THERMO-VISCOELASTIC-VISCOPLASTIC-VISCODAMAGE-HEALING MODELING OF BITUMINOUS MATERIALS: THEORY AND COMPUTATION

A Dissertation

by

MASOUD DARABI KONARTAKHTEH

Submitted to the Office of Graduate Studies of
Texas A&M University
in partial fulfillment of the requirements for the degree of

DOCTOR OF PHILOSOPHY

August 2011

Major Subject: Civil Engineering

Thermo-Viscoelastic-Viscoplastic-Viscodamage-Healing Modeling of Bituminous

Materials: Theory and Computation

THERMO-VISCOELASTIC-VISCOPLASTIC-VISCODAMAGE-HEALING MODELING OF BITUMINOUS MATERIALS: THEORY AND COMPUTATION

A Dissertation

by

MASOUD DARABI KONARTAKHTEH

Submitted to the Office of Graduate Studies of
Texas A&M University
in partial fulfillment of the requirements for the degree of

DOCTOR OF PHILOSOPHY

Approved by:

Co-Chairs of Committee, Rashid K. Abu Al-Rub
                         Eyad A. Masad
Committee Members,   Dallas N. Little
                         Anastasia Muliana
                         Imad Al-Qadi
Head of Department,   John Niedzwecki

August 2011

Major Subject: Civil Engineering

ABSTRACT

Thermo-Viscoelastic-Viscoplastic-Viscodamage-Healing Modeling of Bituminous
Materials: Theory and Computation. (August 2011)

Masoud Darabi Konartakhteh, B.S., Sharif University of Technology;

M.Sc., Sharif University of Technology

Co-Chairs of Advisory Committee: Dr. Rashid K. Abu Al-Rub
Dr. Eyad A. Masad

Time- and rate-dependent materials such as polymers, bituminous materials, and soft materials clearly display all four fundamental responses (i.e. viscoelasticity, viscoplasticity, viscodamage, and healing) where contribution of each response strongly depends on the temperature and loading conditions. This study proposes a new general thermodynamic-based framework to specifically derive thermo-viscoelastic, thermo-viscoplastic, thermo-viscodamage, and micro-damage healing constitutive models for bituminous materials and asphalt mixes. The developed thermodynamic-based framework is general and can be applied for constitutive modeling of different materials such as bituminous materials, soft materials, polymers, and biomaterials. This framework is build on the basis of assuming a form for the Helmohelotz free energy function (i.e. knowing how the material stores energy) and a form for the rate of entropy production (i.e. knowing how the material dissipates energy). However, the focus in this work is placed on constitutive modeling of bituminous materials and asphalt mixes. A viscoplastic softening model is proposed to model the distinct viscoplastic softening response of asphalt mixes subjected to cyclic loading conditions. A systematic procedure for identification of the constitutive model parameters based on optimized experimental effor is proposed. It is shown that this procedure is simple and straightforward and yields unique values for the model material parameters. Subsequently, the proposed model is validated against an extensive experimental data including creep, creep-recovery, repeated creep-recovery, dynamic modulus, constant strain rate, cyclic stress controlled, and cyclic strain controlled tests in both tension and compression and over a wide range

of temperatures, stress levels, strain rates, loading/unloading periods, loading frequencies, and confinement levels. It is shown that the model is capable of predicting time-, rate-, and temperature-dependent of asphalt mixes subjected to different loading conditions.

DEDICATION

TO MY BELOVED PARENTS

Thank you for your endless patience, unconditional support, and continuous encouragement.

TO MY LOVELY WIFE, AZADEH

Your love gave me the support needed in this journey.

ACKNOWLEDGEMENTS

NOMENCLATURE

Symbol	Definition	Symbol	Definition
	New symbols introduced in Chapter II		
ε	Total strain tensor	Y	Damage force
ε^{nve}	Nonlinear viscoelastic strain tensor	Γ^{vd}	Damage viscosity parameter
ε^{vp}	Viscoplastic strain tensor	$Y_0, q, k,\ d^{vd}$	Damage model parameters
e	Deviatoric strain tensor	τ^{vd}	Deviatoric component of the viscodamage force
ε_{kk}	Volumetric strain	χ^{vd}	Viscodamage dynamic loading condition
p	Effective viscoplastic strain	W^R, ε^R	Pseudo strain energy and pseudo strain
ε_{eff}	Total effective strain	D_0, ΔD	Instantaneous and transient creep compliances
σ	Stress tensor	D_n, λ_n	Prony series' coefficients
s	Deviatoric stress tensor	g_0, g_1, g_2	Viscoelastic nonlinear parameters
σ_{kk}	Volumetric stress	ψ	Reduced time
I_1	First stress invariant	a_T, a_s, a_e	Temperature, strain or stress, and environmental shift factors
J_2, J_3	The second and the third deviatoric stress invariants	q_{ij}	Hereditary integral
E, G, K	Elastic, Shear, and bulk moduli	"tr"	Designates trial values

Symbol	Definition	Symbol	Definition
J, B	Shear and bulk compliances	$\dot{\gamma}^{vp}$	Viscoplastic multiplier
ν	Poisson's ratio	f, F	Viscoplastic yield and potential functions
δ_{ij}	Kronecker delta	χ	Viscoplastic dynamic yield surface
"$-$"	Designate the effective (undamaged) configuration	Γ^{vp}	Viscoplastic viscosity parameter
ϕ	Damage density variables	Φ	Overstress function
ζ	Continuity scalar	$N, \alpha, \beta, \kappa_0$, $\kappa_1, \kappa_2, d^{vp}$	Viscoplastic model parameters
A, $\bar{A}$	Cross-sectional area in the damaged and effective configuration	$\langle \ \rangle$	Macaulay brackets
A^D	Area of the micro-damages	σ_y^0	Initial yield stress
ϕ^c	Critical damage density	κ	Isotropic hardening function
τ^{vp}	Deviatoric component of the viscoplasticity yield surface	δ_1, δ_2, δ_3	Temperature coupling term parameters
T	Temperature	T_0	Reference temperature
R	Residual strain	S_{ijkl}	Tangent compliance

New symbols introduced in Chapter III

Symbol	Definition	Symbol	Definition
ρ	Mass density	$\boldsymbol{u}$	Displacement vector
$\boldsymbol{b}$	Body force vector	r_{ext}	External heat

Symbol	Definition	Symbol	Definition
η	Specific entropy	$\boldsymbol{q}$	Heat flux vector
Ψ	Helmholtz free energy	e	Internal energy
$Q^{(m)}$	Thermodynamic conjugate forces associated with the viscoelastic internal state variables $\zeta^{(m)}$	c_p	Tangent specific heat capacity
Π	Rate of energy dissipation	g , G	Damage loading condition and damage potential function
λ	Lagrange Multiplier	Ω	Objective function
ϑ	Temperature coupling term	∇	Gradient operator
σ_v	Viscoplastic overstress	σ_v^{vd}	Viscodamage overstress

New symbols introduced in Chapter IV

Symbol	Definition	Symbol	Definition
"~"	Designate the healing configuration	A^{uh} , A^h	Area of unhealed and healed micro-damages
h	Micro-damage healing variables	A^{uh}	Area of the unhealed micro-damages
$\tilde{\phi}$	Effective damage density	Γ^h	Healing viscosity
E	Secant stiffness modulus	E_t	Tangent stiffness modulus
W	Elastic strain energy	t_R	Rest period
ReL	Reloading	UL	Unloading

New symbols introduced in Chapter V

Symbol	Definition	Symbol	Definition
Θ	Macroscopic recovery parameter	Θ_I	Intrinsic healing function

Symbol	Definition	Symbol	Definition
ξ	Wetting distribution function	σ_b	Bond strength
W_c	Work of cohesion	$\dot{a}_b$	Rate of crack shortening
Δ	Healing process zone	Γ^h, b_1, b_2	Micro-damage healing model parameters

New symbols introduced in Chapter VI

Symbol	Definition	Symbol	Definition
H	Healing force	$\mathbf{X}$	Kinematic hardening
P_{int}	Internal power	P_{ext}	External power
P_{int}^*	Internal virtual power	P_{ext}^*	External virtual power
"ene"	Designates energetic component	"dis"	Designates dissipative component

New symbols introduced in Chapter VII

Symbol	Definition	Symbol	Definition
D^*	Dynamic compliance	D'	Storage compliance
D''	Loss compliance	$\Gamma^{vp,\text{soft}}$	Viscoplastic softening viscosity parameter
q^{vp}	Viscoplastic softening internal state variable	S_1, S_2, S_3	Viscoplastic softening model parameters
$\chi^{vp,\text{soft}}$	Viscoplastic softening dynamic memory surface		

New symbols introduced in Chapter VIII

Symbol	Definition	Symbol	Definition
"^"	Designates nonlocal variables	ℓ	Intrinsic material length scale
∇^2	Laplacian operator	g_{mn}	Nonlocal coefficients

Symbol	Definition	Symbol	Definition
E_t^{ed}	Elastic-damage tangent stiffness	E_t^{alg}	Algorithmic elastic-damage tangent stiffness

TABLE OF CONTENTS

LIST OF FIGURES

FIGURE   Page

FIGURE   Page

FIGURE   Page

LIST OF TABLES

CHAPTER I
INTRODUCTION AND LITERATURE REVIEW

1.1. Problem Statement

Asphalt concrete pavements are one of the largest infrastructure assets in the United States and almost in every other country in the world. Although pavement design has gradually moved from art to science, empirical relations and equations still play a substantial role in design guides and manuals. The complex behavior of the constituents of the pavements along with the environmental effects that pavements experience during their service life has made it extremely difficult to develop fully mechanistic models to predict the performance of pavements during their service life.

Various types of tests and models have been used to characterize the mechanical response of asphalt concrete mixes as one of the main constituents of the pavements. However, most of these models are developed to predict the responses under specific test conditions or design problem, and therefore, are usually ad hoc and do not represent the behavior of these materials under general three dimensional stress states and realistic environmental conditions that actually happens in the field. The reason is that the asphalt concrete mixes show nonlinear responses under different loading conditions.

Asphalt concrete mix and Hot Mix Asphalt (HMA) can be considered to be consist of three scales :(a) the micro-scale (mastic), where fine fillers are surrounded by the asphalt binder; (b) the meso-scale, fine aggregate mixture (FAM), where fine aggregates are surrounded by the mastic; and (c) the macro-scale which includes all the coarse aggregates surrounded by FAM. The complex interactions between these scales are the primary source of nonlinearity in asphalt concrete mixes. Numerous experimental studies have shown that the HMA response is time-, rate-, and temperature-dependent. Several degree of magnitude of differences between the stiffness of the aggregate and the binder makes the strain localization in the binder a dominant reason for the nonlinear behavior of asphalt concrete mixes. Rotation and slippage of aggregates and interaction between binder and aggregates during the loading are also other factors contributing to

_____

This dissertation follows the style of International Journal of Plasticity.

the nonlinear behavior of asphalt concrete mixes. Moreover, the severe temperature sensitivity of asphalt concrete mixes results in substantial changes of the behavior with the temperature change. The combined effect of these phenomena causes the asphalt mixes to show nonlinear responses even at very small strain or stress levels.

Added to this, the evolution of the permanent deformation in asphalt mixes makes the mechanical response of these materials more nonlinear which is also a source of a major distress in asphalt pavements referred to as *rutting*. Figure 1.1 shows a picture of the severe rutting in an asphalt pavement section as a result of evolution of the permanent deformation.

Figure 1.1. Rutting in the asphalt pavements as a result of evolution of the viscoplastic strain. This section is related to US 287 highway in Whichita Falls near Dallas Fort Worth.

Another major source of nonlinearity in the thermo-mechanical response of HMA is the evolution of micro-cracks and micro-voids and rate-dependent plastic (viscoplastic) hardening/softening. Figure 1.2 shows X-Ray computed tomography (CT) images of the cross-section of an asphalt mixture laboratory specimen before loading and at different strain levels. As it is shown in Figure 1.2 (b)-(d), micro-damages (micro-cracks and micro-voids) nucleate and propagate progressively as the material deforms and cause the stiffness to degrade. However, at specific temperature ranges, the binder in

the asphalt mixes and subsequently the asphalt concrete mix has the potential to heal with time and recover part of its strength and stiffness during the rest period. Therefore, an accurate prediction of the thermo-mechanical response of asphalt mixes and bituminous materials require the coupling between viscoelasticty, viscoplasticity, viscodamage, and healing models.
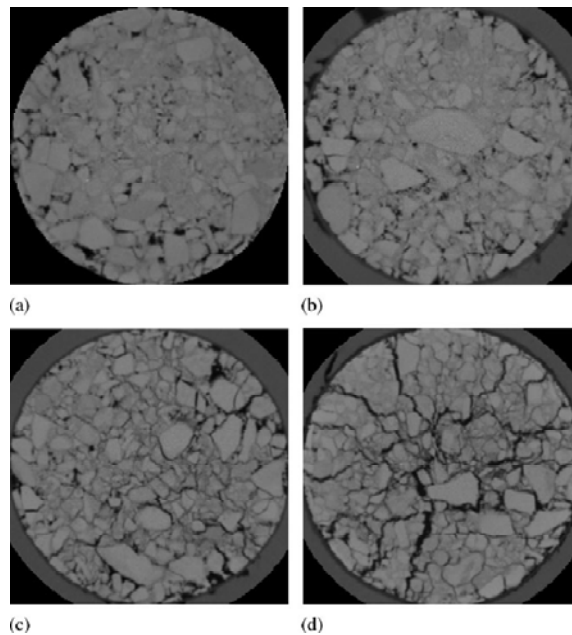
Figure 1.2. X-Ray images of the cross-section of an asphalt mixture laboratory specimen subjected to triaxial loading. (a) Before loading; (b) 2% strain; (c) 4% strain; (d) 8% strain. Micro-damages (i.e. micro-cracks and micro-voids) nucleate and propagate as the material deforms.

In addition to thermo-mechanical loadings, pavements are subjected to environmental conditions such as moisture and oxygen. The moisture at the surface of the asphalt mixes in the forms of water or environmental humidity disperses into the mixture, fully/partially fills the air voids, and diffuses to the solid part through the diffusion process. The infiltrated moisture may yield to stiffness and strength degradation because of chemical, physical, and mechanical processes. This effect is referred to as *moisture damage* in this work and may cause the aggregates in the asphalt

surface to loosen gradually and separate individually from the asphalt layer. On the other hand, the existing oxygen in the air in contact with the asphalt layer of a pavement can also diffuse inside the asphalt layer through the interconnected air voids. Once infiltrated by oxygen, the binder phase in the mix reacts with oxygen resulting in changes in the mechanical properties of asphalt concrete mixes. This phenomenon is known as *aging* which is the result of the chemical reaction of oxygen with binder.

More complication arises because each individual processes (i.e. thermo-viscoelasticity, thermo-viscoplasticity, thermo-viscodamage, healing, moisture damage, and aging) also interact with one another and are in most cases coupled. For instance, crack propagation enables more water and higher amount of oxygen to diffuse inside the mix and accelerates the moisture damage and aging effects. It also yields to the acceleration of accumulative permanent deformation in the mix. Subsequently, the increase in the deformation causes more damage growth which degrades the mechanical properties of the mix in higher extent which obviously makes the mix to be more prone to distresses. This process is very important in predicting the performance prediction of asphalt pavements.

The presence of different mechanical, thermal, and environmental effects in the pavements during their service life makes it necessary to develop a robust constitutive model to predict the multi-physics response of asphalt mixes in the pavements. However, the developed constitutive model should be as general as possible and be validated over extensive experimental measurements to ensure proper model response under complex three-dimensional stress states. In fact, development of such constitutive models for a specific material has been the main challenge of the modern constitutive modeling. This can be effectively achieved, so far, through the thermodynamic principles by enforcing the balancing laws, the conservation of mass, the conservation of linear and angular momentums, and the first and second laws of thermodynamics.

The ultimate goal of developing a robust constitutive model is to provide a reliable tool for predicting the pavement performance during its service time. This raises another challenging task which is the proper computational techniques for pavement

performance predictions. The long life of pavements, very large number of loading cycles (millions of loading cycles), the complex constitutive model, and the complex nature of the applied loading conditions make the development of an accurate and yet affordable computational technique very difficult and challenging task. Even with the current state-of-the-art in computational power, conducting realistic 3D finite element (FE) rutting and/or fatigue performance simulations for pavements subjected to millions of wheel loading cycles by considering realistic wheel/pavement interactions and environmental effects is almost impossible.

Added to the mentioned challenges in developing computational techniques, strain and damage localization phenomena in the asphalt concrete mixes causes instabilities and mesh-dependent results in the FE simulations. In other words, as the loading increases, asphalt binder undergoes a substantial strain levels comparing to the applied strain to the HMA. For example, strain in the binder could range between average of eight times and a maximum of 510 times the bulk strain of the mixture (Kose et al., 2000) and some regions within the mastic can experienced strain levels as high as 30 times the applied strain (Masad and Somadevan, 2002). These localizations lead to the mesh-dependent results in the FE simulations specially at softening regions such that the traditional local continuum theories fail to predict physical response. One alternative to remedy this problem is to use and implement non-classical gradient-dependent continuum theories.

This work tries to contribute in filling the gap in constitutive modeling and computational techniques of bituminous materials and asphalt mixes. Therefore, a thermo-viscoelastic-viscoplastic-viscodamage-healing constitutive model is developed to model the complex response of these materials under more realistic conditions. The term "*visco*" is referred to time- and rate-dependent characteristic of the model, whereas, the term "*thermo*" is related to temperature-dependent response of bituminous materials. The developed model is calibrated, validated, and subsequently implemented in the well-known finite element code Abaqus (2008) through the user material subroutine UMAT.

The implemented model is finally used to predict the complex mechanical response of asphalt mixes and to conduct the performance simulation of asphalt pavements.

1.2. Background and State of the Art

Numerous experimental studies on polymers, bituminous materials, asphalt mixes, and soft materials have shown that the mechanical response of these materials is time- and rate-dependent. These materials clearly display all four fundamental mechanical responses (i.e. viscoelasticity, viscoplasticity, viscodamage, and healing) where contribution of each response strongly depends on the temperature and loading conditions. For example, the viscoelastic response could be dominant at low temperatures and stress levels, whereas viscoelastic and viscoplastic responses are dominant at high temperatures. However, the viscodamage (rate-dependent damage) response becomes very important at post peak stress-strain regions, high stress levels, and long loading periods; whereas for some materials, the healing could be significant in fatigue loadings. This section provides the background and a limited literature review on the modeling efforts to simulate these effects. These previous works are considered as the foundation for developing new theories and modifying the existing ones for each component of the thermo-viscoelastic-viscoplastic-viscodamage-healing model proposed in this work.

1.2.1. Viscoelasticity

Experimental observations have clearly shown that the response of asphalt mixes show both recoverable and irrecoverable components (Perl et al., 1983; Collop et al., 2003; Huang, 2008). The recoverable component is usually modeled using the solid-like viscoelasticity models, whereas, the irrecoverable component is usually modeled using fluid-like viscoelasticity and/or viscoplasticity models.

In terms of the viscoelastic behavior of materials, Biot (1954) derived a formulation for linear viscoelastic materials. Schapery (1969b) used the thermodynamics of irreversible processes and developed a single integral constitutive model for nonlinear viscoelastic materials such as polymers (e.g. Christen, 1968; Schapery, 1969a, b; Sadkin

and Aboudi, 1989; Haj-Ali and Muliana, 2004; Muliana and Haj-Ali, 2008). Schapery's constitutive model has been applied to asphalt mixes by several other researchers (e.g. Huang et al., 2007; Masad et al., 2008; Abu Al-Rub et al., 2009; Saadeh and Masad, 2010; Darabi et al., 2011c). Moreover, Touti and Cederbaum (1998), Haj-Ali and Muliana (2004), Sadd et al. (2003), and Huang et al. (2007) developed algorithms for numerical implementation of Schapery's viscoelastic constitutive model in finite element codes. Recently, Levesque et al. (2008) extended the Schapery's nonlinear viscoelastic model for 3D applications based on laws of thermodynamics. Masad et al. (2009), Abu Al-Rub et al. (2010a), Huang et al. (2011a), and Darabi et al. (2011c) have developed and applied a systematic procedure to characterize and decouple the recoverable (viscoelastic) by analyzing repeated creep-recovery experimental tests using Schapery's nonlinear viscoelastic model.

These studies clearly show that the viscoelastic response of HMA can be well-predicted using Schapery's nonlinear viscoelasticity model (Huang et al., 2007; Masad et al., 2008; Abu Al-Rub et al., 2010a; Darabi et al., 2011c). It should be noted that the Schapery's linear/nonlinear model is a solid-like viscoelastic model and predicts only the recoverable strains.

1.2.2. Viscoplasticity

Two approaches have been used in the literature to model the irrecoverable component of the deformation in bituminous materials and asphalt mixes. The first approach is based on the spring-dashpot analogy and development of fluid-like viscoelasticity models; whereas, the second approach is to use the plastic/viscoplastic models to represent the irrecoverable component of the strain and deformation.

One of the early models for describing the mechanical behavior of bituminous materials is the burger's model (Burgers, 1939) which has also been used and modified by Saal and Labout (1940). Krishnan and Rajagopal (2004, 2005) introduced the concept of the natural configurations and derived a large deformation fluid-like viscoelasticity theory based on the spring-dashpot analogy to predict the mechanical response of asphalt. However, they assumed the incompressibility condition which has not been fully

validated experimentally. In fact, the experimental measurements on the asphalt concrete show the development of significant volumetric strains in deformation (Erkens, 2002). In another attempt, Scarpas, Kringos and their co-workers at Delft University of Technology derived a large deformation viscoplasticity theory using the concept of spring-dashpot analogy (e.g. Scarpas, 2004; Kringos et al., 2007; Kringos et al., 2010).

However, the assumption of small deformations for asphalt mixes and for a range of temperatures is a fairly reasonable assumption which significantly simplifies the viscoplastic component of the constitutive model. Sides et al. (1985) proposed a one-dimensional empirical equation to describe the viscoelastic-viscoplastic response of asphalt mixes subjected to uniaxial loading. Later, Chehab et al. (2003) proposed an elasto-viscoplastic model for one-dimensional state of stress. However, these models were valid only for one-dimensional problems which obviously cannot be used to explain the response of asphalt mixes for three-dimensional stress states. In another attempt, Sousa and Weissman (1994) improved the work of Sousa et al. (1993) by incorporating Von-Misses yield function with kinematic hardening to describe the plastic response of asphalt mixes. However, it is well-known that the irrecoverable response of asphalt mixes is time- and rate-dependent and cannot effectively be explained by time-independent plastic models, instead, time- and rate-dependent plastic models (viscoplastic models). should be used.

In terms of the viscoplastic behavior of asphalt mixes, Perzyna's theory (Perzyna, 1971) has been used by several researchers for predicting the permanent deformation in asphalt mixes. For example, Lu and Wright (1998) and Seibi et al. (2001) used the Perzyna's viscoplastic model with Drucker-Prager type yield surface to predict the viscoplastic response of asphalt mixes. These studies used the associative flow rule for the asphalt mixes. However, several experimental observations have shown that the viscoplastic deformation of HMA, and geomaterials in general, is non-associated (e.g. Zienkiewicz et al., 1975; Oda and Nakayama, 1989; Cristescu, 1994; Florea, 1994; Bousshine et al., 2001). Later, Tashman (2003) used a nonassociative elasto-viscoplastic model to predict the HMA mechanical responses. Dessouky (2005) and Masad et al.

(2007), extended the work of Tashman (2003) by modifying the yield surface to distinguish between the viscoplastic behavior in compression and extension state of loading. However, they also used the time-independent elastic models for the recoverable component of the deformation which is not the case for asphalt mixes. Saadeh et al. (2007), Huang (2008), Abu Al-Rub et al. (2009; 2010a), Darabi et al. (2011c), and Huang et al. (2011a) coupled the nonlinear viscoelasticity model of Schapery and Perzyna's viscoplasticity model to simulate more accurately the nonlinear mechanical response of HMA at high stress levels and high temperatures.

1.2.3. Viscodamage

The coupled viscoelastic-viscoplastic constitutive models yield reasonable predictions of the mechanical response of asphalt mixes prior to the damage. However, the changes in the material's microstructure during deformation cause HMA materials to experience a significant amount of micro-damage (micro-cracks and micro-voids) under service loading conditions, where specific phenomena such as tertiary creep, post-peak behavior of the stress-strain response, and degradation in the mechanical properties of HMA is mostly due to damage and cannot be explained only by viscoelasticity and viscoplasticity constitutive models.

Models based on the continuum damage mechanics (CDM) have been effectively used to model the degradations in materials due to cracks and voids (Kachanov, 1958; Rabotnov, 1969; Fanella and Krajcinovic, 1985; Voyiadjis and Kattan, 1992; Lemaître, 1996; Voyiadjis and Thiagarajan, 1997). Masad et al. (2005) included isotropic (scalar) damage in an elasto-viscoplastic model (modified by Saadeh et al. (2007), Graham (2009), and Saadeh and Masad (2010) to include Schapery's nonlinear viscoelasticity) to simulate the mechanical response of asphalt mixes. Another attempt is made by Uzan (2005) to develop a damage-viscoelastic-viscoplastic model for asphalt mixes, but this model is valid for one-dimensional problems and cannot be used for multi-axial state of stresses. Moreover, in most of these works the damage laws are not time- and rate-dependent which is a challenge in the modeling of asphalt mixes. This argument is experimentally motivated since various experimental studies have shown that the

damage response of bituminous materials depends on temperature, time, and rate of loading (Kim and Little, 1990; Collop et al., 2003; Masad et al., 2007). Several rate-dependent damage models (usually referred to as the creep-damage laws) have been proposed in the literature. Kachanov (1958), Odqvist and Hult (1961), and Rabotnov (1969) pioneered in proposing the creep-damage evolution laws. Later, various types of creep-damage laws in terms of stress, strain, and energy have been proposed by other researchers (Cozzarelli and Bernasconi, 1981; Lee et al., 1986; Voyiadjis et al., 2004; Abu Al-Rub and Voyiadjis, 2005b; Zolochevsky and Voyiadjis, 2005). Although many papers are devoted to improve the damage evolution laws in elastic media (Kachanov, 1986; Lemaître, 1992; Krajcinovic, 1996; Lemaître and Desmorat, 2005), very few damage models have been coupled to viscoelasticity and viscoplasticity in order to predict the mechanical response of time- and rate-dependent materials. In fact, there are few studies that couple damage to viscoelasticity to include time and rate effects on damage evolution laws (Schapery, 1975c; Schapery, 1975a, b; Simo, 1987; Weitsman, 1988; Gazonas, 1993; Sullivan, 2008). Schapery's viscoelastic-damage model (Schapery, 1975b; Schapery, 1987), which has been modified by Schapery (1999) to include viscoplasticity, is currently used to reasonably predict the damage behavior of asphaltic materials (Kim and Little, 1990; Park et al., 1996; Gibson et al., 2003; Kim et al., 2007). This model is based on the elastic-viscoelastic correspondence principle that is based on the pseudo strain for modeling the linear viscoelastic behavior of the material; the continuum damage mechanics based on pseudo strain energy density for modeling the damage evolution; and time-temperature superposition principle for including time, rate, and temperature effects. However, it has the following limitations: (1) it can be used only to predict viscoplasticity and damage evolution in tensile loading conditions; and (2) it treats asphaltic materials as linear viscoelastic materials irrespective of temperature and stress levels. Recently, Darabi et al. (2011c) proposed a phenomenological temperature-dependent viscodamage model and coupled it to Schapery's viscoelasticity and Perzyna's viscoplasticity in order to realistically model the mechanical responses of asphalt mixes.

1.2.4. Micro-Damage Healing

Experimental observations in the last few decades have clearly shown that various classes of engineering materials (e.g. polymers, bitumen, bio-inspired materials, rocks) have the potential to heal with time and recover part of their strength and stiffness under specific circumstances (e.g. Miao et al., 1995; Kessler and White, 2001; Brown et al., 2002; Reinhardt and Jooss, 2003; Guo and Guo, 2006; Kessler, 2007; Bhasin et al., 2008). Constitutive models that do not account for healing of these materials significantly underestimate their fatigue life that will lead to very conservative design of structural systems made of such materials. Therefore, it is imperative to model healing for more accurate fatigue life predictions.

Changes in the material's microstructure during deformation usually cause significant micro-damage (micro-cracks and micro-voids) under service loading conditions. The creation and coalescence of micro-damages lead to degradation in the material's mechanical properties including strength and stiffness. This process of degradation can progressively continue up to complete failure. Theories based on continuum damage mechanics have been successfully used to explain these degradation in different materials.

However, a common assumption in the theories based on continuum damage mechanics is that the damage process is irreversible (e.g. Kachanov, 1958, 1986; Lemaître and Chaboche, 1990; Lemaître, 1992; Voyiadjis and Kattan, 1992; Kattan and Voyiadjis, 1993; Krajcinovic, 1996; Voyiadjis and Park, 1999; Voyiadjis and Deliktas, 2000; Lemaître, 2002; Abu Al-Rub and Voyiadjis, 2003, 2005b; Voyadjis and Abu Al-Rub, 2006). In other words, the damage variable is usually assumed to be a monotonically increasing function. However, during the unloading process and resting time periods some micro-crack and micro-void free surfaces wet and are brought back into contact with one another. In certain materials such as polymers and especially asphalt mixes, micro-cracks and micro-voids gradually reduce in size with a corresponding recovery in strength and stiffness due to micromechanical short-term wetting and long-term diffusion processes as the resting period increases (Wool and

Oconnor, 1981). These healing features are opposite to those normally associated with continuum damage mechanics. In fact, for long resting periods, the damaged area may recover all of its strength and becomes identical to the virgin state of material (Prager and Tirrell, 1981; Carpenter and Shen, 2006; Little and Bhasin, 2007). This process is referred to as *micro-damage healing*.

The importance of the micro-damage healing process depends on loading conditions. For example, the result of the healing process can be significant when the material is subjected to fatigue loading conditions where rest time periods are introduced between the loading cycles. This is the case in asphaltic pavements under traffic loading conditions (Kim and Little, 1989; Lytton et al., 1993; Kim et al., 1994; Si et al., 2002). In other words, the impact of the recovery process is cumulative and depends on variables such as the length of the rest period and the temperature of the asphalt mixture. Moreover, Shen and Carpenter (2005), Carpenter and Shen (2006), and Shen et al. (2006) have documented the efficacy of the dissipated energy approach to fatigue damage as well as the cumulative impact of healing even for very short rest periods during the fatigue damage process. Furthermore, Zhang et al. (2001b) and Kim and Roque (2006) have identified the importance of considering a healing property in fatigue damage and the crack growth process. In another work, Zhang et al. (2001a) introduced the concept of a threshold fracture energy density as a failure criterion for the initiation and propagation of cracks. They state that at the "local level, in front of the crack tip, or in areas of high stress concentration, one could use the fracture energy density as a criterion below which cracks will not initiate or propagate". This is a pertinent observation with regard to healing as this study focuses on the importance of considering the recovery of damage in the area that precedes the crack tip during the healing process.

Several micromechanical- and phenomenological-based models for predicting micro-damage healing in different materials have been proposed (Wool and Oconnor, 1981; Schapery, 1989; Miao et al., 1995; Jacobsen et al., 1996; Ramm and Biscoping, 1998; Ando et al., 2002; Little and Bhasin, 2007). Wool and O'connor (1981) proposed a phenomenological-based theory of crack healing in polymers and introduced a

macroscopic recovery parameter that is the convolution of an intrinsic healing function and the rate of wetting distribution function to relate the healing at micro scale to the changes in the mechanical properties of polymers at the macro scale. Schapery (1989) proposed a fracture mechanics-based model to describe the rate of crack shortening for linear viscoelastic materials using the correspondence principle. Miao et al. (1995) presented a thermodynamic-based model for healing of crushed rock salt. Little and Bhasin (2007) and Bhasin et al. (2008) combined the contributions of Wool and O'connor (1981) with those of Schapery (1989) and defined a macroscopic recovery parameter to quantify healing in bituminous materials. They showed that the rest period have a significant effect on healing.

However, these models are mostly: (1) micromechanical- and fracture mechanics-based that cannot be easily used at the macroscopic level to solve an engineering problem; (2) augmented with several material parameters that are difficult to identify based on available macroscopic experiments; (3) usually developed for specific loading conditions and cannot be used for capturing healing effects under different loading conditions; and (4) not coupled with the viscoelastic, viscoplastic, and/or damage constitutive behavior of the healed material. Hence, development of a general and robust healing model at the continuum level seems appropriate and necessary as a contribution to understanding and modeling the general fatigue damage process. Surprisingly, little attention is devoted to the development of such a healing model and its coupling to the visco-inelastic response of asphaltic materials.

It is noteworthy that the problem of viscoelastic, viscoplastic, damage, and healing in bituminous materials and specially asphalt mixes is very complicated. Therefore, a rigorous thermodynamic basis for modeling the viscoelastic, viscoplastic, damage, and healing mechanisms should be developed in order to explain how these mechanisms store energy and how each of these mechanisms affect the entropy production. Rajagopal and his co-workers have presented a rigorous thermodynamic-based model to explain the viscoelastic response of asphalt mixes (e.g. Krishnan and Rajagopal, 2003; Krishnan and Rajagopal, 2004; Koneru et al., 2008; Ravindran et al.,

2009 and the references quoted therein). The procedure for the development of thermodynamically consistent coupled viscoelastic-viscoplastic-viscodamage-healing constitutive model will be presented in the next chapters of this work.

Moreover, asphalt mixture is a highly complex material which is a mixture of asphalt binder, aggregate, and air voids. The properties of these constituents have significant effect on the overall property of asphalt mixture. Mixture theory is one of the modern techniques to model the behavior of different mixtures such as asphalt mixtures initially proposed for modeling the mixture behavior of fluids (Ingram and Cemal Eringen, 1967; Truesdell, 1969). However, one of the important problems in using the mixture theories is how to handle the boundary condition problem between different constituents (c.f. Rajagopal and Tao, 1996; Krishnan and Rao, 2000). These theories along with the framework of natural configurations (Rajagopal and Wineman, 1992; Rajagopal, 1995) have been used by several researchers to explain the mechanical properties of asphalt mixtures (e.g. Krishnan and Rao, 2000; Krishnan and Rajagopal, 2003; Krishnan and Rajagopal, 2004; Wang et al., 2004; Koneru et al., 2008; Ravindran et al., 2009). Although using the mixture theory is one of the promising approaches for modeling the behavior of asphalt mixes, they are augmented with several model parameters at the mixture level and for each of the constituents. Hence, in this paper we consider a single homogenized continuum approach to model the mechanical response of asphalt mixes.

1.3. Scope and Objective

The main objective of this work is to develop a thermo-viscoelastic-viscoplastic-viscodamage-healing constitutive model and to apply it for predicting the response of bituminous materials, asphalt mixes, and pavements under realistic mechanical conditions. This objective is achieved through the following tasks:

1- Development of a time-, rate-, and temperature-dependent damage model (thermo-viscodamage) and couple it with thermo-viscoelastic and thermo-viscoplastic models.

2- Development of a general framework to model the micro-damage healing in materials with the healing capability.

3- Development of a micro-damage healing model for asphalt mixes for more accurate prediction of the response under cyclic loading conditions.

4- Development of a general thermodynamic framework that provides a systematic procedure for deriving thermodynamically consistent constitutive models.

5- Implementing the proposed thermo-mechanical constitutive model in the finite element (FE) codes.

6- Validating the constitutive model and subsequently applying it for performance prediction of the pavements.

1.4. Organization of the Dissertation

This dissertation is organized following the research paper format. Chapters II, III, IV, V, VI, VII, VIII, and IX are research papers that have been or will be submitted as refereed journal papers.

Chapter I includes the introduction which contains background on modeling asphalt mixture response and performance, problem statement, objectives and the outline of this dissertation. Chapter II presents the development of a thermo-viscoelastic-viscoplatic-viscodamage model for asphaltic materials. Chapter III proposes a thermodynamic-based framework to ensure the consistency of the proposed model. Chapter IV introduces a continuum damage mechanics framework for modeling the micro-damage healing in materials and Chapter V proposes a micro-damage healing model for asphalt mixes. Chapter VI proposes a general thermodynamic-based framework for constitutive modeling of time- and rate-dependent materials. The proposed thermo-mechanical model is validated against another extensive experimental measurements in Chapter VII. Chapter VIII develops a numerical technique for implementation of the gradient-dependent continuum damage mechanics theories and the model is used to conduct the performance simulation of asphalt pavements in

Chapter IX. Final conclusions, recommendations, and future works are presented in Chapter X.

CHAPTER II
A THERMO-VISCOELASTIC-VISCOPLASTIC-VISCODAMAGE MODEL FOR ASPHALTIC MATERIALS

2.1. Introduction

Because of the complex behavior of HMA, the coupling of the nonlinear thermo-viscoelasticity, thermo-viscoplasticity, and temperature- and rate-dependent damage (thermo-viscodamage) modeling seems inevitable. However, surprisingly, very limited work has been focusing on the development of such models, and the current study attempts to close this gap and develops a robust model that overcomes the limitations of the current models for HMA. This chapter proposes a temperature dependent viscodamage model which is coupled to nonlinear temperature-dependent Schapery's viscoelastic model (Schapery, 1969a) and temperature-dependent Perzyna's viscoplasticity model (Perzyna, 1971) to model the nonlinear constitutive behavior of asphalt mixes. The viscodamage model is formulated to be a function of temperature, total effective strain, and the damage driving force which is expressed in terms of the stress invariants of the effective stress in the undamaged (effective) configuration.

However, it is well-recognized that the damage response of asphalt mixes is different in compression and extension state of loading. Therefore, the damage driving force is formulated such that it allows for the distinction between the influence of compression and extension loading conditions on damage nucleation and growth. A systematic procedure is presented to identify temperature-dependent viscoelasticity, viscoplasticity, and viscodamage model parameters. The viscoelastic model parameters are identified by extracting the pure viscoelastic response during the recovery part of the creep-recovery test (Huang, 2008). Subsequently, the viscoplastic response during the creep part of the creep-recovery test is obtained by subtracting the viscoelastic strain from the total strain. This response is then used to identify the viscoplastic model parameters (Abu Al-Rub et al., 2009; Huang et al., 2011a). Finally, the viscodamage model parameters are identified from two creep tests that show the secondary and

tertiary responses (Darabi et al., 2011c). The presented model is implemented in the well-known finite element code Abaqus (2008) through the user subroutine UMAT to validate the model over the experimental data which was not used in the calibration process. The recursive-iterative and radial return algorithms are used for the numerical implementation of the nonlinear viscoelasticity and viscoplasticity models, respectively, whereas the viscodamage model is implemented using the effective (undamaged) configuration concept. It is shown that the presented constitutive model is capable of predicting the nonlinear behavior of asphaltic mixes under different loading conditions.

2.2. Total Strain Additive Decomposition

The total deformation of the Hot Mix Asphalt (HMA) subjected to an applied stress can be decomposed into recoverable and irrecoverable components, where the extent of each is mainly affected by time, temperature, and loading rate. In this study, small deformations are assumed such that the total strain is additively decomposed into a viscoelastic (recoverable) component and a viscoplastic (irrecoverable) component:

$$\varepsilon_{ij} = \varepsilon_{ij}^{nve} + \varepsilon_{ij}^{vp} \qquad (2.1)$$

where ε_{ij} is the total strain tensor, ε_{ij}^{nve} is the nonlinear viscoelastic strain tensor, and ε_{ij}^{vp} is the viscoplastic strain tensor. The constitutive equations necessary for calculating ε_{ij}^{nve} and ε_{ij}^{vp} will be presented in the following sections.

2.3. Effective (Undamaged) Stress Concept

Kachanov (1958) has pioneered the concept of continuum damage mechanics (CDM), where he introduced a scalar measure called continuity, ζ, which is physically defined by Rabotnov (1969) as:

$$\zeta = \frac{\bar{A}}{A} \qquad (2.2)$$

where A is the damaged (apparent) area and $\bar{A}$ is the real area (intact or undamaged area) carrying the load. In other words, $\bar{A}$ is the resulted *effective* area after micro-

damages (micro-cracks and micro-voids) are removed from the damaged area A. The continuity parameter has, thus, values ranging from $\zeta = 1$ for intact (undamaged) material to $\zeta = 0$ indicating total rupture.

Odqvist and Hult (1961) introduced another variable, ϕ, defining the reduction of area because of the micro-damages:

$$\phi = 1 - \zeta = \frac{A - \bar{A}}{A} = \frac{A^D}{A} \tag{2.3}$$

where A^D is the area of micro-damages such that $A^D = A - \bar{A}$. ϕ is the so-called damage variable or damage density which can be interpreted as the density of micro-damages (micro-cracks and micro-voids) with values ranging from 0 (undamaged) to 1 (complete damage). In fact, fracture or complete rupture mostly occurs when $\phi = \phi^c$, where ϕ^c is the critical damage density, which is a material property (Abu Al-Rub and Voyiadjis, 2003). In this study, isotropic damage is assumed such that the stress tensor components are degraded equally in different directions.

Based on CDM definition of an effective area, the relationship between stresses in the undamaged (effective) material and the damaged material is defined as [see Chaboche (2003) for a concise review of effective stress in CDM]:

$$\bar{\sigma}_{ij} = \frac{\sigma_{ij}}{1 - \phi} \tag{2.4}$$

where $\bar{\sigma}$ is the effective stress tensor in the effective (undamaged) configuration and σ is the nominal Cauchy stress tensor in the nominal (damaged) configuration. The schematic representation of the nominal (damaged) and effective (undamaged) configurations is shown in Figure 2.1.
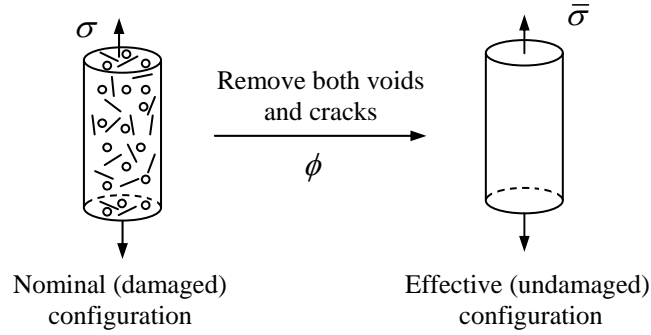
Figure 2.1. Schematic representation of the effective and nominal configurations.

It is noteworthy that the effective stress $\bar{\sigma}$ is the one that drives viscoelastic and viscoplastic deformations. Moreover, it is usually argued that once the material is damaged, further loading can only affect the undamaged material skeleton. Hence, the viscoelastic, viscoplastic, and viscodamage models are defined as functions of variables in the effective configuration. The superimposed "$-$" in this work designates the effective configuration.

However, a transformation hypothesis is required to relate the nominal stress and strain tensors (σ and ε) to the stress and strain tensors in the undamaged configuration ($\bar{\sigma}$ and $\bar{\varepsilon}$). For this purpose, one can either adapt the strain equivalence hypothesis (i.e. the strains in nominal and effective configurations are equal) or the strain energy equivalence hypothesis (i.e. any form of strain energy in the nominal configuration is equal to the corresponding strain energy in the effective configuration) [see Voyiadjis and Kattan (1999) for more details].

Although, the strain energy equivalence hypothesis is intuitively more physically sound, but greatly complicates the constitutive models and their numerical implementation (Abu Al-Rub and Voyiadjis, 2003). Therefore, for simplicity and easiness in the finite element implementation of the subsequent complex constitutive equations, the strain equivalence hypothesis is adopted. Hence, one can assume that the nominal strain tensors ε, ε^{nve}, and ε^{vp} are equal to their counterparts in the effective configuration, $\bar{\varepsilon}$, $\bar{\varepsilon}^{nve}$, and $\bar{\varepsilon}^{vp}$, such that:

$$\varepsilon_{ij} = \overline{\varepsilon}_{ij} \, , \; \varepsilon_{ij}^{nve} = \overline{\varepsilon}_{ij}^{nve} \, , \; \varepsilon_{ij}^{vp} = \overline{\varepsilon}_{ij}^{vp} \tag{2.5}$$

where $\boldsymbol{\varepsilon}^{nve}$ and $\boldsymbol{\varepsilon}^{vp}$ are the nonlinear viscoelastic and viscoplastic strain tensors in the nominal configuration, respectively; whereas $\overline{\boldsymbol{\varepsilon}}^{nve}$ and $\overline{\boldsymbol{\varepsilon}}^{vp}$ are the nonlinear viscoelastic and viscoplastic strain tensors in the effective configuration, respectively. This transformation hypothesis makes the numerical implementation of constitutive equations very easy and avoids the complexities associated with direct couplings between the damage model and different parts of the constitutive model. In fact, for small deformations and isotropic (scalar) damage assumptions, one can assume that the strain differences in the nominal and effective configurations are negligible (Abu Al-Rub and Voyiadjis, 2003), such that postulating the strain equivalence hypothesis seems admissible. However, the strain equivalence hypothesis results in linear variation of the stiffness modulus with the damage density which is not experimentally motivated. To remedy this issue, Cicekli et al. (2007) and Abu Al-Rub and Voyiadjis (2009) modified Eq. (2.4), such that:

$$\overline{\sigma}_{ij} = \frac{\sigma_{ij}}{(1-\phi)^2} \tag{2.6}$$

Eq. (2.6) (which is used in this work) allows the quadratic variation of the damaged stiffness with respect to the damage density when the strain equivalence hypothesis is use.

It should be noted that the equivalency of the strain tensor in the effective and nominal configuration is assumed here for simplicity and might not be an accurate assumption for large deformation theories when damage is significant. In these cases, one may use alternative approaches such as postulating the strain energy equivalence hypothesis, power equivalence hypothesis, or taking into account the changes in the density of the damaged materials by adapting finite deformation theories (c.f. Davison and Stevens, 1973; Davison et al., 1977; Voyiadjis and Kattan, 1992; Lubarda and Krajcinovic, 1995).

2.4. Nonlinear Thermo-Viscoelastic Model

In this study, the Schapery's nonlinear viscoelasticity theory (Schapery, 1966) is used to model the viscoelastic response of HMA. The Schapery's viscoelastic one-dimensional single integral model is expressed here in terms of the effective stress $\bar{\sigma}$, Eq. (2.6), as follows:

$$\bar{\varepsilon}^{nve,t} = g_0(\bar{\sigma}^t, T^t) D_0 \bar{\sigma}^t + g_1(\bar{\sigma}^t, T^t) \int_0^t \Delta D(\psi^t - \psi^\tau) \frac{d\left(g_2(\bar{\sigma}^\tau, T^\tau)\bar{\sigma}^\tau\right)}{d\tau} d\tau \quad (2.7)$$

where D_0 is the instantaneous compliance; ΔD is the transient compliance; g_0, g_1, and g_2 are nonlinear parameters related to the effective stress, $\bar{\sigma}$, strain level, $\bar{\varepsilon}^{nve}$, or temperature T at a specific time τ. The parameter g_0 is the nonlinear instantaneous compliance parameter that measures the reduction or the increase in the instantaneous compliance. The transient nonlinear parameter g_1 measures nonlinearity effects in the transient compliance. The nonlinear parameter g_2 accounts for the loading rate effect on the creep response. Note that D_0, ΔD, g_0, g_1, and g_2 should be determined for undamaged material. In Eq. (2.7), ψ^t is the reduced-time given by:

$$\psi^t = \int_0^t \frac{d\xi}{a_T a_s a_e} \quad (2.8)$$

where a_T, a_s, and a_e are the temperature, strain or stress, and environment (e.g. moisture, aging) shift factors, respectively. It is noteworthy to mention assuming g_0, g_1, and g_2 to be constant and equal to one simplified the Schapery's nonlinear viscoelastic model [Eq. (2.7)] to the Boltzmann superposition integral for linear viscoelastic materials. For numerical convenience, the Prony series is used to represent the transient compliance ΔD, such that:

$$\Delta D^{\psi^t} = \sum_{n=1}^N D_n \left[1 - \exp\left(-\lambda_n \psi^t\right)\right] \quad (2.9)$$

where N is the number of terms, D_n is the nth coefficient of Prony series associated with the nth retardation time λ_n. In the above and subsequent equations, the superimposed t and τ designate the response at a specific time.

As proposed by Lai and Bakker (1996), the one-dimensional nonlinear viscoelastic model in Eq. (2.7) can be generalized to three-dimensional problems by decoupling the response into deviatoric and volumetric parts, such that:

$$\overline{\varepsilon}_{ij}^{nve} = \overline{e}_{ij}^{nve} + \frac{1}{3}\overline{\varepsilon}_{kk}^{nve}\delta_{ij} = \frac{1}{2\overline{G}}\overline{S}_{ij} + \frac{\overline{\sigma}_{kk}}{9\overline{K}}\delta_{ij} = \frac{\overline{J}}{2}\overline{S}_{ij} + \frac{\overline{B}}{3}\overline{\sigma}_{kk}\delta_{ij} \qquad (2.10)$$

where $\overline{e}^{nve}$ and $\overline{\varepsilon}_{kk}^{nve}$ are the deviatoric strain tensor and the volumetric component of the strain tensor, respectively; $\overline{G}$ and $\overline{K}$ are the undamaged shear and bulk moduli, respectively, which are related to the undamaged Young's modulus $\overline{E}$ and Poisson's ratio $\overline{\nu}$ by:

$$\overline{G} = \overline{E}/2(1+\overline{\nu}), \quad \overline{K} = \overline{E}/3(1-2\overline{\nu}) \qquad (2.11)$$

$\overline{J}$ and $\overline{B}$ are the undamaged shear and bulk compliances, respectively; $\overline{S}_{ij} = \overline{\sigma}_{ij} - \overline{\sigma}_{kk}\delta_{ij}/3$ is the deviatoric stress tensor in the effective configuration; δ_{ij} is the Kronecker delta; and $\overline{\sigma}_{kk}$ is the volumetric stress in the effective (undamaged) configuration. Using Schapery's integral constitutive model [Eq. (2.7)] and after some mathematical manipulations, the deviatoric and volumetric components of the nonlinear viscoelastic strain at time t can be expressed, respectively, as follows (Lai and Bakker, 1996):

$$\overline{e}_{ij}^{nve,t} = \frac{1}{2}g_0^t\overline{J}_0\overline{S}_{ij}^t + \frac{1}{2}g_1^t\int_0^t \Delta\overline{J}^{(\psi^t-\psi^\tau)}\frac{d(g_2^\tau\overline{S}_{ij}^\tau)}{d\tau}d\tau \qquad (2.12)$$

$$\overline{\varepsilon}_{kk}^{nve,t} = \frac{1}{3}g_0^t\overline{B}_0\overline{\sigma}_{kk}^t + \frac{1}{3}g_1^t\int_0^t \Delta\overline{B}^{(\psi^t-\psi^\tau)}\frac{d(g_2^\tau\overline{\sigma}_{kk}^\tau)}{d\tau}d\tau \qquad (2.13)$$

where the material constants $\overline{J}_0$ and $\overline{B}_0$ are the instantaneous effective elastic shear and bulk compliances, respectively. The Poisson's ratio $\overline{\nu}$ is assumed to be time-independent which is a fairly reasonable assumption for a range of temperatures and

stress rates in the asphaltic materials (e.g. Di Benedetto et al., 2007). Therefore, one can write:

$$\bar{J}_0 = 2(1+\bar{v})\bar{D}_0 ; \qquad \bar{B}_0 = 3(1-2\bar{v})\bar{D}_0 \tag{2.14}$$

$$\Delta\bar{J}(\psi) = 2(1+\bar{v})\Delta\bar{D}(\psi) ; \qquad \Delta\bar{B}(\psi) = 3(1-2\bar{v})\Delta\bar{D}(\psi) \tag{2.15}$$

Representing the transient compliance as the Prony series, Eq. (2.9), and making use of Eqs. (2.14) and (2.15) yields the following relations for the deviatoric strain tensor $\bar{e}^{nve,t}$ and the volumetric strain $\bar{\varepsilon}_{kk}^{nve,t}$ (Haj-Ali and Muliana, 2004):

$$\begin{aligned} \bar{e}_{ij}^{nve,t} = \frac{1}{2}\left[g_0^t \bar{J}_0 + g_1^t g_2^t \sum_{n=1}^{N} \bar{J}_n - g_1^t g_2^t \sum_{n=1}^{N} \bar{J}_n \frac{1-\exp(-\lambda_n \Delta\psi^t)}{\lambda_n \Delta\psi^t} \right] \bar{S}_{ij}^t - \\ \frac{1}{2} g_1^t \sum_{n=1}^{N} \bar{J}_n \left[\exp(-\lambda_n \Delta\psi^t)q_{ij,n}^{t-\Delta t} - g_2^{t-\Delta t} \frac{(1-\exp(-\lambda_n \Delta\psi^t))}{\lambda_n \Delta\psi^t} \bar{S}_{ij}^{t-\Delta t} \right] \end{aligned} \tag{2.16}$$

$$\begin{aligned} \bar{\varepsilon}_{kk}^{nve,t} = \frac{1}{3}\left[g_0^t \bar{B}_0 + g_1^t g_2^t \sum_{n=1}^{N} \bar{B}_n - g_1^t g_2^t \sum_{n=1}^{N} \bar{B}_n \frac{1-\exp(-\lambda_n \Delta\psi^t)}{\lambda_n \Delta\psi^t} \right] \bar{\sigma}_{kk}^t - \\ \frac{1}{3} g_1^t \sum_{n=1}^{N} \bar{B}_n \left[\exp(-\lambda_n \Delta\psi^t)q_{kk,n}^{t-\Delta t} - g_2^{t-\Delta t} \frac{(1-\exp(-\lambda_n \Delta\psi^t))}{\lambda_n \Delta\psi^t} \bar{\sigma}_{kk}^{t-\Delta t} \right] \end{aligned} \tag{2.17}$$

where the superscript Δt designates the time increment.

It is noteworthy that the only difference between Eqs. (2.7)-(2.17) and those presented in Huang et al. (2011a) is that they are expressed in the effective (undamaged) configuration, which allows one to easily couple viscoelasticity to damage evolution.

2.5. Thermo-Viscoplastic Model

In order to calculate the viscoplastic (unrecoverable) deformations in HMA, Perzyna-type viscoplasticity constitutive equations as outlined in Masad et al. (2005), Tashman et al. (2005), and Huang et al. (2011a) are modified here and expressed in terms of the effective stress tensor $\bar{\sigma}$, Eq. (2.6), instead of the nominal stress tenor σ. The constitutive equations are defined in the effective configuration since it is argued that once the material is damaged, further loading can only affect the undamaged (effective) region such that the viscoplasticity can only affect the undamaged material skeleton.

Taking the time derivative of Eq. (2.1) in the effective configuration implies:

$$\dot{\overline{\varepsilon}}_{ij} = \dot{\overline{\varepsilon}}_{ij}^{nve} + \dot{\overline{\varepsilon}}_{ij}^{vp} \tag{2.18}$$

where $\dot{\overline{\varepsilon}}^{nve}$ and $\dot{\overline{\varepsilon}}^{vp}$ are the nonlinear viscoelastic and the viscoplastic strain rate tensors in the effective configuration, respectively. In Eq. (2.18) and subsequent equations, the superimposed dot indicates derivative with respect to time. The viscoplastic strain rate is defined through the following classical viscoplastic flow rule:

$$\dot{\overline{\varepsilon}}_{ij}^{vp} = \dot{\overline{\gamma}}^{vp} \frac{\partial \overline{F}}{\partial \overline{\sigma}_{ij}} \tag{2.19}$$

where $\dot{\overline{\gamma}}^{vp}$ and $\overline{F}$ are the viscoplastic multiplier and the viscoplastic potential function in the effective configuration, respectively. Physically, $\dot{\overline{\gamma}}^{vp}$ is a positive scalar which determines the magnitude of $\dot{\overline{\varepsilon}}_{ij}^{vp}$, whereas $\partial \overline{F}/\partial \overline{\sigma}_{ij}$ determines the direction of $\dot{\overline{\varepsilon}}_{ij}^{vp}$. Perzyna (1971) expressed the viscoplastic multiplier in terms of an overstress function and a viscosity parameter that relates the rate of viscoplastic strain to the current stresses, such that $\dot{\overline{\gamma}}^{vp}$ can be expressed as follows:

$$\dot{\overline{\gamma}}^{vp} = \Gamma^{vp} \left\langle \Phi\left(\overline{f}\right) \right\rangle^{N} \tag{2.20}$$

where Γ^{vp} is the viscoplastic viscosity parameter such that $1/\Gamma^{vp}$ represents the viscoplasticity relaxation time according to the notion given by Perzyna, N is the viscoplastic rate sensitivity exponent, and Φ is the overstress function which is expressed in terms of the yield function $\overline{f}$. Moreover, $\langle \bullet \rangle$ in Eq. (2.20) is the Macaulay bracket defined by $\langle \Phi \rangle = \left(\Phi + |\Phi|\right)/2$. The following expression can be postulated for the overstress function Φ:

$$\Phi\left(\overline{f}\right) = \frac{\overline{f}}{\sigma_y^0} \tag{2.21}$$

where σ_y^0 is a yield stress quantity used to normalize the overstress function and can be assumed unity. Eqs. (2.19)-(2.21) indicate that viscoplasticity occurs only when the overstress function Φ is greater than zero.

Drucker-Prager-type yield surfaces have been used by number of researchers for describing the viscoplastic flow behavior of HMA since it takes into consideration confinement, aggregates friction, aggregates interlocking, and dilative behavior of HMA (c.f. Abdulshafi and Majidzadeh, 1985; Tan et al., 1994; Bousshine et al., 2001; Seibi et al., 2001; Cela, 2002; Dessouky, 2005; Tashman et al., 2005; Saadeh et al., 2007; Saadeh and Masad, 2010; Huang et al., 2011a). In this study, a modified Drucker-Prager yield function that distinguishes between the distinct behavior of HMA in compression and extension, and also takes into consideration the pressure sensitivity is employed (Dessouky, 2005). However, this modified Drucker-Prager yield function is expressed here as a function of the effective (undamaged) stress tensor, $\bar{\sigma}$, as follows:

$$\bar{f} = \bar{\tau}^{vp} - \alpha \bar{I}_1 - \bar{\kappa}\left(\bar{p}\right) \tag{2.22}$$

where α is a material parameter related to the material's internal friction, $\bar{\kappa}\left(\bar{p}\right)$ is the isotropic hardening function associated with the cohesive characteristics of the material and depends on the effective viscoplastic strain $\bar{p}$, $\bar{I}_1 = \bar{\sigma}_{kk}$ is the first stress invariant, and $\bar{\tau}^{vp}$ is the deviatoric effective shear stress modified to distinguish between the HMA behavior under compression and extension loading conditions, such that:

$$\bar{\tau}^{vp} = \frac{\sqrt{3\bar{J}_2}}{2}\left[1 + \frac{1}{d^{vp}} + \left(1 - \frac{1}{d^{vp}}\right)\frac{3\bar{J}_3}{\sqrt{3\bar{J}_2^3}}\right] \tag{2.23}$$

where $\bar{J}_2 = \frac{1}{2}\bar{S}_{ij}\bar{S}_{ij}$ and $\bar{J}_3 = \frac{1}{2}\bar{S}_{ij}\bar{S}_{jk}\bar{S}_{ki}$ are the second and third deviatoric stress invariants of the effective stress tensor $\bar{\sigma}$, respectively. d^{vp} is a material parameter which gives the distinction of the material's viscoplastic response in compressive and extensive loading conditions. For example, Eq. (2.23) shows that in uniaxial compression $\bar{\tau}^{vp} = \sqrt{3\bar{J}_2}$, whereas in uniaxial tension $\bar{\tau}^{vp} = \frac{\sqrt{3\bar{J}_2}}{d^{vp}}$. Therefore, d^{vp} can simply be defined as the ratio of the yield strength in uniaxial tension to that in uniaxial compression. To ensure the convexity of the viscoplastic loading surface function $\bar{f}$, d^{vp} ranges between 0.78 and 1. Eq. (2.22) simplifies to the classical Drucker-Prager

yield surface when $d^{vp}=1$ and to the von Misses criterion when $d^{vp}=1$ and $\alpha=0$. However, $d<1$ indicates that the strength of the material in tension is lower than that in compression. Figure 2.2 (a) and (b) show the schematic illustration of the yield surface [Eq. (2.22)] in the deviatoric plane and the meridional plane, respectively.

Further illustration of the effect of the parameter d^{vp} on the viscoplastic response of bituminous materials is shown schematically in Figure 2.3. Point "A" in this figure represents a point that is under the hydrostatic pressure. Increasing the axial stress causes both the first stress invariant $\bar{I}_1$ and the second deviatoric stress invariant $\bar{J}_2$ to increase. Hence, point "A" follows the stress path "AB" until the material yields at point "B". On the other hand, by decreasing the axial stress (extension test), point "A" follows the stress path "AC". For the conventional Drucker-Prager yield surface (i.e. $d^{vp}=1$), the material yields at point "C". However, the modified Drucker-Prager yield surface shows that the material yields sooner at point "C'" since the inclusion of the d^{vp} parameter reduces both the internal slope α and the hardening $\bar{\kappa}$ to α' and $\bar{\kappa}'$, respectively. This is an interesting feature of the modified Drucker-Prager yield function in distinguishing the yield behavior in the compression or extension mode of loading.

(a)   (b)
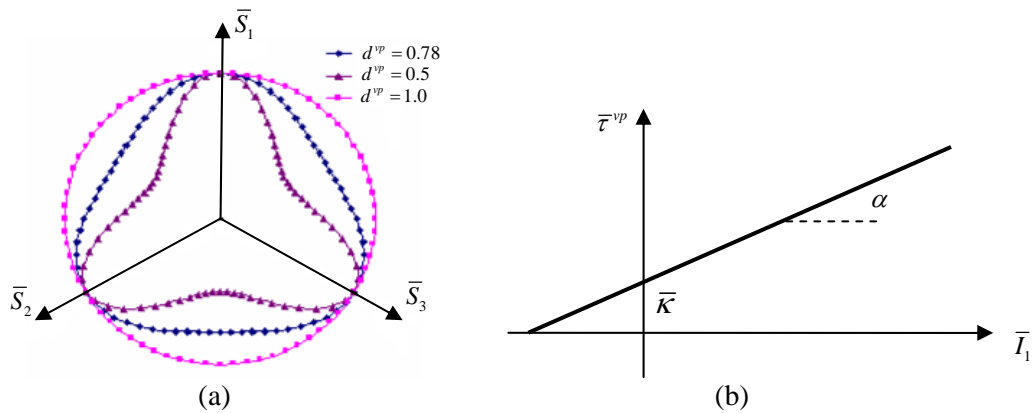
Figure 2.2. Schematic illustration of the extended Drucker-Prager yield surface [Eqs. (2.22) and (2.23)]. (a) In the deviatoric plane; (b) In the meridional plane.
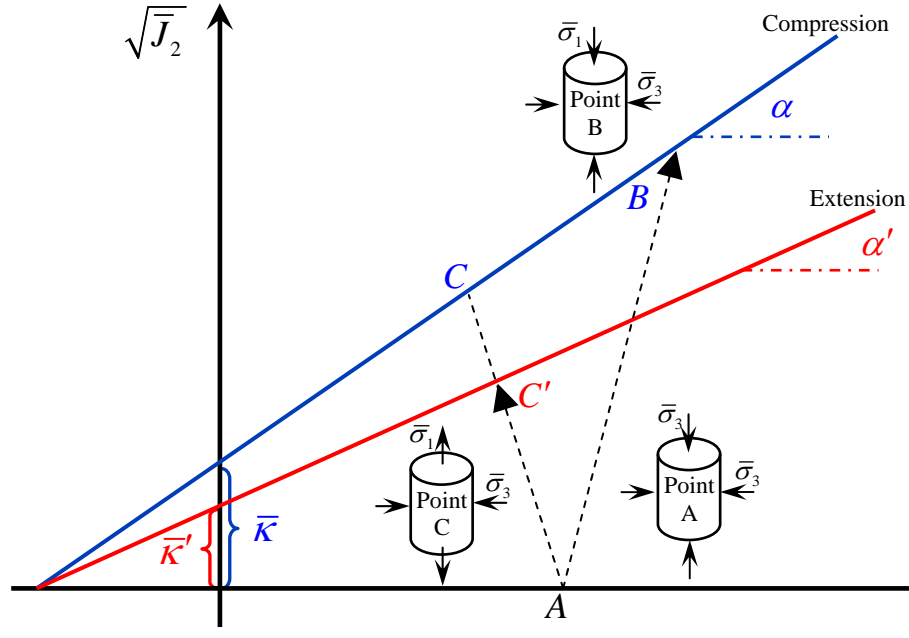
Figure 2.3. Schematic illustration of the influence of the stress path on the modified Drucker-Prager yield surface.

Following the work of Lemaître and Chaboche (1990), the isotropic hardening function $\bar{\kappa}(\bar{p})$ is expressed as an exponential function of the effective viscoplastic strain $\bar{p}$, such that:

$$\bar{\kappa}(\bar{p}) = \kappa_0 + \kappa_1\left[1 - \exp(-\kappa_2\bar{p})\right] \tag{2.24}$$

where κ_0, κ_1, and κ_2 are material parameters; κ_0 defines the initial yield stress, $\kappa_0 + \kappa_1$ determines the saturated yield stress, and κ_2 is the strain hardening rate.

As mentioned in Chapter I, several studies have shown that the viscoplastic deformation of HMA is non-associated which requires assuming a plastic potential function $\bar{F}$ to be different than the yield function $\bar{f}$. Hence, the direction of the viscoplastic strain increment is not normal to the yield surface, but to the plastic potential surface. The use of an associated flow rule (i.e. $\bar{F} = \bar{f}$) overestimates the dilation behavior of HMA when compared to experimental measurements (Masad et al., 2005; 2007). In order to obtain non-associative viscoplasticity, the Drucker-Prager-type

function can still be used where the parameter α is replaced by another parameter, β; defining the viscoplastic potential function as follows:

$$\bar{F} = \bar{\tau}^{vp} - \beta \bar{I}_1 \tag{2.25}$$

where β is a material parameter that describes the dilation or contraction behavior of the material. The effective viscoplastic strain rate $\dot{\bar{p}}$ is expressed as (Dessouky, 2005):

$$\dot{\bar{p}} = a^{-1}\sqrt{\dot{\bar{\varepsilon}}_{ij}^{vp}\dot{\bar{\varepsilon}}_{ij}^{vp}} \quad \text{where} \quad a = \sqrt{1 + 2\left(\frac{0.5 + \beta/3}{1 - \beta/3}\right)^2} \tag{2.26}$$

From Eq. (2.25), one can write:

$$\frac{\partial \bar{F}}{\partial \bar{\sigma}_{ij}} = \frac{\partial \bar{\tau}^{vp}}{\partial \bar{\sigma}_{ij}} - \frac{1}{3}\beta\delta_{ij} \tag{2.27}$$

where δ_{ij} is the Kronecker delta and $\partial\bar{\tau}^{vp}/\partial\bar{\sigma}_{ij}$ is given by:

$$\frac{\partial \bar{\tau}^{vp}}{\partial \bar{\sigma}_{ij}} = \frac{1}{2}\left[\frac{\sqrt{3}}{2}\left(1+\frac{1}{d^{vp}}\right)\frac{\partial \bar{J}_2}{\partial \bar{\sigma}_{ij}}\bar{J}_2^{-1/2} + 3\left(1-\frac{1}{d^{vp}}\right)\left(\frac{\partial \bar{J}_3}{\partial \bar{\sigma}_{ij}}\bar{J}_2^{-1} - \frac{\partial \bar{J}_2}{\partial \bar{\sigma}_{ij}}\bar{J}_3\bar{J}_2^{-2}\right)\right] \tag{2.28}$$

Substituting Eq. (2.28) into Eq. (2.27) and noting that $\partial\bar{J}_2/\partial\bar{\sigma}_{ij} = \bar{S}_{ij}$ and $\partial\bar{J}_3/\partial\bar{\sigma}_{ij} = \frac{3}{2}\bar{S}_{ik}\bar{S}_{kj} - \bar{J}_2\delta_{ij}$ imply:

$$\frac{\partial \bar{F}}{\partial \bar{\sigma}_{ij}} = \frac{\sqrt{3}}{4}\left(1+\frac{1}{d^{vp}}\right)\bar{S}_{ij}\bar{J}_2^{-1/2} +$$
$$\frac{3}{2}\left(1-\frac{1}{d^{vp}}\right)\left(\frac{3}{2}\bar{S}_{ik}\bar{S}_{kj}\bar{J}_2^{-1} - \bar{S}_{ij}\bar{J}_3\bar{J}_2^{-2} - \delta_{ij}\right) - \frac{1}{3}\beta\delta_{ij} \tag{2.29}$$

2.6. Thermo-Viscodamage Model

Time-, rate-, and temperature-independent evolution equations for the damage variable ϕ are not appropriate for predicting the damage nucleation and growth in HMA materials. Generally, the damage evolution $\dot{\phi}$ can be a function of stress tensor $\bar{\sigma}$, hydrostatic stress $\bar{\sigma}_{kk}$, strain tensor $\bar{\varepsilon}$, strain rate tensor $\dot{\bar{\varepsilon}}$, temperature T, and damage history ϕ, such that:

$$\dot{\phi}(t) = \phi\left[\overline{\boldsymbol{\sigma}}(t), \overline{\sigma}_{kk}(t), \overline{\boldsymbol{\varepsilon}}(t), \dot{\overline{\varepsilon}}(t), T(t), \phi(t)\right] \tag{2.30}$$

Kachanov (1958) was the first to postulate a time-dependent damage law to describe creep damage, which had the following form:

$$\dot{\phi} = \left[\frac{\sigma}{C_1(1-\phi)}\right]^{C_2} \tag{2.31}$$

where C_1 and C_2 are material constants, and σ is the applied stress. Rabotnov (1969) assumed that damage also affects the rate of creep strain, $\dot{\varepsilon}$, and proposed the following evolution equations for creep strain and damage variable:

$$\dot{\varepsilon} = C_1\sigma^n(1-\phi)^{-m}, \qquad \dot{\phi} = C_2\sigma^\gamma(1-\phi)^{-\mu} \tag{2.32}$$

where C_1, C_2, n, m, γ, and μ are material constants. Since most processes are stress controlled, the evolution law of equations (2.31) and (2.32) are functions of stress. However, for other types of loading conditions the dependency of evolution law on strain and other factors is inevitable. Hence, in several works, first of which was proposed by Rabotnov (1969), the evolution law was expressed in terms of strain. He eliminated the stress from the evolution law and proposed an exponential form in terms of strain as follows:

$$\dot{\phi} = C\exp(k\varepsilon)(1-\phi)^{-\mu} \tag{2.33}$$

where k is a material constant. Belloni et al. (1979) proposed the following creep damage law:

$$\phi = C\varepsilon^\alpha \exp(-\frac{\beta}{T})\sigma^\gamma t^\delta \tag{2.34}$$

where C, α, β, γ, δ are material constants, and t is time. Afterwards, relying on several sets of experiments, they implied that strain is the most important one, and proposed the first approximation for the damage variable as:

$$\phi = C\varepsilon^\alpha \tag{2.35}$$

Cozzarelli and Bernasconi (1981) and Lee et al. (1986) used this idea and proposed the following differential evolution law:

$$\phi(t) = C\varepsilon_c(t)^\alpha \left[\int_0^t (\sigma(\tau))^{\frac{\gamma}{\delta}} d\tau \right]^\delta \tag{2.36}$$

where C, α, γ, and δ are material constants, ε_c is the creep strain, and $\sigma(\tau)$ is the applied stress at specific time τ.

Schapery (1990) used the concept of viscoelastic fracture mechanics (Schapery, 1975c; 1984; 1987) along with the elastic-viscoelastic correspondence principle and continuum damage mechanics to model the growing damage in viscoelastic media, where the following power-law evolution eqaution has been proposed for a damage parameter designated as S :

$$\dot{S} = \left[-\frac{\partial W^R}{\partial S} \right]^\alpha \tag{2.37}$$

where α is a material constant, and W^R is the pseudo strain energy density defined as

$$W^R = \frac{1}{2} E^R (\varepsilon^R)^2 \tag{2.38}$$

with ε^R being the pseudo strain given by

$$\varepsilon^R = \frac{1}{E^R} \int_0^t E(\psi^t - \psi^\tau) \frac{d\varepsilon}{d\tau} d\tau \tag{2.39}$$

where $E(t)$ is the relaxation modulus in uniaxial loading, $E^R = 1$ is a reference modulus, and ψ^t is the reduced time defined in Eq. (2.8). However, in addition to the limitations of the model discussed in Chapter I, the introduced damage parameter S did not have a clear physicall meaning and could range between zero and infinity. Moreover, Park et al. (1996), Chehab et al. (2002), Kim et al. (2005; 2008), and Underwood et al. (2006) have used Schapery's model to simulate the damage evolution in HMA.

Motivated and guided by the aforementioned damage evolution laws, in this study, the first approximation of the damage evolution law is proposed as an exponential form of the total effective strain:

$$\dot{\phi} = \Gamma^{vd} \exp\left(k \bar{\varepsilon}_{eff} \right) \tag{2.40}$$

where Γ^{vd} is a damage viscousity parameter, $\bar{\varepsilon}_{eff} = \sqrt{\bar{\varepsilon}_{ij}\bar{\varepsilon}_{ij}}$ is the effective total strain in the effective configuration. $\bar{\varepsilon}_{ij}$ includes both viscoelastic and viscoplastic components [Eq. (2.1)] and k is a material parameter. The dependence of the damage density evolution equation on the total strain implicitly couples the damage model to the viscoelasticity and viscoplasticity models. Hence, changes in loading time, rate, and temperature implicitly affects the damage evolution through changes in viscoelastic and viscoplastic strains. However, time of rupture in creep tests and peak point in the stress-strain diagram for the constant strain rate tests are highly stress dependent. Therefore, one may assume the damage viscousity variable [in Eq. (2.40)] to be a function of stress. Here, a power law function is postulated for expressing the stress dependency of the damage viscousity parameter, such that:

$$\Gamma^{vd} = \Gamma_0^{vd} \left\langle \frac{Y}{Y_0} \right\rangle^q \tag{2.41}$$

where q is the stress dependency parameter; Γ_0^{vd} and Y_0 are the reference damage viscousity parameter and the reference damage force obtained at a reference stress for a creep test; and Y is the damage driving force in the nominal (damaged) configuration, which can be assumed to have a modified Drucker-Prager-type form, such that:

$$Y = \tau^{vd} - \alpha I_1 \tag{2.42}$$

The brackets $\langle \bullet \rangle$ in Eq. (2.41) are the Macaulay brackets defined by $\langle x \rangle = (x + |x|)/2$ to ensure that the non-positive values of $(\tau^{vd} - \alpha I_1)$ load to $\dot{\phi} = 0$. The term $\langle \tau^{vd} - \alpha I_1 \rangle$ in Eq. (2.41) is the component of the damage force in the nominal configuration which is assumed to have the form of the modified Drucker-Prager criterion in order to include the pressure effects on damage nucleation and growth. Moreover, α is a parameter that reflects the material internal friction. Eqs. (2.41) and (2.42) state that the damage starts when the deviatoric stress τ^{vd} dominates the confinement effect αI_1 (i.e. $\tau^{vd} - \alpha I_1 > 0$). In this work, it is assumed that damage does not evolve due to hydrostatic pressure, and damage starts nucleating when the deviatoric stress exceeds the confinement effect term.

Note that τ is expressed in the nominal configuration and is a function of the nominal stress σ_{ij} instead of the effective stress $\bar{\sigma}_{ij}$. In continuum damage mechanics, Y is interpreted as the energy release rate necessary for damage nucleation and growth (Abu Al-Rub and Voyiadjis, 2003). Assuming the damage viscousity parameter to be a function of the damage force, Y, in the nominal (damaged) configuration instead of the effective (undamaged) configuration allows one to include damage history effects, such that by using the effective stress concept in Eq. (2.6) one can rewrite Y as follows:

$$Y = \bar{Y}\left(1 - \phi\right)^2 \tag{2.43}$$

Moreover, the following form is postulated for $\bar{\tau}^{vd}$:

$$\bar{\tau}^{vd} = \frac{\sqrt{3\bar{J}_2}}{2}\left[1 + \frac{1}{d^{vd}} + \left(1 - \frac{1}{d^{vd}}\right)\frac{3\bar{J}_3}{\sqrt{3\bar{J}_2^3}}\right] \tag{2.44}$$

where $\bar{J}_2 = \frac{1}{2}\bar{S}_{ij}\bar{S}_{ij}$ and $\bar{J}_3 = \frac{1}{2}\bar{S}_{ij}\bar{S}_{jk}\bar{S}_{ki}$ are the second and third deviatoric stress invariants of the effective stress tensor $\bar{\sigma}$, respectively. Parameter d^{vd} in Eq. (2.44) captures different damage nucleation and growth conditions in extension (not necessarily tension) and contraction (not necessarily compression) loading conditions and can be defined as the ratio of the damage force in the uniaxial tension to that in the uniaxial compression. For example, in uniaxial compression, Eq. (2.44) indicates $\frac{3\bar{J}_3}{\sqrt{3\bar{J}_2^3}} = 1$ and $\bar{\tau}^{vd} = \sqrt{3\bar{J}_2}$, whereas in uniaxial tension $\frac{3\bar{J}_3}{\sqrt{3\bar{J}_2^3}} = -1$ and $\bar{\tau}^{vd} = \frac{\sqrt{3\bar{J}_2}}{d^{vd}}$. Hence, d^{vd} can be defined as the ratio of the damage force in uniaxial tension to that in uniaxial compression.

Moreover, the damage density evolution highly depends on temperature. In this work, the proposed damage evolution law is coupled with temperature through a damage temperature function $G(T)$, which should be identified based on experimental data. Hence, the following damage evolution law can be obtained using Eqs. (2.40), (2.41), and (2.43):

$$\dot{\phi} = \Gamma_0^{vd} \left\langle \frac{\overline{Y}(1-\phi)^2}{Y_0} \right\rangle^q \exp\left(k\varepsilon_{eff}\right) G(T) \qquad (2.45)$$

Assuming the damage force to have a Drucker-Prager-type form is a smart choice since it allows the damage evolution to depend on confining pressures, and to take into consideration the distinct response of asphalt concrete mixes under extention and compression loading conditions through the parameter d^{vd} in Eq. (2.44).

It should be emphasized that Eqs. (2.42) and (2.45) provide both the nucleation criterion and the growth function for the viscodamage model. The inherent assumption in these equations is that the damage rate will have a non zero value when the term inside the bracket has a positive value (i.e. $\overline{\tau}^{vd} - \alpha \overline{I}_1 > 0$). In other words, the damage grows only in extension mode of loading where the deviatoric stress dominants the confinement effect. Figure 2.4 shows a schematic illustration of the damage surface. The effect of d^{vd} in Eq. (2.44) on the viscodamage nucleation criterion is very similar to the effect of d^{vd} in Eq. (2.23) on the viscoplastic yield surface as shown in Figures 2.2 and 2.2.
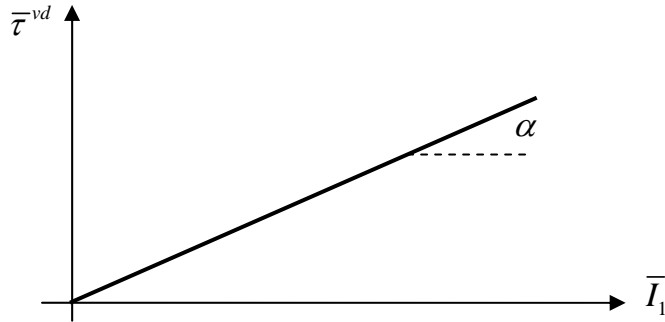
Figure 2.4. Schematic illustration of the viscodamage nucleation criterion. Damage starts growing when the deviatoric stress $\overline{\tau}^{vd}$ dominates the confinement effect $\alpha \overline{I}_1$.

In the following section, numerical algorithms for integrating the presented thermo-mechanical viscoelastic, viscoplastic, and viscodamage evolution equations will

be detailed, and the associated material constants will be indentified based on available experimental data.

2.7. Numerical Implementation

As mentioned in the previous sections, the constitutive models are presented in the effective (undamaged) configuration. This approach substantially simplifies the numerical implementation since it avoids the complexities associated with the direct couplings of the damage model to the viscoelastic and viscoplastic models. In other words, one can first update the stress tensor in the effective configuration $\bar{\sigma}$ using the viscoelastic and viscoplastic models, then calculate the damage variable which is functions of the stress in the effective configuration, and finally update the nominal strain and stress tensors. The strain increment in the nominal configuration is known $\Delta \varepsilon_{ij}^t$ at the beginning the analysis. For the strain equivalence hypothesis, the strain increments in the effective and nominal configurations are the same. However, this is not the case for other transformation hypotheses such as strain energy equivalence hypothesis or power equivalence hypothesis. For these hypotheses, another iteration scheme should be added to the numerical implementation in order to obtain the converged strain increment in the effective configuration. Having the given strain increment, $\Delta \bar{\varepsilon}_{ij} = \bar{\varepsilon}_{ij}^t - \bar{\varepsilon}_{ij}^{t-\Delta t}$, and values of the stress and internal variables from the previous step (i.e. at time $t - \Delta t$), one can obtain the updated values at the end the time increment (i.e. at time t). Therefore, one can decompose the total strain in Eq. (2.1), the effective viscoplastic strain in Eq. (2.26), and the effective stress tensor $\bar{\sigma}_{ij}$, respectively, at the current time t as follows:

$$\bar{\varepsilon}_{ij}^t = \bar{\varepsilon}_{ij}^{nve,t} + \bar{\varepsilon}_{ij}^{vp,t} = \bar{\varepsilon}_{ij}^{t-\Delta t} + \Delta \bar{\varepsilon}_{ij}^t = \bar{\varepsilon}_{ij}^{nve,t-\Delta t} + \bar{\varepsilon}_{ij}^{vp,t-\Delta t} + \Delta \bar{\varepsilon}_{ij}^{nve,t} + \Delta \bar{\varepsilon}_{ij}^{vp,t} \quad (2.46)$$

$$\bar{p}^t = \bar{p}^{t-\Delta t} + \Delta \bar{p}^t \quad (2.47)$$

$$\bar{\sigma}_{ij}^t = \bar{\sigma}_{ij}^{t-\Delta t} + \Delta \bar{\sigma}_{ij}^t \quad (2.48)$$

In the next subsections, the procedure for determination of $\Delta\bar{\varepsilon}_{ij}^{ve,t}$, $\Delta\bar{\varepsilon}_{ij}^{vp,t}$, $\Delta\bar{p}^t$, and $\Delta\bar{\sigma}_{ij}^t$ will be explained. Moreover, in the following subsections, the constitutive model is assumed to be at the reference temperature (i.e. $T = T_0$), such that all temperature coupling terms have the value of one. In this section, a step by step procedure for implementation of the proposed complex constitutive model is presented. In other words, at the beginning, the procedure for implementation of the viscoelastic model is explained, then the viscoelastic model is coupled to viscoplasticity, and finally the coupled viscoelastic-viscoplastic model will be coupled to the damage models.

2.7.1. Implementation of the Viscoelastic Model

Deviatoric and volumetric components of the viscoelastic strain tensor can be rewritten as follows by using (2.16) and (2.17) (Haj-Ali and Muliana, 2004):

$$\Delta\bar{e}_{ij}^{nve,t} = \bar{e}_{ij}^{nve,t} - \bar{e}_{ij}^{nve,t-\Delta t}$$

$$= \bar{J}^t \bar{S}_{ij}^t - \bar{J}^{t-\Delta t} \bar{S}_{ij}^{t-\Delta t} - \frac{1}{2}\sum_{n=1}^{N} \bar{J}_n \left[g_1^t \exp(-\lambda_n \Delta t^t) - g_1^{t-\Delta t} \right] q_{ij,n}^{t-\Delta t} - \qquad (2.49)$$

$$\frac{1}{2} g_2^{t-\Delta t} \sum_{n=1}^{N} \bar{J}_n \left\{ g_1^{t-\Delta t}\left[\frac{1-\exp(-\lambda_n \Delta t^{t-\Delta t})}{\lambda_n \Delta t^{t-\Delta t}} \right] - g_1^t \left[\frac{1-\exp(-\lambda_n \Delta t^t)}{\lambda_n \Delta t^t} \right] \right\} \bar{S}_{ij}^{t-\Delta t}$$

$$\Delta\bar{\varepsilon}_{kk}^{nve,t} = \bar{\varepsilon}_{kk}^{nve,t} - \bar{\varepsilon}_{kk}^{nve,t-\Delta t}$$

$$= \bar{B}^t \bar{\sigma}_{kk}^t - \bar{B}^{t-\Delta t} \bar{\sigma}_{kk}^{t-\Delta t} - \frac{1}{3}\sum_{n=1}^{N} \bar{B}_n \left[g_1^t \exp(-\lambda_n \Delta t^t) - g_1^{t-\Delta t} \right] q_{kk,n}^{t-\Delta t} - \qquad (2.50)$$

$$\frac{1}{3} g_2^{t-\Delta t} \sum_{n=1}^{N} \bar{B}_n \left\{ g_1^{t-\Delta t}\left[\frac{1-\exp(-\lambda_n \Delta t^{t-\Delta t})}{\lambda_n \Delta t^{t-\Delta t}} \right] - g_1^t \left[\frac{1-\exp(-\lambda_n \Delta t^t)}{\lambda_n \Delta t^t} \right] \right\} \bar{\sigma}_{kk}^{t-\Delta t}$$

where the variables $q_{ij,n}^{t-\Delta t}$ and $q_{kk,n}^{t-\Delta t}$ are the deviatoric and volumetric components of the hereditary integrals for each term n of the Prony series at previous time step $t - \Delta t$, respectively. The hereditary integrals are updated at the end of each converged time increment, which will be used for the next time increment, and are expressed as follows (Haj-Ali and Muliana, 2004):

$$q_{ij,n}^t = \exp(-\lambda_n \Delta\psi^t)q_{ij,n}^{t-\Delta t} + (g_2^t \bar{S}_{ij}^t - g_2^{t-\Delta t}\bar{S}_{ij}^{t-\Delta t})\frac{1-\exp(-\lambda_n \Delta\psi^t)}{\lambda_n \Delta\psi^t} \qquad (2.51)$$

$$q_{kk,n}^t = \exp(-\lambda_n \Delta \psi^t) q_{kk,n}^{t-\Delta t} + (g_2^t \overline{\sigma}_{kk}^t - g_2^{t-\Delta t} \overline{\sigma}_{kk}^{t-\Delta t}) \frac{1 - \exp(-\lambda_n \Delta \psi^t)}{\lambda_n \Delta \psi^t} \tag{2.52}$$

The problem in solving Eqs. (2.49) and (2.50) is that the nonlinear functions are not known at the current increment t. Therefore, an iterative method can be used to find the correct stress state. Hence, Eqs. (2.49) and (2.50) are further linearized by assuming that $g_\alpha^t = g_\alpha^{t-\Delta t}$, such that the trial stress increment can be written as follows:

$$\Delta \overline{S}_{ij}^{t,tr} = \frac{1}{\overline{J}^{t,tr}} \left\{ \Delta \overline{e}_{ij}^t + \frac{1}{2} g_1^{t,tr} \sum_{n=1}^{N} J_n \left[\exp(-\lambda_n \Delta t) - 1 \right] q_{ij,n}^{t-\Delta t} \right\} \tag{2.53}$$

$$\Delta \overline{\sigma}_{kk}^{t,tr} = \frac{1}{\overline{B}^{t,tr}} \left\{ \Delta \overline{\varepsilon}_{kk}^t + \frac{1}{3} g_1^{t,tr} \sum_{n=1}^{N} B_n \left[\exp(-\lambda_n \Delta t) - 1 \right] q_{kk,n}^{t-\Delta t} \right\} \tag{2.54}$$

where $\overline{J}^{t,tr}$ and $\overline{B}^{t,tr}$ can be obtained using Eqs. (2.16) and (2.17) when the nonlinear parameters are functions of the trial stress. This study employs the iterative scheme to obtain the correct stress for a given strain increment. Before the onset of viscoplasticity, the residual strain will be defined as follows:

$$\overline{R}_{ij}^{ve,t} = \Delta \overline{e}_{ij}^{ve,t} + \frac{1}{3} \Delta \overline{\varepsilon}_{kk}^{ve,t} - \Delta \overline{\varepsilon}_{ij}^t \tag{2.55}$$

The Newton-Raphson method will be used to minimize the strain residual in Eq. (2.55). Moreover, when the strain is totally viscoelastic, the program uses the consistent Jacobian matrix which is the consistent tangent compliance and is determined as:

$$\begin{aligned}
\overline{S}_{ijkl}^{ve} &= \frac{\partial \overline{R}_{ij}^{ve,t}}{\partial \overline{\sigma}_{ij}^t} = \hat{J}^t \delta_{ik} \delta_{jl} + \frac{1}{3} \left(\hat{B}^t - \hat{J}^t \right) \delta_{ij} \delta_{kl} + \\
&\quad \frac{\partial \overline{\sigma}_{eff}^t}{\partial \sigma_{kl}^t} \left\{ \frac{\partial \hat{J}^t}{\partial \overline{\sigma}_{eff}^t} \overline{\sigma}_{ij}^t + \frac{1}{3} \left(\frac{\partial \hat{B}^t}{\partial \overline{\sigma}_{eff}^t} - \frac{\partial \hat{J}^t}{\partial \overline{\sigma}_{eff}^t} \right) \overline{\sigma}_{kk}^t \delta_{ij} \right. \\
&\quad \left. - \frac{1}{2} \frac{\partial g_1^t}{\partial \overline{\sigma}_{eff}^t} \sum_{n=1}^{N} \hat{J}_n \left[\exp(-\lambda_n \Delta t^t) q_{ij,n}^{t-\Delta t} - g_2^{t-\Delta t} \left(\frac{1 - \exp(-\lambda_n \Delta t^t)}{\lambda_n \Delta t^t} \right) \overline{S}_{ij}^{t-\Delta t} \right] \right. \\
&\quad \left. - \frac{1}{9} \frac{\partial g_1^t}{\partial \overline{\sigma}_{eff}^t} \sum_{n=1}^{N} \hat{B}_n \left[\exp(-\lambda_n \Delta t^t) q_{kk,n}^{t-\Delta t} - g_2^{t-\Delta t} \left(\frac{1 - \exp(-\lambda_n \Delta t^t)}{\lambda_n \Delta t^t} \right) \overline{\sigma}_{kk}^{t-\Delta t} \right] \delta_{ij} \right.
\end{aligned} \tag{2.56}$$

It should be noted that Eqs. (2.55) and (2.56) are not valid in the presence of the viscoplastic strains. These equations will be updated in the next subsection. Figure 2.5

shows the flowchart for implementation of the viscoelastic model. Note that, this flowchart is valid in the absence of viscoplasticity and damage. Hence, the nominal strain increment will be the same as the strain increment in the healed configuration.
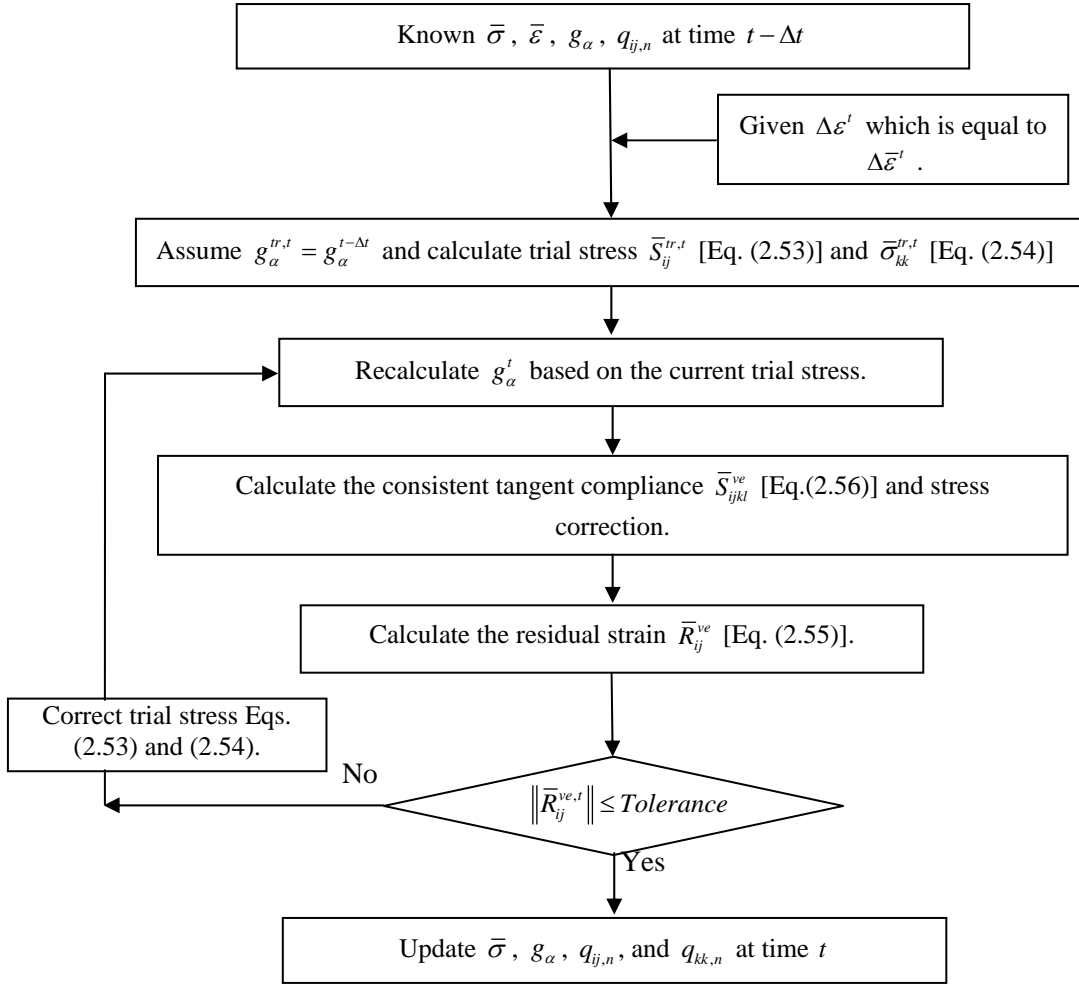
Figure 2.5. The flow chart of the recursive-iterative algorithm for implementation of the viscoelastic model.

2.7.2. Implementation of the Viscoplastic Model

The viscoplastic strain increment in Eqs. (2.19) and (2.20) can be rewritten as follows:

$$\Delta \overline{\varepsilon}_{ij}^{vp,t} = \Gamma^{vp} \left\langle \Phi\left(\overline{f}\right)\right\rangle^N \frac{\partial \overline{F}}{\partial \overline{\sigma}_{ij}} \Delta t = \Delta \overline{\gamma}^{vp,t} \frac{\partial \overline{F}}{\partial \overline{\sigma}_{ij}} \tag{2.57}$$

where $\Delta \overline{\gamma}^{vp,t}$ can be written from Eqs. (2.20) and (2.21) as follows:

$$\Delta \overline{\gamma}^{vp,t} = \Delta t \Gamma^{vp} \left\langle \Phi\left(\overline{f}\right)\right\rangle^N = \Delta t \Gamma^{vp} \left[\frac{f\left(\overline{\sigma}_{ij}^t, \overline{\varepsilon}_e^{vp,t}\right)}{\sigma_y^0}\right]^N \tag{2.58}$$

Substituting Eqs. (2.26), and (2.57) into Eq. (2.47), the effective viscoplastic strain increment can be written as:

$$\overline{\varepsilon}_e^{vp,t} = \overline{\varepsilon}_e^{vp,t-\Delta t} + \Delta \overline{\varepsilon}_e^{vp,t} = \overline{\varepsilon}_e^{vp,t-\Delta t} + \frac{\Delta \overline{\gamma}^{vp,t}}{a} \sqrt{\frac{\partial \overline{F}}{\partial \overline{\sigma}_{ij}} \frac{\partial \overline{F}}{\partial \overline{\sigma}_{ij}}} \tag{2.59}$$

According to Wang et al. (1997), one can define a consistency condition for rate-dependent plasticity (viscoplasticity) similar to the classical rate-independent plasticity theory such that a dynamic (rate-dependent) yield surface, χ, can be expressed from Eqs. (2.20), (2.21), and (2.22) as follows:

$$\chi = \overline{\tau}^{vp} - \alpha \overline{I}_1 - \overline{\kappa}\left(\overline{p}\right) - \sigma_y^0 \left(\frac{\dot{\overline{\gamma}}^{vp}}{\Gamma^{vp}}\right)^{1/N} \leq 0 \tag{2.60}$$

The Kuhn-Tucker loading-unloading condition (consistency) is valid also for the dynamic yield surface χ, such that:

$$\chi \leq 0; \quad \dot{\overline{\gamma}}^{vp} \geq 0; \quad \dot{\overline{\gamma}}^{vp}\chi = 0; \quad \dot{\chi} = 0 \tag{2.61}$$

A trial dynamic yield surface function χ^{tr} can be defined using Eqs. (2.53), (2.54), and (2.60), such that:

$$\chi^{tr} = \overline{\tau}^{vp,tr} - \alpha \overline{I}_1^{tr} - \overline{\kappa}\left(\overline{p}^{t-\Delta t}\right) - \sigma_y^0 \left(\frac{\Delta \overline{\gamma}^{vp,t-\Delta t}}{\Delta t \Gamma^{vp}}\right)^{1/N} \tag{2.62}$$

$\Delta \overline{\gamma}^{vp,t}$ and $\overline{p}^t$ can be obtained by iteratively solving Eq. (2.62) using the Newton-Raphson scheme. Once $\Delta \overline{\gamma}^{vp,t}$ is obtained, the viscoplastic strain increment $\Delta \overline{\varepsilon}_{ij}^{vp}$ can then be obtained from Eq. (2.57). In the Newton-Raphson scheme, the differential of χ with respect to $\Delta \overline{\gamma}^{vp}$ is needed, which can be expressed as follows:

$$\frac{\partial \chi}{\partial \Delta \gamma^{vp}} = -\frac{\partial \overline{\kappa}}{\partial \Delta \overline{p}} \frac{\partial \Delta \overline{p}}{\partial \Delta \overline{\gamma}^{vp}} - \frac{\sigma_y^0}{\Delta \overline{\gamma}^{vp} N} \left(\frac{\Delta \overline{\gamma}^{vp}}{\Delta t \Gamma^{vp}} \right)^{\frac{1}{N}} \tag{2.63}$$

At the $k+1$ iteration, the viscoplastic multiplier can be calculated as follows:

$$\left(\Delta \overline{\gamma}^{vp,t} \right)^{k+1} = \left(\Delta \overline{\gamma}^{vp,t} \right)^k - \left[\left(\frac{\partial \chi}{\partial \Delta \overline{\gamma}^{vp,t}} \right)^k \right]^{-1} \chi^k \tag{2.64}$$

The above recursive-iterative algorithm with the Newton-Raphson method is used to obtain the current effective stress and the updated values of viscoelastic and viscoplastic strain increments by minimizing the residual strain defined as:

$$\overline{R}_{ij} = \Delta \overline{\varepsilon}_{ij}^{nve,t} + \Delta \overline{\varepsilon}_{ij}^{vp,t} - \Delta \overline{\varepsilon}_{ij}^t \tag{2.65}$$

The stress increment at the $k+1$ iteration is calculated by:

$$\left(\Delta \overline{\sigma}_{ij}^t \right)^{k+1} = \left(\Delta \overline{\sigma}_{ij}^t \right)^k - \left[\left(\frac{\partial \overline{R}_{ij}^t}{\partial \overline{\sigma}_{kl}^t} \right)^k \right]^{-1} \left(\overline{R}_{kl}^t \right)^k \tag{2.66}$$

where the differential of $\overline{R}_{ij}^t$ gives the consistent tangent compliance, which is necessary for speeding convergence and can be derived as follows:

$$\overline{S}_{ijkl} = \frac{\partial \overline{R}_{ij}^t}{\partial \overline{\sigma}_{kl}} = \frac{\partial \Delta \overline{\varepsilon}_{ij}^{nve,t}}{\partial \overline{\sigma}_{kl}} + \frac{\partial \Delta \overline{\varepsilon}_{ij}^{vp,t}}{\partial \overline{\sigma}_{kl}} = \overline{S}_{ijkl}^{nve,t} + \overline{S}_{ijkl}^{vp,t} \tag{2.67}$$

where $\overline{S}_{ijkl}^{nve,t} = \dfrac{\partial \Delta \overline{\varepsilon}_{ij}^{nve,t}}{\partial \overline{\sigma}_{kl}}$ is the nonlinear viscoelastic tangent compliance which is derived

in Eq. (2.56). The viscoplastic tangent compliance can be derived using Eqs. (2.22), (2.57), and (2.58), such that:

$$\begin{aligned} \overline{S}_{ijkl}^{vp,t} &= \frac{\partial \Delta \overline{\varepsilon}_{ij}^{vp,t}}{\partial \overline{\sigma}_{kl}} = \frac{\partial \overline{F}}{\partial \overline{\sigma}_{ij}} \frac{\partial \Delta \overline{\gamma}^{vp,t}}{\partial \overline{\sigma}_{kl}} + \Delta \overline{\gamma}^{vp,t} \frac{\partial^2 \overline{F}}{\partial \overline{\sigma}_{ij} \partial \overline{\sigma}_{kl}} \\ &= \frac{\Delta t \Gamma^{vp} N}{\sigma_y^0} \left(\frac{\overline{f}}{\sigma_y^0} \right)^{N-1} \frac{\partial \overline{F}}{\partial \overline{\sigma}_{ij}} \frac{\partial \overline{f}}{\partial \overline{\sigma}_{kl}} + \Delta t \Gamma^{vp} \left(\frac{\overline{f}}{\sigma_y^0} \right)^N \frac{\partial^2 \overline{F}}{\partial \overline{\sigma}_{ij} \partial \overline{\sigma}_{kl}} \end{aligned} \tag{2.68}$$

The tangent compliance for the coupled viscoelastic-viscoplastic model can now be obtained by substituting Eqs. (2.56) and (2.68) into Eq. (2.67). The flowchart for implementing the coupled viscoelastic-viscoplastic model is presented in Figure 2.6.

2.7.3. Implementation of the Viscodamage Model

Damage is implemented using the effective configuration concept. Using the effective configuration concept substantially simplifies the numerical implementation of the damage model and avoids the complexities associated with the direct couplings of the viscoelastic and viscoplastic models to the damage model.

In other words, the stress in the effective configuration can be first updated using the viscoelastic and viscoplastic models. The damage force which is expressed in terms of the quantities in the effective configuration can be calculated and used to calculate the damage rate. The damage dynamic surface can be obtained using Eq. (2.45), such that:

$$\chi^{vd} = \left[\frac{\overline{Y}(1-\phi)}{Y_0}\right]^q \exp\left(k\overline{\varepsilon}_{eff}\right) - \frac{\dot{\phi}}{\Gamma^{vd}} = 0 \tag{2.69}$$

where $\overline{Y}$ is the damage force and χ^{vd} is the damage loading condition. A trial value for viscodamage loading surface can be defined as:

$$\chi^{vd,tr} = \left[\frac{\overline{Y}\left(1-\phi^{t-\Delta t}\right)}{Y_0}\right]^q \exp\left(k\overline{\varepsilon}_{eff}\right) - \frac{\Delta\phi^{t-\Delta t}}{\Gamma^{vd}\Delta t} = 0 \tag{2.70}$$

Very similar to viscoplasticity, the damage increment can be obtained using the Newton-Raphson scheme. However, it should be noted that the values of $\overline{Y}$ and $\overline{\varepsilon}_{eff}$ are constant during these trials, which substantially simplifies the implementation, since they are expressed in the healed configuration. However, the differential of the χ^{vd} with respect to $\Delta\phi$ is needed which can be expressed as follows:

$$\frac{\partial\chi^{vd}}{\partial\Delta\phi} = -\left(\frac{\overline{Y}}{Y_0}\right)\left[\frac{\overline{Y}(1-\phi)}{Y_0}\right]^{q-1} \exp\left(k\overline{\varepsilon}_{eff}\right) - \frac{1}{\Gamma^{vd}\Delta t} \tag{2.71}$$

Known $\bar{\sigma}$, $\bar{\varepsilon}^{ve}$, $\bar{\varepsilon}^{vp}$, g_α, $q_{ij,n}$, $\bar{p}$, $\Delta\bar{\gamma}^{vp}$ at time $t - \Delta t$

Given $\Delta\varepsilon^t$ which is equal to $\Delta\bar{\varepsilon}^t$.

Calculate trial stress $\bar{S}_{ij}^{tr,t}$ [Eq. (2.53)] and $\bar{\sigma}_{kk}^{tr,t}$ [Eq. (2.54)].

Yes

No

$f = \bar{\tau}^{vp} - \alpha\bar{I}_1 - \kappa \geq 0$

Put $\Delta\bar{\varepsilon}_{ij}^{vp,t} = 0$.

Recalculate g_α^t based on the current trial stress.

Calculate the consistent tangent compliance $\bar{S}_{ijkl}$ [Eq. (2.67)] and stress correction [Eq. (2.66)].

Calculate $\Delta\bar{e}_{ij}^{ve}$ and $\Delta\bar{\varepsilon}_{kk}^{ve}$ from Eqs. (2.49) and (2.50).

Calculate $\Delta\bar{\varepsilon}_{ij}^{vp}$ and $\Delta\bar{p}$ based on the current trial stress by using the local Newton-Raphson method [Eq. (2.64)].

Calculate the residual strain $\bar{R}_{ij}$ [Eq. (2.65)].

Correct trial stress [Eq.(2.66)].

No

$\|\bar{R}_{ij}^t\| \leq Tolerance$

No

Yes

Yes

Update $\bar{\sigma}$, $\bar{\varepsilon}^{ve}$, $\bar{\varepsilon}^{vp}$, g_α, $q_{ij,n}$, $\bar{p}$ at time t

Figure 2.6. The flow chart of the recursive-iterative Newoton-Raphson algorithm for implementation of the coupled viscoelastic-viscoplastic model.

Hence, the damage density increment at the $k+1$ iteration can be obtained as follows:

$$\left(\Delta\phi^{t}\right)^{k+1} = \left(\Delta\phi^{t}\right)^{k} - \left[\left(\frac{\partial\chi^{vd}}{\partial\Delta\phi^{t}}\right)^{k}\right]^{-1}\chi^{vd} \qquad (2.72)$$

The damage density ϕ can then be obtained, such that:

$$\phi^{t} = \phi^{t-\Delta t} + \dot{\phi}^{t}\Delta t \qquad (2.73)$$

Finally, Eq. (2.6) can be used to update the final nominal stress. It should be noted that the healing process is not included in this damage model. Hence, negative damage density rates are not accepted and are set to zero.

The above formulated numerical algorithms are implemented in the well-known commercial finite element code Abaqus (2008) via the user material subroutine UMAT. The finite element model considered here is simply a three-dimensional single element (C3D8R) available in Abaqus.

This subsection concludes the numerical implementation of the proposed viscoelastic-viscoplastic-viscodamage-healing model.

2.8. Application of the Model to Asphalt Concrete: Model Calibration

In this section, the presented thermo-viscoelastic-viscoplastic-viscodamage constitutive model is calibrated using a set of experimental data on asphalt concrete tested at different stress levels, strain rates, and temperatures. The asphalt concrete used in this study is described as 10 mm Dense Bitumen Macadam (DBM) which is a continuously graded mixture with asphalt binder content of 5.5%. Granite aggregates and an asphalt binder with a penetration grade of 70/100 are used in preparing the asphalt mixtures. Cylindrical specimens with a diameter of 100mm and a height of 100mm are compacted using the gyratory compactor. Single creep-recovery test under direct compression at the reference temperature is conducted to identify the viscoelastic and viscoplastic model parameters, whereas, two creep tests that include the tertiary creep response at the reference temperature are conducted to identify the viscodamage model parameters. The healing model parameters are also identified using the repeated creep-recovery test with

rest period at the reference temperature. The temperature coupling term parameters are then identified by comparing the results at different temperatures. Moreover, the parameters that distinguish between compressive and extensive loading conditions (i.e. d^{vp} and d^{vd}) are identified by comparing several tests in tension and compression.

Finally, the identified model parameters are used to predict the mechanical response of asphalt concrete over an extensive experimental data including creep-recovery, creep, constant strain rate test, and repeated creep-recovery tests over a range of temperatures, stress levels, loading-unloading times, and strain rates in both tension and compression. Table 2.1 lists the summary of the tests used for calibration of the model.

The procedure for identification of the viscoelastic, viscoplastic, and viscodamage model parameters is presented by Darabi et al. (2011c). The procedure for identification of the model parameters will be explained in the next sub-sections.

Table 2.1. The summary of the tests used to identify the model parameters.

	Test	Temperature (^{o}C)	Stress level (kPa)	Loading time (Sec)
Compression	Creep-recovery	20	1500	30
	Creep	10	2000	
		20	1000, 1500	
		40	500	
Tension	Creep	20	300, 500	

2.8.1. Identification of the Viscoelastic Model Parameters

The first step in calibration process is to determine the viscoelastic model parameters at the reference temperature. To achieve this, the viscoelastic and viscoplastic responses in the recovery part of a single creep-recovery test should be separated. The advantage of conducting a creep-recovery test is that the viscoplastic strain during the recovery remains constant which makes it possible to separation the viscoelastic and viscoplastic strains. Figure 2.7 (a) shows a schematic single creep-recovery test in which the stress

level σ is kept constant up to time t_a and is removed after time t_a. The strain response of the creep-recovery loading [Figure 2.7 (a)] is presented in Figure 2.7 (b).

It should be noted that the stress level in the conducted creep-recovery test should be low and/or the loading time should be short such that the material does not get damaged or at least the induced damage can be assumed to be negligible. The strain response at the end of the loading time t_a can be decomposed into viscoelastic and viscoplastic components, such that:

$$\overline{\varepsilon}\left(t_a\right) = \overline{\varepsilon}^{ve}\left(t_a\right) + \overline{\varepsilon}^{vp}\left(t_a\right) \tag{2.74}$$
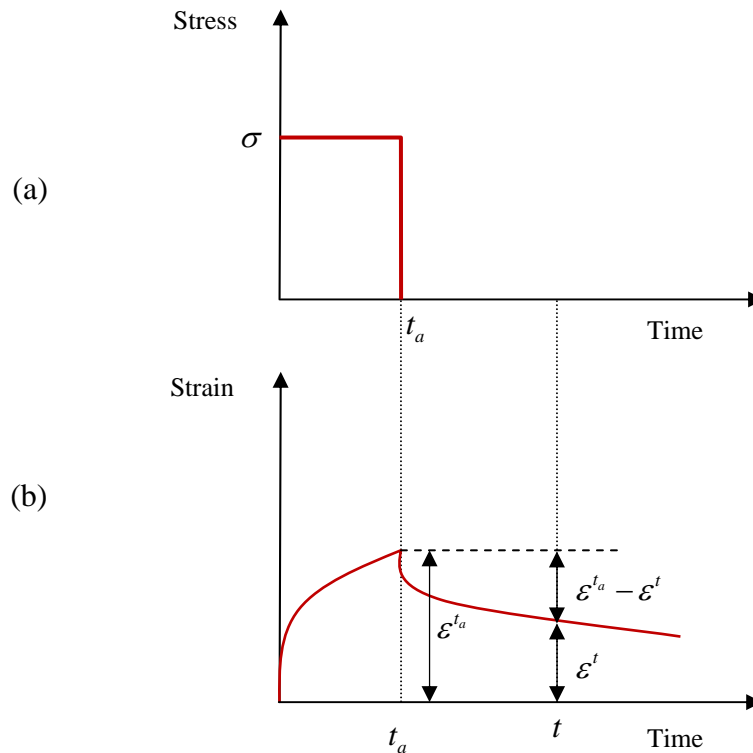
Figure 2.7. A schematic creep-recovery test.

The same strain decomposition can be assumed for any time t after the unloading time t_a (i.e. $t > t_a$). However, the stress is zero during the recovery. Hence, the viscoplastic strain remains constant after the unloading time t_a (i.e.

$\overline{\varepsilon}^{vp}\left(t \geq t_a\right) = \overline{\varepsilon}^{vp}\left(t_a\right)$). Hence, one can write the following strain decomposition at point $t \geq t_a$:

$$\overline{\varepsilon}\left(t \geq t_a\right) = \overline{\varepsilon}^{ve}\left(t\right) + \overline{\varepsilon}^{vp}\left(t_a\right) \tag{2.75}$$

Subtracting Eq. (2.75) from Eq. (2.74) and calculating $\overline{\varepsilon}^{ve}\left(t_a\right)$ and $\overline{\varepsilon}^{ve}\left(t\right)$ using Eqs. (2.7) and (2.9) yield:

$$\Delta\overline{\varepsilon}_1^{ve} = \overline{\varepsilon}\left(t_a\right) - \overline{\varepsilon}^{ve}\left(t\right) = g_0 D_0 \overline{\sigma} + g_1 g_2 \left[\Delta D\left(t_a\right) - \Delta D\left(t\right) + \Delta D\left(t - t_a\right)\right]\overline{\sigma} \tag{2.76}$$

A low stress level is applied in this creep-recovery test and , hence, the nonlinear viscoelastic parameters can be assumed to be one (i.e. $g_0 = g_1 = g_2 = 1$). Therefore, Eq. (2.76) can be simplified as follows for low stress levels:

$$\Delta\overline{\varepsilon}_1^{ve} = \overline{\varepsilon}\left(t_a\right) - \overline{\varepsilon}^{ve}\left(t\right) = D_0 \overline{\sigma} + \left[\Delta D\left(t_a\right) - \Delta D\left(t\right) + \Delta D\left(t - t_a\right)\right]\overline{\sigma} \tag{2.77}$$

$\Delta\overline{\varepsilon}_1^{ve}$ can be calculated for each test data in the recovery region. Note that the right hand side of Eq. (2.77) is only a function of viscoelastic properties. Therefore, the linear viscoelastic model parameters D_n and λ_n (i.e. the Prony series coefficients, Eq. (2.9)) can be identified by minimizing the error between the experimental measurements for $\Delta\varepsilon_1^{ve}$ and Eq. (2.77).

2.8.2. Identification of the Viscoplastic Model Parameters

The next step in the model calibration process is to identify the viscoplastic model parameters. Basically, the creep part of the analyzed creep-recovery test [Figure 2.7] can be used to identify the viscoplastic model parameters at the reference temperature. In other words, the viscoplastic strain in the creep part can be obtained by subtracting the model prediction for the viscoelastic strain (using the viscoelastic model parameters obtained in the previous sub-section) from the total experimental measurements.

The dynamic viscoplastic yield surface in Eq. (2.60) for a uniaxial compression step-loading is expressed as:

$$\chi = \overline{\sigma} - \alpha\frac{\overline{\sigma}}{3} - \left[\kappa_0 + \kappa_1\left(1 - \exp\left(-\kappa_2\overline{p}\right)\right)\right] - \sigma_0^y\left(\frac{\dot{\overline{\gamma}}^{vp}}{\Gamma^{vp}}\right)^{\frac{1}{N}} \cong 0 \tag{2.78}$$

where $\bar{\sigma}$ is the applied uniaxial compressive stress. Rearranging Eq. (2.78) yields:

$$\frac{\Delta \bar{\gamma}^{vp}}{\Delta t} = \Gamma^{vp} \left(\frac{\bar{\sigma} - \alpha \dfrac{\bar{\sigma}}{3} - \left[\kappa_0 + \kappa_1 \left(1 - \exp\left(-\kappa_2 \bar{p}\right)\right)\right]}{\sigma_0^y} \right)^N \tag{2.79}$$

where $\Delta \bar{\gamma}^{vp}$ can be obtained using the separated viscoplastic strain in the creep region $\Delta \varepsilon_1^{vp,t}$ using the following expression [Eq. (2.57)]:

$$\Delta \bar{\gamma}^{vp} = \frac{\Delta \bar{\varepsilon}_1^{vp,t}}{\left(1 - \dfrac{\beta}{3} \right)} \tag{2.80}$$

Moreover, the effective viscoplastic strain for the uniaxial compression can be calculated using Eq. (2.59) as follows:

$$\Delta \bar{p} = \frac{1}{a} \sqrt{\left(\Delta \bar{\varepsilon}_1^{vp} \right)^2 + 2 \left(\Delta \bar{\varepsilon}_2^{vp} \right)^2} \tag{2.81}$$

where $a = \sqrt{1 + 2 \left(\dfrac{0.5 + \beta/3}{1 - \beta/3} \right)^2}$. $\Delta \bar{\varepsilon}_1^{vp}$ and $\Delta \bar{\varepsilon}_2^{vp}$ are the axial and radial viscoplastic strain increments, respectively. However, the available experimental data does not include $\Delta \bar{\varepsilon}_2^{vp}$. Hence, one can calculate $\Delta \bar{\varepsilon}_2^{vp}$ using Eq. (2.19), such that:

$$\frac{\Delta \bar{\varepsilon}_2^{vp,t}}{\Delta \bar{\varepsilon}_1^{vp,t}} = - \left(\frac{\partial \bar{F}}{\partial \bar{\sigma}_{22}} \right) \Big/ \left(\frac{\partial \bar{F}}{\partial \bar{\sigma}_{11}} \right) = \frac{1.5 + \beta}{3 - \beta} \tag{2.82}$$

Once $\Delta \bar{p}$ is calculated from the analyzed experimental data using Eqs. (2.80) and (2.81), the viscoplastic model parameters Γ^{vp}, N, κ_0, κ_1, and κ_2 can be identified by minimizing the error between the measurements and Eqs. (2.79) and (2.81).

Figure 2.8 shows the separation of the viscoelastic and viscoplastic strains at the reference temperature (i.e. $T = 20^o C$) when the applied stress is 1500 kPa and the loading time is 30 sec. As mentioned before, the shortest loading time is selected to identify the viscoelastic and viscoplastic model parameters such that one can reasonably assume that the induced damage is negligible at these loading conditions. The viscoelastic and viscoplastic model parameters can now be identified by fitting the

separated viscoelastic and viscoplastic strains as shown in Figure 2.8(b). Finally, the model predictions and experimental measurements for the total strain at the reference temperature are presented in Figure 2.8(c).
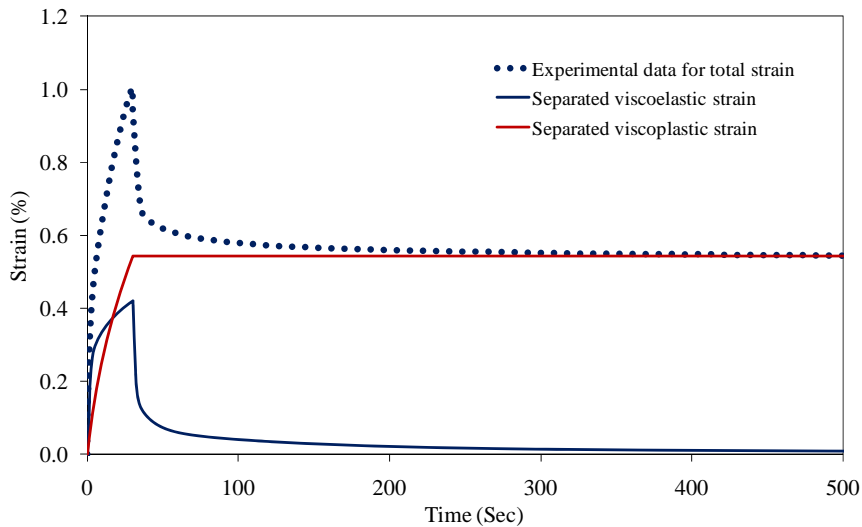
(a)
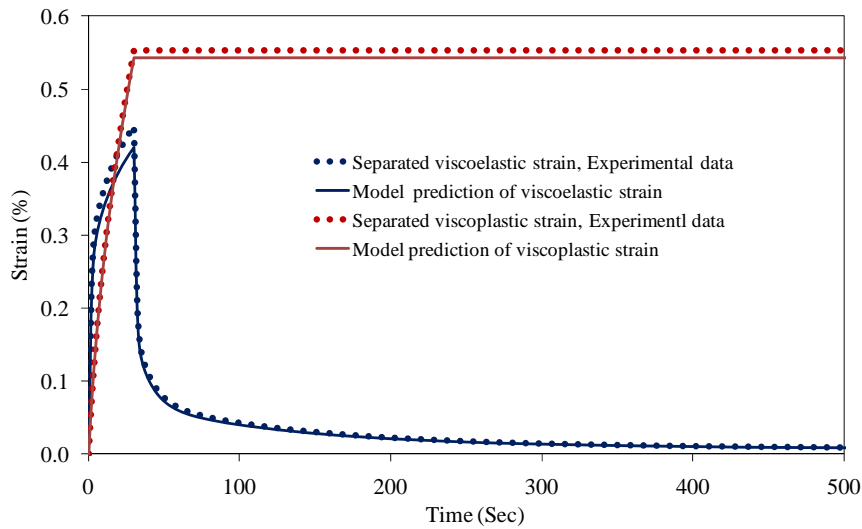
(b)

Figure 2.8. Identification of the viscoelastic and viscoplastic model parameters using a creep-recovery test at the reference temperature (i.e. $T = 20^{o}C$) when the applied stress is 1500kPa and the loading time is 30 sec. (a) Separation of the viscoelastic and viscoplastic strains using the experimental data; (b) Experimental and model predictions for the viscoelastic strain and the viscoplastic strain; (c) Experimental and model prediction of the total strain.
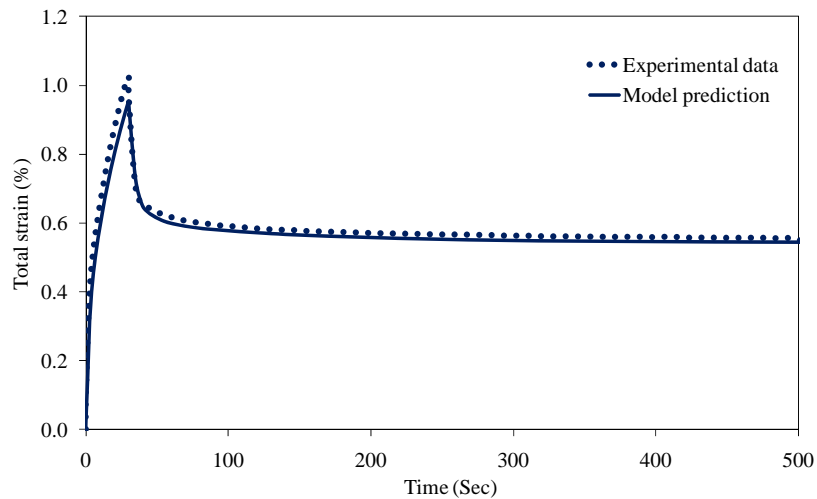
(c)

Figure 2.8. Continued.

2.8.3. Identification of the Viscodamage Model Parameters

The loading times in the creep-recovery tests conducted to identify the viscoelastic and viscoplastic model parameters are too short for the material to get damaged. However, in other tests such as the creep tests, the load usually remains on the specimen until failure. The loading time in these tests are long enough for damage to evolve causing the secondary and tertiary creep responses. The damage model is calibrated using the secondary and tertiary creep responses in a creep test since these regions are mostly caused by damage. Moreover, during the creep loading, healing does not occur in the material which makes it possible to calibrate the damage model independent of the healing effects. To calibrate the viscodamage model at the reference temperature (i.e. $T = 20^{o}C$), the identified viscoelastic and viscoplastic model parameters at the reference temperature are used to predict the creep tests. These predictions usually match for the initial response and start deviating from the experimental measurements in secondary and tertiary creep regions. This deviation should be compensated for by using the viscodamage model.

At the reference temperature, the viscodamage temperature coupling term has the value of one [i.e. $G(T_0) = 1$]. Therefore, at the reference temperature, Eq. (2.45) simplifies as follows:

$$\dot{\phi} = \Gamma_0^{vd} \left[\frac{\overline{Y}(1-\phi)^2}{Y_0} \right]^q \exp\left(k\overline{\varepsilon}_{eff}\right) \tag{2.83}$$

The first step in identifying the viscodamage model parameters is to select an arbitrary reference stress level (which is selected to be 1000kPa in this work). The reference damage force Y_0 can be calculated easily using Eq. (2.42) as the reference damage force. The damage evolution law of Eq. (2.83) can be expressed in terms of the damage force in the nominal configuration by making use of Eq. (2.43), such that:

$$\dot{\phi} = \Gamma_0^{vd} \left[\frac{Y}{Y_0} \right]^q \exp(k\overline{\varepsilon}_{eff}) \tag{2.84}$$

However, the nominal stress during the creep test is constant. Hence, at the reference stress level, the damage force Y is the damage force at the reference stress level. Therefore, at the reference stress level, Eq. (2.84) can be simplified further as:

$$\dot{\phi} = \Gamma_0^{vd} \exp(k\overline{\varepsilon}_{eff}) \tag{2.85}$$

Now, the damage viscosity parameter Γ^{vd} and the strain dependency parameter k can be identified using a creep test at the reference temperature and stress level. The viscodamage stress dependency parameter q can finally be identified by comparing the experimental results and model predictions for a creep at another stress level (i.e. 1500kPa in this work) which is different from the reference stress level.

The identified model viscoelastic-viscoplastic-viscodamage model parameters at the reference temperature are listed in Table 2.2.

Figure 2.9 shows the comparison between the model prediction and the experimental data for those creep tests that have been used to identify the viscodamage model parameters. Figure 2.9 clearly shows that the model is capable of capturing both secondary and tertiary behavior in the creep test.

Table 2.2. The identified viscoelastic-viscoplastic-viscodamage model parameters at the reference temperature.

Viscoelastic model parameters					
n	1	2	3	4	5
λ_n (sec^{-1})	10	1	0.1	0.01	0.001
D_n (kPa^{-1})	1.98×10^{-7}	1.48×10^{-6}	6.56×10^{-7}	1.43×10^{-6}	2.74×10^{-6}
D_0 (kPa^{-1})	3.5×10^{-6}				

Viscoplastic model parameters						
α	β	Γ^{vp} (sec^{-1})	N	κ_0 (kPa)	κ_1 (kPa)	κ_2
0.3	0.15	5×10^{-4}	3.63	35	610	215

Viscodamage model parameters			
Γ^{vd} (sec^{-1})	Y_0 (kPa)	q	k
4×10^{-5}	700	5	30
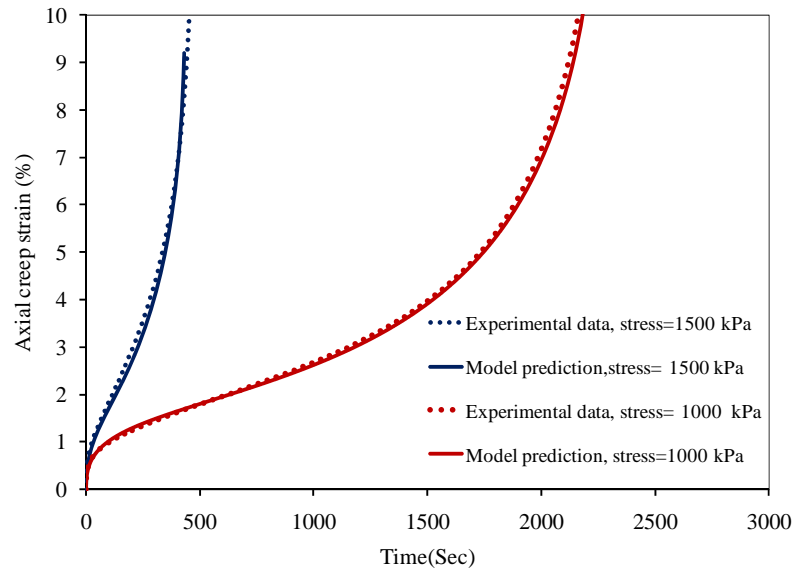
Figure 2.9. Model predictions and experimental measuremenst for the creep test at the reference temperature (i.e. $T = 20^o C$) and two different stress levels. These two test are used to identify the viscodamage model parameters.

2.8.4. Identification of the Model Parameters Distinguishing between Loading Modes

One of the main advantages of the model is the presence of two parameters d^{vp} and d^{vd} that enables the model to distinguish between the compressive or extension mode of loadings. d^{vp} is a material parameter representing the sensitivity of yield behavior to the

hydrostatic pressure $\bar{I}_1$. This parameter can also be defined as the ratio of the yield strength in uniaxial tension to that in uniaxial compression (i.e. $d^{vp} = \bar{\sigma}_y^t / \bar{\sigma}_y^c$). Similarly, d^{vd} captures the different damage responses in extension and compression. In fact, d^{vd} magnifies the damage force $\bar{Y}$ in tensile loading modes. These two parameters can be obtained by comparing experimental measurements and model predictions in tension and compression. In this study, $d^{vp} = 0.78$ and $d^{vp} = 0.16$ are identified. Figure 2.10 shows the model prediction and experimental measurements of the creep test at 20$^\text{o}$C when the applied tensile stresses are 300kPa and 500kPa. Figure 2.10 clearly shows that using d^{vp} and d^{vd} parameters enhance the model predictions through distinguishing the behaviors in tension and compression.
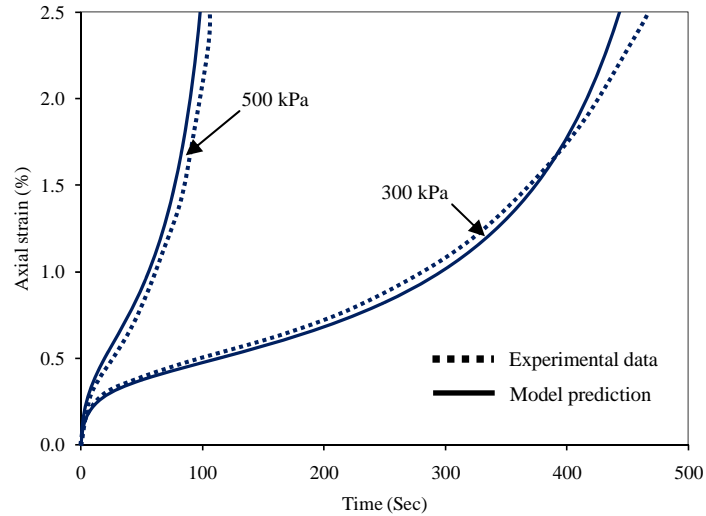
Figure 2.10. Model predictions and experimental measuremenst for the creep test in tension at 20$^\text{o}$C and different stress levels. These tests are utilized to identify d^{vp} and d^{vd} model parameters.

2.8.5. Identification of the Temperature Coupling Term Model Parameters

It is not convenient to introduce a whole different set of material parameters for each temperature as done by Abu Al-Rub et al. (2009) and Huange et al. (2011a). Therefore,

in this study, the model's ability to predict the response at other temperatures is achieved through the temperature coupling terms as discussed next.

The viscoelastic-viscoplastic material responses at other temperatures can be captured using the temperature time-shift factor for both viscoelasticity and viscoplasticity. The reduced time concept [Eq. (2.8)] can be used for introducing the temperature time-shift factor a_T^{ve} in the viscoelasticity constitutive equations; whereas, the viscoplasticity constitutive equations are coupled to temperature by replacing the time increment Δt with the reduced time increment $\Delta t / a_T^{vp}$, such that the dynamic viscoplasticity yield surface in Eq. (2.60) can be rewritten as follows:

$$\chi = \overline{\tau}^{vp} - \alpha \overline{I}_1 - \kappa(\overline{p}) - \sigma_y^0 \left(\frac{\Delta \overline{\gamma}^{vp}}{\frac{\Delta t}{a_T^{vp}} \Gamma^{vp}} \right)^{1/N} \leq 0 \tag{2.86}$$

where a_T^{vp} is the viscoplasticity temperature coupling term or the viscoplasticity temperature time-shift factor. Note that Eq. (2.86) implies that the viscoplasticity temperature coupling term should also be introduced in the viscoplasticity flow rule, Eq. (2.19), such that:

$$\Delta \overline{\varepsilon}_{ij}^{vp,t} = \Gamma^{vp} \left\langle \Phi(\overline{f}) \right\rangle^N \left(\frac{\Delta t}{a_T^{vp}} \right) \frac{\partial \overline{F}}{\partial \overline{\sigma}_{ij}} \tag{2.87}$$

In this study, the same temperature coupling terms are assumed for both the viscoelastic and viscoplastic models (i.e. $a_T = a_T^{ve} = a_T^{vp}$) as suggested by the experimental study of Schwartz et al. (2002) on asphalt mixtures. The values of the viscoelastic and viscoplastic temperature coupling parameters are obtained from the creep-recovery tests at different temperatures. The creep compliance $D(t)$ can be calculated using experimental data at different temperatures [see Figure 2.10] using the following relation:

$$D(t) = \frac{\overline{\varepsilon}(t)}{\overline{\sigma}} \tag{2.88}$$

Figures 2.11 (a) and (b) show the experimental data at different temperatures before and after shifting, respectively. By shifting the experimental data horizontally, one can get the viscoelastic-viscoplastic temperature time-shift factor, a_T, for each temperature.

(a)

(b)
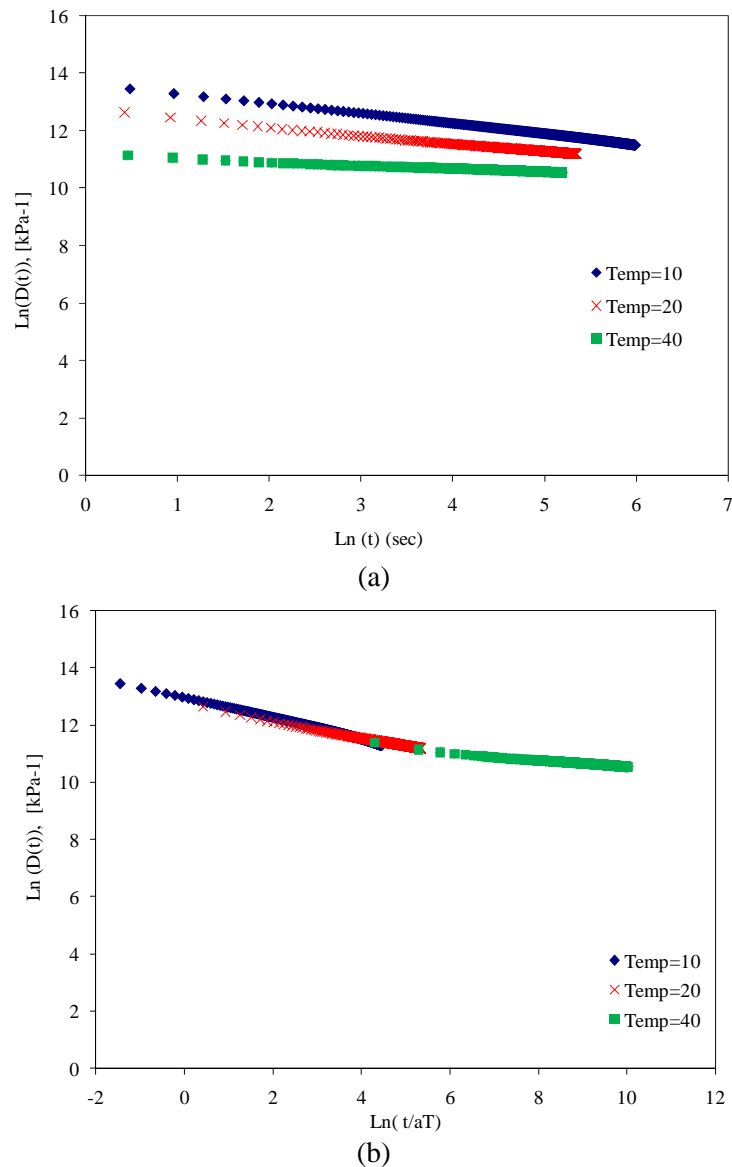
Figure 2.11. Experimental data for creep compliance at $T = 10$, 20, and $40^o C$. (a) Before applying the temperature time-shift factor. (b) After applying the temperature time-shift factor.

The reduced time (or time-shift) concept as used in viscoelasticity and viscoplasticity for including temperature effects can also be used in the viscodamage model for predicting the damage evolution in asphalt mixes at different temperatures.

Similarly, one can replace the time increment Δt in the damage evolution equation [Eq. (2.45)] with the reduced time $\Delta t / a_T^{vd}$, such that Eq. (2.45) can be rewritten as:

$$\Delta \phi = \Gamma_0^{vd} \left(\frac{Y}{Y_0} \right)^q \exp\left(k \overline{\varepsilon}_{eff} \right) \frac{\Delta t}{a_T^{vd}} \tag{2.89}$$

where $a_T^{vd} = \dfrac{1}{G(T)}$ is the viscodamage temperature time-shift factor. In this study, two creep tests at temperatures 10^oC and 40^oC are used to determine the temperature coupling terms. Figure 2.12 represents the model predictions and experimental measurements for the creep test at 10^oC and 40^oC. These two tests are used in order to identify the temperature coupling term model parameters.
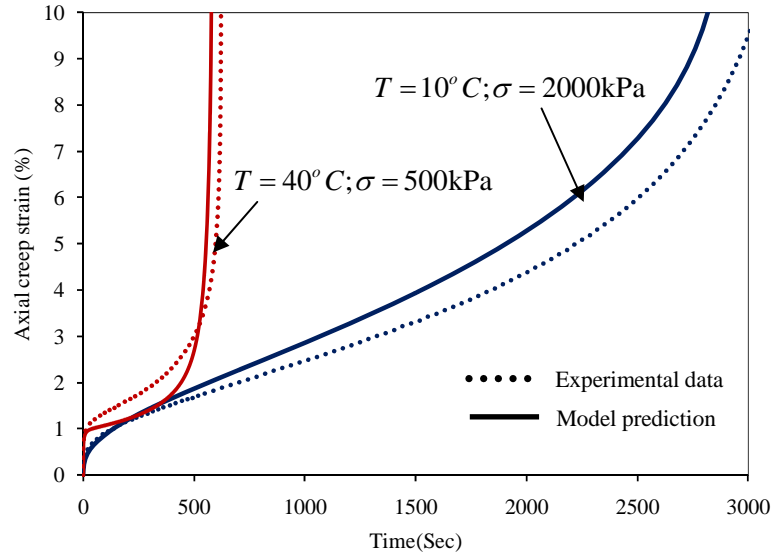
Figure 2.12. Model predictions and experimental measuremenst for the creep test at different temperatures in order to identify the temperature coupling term parameters for the viscodamage model.

Arrhenius-type equations are used for expressing the viscoelastic, viscoplastic, and viscodamage temperature coupling terms, such that one can write:

$$a_T = a_T^{vp} = \exp\left[-\delta_1\left(1-\frac{T}{T_0}\right)\right] \qquad (2.90)$$

$$a_T^{vd} = \exp\left[-\delta_2\left(1-\frac{T}{T_0}\right)\right] \qquad (2.91)$$

where δ_1 and δ_2 are material parameters and T_0 is the reference temperature. . The identified temperature coupling term parameters are listed in Table 2.3.

Table 2.3. Temperature coupling term model parameters [Eqs. (2.90) and (2.91)].

δ_1	δ_2
-4.64	-5.89

It is noteworthy that assuming the same temperature time-shift factor for both viscoelasticity and viscoplasticity saves significant amount of experimental tests needed for calibrating the thermo-viscoplastic response of asphaltic materials. Figure 2.13 shows the flowchart for obtaining the model parameters in a systematic manner.

Separate viscoelastic response in the recovery part of the creep-recovery tests using Eq. (2.76).

↓

Identify the Prony series coefficients D_n and λ_n at the reference temperature using Eqs. (2.9) and (2.76).

↓

Calculate $\Delta\bar{\varepsilon}_1^{vp}$, $\Delta\bar{\varepsilon}_2^{vp}$, and $\Delta\bar{p}$ from the creep part of the creep-recovery tests using Eqs. (2.80), (2.81), and (2.82).

↓

Identify the viscoplastic model parameters at the reference temperature by minimizing the error between the experimental measurements and Eq. (2.79).

↓

Identify Γ^{vd} and k from a creep test at the reference temperature and stress level using Eq. (2.85).

↓

Identify viscodamage stress dependency parameter q from a creep test at the reference temperature, when $\sigma \neq \sigma_{ref}$ using Eq. (2.84).

↓

Identify temperature coupling terms model parameters by comparing experimental data and model predictions at different temperatures using Eqs. (2.90) and (2.91).

↓

Identify d^{vp} and d^{vp} from two creep tests in tension using Eqs. (2.23) and. (2.44).

Figure 2.13. The procedure for identification of the thermo-viscoelastic-viscoplastic-viscodamage constitutive model parameters.

2.9. Application of the Model to Asphalt Concrete: Model Validation

The identified model parameters listed in Tables 2.2 and 2.3 are used to validate the model against another set of experimental data listed in Table 2.4 which have not been used in the calibration process. Table 2.4 shows that the model is to be validated against different sets of experimental data including creep-recovery, creep, repeated creep-recovery, and uniaxial constant strain rate tests in both tension and compression at different temperatures, stress levels, and strain rates.

Table 2.4. The summary of the tests used for validating the model.

	Test	Temperature (^oC)	Stress level (kPa)	Loading time (Sec)	Strain rate (Sec^{-1})
Compression	Creep-recovery	10	2000	400, 600	
			2500	350, 300	
		20	1000	40, 210	
			1500	130	
		40	500	130, 180	
			750	35	
	Creep	10	2500		
		40	750		
	Constant strain rate	10			0.005, 0.0005, 0.00005
		20			0.005, 0.0005, 0.00005
		40			0.005, 0.0005
	Repeated creep-recovery	20	1500	120 (100)*, 60 (100), 60 (1500)	
Tension	Creep	10	500, 1000, 1500		
		20	700		
		35	100, 150		
	Constant strain rate	20			0.0167, 0.00167
	Repeated creep-recovery	20	300	120 (100), 60 (50), 60 (100), 60 (1500)	

*Unloading time in second.

2.9.1. Model Validation against Creep-Recovery Tests

Creep-recovery tests at 10, 20, and 40°C for different stress levels and loading times are conducted in this section in order to validate the model. Model predictions and experimental measurements for the creep-recovery test in compression at temperatures 10, 20 , and 40^oC are shown in Figures 2.14, 2.15, and 2.16, respectively. Figures 2.14 and 2.15 show that at temperatures 10^oC and 20^oC the model can reasonably predict the experimental data at different stress levels and loading times. Figure 2.16 shows that the model underestimates the experimental measurements at temperature 40^oC at tress level 500 kPa. Although Figure 2.16 shows that the model yields reasonable predictions at stress level 750 kPa, more experimental measurements at high temperatures are still needed to more accurately identify the viscoelastic-viscoplastic temperature coupling terms.
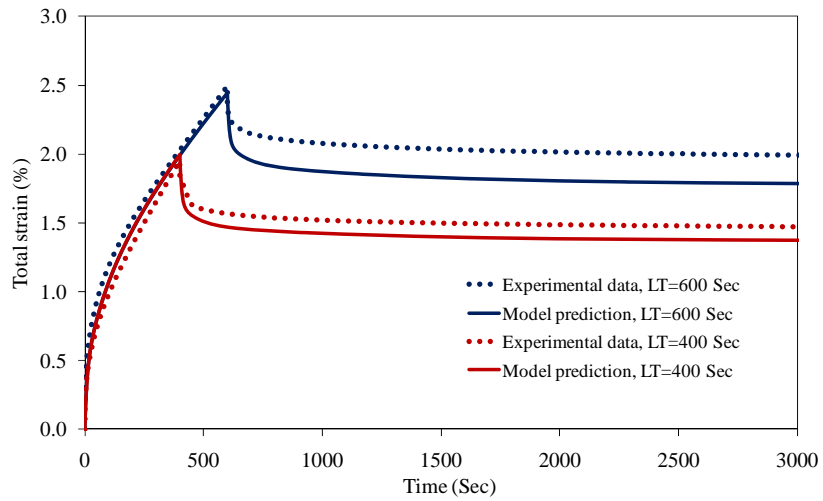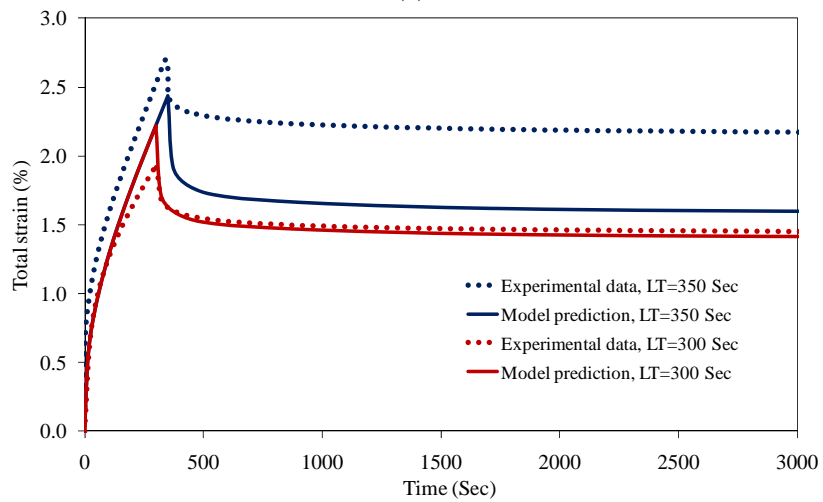
Figure 2.14. Experimental measurements and model predictions for creep-recovery test in compression at $T = 10^o C$; (a) $\sigma = 2000$ kPa, (b) $\sigma = 2500$ kPa.
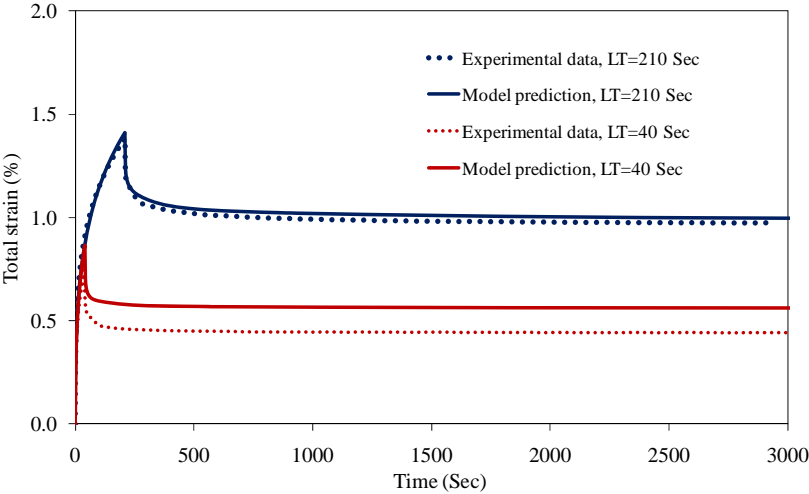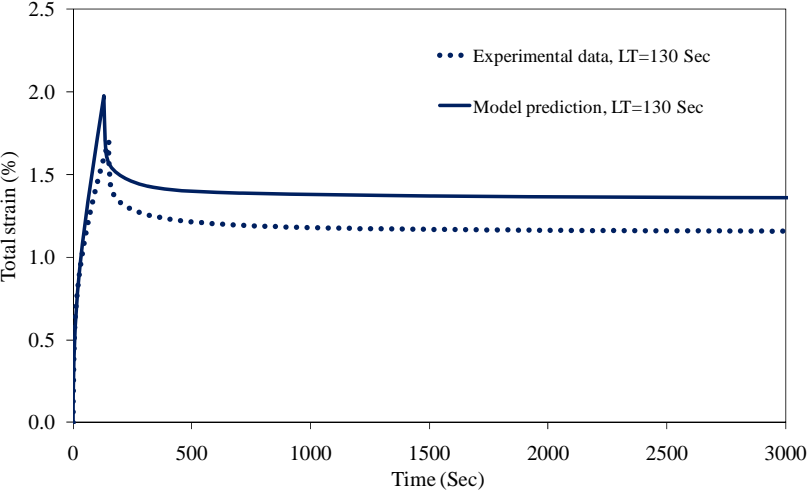
Figure 2.15. Experimental measurements and model predictions for creep-recovery test in compression at $T = 20^{o}C$; (a) $\sigma = 1000$ kPa, (b) $\sigma = 1500$ kPa.
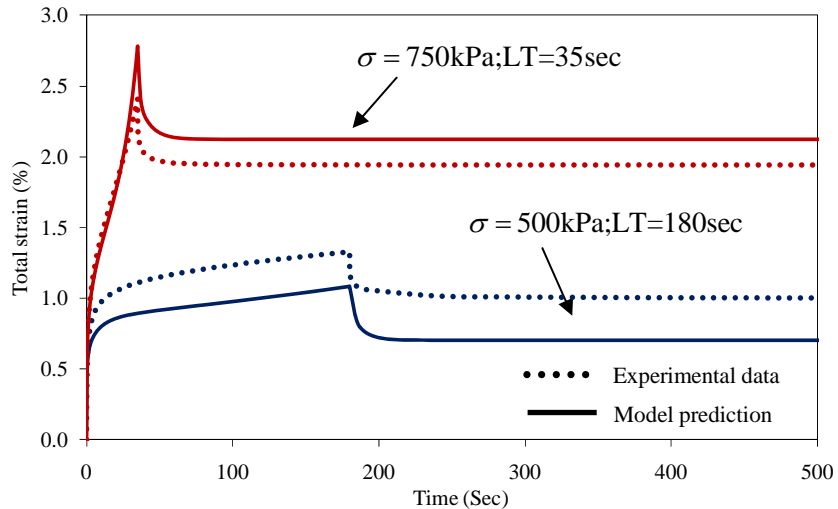
Figure 2.16. Experimental measurements and model predictions for creep-recovery test in compression at $T = 40^o C$.

2.9.2. Model Validation against Creep Tests

Figure 2.17 shows the model predictions and experimental measurements for creep test in compression for different temperatures and stress levels. Figure 2.17 shows that the model is able to capture the tertiary behavior very close to the experimental measurements. It is noteworthy that the failure time changes drastically from thousands of seconds to couple of hundred seconds as the stress level changes. Figure 2.17(b) shows that even at temperature $40^o C$ the model can capture secondary and tertiary creep reasonably.

The model is further validated by comparing the model predictions and experimental measurements for the creep tests in tension at different temperatures and stress levels. Model predictions and experimental measurements for the creep-test in tension for a range of temperatures and stress levels are compared in Figure 2.18.
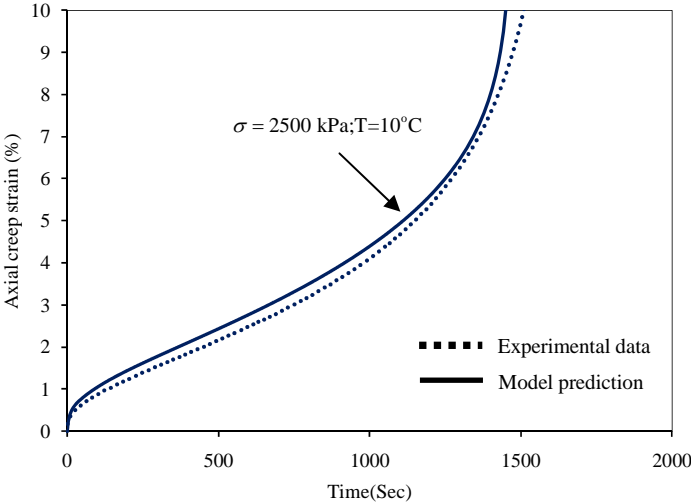
(a)
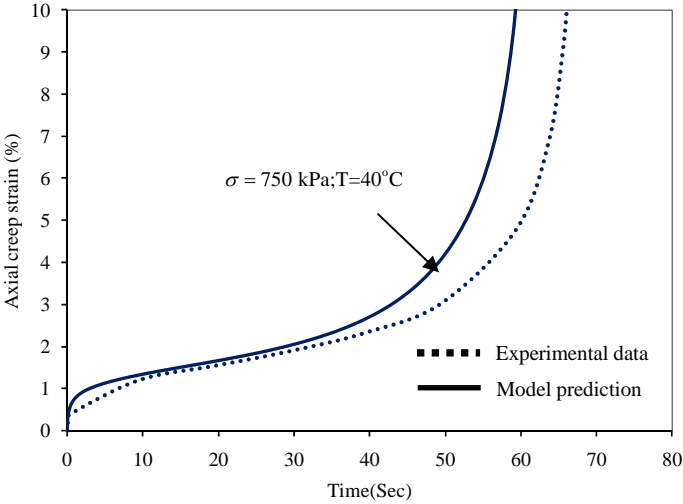
(b)

Figure 2.17. Experimental measurements and model predictions for the creep test in compression at different temperatures and stress levels. (a) $T = 10^o C; \sigma = 2500 \text{kPa}$; (b) $T = 40^o C; \sigma = 750 \text{kPa}$.
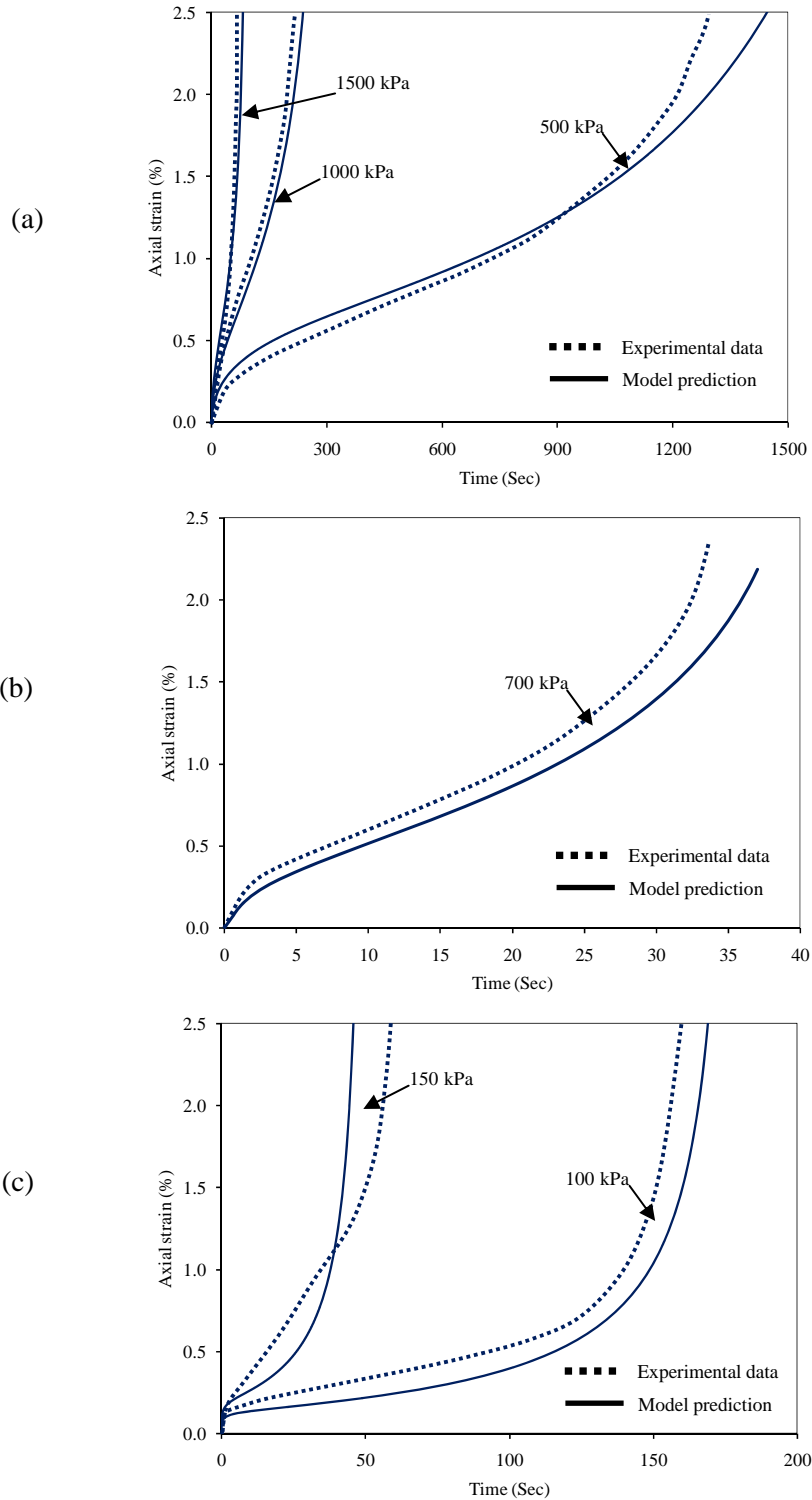
Figure 2.18. Experimental measurements and model predictions for creep test in tension. (a) $T = 10^o C$; (b) $T = 20^o C$; (c) $T = 35^o C$.

Figure 2.18 shows that the model is also capable of predicting the tertiary behavior in tension. This figure shows that at temperatures 10 and $20^o C$ the model can predict the experiments well. Although model predictions and experimental measurements are not quite the same at temperature $35^o C$, the model can still predict the tertiary behavior rather reasonably. It should be mentioned that the distinction between compression and tension is brought to the model through d^{vp} and d^{vd} parameters.

2.9.3. Model Validation against Uniaxial Constant Strain Rate Tests

Different predictions are conducted in this chapter to validate the model in capturing the time-, temperature-, and rate-dependent properties of bituminous materials. Therefore, the model is also validated against the monotonic uniaxial constant strain rate tests in compression at different temperatures in order to test the model capability in capturing the temperature-dependent response of bituminous materials. Figure 2.19 shows the stress-strain plots at different temperatures when the strain rate is 0.005/sec. Figure 2.19 clearly shows that the model is able to capture the temperature effects on the initial, peak point, and post peak responses in the stress-strain diagram using the identified model parameters presented in Tables 2.2 and 2.3. The plots of the predicted damage density versus the total strain for strain rate of 0.005/sec is shown in Figure 2.19(b). Figure 2.19(b) shows that the damage density is close to zero at low strain levels and increases as strain and stress levels increases. However, the rate of damage decreases after the strain reaches close to 3%. This strain level corresponds to the strain at which the maximum value of the stress occurs. This behavior is due to the presence of the damage history term [i.e. $(1-\phi)^2$] in the damage model in Eq. (2.45). In other words, the history term causes the damage rate to decrease after the stress-strain peak point. Hence, one may consider the inflection point of the damage-strain diagram as the strain corresponds to the peak stress at the stress-strain diagram.
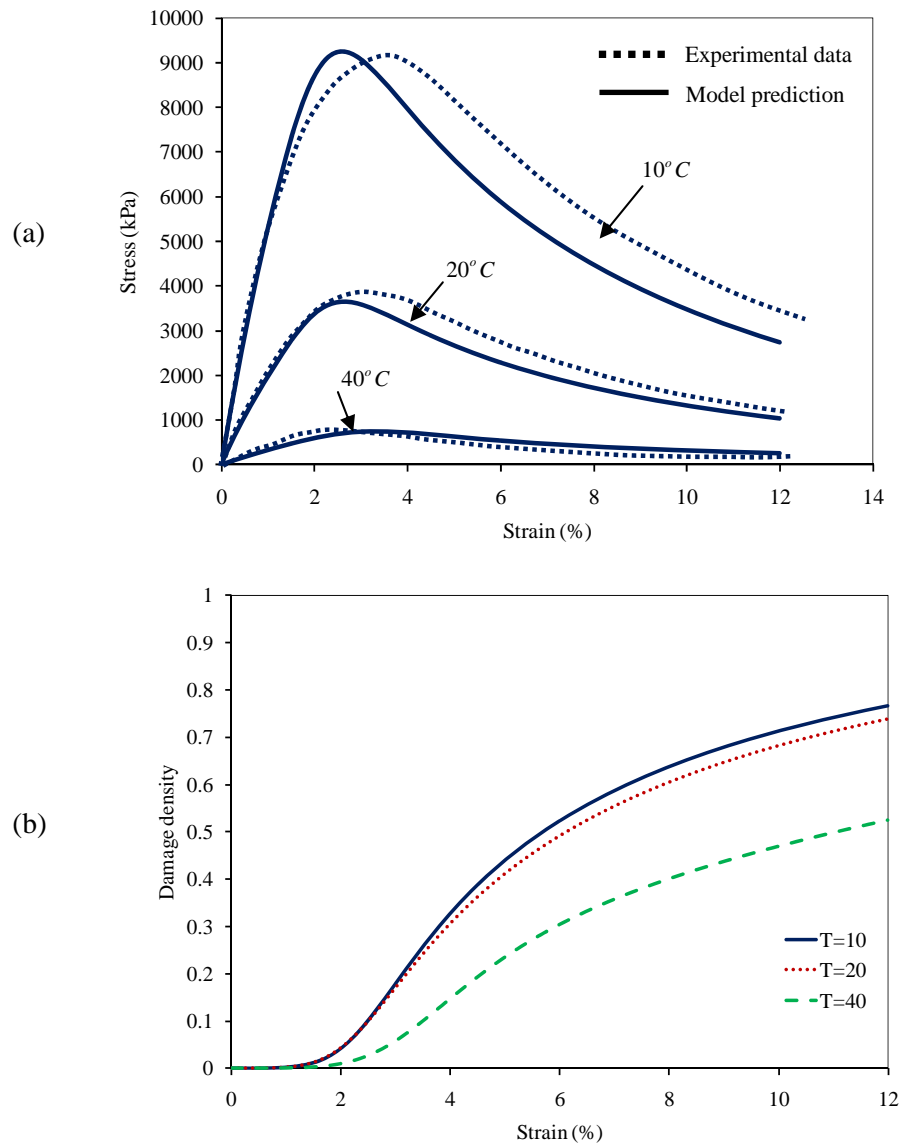
Figure 2.19. (a) Comparison of experimental measurements and model predictions for the constant strain rate test in compression when $\dot{\varepsilon} = 0.005$ sec^{-1}. (b) Damage density versus strain for model predictions presented in (a).

Moreover, the presence of the history term causes the damage-strain diagram to have the S-like shape which is intuitively sound. Furthermore, Figure 2.19(b) shows that at the same strain level the damage density at low temperatures is higher than the damage density at high temperatures. This behavior is expected for bituminous materials

since they are more susceptible to damage at low temperatures. Moreover, the same test (i.e. constant strain rate test is conducted at two other strain rates of 0.0005/sec, and 0.00005/sec to test the model capability in capturing the rate-dependent response of bituminous materials. Figures 2.20(a) and 2.21(a) show that the model can reasonably predict experimental data at different strain rates as well.

(a)

(b)
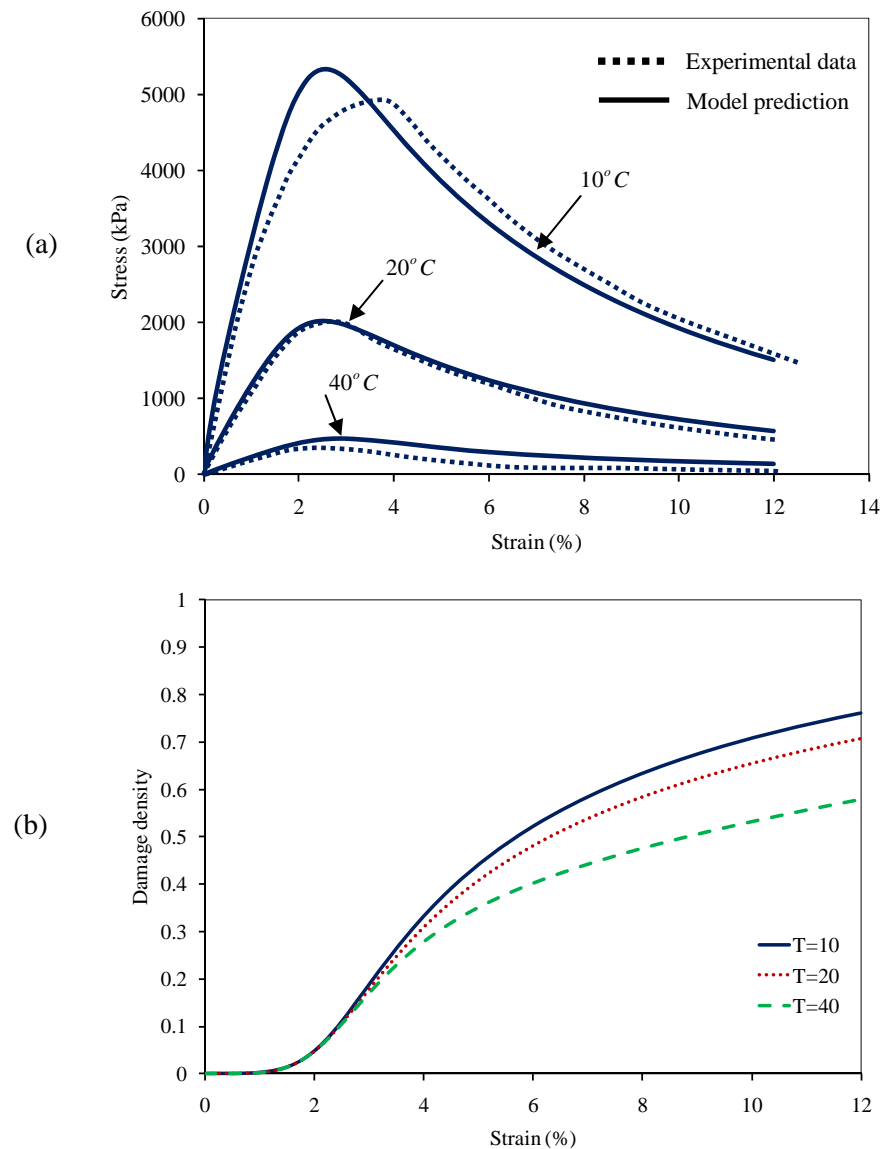
Figure 2.20. (a) Comparison of experimental measurements and model predictions for the constant strain rate test in compression when $\dot{\varepsilon} = 0.0005\,\text{sec}^{-1}$. (b) Damage density versus strain for model predictions presented in (a).

Figures 2.19-2.21 clearly show that the model can reasonably predict the rate and temperature effects on the initial, peak point, and post peak responses of bituminous materials. The plots of the predicted damage density versus the total strain for strain rates 0.0005, and 0.00005/sec are shown in Figures 2.20(b) and 2.21(b), respectively.
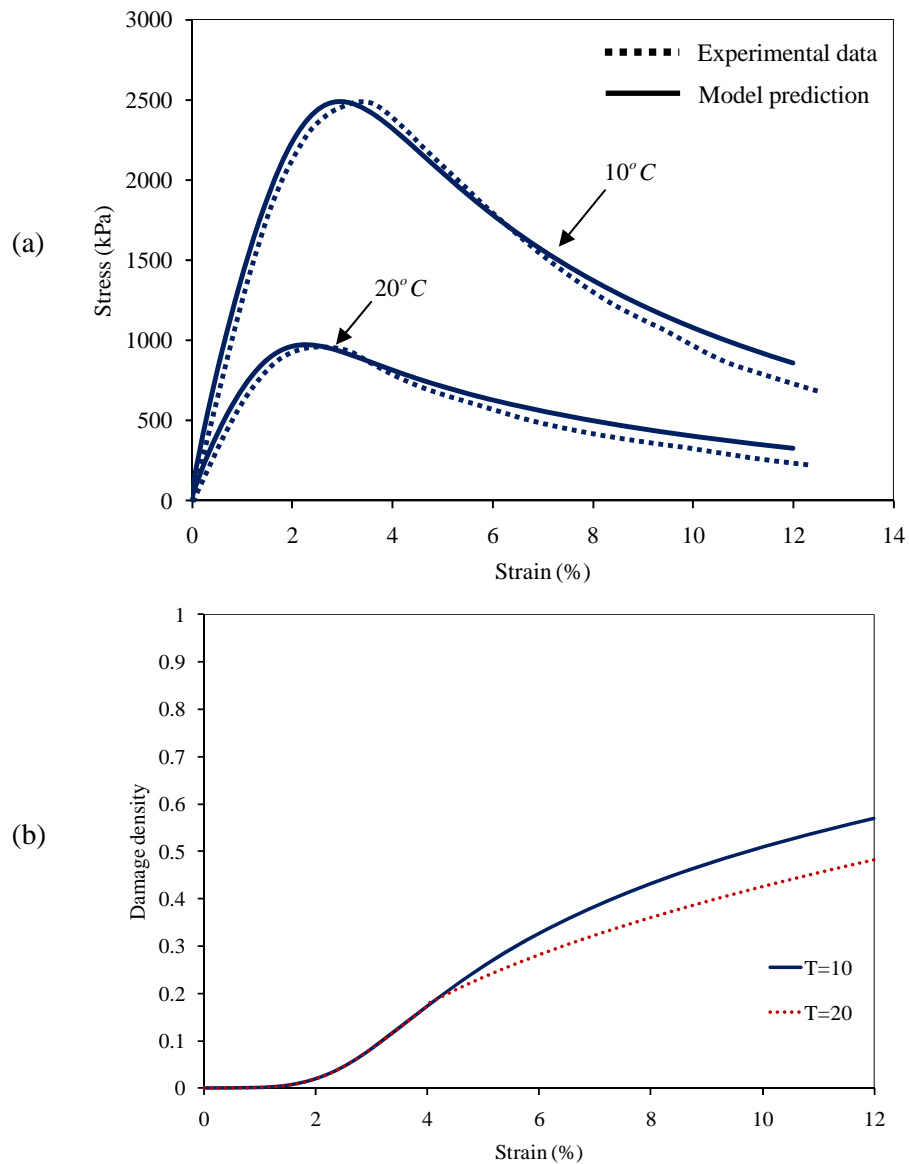
Figure 2.21. (a) Comparison of experimental measurements and model predictions for the constant strain rate test in compression when $\dot{\varepsilon} = 0.00005\ \mathrm{Sec}^{-1}$. (b) Damage density versus strain for model predictions presented in (a).

Because of the lack of experimental tension data at different temperatures, model predictions and experimental results for the constant strain rate in tension are only compared at one temperature, $T = 20^{o}C$, and two strain rates, 0.0167/sec and 0.00167/sec. These comparisons are shown in Figure 2.22.
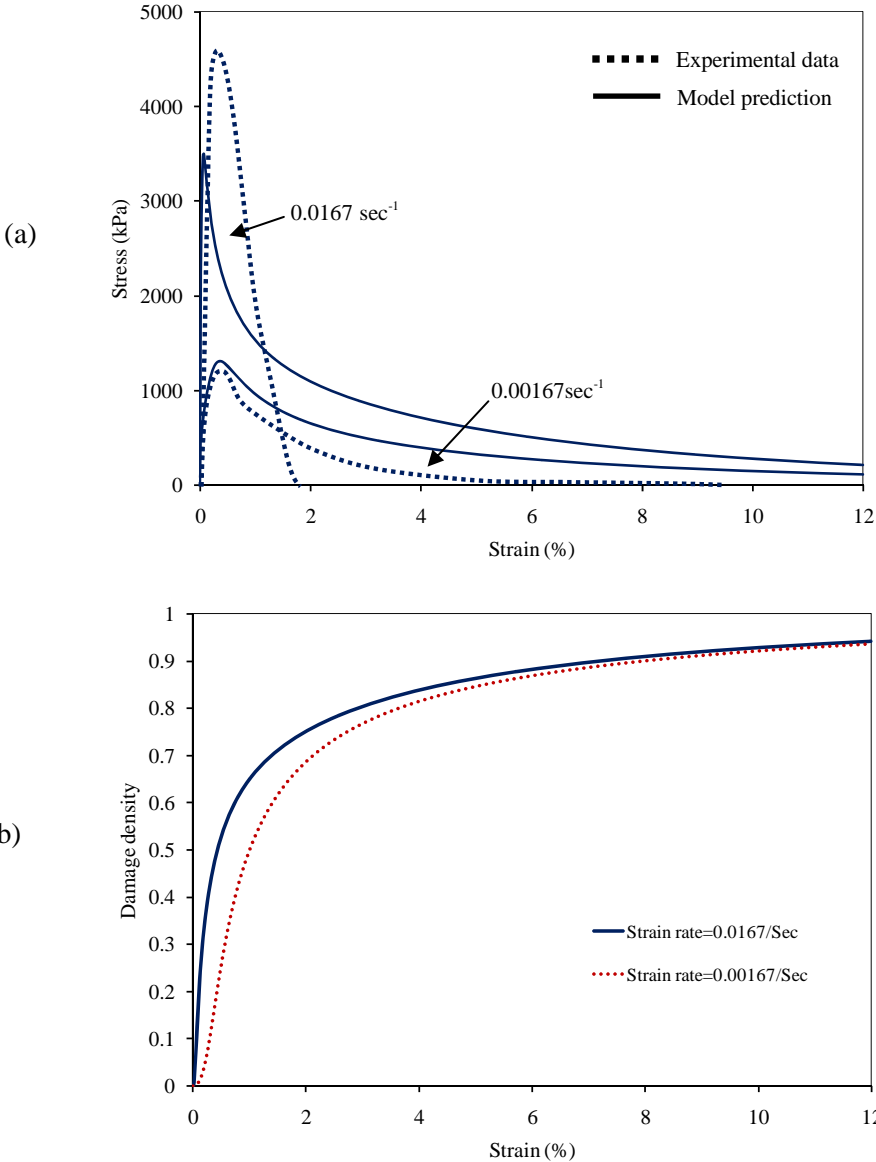
Figure 2.22. (a) Experimental measurements and model predictions for the constant strain test in tension when $T = 20^{o}C$. (b) Damage density versus strain for model predictions presented in (a).

Figure 2.22(a) shows that the model underestimates the experimental data at strain rate of 0.0167/sec. However, reasonable predictions are obtained when at the strain rate is 0.00167. Plots of the damage density versus the total strain for the predictions presented in Figure 2.22(a) are shown in Figure 2.22(b). One can also see the S-like shape of damage-strain diagram in Figure 2.22(b). However, since the peak stress occurs very rapidly in tension, this S-like is not very clear, especially at higher strain rates.

2.9.4. Model Validation against Repeated Creep-Recovery Tests

The ultimate goal of the current work is to develop a unified continuum model for predicting the behavior of asphalt mixes during their service life. However, pavements are subjected to repeated loading during the service life where fatigue damage becomes very important. Thus, several repeated creep-recovery tests with different loading and unloading times are utilized from the University of Nottingham database at the reference temperature and compared with the model predictions. The applied stress level in repeated creep-recovery tests in compression is 1500 kPa. Figure 2.23 shows the creep strain-time diagram when the loading time is 120sec and the unloading time is 100sec. As it is shown in Figure 2.23(a), the proposed model predictions compare well with the experimental measurements. The damage evolution versus time is also presented in Figure 2.23(b), which shows a stair case-type diagram for damage evolution which is expected in repeated creep-recovery loading in case micro-damage healing (i.e. micro-crack healing) is neglected. Figure 2.23 shows that during the loading period damage evolves and during the unloading period the value of the damage density remains constant in case the micro-damage healing is neglected.
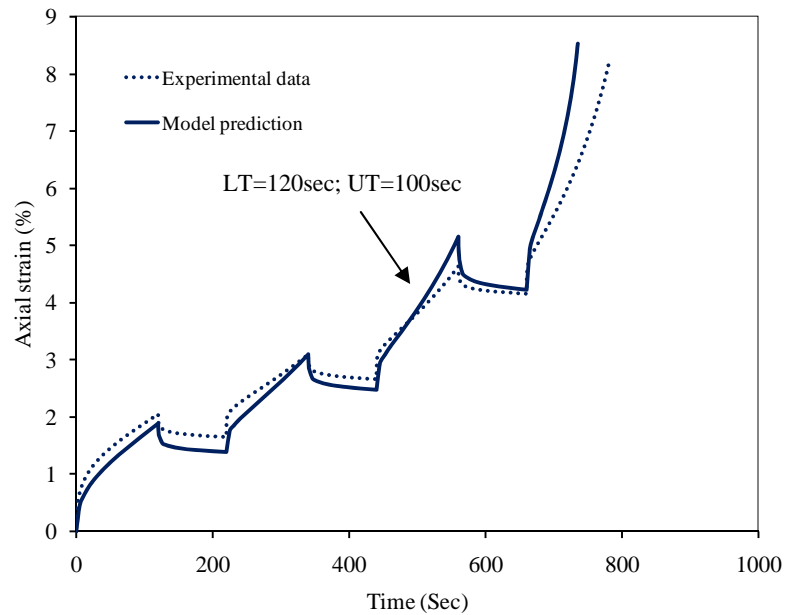
(a)
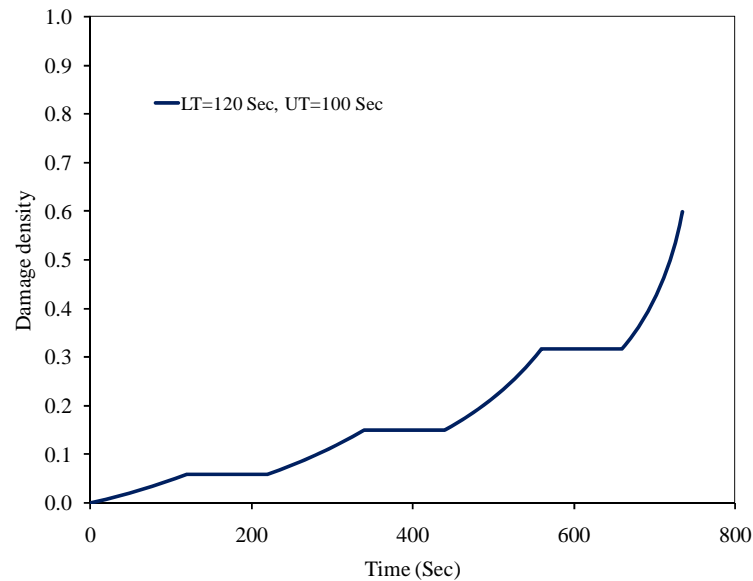
(b)

Figure 2.23. (a) Comparison between model results and experiments for repeated creep-recovery test in compression when LT= 120 sec and UT=100 sec. (b) Damage density versus time.

However, several studies have shown that asphalt mixes experience healing during the unloading duration (rest period) (Kim and Little, 1990; Lee and Kim, 1998; Lee et al., 2000; Si et al., 2002; Little and Bhasin, 2007; Bhasin et al., 2008). In fact,

during the unloading process and resting time periods some micro-crack and micro-void free surfaces wet and are brought back into contact with one another due to the effect of the surface free energy. In certain materials such as polymers and especially asphalt mixes, micro-cracks and micro-voids gradually reduce in size with a corresponding recovery in strength and stiffness due to micromechanical short-term wetting and long-term diffusion processes as the resting period increases (c.f. Wool and Oconnor, 1981). The underlying mechanism of micro-damage healing is usually described as a combination of wetting and intrinsic healing processes that occur across a crack surface. In the wetting process the cracked surfaces coming into contact with each other. However, during the intrinsic healing process the wetted crack surfaces gain strength over time. Surface free energy is usually considered as the driving force for wetting and the initial phase of the intrinsic healing in asphalt mixes. However, the subsequent time-dependent intrinsic healing is usually assumed to be due to the self-diffusion of asphalt cement molecules across the crack interface (c.f. Wool and Oconnor, 1981; Bhasin et al., 2011).

These healing features are opposite to those normally associated with continuum damage mechanics. In fact, for long resting periods, the damaged area may recover all of its strength and becomes identical to the virgin state of material (e.g. Prager and Tirrell, 1981; Carpenter and Shen, 2006; Little and Bhasin, 2007; Abu Al-Rub et al., 2010a). This process is referred to as micro-damage healing. The importance of the micro-damage healing process depends on specific loading conditions. For example, the result of the healing process can be significant when the material is subjected to fatigue loading conditions where rest time periods are introduced between the loading cycles. In other words, the impact of the recovery process is cumulative and depends on variables such as the length of the rest period. This behavior is evident for the repeated creep-recovery tests. Figure 2.24(a) and (b) show the results of repeated creep-recovery test in compression for the same loading time of 60sec but different unloading time of 100sec and 1500sec, respectively. As it is shown in Figure 2.24, deviation of the model

prediction from the experimental measurements increases when the length of the rest period increases.
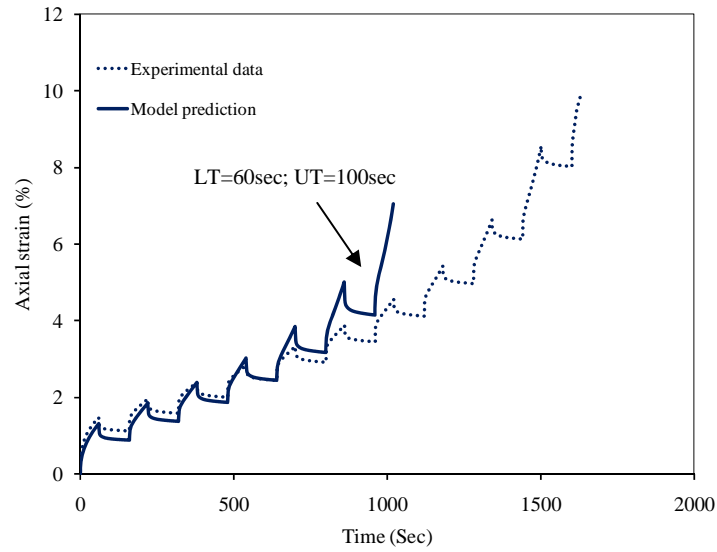
(a)
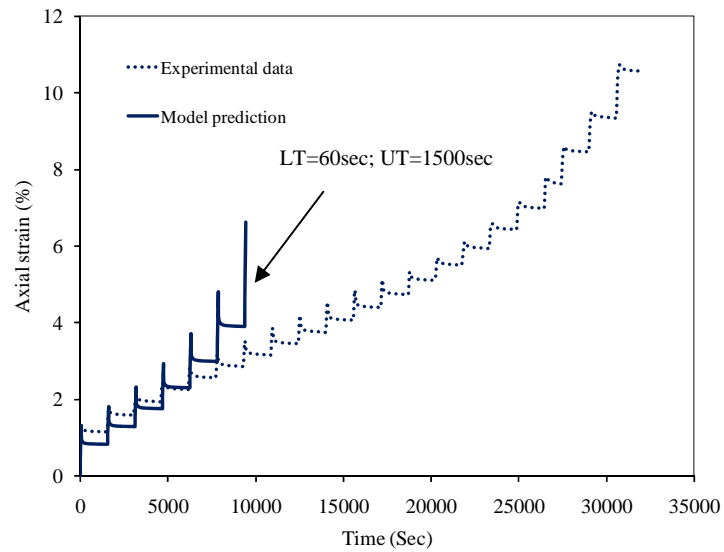
(b)

Figure 2.24. Comparison between model results and experiments for repeated creep-recovery test in compression. (a) LT= 60sec and UT=100sec; (b) LT= 60sec and UT=1500sec.

From the experimental data presented in Figures 2.23(a), 2.24(a), and 2.24(b), one can see that the failure in the repeated creep-recovery occurs mostly because of the damage since at large number of loading cycles the shape of the strain-time diagram at failure is very similar to the tertiary creep response. These figures also show that during the first few cycles the model predictions and experimental measurements compared well. However, the model predictions start to deviate significantly from experimental measurements as the number of cycles increases such that the model predicts failure much earlier. This deviation from experimental results increases as the unloading time increases. It is believed that this deviation is attributed to not incorporating the micro-crack healing during the resting time periods or unloading times. If micro-crack healing is incorporated, then damage and complete failure will be delayed and more reasonable predictions will be obtained.

Furthermore, the model predictions are compared to experimental measurements for repeated creep-recovery tests in tension for different loading and unloading times. These tests are conducted at reference temperature when the applied stress level is 300 kPa. Two different loading times are considered for these tests in tension. Figure 2.25 shows the results when the loading time is 120sec and the unloading time is 100sec. Figure 2.25(a) shows reasonable comparisons between model and experimental results for creep strain versus time, but significant deviation as failure is approached. Damage density versus time is also plotted in Figure 2.25(b). Model predictions and experimental results when the loading time is 60sec are plotted in Figure 2.26. Figures 2.26(a), (b), and (c) show the results when the unloading time is 50, 100, and 1500sec, respectively. Again, one sees that the current model predictions deviate significantly from the experimental data as failure is approached. These deviations are more significant for longer unloading times. This should be corrected in case micro-crack healing is modeled.

Figures 2.25(a) and 2.26(a)-(c) confirm that the model is able to predict the experimental results for repeated creep-recovery test when unloading time period is

small. However, similar to the results obtained for repeated creep-recovery test in compression the model fails to predict the experiments at large unloading times.
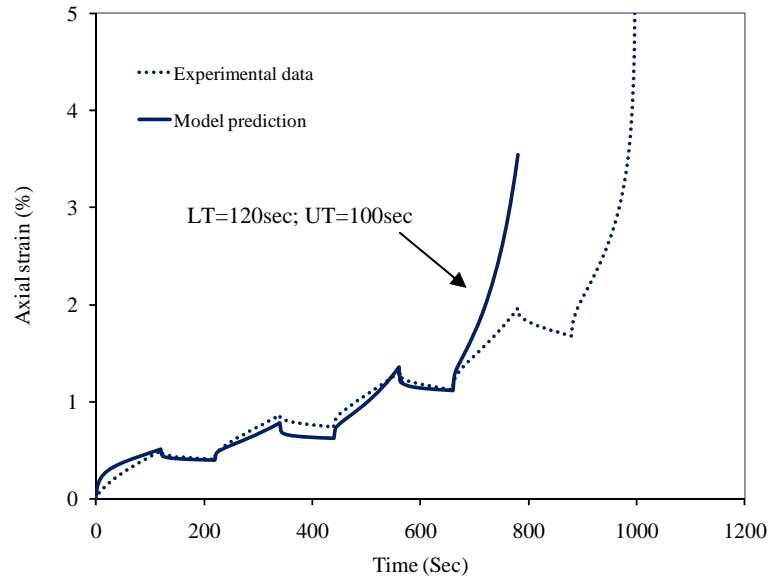
(a)
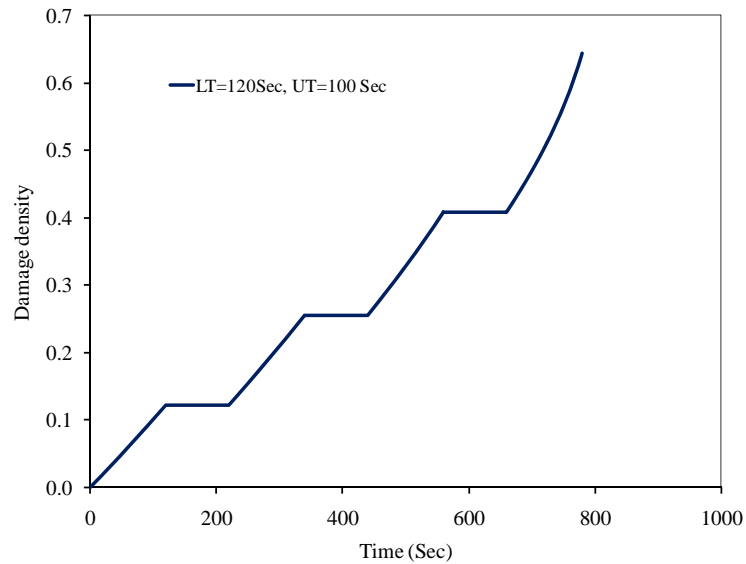
(b)

Figure 2.25. (a) Comparison between model results and experiments for repeated creep-recovery test in tension when LT= 120 sec and UT=100 sec. (b) Damage density versus time.

This is attributed to the healing phenomenon. Hence, the inclusion of the healing in a unified continuum model for predicting fatigue behavior of asphalt mixes is inevitable especially for large rest period times. This issue will be discussed in more details in the following chapters.
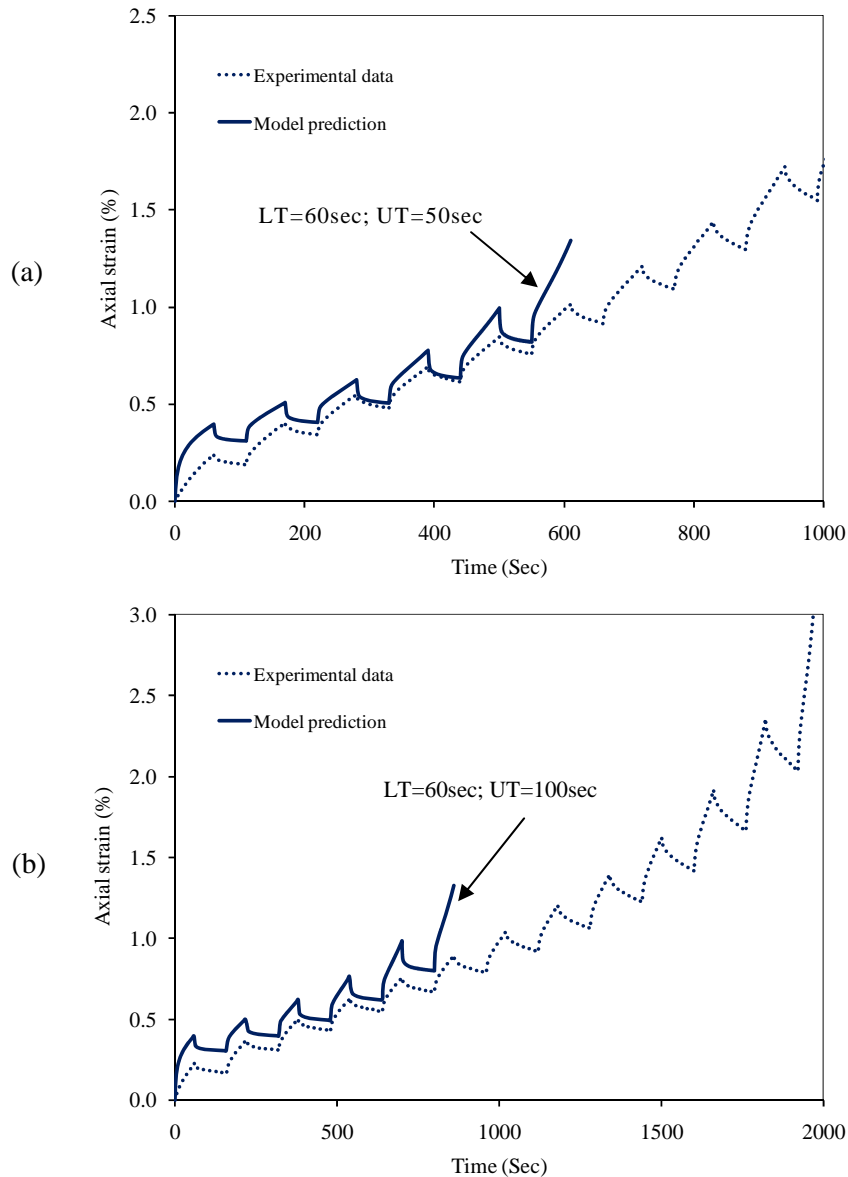
Figure 2.26. Comparison between model results and experiments for repeated creep-recovery test in tension. (a) LT= 60sec and UT=50sec; (b) LT= 60sec and UT=100sec; (c) LT=60sec and UT=1500sec.
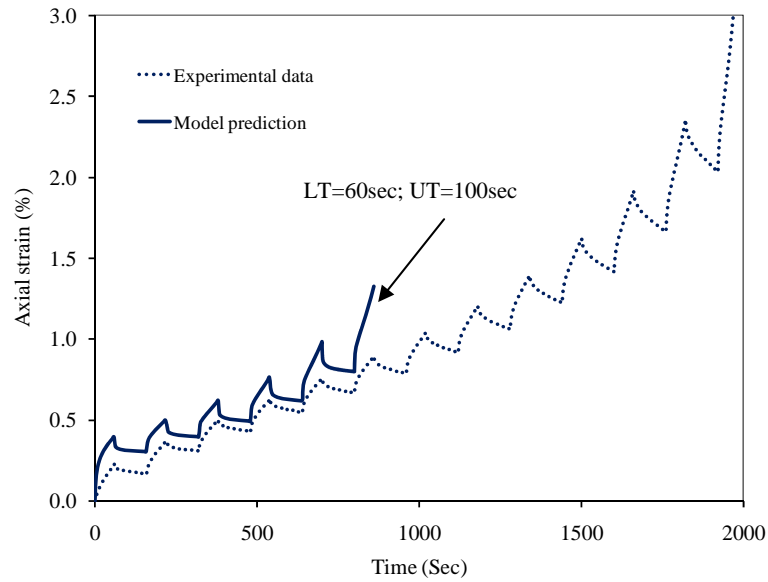
(c)

Figure 2.26. Continued.

2.10. Conclusions

In this work, a thermo-viscoelastic-viscoplastic-viscodamage constitutive model is presented and applied to predict the highly nonlinear response of asphalt mixes. The viscodamage model is coupled to other parts of the constitutive model by using the concept of the effective (undamaged) configuration within the continuum damage mechanics framework. This procedure simplifies the numerical implementation of the presented nonlinear model to a great deal since it avoids the complexities associated with the direct couplings of the damage to the rest of the constitutive equations and allows natural coupling of viscoelasticity and viscoplasticity to damage evolution. A straightforward procedure for identifying the associated material parameters of the presented model is discussed. The viscodamage model is formulated to be a function of stress, total strain, and the damage history. Also, both viscoplasticity and viscodamage models are enhanced by incorporating a parameter that accounts for the difference in viscoplastic and damage responses in compression and in tension. The temperature

coupling is brought into the model explicitly by introducing multiplicative temperature coupling terms in the Helmholtz free energy density function.

One set of material parameters identified from some specific tests is then used to validate the model for different tests. Validation is based on a comprehensive set of experimental data on a hot asphalt mix that include creep-recovery, creep, monotonic constant strain rate, and repeated creep-recover tests in both tension and compression and over a wide range of temperatures, stress levels, and strain rates. Comparing the experimental measurements with the model predictions show that the model can predict the complex mechanical responses of the bituminous materials reasonably well for the majority of the test data. Also, creep tests show that the model is capable of predicting the tertiary behavior in both tension and compression. The constant strain rate tests at different temperatures and strain rates show that the model is able to capture the peak point, post-peak behavior, and initial response in the stress-strain diagram. It is shown that the dependence of the viscodamage model on the history makes the damage density-strain diagram to have an S-like shape. Hence, one can consider the inflection point of the damage-strain curve as the point after which the post-peak behavior occurs. Moreover, the comparisons between the model predictions and experimental measurements for repeated creep-recovery test show that the model is capable of predicting the experiments for low rest period times. However, once the rest period increases the model predictions and experimental measurements deviate because of the healing phenomenon which is substantial at large resting time periods.

The present analysis considers creep-recovery, repeated creep-recovery, creep, and uniaxial constant strain rate tests at different temperatures, stress levels, and strain rates in both tension and compression. However, more tests are still needed to fully validate the proposed model. This necessity is very critical at high temperatures specially for calibrating the viscoelastic-viscoplastic temperature coupling term more accurately. Furthermore, since the ultimate goal is to predict the response of the bituminous materials and specially the asphalt mix during its service life, the inclusion of the healing

in the model is also critical since experimental studies have shown that asphalt mixes undergo healing during their service life.

Furthermore, although the presented model is calibrated over a large set of experimental data, the model should be thermodynamically consistent such that it also provides reasonable material response for the general loading scenarios. This will be the subject of the next chapter.

CHAPTER III
THERMODYNAMIC CONSISTENCY OF THE THERMO-VISCOELASTIC-VISCOPLASTIC-VISCODAMAGE CONSTITUTIVE MODEL

3.1. Introduction

One of the main challenges of the modern constitutive modeling is to derive the constitutive models which are consistent with the fundamental laws of thermodynamics. Therefore, in the past decades the development of the thermodynamic-based constitutive models for different materials has reached a great attention in the literature. Hence, numerous works have been devoted to development of thermodynamic-based formulations for modeling viscoelastic, viscoplastic, and/or damage behavior of different materials, especially metals and polymers (Kachanov, 1986; Voyiadjis and Kattan, 1990; Lemaître, 1992; Schapery, 1999; Voyiadjis and Park, 1999; Tao et al., 2001; Abu Al-Rub and Voyiadjis, 2003; Boubakar et al., 2003; Abu Al-Rub et al., 2007; Ghorbel, 2008; Levesque et al., 2008). Although the literature in developing thermodynamic-based constitutive models for materials is rather mature and rich, few attempts are available for developing such constitutive models for bituminous materials and especially asphalt mixes.

Therefore, based on the continuum damage mechanics, a general and comprehensive thermodynamic-based framework for coupling the temperature-dependent viscoelastic, viscoplastic, and viscodamage behaviors of bituminous materials is presented. This general framework derives systematically Schapery-type nonlinear viscoelasticity, Perzyna-type viscoplasticity, and a viscodamage model analogous to the Perzyna-type viscoplasticity.

The emphasis in this chapter is placed on deriving the constitutive model presented in Chapter II based on laws of thermodynamics (Darabi et al., 2011d).

Note that in this chapter indices m and n range from 1 to M_{int}^{ve} (the maximum number of internal state variables associated with the viscoelastic processes) while the other indices range from 1 to 3. Moreover, bold letters indicate that variables are tensors or matrices.

Moreover, the concept of the stress in the effective configuration [Eq. (2.4)] along with the strain equivalence hypothesis [Eq. (2.5)] is used in this chapter.

3.2. Basic Thermodynamic Formulations

Development of proper constitutive equations for a specific material and determination of the evolution laws for assumed internal state variables characterizing the material's behavior are the main challenges of the modern constitutive modeling. This can be effectively achieved, so far, through the thermodynamic principles by enforcing the balancing laws, the conservation of mass, the conservation of linear and angular momentums, and the first and second laws of thermodynamics. In this work, small deformations are assumed. The fundamental laws can be written as follows (Coleman and Gurtin, 1967; Lemaître and Chaboche, 1990; Lubliner, 1990, 2008):

$$\dot{\rho} + \rho \dot{u}_{i,i} = 0 \tag{3.1}$$

$$\sigma_{ij,j} + \rho b_i = \rho \ddot{u}_i \tag{3.2}$$

$$\sigma_{ij} = \sigma_{ji} \tag{3.3}$$

$$\rho \dot{e} = \sigma_{ij} \dot{\varepsilon}_{ij} + \rho r_{ext} - q_{i,i} \tag{3.4}$$

$$\sigma_{ij} \dot{\varepsilon}_{ij} - \rho(\dot{\Psi} + \eta \dot{T}) - \frac{1}{T} q_i \nabla_i T \geq 0 \tag{3.5}$$

where ρ , u , ρb , ρe , ρr_{ext} , $\rho \eta$, q , $\rho \Psi$, and T are the mass density, the displacement vector, the body force density vector, the internal energy density, the density of external heat, the specific entropy density, the heat flux vector, the Helmholtz free energy density, and temperature, respectively. Eq. (3.1) represents the conservation of mass; Eqs. (3.2) and (3.3) represent the balance of linear momentum and angular momentum, respectively. Eq. (3.4) is the conservation of energy or the first law of thermodynamics;

finally, Eq. (3.5) expresses the Clausius-Duhem inequality. Meanwhile, Ψ, e, T, and η are related through the following equation:

$$\Psi = e - T\eta \qquad (3.6)$$

Moreover, it is usually argued that once the material is damaged, further loading can only affect the undamaged material skeleton. Hence, the viscoelastic, viscoplastic, and viscodamage models are defined as functions of variables in the effective configuration. This assumption makes the assumed state variables independent as it should be in formulating a thermodynamically consistent constitutive model.

In this work, viscoelastic (creep and relaxation properties), viscoplastic (rate-dependent plasticity), and viscodamage (rate-dependent damage) material responses are coupled to the temperature to explain the temperature-, time-, and rate-dependent responses of asphalt mixes. Hence, the constitutive model is considered to be a function of the viscoelastic strain tensor in the effective configuration $\bar{\varepsilon}^{ve}$, M_{int}^{ve}- of phenomenological internal state variables associated with the viscoelastic processes $\bar{\zeta}^{(m)}$ ($m = 1,..., M_{int}^{ve}; M_{int}^{ve} \geq 1$), the isotropic damage density ϕ, the accumulative viscoplastic strain in the effective configuration $\bar{p}$ which is responsible for the isotropic hardening in the viscoplastic yield function, and the temperature T, such that one can express the Helmholtz free energy Ψ as a function of the state variables in the effective configuration as follows:

$$\Psi = \Psi(\bar{\varepsilon}_{ij}^{ve}, \bar{\zeta}^{(m)}, \bar{p}, \phi, T) \qquad (3.7)$$

The internal state variables associated with the viscoelastic process ($\bar{\zeta}^{(m)}$) are hidden state variables. These hidden state variables are associated with internal phenomena such as chain mobility in polymers that causes the evolution of the viscoelastic strain $\bar{\varepsilon}_{ij}^{ve}$ which is an observable variable that can be measured experimentally. However, although these hidden state variables finally result in the evolution of the viscoelastic strain tensor, their contribution to the stored and dissipated energies should be considered for more accurate estimation of stored and dissipated energies in the viscoelastic materials (as will be shown in the next sections). Schapery

(1966) defines these viscoelastic internal state variables as the generalized coordinates which could be physically interpreted as the variables representing molecular configurations in polymers or location of interstitial atoms in metals (please refere to Schapery, 1964; 1966 for more information).

Rewriting the Clausius-Duhem inequality in the effective configuration yields:

$$\bar{\sigma}_{ij}\dot{\bar{\varepsilon}}_{ij} - \rho(\dot{\Psi} + \eta\dot{T}) - \frac{1}{T}q_i\nabla_iT \geq 0 \tag{3.8}$$

Using the chain rule for taking the time derivative of the Helmholtz free energy Ψ [Eq. (3.7)] with respect to its state variables implies:

$$\dot{\Psi} = \frac{\partial\Psi}{\partial\bar{\varepsilon}_{ij}^{ve}}\dot{\bar{\varepsilon}}_{ij}^{ve} + \frac{\partial\Psi}{\partial\overline{\zeta}^{(m)}}\dot{\overline{\zeta}}^{(m)} + \frac{\partial\Psi}{\partial\overline{p}}\dot{\overline{p}} + \frac{\partial\Psi}{\partial\phi}\dot{\phi} + \frac{\partial\Psi}{\partial T}\dot{T} \tag{3.9}$$

where the superimposed dot indicates derivative with respect to time. Here, small deformations are considered. Thus, the total effective strain tensor, $\bar{\varepsilon}$, can be additively decomposed into the viscoelastic strain tensor, $\bar{\varepsilon}^{ve}$, and the viscoplastic strain tensor, $\bar{\varepsilon}^{vp}$, such that one can write:

$$\dot{\bar{\varepsilon}}_{ij} = \dot{\bar{\varepsilon}}_{ij}^{ve} + \dot{\bar{\varepsilon}}_{ij}^{vp} \tag{3.10}$$

Substituting the rate of the Helmholtz free energy [Eq. (3.9)] into the Clausius-Duhem inequality [Eq.(3.8)] and making use of Eq. (3.10) yield the following thermodynamic constraint (Coleman and Noll, 1963; Coleman and Gurtin, 1967):

$$\left(\bar{\sigma}_{ij} - \rho\frac{\partial\Psi}{\partial\bar{\varepsilon}_{ij}^{ve}}\right)\dot{\bar{\varepsilon}}_{ij}^{ve} - \rho\frac{\partial\Psi}{\partial\overline{\zeta}^{(m)}}\dot{\overline{\zeta}}^{(m)} + \bar{\sigma}_{ij}\dot{\bar{\varepsilon}}_{ij}^{vp} - \rho\frac{\partial\Psi}{\partial\overline{p}}\dot{\overline{p}} -$$
$$\rho\frac{\partial\Psi}{\partial\phi}\dot{\phi} - \rho\left(\frac{\partial\Psi}{\partial T} + \eta\right)\dot{T} - \frac{1}{T}q_i\nabla_iT \geq 0 \tag{3.11}$$

The following thermodynamic conjugate forces and state laws can be defined by making use of Eq. (3.11) (Coleman and Noll, 1963; Coleman and Gurtin, 1967):

$$\bar{L}_{ij} \equiv \bar{\sigma}_{ij} - \rho\frac{\partial\Psi}{\partial\bar{\varepsilon}_{ij}^{ve}} \tag{3.12}$$

$$\bar{Q}^{(m)} \equiv -\rho\frac{\partial\Psi}{\partial\overline{\zeta}^{(m)}} \tag{3.13}$$

$$\bar{\kappa} \equiv \rho \frac{\partial \Psi}{\partial \bar{p}} \tag{3.14}$$

$$\bar{Y} \equiv -\rho \frac{\partial \Psi}{\partial \phi} \tag{3.15}$$

$$\eta = -\frac{\partial \Psi}{\partial T} \tag{3.16}$$

Eqs. (3.12)-(3.16) describe the relation between the internal state variables and their associated thermodynamic conjugate forces, where $\bar{Q}^{(m)}$, $\bar{\kappa}$, $\bar{Y}$, and η are the conjugate forces associated with the internal state variables $\bar{\zeta}^{(m)}$, $\bar{p}$, ϕ, and T, respectively. The forces $\bar{Q}^{(m)}$ measure the changes in the internal structure due to viscoelastic process; the conjugate force $\bar{\kappa}$ is a measure of the changes in the material due to the accumulation of viscoplastic strain; and $\bar{Y}$ is measure of the changes in the internal structure due to micro-damage evolution. Moreover, as it will be shown later, tensor $\bar{L}$ will be null since the Cauchy stress tensor is the conjugate force of the viscoelastic strain tensor [Eq. (3.30)]; (i.e. $\bar{L}_{ij} \equiv \bar{\sigma}_{ij} - \rho \frac{\partial \Psi}{\partial \bar{\varepsilon}_{ij}^{ve}} = 0_{ij}$).

One can now define the expression for the rate of the total energy dissipation Π by substituting the thermodynamic state laws (3.12)-(3.16) into Eq. (3.11), such that:

$$\Pi = \bar{L}_{ij} \dot{\bar{\varepsilon}}_{ij}^{ve} + \bar{Q}^{(m)} \dot{\bar{\zeta}}^{(m)} + \bar{\sigma}_{ij} \dot{\bar{\varepsilon}}_{ij}^{vp} - \bar{\kappa} \dot{\bar{p}} + \bar{Y}\dot{\phi} - \frac{1}{T} q_i \nabla_i T \geq 0 \tag{3.17}$$

One can interpret from Eq. (3.17) that the total rate of energy dissipation can be decomposed into viscoelastic, viscoplastic, viscodamage, and thermal components, such that:

$$\Pi = \Pi^{ve} + \Pi^{vp} + \Pi^{vd} + \Pi^{th} \geq 0 \tag{3.18}$$

where

$$\Pi^{ve} = \bar{L}_{ij} \dot{\bar{\varepsilon}}_{ij}^{ve} + \bar{Q}^{(m)} \dot{\bar{\zeta}}^{(m)} \geq 0 \tag{3.19}$$

$$\Pi^{vp} = \bar{\sigma}_{ij} \dot{\bar{\varepsilon}}_{ij}^{vp} - \bar{\kappa} \dot{\bar{p}} \geq 0 \tag{3.20}$$

$$\Pi^{vd} = \bar{Y}\dot{\phi} \geq 0 \tag{3.21}$$

$$\Pi^{th} = -\frac{1}{T}q_i\nabla_i T \geq 0 \tag{3.22}$$

The evolution laws for $\overline{\boldsymbol{\varepsilon}}^{ve}$, $\overline{\boldsymbol{\varepsilon}}^{vp}$, $\overline{p}$, and ϕ can be obtained using the calculus of several variables with Lagrange multipliers $\dot{\lambda}^{vp}$ and $\dot{\lambda}^{vd}$. This can be achieved by subjecting the viscoinelastic rate of energy dissipation (i.e. $\Pi^{vi} = \Pi^{vp} + \Pi^{vd}$) to two constraints $f = 0$ and $g = 0$, such that (Simo, 1998):

$$\Omega = \Pi^{vp} + \Pi^{vd} - \dot{\lambda}^{vp}f - \dot{\lambda}^{vd}g \tag{3.23}$$

where f and g are viscoplastic and viscodamage loading surface functions, respectively. It should be noted that the loading surface functions are selected as constraints since the selected constraints should always have a zero value.

The maximum viscoinelastic dissipation principle states that the actual states of the thermodynamic forces are those which maximize the inelastic dissipation function over all possible states. One can now use this principle to obtain the evolution laws for the viscoinelastic state variables (i.e. $\dot{\overline{\varepsilon}}_{ij}^{vp}$, $\dot{\overline{p}}$, and $\dot{\phi}$) by satisfying the necessary conditions for the objective function, Ω, as follows:

$$\frac{\partial\Omega}{\partial\overline{\sigma}_{ij}} = 0 \; , \; \frac{\partial\Omega}{\partial\overline{\kappa}} = 0, \; \frac{\partial\Omega}{\partial\overline{\overline{Y}}} = 0 \tag{3.24}$$

By substituting Eq. (3.23) into Eq. (3.24) and making use of Eqs. (3.20) and (3.21), one obtains the thermodynamic laws corresponding to the evolution of the viscoplastic strain $\overline{\varepsilon}_{ij}^{vp}$, the effective viscoplastic strain $\overline{p}$, and the damage variable ϕ, such that:

$$\dot{\overline{\varepsilon}}_{ij}^{vp} = \dot{\lambda}^{vp}\frac{\partial f}{\partial\overline{\sigma}_{ij}} \tag{3.25}$$

$$\dot{\overline{p}} = -\dot{\lambda}^{vd}\frac{\partial f}{\partial\overline{\kappa}} \tag{3.26}$$

$$\dot{\phi} = \dot{\lambda}^{vd}\frac{\partial g}{\partial\overline{\overline{Y}}} \tag{3.27}$$

Eqs. (3.25), (3.26), and (3.27) provide evolution functions for the viscoplastic strain, effective viscoplastic strain, and damage density, respectively. Lagrange

multipliers $\dot{\lambda}^{vp}$ and $\dot{\lambda}^{vd}$ can be determined by satisfying the consistency conditions for viscoplasticity and viscodamage loading surfaces (i.e. $\dot{f} = 0$ and $\dot{g} = 0$). However, several experimental works on bituminous materials show that the viscoplastic deformation of these materials is non-associative (Oda and Nakayama, 1989; Cristescu, 1994; Florea, 1994; Bousshine et al., 2001; Masad et al., 2005; Tashman et al., 2005; Masad et al., 2007). Therefore, Eqs. (3.25) and (3.26) are modified to reflect the nonassociative behavior of bituminous materials, such that:

$$\dot{\bar{\varepsilon}}_{ij}^{vp} = \dot{\lambda}^{vp} \frac{\partial F}{\partial \bar{\sigma}_{ij}} \tag{3.28}$$

$$\dot{\bar{p}} = -\dot{\lambda}^{vd} \frac{\partial F}{\partial \bar{\kappa}} \tag{3.29}$$

where F is the viscoplastic potential function which is different from the viscoplastic loading surface function f. The same modifications can be made to make the viscodamage flow rule nonassociative. However, an associative viscodamage flow rule is used in this paper (i.e. $G = g$; G being the viscodamage potential function). Eq. (3.27) shows that damage can evolve even before the viscoplasticity ($\dot{\lambda}^{vp} = 0$). The next step in formulating the constitutive equations is to assume a proper form for the Helmholtz free energy density, loading surface functions, and potential functions for viscoplastic and viscodamage models. These assumptions are made in the subsequent sections to obtain viscoelastic, viscoplastic, and viscodamage constitutive models for asphalt mixes. It should be noted that different constitutive equations can be obtained by postulating different forms for the Helmholtz free energy, loading surface functions, and potential functions. However, in this work, specific forms are assumed such that one can obtain Schapery's viscoelasticity model, Perzyna's viscoplasticity model, and a viscodamage model that predicts the degradation in mechanical response of asphalt mixes due to induced damages.

It is noteworthy that the Clausius-Duhem inequality [Eq. (3.11)] is valid for all load histories. Therefore, let one assume a reversible load history under which neither viscoplasticity nor viscodamage have occurred in the material. Hence, rates of the

effective viscoplastic strain and the damage density variable are zero under this hypothetical loading history. Also, let one assume that this load history is such that the viscoelastic state variables remain constant. For this hypothetical reversible load history, the rate of the state variables vanishes (i.e. $\dot{\bar{p}} = 0$; $\dot{\phi} = 0$; and $\dot{\bar{\zeta}}^{(m)} = 0$, $m \in [1...M_{int}^{ve}]$), such that Eq. (3.11) yields the following thermodynamic state law:

$$\bar{\sigma}_{ij} = \rho \frac{\partial \Psi}{\partial \bar{\varepsilon}_{ij}^{ve}} \tag{3.30}$$

The above thermodynamic framework based on internal state variables is classical and used by many researchers for deriving constitutive theories. However, very few studies can be found on using this thermodynamic framework for deriving viscoelasticity theories. For example, Levesque et al. (2008) used this procedure and derived the Schapery-type viscoelastic model successfully.

3.3. Specific Free Energy Function

The complexity of the model is directly related to the definition of the Helmholtz free energy function Ψ and the number of assumed internal state variables. Hence, the definition of the Helmholtz free energy is a crucial step in formulating the constitutive equations. Different assumptions for the form of the Helmholtz free energy function yield different types of constitutive equations. In this paper, it is assumed that bituminous materials undergo three processes (i.e. viscoelasticity, viscoplasticity, and viscodamage) under loading and deformation. In this paper, the Helmholtz free energy is decomposed into three components (i.e. thermo-viscoelastic, thermo-viscoplastic, and thermo-viscodamage) in order to describe the changes in stored energy associated with each process. The decomposition of the Helmholtz free energy into the elastic and the viscoplastic components for elasto-viscoplastic materials is well established (Lemaître and Chaboche, 1990; Lubliner, 1990; Voyiadjis and Kattan, 1999). The addition of the damage component of the Helmholtz free energy is an assumption based on the fact that damage has a distinct morphology that is different from the other deformation mechanisms (Voyiadjis and Kattan, 1999; Voyiadjis et al., 2004). However, this

assumption is adopted here for decomposing the Helmholtz free energy into viscoelastic, viscoplastic, and viscodamage components, such that one can write:

$$\Psi(\overline{\varepsilon}_{ij}^{ve}, \overline{\zeta}^{(m)}, \overline{p}, \phi, T) = \Psi^{tve}(\overline{\varepsilon}_{ij}^{ve}, \overline{\zeta}^{(m)}, T) + \Psi^{tvp}(\overline{p}, T) + \Psi^{tvd}(\phi, T) \qquad (3.31)$$

where Ψ^{tve}, Ψ^{tvp}, and Ψ^{tvd} are the thermo-viscoelastic, thermo-viscoplastic, and thermo-viscodamage components of the Helmholtz free energy function, respectively. It should be noted that one can decompose the free energy function into its components and yet capture the coupling between different processes via the viscoplastic and viscodamage potential functions (Voyiadjis et al., 2004). Moreover, to obtain a more realistic description for the evolution of state variables and also to couple the constitutive equation to the temperature, multiplicative terms of temperature are introduced in the viscoelastic, viscoplastic, and viscodamage constitutive laws (as will be shown in the following sections).

In the classical theory of viscoelasticity it is usually assumed that the Helmholtz free energy can be expressed as a Taylor expression of the state variables around a reference state where $\sigma = \varepsilon^{ve} = \zeta = 0$ (Levesque et al., 2008). However, Schapery (1969b) proposed a nonlinear viscoelastic model by introducing nonlinear dependency scalars at various steps of the development of the constitutive theory (e.g. introducing the nonlinear dependency scalars in the definition of the Helmholtz free energy). Hence, the thermo-viscoelastic component of the Ψ can be written as:

$$\rho\Psi^{tve} = \left[\frac{1}{2}a_0\left(\overline{\boldsymbol{\varepsilon}}^{ve}\right)P_{ijkl}\overline{\varepsilon}_{ij}^{ve}\overline{\varepsilon}_{kl}^{ve} + a_1\left(\overline{\boldsymbol{\varepsilon}}^{ve}\right)P'_{ijm}\overline{\varepsilon}_{ij}^{ve}\overline{\zeta}^{(m)} + \frac{1}{2}P''_{mn}\overline{\zeta}^{(m)}\overline{\zeta}^{(n)}\right]\mathcal{G}^{ve}(T) \quad (3.32)$$

where $a_0\left(\overline{\boldsymbol{\varepsilon}}^{ve}\right)$ and $a_1\left(\overline{\boldsymbol{\varepsilon}}^{ve}\right)$ are nonlinear dependency scalars and are functions of viscoelastic strain tensor. $\mathcal{G}^{ve}(T)$ is an Arrhenius-type temperature term for coupling temperature to the viscoelastic constitutive law and is defined as follows:

$$\mathcal{G}^{ve}(T) = \exp\left[-\delta_1\left(1 - \frac{T}{T_0}\right)\right] \qquad (3.33)$$

where δ_1 is a material parameter and T_0 is the reference temperature.

For the viscoplastic component of the Helmholtz free energy the following form is postulated (Abu Al-Rub and Voyiadjis, 2003; Voyiadjis and Abu Al-Rub, 2003):

$$\rho\Psi^{tvp} = \left[\kappa_0 \overline{p} + \kappa_1 \left(\overline{p} + \frac{1}{\kappa_2} \exp(-\kappa_2 \overline{p}) \right) \right] \vartheta^{vp}(T) \tag{3.34}$$

where κ_0, κ_1, and κ_2 are material constants obtained at the reference temperature; and $\vartheta^{vp}(T)$ is another Arrhenius-type temperature term for coupling temperature to viscoplastic constitutive laws. Viscoelastic and viscoplastic temperature coupling terms are assumed to be the same for bituminous materials and asphalt mixes, which is proved experimentally by Schwartz et al. (2002), such that:

$$\vartheta^{vp}(T) = \vartheta^{ve}(T) = \exp\left[-\delta_1 \left(1 - \frac{T}{T_0} \right) \right] \tag{3.35}$$

Wu et al. (2006) proposed an energy-based plastic-damage model for concrete in which the Helmholtz free energy in the presence of damage is expressed as a function of the stress invariants and the damage variable. Similar assumptions have been made by Voyiadjis et al. (2004), Voyiadjis and Abu AL-Rub (2006), and Abu Al-Rub and Kim (2009). Therefore, the following form is postulated for the thermo-viscodamage component of the Helmholtz free energy in order to consider the confinement effects, the different effects of damage in tensile and compressive loading conditions, and the effect of temperature on damage evolution and growth; such that one can write:

$$\rho\Psi^{tvd} = \frac{1}{b_1} \left[(1-\phi)^{b_1} \left\langle \overline{\tau}^{vd} - \alpha \overline{I}_1 \right\rangle \exp\left(b_2 \overline{\varepsilon}_{eff} \right) \right] \vartheta^{vd}(T) \tag{3.36}$$

where b_1, b_2, and α are model parameters and $\vartheta^{vd}(T)$ is the viscodamage temperature coupling term, such that:

$$\vartheta^{vd}(T) = \exp\left[-\delta_2 \left(1 - \frac{T}{T_0} \right) \right] \tag{3.37}$$

where δ_2 is a material parameter. The brackets $\langle \bullet \rangle$ in Eq. (3.36) are the Macaulay brackets defined by $\langle x \rangle = (x + |x|)/2$ to ensure that the nonpositive values of $\left(\overline{\tau}^{vd} - \alpha \overline{I}_1 \right)$

load to $\rho\Psi^{tvd} = 0$. The term $\left\langle \bar{\tau}^{vd} - \alpha\bar{I}_1 \right\rangle$ in Eq. (3.36) is the component of the damage force in the effective configuration which is assumed to have the form of the modified Drucker-Prager criterion in order to include the pressure effects on damage nucleation and growth. Moreover, α is a parameter that reflects the material internal friction. Eq. (3.36) states that the damage starts when the deviatoric stress $\bar{\tau}^{vd}$ dominates the confinement effect $\alpha\bar{I}_1$ (i.e. $\bar{\tau}^{vd} - \alpha\bar{I}_1 > 0$). In this paper, it is assumed that damage does not evolve due to hydrostatic pressure, and damage starts nucleating when the deviatoric stress exceeds the confinement effect term. The form for $\bar{\tau}^{vd}$ is presented in Eq. (2.44).

As mentioned in the previous chapter, parameter d^{vd} in Eq. (2.44) captures different damage nucleation and growth conditions in extension (not necessarily tension) and contraction (not necessarily compression). Eq. (2.44) has been used by several researchers for distinguishing the plastic response of materials in tension and compression (Drucker et al., 1957; Chen and Mizuno, 1990; Dessouky, 2005; Han et al., 2008). Making use of this function in the viscodamage component of the Helmholtz free energy function is a wise choice for pressure sensitive materials (such as asphaltic materials) that show different damage responses in tension and compression. Note that when $\phi = 0$ (i.e. no damage) the viscodamage component of the Helmholtz free energy has its initial value. However, when the damage variable increases the viscodamage component of the free energy function decreases and eventually reaches zero at complete failure (i.e. $\phi = 1$). Furthermore, the viscodamage component of the Helmholtz free energy is assumed to be a function of the total effective strain in the effective configuration (i.e. $\bar{\varepsilon}_{eff} = \sqrt{\bar{\varepsilon}_{ij}\bar{\varepsilon}_{ij}}$) in order to bring more couplings between viscoelasticity, viscoplasticity, and viscodamage models.

Substituting Eq. (3.31) into Eq. (3.16) implies:

$$\eta = -\frac{\partial\Psi^{tve}}{\partial T} - \frac{\partial\Psi^{tvp}}{\partial T} - \frac{\partial\Psi^{tvd}}{\partial T} \tag{3.38}$$

Therefore, one can decompose the entropy function to its components due to thermo-viscoelastic, thermo-viscoplastic, and thermo-viscodamage processes, such that:

$$\eta = \eta^{tve} + \eta^{tvp} + \eta^{tvd} \tag{3.39}$$

where η^{tve}, η^{tvp}, and η^{tvd} are the entropy function due to thermo-viscoelastic, thermo-viscoplastic, and thermo-viscodamage processes, respectively.

$$\eta^{tve} = -\frac{\partial \Psi^{tve}}{\partial T}; \quad \eta^{tvp} = -\frac{\partial \Psi^{tvp}}{\partial T}; \quad \eta^{tvd} = -\frac{\partial \Psi^{tvd}}{\partial T} \tag{3.40}$$

Substituting Eqs. (3.32), (3.34), and (3.36) into Eq. (3.40) implies the following constitutive equations for entropy function:

$$\eta^{tve} = \frac{1}{\rho} \left[\frac{1}{2} a_0 \left(\overline{\boldsymbol{\varepsilon}}^{ve} \right) P_{ijkl} \overline{\varepsilon}_{ij}^{ve} \overline{\varepsilon}_{kl}^{ve} + a_1 \left(\overline{\boldsymbol{\varepsilon}}^{ve} \right) P_{ijm}' \overline{\varepsilon}_{ij}^{ve} \overline{\zeta}^{(m)} + \frac{1}{2} P_{mn}'' \overline{\zeta}^{(m)} \overline{\zeta}^{(n)} \right] Z^{ve} (T) \tag{3.41}$$

$$\eta^{tvp} = \frac{1}{\rho} \left[\kappa_0 \overline{p} + \kappa_1 \left(\overline{p} + \frac{1}{\kappa_2} \exp(-\kappa_2 \overline{p}) \right) \right] Z^{vp} (T) \tag{3.42}$$

$$\eta^{tvd} = \frac{1}{\rho b_1} \left[(1-\phi)^{b_1} \left\langle \overline{\tau}^{vd} - \alpha \overline{I}_1 \right\rangle \exp\left(b_2 \overline{\varepsilon}_{eff} \right) \right] Z^{vd} (T) \tag{3.43}$$

where

$$Z^a (T) = -\frac{\partial \vartheta^a (T)}{\partial T}; \quad (a = ve, vp, vd) \tag{3.44}$$

3.4. Viscoelastic Constitutive Model

Schapery (1969b) used the thermodynamics of irreversible processes to develop a single integral constitutive model for non-linear viscoelastic materials. Recently, Levesque et al. (2008) extended the Schapery's nonlinear viscoelastic model for 3D applications based on laws of thermodynamics. Here, a similar procedure is used for derivation of the viscoelastic model. However, the viscoelastic model is then coupled to viscoplastic model, viscodamage model, and temperature in order to more accurately predict the complex behavior of bituminous materials.

One of the hypotheses in the linear viscoelasticity theories is that the thermodynamic conjugate forces have linear relationships with the variation of state variables. Hence, one can write:

$$\dot{\bar{\zeta}}^{(m)} = C_{mn}\bar{Q}^{(n)} / a_2, \qquad m \in [1...M_{int}^{ve}] \tag{3.45}$$

where C_{mn} is a constant, positive, and semi-definite tensor; and a_2 is another nonlinear dependency scalar that can be a function of viscoelastic strain $\bar{\varepsilon}_{ij}^{ve}$ which takes into account the nonlinearity in the viscoelastic model. Substituting Eq. (3.32) into Eq. (3.13) yields:

$$\bar{Q}^{(m)} = -\rho\frac{\partial\Psi}{\partial\bar{\zeta}^{(m)}} = -\rho\frac{\partial\Psi^{tve}}{\partial\bar{\zeta}^{(m)}} = -a_1 P'_{ijm}\bar{\varepsilon}_{ij}^{ve}\vartheta^{ve} - P''_{mn}\bar{\zeta}^{(n)}\vartheta^{ve} \tag{3.46}$$

Substituting Eq. (3.45) into Eq. (3.46) implies:

$$a_2 C_{mn}^{-1}\dot{\bar{\zeta}}^{(n)} = -a_1 P'_{ijm}\bar{\varepsilon}_{ij}^{ve}\vartheta^{ve} - P''_{mn}\bar{\zeta}^{(n)}\vartheta^{ve} \tag{3.47}$$

One can rewrite Eq. (3.47), such that:

$$\frac{a_2}{\vartheta^{ve}}C_{mn}^{-1}\dot{\bar{\zeta}}^{(n)} + P''_{mn}\bar{\zeta}^{(n)} + a_1 P'_{ijm}\bar{\varepsilon}_{ij}^{ve} = 0 \tag{3.48}$$

Eq. (3.48) represents a coupled system of differential equations expressing the evolution of viscoelastic internal state variables $\bar{\zeta}^{(n)}$ as a function of the observed variable $\bar{\varepsilon}_{ij}^{ve}$. One can also use the reduced-time parameter defined as follows:

$$\psi = \int_0^t \frac{dt}{a_2} \tag{3.49}$$

The reduced-time introduces the time-shifting concept. Classically, the nonlinear parameter a_2 can be a functions of strain, stress, temperature, moisture, and aging (Schapery, 1969b). Therefore, Schapery's viscoelastic model is usually coupled to temperature through the temperature time-shifting parameter instead of using the temperature coupling term $\vartheta^{ve}(T)$. However, in this paper, the viscoelastic temperature coupling term $\vartheta^{ve}(T)$ is utilized for coupling the temperature to the viscoelastic model because it makes the thermo-mechanical coupling terms much simpler. Substituting the definition of the reduced time, Eq. (3.49), into Eq. (3.48) implies:

$$\left(\frac{C_{mn}^{-1}}{\vartheta^{ve}}\right)\frac{d\bar{\zeta}^{(n)}}{d\psi} + P''_{mn}\bar{\zeta}^{(n)} + a_1 P'_{ijm}\bar{\varepsilon}_{ij}^{ve} = 0 \quad \text{(No sum on } n) \tag{3.50}$$

Since $\mathbf{C}^{-1}$ and $\mathbf{P}''$ are symmetric and $\mathbf{P}''$ is positive definite, it is always possible to find a basis in which these tensors are diagonal (Levesque et al., 2008). Suppose for simplicity that these tensors are already expressed in this basis. Then Eq. (3.50) becomes:

$$\left(\frac{C_{mn}^{-1}}{\vartheta^{ve}}\right)\frac{d\overline{\zeta}^{(m)}}{d\psi} + P_{mm}''\overline{\zeta}^{(m)} + a_1 P_{ijm}'\overline{\varepsilon}_{ij}^{ve} = 0 \quad \text{(No sum on } m) \tag{3.51}$$

Eq. (3.51) is a set of uncoupled uni-dimensional differential equations. Using the Laplace transform one can write:

$$\overline{\zeta}^{(m)}(\psi) = -\frac{P_{ijm}'}{P_{mm}''}\int_0^\psi \left(1-\exp[-\omega_m(\psi^t-\psi^\tau)]\right)\frac{d(a_1\overline{\varepsilon}_{ij}^{ve})}{d\tau}d\tau \quad \text{(No sum on } m)(3.52)$$

where

$$\omega^{(m)} = P_{mm}''C_{mm}\vartheta^{ve}(T) \tag{3.53}$$

Eq. (3.52) represents the relationship between the viscoelastic internal state variables and the viscoelastic strain tensor. Substituting Eq. (3.32) into Eq. (3.30) yields:

$$\overline{\sigma}_{ij} = \left[A_{ijtu}^0 P_{tukl}\overline{\varepsilon}_{kl}^{ve} + A_{ijtu}^1 P_{tum}'\overline{\zeta}^{(m)}\right]\vartheta^{ve}(T) \tag{3.54}$$

where A_{ijtu}^0 and A_{ijtu}^1 are nonlinear tensors related to the instantaneous and transient viscoelastic responses, respectively. Eq. (3.54) shows that the instantaneous nonlinear parameters are no longer scalars for 3D Schapery-type models and defined as follows:

$$A_{ijtu}^0 = a_0\delta_{it}\delta_{ju} + \frac{1}{2}\frac{\partial a_0}{\partial\overline{\varepsilon}_{ij}^{ve}}\overline{\varepsilon}_{tu}^{ve} \tag{3.55}$$

$$A_{ijtu}^1 = a_1\delta_{it}\delta_{ju} + \frac{\partial a_1}{\partial\overline{\varepsilon}_{ij}^{ve}}\overline{\varepsilon}_{tu}^{ve} \tag{3.56}$$

The stress as a function of viscoelastic strain can now be obtained by substituting Eq. (3.52) into Eq. (3.54), such that:

$$\begin{aligned}\overline{\sigma}_{ij} = &\, G_{ijtu}^{(0)}\vartheta^{ve}(T)E_{tukl}^{(0)}\overline{\varepsilon}_{kl}^{ve} + \\ &\, G_{ijtu}^{(1)}\vartheta^{ve}(T)\int_0^\psi\sum_{m=1}^M\left[E_{tukl}^{(m)}\left(1-\exp[-\omega_m(\psi^t-\psi^\tau)]\right)\right]\frac{d(g^{(2)}\overline{\varepsilon}_{kl}^{ve})}{d\tau}d\tau\end{aligned} \tag{3.57}$$

where

$$G_{ijtu}^{(0)} E_{tukl}^{(0)} = A_{ijtu}^0 P_{tukl} - A_{ijtu}^1 \frac{P'_{tum} P'_{klm}}{P''_{mm}} \tag{3.58}$$

$$G_{ijtu}^{(1)} = A_{ijtu}^1 ; \quad E_{tukl}^{(m)} = \frac{P'_{tum} P'_{klm}}{P''_{mm}} ; \quad g^{(2)} = a_1 \tag{3.59}$$

Eqs. (3.57), (3.58), and (3.59) show that the general form of the thermodynamically consistent Schapery's nonlinear equation for 3D applications has a complex form in which the nonlinear parameter are no longer scalars. For the case of linear viscoelasticity the nonlinear parameters $\boldsymbol{G}^{(0)}$, $\boldsymbol{G}^{(1)}$, and $g^{(2)}$ should always be unity (i.e. $\boldsymbol{G}^{(0)} = \boldsymbol{G}^{(1)} = \boldsymbol{I}$ and $g^{(2)} = 1$). Moreover, one can still use scalar variables for nonlinear parameters by setting $G_{ijtu}^{(0)} = g^{(0)} I_{ijtu}$ and $G_{ijtu}^{(1)} = g^{(1)} I_{ijtu}$; $\boldsymbol{I}$ being the fourth order unit tensor to retrieve the original Schapery's nonlinear viscoelastic equation, such that:

$$\bar{\sigma}_{ij} = g^{(0)} E_{ijkl}^{(0)} \bar{\varepsilon}_{kl}^{ve} \vartheta^{ve} + g^{(1)} \vartheta^{ve} \int_0^\psi \sum_{m=1}^M \left[E_{ijkl}^{(m)} \left(1 - \exp[-\omega_m (\psi^t - \psi^\tau)]\right) \right] \frac{d(g^{(2)} \bar{\varepsilon}_{kl}^{ve})}{d\tau} d\tau \tag{3.60}$$

Eq. (3.57) shows that the temperature coupling term ϑ^{ve} captures the temperature effects on the instantaneous viscoelastic response, whereas temperature coupling term ϑ^{ve} and retardation time [Eq. (3.53)] introduces the temperature effects on the transient response.

The viscoelastic strain as a function of stress can also be obtained using the Laplace transform. In other words, one can express the viscoelastic strain as a function of stress in Laplace domain and then perform the inverse Laplace transform in order to obtain the viscoelastic strain as a function of the stress in the time domain. It is noteworthy that Schapery (1969b) used the thermodynamics of irreversible processes and derived the relationship for viscoelastic strains as a function of stresses. His formulation for linear viscoelasticity in the effective stress space can be written as follows:

$$\bar{\varepsilon}_{ij}^{ve} = D_{ijkl}^0 (T) \bar{\sigma}_{kl} + \int_0^\psi \Delta D_{ijkl} \left(\psi^t - \psi^\tau\right) \frac{d\bar{\sigma}_{kl}}{d\tau} d\tau \tag{3.61}$$

where $\boldsymbol{D} = \boldsymbol{D}^0 + \Delta \boldsymbol{D}(t)$ is the fourth-order creep compliance tensor with $\boldsymbol{D}^{(0)}$ being the instantaneous compliance tensor and $\Delta \boldsymbol{D}$ being the transient time-dependent compliance

tensor. For the case of isotropic and homogenous materials one can express the temperature-dependent instantaneous creep compliance $D^0(T)$ as follows:

$$D^0(T) = D^0 \exp\left[-\mu\left(1 - \frac{T}{T_0}\right)\right]$$ (3.62)

where D^0 is the instantaneous compliance at reference temperature T_0, and μ is a material constant. In Eq. (3.61), ΔD is the transient time-dependent compliance that can be expressed as a Prony series as follows:

$$\Delta D^{\psi^t} = \sum_{n=1}^{N} D_n \left[1 - \exp\left(-\lambda_n \psi^t\right)\right]$$ (3.63)

where N is the number of Prony series terms, D_n is the nth coefficient of Prony series associated with the nth retardation time λ_n, which is defined as:

$$\lambda_n = \lambda_n^0 \mathcal{G}^{ve} = \lambda_n^0 \exp\left[-\delta\left(1 - \frac{T}{T_0}\right)\right]$$ (3.64)

Note that here the viscoelasticity temperature coupling term is included in the retardation time instead of the reduced-time [see Eq. (3.53)]. Also, λ_n^0 in Eq. (3.64) is the nth retardation time at the reference temperature.

3.5. Viscoplastic Constitutive Model

As argued previously, once the material is damaged, further loading can only affect the undamaged material skeleton. Hence, the viscoplasticity and damage loading surfaces (f and g) and potential functions (F and G) are represented in the effective configuration. A modified Drucker-Prager-type function is used here for the yield surface since it captures the confinement effects, inter-particle friction effects, and distinguishes between the viscoplastic response of asphalt mixes in tension and compression. This function has been successfully applied to pressure sensitive materials by several researchers (Dessouky, 2005; Masad et al., 2005). Hence, one can express the yield condition as follows:

$$f = \bar{\tau}^{vp} - \alpha \bar{I}_1 - \bar{\kappa}(\bar{p},T) \leq 0 \tag{3.65}$$

where α is a material parameter related to the material's internal friction, $\bar{\kappa}(\bar{p},T)$ is the isotropic hardening function associated with the cohesive characteristics of the material and depends on the effective viscoplastic strain $\bar{p}$. Moreover, $\bar{\tau}^{vp}$ is the deviatoric effective shear stress modified to distinguish between different viscoplastic responses of the asphaltic material under compression and extension loading conditions, which is defined in Eq. (2.23).

The isotropic hardening function can now be determined using Eqs. (3.14) and (3.34), such that:

$$\bar{\kappa}(\bar{p},T) = \rho \frac{\partial \Psi}{\partial \bar{p}} = \rho \frac{\partial \Psi^{tvp}}{\partial \bar{p}} = \left[\kappa_0 + \kappa_1\left(1 - \exp(-\kappa_2\bar{p})\right)\right]\vartheta^{vp}(T) \tag{3.66}$$

The temperature-independent version of Eq. (3.66) is compatible with the form proposed by Lemaître and Chaboche (1990). Moreover, viscoelastic and viscoplastic temperature coupling terms are assumed to be the same for bituminous materials and asphalt mixes (i.e. $\vartheta^{vp}(T) = \vartheta^{ve}(T)$) [see Eq. (3.35)].

Several experimental works on bituminous materials show that the viscoplastic deformation of these materials is non-associative. Therefore, in this work, the following Drucker-Prager-type function (which is different from the yield surface function) is postulated for the viscoplastic potential function:

$$F = \bar{\tau}^{vp} - \beta \bar{I}_1 \tag{3.67}$$

where β is a material parameter that describes the dilation or contraction behavior of the material.

Eq. (3.65) can now be extended to include rate-dependent plasticity (viscoplasticity) using the overstress concept (Zener and Hollomon, 1944; Malvern, 1951; Perzyna, 1986; Perzyna and Korbel, 1998). However, the stress state is not constrained anymore to remain on the yield surface (i.e. $f \geq 0$). Hence, the overstress which expresses the difference between the stress state and the yield surface can be defined as:

$$\bar{\sigma}_v = \left\langle \bar{\tau}^{vp} - \alpha \bar{I}_1 - \bar{\kappa}\left(\bar{p}, T\right) \right\rangle \tag{3.68}$$

where $\bar{\sigma}_v$ is the overstress (or viscous stress) in the effective configuration. Eq. (3.68) shows that the overstress function is also temperature-dependent. The overstress function states that an inelastic process can take place only when the overstress function is positive (i.e. $\bar{\sigma}_v \geq 0$); as a result $f \geq 0$. The dynamic viscoplasticity yield surface χ^{vp} can now be defined from Eq. (3.68), such that:

$$\chi^{vp} \equiv \bar{\tau}^{vp} - \alpha \bar{I}_1 - \bar{\kappa}\left(\bar{p}, T\right) - \bar{\sigma}_v = 0 \tag{3.69}$$

Based on the assumed form for the yield surface function and the plastic potential function, the following relation between the viscoplastic Lagrange multiplier $\dot{\lambda}^{vp}$ and the effective viscoplastic strain can be obtained, such that:

$$\dot{\bar{p}} = \left(1 - \frac{\beta}{3}\right) \dot{\lambda}^{vp} \tag{3.70}$$

Different admissible forms for the viscoplastic Lagrange multiplier can be substituted in Eq. (3.28). Several physically- and phenomenological-based evolution equations for $\dot{\lambda}^{vp}$ have been proposed in the literature. One of the most widely used models is due to Perzyna (Perzyna, 1963, 1971, 1986; Perzyna and Korbel, 1998), which can be considered as the penalty regularization of the rate-dependent plasticity. In Perzyna-type models $\dot{\lambda}^{vp}$ can be replaced by an increasing function of the overstress. In this paper the following form is postulated for bituminous materials:

$$\dot{\lambda}^{vp} = \Gamma^{vp}\left(T\right) \left\langle \frac{\bar{\sigma}_v}{\bar{\tau}^{vp} - \alpha \bar{I}} \right\rangle^N \tag{3.71}$$

where N is the viscoplastic rate sensitivity exponent and $\Gamma^{vp}\left(T\right)$ is the temperature-dependent viscoplasticity viscosity parameter. Making Γ^{vp} temperature-dependent is experimentally motivated for HMA materials (Huang et al., 2002). However, the same viscoplastic temperature coupling term ϑ^{vp} [Eq. (3.35)] is used here to make the viscosity parameter temperature-dependent. Hence, using the temperature-dependent

viscoplasticity viscosity parameter does not increase the number of the model parameters. Therefore, one can write:

$$\Gamma^{vp}(T) = \Gamma_0^{vp} \mathcal{G}^{vp} \tag{3.72}$$

where Γ_0^{vp} is the viscoplasticity viscosity parameter at the reference temperature. Substituting Eq. (3.72) into Eq. (3.71) and rearranging Eq. (3.71) yield the following expression for the overstress function:

$$\bar{\sigma}_v = (\bar{\tau}^{vp} - \alpha \bar{I}_1) \left(\frac{\dot{\lambda}^{vp}}{\Gamma_0^{vp} \mathcal{G}^{vp}} \right)^{1/N} \tag{3.73}$$

The dynamic viscoplasticity yield surface χ^{vp} can now be obtained by substituting the overstress function [Eq. (3.73)] into Eq. (3.69), such that:

$$\chi^{vp} = \bar{\tau}^{vp} - \alpha \bar{I}_1 - \bar{\kappa}(\bar{p},T) - [\bar{\tau}^{vp} - \alpha \bar{I}_1] \left(\frac{\dot{\lambda}^{vp}}{\Gamma_0^{vp} \mathcal{G}^{vp}} \right)^{1/N} = 0 \tag{3.74}$$

Eq. (3.74) defines the temperature-dependent dynamic yield surface which is the generalization of the yield surface for the rate-independent plasticity given in Eq. (3.65). It is noteworthy that for large values of Γ_0^{vp} the dynamic yield surface and its static counterpart are the same ($\chi^{vp} = f \leq 0$). Also, in the elastic domain both f and χ^{vp} are the same since the rate of the effective viscoplastic strain $\dot{\bar{p}}$ and as a result the viscoplastic multiplier $\dot{\lambda}^{vp}$ are both zero ($\dot{\bar{p}} = \dot{\lambda}^{vp} = 0$). Hence, the admissible stress states remain within or on the viscoelastic domain such that similar to rate-independent plasticity $\chi^{vp} \leq 0$. However, the condition $\chi^{vp} < 0$ does not necessary imply that the stress state is in the viscoelastic domain. For example, during the unloading process for a specific strain rate the stress state may satisfy the condition $\chi^{vp} < 0$ while it is still in the viscoplastic domain. In this case the viscoplastic strain still continues with a smaller strain rate. Moreover, for large values of the viscoplasticity viscosity parameter Γ_0^{vp} the viscoplasticity multiplier remains finite and positive since the overstress goes to zero. Furthermore, the standard Kuhn-Tucker loading/unloading conditions can also be applied to the dynamic yield surface such that:

$$\chi^{vp} \leq 0, \quad \dot{\lambda}^{vp} \geq 0, \quad \dot{\lambda}^{vp} \chi^{vp} = 0, \quad \dot{\lambda}^{vp} \dot{\chi}^{vp} = 0 \tag{3.75}$$

Moreover, the dynamic yield surface can expand and shrink due to both softening/hardening effects and softening/hardening rate effects. The non-associative viscoplasticity flow rule can now be obtained by substitute Eqs. (3.71) and (3.72) into Eq.(3.28), such that:

$$\dot{\bar{\varepsilon}}_{ij}^{vp} = \Gamma_0^{vp} \vartheta^{vp} \left\langle \frac{\bar{\sigma}_v}{\bar{\tau}^{vp} - \alpha \bar{I}} \right\rangle^N \frac{\partial F}{\partial \bar{\sigma}_{ij}} \tag{3.76}$$

Eqs. (3.74) and (3.76) show that the viscoplastic temperature coupling term should be included in both the flow rule and the dynamic viscoplasticity yield surface.

3.6. Viscodamage Constitutive Model

In this work, the constitutive models are expressed in the effective stress space. In this section, the thermo-viscodamage model will be formulated and will be coupled to the thermo-viscoelastic and thermo-viscoplastic models. Therefore, expressing the viscodamage model elements (i.e. the damage potential function G and damage surface function g) in the effective stress space seems quiet natural since damage also affects the undamaged skeleton of material. The damage force can be derived from the Helmholtz free energy function by substituting Eq.(3.36) into Eq. (3.15), such that:

$$\bar{Y} = -\rho \frac{\partial \Psi}{\partial \phi} = -\rho \frac{\partial \Psi^{tvd}}{\partial \phi} = \left[(1-\phi)^{b_1-1} \left\langle \bar{\tau}^{vd} - \alpha \bar{I}_1 \right\rangle \exp\left(b_2 \bar{\varepsilon}_{eff}\right) \right] \vartheta^{vd}(T) \tag{3.77}$$

An analogous procedure for formulating the viscoplastic model is used to formulate the viscodamage model. In this work the damage growth surface g is assumed to be the same as the damage potential function G (i.e. associative viscodamage). One can define a very simple static damage loading surface, such that:

$$g = \bar{Y} - Y_0 \leq 0 \tag{3.78}$$

where $\bar{Y}$ is the damage force [Eq. (3.77)] and Y_0 is the threshold damage force. Very similar to the viscoplasticity, one can extend Eq. (3.78) to include the rate-dependent damage (viscodamage) such that:

$$\chi^{vd} = g - \bar{\sigma}_v^{vd} = 0 \tag{3.79}$$

where χ^{vd} is the dynamic damage loading surface and $\bar{\sigma}_v^{vd}$ is the damage overstress defined as:

$$\bar{\sigma}_v^{vd} = \left\langle \bar{Y} - Y_0 \right\rangle \tag{3.80}$$

A form similar to the form selected for the admissible viscoplastic Lagrange multiplier is postulated for the damage Lagrange multiplier $\dot{\lambda}^{vd}$. Hence, the following form which is an increasing function of the damage overstress is postulated for the damage Lagrange multiplier:

$$\dot{\lambda}^{vd} = \Gamma^{vd} \left\langle \frac{\bar{\sigma}_v^{vd} + Y_0}{Y_0} \right\rangle^q \tag{3.81}$$

where Γ^{vd} is the damage viscosity parameter and q is a material constant. From Eq. (3.81) one can simply determine the damage overstress as:

$$\bar{\sigma}_v^{vd} = Y_0 \left[\left(\frac{\dot{\lambda}^{vd}}{\Gamma^{vd}} \right)^{1/q} - 1 \right] \tag{3.82}$$

Substituting Eq. (3.78) into Eq. (3.27) implies that the damage multiplier $\dot{\lambda}^{vd}$ is the same as the damage rate (i.e. $\dot{\lambda}^{vd} = \dot{\phi}$). Finally, the dynamic viscodamage loading surface can be obtained by substituting Eqs. (3.77) and (3.78) into Eq. (3.79), such that:

$$\chi^{vd} = \bar{Y} - Y_0 \left(\frac{\dot{\phi}}{\Gamma^{vd}} \right)^{1/q} = 0 \tag{3.83}$$

Substituting Eq. (3.77) into Eq. (3.83) yields:

$$\chi^{vd} = \left[(1-\phi)^{b_1-1} \left\langle \bar{\tau}^{vd} - \alpha \bar{I}_1 \right\rangle \exp\left(b_2 \bar{\varepsilon}_{eff} \right) \right] \vartheta^{vd} - Y_0 \left(\frac{\dot{\phi}}{\Gamma^{vd}} \right)^{1/q} = 0 \tag{3.84}$$

The temperature-dependent dynamic viscodamage loading function, $\chi^{vd} = 0$, defined in Eq. (3.84) is the generalization of its static counterpart $g \leq 0$ [Eq. (3.78)]. Similar to the viscoplasticity loading surface, the static damage loading surface can be recovered for large values of the damage viscosity parameter Γ^{vd}. In the undamaged domain g and

χ^{vd} are the same since there is no damage evolution (i.e. $\dot{\lambda}^{vd} = \dot{\phi} = 0$). In this case the allowable stress states are forced to remain on or within the viscoelastic domain, so that one has similar to rate-independent damage $g \leq 0$. Again analogous to the viscoplasticity, during the unloading process and for a particular damage rate, $\chi^{vd} < 0$ does not necessarily imply that the material is in the undamaged domain, but the material could still be in the damage state with a smaller damage rate. The generalized Kuhn-Tucker loading/unloading conditions can also be applied to the dynamic viscodamage surface, such that:

$$\chi^{vd} \leq 0, \quad \dot{\lambda}^{vd} \geq 0, \quad \dot{\lambda}^{vd} \chi^{vd} = 0, \quad \dot{\lambda}^{vd} \dot{\chi}^{vd} = 0 \tag{3.85}$$

The evolution law for the thermo-viscodamage model can be obtained by rearranging Eq. (3.84), such that:

$$\dot{\phi} = \Gamma^{vd} \left[\frac{(1-\phi)^{b_1 - 1} \langle \bar{\tau}^{vd} - \alpha \bar{I}_1 \rangle}{Y_0} \right]^q \exp\left(b_2 q \bar{\varepsilon}_{eff} \right) \left(\vartheta^{vd} \right)^q \tag{3.86}$$

where the viscodamage temperature coupling term can be defined as:

$$\tilde{\vartheta}^{vd} = \left(\vartheta^{vd} \right)^q = \exp\left[-\gamma_1 \left(1 - \frac{T}{T_0} \right) \right] \tag{3.87}$$

As explained in the previous chapter, the proposed viscodamage model has the advantage that allows a systematic and straightforward procedure for determination of unique model parameters which makes its calibration very simple.

3.7. The Heat Equation

Bituminous materials and asphalt mixes are temperature- sensitive materials. Asphalt mixes are subjected to thermal loadings due to the daily and seasonal fluctuations in temperature during their service life. Also, some specific phenomena such as compaction of hot mix asphalt in the field are associated with drastic temperature changes. Moreover, local temperature changes because of the energy dissipation associated with the deformation processes influence the mechanical properties of asphalt mixes. Hence, including the temperature evolution in the constitutive model seems inevitable for

accurate modeling of the mechanical response of asphalt mixes. In this subsection, the heat equation is derived.

Substituting the internal energy per unit mass, e, from Eq. (3.6) into the first law of thermodynamics [Eq. (3.4)] for the effective configuration implies the following energy balance equation:

$$\rho\left(\dot{\Psi}+\dot{T}\eta+T\dot{\eta}\right)-\bar{\sigma}_{ij}\dot{\bar{\varepsilon}}_{ij}-\rho r_{ext}+q_{i,i}=0 \tag{3.88}$$

Substituting $\dot{\Psi}$ from Eq. (3.9) into the above energy balance equation and making use of results in Eqs. (3.13), (3.14), (3.15), (3.16), and (3.30) yield the following equation:

$$\rho T\dot{\eta}=\bar{\sigma}_{ij}\dot{\bar{\varepsilon}}_{ij}^{vp}+\bar{Q}^{(m)}\dot{\bar{\zeta}}^{(m)}-\bar{\kappa}\dot{\bar{p}}+\bar{Y}\dot{\phi}+\rho r_{ext}-q_{i,i} \tag{3.89}$$

On the other hand, Substituting Eqs. (3.19), (3.20), (3.21), and (3.30) into Eq. (3.89) gives:

$$\rho T\dot{\eta}=\Pi^{ve}+\Pi^{vp}+\Pi^{vd}+\rho r_{ext}-q_{i,i} \tag{3.90}$$

Looking at Eqs. (3.41), (3.42), (3.43), and (3.44) reveals that:

$$\eta=\tilde{\eta}\left(\bar{\varepsilon}_{ij}^{ve},\bar{\zeta}^{(m)},\bar{p},\phi,T\right) \tag{3.91}$$

Taking the time derivative of Eq. (3.91) yields:

$$\dot{\eta}=\frac{\partial\eta}{\partial\bar{\varepsilon}_{ij}^{ve}}\dot{\bar{\varepsilon}}_{ij}^{ve}+\frac{\partial\eta}{\partial\bar{\zeta}^{(m)}}\dot{\bar{\zeta}}^{(m)}+\frac{\partial\eta}{\partial\bar{p}}\dot{\bar{p}}+\frac{\partial\eta}{\partial\phi}\dot{\phi}+\frac{\partial\eta}{\partial T}\dot{T} \tag{3.92}$$

Substituting Eq. (3.92) into Eq. (3.90) yields the thermo-mechanical heat balance equation, such that:

$$\rho c_p\dot{T}=\Pi^{ve}+\Pi^{vp}+\Pi^{vd}+\underbrace{\left[\frac{\partial\bar{Q}^{(m)}}{\partial T}\dot{\bar{\zeta}}^{(m)}-\frac{\partial\bar{\sigma}_{ij}}{\partial T}\dot{\bar{\varepsilon}}_{ij}^{ve}-\frac{\partial\bar{\kappa}}{\partial T}\dot{\bar{p}}+\frac{\partial\bar{Y}}{\partial T}\dot{\phi}\right]T}_{\text{Thermo-mechanical coupling terms}}+\rho r_{ext}-q_{i,i} \tag{3.93}$$

where $c_p=T\,\partial\eta/\partial T$ is the tangent specific heat capacity at constant pressure. Therefore, from the above equation, one can calculate the increase in temperature associated with the energy dissipation during the viscoelastic, viscoplastic, and viscodamage deformation processes, and due to the external heat sources and conduction.

The thermo-mechanical terms in Eq. (3.93) can be obtained using Eqs. (3.44), (3.46), (3.52), (3.53), (3.57), (3.66), and (3.77), such that:

$$\frac{\partial \overline{Q}^{(m)}}{\partial T} = \left(a_1 P'_{ijm} \overline{\varepsilon}^{ve}_{ij} + P''_{mn} \overline{\zeta}^{(n)} \right) Z^{ve} \tag{3.94}$$

$$-\frac{\partial \overline{\sigma}_{ij}}{\partial T} = G^{(0)}_{ijtu} E^{(0)}_{tukl} \overline{\varepsilon}^{ve}_{kl} Z^{ve} -$$

$$\frac{Z^{ve}}{\mathcal{G}^{ve}} G^{(1)}_{ijtu} \int_0^\psi \left\{ \sum E^{(m)}_{tukl} \left[\omega_m (\psi - \psi^\tau) \right] \exp \left[-\omega_m \left(\psi - \psi^\tau \right) \right] \right\} \frac{d(g^{(2)} \overline{\varepsilon}^{ve}_{kl})}{d\tau} d\tau \tag{3.95}$$

$$-\frac{\partial \overline{\kappa}}{\partial T} = \left[\kappa_0 + \kappa_1 \left(1 - \exp(-\kappa_2 \overline{p}) \right) \right] Z^{vp} \tag{3.96}$$

$$\frac{\partial \overline{Y}}{\partial T} = -\left[(1-\phi)^{b_1-1} \left\langle \overline{\tau}^{vd} - \alpha \overline{I}_1 \right\rangle \exp \left(b_2 \overline{\varepsilon}_{eff} \right) \right] Z^{vd} \tag{3.97}$$

where $Z = -\partial \mathcal{G} / \partial T$. The heat flux vector, $\mathbf{q}$, can also be determined using the well-known Fourier's heat conduction law, such that:

$$q_i = -k_{ij} \nabla_j T \tag{3.98}$$

By substituting Eqs. (3.52), (3.94), (3.95), (3.96), (3.97), and (3.98) into Eq. (3.93) one realizes that the right hand side of thermo-mechanical heat balance [Eq. (3.93)] becomes a function of viscoelastic strain tensor, $\overline{\varepsilon}^{ve}$, effective viscoplastic strain, $\dot{\overline{p}}$, damage density, ϕ, and temperature, T. Eq. (3.93) expresses the changes in the temperature during the deformation processes.

3.8. Conclusions

In this work, a systematic and consistent thermodynamic-based framework for constructing a temperature-, time-, and rate-dependent constitutive model for bituminous materials, which provides a coupling among temperature, viscoelasticity, viscoplasticity, and viscodamage, is presented.

The viscodamage model is coupled to other parts of the constitutive model by using the concept of the effective (undamaged) configuration within the continuum damage mechanics framework. Hence, the Helmholtz free energy function is expressed in terms of the internal state variables in the effective configuration.

This thermodynamic framework which is based on the Clausius-Duhem inequality is used to derive the constitutive models presented in Chapter II. It is shown that the presented constitutive model is thermodynamically consistent.

However, as mentioned in Chapter II, the presented constitutive model does not include the micro-damage healing effect which makes the constitutive model unable to predict reasonable responses in the presence of the rest period. This very crucial issue will be discussed for general cases in Chapter IV and for the asphalt mixes in Chapter V.

CHAPTER IV
A CONTINUUM DAMAGE MECHANICS FRAMEWORK FOR MODELING MICRO-DAMAGE HEALING

4.1. Introduction

Followed by Kachanov (1958) pioneering work on continuum damage mechanics, many researchers have used the effective configuration concept to model the irreversible damage processes in engineering materials. However, experimental observations in the last decade have clearly shown that various classes of engineering materials such as polymers, biomaterials, and asphalt binder have the potential to heal and retrieve part of their strength and stiffness under specific conditions.

The intrinsic healing capability of biomaterials and biological systems is a well-known and well-established fact (e.g. Yasko et al., 1992; Rodeo et al., 1993; Arrington et al., 1996; Strauer et al., 2002; Werner and Grose, 2003). Moreover, several procedures for synthesizing self-healing polymers are recently developed inspired by these unique features of biological systems and materials (e.g. White et al., 2001; Brown et al., 2005; Bond et al., 2007; Rong et al., 2007; White et al., 2008; Yin et al., 2008; Yuan et al., 2008). Another category of the engineering materials that tend to heal is the composite materials whose matrix is intrinsically tend to heal at elevated temperatures and during the rest periods (Little and Bhasin, 2007; Bhasin et al., 2008; Bhasin et al., 2011). Interestingly, from the continuum point of view, the common feature of the healing phenomenon in all of these materials (e.g. self-healing polymers and biomaterials) is that the induced micro-damages (e.g. micro-cracks, micro-voids) gradually reduce in size and subsequently cause the material to recover partially or fully its strength and stiffness. Therefore, it seems quite natural to relate the modeling of the healing phenomenon to the size and density of the healed micro-damages.

The common modeling practice in predicting the damage evolution and growth in the context of continuum damage mechanics is to treat the damage nucleation and growth analogously to time-independent plasticity by introducing a damage surface

(analogous to the yield surface) which determines the damage nucleation criterion and a damage evolution function which quantifies the damage density (Kachanov, 1986; Lemaître and Chaboche, 1990; Voyiadjis and Kattan, 1990; Krajcinovic, 1996). This modeling treatment of continuum damage mechanics yields to the fact that damage does not evolve during the unloading where the material point is located in the damage loading surface. Subsequently, the stiffness modulus remains constant during the unloading resulting in a linear response in the stress-strain diagram during the unloading. Figure 4.1 shows a schematic representation of the stress-strain response for a complete unloading-loading cycle (e.g. Karsan and Jirsa, 1969).
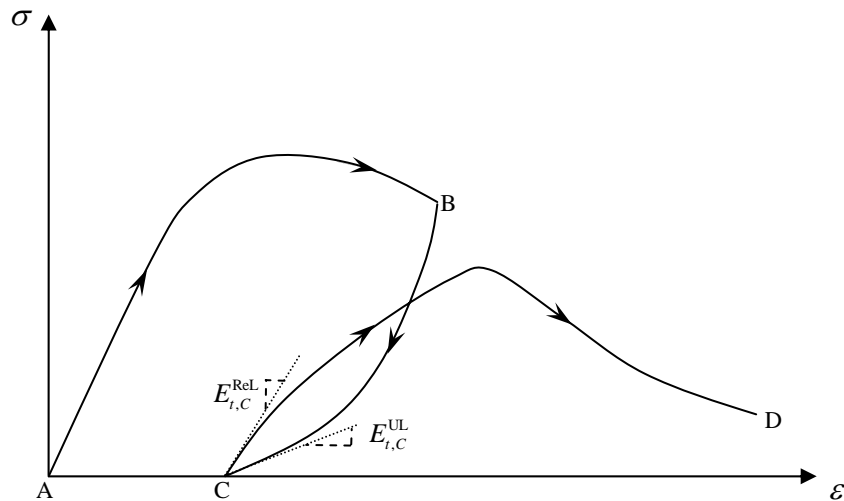
Figure 4.1. Schematic representation of the stress-strain response for a loading (path "AB"), unloading (Path "BC"), and reloading (path "CD") cycle. The stress-strain response during the unloading is nonlinear and also the tangent stiffness at the end of the unloading (i.e. $E_{t,C}^{\mathrm{UL}}$) is less than the tangent stiffness modulus at the beginning of the reloading (i.e. $E_{t,C}^{\mathrm{ReL}}$).

As shown schematically in Figure 4.1 and has also been reported in numerous experimental studies on engineering materials, the stress-strain response during the unloading [path "BC" in Figure 4.1] is nonlinear (e.g. Sinha et al., 1964; Karsan and

Jirsa, 1969; Ortiz, 1985; Bari and Hassan, 2000; Mirmiran et al., 2000; Eggeler et al., 2004; Palermo and Vecchio, 2004; Sima et al., 2008).

In this work, the nonlinear response of the stress-strain diagram during the unloading is related to extra damage growth during the unloading. It should be noted that Ortiz (1985) was the first to model the nonlinear response of the stress-strain diagram during the unloading by considering the anisotropic damage and crack closure. In this work, the damage anisotropy is not included; instead, the damage function is allowed to evolve with a slower rate during the unloading to model this distinct behavior. Moreover, the arguments in the subsequent sections show that the underlying assumptions of this work are physically in line with the fundamental assumptions of Ortiz (1985).

Moreover, the experimental observations on cyclic loading of several materials show a jump in the tangent stiffness modulus at the unloading-loading points [point "C" in Figure 4.1] (Sinha et al., 1964; Karsan and Jirsa, 1969; Ortiz, 1985; Hassan et al., 1992; Eggeler et al., 2004; Sima et al., 2008). In other words, as shown schematically in Figure 4.1, the material recovers part of its stiffness at unloading-loading point such that the tangent stiffness at the beginning of the subsequent loading cycle [$E_{t,C}^{\mathrm{ReL}}$ in Figure 4.1] is greater than the tangent stiffness modulus at the end of the unloading [$E_{t,C}^{\mathrm{UL}}$ in Figure 4.1]. This jump in the tangent stiffness at the unloading-loading point becomes more significant if rest periods (or unloading times) are introduced between the loading cycles. The current study shows that this distinct behavior could be related to micro-damage healing at low strain levels. In other words, at the end of the unloading, the strain levels becomes close to zero such that the faces of the induced micro-damages wet each other and retrieve part of their bond strength. The wetting of the micro-damage surfaces results in partial healing and subsequently partial recovery in the tangent stiffness modulus at unloading-loading point. This phenomenon is usually referred to as *instantaneous healing* (Wool and Oconnor, 1981). More healing will occur (e.g. due to cohesion and inter-molecular diffusion process between the micro-crack faces in polymers, biomaterials, and bituminous materials) if the wetted surfaces of the micro-

damages put into rest for a while before the next loading cycle is applied. This phenomenon is usually referred to as the *time-dependent (or long-term) healing* in the literature (Wool and Oconnor, 1981).

Several phenomenological-based formulations for describing the healing phenomena in different materials have been proposed in the literature (e.g. Jacobsen et al., 1996; Ramm and Biscoping, 1998; Ando et al., 2002). However, little attention is devoted to the proper coupling of the healing to continuum damage mechanics. Miao et al. (1995) proposed a constitutive model for compaction of crushed rock salts, Barbero et al. (2005) proposed a thermodynamic-based continuum damage-healing constitutive model for self-healing composites, and Voyiadjis et al. (2011) extended the work of Barbero et al. (2005) by incorporating the isotropic hardening in damage and healing models. However, more studies are needed to develop a robust and simple computational technique to model the phenomena associated with the micro-damage healing in materials that tend to heal. Therefore, this study aims to contribute in filling this gap by proposing a micro-damage healing framework in the context of the continuum damage mechanics. The proposed framework introduces a healing configuration which enriches the continuum damage mechanics theories in modeling the micro-damage healing phenomenon. The well-known transformation hypotheses of continuum damage mechanics from the effective (undamaged) to the nominal (damaged) configurations are extended here to incorporate self-healing. Moreover, analytical relations are derived to relate the stiffness moduli in different configurations. Several numerical examples are presented in order to demonstrate the capabilities of the proposed framework in capturing interesting phenomena such as: (a) the stiffness and strength recovery in cyclic loading upon the application of rest periods; (b) the nonlinear response of the stress-strain diagram during unloading; and (c) the jump in the tangent stiffness modulus at the unloading-loading point (Darabi et al., 2011b).

4.2. Micro-Damage Healing Configuration

In the classical continuum damage mechanics (CDM) framework, a scalar variable, the damage variable, for the case of the isotropic damage or a higher-order tensor, the damage tensor, for the case of the anisotropic damage is usually used to explain the degradation behavior of materials due to micro-damage (micro-cracks and micro-voids) nucleation and growth [see e.g. Voyiadjis and Kattan (1999) for a comprehensive review of the this subject]. For simplicity and without loss of generality, the case of isotropic damage is considered here. In this work, the *effective (undamaged) configuration* is generalized to the cases when materials undergo micro-damage healing or partial/full recovery of the damaged stiffness.

Figure 4.2(a) shows a cylinder under a uniaxial tensile load T at the current time "t". During the loading-unloading processes, some new micro-cracks and micro-voids nucleate and propagate upon satisfaction of the damage nucleation and growth conditions. On the other hand, for certain materials (e.g. polymers, bituminous materials, and biological materials) some of these micro-cracks may heal during the resting period (or the unloading process). Therefore, one can divide the total cross-sectional area, A, of the cylinder into three parts: (a) the area that has not been damaged (i.e. intact area), $\bar{A}$, which can be considered as the *effective* (undamaged) area in CDM; (b) the area of unhealed cracks and voids, A^{uh}, where damage is considered irreversible; (c) the area of micro-cracks and micro-voids that have been healed during the unloading process or the rest period, A^h. Figure 4.2(b) shows the cross-sectional area of the cylinder at time "t" in the *nominal (damaged) configuration*. One can assume that the area of the completely healed micro-damages have the same properties of the intact material. Hence, once a micro-crack heals completely, it retrieves all of its strength such that its mechanical properties become identical to those of the intact material. Figure 4.2(c) shows the *healing configuration*.

(a)

Remove both healed and unhealed damages (micro-cracks and micro-voids)

Remove all unhealed
damages

Remove healed damages

A, σ, E

$\tilde{A} = A - A^{uh}, \tilde{\sigma}, \tilde{E}$

$\bar{A} = A - A^{h} - A^{uh}, \bar{\sigma}, \bar{E}$

Nominal (damaged)
configuration

Healing
configuration

Effective (undamaged)
configuration

(b)

(c)

(d)
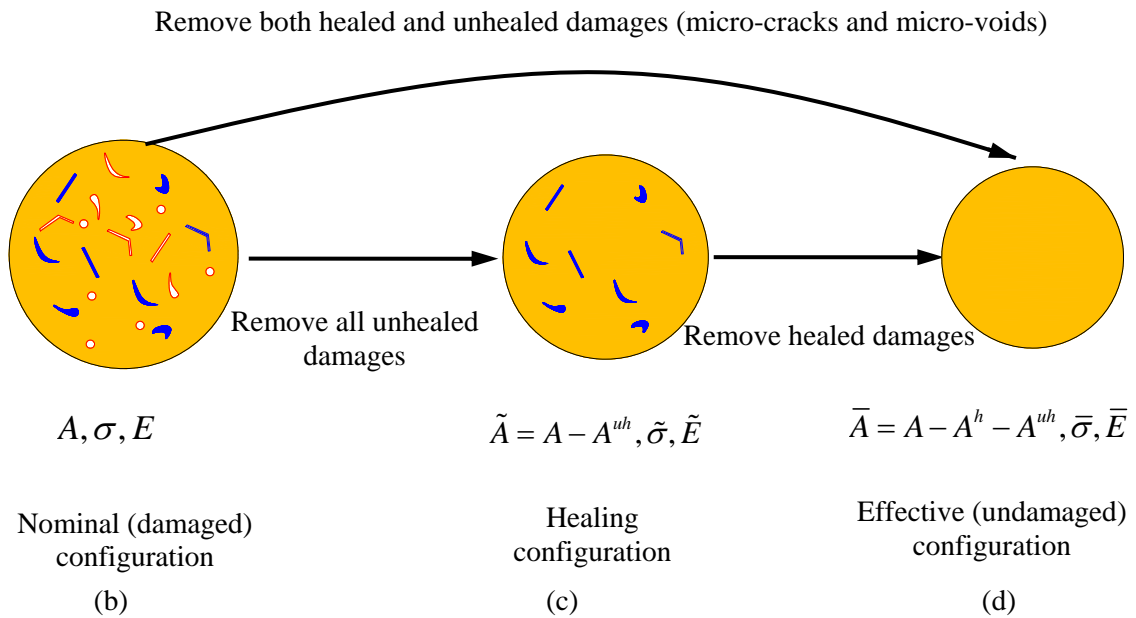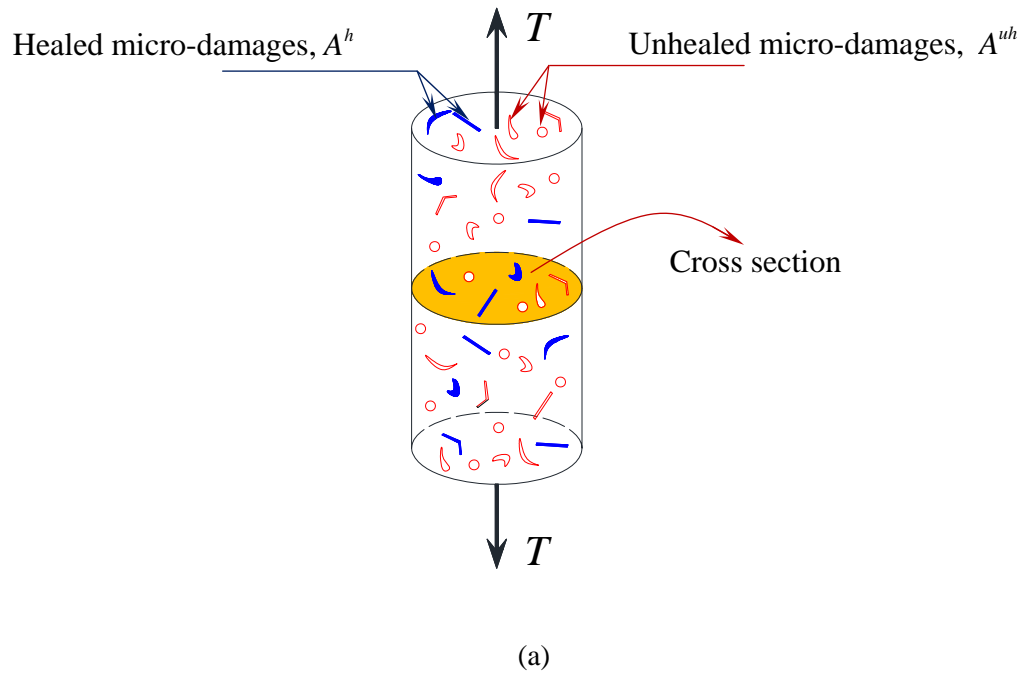
Figure 4.2. Schematic representation of: (a) the damaged partially healed cylinder in tension; (b) the nominal configuration; (c) the healing configuration; and (d) the effective configuration. The nominal configuration includes the intact material, unhealed damages, and healed micro-damages; the healing configuration includes the intact material and the healed micro-damages and the effective configuration only includes the intact material.

This fictitious configuration results when unhealed cracks and voids are removed from the damaged configuration. The *effective (undamaged) configuration* is shown in Figure 4.2(d). This fictitious configuration includes the materials that have never been damaged (intact) during the loading-unloading history. This configuration is identical to the so-called effective configuration in CDM when healing does not occur. Therefore, one can write from Figure 4.2:

$$A = \bar{A} + A^D = \tilde{A} + A^{uh} \tag{4.1}$$

$$A^D = A^{uh} + A^h \tag{4.2}$$

where A, $\bar{A}$, and $\tilde{A}$ are the cross-sectional area in the *nominal* (damaged), *effective* (undamaged), and *healing* configurations, respectively; and A^D is the summation of both healed micro-cracks and micro-voids, A^h, and unhealed micro-cracks and micro-voids, A^{uh}.

As it is assumed in CDM, cracks and voids cannot carry load. In fact, load is carried by the area of the intact material and the healed micro-damages. Therefore, one can assume that the applied forces in the nominal and healing configurations are equal, such that:

$$T = \sigma A = \tilde{\sigma} \tilde{A} \tag{4.3}$$

where σ is the nominal (apparent) stress and $\tilde{\sigma}$ is the stress in the healing configuration (true or net stress). In this paper, the superscripts "‾" and "~" designate the effective and healing configurations, respectively. The following definitions are introduced for the damage and healing internal state variables, respectively:

$$\phi = \frac{A^D}{A} \tag{4.4}$$

$$h = \frac{A^h}{A^D} \tag{4.5}$$

For the cases when healing is not considered, ϕ is the classical irreversible damage density variable ranging from $0 \leq \phi \leq 1$, which is interpreted as the micro-damage density such that $\phi = 0$ indicates no damage and $\phi = 1$ indicates complete damage (or

fracture). However, when healing is included, ϕ is interpreted as an internal state variable representing the damage history such that A^D is the accumulative damaged area. On the other hand, h is the *healing internal variable* defined as the ratio of the accumulative area of healed micro-damages over the accumulative damaged area. Therefore, h represents the healed fraction of the total accumulative damaged area. The healing variable ranges from $0 \leq h \leq 1$; $h = 0$ for no healing and $h = 1$ when all micro-cracks and micro-voids are healed.

Substituting Eqs. (4.1), (4.2), (4.4), and (4.5) into Eq. (4.3) yields:

$$\tilde{\sigma} = \frac{\sigma}{1 - \tilde{\phi}} \tag{4.6}$$

where $\tilde{\phi}$ is the effective damage density ranging from $0 \leq \phi_{eff} \leq 1$, such that:

$$\tilde{\phi} = \phi(1 - h) \tag{4.7}$$

such that $\tilde{\phi} = 0$ indicates that either the material has not been damaged yet or all induced damages have already been healed; whereas, $\tilde{\phi} = 1$ indicates complete damage (or fracture). It should be noted that the effective damage density variable is no longer irreversible and can decrease upon micro-damage healing.

It is noteworthy that the healing variable in Eq. (4.7) has a similar effect to the stiffness-recovery parameter introduced in the work of Lee and Fenves (1998) for modeling the stiffness recovery in concrete materials during the transition from tension to compression loading. However, the physics behind the stiffness-recovery parameter by Lee and Fenves (1998) is different than the current proposed micro-damage healing variable h. Lee and Fenves (1998) interpreted the area of healed micro-cracks in Eq. (4.5), A^h, as the area of closed micro-cracks (not healed) during the loading transition from tension to compression. Therefore, the current proposed healing variable is more general as it can be interpreted as a crack-closure parameter or as a healing parameter, but with a different evolution law, depending on the intended application.

Eqs. (4.6) and (4.7) relate the stress in the healing configuration to the nominal stress as a function of the damage and healing internal variables. This expression

represents the proper coupling between the damage and healing variables and modifies the classical definition of the effective stress in CDM [i.e. $\tilde{\sigma} = \bar{\sigma} = \sigma/(1-\phi)$ when healing is not considered (i.e. $h = 0$)].

Eq. (4.6) can be simply generalized for three-dimensional cases for the case of the isotropic (scalar) damage, such that:

$$\tilde{\sigma} = \frac{\sigma}{1-\tilde{\phi}} = \frac{\sigma}{1-\phi(1-h)} \tag{4.8}$$

where σ is the nominal stress tensor in the damaged configuration and $\tilde{\sigma}$ is the true stress tensor in the healing configuration.

Moreover, the following relationship between the stress tensors in the healing and effective configurations will be obtained if one assumes that the tensile forces in the effective and healing configurations are the same (i.e. $\bar{\sigma}\bar{A} = \tilde{\sigma}\tilde{A}$ in Figure 4.2), such that:

$$\bar{\sigma} = \tilde{\sigma}\left[\frac{1-\phi(1-h)}{1-\phi}\right] \tag{4.9}$$

Eq. (4.9) clearly shows that the stress tensors in the healing and effective configurations will be the same only for two cases: (1) damage variable is zero (i.e. $\phi = 0$), where in this case the stress tensors in the effective and healing configurations (i.e. $\bar{\sigma}$ and $\tilde{\sigma}$) will be the same as the stress tensor in the nominal configuration (i.e. σ) since damage has not started yet; (2) healing variable is zero (i.e. $h = 0$), where in this case the stress tensors in the effective and healing configurations will be the same since healing is not considered. For other cases, the stress tensor in the fictitious effective configuration will be always greater than the stress tensor in the healing configuration (i.e. $\bar{\sigma} \geq \tilde{\sigma}$). In other words, the effective configuration (Figure 4.2(d)) is obtained by removing the healed micro-damage areas from the healing configuration (Figure 4.2(c)) such that these healed micro-damages can tolerate load and carry stress in the healing configuration. Therefore, the stress tensor in the effective configurations should be magnified comparing to the stress tensor in the healing configuration in order to compensate for the stresses carried by the removed healed micro-damages.

In the above, the relations between the stresses in different configurations are derived. In the following sections, the relations among the strain tensors and stiffness moduli in different configurations will be derived.

4.3. The Stiffness Moduli in Different Configurations

As mentioned in previous Section, completely healed micro-cracks and micro-voids recover their total strength and stiffness such that they become identical to the intact material. Hence, one can assume that the stiffness moduli in the effective and healing configurations are the same and equal to the stiffness modulus of the virgin state of the material that does not change during the loading-unloading history, such that:

$$\bar{E}_t = \tilde{E}_t \tag{4.10}$$

where $\bar{E}_t$ and $\tilde{E}_t$ are the tangent stiffness moduli in the effective and healing configurations, respectively. The tangent stiffness modulus is used in this paper instead of the commonly used secant stiffness modulus in CDM theories. The nominal tangent stiffness modulus is defined as:

$$E_t = \frac{d\sigma}{d\varepsilon} \tag{4.11}$$

The secant stiffness modulus is commonly used in CDM to capture the degradation of the stiffness modulus with damage evolution. However, the tangent stiffness modulus could capture the nonlinear response of materials easier and is commonly used instead of the secant stiffness modulus for the numerical implementation purposes. Figure 3 schematically illustrates the advantages of using tangent stiffness modulus rather than the secant stiffness modulus. Figure 4.3 shows three different paths that point "A" may continue on the stress-strain curve. Path (1) represents a path on which the material shows hardening behavior; the material goes to the softening region on path (2); and path (3) represents a schematic unloading path. The secant stiffness modulus of point "A" (i.e. E_A) will be the same for all these three different paths as shown in Figure 4.3. However, the tangent stiffness modulus at point "A" for each of these paths will be different (i.e. $E_{t,A,1}$, $E_{t,A,2}$, and $E_{t,A,3}$ corresponding to paths (1), (2), and (3),

respectively). Therefore, these different paths will clearly be distinguished by looking at the tangent stiffness moduli at point "A". Moreover, physically speaking, a material point at a specific time feels the tangent stiffness modulus as the measure of its stiffness. In other words, if the tangent modulus at an arbitrary point "c" on the stress-strain curve is greater than that of point "d", it can simply be implied that the material has the capacity to build up larger stress increment at point "c" rather than point "d" for the same strain increment. However, this simple argument cannot be made by looking at the values of the secant modulus at those points unless the history of the secant modulus is studied [please see Eq. (4.15)].
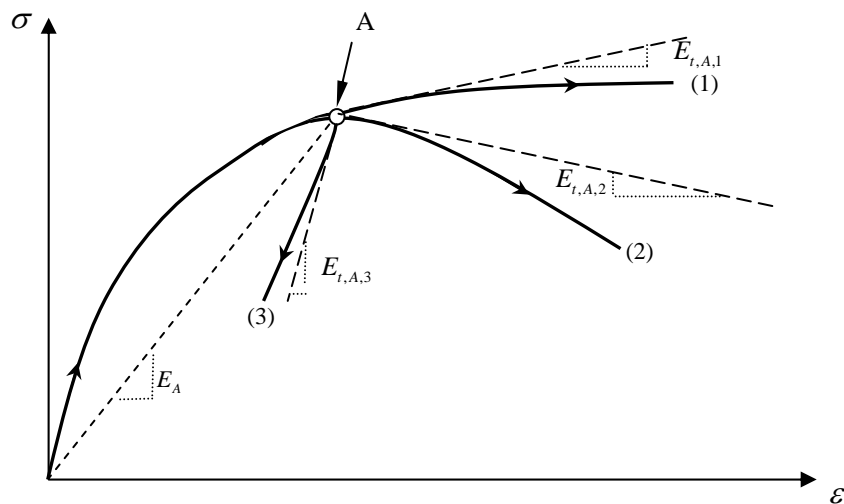
Figure 4.3. Schematic illustration of three possible paths for point "A" on the stress-strain curve. Path (1) represents the path on which the material shows hardening behavior; material point goes to softening region on path (2), and path (3) represents a schematic unloading path. The secant stiffness modulus of point "A" will be the same for all these three paths. However, these paths can be distinguished by looking at the tangent stiffness modulus of point "A" for each stress-strain path.

However, one can simply derive the relationship between the tangent and secant stiffness moduli as illustrated in the following developments. For the *secant* stiffness modulus, one can write:

$$\boldsymbol{\sigma} = \boldsymbol{E} : \boldsymbol{\varepsilon} \tag{4.12}$$

where $E = E\left(\bar{E}, \phi, h\right)$ is the fourth-order damaged-healed secant stiffness tensor, and ε is the strain tensor in the nominal configuration. Taking the time derivative of Eq. (4.12) yields:

$$\dot{\sigma} = E : \dot{\varepsilon} + \dot{E} : \varepsilon = \left(E + \dot{E} : \varepsilon \dot{\varepsilon}^{-1}\right) : \dot{\varepsilon} \tag{4.13}$$

The superimposed dot in this equation and all subsequent equations indicates derivative with respect to time. Also, "A^{-1}" indicates the inverse of "A". On the other hand, for the *tangent* stiffness modulus, one can write:

$$\dot{\sigma} = E_t : \dot{\varepsilon} \tag{4.14}$$

The relation between the tangent and secant moduli is obtained by comparing Eqs. (4.13) and (4.14), such that:

$$E_t = E + \dot{E} : \varepsilon \, \dot{\varepsilon}^{-1} \tag{4.15}$$

Different expressions for $\dot{E}$ are derived next based on adapting three different transformation hypotheses to relate the healing configuration to the damaged configuration.

   As argued before, the stiffness moduli in the effective and healing configurations are the same [Eq. (4.10)] and do not change during the loading-unloading history or as the material damages or heals. Hence, one can simply imply that for elastic-damage-healing materials, the secant and tangent stiffness moduli in both effective and healing configurations are the same as the initial undamaged stiffness modulus of the intact materials, such that:

$$\bar{E} = \tilde{E} = \bar{E}_t = \tilde{E}_t \tag{4.16}$$

Moreover, stress and strain tensors and their rates are related through the following relationships:

$$\tilde{\sigma} = \tilde{E} : \tilde{\varepsilon}; \quad \dot{\tilde{\sigma}} = \tilde{E}_t : \dot{\tilde{\varepsilon}} \tag{4.17}$$

Taking the time derivative of Eq. (4.8) yields:

$$\dot{\sigma} = \left[1 - \phi(1-h)\right]\dot{\tilde{\sigma}} + \left(-\dot{\phi} + \dot{\phi}h + \phi\dot{h}\right)\tilde{\sigma} \tag{4.18}$$

Now, several transformation hypotheses from the healing configuration to the damage configuration are discussed. It should be noted that Eqs. (4.9) and (4.16) relate the stress tensors and stiffness moduli in the effective and healing configurations. One can also establish a general relationship between the strain tensors in the effective and healing configurations. Eq. (4.16) yields:

$$\bar{E} = \tilde{E} \Rightarrow \bar{\sigma} : \bar{\varepsilon}^{-1} = \tilde{\sigma} : \tilde{\varepsilon}^{-1} \tag{4.19}$$

Substituting Eq. (4.9) into Eq. (4.19) gives:

$$\bar{\varepsilon} = \left[\frac{1 - \phi(1-h)}{1-\phi} \right] \tilde{\varepsilon} \tag{4.20}$$

Eq. (4.20) relates the strain tensors in the effective and healing configurations and shows that these two tensors will be the same when healing is not included (i.e. $h=0$) or when there is no damage (i.e. $\phi=0$). Otherwise, there will be differences between the strain tensors in the effective and healing configurations depending on the levels of damage and healing. Also, Eq. (4.20) is true independent of the following postulated transformation hypotheses.

In the next sub-sections, the relationships between the strain tensors and stiffness moduli in the nominal (damaged) and healing configurations will be established for different transformation hypotheses. Relations between the stress tensors, stiffness moduli, and strain tensors in the healing and effective configurations can evidently be obtained using Eqs. (4.9), (4.16), and (4.20), respectively.

4.3.1. Strain Equivalence Hypothesis

The first commonly used hypothesis in CDM to relate the nominal stress and strain tenors (σ and ε) to the stress and strain tensors in the undamaged effective configuration ($\bar{\sigma}$ and $\bar{\varepsilon}$) is the strain equivalence hypothesis which states that the strain tenors in the nominal and effective configurations are equal (Lemaître and Chaboche, 1990). This is the simplest transformation hypothesis that one can think about and makes the theoretical derivation and numerical implementation of constitutive models relatively easier. However, this hypothesis is inaccurate in case of large deformations and/or

significant damage evolution. This hypothesis is extended here for the healing configuration such that one can assume that the strain tensors in the nominal and healing configurations are equal, such that:

$$\boldsymbol{\varepsilon} = \tilde{\boldsymbol{\varepsilon}} \;\Rightarrow\; \dot{\boldsymbol{\varepsilon}} = \dot{\tilde{\boldsymbol{\varepsilon}}} \tag{4.21}$$

It should be noted that equivalency of the strain tensors in the healing and nominal configurations does not imply the equivalency of the strain tensors in the effective and healing configurations when healing is included. In fact, Eq. (4.20) relates the strain tensors in the healing and effective configurations when healing is included. Substituting Eq. (4.18) into $\dot{\boldsymbol{\varepsilon}} = \boldsymbol{E}_t^{-1} : \dot{\boldsymbol{\sigma}}$ [Eq. (4.14)] yields:

$$\dot{\boldsymbol{\varepsilon}} = \left[1 - \phi(1-h)\right]\boldsymbol{E}_t^{-1} : \dot{\tilde{\boldsymbol{\sigma}}} + \left(-\dot{\phi} + \dot{\phi}h + \phi\dot{h}\right)\boldsymbol{E}_t^{-1} : \tilde{\boldsymbol{\sigma}} \tag{4.22}$$

Substituting Eq. $(4.17)_2$ into Eq. (4.22) yields:

$$\dot{\boldsymbol{\varepsilon}} = \left[1 - \phi(1-h)\right]\boldsymbol{E}_t^{-1} : \tilde{\boldsymbol{E}}_t : \dot{\tilde{\boldsymbol{\varepsilon}}} + \left[-\dot{\phi} + \dot{\phi}h + \phi\dot{h}\right]\boldsymbol{E}_t^{-1} : \tilde{\boldsymbol{E}}_t : \tilde{\boldsymbol{\varepsilon}} \tag{4.23}$$

Furthermore, substituting Eq. (4.21) into Eq. (4.23) gives:

$$\boldsymbol{E}_t = \left[1 - \phi(1-h) + \left(\dot{\phi}h + \phi\dot{h} - \dot{\phi}\right)\boldsymbol{\varepsilon} : \dot{\boldsymbol{\varepsilon}}^{-1}\right]\tilde{\boldsymbol{E}}_t \tag{4.24}$$

Eq. (4.24) expresses the changes in the nominal tangent stiffness as a function of the damage variable, the healing variable, the strain level, and their rates. As will be shown in the subsequent developments, Eq. (4.24) is able to capture the nonlinear response of the material during the loading as well as the unloading processes. Another feature of Eq. (4.24) is that it takes into account the deformation history by including the strain level. This equation can also capture the changes in the stiffness modulus at the loading-unloading point in the cyclic loading which is triggered by the presence of the strain rate in Eq. (4.24).

One can also simply derive the relation between the secant stiffness modulus and its rate in the nominal and healing configurations by substituting Eqs. (4.12), $(4.17)_1$, and (4.21) into Eq. (4.8), such that:

$$\boldsymbol{E} = \left[1 - \phi(1-h)\right]\tilde{\boldsymbol{E}} \tag{4.25}$$

Taking the time derivative of Eq. (4.25) and noting that the secant modulus in the healing configuration is constant (i.e. $\dot{\tilde{E}} = 0$) imply:

$$\dot{E} = \left(-\dot{\phi} + \dot{\phi}h + \phi\dot{h}\right)\tilde{E} \tag{4.26}$$

Eqs. (4.25) and (4.26) relate the secant stiffness modulus and its rate in the nominal configuration to their corresponding counterparts in the healing configuration. It should be noted that Eq. (4.24) can be derived simply by substituting Eqs. (4.16), (4.25), and (4.26) into Eq. (4.15).

4.3.2. Elastic Strain Energy Equivalence Hypothesis

Another commonly used transformation hypothesis in CDM is the elastic strain energy equivalence hypothesis (Cordebois and Sidoroff, 1982; Voyiadjis and Kattan, 1993; Lemaître et al., 2000), which is more physically sound comparing to the strain equivalence hypothesis (Abu Al-Rub and Voyiadjis, 2003). The elastic strain energy densities in the nominal and healing configurations for the elastic-damage-healing materials can be written as follows:

$$W = \frac{1}{2}\sigma : \varepsilon ; \quad \tilde{W} = \frac{1}{2}\tilde{\sigma} : \tilde{\varepsilon} \tag{4.27}$$

The elastic strain energy equivalence hypothesis states that the elastic strain energy densities in the nominal and effective configurations are the same (i.e. the elastic strain energy is stored in the intact material). This hypothesis is postulated here for the nominal and healing configurations, such that:

$$W = \tilde{W} \tag{4.28}$$

However, this hypothesis does not imply the equivalency of the elastic strain energy in the nominal and effective configurations when healing is included. The relationship between the elastic strain energies in the effective, nominal, and healing configurations can be obtained using Eqs. (4.9), (4.20), and (4.28), such that:

$$W = \tilde{W} = \left[\frac{1-\phi}{1-\phi(1-h)}\right]^2 \bar{W} \tag{4.29}$$

where $\bar{W} = \bar{\boldsymbol{\sigma}} : \bar{\boldsymbol{\varepsilon}}/2$. Eq. (4.29) shows that the elastic strain energy in the effective configuration will be equivalent to that in the nominal and healing configurations only when the healing variable is zero (i.e. healing is not included) or when there is no damage. Substituting Eqs. (4.8) and (4.27) into Eq. (4.28) yields:

$$\tilde{\boldsymbol{\varepsilon}} = \left[1 - \phi(1-h)\right]\boldsymbol{\varepsilon} \tag{4.30}$$

Eq. (4.30) relates the strain tensors in the nominal and healing configurations. The relationship between the tangent moduli in the nominal and healing configurations can then be obtained by substituting Eqs. (4.12), (4.14), (4.16), (4.17), and (4.30) into Eq. (4.18), such that:

$$\boldsymbol{E}_t = \left\{\left[1 - \phi(1-h)\right]^2 + 2\left(-\dot{\phi} + \dot{\phi}h + \phi\dot{h}\right)\left[1 - \phi(1-h)\right]\boldsymbol{\varepsilon} : \dot{\boldsymbol{\varepsilon}}^{-1}\right\}\tilde{\boldsymbol{E}}_t \tag{4.31}$$

Furthermore, the relations between the secant stiffness modulus and its rate in the nominal and healing configurations can be derived by substituting Eqs. (4.12), (4.16), (4.17)$_1$, and (4.30) into Eq. (4.8), such that:

$$\boldsymbol{E} = \left[1 - \phi(1-h)\right]^2 \tilde{\boldsymbol{E}} \tag{4.32}$$

$$\dot{\boldsymbol{E}} = 2\left(-\dot{\phi} + \dot{\phi}h + \phi\dot{h}\right)\left[1 - \phi(1-h)\right]\tilde{\boldsymbol{E}} \tag{4.33}$$

Equivalently, substituting Eqs. (4.32) and (4.33) into Eq. (4.15) confirms Eq. (4.31).

4.3.3. Power Equivalence Hypothesis

Another transformation hypothesis to relate strains and stiffness moduli in the nominal and effective configurations in the absence of micro-damage healing is the power equivalence hypothesis. This hypothesis has been used by several researchers to derive constitutive models associated with dissipative processes such as viscoelasticity and viscoplasticity. To name a few, Lee et al. (1985), Voyiadjis and Thiagarajan (1997), and Voyiadjis et al. (2004) used this hypothesis to couple damage to plasticity and/or viscoplasticity models. This hypothesis is extended here to the healing configuration (instead of the effective configuration) such that one can assume that the power expenditures in the nominal and healing configurations are the same. This hypothesis is attractive for mechanisms associated with dissipation processes since the correct

estimation of the dissipated energy is generally needed. It is noteworthy that using the power equivalence hypothesis along with the concept of the stress in the healing configuration is both numerically and physically interesting. Using the concept of the stress in the healing configuration eliminates numerical complexities associated with direct coupling between the damage and healing constitutive equations and at the same time makes these simplifications physically sound since it allows the accurate estimation of the dissipated energy in the healing configuration.

The power expenditures in the nominal and healing configurations can be written as:

$$\Pi = \frac{1}{2}\boldsymbol{\sigma} : \dot{\boldsymbol{\varepsilon}}\,; \quad \tilde{\Pi} = \frac{1}{2}\tilde{\boldsymbol{\sigma}} : \dot{\tilde{\boldsymbol{\varepsilon}}} \tag{4.34}$$

Power equivalence hypothesis states that the power expenditure in the nominal, Π, and healing, $\tilde{\Pi}$, configurations are the same, such that:

$$\Pi = \tilde{\Pi} \tag{4.35}$$

Substituting Eqs. (4.8) and (4.34) into Eq. (4.35) yields:

$$\dot{\tilde{\boldsymbol{\varepsilon}}} = \left[1 - \phi(1-h)\right]\dot{\boldsymbol{\varepsilon}} \tag{4.36}$$

which relates the rate of the nominal strain tensor to its rate in the healing configuration. Substituting $\boldsymbol{\sigma}$ from Eq. (4.8) along with $\dot{\boldsymbol{\varepsilon}}$ from Eq. (4.14) into Eq. (4.34)$_1$ gives:

$$\Pi = \frac{1}{2}\left[1 - \phi(1-h)\right]\tilde{\boldsymbol{\sigma}} : \boldsymbol{E}_t^{-1} : \dot{\boldsymbol{\sigma}} \tag{4.37}$$

Substituting Eqs. (4.16), (4.17)$_2$, and (4.18) into Eq. (4.37) gives:

$$\Pi = \frac{1}{2}\left[1 - \phi(1-h)\right]^2 \tilde{\boldsymbol{\sigma}} : \boldsymbol{E}_t^{-1} : \tilde{\boldsymbol{E}}_t : \dot{\tilde{\boldsymbol{\varepsilon}}} +$$
$$\frac{1}{2}\left[1 - \phi(1-h)\right]\left(-\dot{\phi} + \dot{\phi}h + \phi\dot{h}\right)\tilde{\boldsymbol{\sigma}} : \boldsymbol{E}_t^{-1} : \tilde{\boldsymbol{E}}_t : \tilde{\boldsymbol{\varepsilon}} \tag{4.38}$$

Using the power equivalence hypothesis [Eq. (4.35)] along with Eqs. (4.34) and (4.38), one obtains the following expression for the tangent moduli:

$$\boldsymbol{E}_t = \left\{\left[1 - \phi(1-h)\right]^2 + \left[1 - \phi(1-h)\right]\left(-\dot{\phi} + \dot{\phi}h + \phi\dot{h}\right)\tilde{\boldsymbol{\varepsilon}} : \dot{\tilde{\boldsymbol{\varepsilon}}}^{-1}\right\}\tilde{\boldsymbol{E}}_t \tag{4.39}$$

The expressions in Eqs. (4.24), (4.31), and (4.39) show different relations between the tangent moduli in the nominal and healing configurations when different transformation hypotheses are postulated. Note that the right-hand-side of Eq. (4.39) is expressed as a function of the strain tensor, $\tilde{\varepsilon}$, and its rate, $\dot{\tilde{\varepsilon}}$, in the healing configuration. One may still represent the right-hand-side of Eq. (4.39) as a function of the strain tensor in the nominal configuration by using Eq. (4.36), such that:

$$\tilde{\varepsilon} = \int_0^t \left[1 - \phi(1-h)\right]\dot{\varepsilon}\,dt \tag{4.40}$$

Applying the integration by parts to Eq. (4.40) implies:

$$\tilde{\varepsilon} = \left[1 - \phi(1-h)\right]\varepsilon - \int_0^t \left(-\dot{\phi} + \dot{\phi}h + \phi\dot{h}\right)\varepsilon\,dt \tag{4.41}$$

Eqs. (4.30) and (4.41) show that postulating the power equivalence hypothesis yields a more general relationship between the strain tensors in the nominal and healing configurations as compared to the relations obtained by postulating the elastic strain energy or strain equivalence hypotheses. The difference between Eqs. (4.30) and (4.41) will be negligible for very slow processes where rate of the healing and damage variables are close to zero. Otherwise, there will be significant difference between these two expressions. Eq. (4.39) can now be expressed in terms of the nominal strain tensor by substituting Eqs. (4.36) and (4.41) into Eq. (4.39), such that:

$$
\begin{aligned}
\boldsymbol{E}_t = \Big\{ &\left[1 - \phi\left(1-h\right)\right]^2 + \varepsilon : \dot{\varepsilon}^{-1}\left[1 - \phi\left(1-h\right)\right]\left(-\dot{\phi} + \dot{\phi}h + \phi\dot{h}\right) \\
&- \left(-\dot{\phi} + \dot{\phi}h + \phi\dot{h}\right)\left[\int_0^t \left(-\dot{\phi} + \dot{\phi}h + \phi\dot{h}\right)\varepsilon\,dt\right] : \dot{\varepsilon}^{-1} \Big\} \tilde{\boldsymbol{E}}_t
\end{aligned}
\tag{4.42}
$$

Furthermore, the relationship between the secant stiffness moduli in the nominal and healing configurations can be obtained by substituting Eqs. (4.12), (4.17)$_1$, and (4.41) into Eq. (4.8), such that:

$$\boldsymbol{E} = \left\{ \left[1 - \phi\left(1-h\right)\right]^2 - \left[1 - \phi\left(1-h\right)\right]\left[\int_0^t \left(-\dot{\phi} + \dot{\phi}h + \phi\dot{h}\right)\varepsilon\,dt\right] : \dot{\varepsilon}^{-1} \right\} \tilde{\boldsymbol{E}} \tag{4.43}$$

Moreover, taking the time derivative of Eq. (4.43) yields:

$$\dot{\boldsymbol{E}} = \left\{ \left[1 - \phi(1-h) \right] \left(-\dot{\phi} + \dot{\phi}h + \phi\dot{h} \right) - \left(-\dot{\phi} + \dot{\phi}h + \phi\dot{h} \right) \left[\int_0^t \left(-\dot{\phi} + \dot{\phi}h + \phi\dot{h} \right) \boldsymbol{\varepsilon} \, dt \right] : \boldsymbol{\varepsilon}^{-1} \right.$$
$$\left. \left[1 - \phi(1-h) \right] \left[\int_0^t \left(-\dot{\phi} + \dot{\phi}h + \phi\dot{h} \right) \boldsymbol{\varepsilon} \, dt \right] : \boldsymbol{\varepsilon}^{-1} : \dot{\boldsymbol{\varepsilon}} : \boldsymbol{\varepsilon}^{-1} \right\} \tilde{\boldsymbol{E}} \tag{4.44}$$

Eqs. (4.39) and (4.42) show the expressions for relating the damaged (nominal) tangent stiffness modulus to the stiffness of the intact material as a function of the damage density, healing variable, strain, and their rates. These relations can be used to capture the nonlinear change in the stiffness during the unloading since during the unloading both the strain and the healing variable change. Furthermore, the presence of the strain rate enriches Eqs. (4.24), (4.31), and (4.39) to capture the changes in the stiffness modulus of the loading-unloading point in the cyclic loading. These important features of these equations will be shown in the following section in order to show the capabilities of the model in cyclic loading.

4.4. Damage and Healing Models and the Numerical Implementation

4.4.1. Damage and Healing Evolution Functions

Several examples are presented in this section to show the capabilities of the proposed healing framework in capturing the nonlinear response of materials under cyclic loading. Recently, Darabi et al. (2011c) and Abu Al-Rub et al. (2010a) have proposed and validated rate-dependent damage (viscodamage or delay-damage) and healing models, respectively, and coupled those to viscoelasticity and viscoplasticity constitutive models to predict the mechanical response of bituminous materials. *Simplified* forms of these models are used in this work to investigate the effect of the healing on the mechanical response of elastic-damage-healing materials. The *simplified* form of the rate-dependent damage evolution function in the healing configuration (viscodamage) is given as follows (Darabi et al., 2011c):

$$\dot{\phi} = \Gamma^{vd} \left(\frac{\tilde{Y}}{Y_{th}} \right) (1-\phi)^2 \exp(k\tilde{\varepsilon}_{eff}) \tag{4.45}$$

where Γ^{vd} is the viscodamage viscosity parameter that controls how fast damage nucleates and grows, k is a material constant, $\tilde{\varepsilon}_{eff} = \sqrt{\tilde{\varepsilon}_{ij}\tilde{\varepsilon}_{ij}}$ is the effective (or equivalent) strain, Y_{th} is the threshold damage force, and $\tilde{Y}$ is the damage driving force which is assumed to have the following simple form (Darabi et al., 2011c):

$$\tilde{Y} = \sqrt{\tilde{J}_2} \qquad (4.46)$$

where $\tilde{J}_2 = \frac{1}{2}\tilde{s}_{ij}\tilde{s}_{ij}$ is the second invariant of the deviatoric stress in the healing configuration with $\tilde{s}_{ij} = \tilde{\sigma}_{ij} - \frac{1}{3}\tilde{\sigma}_{kk}\delta_{ij}$ being the deviatoric stress and δ_{ij} being the Kronecker delta.

The presented viscodamage model in Eq. (4.45) can be treated analogous to viscoplasticity models such that the damage variable evolves when the material state is on or outside the viscodamage surface. The viscodamage surface can simply be extracted from the damage evolution function, Eq. (4.45), such that:

$$f^{vd} = \tilde{Y} - Y_{th}\frac{\dot{\phi}}{\Gamma^{vd}}\left(1-\phi\right)^{-2}\exp(-k\tilde{\varepsilon}_{eff}) \leq 0 \qquad (4.47)$$

where f^{vd} is the viscodamage loading surface [please refer to Darabi et al. (2011c; 2011d) for more details]. Hence, the damage variable ϕ evolves when the viscodamage surface is equal or greater than zero.

Since the main aim of this section is to show qualitative effects of micro-damage healing on responses of elastic-damage-healing materials, a simple phenomenological-based healing evolution function is adapted (Abu Al-Rub et al., 2010a), such that:

$$\dot{h} = \Gamma^h\left[\left(1-\phi\right)\left(1-h\right)\right]^a \qquad (4.48)$$

where Γ^h is the healing viscosity parameter controlling the rate of the micro-damage healing, and a is a material parameter. The following initiation condition is also postulated for the healing model:

$$f^h = \tilde{\varepsilon}_{th}^h - \tilde{\varepsilon}_{eff} \leq 0 \qquad (4.49)$$

where f^h is the healing loading surface, $\tilde{\varepsilon}_{th}^h$ is the healing threshold strain, and $\tilde{\varepsilon}_{eff}$ is the effective strain. Eq. (4.49) assumes that the healing variable evolves when the total effective strain is smaller than the healing threshold strain. In other words, the healing occurs at very small strains such that the micro-crack faces are close to each other and can wet each other in order for healing to occur. Moreover, it should be noted that healing cannot occur during the damage process and vice versa (i.e. a micro-crack cannot propagate and heal at the same time; either propagates or heals). Hence, rate of the healing variable will be zero when damage is evolving (i.e. when $\dot{\phi} \geq 0$).

In the following subsections, the effect of assuming rate-dependent damage versus rate-independent damage on the mechanical responses will also be investigated. Therefore, the following function is assumed to describe the rate-independent damage model, such that:

$$\phi = \gamma \left(\frac{\tilde{Y}}{Y_{th}} \right) \exp(k\tilde{\varepsilon}_{eff}) \tag{4.50}$$

The main difference between Eq. (4.45) and (4.50) is that the former is time- and rate-dependent which considers the loading time as well as the loading rate while the later is time- and rate-independent.

It is noteworthy that the presented models will be used to show qualitative effects of damage and healing on the mechanical response of elastic-damage-healing materials. Obviously, the evolution functions for the damage and healing models can be different for different materials, but similar qualitative trends will be obtained by following the above formulated continuum damage mechanics framework considering micro-damage healing.

4.4.2. Numerical Implementation for Different Transformation Hypotheses

The implementation procedure for the presented elastic-damage-healing model using different transformation hypotheses is discussed in this sub-section. However, as it will be discussed, the implementation procedure is general and independent of the selected evolution functions for the damage and healing models.

The use of the concept of the stress in the healing configurations substantially simplifies the numerical implementation of the damage and healing models, especially, for complex constitutive models where damage and healing models are coupled to viscoelasticity and/or viscoplasticity models. In other words, one can update the stress tensor in the healing configuration $\tilde{\sigma}^{t+\Delta t}$ without facing the complexities associated with the direct couplings of the damage and healing models to the rest of the constitutive model. The updated stress in the healing configuration can then be used to update the damage and healing variables and subsequently the nominal stress tensor. It should be noted that the nominal strain increment tensor $\Delta \varepsilon^{t+\Delta t}$ as well as the nominal total strain tensor $\varepsilon^{t+\Delta t}$ at the current time $t+\Delta t$ are given at the beginning of each increment. The nominal strain tensor and its increment will be the same as those in the healing configuration if the strain equivalence hypothesis is used. However, the nominal strain tensor and its increment will be different from their corresponding values in the healing configuration if either the elastic strain energy equivalence or the power equivalence hypotheses are used. Therefore, an iterative scheme is needed to obtain the total strain and the strain increment tensors in the healing configuration at time $t+\Delta t$ when the elastic strain energy equivalence or power equivalence hypotheses are used. The total nominal strain tensor and its increment at the current time $t+\Delta t$, the values of the internal state variables (i.e. ϕ, h, and $\tilde{\phi}$) at previous time t, and the stress tensors in the nominal and healing configurations at previous time t are known. The objective is to update the current stress tensors in the nominal and healing configurations as well as the strain tensor in the healing configuration at the current time $t+\Delta t$. Hence, one can start with a trial strain tensor in the healing configuration when the elastic strain energy equivalence hypothesis is used, such that:

$$\tilde{\varepsilon}^{tr,t+\Delta t} = \left(1-\tilde{\phi}^{t}\right)\varepsilon^{t+\Delta t} \tag{4.51}$$

Similarly, one can start with a trial strain increment in the healing configuration when the power equivalence hypothesis is used, such that:

$$\Delta\tilde{\varepsilon}^{tr,t+\Delta t} = \left(1-\tilde{\phi}^{t}\right)\Delta\varepsilon^{t+\Delta t} \tag{4.52}$$

Subsequently, the total trial strain tensor in the healing configuration can be obtained for the power equivalence hypothesis [using Eq. (4.52)], such that:

$$\tilde{\varepsilon}^{tr,t+\Delta t} = \tilde{\varepsilon}^{t} + \Delta\tilde{\varepsilon}^{tr,t+\Delta t} \tag{4.53}$$

The trial strain in the healing configuration [Eq. (4.51) for the elastic strain energy equivalence hypothesis; Eqs. (4.52) and (4.53) for the power equivalence hypothesis] can then be fed to the Hooke's law [Eq. (4.17)] to update the stress in the healing configuration. The next step is to calculate the damage and healing variables based on the obtained trial strain and stress tensors in the healing configuration. The damage density can then be obtained by calculating the damage density rate using Eq. (4.45), such that:

$$\phi^{t+\Delta t} = \phi^{t} + \dot{\phi}^{t+\Delta t}\Delta t \tag{4.54}$$

The same procedure can be applied to calculate the healing variable. In other words, the rate of the healing variable $\dot{h}^{t+\Delta t}$ (if the healing criterion is met) should be calculated first using Eq. (4.48). However, as mentioned earlier, healing does not occur during the damage process and vice versa. Hence, the healed area A^{h} remains constant during the damage evolution. However, during the healing process both the healing area A^{h} and the total damage area $A^{D} = A^{h} + A^{uh}$ which is the summation of the healed and unhealed damage areas will also evolve. Taking the time derivative of Eq. (4.5) and making use of Eq. (4.4) yield the following relations for the updated healing variable:

$$\begin{cases} h^{t+\Delta t} = \dfrac{\phi^{t}}{\phi^{t+\Delta t}} h^{t}; & \dot{\phi}^{t+\Delta t} \geq 0 \\ h^{t+\Delta t} = h^{t} + \dot{h}^{t+\Delta t}\Delta t; & \dot{\phi}^{t+\Delta t} = 0 \end{cases} \tag{4.55}$$

The new trial strain tensor in the healing configuration will then be recalculated using updated damage and healing variables. At the end of the iteration, the new and old values of the strain tensor in the healing configuration will be compared to check the convergence. Figure 4.4 shows the flowchart for implementation of the presented elastic-damage-healing constitutive model using different transformation hypotheses.

Known $\boldsymbol{\sigma}^t$, $\boldsymbol{\varepsilon}^t$, $\tilde{\boldsymbol{\sigma}}^t$, $\tilde{\boldsymbol{\varepsilon}}^t$, ϕ^t, h^t, and $\tilde{\phi}^t$.

Given $\Delta\boldsymbol{\varepsilon}^{t+\Delta t}$ and as a result $\boldsymbol{\varepsilon}^{t+\Delta t}$.

Elastic strain energy equivalence hypothesis

Power equivalence hypothesis

Strain equivalence hypothesis

Set $\tilde{\boldsymbol{\varepsilon}}^{t+\Delta t,tr} = \boldsymbol{\varepsilon}^{t+\Delta t}$.

Calculate the trial strain in the healing configuration
$$\tilde{\boldsymbol{\varepsilon}}^{t+\Delta t,tr} = \left(1-\tilde{\phi}^t\right)\boldsymbol{\varepsilon}^{t+\Delta t}.$$

Calculate the trial strain and strain increment in the healing configuration;
$$\Delta\tilde{\boldsymbol{\varepsilon}}^{t+\Delta t,tr} = \left(1-\tilde{\phi}^t\right)\Delta\boldsymbol{\varepsilon}^{t+\Delta t}$$
$$\tilde{\boldsymbol{\varepsilon}}^{t+\Delta t,tr} = \tilde{\boldsymbol{\varepsilon}}^t + \Delta\tilde{\boldsymbol{\varepsilon}}^{t+\Delta t,tr}.$$

Update $\tilde{\boldsymbol{\sigma}}^{t+\Delta t}$ using the trial strain in the healing configuration, Eq. (4.17)

Update damage variable using the updated stress $\tilde{\boldsymbol{\sigma}}^{t+\Delta t}$ [Eqs. (4.45), (4.54)].

Update healing variable using the updated stress $\tilde{\boldsymbol{\sigma}}^{t+\Delta t}$ [Eqs. (4.48), and (4.55)].

$$\tilde{\boldsymbol{\varepsilon}}^{t+\Delta t} = \left(1-\tilde{\phi}^{t,t+\Delta t}\right)\boldsymbol{\varepsilon}^{t+\Delta t}$$

$$\tilde{\boldsymbol{\varepsilon}}^{t+\Delta t} = \boldsymbol{\varepsilon}^{t+\Delta t}$$

$$\Delta\tilde{\boldsymbol{\varepsilon}}^{t+\Delta t} = \left(1-\tilde{\phi}^{t+\Delta t}\right)\Delta\boldsymbol{\varepsilon}^{t+\Delta t}$$
$$\tilde{\boldsymbol{\varepsilon}}^{t+\Delta t} = \tilde{\boldsymbol{\varepsilon}}^t + \Delta\tilde{\boldsymbol{\varepsilon}}^{t+\Delta t}$$

Correct the trial strain in the healing configuration
$$\tilde{\boldsymbol{\varepsilon}}^{t+\Delta t,tr} = \tilde{\boldsymbol{\varepsilon}}^{t+\Delta t}.$$

No

$$\left\|\tilde{\boldsymbol{\varepsilon}}^{t+\Delta t} - \tilde{\boldsymbol{\varepsilon}}^{t+\Delta t,tr}\right\| \leq \text{Tol}$$

No

Correct the trial strain in the healing configuration
$$\Delta\tilde{\boldsymbol{\varepsilon}}^{t+\Delta t,tr} = \Delta\tilde{\boldsymbol{\varepsilon}}^{t+\Delta t}$$
$$\tilde{\boldsymbol{\varepsilon}}^{t+\Delta t,tr} = \tilde{\boldsymbol{\varepsilon}}^t + \Delta\tilde{\boldsymbol{\varepsilon}}^{t+\Delta t}.$$

Yes   Yes   Yes

Update $\tilde{\boldsymbol{\sigma}}^{t+\Delta t}$, $\tilde{\boldsymbol{\varepsilon}}^{t+\Delta t}$, $\phi^{t+\Delta t}$, $h^{t+\Delta t}$, and $\tilde{\phi}^{t+\Delta t}$.

Update the nominal stress tensor $\boldsymbol{\sigma}^{t+\Delta t}$ using Eq. (4.8).

Figure 4.4. A flowchart showing the general finite element implementation procedure of the elastic-damage-healing model using different transformation hypotheses.

4.5. Numerical Results and Examples

The presented elastic-damage-healing model is implemented in the well-known commercial finite element code Abaqus (2008) via the user material subroutine UMAT. The finite element model considered here is simply a three-dimensional single element (C3D8R) available in Abaqus.

4.5.1. Example 1: Different Transformation Hypotheses

The effect of postulating different transformation hypotheses on the mechanical responses is investigated in this subsection. The rate-dependent damage and healing models [Eqs. (4.45) and (4.48)] along with the model parameters listed in Table 4.1 are used for the examples presented in this section.

Table 4.1. Model parameters associated with the presented elastic-damage-healing constitutive model.

$\tilde{E}$ (GPa)	v	γ	Γ^{vd} (s^{-1})	k	Y_{th} (MPa)	Γ^{h} (s^{-1})	a	$\tilde{\varepsilon}_{th}^{h}$
2	0.25	0.25	5×10^{-7}	75	2	0.03	2	0.001

The first simulated example is the uniaxial constant strain rate test (i.e. strain-controlled uniaxial test). The strain rate is selected as 0.005/sec. The loading history for this test is shown in Figure 4.5(a). Therefore, during this numerical test, no healing is expected. The stress-strain responses using different transformation hypotheses are shown in Figure 4.5(b). Figure 4.5(b) shows that the response of all transformation hypotheses is close to each other at small strains. However, these responses deviate when the strain and subsequently the damage density increase. Figure 4.5(b) shows different responses for the peak point of the stress-strain diagram and the post peak region in the stress-strain diagram when different transformation hypotheses are postulated. Furthermore, it shows that the stress-strain response using the power equivalence hypothesis lies between the numerical results from the strain equivalence and elastic strain energy equivalence hypotheses.
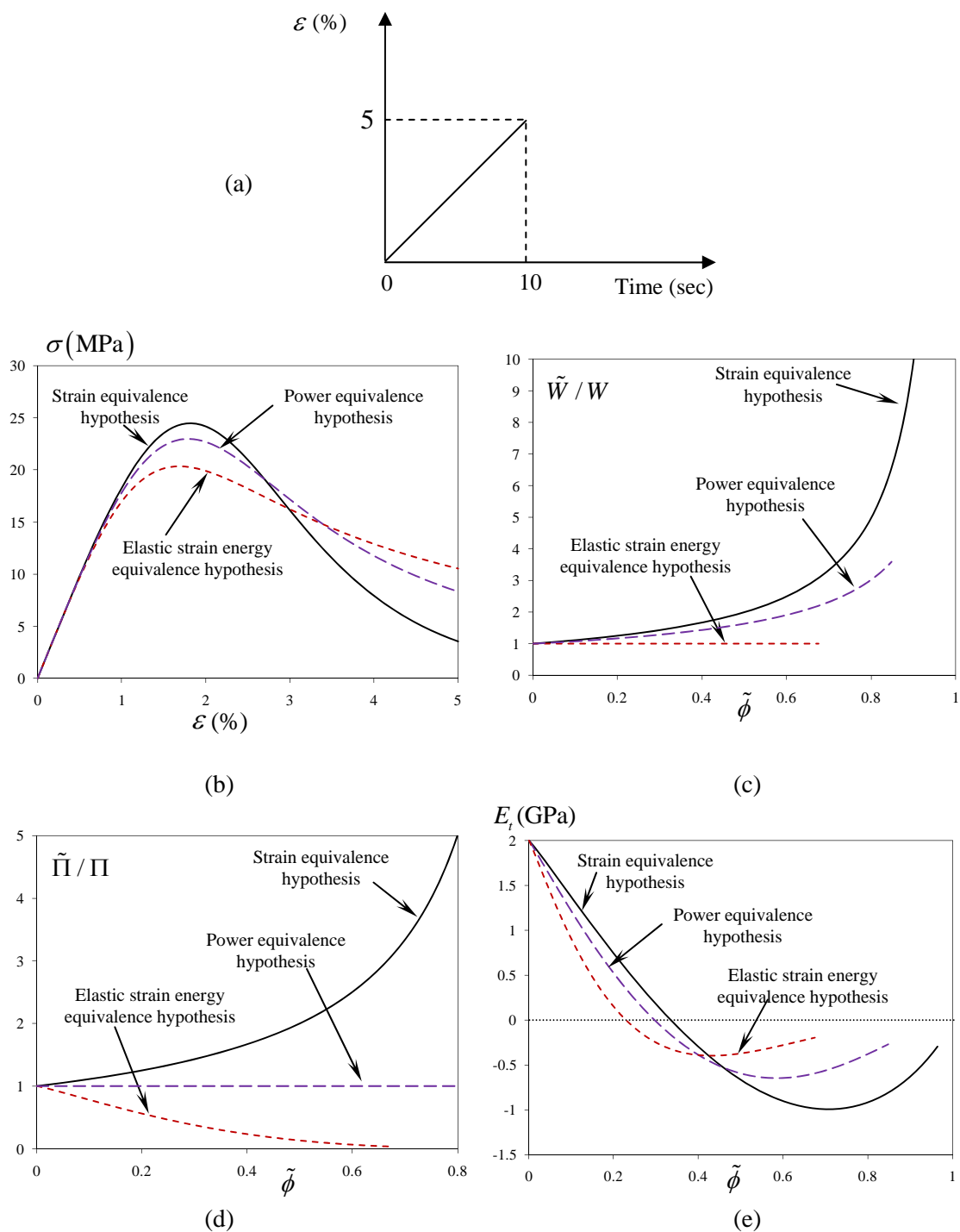
Figure 4.5. Model predictions for a uniaxial constant strain rate test using different transformation hypothesis. (a) Loading history; (b) stress-strain responses; (c) ratio of the elastic strain energy in the healing configuration over that in the nominal configuration; (d) ratio of the expended power in the healing configuration over that in the nominal configuration; and (e) tangent stiffness moduli.

The ratio of the elastic strain energy and the expended power in the healing configuration to their corresponding values in the nominal configuration for different transformation hypotheses are plotted in Figures 4.5(c) and 4.5(d), respectively. Figure 4.5(c) shows that both the strain equivalence and power equivalence hypotheses predict higher values for the elastic strain energy in the healing configuration comparing to their corresponding values in the nominal configuration. However, this deviation is much significant when the strain equivalence hypothesis is used. On the other hand, Figure 4.5(d) shows that the strain equivalence hypothesis predicts larger values for the expended power in the healing configuration comparing to its corresponding value in the nominal configuration; whereas, the elastic energy equivalence hypothesis predicts lower values for the expended power in the healing configuration comparing to that in the nominal configuration. However, it should be noted that the main purpose of using the fictitious healing and/or effective configurations along with a specific transformation hypothesis is to make the implementation simpler while the underlying physics is preserved. Also, a proper transformation hypothesis is a one that leads to a constitutive model that is equivalent when expressed in both the nominal and healing configurations since both configurations are tools to represent the same material behavior. It is also interesting to look at this problem from the thermodynamic point of view. As stated by Ziegler (1977) and have used by many other researchers (Coleman and Gurtin, 1967; Rice, 1971; Ziegler, 1983; Ziegler and Wehrli, 1987; Fremond and Nedjar, 1996; Collins and Houlsby, 1997; Shizawa and Zbib, 1999) the constitutive equations for a material are fully determined by the knowledge of the Helmholtz free energy and a dissipation function such as the rate of the energy dissipation. Therefore, two systems will be thermodynamically equivalent if they predict equivalent responses for an energetic function such as the stored energy and for a dissipative function such as dissipated power. As shown in Figures 4.5(c) and 4.5(d), none of these hypotheses predict the same value for both of these two energetic measures (i.e. strain energy and energy power) functions in nominal and healing configurations. Therefore, qualitative investigation of

the responses of each transformation hypothesis is extremely important in deciding the properness of a specific transformation hypothesis for a specific type of material.

For example, one can use the strain equivalence hypothesis for simplicity if the damage density is expected to be low. On the other hand, one may use the elastic energy equivalence hypothesis for the elastic-damage materials where the elastic strain energy could be the driving force for the damage evolution. Finally, the power equivalence hypothesis could be used for complex constitutive models including viscoelasticity and viscoplasticity in which case the elastic strain energy is negligible comparing to the total strain energy and also the dissipative power and energy becomes of great interest. Development of a transformation hypothesis that yields to the thermodynamically equivalent systems in the healing and nominal configurations will be the focus of a future work by the authors.

Finally, the tangent stiffness moduli for different transformation hypotheses are plotted in Figure 4.5(e). The negative values of the tangent stiffness modulus show that the material is in the post peak (softening) region.

The above simulation is repeated for the case of a uniaxial constant stress rate test as well (i.e. stress-controlled uniaxial test). The loading history, stress-strain response, the ratio of the elastic energy in the healing and nominal configuration, the ratio of the power expenditure in the healing and nominal configurations, and the tangent stiffness using different transformation hypotheses are shown in Figures 4.6(a)-4.6(e), respectively. Comparing Figures 4.5 and 4.6 yield similar observations for both uniaxial constant strain rate test and uniaxial constant stress rate test.

The predicted secant stiffness moduli using different transformation hypotheses are plotted in Figure 4.7 for both uniaxial constant strain rate and uniaxial constant stress rate tests. Figure 4.7 shows that the predicted secant moduli using the strain equivalence and elastic strain energy equivalence hypotheses are both path-independent.
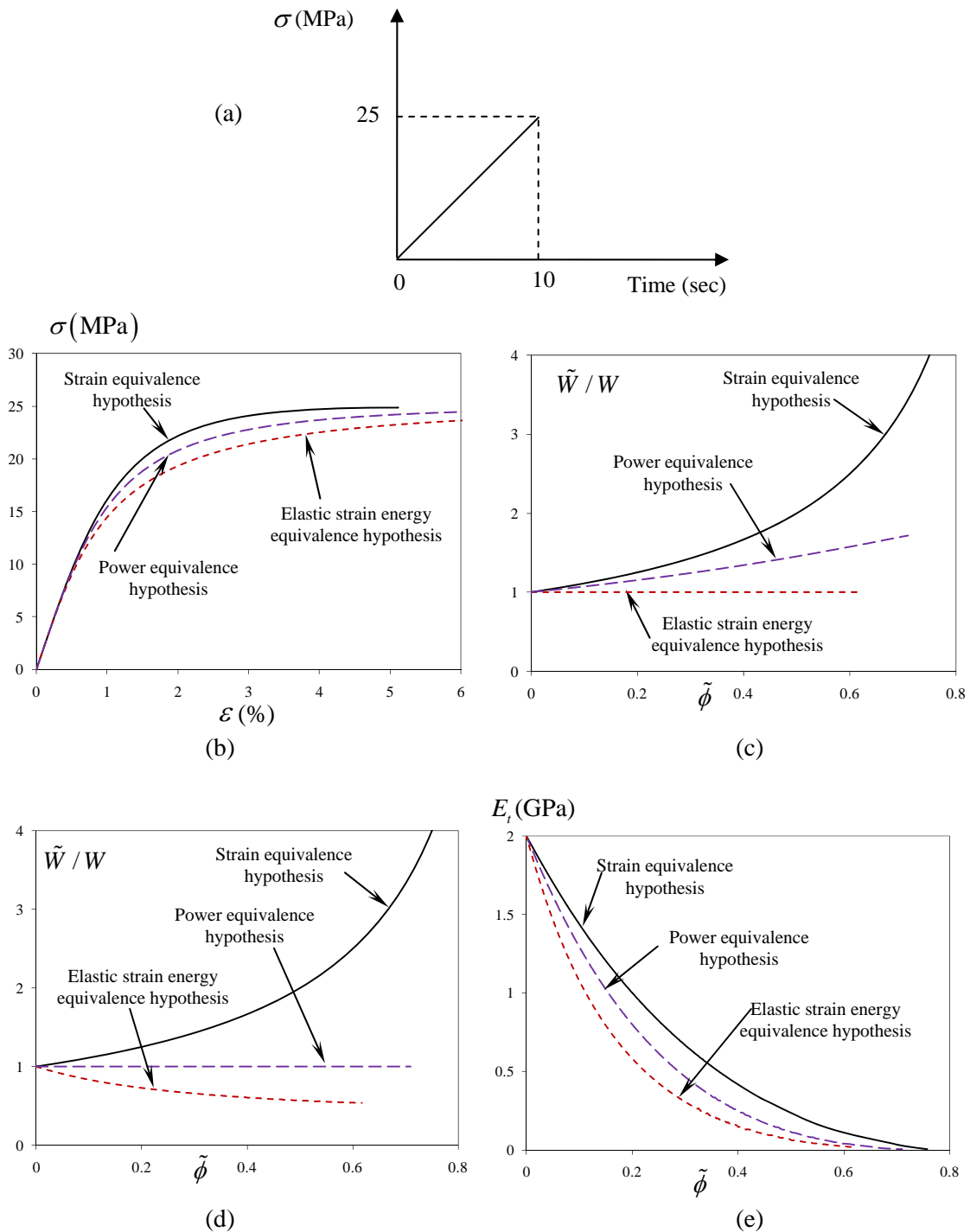
Figure 4.6. Model predictions for a uniaxial constant stress rate test using different transformation hypothesis. (a) Loading history; (b) stress-strain responses; (c) ratio of the elastic strain energy in the healing configuration over that in the nominal configuration; (d) ratio of the expended power in the healing configuration over that in the nominal configuration; and (e) tangent stiffness moduli.

This behavior is expected according to Eq. (4.25) and Eq. (4.32) for strain equivalence and elastic strain energy equivalence hypotheses, respectively. In fact, Eq. (4.25) shows that the secant stiffness modulus changes linearly as a function of the damage density for strain equivalence hypothesis; whereas, Eq. (4.32) shows that the secant stiffness modulus changes quadratic as a function of the damage density when the elastic strain energy hypothesis is postulated. On the other hand, the secant stiffness modulus becomes path-dependent when the power equivalence hypothesis is used, as shown in Figure 4.7.
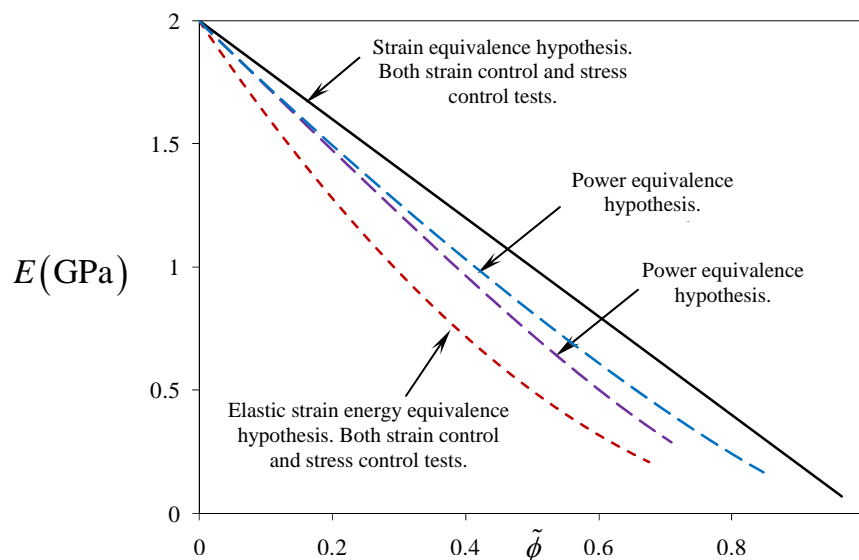
Figure 4.7. Model predictions of the secant stiffness moduli for both uniaxial constant stress and uniaxial constant strain rate tests using different transformation hypotheses. The secant stiffness modulus is path-independent when strain equivalence or elastic strain energy equivalence hypotheses are used. However, secant stiffness modulus depends on loading history when the power equivalence hypothesis is used.

This behavior is also expected by investigating Eq. (4.43). Eq. (4.43). These equations clearly show that the secant stiffness modulus is a function of the strain and strain rate in addition to the damage density value when the power equivalence hypothesis is assumed. This is a very interesting conclusion that needs to be verified experimentally, which will be the focus of a future work. Such experimental verification

will be useful to decide which transformation hypothesis is more physically sound since this issue is still an open area of research. Many argue that the strain energy equivalence hypothesis is more physically sound than the strain equivalence hypothesis (e.g. Lemaitre and Chaboche, 1990; Voyiadjis and Kattan, 1999; Abu Al-Rub and Voyiadjis, 2003). In fact, the current comparison, shows that the power equivalence hypothesis is more physically attractive since it takes into consideration the loading path-dependency of damage evolution.

The above examples show how assuming different transformation hypotheses affect the numerical results. Therefore, each of these transformation hypotheses can be selected according to the importance of the specific quantities for a specific material. For example, the strain equivalence hypothesis can be used for simplicity when the damage density is not expected to have a significant value. The elastic energy equivalence hypothesis can be used for the elastic-damage materials where the elastic strain energy could be the driving force for the damage evolution. Finally, one may use the power equivalence hypothesis for constitutive models with the dissipative nature (such as viscoelasticity and viscoplasticity) where the elastic strain energy is negligible comparing to the total strain energy and also the dissipative power and energy becomes of great interest.

4.5.2. Effect of Healing on Stiffness Recovery

In this subsection, the effect of the healing on the mechanical response of the elastic-damage-healing materials is investigated. The elastic strain energy equivalence hypothesis is used in this example since in the current elastic-damage-healing model the driving force for the damage evolution is related to the elastic strain energy. However, adapting the other transformation hypotheses will not affect the qualitative results obtained in this subsection. The rate-dependent damage and healing models are used [Eqs. (4.45) and (4.48)]. The model parameters used in this section are listed in Table 4.1. The loading history shown in Figure 4.8 can be summarized as follows:

- The material is loaded with a constant strain rate until it is partially damaged (up to 3% strain in this case).

- The load is removed with the same rate until the strain reaches zero.
- Material remains in rest for time t_R such that the induced micro-damages can partially heal. As explained before, Eq. (4.48) is time-dependent. Hence, more damages will heal for longer rest periods. Therefore different rest periods t_R are examined to investigate the effect of different healing levels on the stiffness recovery during the reloading.
- Material is reloaded with the same strain rate until significant amount of damage is developed.
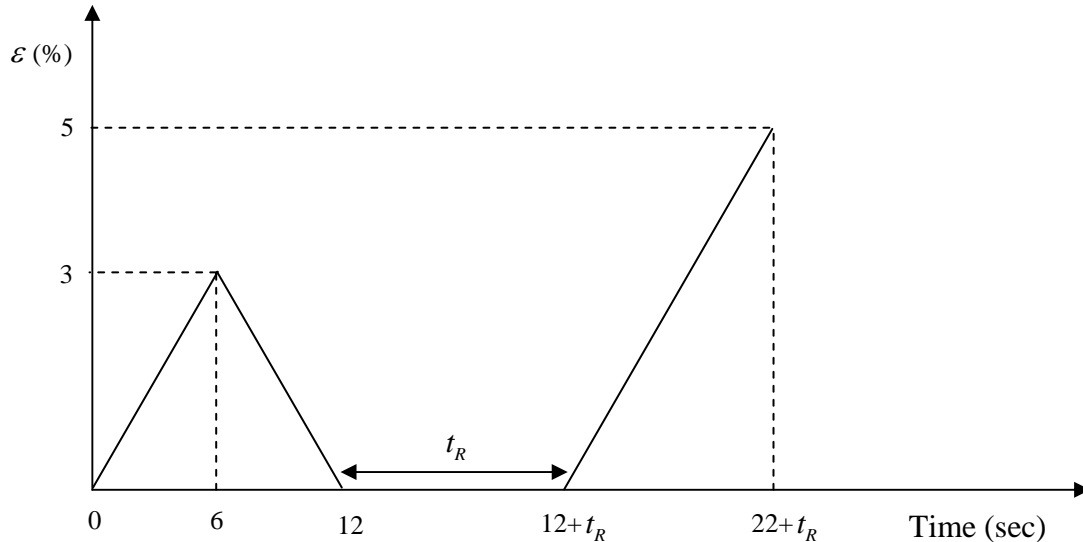
Figure 4.8. Loading history for the example simulated in Section 4.5.2. Different rest times t_R are introduced between the loading cycles to investigate the effect of the healing level on stiffness and strength recovery.

Four different rest periods of 0, 50, 200, and 500 sec are assumed in this example. Figures 4.9(a) and 4.9(b) show the stress-time and stress-strain responses for different rest periods t_R, respectively. As shown in Figures 4.9and 4.10, the material recovers part of its strength and also restores its ability to carry more stress during the reloading as the rest period increases (or equivalently as the healing variable increases).

Moreover, the mechanical response during the reloading becomes closer to the response of the monotonic loading as the rest period increases.
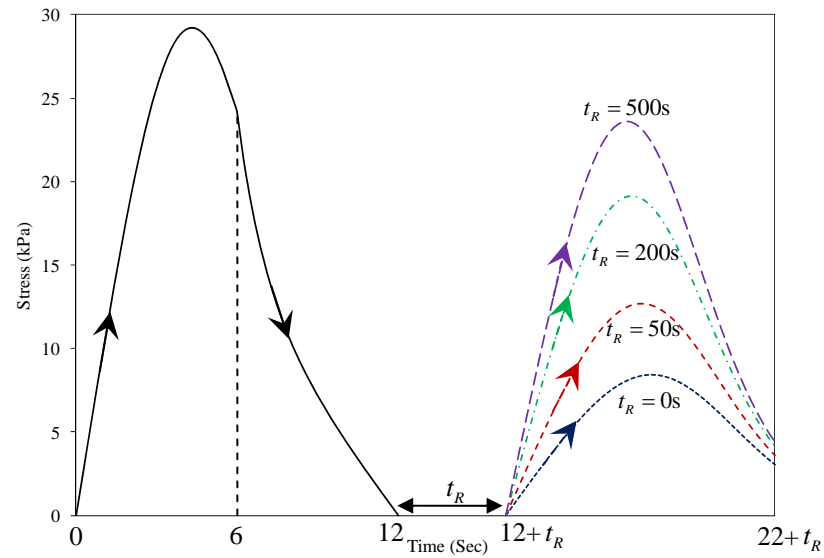
(a)
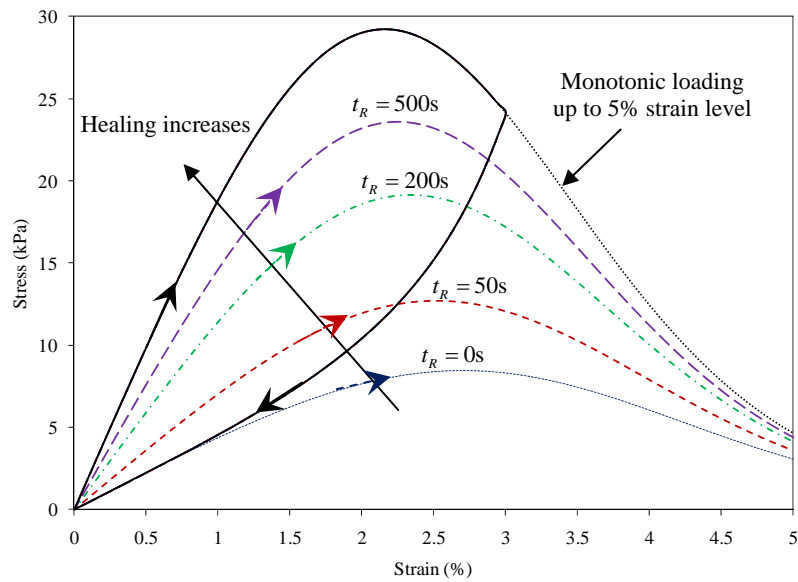
(b)

Figure 4.9. (a) Stress-time; (b) stress-strain diagrams for the loading history shown in Figure 4.7. Model predictions show more recovery in the stiffness during the reloading as t_R and consequently the healing variable increases.
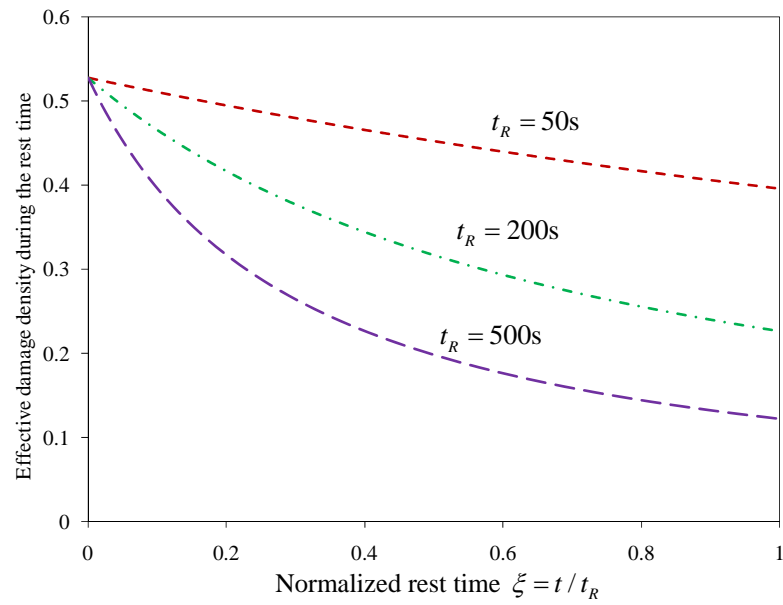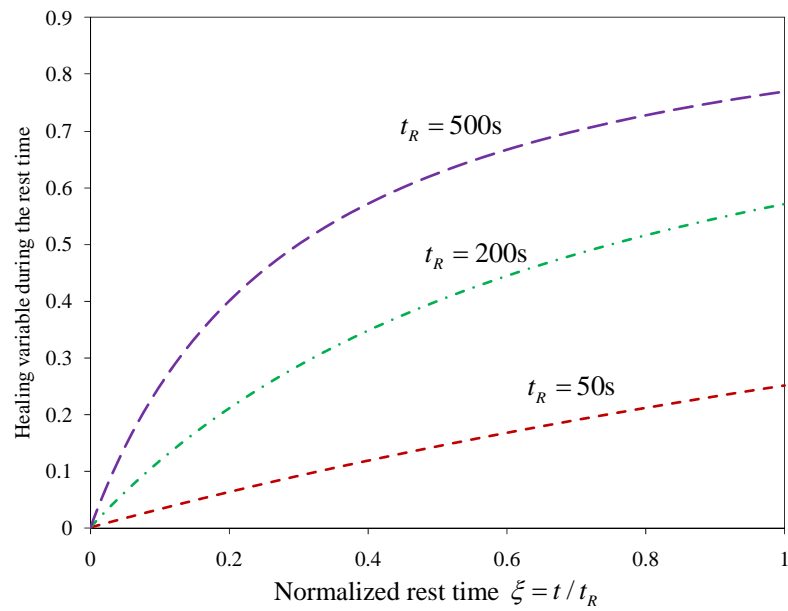
Figure 4.10. (a) Effective damage density versus the normalized rest time; smaller values for the effective damage density at the end of the rest time as the rest time increases; and (b) healing variable versus the normalized rest time; more damages heal as the rest time increases.

A normalized rest time $\xi = t/t_R$ is defined to make the comparison of the effective damage density, $\tilde{\phi}$, and healing, h, variables for different rest periods easier. Hence, $\xi = 0$ indicates the start of the rest period, whereas $\xi = 1$ indicates the end of the rest period. The effective damage density and healing variables are plotted versus the normalized rest time ξ in Figures 4.10(a) and 4.10(b), respectively. Figure 4.10(a) shows that at the beginning of the rest period the effective damage density is the same for all cases. However, the effective damage density variable decreases during the rest period as a result of healing. Figure 4.10(a) shows that the longer the rest period, the lower the effective damage density at the end of rest period. One would expect that the effective damage density to reach zero and the healing variable to reach one if long enough rest period is introduced between the loading cycles. In other words, the model shows that the material can retrieve all its strength and stiffness and as a result becomes identical to the virgin state of the material if put in rest for a long enough time. This can also be explained by looking at Figure 4.9(b) showing that for long rest periods the material response during the reloading converges to the response of the monotonic loading.

4.5.3. Effect of Healing and Damage Models on Predicting the Fatigue Damage

Other features of the healing model as well as the consequences of postulating rate-dependent versus rate-independent damage models are investigated in this subsection. To this end, the stress response for a cyclic loading shown in Figure 4.11 is investigated.

It should be mentioned that the elastic strain energy equivalence hypothesis is used for this examples and the ones presented in the subsequent sections. The selection of a specific transformation hypothesis will not affect the qualitative results obtained in the following examples.
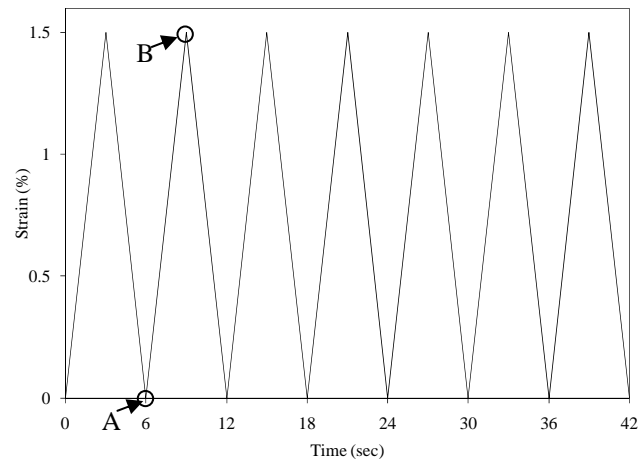
Figure 4.11. The loading history for the examples presented in Section 4.5.3.

4.5.3.1. Rate-independent damage model

The damage function presented in Eq. (4.50), with $\gamma = 5 \times 10^{-7}$ and $k = 50$, is used for the rate-independent damage model. The stress-strain response and the damage density versus time for the elastic-damage model are shown in Figures 4.12(a) and 4.12(b), respectively. As shown in Figure 4.12(a), the unloading occurs linearly and no hysteresis loop occurs after the first loading cycle. In other words, both loading and unloading occur linearly after the first loading cycle. In this work, the damage kinematic hardening is not considered. Therefore, the damage model is a function of strain and stress level in the healing configuration which makes the damage variable to evolve only if the strain and/or stress level in the healing configuration exceed its maximum corresponding value in the first loading cycle. Obviously, the stress and strain reach its maximum value during the first loading cycle. Hence, damage does not evolve during the unloading as well as the next loading cycle which makes the presented rate-independent model incapable of predicting the nonlinear response during the unloading.
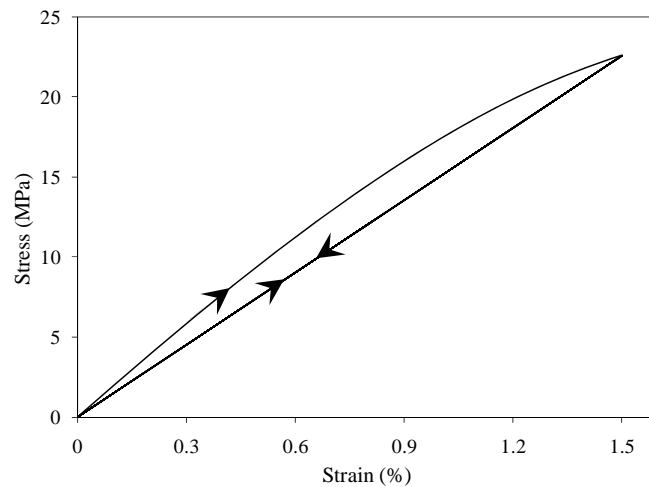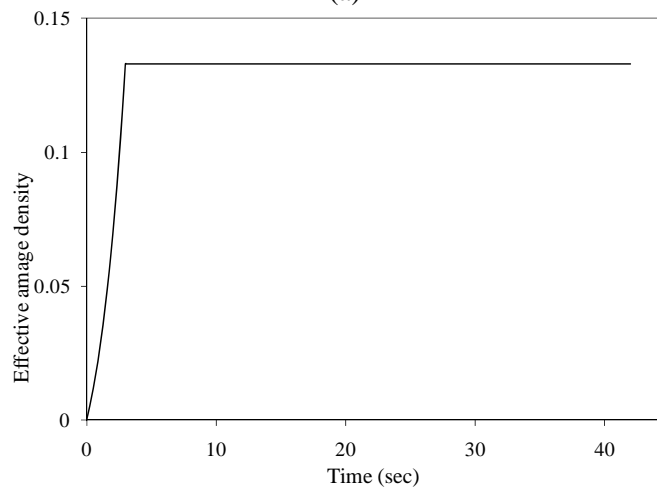
Figure 4.12. Model response when using the rate-independent damage model. (a) Stress-strain response; after the first loading cycle both loading and unloading are linear. (b) Damage density versus time; damage density evolves only during the first loading cycle and remains constant during the unloading as well as during the next cycles.

4.5.3.2. Rate-dependent damage model

The rate-dependent damage evolution function presented in Eq. (4.45) and the model parameters listed in Table 4.1 are used in this subsection. However, healing is not considered in this example. Assuming the rate-dependent damage model allows the damage density to evolve during both loading and unloading. In other words, damage density evolves as long as the damage driving force $\tilde{Y}$ is greater than the threshold

damage force Y_{th}. However, damage evolves with slower rate during the unloading. The stress-strain response and evolution of the effective damage density [i.e. $\tilde{\phi} = \phi(1-h)$ where $h = 0$ since healing is not incorporated] are shown in Figures 4.13(a) and 4.13(b), respectively. Figure 4.13(a) shows that the model gives a nonlinear response during the unloading as well as during the loading. This is attributed to the fact that the damage density can also evolve during the unloading, as shown in Figure 4.13(b).
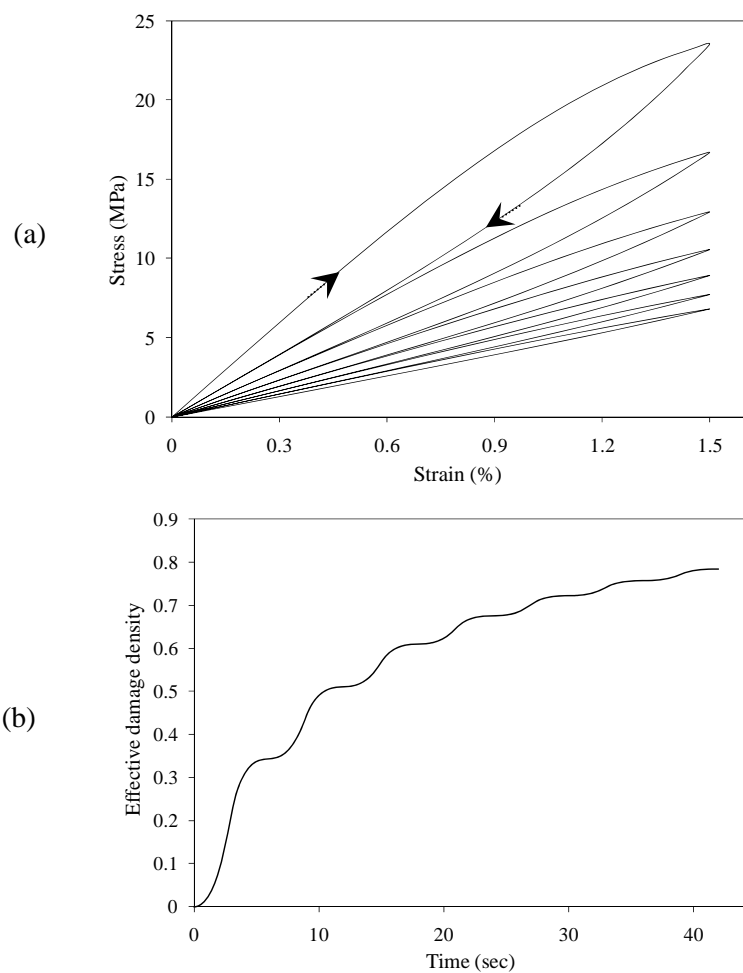
Figure 4.13. Model responses for the rate-dependent damage model when healing is not considered. (a) Stress-strain response; model predicts nonlinear response during the unloading and loading, hysteresis loops form and energy dissipates at each cycle; (b) Effective damage density versus time; damage density evolves during both loading and unloading at each cycle; however, the rate of damage evolution decreases as the number of loading cycles increases.

It should be noted that Ortiz (1985) was the first to model the nonlinear response of the stress-strain diagram during unloading by considering the anisotropic damage and crack closure effects. The fundamental assumptions underlying his pioneering work are schematically illustrated in Figure 4.14.

(a)   (b)   (c)
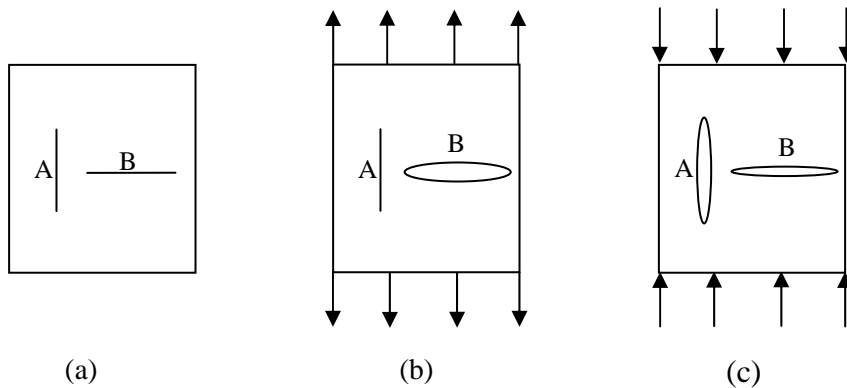
Figure 4.14. Illustration of the anisotropic damage which has been postulated by Ortiz (1985) to model the nonlinear stress-strain response during the unloading. (a) A schematic RVE with two embedded cracks "A" and "B"; (b) during the loading crack "B" opens and contributes to the degradation of the stiffness; and (c) during the unloading crack "A" opens while partial crack closure occurs at crack "B". However, the net effect causes the stiffness modulus to degrade during the unloading.

Figure 4.14(a) shows a schematic RVE with two embedded cracks "A" and "B" in vertical and horizontal directions, respectively. The RVE presented in Figure 4.14(a) is subjected to a uniaxial loading-unloading history. During the loading phase [Figure 4.14(b)], crack "B" opens and starts growing which subsequently causes the stiffness modulus of the material to degrade. However, while crack "B" starts closing and reduces in size during the unloading phase [Figure 4.14(c)], crack "A" opens and starts growing as shown in Figure 4.14(c). The reduction in size of crack "B" contributes to the partial recovery in the stiffness modulus, whereas, the opening of crack "A" during the unloading contributes to the degradation of the stiffness modulus. Therefore, the change in the stiffness modulus during the unloading is a competing mechanism between the effect of the crack closure and crack opening on the stiffness during the unloading.

According to the experimental observations, the tangent stiffness modulus usually decreases gradually during the unloading which is an indication of greater contribution of the crack opening during the unloading (e.g. Sinha et al., 1964; Karsan and Jirsa, 1969; Ortiz, 1985; Hassan et al., 1992; Eggeler et al., 2004; Sima et al., 2008). In this work, the anisotropic damage is not considered. However, the nonlinear response during the unloading is modeled by allowing a time-dependent degradation during the unloading through a delay-damage (i.e. viscodamage) evolution law. The net contribution of the closure of crack "A" and opening of crack "B" (Figure 4.14) on the stiffness reduction during the unloading is captured by allowing the material to gradually feel the presence of existing cracks during the unloading through crack closure/opening processes. In other words, at the onset of unloading the material memorizes the damaged stiffness from the previous loading cycle such that the presence of the newly developed micro-cracks during the current loading cycle is not felt yet by the material. However, upon more unloading a gradual opening/closure of existing cracks occurs so that the material starts gradually feel the presence of those newly developed cracks that will subsequently cause a gradual stiffness reduction until the complete unloading as schematically shown in Figure 4.1.

Consequently, one may argue that the commonly observed nonlinear response in the stress-strain diagram during the unloading could be due to more damage accumulation. However, careful and extensive experimental measurements should be conducted before one may prove this argument for a specific type of material. Moreover, Figure 4.13(a) shows that when damage is allowed to evolve during the unloading, hysteresis loops form for each loading-unloading cycle. Hence, energy dissipation continues even after the first loading-unloading cycle which could trigger the fatigue damage.

The experimental investigations on the cyclic loading of several materials also show a jump in the tangent stiffness modulus at the unloading-loading points (e.g. point "A" in the loading history presented in Figure 4.11) (e.g. Sinha et al., 1964; Karsan and Jirsa, 1969; Ortiz, 1985; Hassan et al., 1992). In other words, the tangent stiffness at the

end of the unloading is usually less than the tangent stiffness at the beginning of the next reloading. However, the rate-dependent damage model is not able to predict this phenomenon as shown in Figure 4.13(a).

4.5.3.3. Rate-dependent damage and healing model

The rate-dependent damage and healing models presented respectively in Eqs. (4.45) and (4.48) are used in this section. The damage model parameters are as listed in Table 4.1. However, the healing model parameters are modified to expedite the healing evolution ($\Gamma^h = 0.8 \text{ s}^{-1}$, $a = 1$, $\tilde{\varepsilon}_{th}^h = 0.001$) in order to magnify the healing effect. The stress-strain response, evolution of the effective damage density [i.e. $\tilde{\phi} = \phi(1-h)$], and the evolution of the healing variable are shown in Figures 4.15(a), 4.15(b), and 4.15(c), respectively. Figure 4.15(a) shows the model's capability in predicting the nonlinear responses during the unloading. It also shows the formation of hysteresis loops for each loading cycles. However, interestingly, the model shows the jump in the tangent stiffness at unloading-loading point (e.g. point "A" in Figure 4.11) when healing is included (this jump can be seen more clearly in Figure 4.9(b) where the tangent stiffness at the end of unloading is less than that at the beginning of the reloading when healing is considered). Moreover, the hysteresis loops converge to a single loop at high loading cycles and tend to stabilize as shown in Figure 4.15(a) [Figure 4.15(a) shows that the hysteresis loop for loading cycles 5-7 are very close together and tend to converge to a single loop]. As mentioned before, the healing condition presented in Eq. (4.49) indicates that the healing variable starts evolving once the total effective strain is less than the threshold healing strain. Hence, in the regions close to unloading-loading point (e.g. point "A" in Figure 4.11) where strain is close to zero, the healing variable increases and subsequently the effective damage density decreases. Therefore, the material recovers part of its strength and stiffness at unloading-loading point that causes the stiffness to show a jump at this point. This observation can also be explained by looking at the effective damage density variable. As shown in Figure 4.15(b), the effective damage density reaches a plateau as the number of loading cycle increases. In other words, the newly nucleated micro-

damages at large number of loading cycle heals at unloading-loading point, and hence, the effective damage density reaches a plateau where no more damage accumulation occurs during the next loading cycle. It also shows that, unlike the commonly postulated assumptions in CDM, the effective damage density is reversible as a result of micro-damage healing. Therefore, one may argue that the jump in stiffness at unloading-loading points might be due to micro-damage healing at low strain levels. Again, careful experimental tests should be conducted to prove this argument. Figure 4.15(c) shows that the healing variable decreases during the loading. This decrease can be explained according to Eq. (4.55). During loading, the area of unhealed damages A^{uh} increases. Therefore, although the area of the healed damages A^{h} does not change during the loading, the healing variable decreases since it is defined as the ratio of the healed damages' area over the total damaged area (i.e. $h = A^{h}/A^{D}$).

(a)
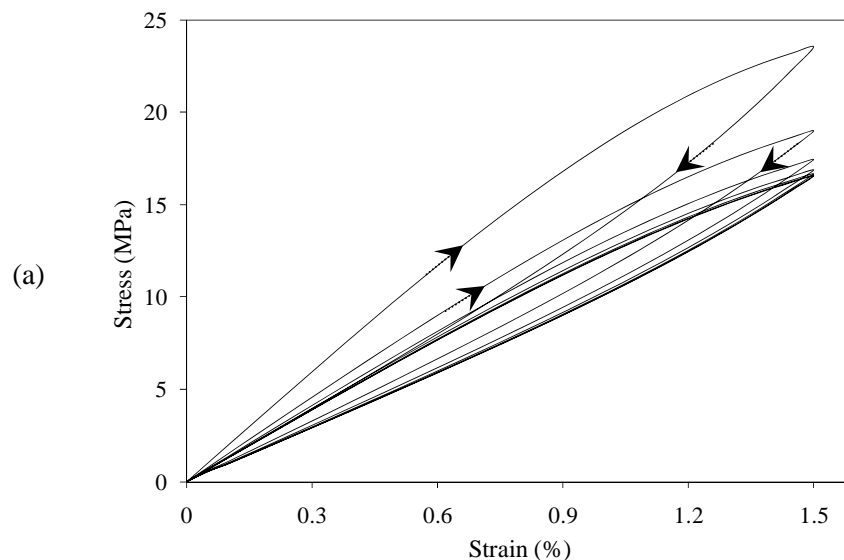
Figure 4.15. Model response for the rate-dependent damage and healing models. (a) Stress-strain response; the hysteresis loops tend to converge to a single one as the number of loading cycles increases and model predictions also show the jump in the tangent stiffness modulus at unloading-loading point. (b) Effective damage density versus time; the effective damage density decreases during the unloading as a result of healing and reaches a plateau at large number of loading cycles. (c) Healing variable versus time; healing variable increases at small strain levels (close to unloading-loading points), and healing variable decreases during the loading since the total damaged area increases.
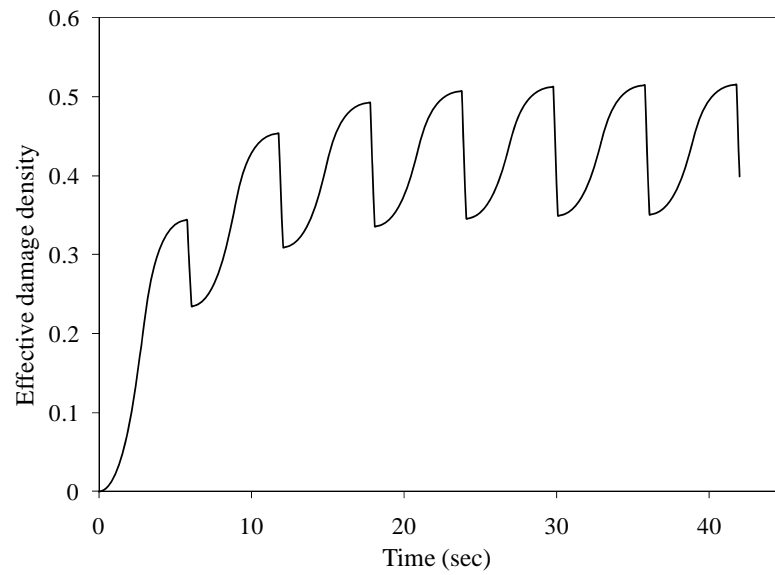
(b)
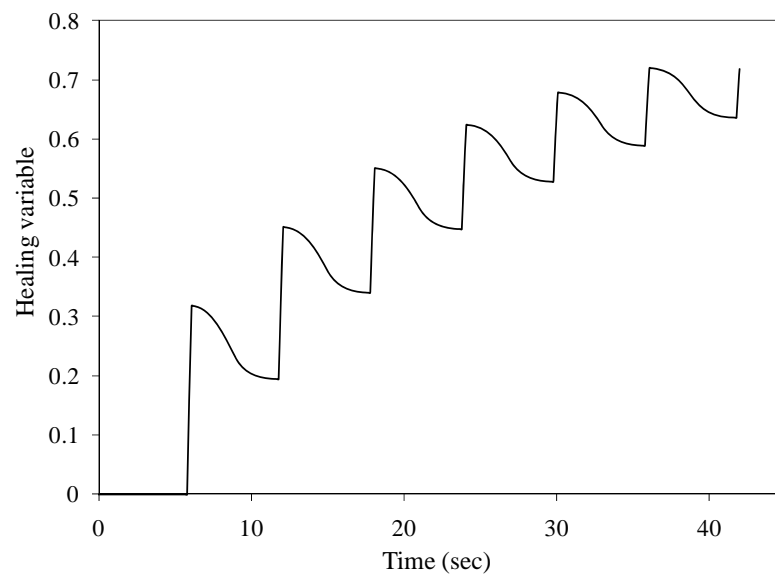
(c)

Figure 4.15. Continued.

4.6. Conclusions

A novel continuum damage mechanics-based framework is proposed in this paper to enhance the continuum damage mechanics theories in modeling the micro-damage healing phenomenon in materials that tend to self-heal. This framework is proposed by

extending the concept of the effective configuration and effective stress to the healing configuration.

Three well-known transformation hypotheses of the continuum damage mechanics theories (i.e. strain, elastic strain energy, and power equivalence hypotheses) are also extended for the materials with healing ability. Analytical relations are derived for each transformation hypothesis to relate the strain tensors, secant stiffness moduli, and tangent stiffness moduli in the damaged (nominal) and healing configurations.

The presented examples show that the proposed healing framework captures the recovery in strength and stiffness modulus when healing occurs. The presented example on the effect of rest periods between loading cycles show that the model predicts more recovery in the stiffness and strength when the rest time increases such that the material can recover even all of its strength and stiffness if put in rest for a long enough time.

It is argued that the commonly observed nonlinear responses during the unloading in the stress-strain response can be modeled using the rate- and time-dependent damage models. Therefore, it is implied that these nonlinear responses could be because of more damage accumulation during the unloading.

It is also shown that the jump in the tangent stiffness modulus at unloading-loading points might be related to micro-damage healing at very small strains. This framework will be used to model the micro-damage healing in asphaltic materials in the next chapter. It will be shown that the inclusion of the micro-damage healing significantly enhances the prediction of the fatigue life in asphalt mixes.

CHAPTER V

A MICRO-DAMAGE HEALING MODEL THAT IMPROVES PREDICTION OF FATIGUE LIFE IN ASPHALT MIXES

5.1. Introduction

As mentioned in Chapters I, II, and IV, various classes of engineering materials including asphalt binders and asphalt mixes have the potential to heal and retrieve part of their strength and stiffness with time. In this study, a continuum-based healing model is proposed in the light of the previous micromechanical and fracture-based models in order to close the gap in the development of a comprehensive constitutive model for accurate prediction of the fatigue life of asphaltic materials. The effect of healing is incorporated into the model by introducing the effective damage density parameter in which micro-damage healing is considered. This effective damage density is no longer irreversible. In other words, the effective damage density can decrease during the rest periods. Consequently, with this effective damage density parameter included, the continuum model has the capability of capturing changes in material properties such as strength and stiffness increases during rest period. In addition, a time-dependent evolution law for the healing parameter is proposed. The proposed evolution law possesses three model parameters, one of which is directly linked to previous micromechanical studies (Schapery, 1989; Little and Bhasin, 2007).

The proposed healing model is then coupled to viscoelastic, viscoplastic, and viscodamage models to enhance that model's ability to capture the effect of micro-damage healing and its impact on the mechanical response of asphalt mixes subjected to repeated loadings in both tension and compression. It is shown that considering the effect of micro-damage healing significantly enhances the ability of the model to predict responses under repeated loading during which variable unloading schemes are introduced. The model predictions show that the fatigue life increases as the rest period increases (Abu Al-Rub et al., 2010a).

5.2. Healing Natural Configuration

In classical CDM, the stresses in a fictitious undamaged (but not healed) configuration are related to the stresses in the nominal (damaged) configuration as follows:

$$\overline{\sigma}_{ij} = \frac{\sigma_{ij}}{1-\phi} \tag{5.1}$$

where $\overline{\sigma}$ is the undamaged stress tensor, σ is the damaged (nominal) stress tensor, and ϕ is the so-called damage variable or damage density. The damage process is primarily assumed to be irreversible in continuum damage mechanics. Hence, an increasing function with time is usually postulated for describing the damage variable ϕ (Kachanov, 1958, 1986; Lemaître, 1992; Kattan and Voyiadjis, 1993; Krajcinovic, 1996; Abu Al-Rub and Voyiadjis, 2005b).

However, as discussed in Chapter IV, some engineering materials and specifically asphalt mixtures have the potential to heal and recover part of their strength and stiffness under specific conditions such as resting periods during repeated or fatigue loading. Hence, a proper CDM framework should be developed in order to describe the changes in the material's microstructure during the healing process (see Figure 5.1).
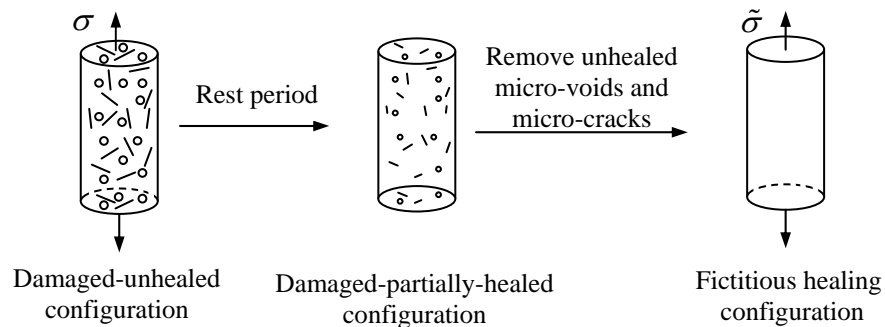
Figure 5.1. Extension of the effective stress concept in continuum damage mechanics to damaged-healed materials.

Therefore, the micro-damage healing framework proposed in Chapter IV is adopted to define a natural configuration named the healing configuration as shown in Figure 5.1.

In this natural configuration, one can simply define an effective damage density, $\tilde{\phi}$, that considers the density of healed micro-cracks and micro-voids as follows:

$$\tilde{\phi} = \phi(1-h) \tag{5.2}$$

where h is referred to in this paper as the micro-damage healing internal state variable since it defines the density of healed micro-cracks and micro-voids. Using the definition proposed in Eq. (5.2), one can replace the definition of the effective stress in Eq. (5.1) by another effective stress that considers micro-damage healing, such that:

$$\tilde{\sigma}_{ij} = \frac{\sigma_{ij}}{1-\tilde{\phi}} = \frac{\sigma_{ij}}{1-\phi(1-h)} \tag{5.3}$$

where $\tilde{\sigma}$ is the stress tensor in the healing configuration as demonstrated in Figure 5.1. In the above and subsequence, the superimposed "~" designates the healing configuration of the material. Note that when $h=0$ (i.e. $\tilde{\phi} = \phi$), Eqs. (5.1) and (5.3) are identical which implies that no healing has occurred in the material. On the other hand, when $h=1$ (i.e. $\tilde{\phi} = 0$), the nominal stress tensor σ and the effective stress tensor in the healing configuration $\tilde{\sigma}$ are the same, which implies that all micro-damage has healed; and hence, the material has completely recovered its strength and stiffness. Moreover, one notice that when the material is initially undamaged, $\phi = h = 0$ and $\sigma = \tilde{\sigma}$.

It is assumed here that once a material is damaged, further loading only affects the portion of the material that is intact and partially or completely healed. In other words, further loading is carried out by the material in the healing configuration shown in Figure 5.1. Hence, in the subsequent developments, the constitutive equations are expressed in the healing configuration.

5.3. Constitutive Model

5.3.1. Thermo-Viscoelastic-Viscoplastic-Viscodamage Model

The viscoelastic-viscoplastic-viscodamage constitutive model remains the same as presented in Chapter II with the difference that they should be represented in the healing configuration instead of the effective (undamaged) configuration. In other words one can simply replace the superimposed "$-$" by "$\sim$" in order to represent the thermo-viscoelastic-viscoplastic-viscodamage model in the undamaged-healed configuration (please refer to Chapter II for a complete detail on the constitutive model). Therefore, in order to avoid the repetition, the thermo-viscoelastic-viscoplastic-viscodamage constitutive model is not presented in this chapter.

5.3.2. Proposed Micro-Damage Healing Model

Wool and O'connor (1981) proposed a phenomenological-based theory for the crack healing in polymers. They defined a macroscopic recovery parameter that relates the healing at the micro-scale to the changes in the mechanical properties of polymers at the macro scale. They introduced the macroscopic recovery parameter Θ as the ratio of the mechanical properties of the material such as the fracture stress, the failure strain, the tensile modulus, and the fracture energy subjected to a healing history over the corresponding mechanical properties of the material in the original state (Wool and Oconnor, 1981). They defined Θ through the following convolution integral:

$$\Theta = \int_{-\infty}^{t} \Theta_I \left(t - \tau \right) \frac{d\xi\left(\tau, X \right)}{d\tau} d\tau \qquad (5.4)$$

where $\Theta_I \left(t \right)$ is an intrinsic healing function that incorporates wetting (i.e. the free surfaces of a crack get closer and touch each other) and diffusion (i.e. inter-molecular flow of matter) and defines the rate at which the two wetted surfaces heal and recover part of their original strength. Therefore, the intrinsic healing function is additively decomposed into an intrinsic healing due to short-term wetting Θ_I^0, which is controlled by the surface energy, and the intrinsic healing due to long-term diffusion, Θ_I^d.

Moreover, $\xi(X,t)$ in Eq. (5.4) is defined as the wetting distribution function. Wool and O'connor (1981) also investigated two cases for $\xi(X,t)$; instantaneous wetting and constant rate wetting. In the case of instantaneous wetting, the two crack surfaces touch each other immediately which implies:

$$\dot{\xi}(t,X) = \delta(t) \tag{5.5}$$

where $\delta(t)$ is the Dirac-delta function. As a result, the macroscopic recovery parameter Θ in Eq. (5.4) and the intrinsic healing function become identical, such that:

$$\Theta = \Theta_I(t) = \Theta_I^0 + \Theta_I^d(t) \tag{5.6}$$

However, for a constant rate of wetting one can write:

$$\dot{\xi}(t,X) = k_w U(t) \tag{5.7}$$

where k_w is the wetting rate and $U(t)$ is the Heaviside step function (i.e. $U = 1$ for $t \geq 0^+$ and $U = 0$ for $t < 0^-$). In this case, the macroscopic recovery parameter Θ can be expressed as:

$$\Theta = k_w \Theta_I^0 t + \Theta^d(t) \tag{5.8}$$

where $\Theta^d(t)$ is the component of the macroscopic recovery parameter due to diffusion. Power or exponential expressions can be assumed for Θ^d such that $\Theta^d = c_1 t^{c_2}$ or $\Theta^d = c_1[1 - \exp(-c_2 t)]$, respectively, where c_1 and c_2 are material parameters. Comparing Eqs. (5.6) and (5.8) reveals that the wetting component of the macroscopic recovery parameter is time-independent in case of instant wetting and time-dependent for the case of constant wetting rate. Using Eq. (5.6), Eq. (5.8), or another expression depends on how experimental data shows the variation of Θ with the healing time. Therefore, it is obvious that Eqs. (5.6) or (5.8) are fitting functions that can be empirically assumed with a large number of material constants without explicit consideration of the driving forces for healing.

On the other hand, Schapery (1989) has developed a model for rate of crack size reduction $\dot{a}_b$ in linear, isotropic, viscoelastic materials based on fracture mechanics. He

related $\dot{a}_b$ to fundamental material properties such as the size of the fracture processed zone, Δ, the surface energy, Γ, the interface bond strength, σ_b, the Poisson's ratio ν, and the viscoelastic material properties. It is noteworthy to mention that in the Schapery's formulation (1989) the whole healing process is considered. In other words, he did not distinguish between the healing due to wetting and the healing due to diffusion since he assumed that the healed part of a crack retrieves its total original strength.

Little and Bhasin (2007) and Bhasin et al. (2008) used the work of Wool and O'connor (1981) and Schapery (1989) and utilized the macroscopic recovery parameter R in Eq. (5.4) to describe the effect of healing in bituminous materials. They used a simplified form of the crack shortening rate (Schapery, 1989) as the rate of the wetting function, such that:

$$\frac{d\xi(t,X)}{dt} = \dot{a}_b = \Delta \left[\frac{1}{D_1 k_m} \left(\frac{\pi W_c}{4(1-\nu^2)\sigma_b^2 \Delta} - D_0 \right) \right]^{-\frac{1}{m}} \tag{5.9}$$

where D_0, D_1, and m are obtained by assuming a power law function for the transient creep compliance in Eq. (2.9) (i.e. $\Delta D = D_1 t^m$), and k_m is a material constant expressed in terms of m. Moreover, $W_c = 2G$ is the work of cohesion and is related to the material's surface energy G. In obtaining Eq. (5.9), Schapery (1989) assumed that the bond strength, σ_b, along in the healing process zone, Δ, is constant. Therefore, one concludes that the rate of wetting function in Eq. (5.9) utilized by Little and Bhasin (2007) and Bhasin et al. (2008) is constant. This reduces the healing convolution integral in Eq. (5.4) to the form in Eq. (5.8) such that $k_w = \dot{a}_b$. Also, Little and Bhasin (2007) have assumed a three-parameter expression for Θ^d in Eq. (5.8) such that $\Theta^d = c_1[1 - \exp(-c_2 t^{c_3})]$. Therefore, identifying these parameters (c_1, c_2, c_3) in addition to those in Eq. (5.9) for an asphalt mixture is a challenge. Moreover, based on limited experimental data, they showed that healing in asphalt binders follow Eq. (5.6) and not

Eq. (5.8), which implies that instantaneous healing occurs upon the wetting of cracks free surfaces.

However, one realizes that the aforementioned healing models are mostly fracture mechanics-based and micromechanically-based and cannot be used easily at the scale of the asphalt mixture. These models are also augmented with many material parameters that are difficult to identify experimentally. Furthermore, their coupling to the viscoelastic, viscoplastic, and rate- and time-dependent damage response of materials is not clear. On the other hand, one need an evolution law for the micro-damage healing internal state variable in Eq. (5.3) to establish this coupling and incorporates healing into the current constitutive equations. According to the aforementioned healing models and intuitively, one expects that the proposed healing variable h should be a function of resting period (or healing time), temperature, level of damage, and the history of healing. Hence, one can incorporate all these effects into the following postulated phenomenological-based healing evolution equation:

$$\dot{h} = \Gamma^h(T)\left(1 - \tilde{\phi}\right)^{b_1}\left(1 - h\right)^{b_2} \tag{5.10}$$

where $\dot{h} = dh/dt$ is the rate of the healing variable, $\Gamma^h(T)$ is the healing viscosity parameter that determines how fast the material heals which is a function of temperature T; and b_1 and b_2 are material constants. Moreover, the following expression can be assumed for $\Gamma^h(T)$:

$$\Gamma^h(T) = \Gamma_0^h \exp\left[-\delta_3\left(1 - \frac{T}{T_0}\right)\right] \tag{5.11}$$

where Γ_0^h is the healing viscosity parameter at reference temperature T_0, and δ_3 is the healing temperature coupling model parameter. Eqs. (5.10) and (5.11) state that the healing rate increases as the temperature exceeds the reference temperature and decreases for temperatures less than the reference temperature. Also, the parameter Γ_0^h has the unit of Sec^{-1} and determines how fast the material heals. One can argue that Γ_0^h increases as the surface energy increases and shows that a material with larger surface

energy heals faster than a material with smaller surface energy. Note that at reference temperature and when $b_1 = b_2 = 0$, Eq. (5.10) simplifies as follows:

$$\dot{h} = \Gamma_0^h \tag{5.12}$$

which states that the rate of healing is constant. This is the simplest evolution equation one can assume for the healing variable h. In fact, this is the case in Eq. (5.9)that is derived by Schapery (1989) based on the assumption of a constant bond strength, σ_b, along the healing process zone, Δ. Therefore, by assuming $\dot{h} \propto \dot{a}_b / \Delta$, one may relate Γ_0^h to more fundamental material properties by comparing Eqs. (5.9) and (5.12), such that:

$$\Gamma_0^h \propto \left[\frac{1}{D_1 k_m} \left(\frac{2\pi G}{4(1-v^2)\sigma_b^2 \Delta} - D_0 \right) \right]^{-\frac{1}{m}} \tag{5.13}$$

Eq. (5.13) bridges the gap between the model developed at the micro-scale, Eq. (5.9), and the proposed model at the macro-scale, Eq. (5.10).

It is noteworthy that, for the general case (i.e. $b_1 > 0$ and $b_2 > 0$) in Eq. (5.10), the healing viscosity parameter can be considered as the maximum rate at which the healing occurs. In other words, the healing rate decreases either when the healing variable increases [controlled by $(1-h)$ term] or when the density of micro-cracks increases [controlled by $(1-\tilde{\phi})$ term]. These arguments are in agreement with those by Schapery (1989) and the experimental observations by Little and Bhasin (2007) and Bhasin et al. (2008).

Moreover, one can obtain the evolution expression in Eq. (5.10) based on the laws of thermodynamics through assuming h to be an internal state variable in the Helmholtz free energy Ψ. Thus, the corresponding thermodynamic conjugate force, H, can be interpreted as the *strain energy recovery rate*, such that

$$H = \frac{\partial \Psi}{\partial h} \tag{5.14}$$

where $\dot{h} = cH$ with c being a material property. Thus, using Eqs. (5.10) and (5.14), one can obtain an expression for Ψ and H that yields the evolution equation for the healing variable h. Details of this thermodynamic approach are presented by Darabi et al. (2011d).

5.4. Finite Element Implementation

The finite element implementation of the thermo-viscoelastic-viscoplastic component of the constitutive model remains the same as explained in Chapter II. However, as mentioned before, the viscoelastic and viscoplastic models are presented in the healing configuration. The viscodamage and micro-damage healing models are incorporated into the model using the concept of the undamaged-healed stress space.

Hence, once the updated stress in the healing configuration, then calculate the rate of the damage density and the rate of healing variable using Eqs. (2.45) and (5.10) such that the total damage density and healing variables can then be obtained as follows:

$$\phi^t = \phi^{t-\Delta t} + \dot{\phi}^t \Delta t \tag{5.15}$$

$$h^t = h^{t-\Delta t} + \dot{h}^t \Delta t \tag{5.16}$$

Finally, the nominal stress tensor can be updated using Eq. (5.3) [refer to Chapter IV for a detailed description of implementation procedure of the healing and damage models]. To clarify the implementation steps, a flowchart showing the implementation process in a straightforward manner is presented in Figure 5.2.

The formulated numerical algorithms presented in this section are implemented in the well-known finite element code Abaqus (2008) via the user material subroutine UMAT.
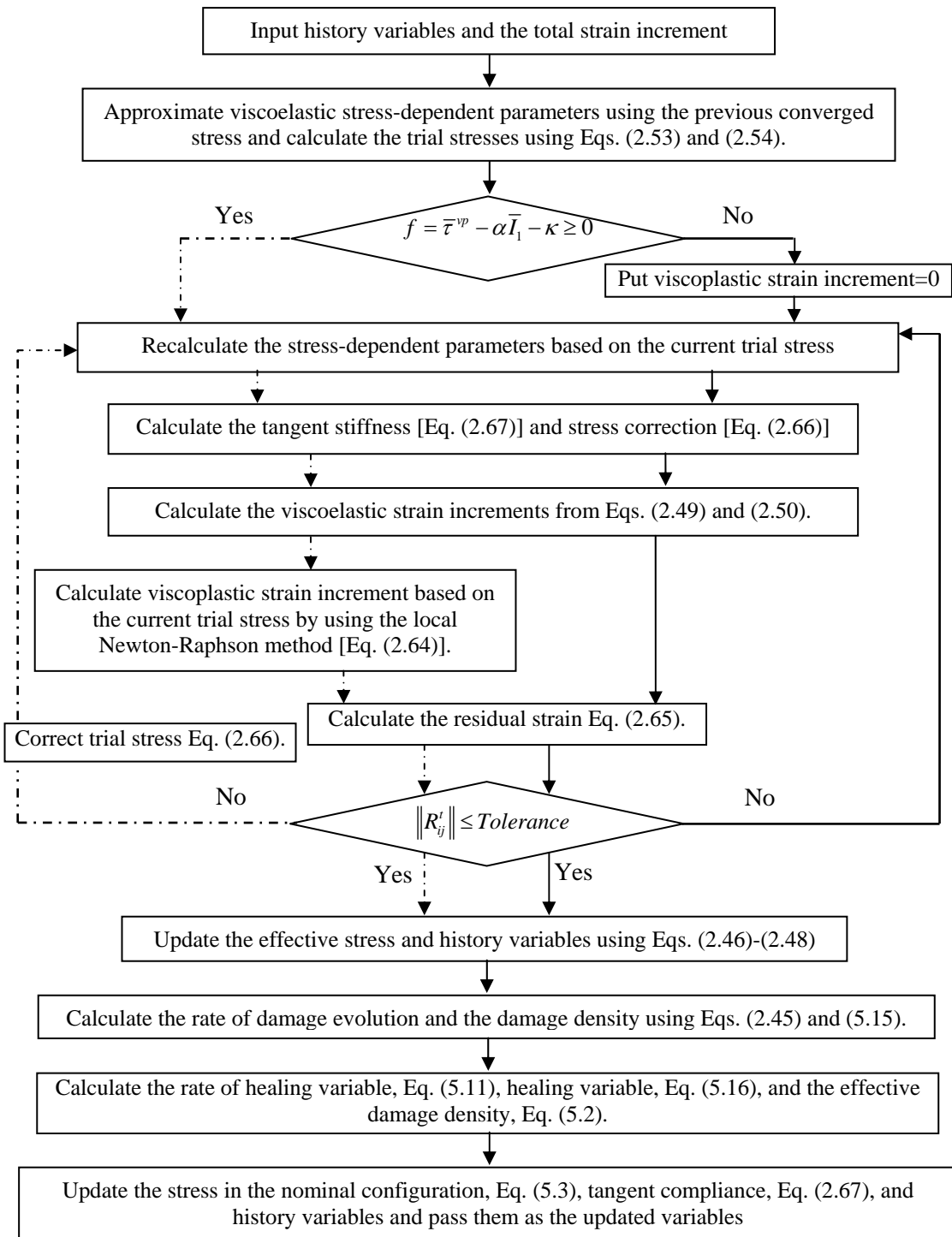
Figure 5.2. Flowchart for numerical implementation of the proposed coupled thermo-viscoelastic-viscoplastic-viscodamage-healing constitutive model.

5.5. Application of the Model for Prediction of Response of Asphalt Mixes

5.5.1. Identification of the Micro-Damage Healing Model Parameters

It was shown in Chapter II that the coupled thermo-viscoelastic-viscoplastic-viscodamage model fails to predict reasonable behavior for the repeated creep-recovery tests with the introduced rest period. In this chapter, the proposed micro-damage healing model is coupled to the rest of the constitutive model to enhance the model in predicting the fatigue behavior of asphalt mixes. The identified thermo-viscoelastic-viscoplastic-viscodamage model parameters for the Dense Bitumen Macadam mixture discussed in Chapter II listed in Table 2.2 and 2.3.

The identified viscoelastic, viscoplastic, and viscodamage model parameters can now be used for prediction of repeated creep-recovery tests. However, the model without the healing component predicts shorter fatigue life comparing to experimental measurements, as discussed earlier. In other words, the model predicts higher creep strains comparing to experimental data. This effect is due to the fact that the damage density in the viscodamage model is considered to be irreversible, and hence, does not allow for damage recovery or healing during the rest period. This effect will be more pronounced for long rest periods. Hence, one can conclude that the difference between the experimental measurements and model predictions of creep strain should be compensated with the healing model. Hence, one can determine the healing viscosity parameter Γ_0^h at reference temperature and the history parameters b_1 and b_2 by adjusting the model predictions to be comparable with the experimental measurements. In this study, the repeated creep-recovery test in compression when loading time is 60 sec and unloading time is 100 sec is selected for determination of healing model parameters. The identified healing model parameters in Eq. (5.11) are $\Gamma_0^h = 2.5 \times 10^{-3} \, \text{Sec}^{-1}$, $b_1 = 3$, and $b_2 = 6$. The flowchart for describing the procedure for calibrating the model in the presence of the micro-damage healing is updated and presented in Figure 5.3.

| Separate viscoelastic response in the recovery part of the creep-recovery tests using Eq. (2.76). |

| Identify the Prony series coefficients D_n and λ_n at the reference temperature using Eqs. (2.9) and (2.76). |

| Calculate $\Delta\bar{\varepsilon}_1^{vp}$, $\Delta\bar{\varepsilon}_2^{vp}$, and $\Delta\bar{p}$ from the creep part of the creep-recovery tests using Eqs. (2.80), (2.81), and (2.82). |

| Identify the viscoplastic model parameters at the reference temperature by minimizing the error between the experimental measurements and Eq. (2.79). |

| Identify Γ^{vd} and k from a creep test at the reference temperature and stress level using Eq. (2.85). |

| Identify viscodamage stress dependency parameter q from a creep test at the reference temperature, when $\sigma \neq \sigma_{ref}$ using Eq. (2.84). |

| Identify temperature coupling terms model parameters by comparing experimental data and model predictions at different temperatures using Eqs. (2.90) and (2.91). |

| Identify d^{vp} and d^{vp} from two creep tests in tension using Eqs. (2.23) and. (2.44). |

| Get healing model parameters Γ_0^h, b_1, and b_2 using a repeated creep-recovery test in compression [Eq.(5.11)]. |

Figure 5.3. The procedure for identification of the coupled thermo-viscoelastic-viscoplastic-viscodamage-healing constitutive model parameters.

5.5.2. Prediction of Fatigue Life in Asphalt Mixes

Recently, Gibson et al. (2009) have simulated several pavement structures with eight inch asphalt layer subjected to dual tires with both 80 kN and 178 kN single axle loads. They calculated the first stress invariant I_1 and the second deviatoric stress invariant

$\sqrt{J_2}$ at different positions under the dual tire configuration. These multiaxial states of stresses relatively represent the actual state of stress in asphalt pavements subjected to wheel loads.

In this work, the applied stress level for the repeated creep-recovery test in compression is assumed to be 1500 kPa whereas the applied stress level for the repeated creep-recovery test in tension is assumed to be 300 kPa. These two stress levels are close to the maximum compressive and tensile stress levels in the asphalt layer analyzed by Gibson et al. (2009).These tests are conducted at temperature of 20°C.

Figures 5.4(a), 5.5(a), and 5.6(a) show the experimental results and model predictions for repeated creep-recovery tests in compression where the applied stress level is 1500 kPa. Figure 5.4(a) shows the creep strain versus time when the loading time is 120 sec and the unloading time is 100 sec. As it is shown in Figure 5.4(a), the model predictions when healing is included are significantly improved as compared to the experimental data and the predictions when healing is not included. The evolution of the effective damage density (i.e. $\tilde{\phi} = \phi$ without healing and $\tilde{\phi} = \phi(1-h)$ with healing) is shown in Figure 5.4(b). As shown in Figure 5.4(b), for model predictions where healing is not considered, the effective damage density increases rapidly during loading and remains constant during unloading, whereas the model predictions when healing is included show that the effective damage density decreases during the resting periods. In other words, by including the healing parameter the effective damage density is no longer irreversible and can decrease during the resting time. Moreover, the model predictions without healing and damage significantly underestimate the total creep strain. It is noteworthy that failure in the simulated repeated creep-recovery test in, for example, Figure 5.4(a) is defined by the onset that the compliance reaches a very large value close to infinity or when the stiffness modulus reaches a very small value close to zero. One notice from Figure 5.4(b) that the damage density increases with increasing loading cycles such that at some loading cycles the creep response in Figure 5.4(a) reaches the tertiary stage with an exponential increase in the total creep strain during the loading cycles.
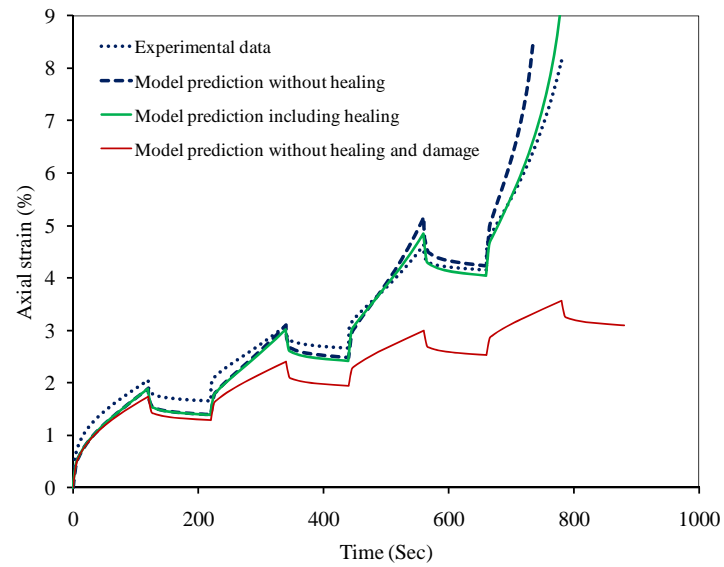
(a)
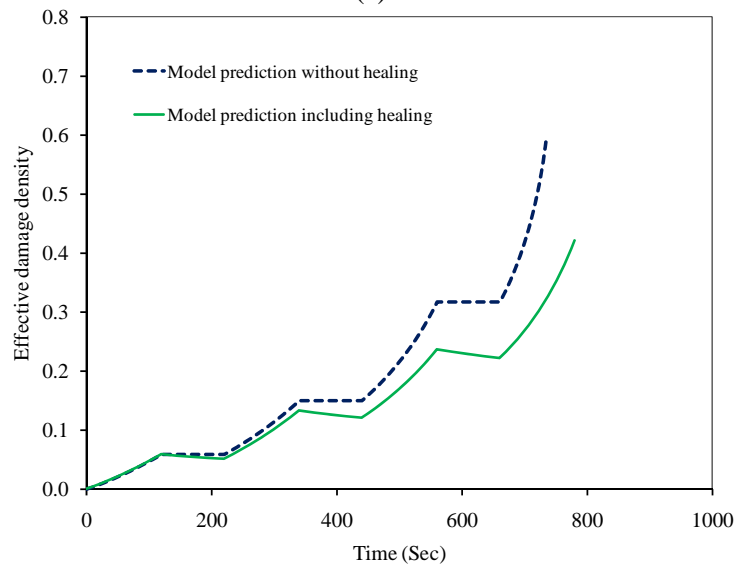
(b)

Figure 5.4. Repeated creep-recovery test in compression with 120sec loading time and 100sec resting period. (a) Compared creep strain, and (b) the evolution of the effective damage density.

The end of the cyclic tertiary stage indicates the failure is similar to a standard creep test. Figure 5.5 shows the results when the loading time is 60 sec and the resting period is 100 sec.
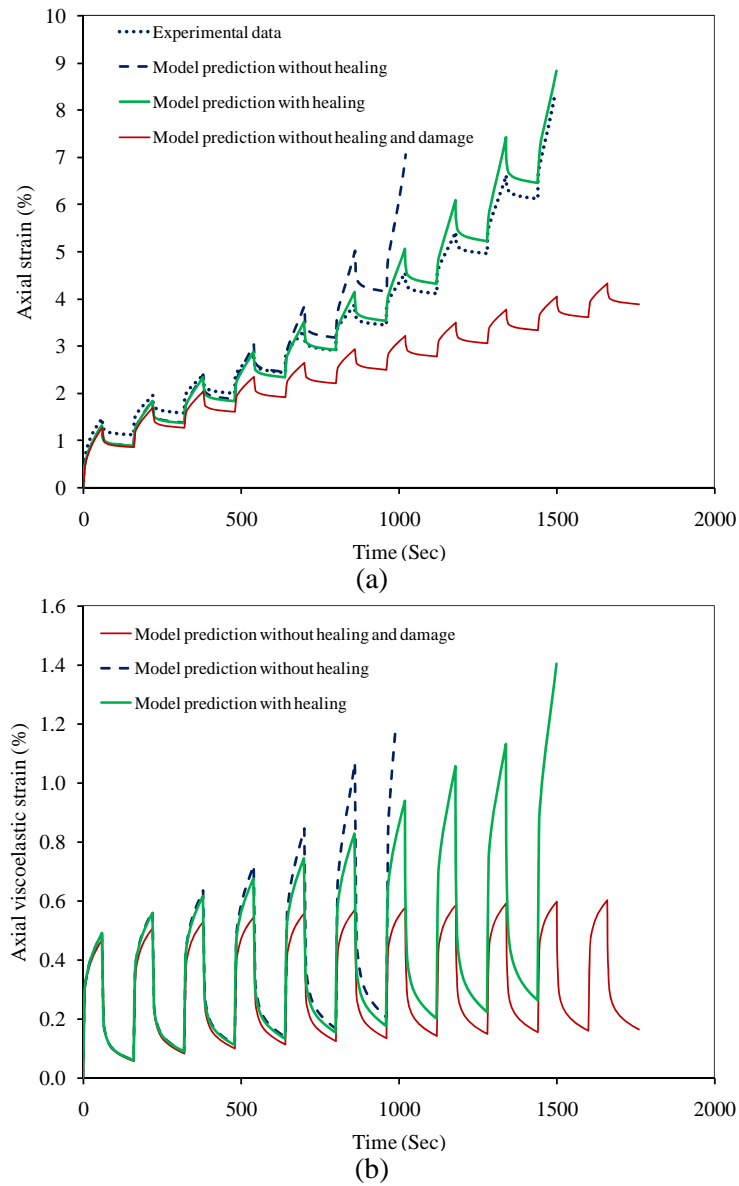
Figure 5.5. Repeated creep-recovery test in compression with 60sec loading time and 100sec resting period. (a) Total experimental creep strain, and model predictions of total creep strain with and without damage and healing components, (b) model predictions for viscoelastic strain with and without damage and healing components, (c) model predictions for viscoplastic strain with and without damage and healing components, and (d) the evolution of the effective damage density.

(c)

(d)
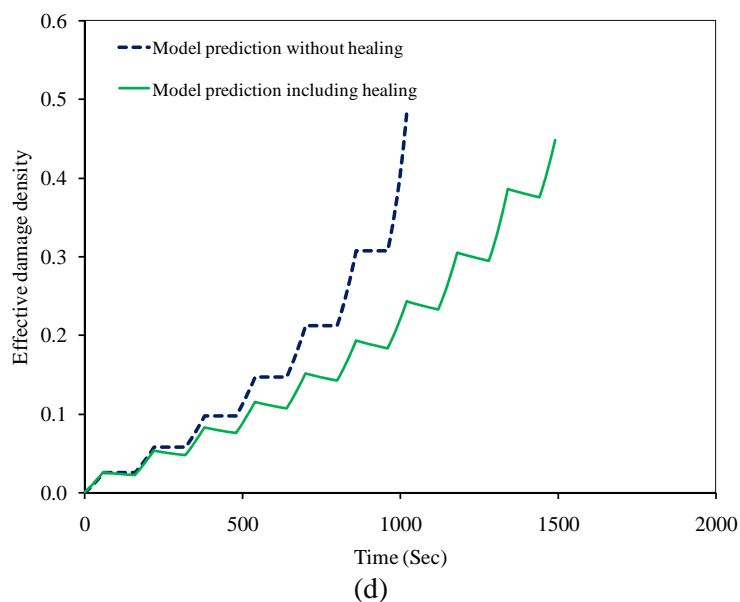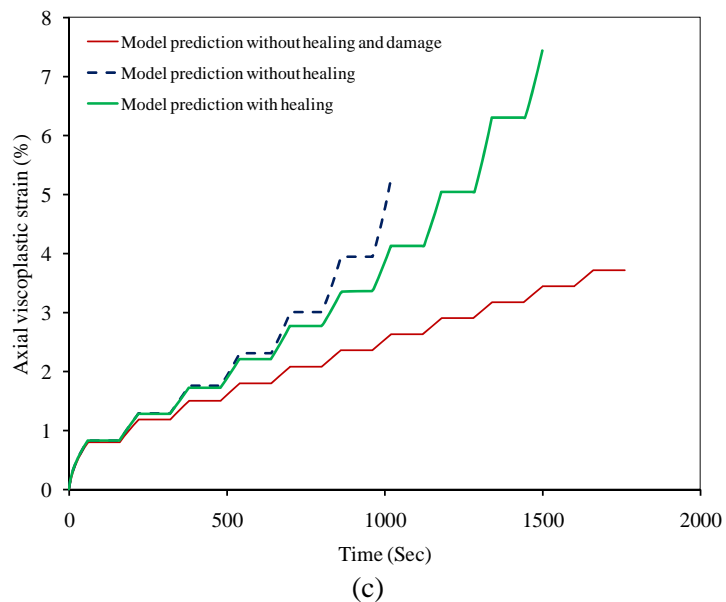
Figure 5.5. Continued.

Figure 5.5(a) shows that the model without healing predicts failure after only 6 cycles; whereas, the model without damage and healing significantly underestimates the creep strain and also is not able to predict failure. However, experimental measurements and model predictions when healing is considered are in good agreement and show that the material can sustain more loading cycles. In order to study the effects of damage and

healing on viscoelastic and viscoplastic deformations, the model predictions for viscoelastic and viscoplastic strains with and without damage and healing are presented in Figures 5.5(b) and 5.5(c), respectively. Figures 5.5(b) and 5.5(c) show that the proposed model predicts larger values for both the viscoelastic and viscoplastic strains when damage and healing are activated. However, the increase in the viscoplastic strain is much larger than that in the viscoelastic strain. Moreover, Figure 5.5(d) shows that the damage density reaches a large value after few cycles when not considering healing; whereas, the effective damage density evolves at a much slower rate when the healing is included.

The effect of healing becomes more pronounced when the total duration of resting period increases. Interesting results are shown in Figure 5.6 when the loading duration is 60 sec and the resting time is 1500 sec. The long resting period provides enough time for significant healing to take place. The model predictions without considering healing show that the material fails after 6 cycles as shown in Figure 5.6(a). However, experimental results demonstrate that the material can tolerate loading for many more loading cycles.

As shown in Figure 5.6(a), the model that considers healing is able of capturing this behavior and is also able to predict the experimental measurements fairly well. Figure 5.6(a) also shows that the model predictions without healing and damage significantly underestimate the total creep strain. Again, as shown in Figure 5.6(b), the effective damage density when healing is not included grows rapidly; whereas, the inclusion of healing reduces the amount of damage and extends the fatigue life the asphalt mix.
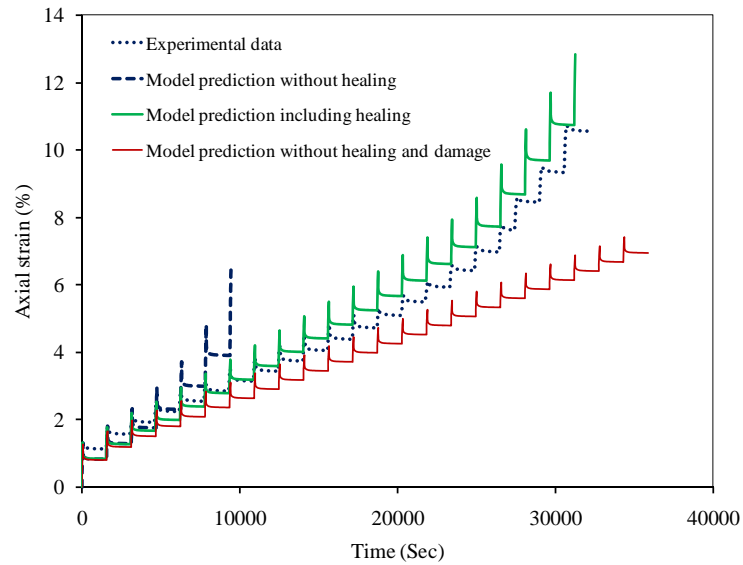
(a)
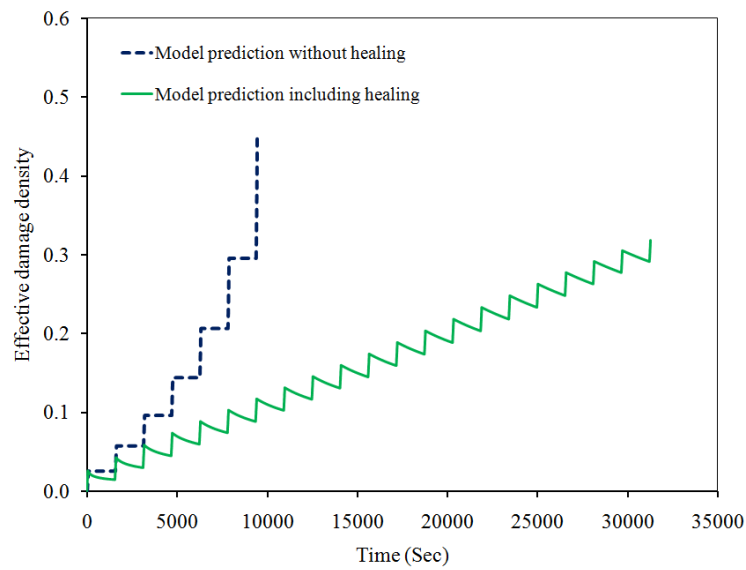
(b)

Figure 5.6. Repeated creep-recovery test in compression with 60sec loading time and 1500sec resting period. (a) Compared creep strain, and (b) the evolution of the effective damage density.

The repeated creep-recovery test is also performed in tension as well and used to validate the healing model. Tensile creep-recovery tests Figures 5.7(a)-5.10(a)) are conducted at room temperature where the applied stress is 300kPa. Two different loading times of 120 sec and 60 sec are considered. Figure 5.7 shows the model

predictions with and without consideration of the healing compared to experimental measurements with 120 sec loading time and 100 sec resting period.
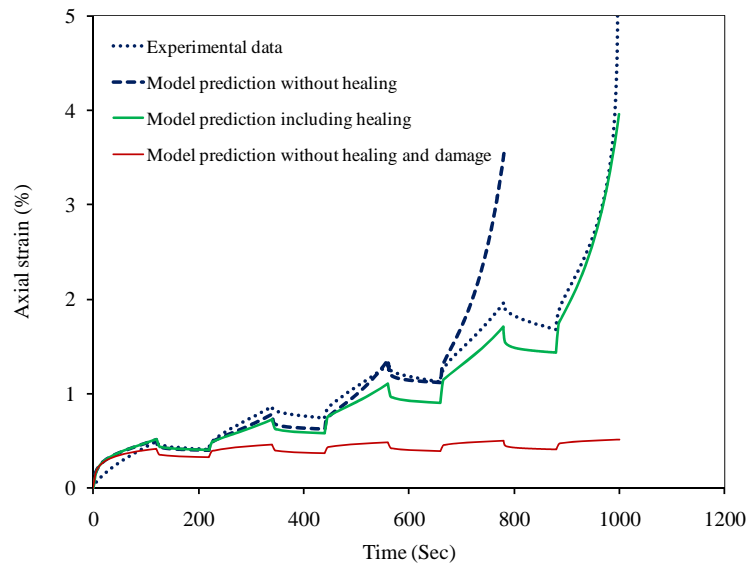
(a)
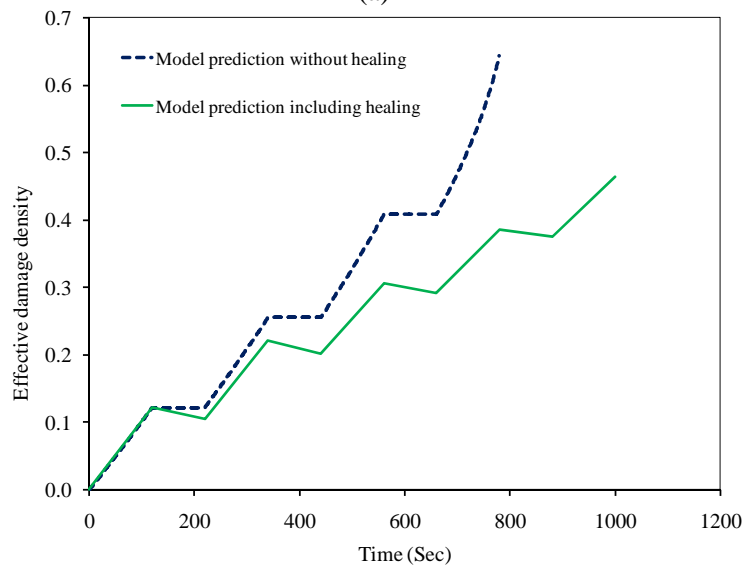
(b)

Figure 5.7. Repeated creep-recovery test in tension with 120sec loading time and 100sec resting period. (a) Compared creep strain, and (b) the evolution of the effective damage density.

Obviously, since damage is more severe in tension than in compression, the model predictions of the repeated creep-recovery response without considering healing significantly overestimates the amount of creep strain and damage evolution. Therefore, it is essential to incorporate healing into the fatigue damage predictions especially under tensile fatigue loading conditions. The evolution of the effective damage density is also shown in Figure 5.7(b). Moreover, experimental measurements and model predictions with and without healing for a loading time duration of 60 sec and for three different unloading times (50, 100, and 1500 sec) are compared in Figures 5.8, 5.9, and 5.10, respectively.

The model predictions when the healing parameter is considered significantly improve the prediction of experimental data. The calculated effective damage density when the loading duration is 60 sec and the unloading durations are 50, 100, and 1500 sec are plotted in Figures 5.8(b), 5.9(b), and 5.10(b), respectively. These figures show that when the micro-damage healing is considered the damage density decreases during the rest period due to the micro-damage healing. Also, one can clearly notice from Figure 5.10(b) that the damage density per loading cycle decreases as the number of cycles increases.
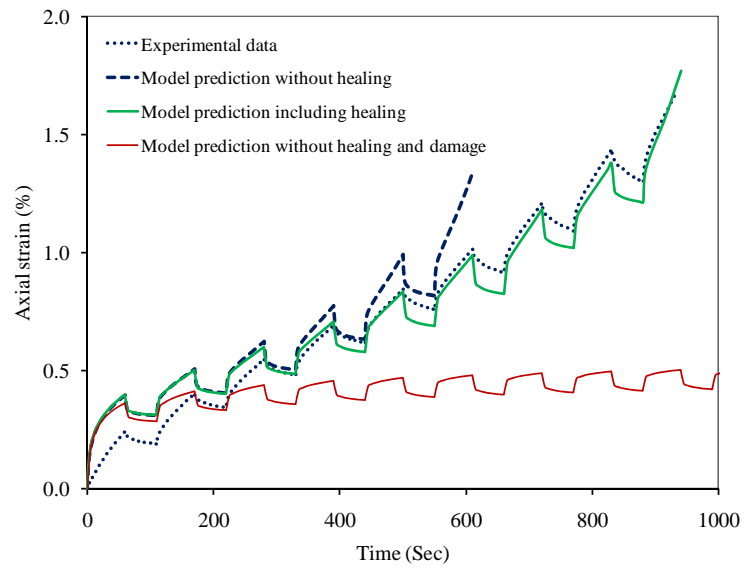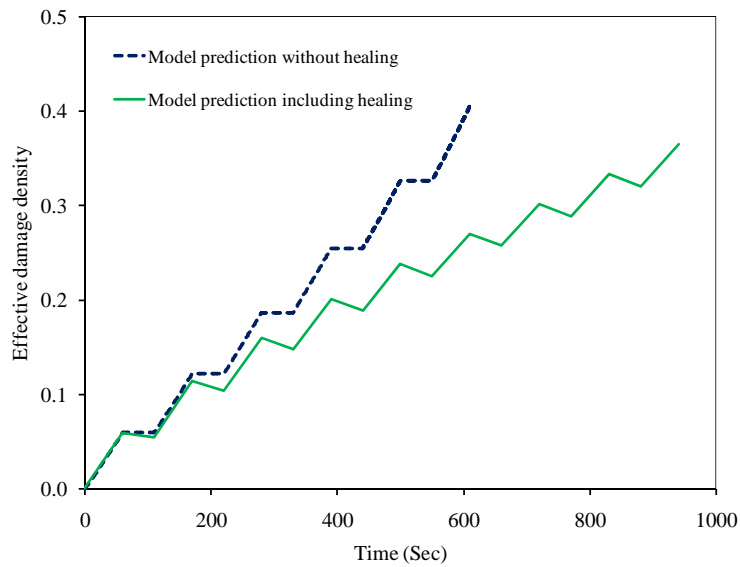
Figure 5.8. Repeated creep-recovery test in tension with 60sec loading time and 50sec resting period. (a) Compared creep strain, and (b) the evolution of the effective damage density.
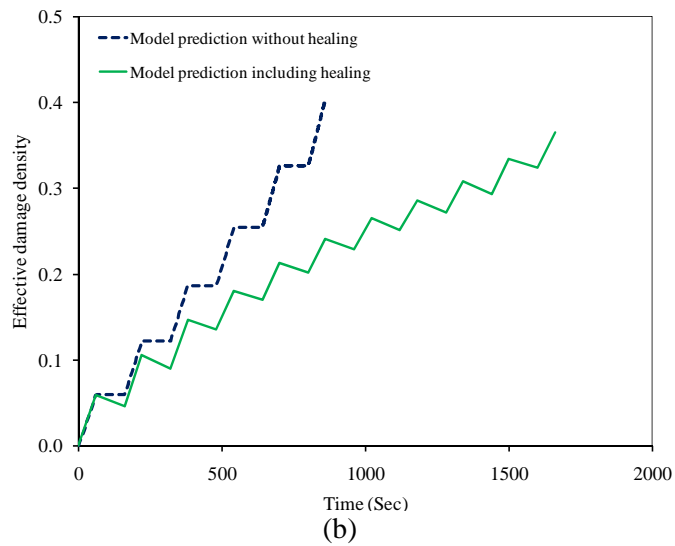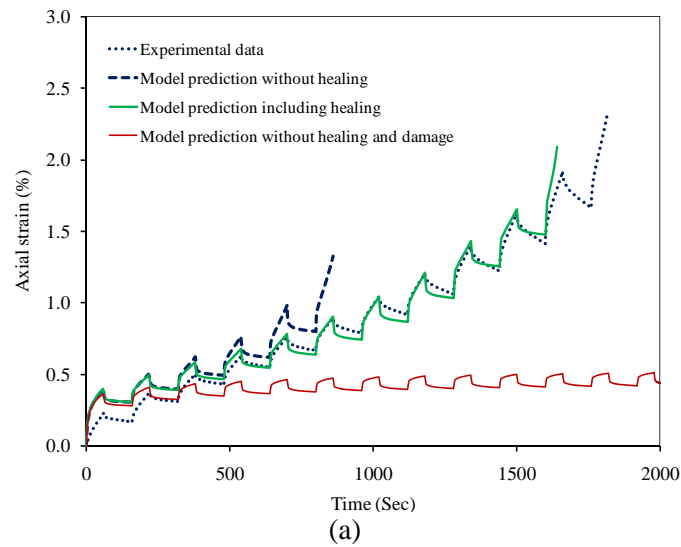
Figure 5.9. Repeated creep-recovery test in tension with 60sec loading time and 100sec resting period. (a) Compared creep strain, and (b) the evolution of the effective damage density.
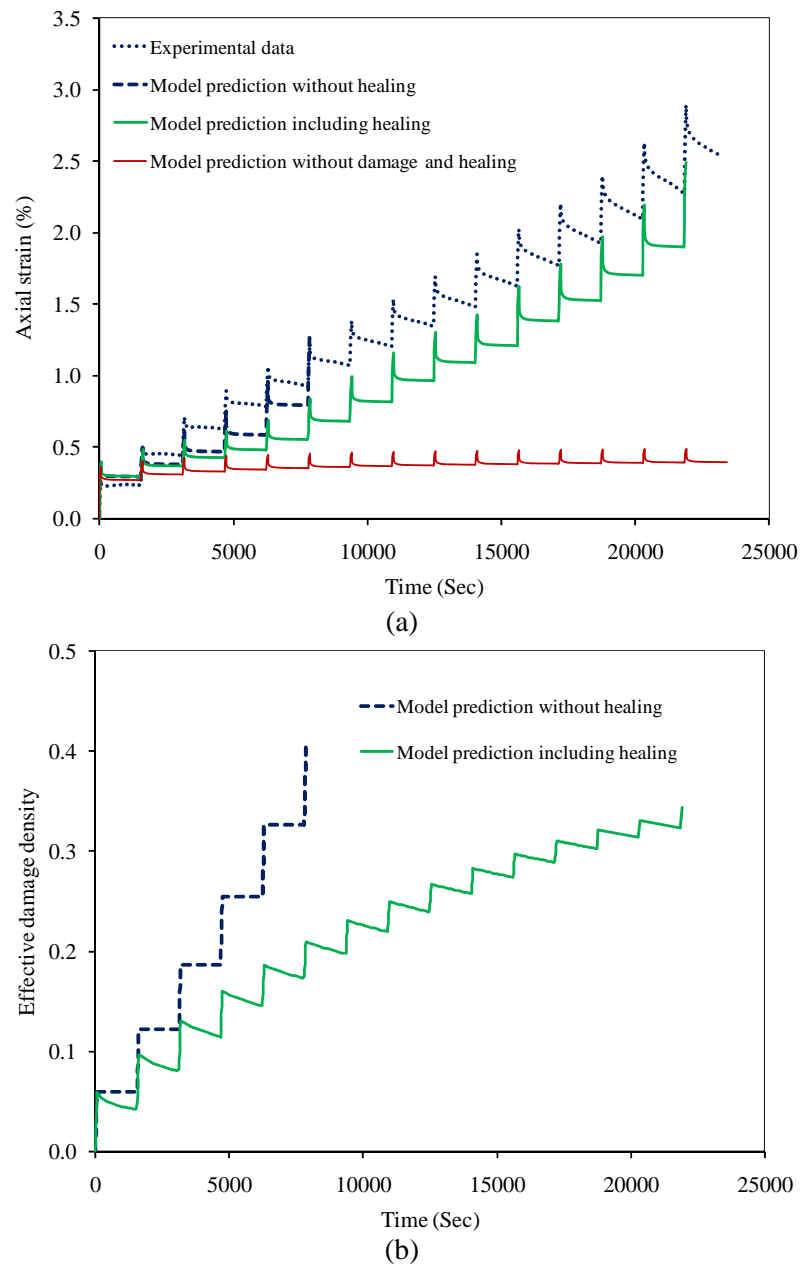
Figure 5.10. Repeated creep-recovery test in tension with 60sec loading time and 1500sec resting period. (a) Compared creep strain, and (b) the evolution of the effective damage density.

These reported results clearly show that considering the effect of the micro-damage healing significantly improves the ability of the current viscoelastic, viscoplastic, and viscodamage constitutive model in predicting the fatigue life of asphalt mixtures in the presence of rest periods. Whereas, neglecting micro-damage healing

makes such a complex constitutive model significantly underestimates the fatigue life, and in turn to very conservative designs of our asphalt pavements. However, more experimental data for different loading conditions, especially at different temperatures, is needed for validating and improving the predictions of the proposed healing model.

It is noteworthy that for healing to impact the damage process, micro-crack development must occur. The damage that is recorded during the currently utilized repeated creep and recovery tests is consistent with the development of micro-cracks. This is because the experiments are performed at 20°C and the periods of loading under large stress levels are sufficiently long to cause micro-crack development and growth. Therefore, although these cyclic creep and recovery experiments do not represent what might be considered as "classical" fatigue experiments to most pavement engineers where thousands of loading cycles at low stress or strain levels are applied to cause failure, it does indeed represent the type of damage and recovery in asphalt pavements that leads to fatigue failure.

5.6. Effect of Healing Model Parameters

In this section, the effect of healing model parameters on damage performance of asphalt mixes is investigated. For this purpose, the repeated creep-recovery test subjected to 1500 kPa compressive load when loading time is 60 sec and unloading time is 100 sec is re-simulated using different values for the healing model parameters Γ_0^h, b_1, and b_2. Figure 5.11 shows the effect of healing viscosity parameter, Γ_0^h, on the fatigue life prediction. The values of history parameters are set to be zero (i.e. $b_1 = b_2 = 0$) in this figure. As is shown in Figure 5.11(a) the fatigue life increases as Γ_0^h increases due to the increased levels of micro-crack healing. Therefore, Γ_0^h controls the rate at which healing occurs such that one can classify different materials for their potential to heal based on the value of this parameter. Figure 5.11(b) shows the corresponding evolution of the effective damage density, $\tilde{\phi}$. This figure shows that for very large values of Γ_0^h the effective damage density approaches zero indicating that the accumulated resting

period is sufficient for complete healing of existing micro-cracks. However, as the healing viscosity parameter decreases, the decrease in the effective damage density during the rest period slows down, and hence, the model predicts shorter fatigue lives. The effects of the history parameters b_1 and b_2 are shown in Figures 5.12 and 5.13, respectively.
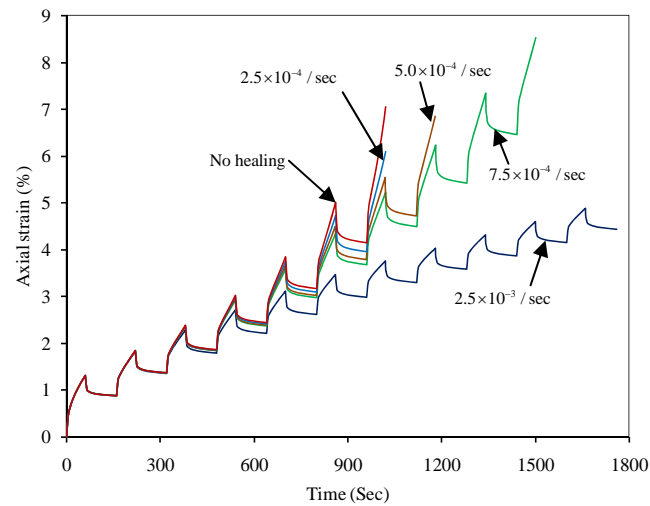
(a)
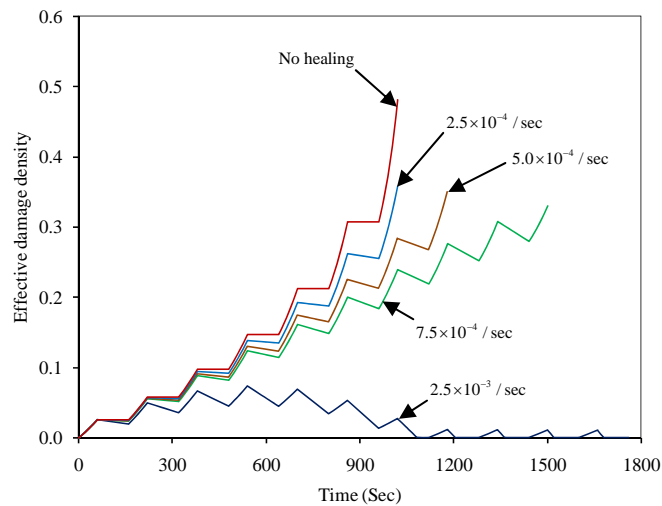
(b)

Figure 5.11. Effect of healing viscosity parameter Γ_0^h on fatigue behavior of asphalt mixes. (a) total strain versus time and (b) effective damage density versus time.

Figure 5.12 shows the effect of damage history parameter b_1 when $\Gamma_0^h = 10^{-3}$ / sec and $b_2 = 0$. Figures 5.12(a) and 5.12(b) show that the material's potential to heal increases as b_1 decreases. Therefore, the healing rate decreases as the damage density increases. In other words, it becomes more difficult to heal the crack as it grows bigger and bigger.
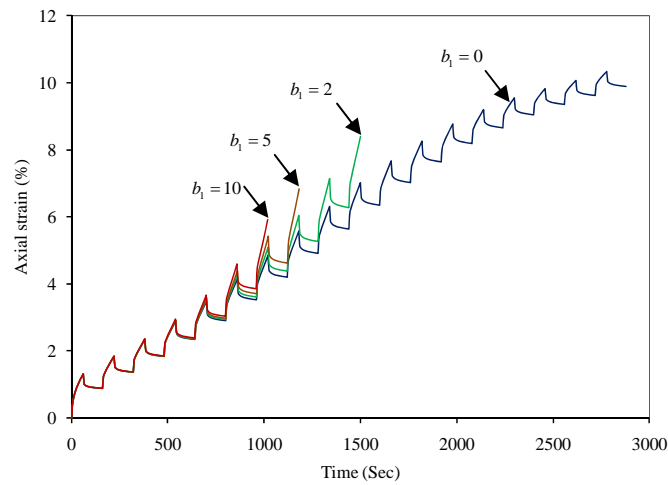
(a)
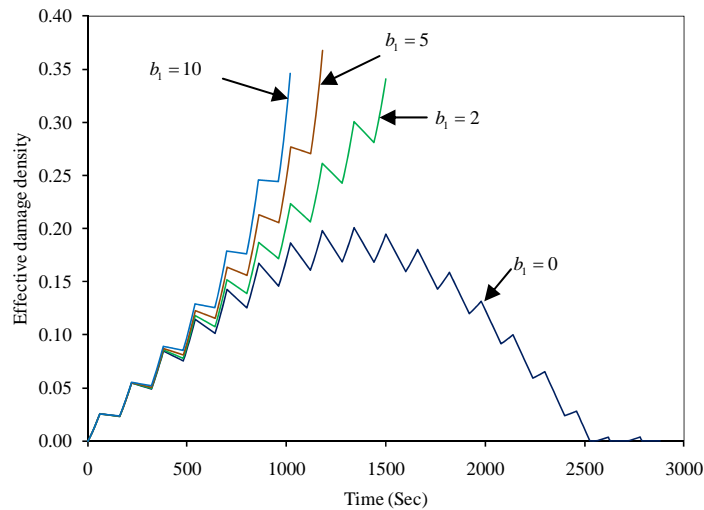
(b)

Figure 5.12. Effect of damage history parameter b_1 on fatigue behavior of asphalt mixes when $\Gamma_0^h = 1.0 \times 10^{-3}$ / sec and $b_2 = 0$. (a) total strain versus time and (b) effective damage density versus time.

The effect of the healing history parameter b_2 on the total strain and effective damage density is presented in Figures 5.13(a) and 5.13(b), respectively. Figures 5.13(a) and 5.13(b) show trends similar to that in Figure 5.12(a) and Figure 5.12(b), respectively. This is in qualitative agreement with the experimental results by Little and Bhasin (2007) who showed that the rate of healing approaches zero upon complete healing of micro-cracks. Therefore, results for negative values for b_2 are not shown here. However, more experimental studies are needed to verify and validate the aforementioned qualitative predictions of the proposed micro-damage healing model.

5.7. Conclusions

In this chapter, a micro-damage healing model is proposed based on extending the effective stress concept in classical continuum damage mechanics by introducing a fictitious effective undamaged-healed natural configuration. The proposed micro-damage healing model is coupled with temperature-dependent nonlinear viscoelastic, viscoplastic, and viscodamage constitutive models that can predict the highly nonlinear mechanical responses of asphalt mixtures subjected to repeated loading conditions.

Moreover, motivated by previously developed micromechanical- and fracture-based healing models, a phenomenological healing equation is proposed for the evolution of the micro-damage healing internal state variable. The healing evolution equation is time, temperature, and loading/unloading history dependent model that explicitly affect the stress state and the viscoelastic, viscoplastic, and viscodamage response of the material while undergoing micro-damage healing. Moreover, an attempt is made to relate the material parameter that controls the rate of healing to the surface energy and bond strength of the material. Finally, the model is calibrated and validated against repeated creep-recovery experimental data on an asphalt mixture with different loading and unloading times and under tensile compressive stress states.
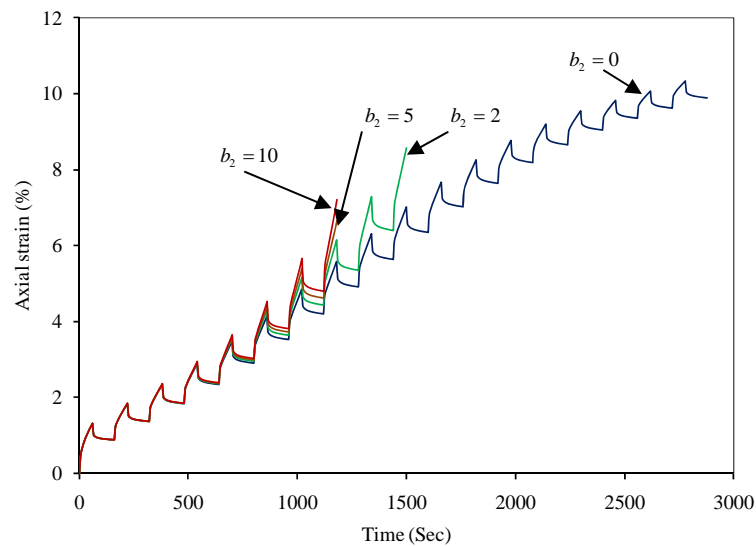
(a)
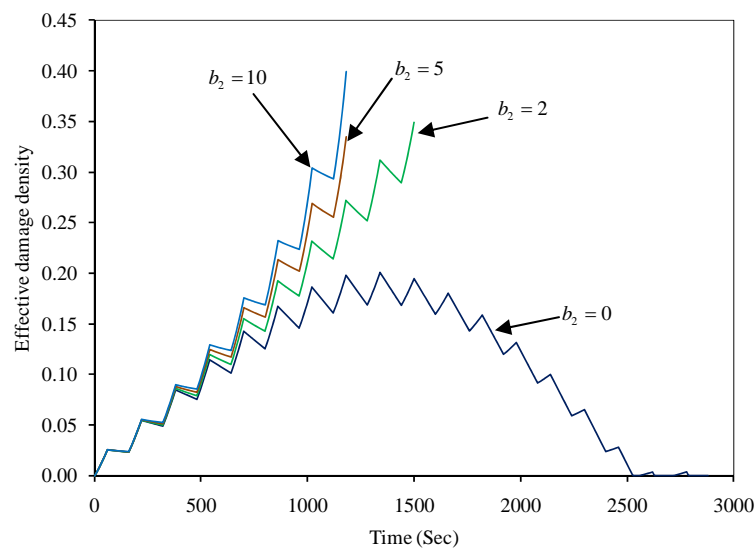
(b)

Figure 5.13. Effect of healing history parameter b_2 on fatigue behavior of asphalt mixes when $\Gamma_0^h = 1.0 \times 10^{-3}$ / sec and $b_1 = 0$. (a) total strain versus time and (b) effective damage density versus time.

It is shown that for the accurate prediction of the fatigue life of asphalt mixtures subjected to repeated loading-unloading conditions, a robust micro-damage healing model should be incorporated into the constitutive behavior of materials. Neglecting the

micro-damage healing phenomenon leads to significant deviations between the constitutive model predictions and the fatigue life of materials that have potential to heal. In fact, very conservative designs are made if such models are used in guiding the design of structural systems made of such material.

The model predictions when micro-damage healing is considered show that the effective damage density decreases during the rest period; and thus, fatigue life increases. It is shown that for long unloading or resting periods the effective damage density (i.e. density of the unhealed micro-cracks and micro-voids) increases at a very low rate as the number of loading cycle increases. Hence, the proposed micro-damage healing model can be used effectively to predict the pavement performance during the service life since pavements are, at least intermittently, subjected to repeated loading conditions with relatively long rest periods compared to the duration of loading periods.

The present analysis considers repeated creep-recovery tests with different loading and unloading times in both tension and compression at room temperature. However, more tests are needed to fully validate the model, especially at different temperatures. Furthermore, the inclusion of environmental factors such as moisture and aging is necessary since the ultimate goal is to predict the response of the asphalt pavements during their service life.

Moreover, the proposed constitutive model is used specifically for asphalt mixes. However, a wide range of materials show time-, temperature-, and rate-dependent viscoelastic, viscoplastic, viscodamage, and healing responses. Therefore, it is imperative to develop a general and robust thermodynamic framework with the capability to derive new constitutive models for different materials or to enhance the existing ones without violating the very fundamental laws of thermodynamic. This investigation will be the subject of the next chapter.

CHAPTER VI

A NEW GENERAL THERMODYNAMIC-BASED FRAMEWORK FOR CONSTITUTIVE MODELING OF TIME- AND RATE-DEPENDENT MATERIALS

6.1. Introduction

As mentioned in the previous chapters, accurate prediction of mechanical response of time- and rate-dependent materials requires the coupling between temperature-dependent viscoelasticity, viscoplasticity, viscodamage, and healing models. These models, on the other hand, should be general such that they can be applied for a wide range of loading conditions and the complex three dimensional stress states. One of the approaches is to derive the models from the fundamental laws of mechanics such that they do not violate the fundamental laws of thermodynamics. This approach makes the model more consistent and reliable.

However, even derivation of the models based on the fundamental laws of the thermodynamics is usually associated with certain assumptions. These assumptions may reduce the reliability of the derived constitutive models. Therefore, this chapter is devoted to development of a general thermodynamic-based framework which can be used to derive different constitutive models for the time- and rate-dependent materials with the least possible assumptions. This framework is general and can be used for derivation of constitutive models for a wide variety of materials including bituminous materials, polymers, bio-inspired materials, and soft materials.

Numerous thermodynamic-based models have been proposed in the literature to couple one or two of the mechanisms such as viscoelastic, viscoplastic, and/or viscodamage to describe the behavior of different materials such as metals, polymers, soft materials, and bio-inspired materials (e.g. Kachanov, 1986; Voyiadjis and Kattan, 1990; Lemaître, 1992; Schapery, 1999; Voyiadjis and Park, 1999; Rajagopal and Srinivasa, 2000; Tao et al., 2001; Abu Al-Rub and Voyiadjis, 2003; Boubakar et al., 2003; Barot et al., 2008; Ghorbel, 2008; Levesque et al., 2008; Karra and Rajagopal,

2009). However, depending on the loading conditions, many types of time- and rate-dependent materials show all four mechanisms under thermo-mechanical loading which makes it necessary to develop a general framework for coupling all four mentioned mechanisms.

Schapery (1969a) derived a single integral equation using the thermodynamics of irreversible processes for constitutive modeling of non-linear viscoelastic materials such as polymers. Several authors have extended the 1D Schapery's constitutive theory to the 3D viscoelastic models directly from the one-dimensional model presented by Schapery (Henriksen, 1984; Touati and Cederbaum, 1998; Beijer and Spoormaker, 2002; Haj-Ali and Muliana, 2004; Levesque et al., 2004). Recently, Levesque et al. (2008) showed that these 3D applications were thermodynamically inconsistent extensions of the 1D Schapery's viscoelastic model, and formulated a thermodynamically consistent 3D Schapery-type viscoelastic model. However, they considered the Cauchy stress tensor as the thermodynamic conjugate force of the total viscoelastic strain tensor. This assumption is valid only for a reversible load history for which the state variables associated with viscoelastic process remain constant and, hence, is not general.

In terms of the viscoplastic behavior of rate-dependent materials, Perzyna's viscoplastic model (Perzyna, 1971) has been used by several researchers to predict the permanent deformation in these materials (e.g. Masad et al., 2005; Saadeh et al., 2007; Huang, 2008; Abu Al-Rub et al., 2009). Many researchers have also re-derived Perzyna's viscoplastic model based on laws of thermodynamics and coupled it to temperature, damage, and/or viscoelasticity to predict more accurately the constitutive behavior of materials (e.g. Dornowski and Perzyna, 2002; Voyiadjis and Abed, 2006; Hallberg et al., 2009). These models are usually derived using the overstress concept (Zener and Hollomon, 1944; Malvern, 1951; Perzyna and Korbel, 1998).

In terms of the damage behavior of time- and rate-dependent materials, several time-independent and time-dependent damage models have been proposed in the literature (e.g. Kachanov, 1958; Odqvist and Hult, 1961; Rabotnov, 1969; Cozzarelli and Bernasconi, 1981; Schapery, 1987; Lemaître, 1992; Abu Al-Rub and Voyiadjis, 2003;

Sullivan, 2008). However, very few damage laws have been coupled to viscoelasticity and viscoplasticity to predict time- and rate-dependent responses of materials (e.g. Schapery, 1999; Darabi et al., 2011c).

Moreover, experimental observations in the last few decades have clearly shown that various classes of engineering materials (e.g. polymers, bitumen, bio-inspired materials, and rocks) have the potential to heal with time and recover part of their strength and stiffness under specific circumstances (e.g. Miao et al., 1995; Kessler and White, 2001; Brown et al., 2002; Reinhardt and Jooss, 2003; Barbero et al., 2005; Guo and Guo, 2006; Bhasin et al., 2008). Although one can find several studies in analyzing different healing processes in a phenomenological point of view (e.g. Jacobsen et al., 1996; Ramm and Biscoping, 1998; Ando et al., 2002), few attempts are available for deriving healing models based on laws on thermodynamics (e.g. Miao et al., 1995; Barbero et al., 2005). To the authors' best knowledge, we are the first to propose a thermodynamic-based model that couples the viscoelastic, viscoplastic, viscodamage, and healing models to model more accurately the mechanical response of time- and rate-dependent materials.

Furthermore, in most cases the thermodynamic-based constitutive models suffer the accurate estimation of the rate of energy dissipation since in most of these models only the Helmholtz free energy function along with the Clausius-Duhem inequality are not used consistently to derive different components of the constitutive models which leads to the underestimation of rate of energy dissipation.

In his celebrated book on continuum thermodynamics, Ziegler (1977) showed that the correct estimation of the rate of energy dissipation requires the decomposition of the thermodynamic conjugate forces into energetic (or quasiconservative according to his notion) and dissipative components. This general theory is also summarized in his later works (Ziegler, 1983; Ziegler and Wehrli, 1987). In these works, he showed that the energetic components of the thermodynamic conjugate forces are related to the Helmholtz free energy function, whereas the dissipative components of the thermodynamic conjugate forces are related to the rate of energy dissipation. Several

researchers have used this theory to develop constitutive models for different materials. To name a few, Freemond and Nedjar (1996) used this theory and applied it to gradient-dependent damage mechanics. Later, Shizawa and Zbib (1999), and Gurtin and his co-workers (Gurtin, 2003; Gurtin and Anand, 2005; Gurtin et al., 2007; Gurtin and Anand, 2009) applied this theory to gradient-dependent plasticity theories. However, Gurtin and his co-workers did not decompose all the thermodynamic conjugate forces into energetic and dissipative components. They assumed the dragstress to have only the dissipative component. In these works, different mathematical forms are postulated to describe energetic and dissipative components of the thermodynamic conjugate forces.

However, it is noteworthy to mention that assuming different forms for energetic and dissipative components of the thermodynamic conjugate forces is not quiet in line of the key assumption in Ziegler's approach which states that the constitutive equations for materials are fully determined by knowledge of the Helmholtz free energy and the dissipation function. Moreover, Collins and Houlsby (1997) used the works of Ziegler (1969), Houlsby (1981, 1982), and Modaressi et al. (1994) and applied these theories to model plastic behavior of geotechnical materials. They showed that when the rate of the plastic energy dissipation is a function of the current stress or the total or elastic strain in addition to the plastic strain and plastic strain rate, the flow rule is not necessarily associated (Collins and Houlsby, 1997; Collins and Kelly, 2002). However, as we will show in this paper, there is no need to make these kinds of assumptions to get the non-associated flow rules for plasticity/viscoplasticity theories. In fact, we will show that the non-associated plasticity/viscoplasticity theories are direct consequences of using the principle of virtual power.

Although several researchers have worked and extended the initial work of Ziegler (as we named a few here), we believe that the robustness and capabilities of Ziegler's approach specifically in using the energetic and dissipative forces to construct different constitutive models has not been given enough attention. Hence, we present a general thermodynamic framework to derive constitutive models for time- and rate-dependent materials with emphasis on the decomposition of thermodynamic conjugate

forces into energetic and dissipative components. We also present a systematic procedure to determine energetic and dissipative components directly from the Helmholtz free energy function and the rate of energy dissipation. The capabilities and robustness of the presented thermodynamic framework is shown through several examples which derive Schapery-type thermo-viscoelastic model, Perzyna-type thermo-viscoplastic model, the thermo-viscodamage model proposed by Darabi et al. (2011c), and the healing model proposed by Abu Al-Rub et al. (2010a).

Moreover, for the first time, we show that the viscoelastic, viscodamage, and healing microforce balances, derived directly from principle of virtual power, along with the decomposition of thermodynamic conjugate forces yield to a general partial differential equation governing the viscoelastic, viscodamage, and healing processes. We also show that this framework yields a more general constitutive model for viscoelasticity comparing to the viscoelastic models presented by Schapery (1969a) and Levesque et al. (2008). We also discuss that the derived viscoelastic constitutive model is valid for general cases and there is no need to assume a hypothetical reversible load history for which the state variables associated with viscoelastic process remain constant. Moreover, using the proposed thermodynamic framework, we derive a modified non-associated Perzyna-type viscoplastic model with kinematic hardening without using the concept of overstress function and postulating a viscoplastic potential function. Also, we show that the non-associative plasticity/viscoplasticity can be derived using the principle of virtual power. Furthermore, based on the presented framework, we derive a modified version of Armstrong and Frederick model (1966) for evolution of backstress. All these models are then coupled together and to temperature to model the complex mechanical response of time- and rate-dependent materials. Finally, we derive the well-known Fourier heat conduction law and the heat equation for the presented constitutive model (Darabi and Abu Al-Rub, 2011).

6.2. Natural Healing Configuration and Transformation Hypothesis

The healing configuration proposed in Chapter IV is adopted in this work to couple healing and damage models to the rest of the constitutive model. The relationship between the stress tensors in the nominal and healing configurations are recalled as follows:

$$\tilde{\sigma}_{ij} = \frac{\sigma_{ij}}{1-\tilde{\phi}} = \frac{\sigma_{ij}}{1-\phi(1-h)} \tag{6.1}$$

Eq. (6.1) makes it possible to extend the developed techniques for implementation of damage models to the healing models.

One of the transformation hypotheses that can be used for the constitutive models accompanied with the dissipative processes such as viscoelasticity and viscoplasticity is based on the equivalency of the power of dissipation in the effective and nominal configurations. Lee et al. (1985) proposed this hypothesis and assumed that the power dissipation associated with the plasticity is equivalent in the nominal and effective configurations. Based on this transformation hypothesis, they derived an elastoplastic-anisotropic damage constitutive model for metal plates. Voyiadjis and Thiagarajan (1997) also used this hypothesis and proposed an uncoupled plastic-anisotropic damage model for metal-matrix composites. Later Voyiadjis et al. (2004) adopted this hypothesis for viscoplasticity and derived a gradient-dependent viscoplasticity-, anisotropic-viscodamage constitutive model.

The small deformation theories are postulated in this work such that the total strain tensor and its rate can additively be decomposed into viscoelastic and viscoplastic components. Assuming the small deformations in the nominal configuration naturally means that the deformation in the healing configuration is also small. Therefore, the additive decomposition of strain tensor and its rate is also valid in the healing configuration, such that:

$$\tilde{\varepsilon}_{ij} = \tilde{\varepsilon}_{ij}^{ve} + \tilde{\varepsilon}_{ij}^{vp} \; ; \quad \dot{\tilde{\varepsilon}}_{ij} = \dot{\tilde{\varepsilon}}_{ij}^{ve} + \dot{\tilde{\varepsilon}}_{ij}^{vp} \tag{6.2}$$

In this work, the power-correlating hypothesis which states that the power expenditure associated with each type of the dissipative process is the same in the

nominal and effective configurations is adopted. However, this hypothesis is extended for correlating the power in the nominal and healing configurations. Postulating this hypothesis along with using continuum damage-healing mechanics based on the healing stress space are both numerically and physically interesting. In other words, using the healing stress space eliminates numerical complexities associated with direct couplings of the damage and healing models with the rest of the constitutive model; whereas, power-correlating hypothesis makes these simplifications physically sound since it allows the accurate estimation of the dissipated energy in the healing stress space. Therefore, it is assumed that the dissipated power resulting from the viscoelastic and viscoplastic processes are the same in the nominal and healing configurations. In this study, the isotropic damage and healing variables are used in order to present the general steps of the thermodynamic framework in a much clearer and simpler way. Applying the power equivalence hypothesis for the isotropic damage and healing cases yields the following relations between different components of the strain tensor in the nominal and healing configurations:

$$\dot{\tilde{\varepsilon}}_{ij}^{ve} = \left[1-\phi(1-h)\right]\dot{\varepsilon}_{ij}^{ve}; \quad \dot{\tilde{\varepsilon}}_{ij}^{vp} = \left[1-\phi(1-h)\right]\dot{\varepsilon}_{ij}^{vp}; \quad \dot{\tilde{\varepsilon}}_{ij} = \left[1-\phi(1-h)\right]\dot{\varepsilon}_{ij} \quad (6.3)$$

6.3. Thermodynamic Framework

6.3.1. Internal and External Expenditures of Power

Axioms of equilibrium and thermodynamics should be satisfied to formulate a proper material constitutive model. In this section, expressions for the internal and external expenditures of power are defined following the framework of Gurtin (2003), but with the consideration of viscoelasticity, damage, and healing. Definition of the internal and external expenditures of power is often thought to be very fixed. However, Fremond and Nedjar (1996) modified the definition of the classical form of the internal virtual power by including, in addition to the classical terms involving strain rates, the damage rate and its gradient. They also modified the expression of the external expenditure of power by including the effects of the external sources of the body and surface damage forces to explain the microscopic movements that produce damage. Based on these modifications,

they formulated an elastic- gradient-dependent damage model. A similar line of thought is followed here to derive a constitutive equation that couples viscoelastic (creep and relaxation properties), viscoplastic (rate-dependent plasticity), viscodamage (rate-dependent damage), and healing material responses to explain the time- and rate-dependent mechanical response of materials. However, the present treatment is limited to local viscoelasticity, viscoplasticity, damage, and healing where higher-order nonlocal gradient-dependent variables are neglected.

Let Γ to be an arbitrary sub-body and let $\boldsymbol{n}$ denote the outward unit normal on the boundary $\partial\Gamma$ of Γ. In this work, the internal expenditure of power is assumed to be characterized by the Cauchy stress tensor $\boldsymbol{\sigma}$ defined over Γ for all times, the back stress $\mathbf{X}$ associated with kinematic hardening, the dragstress κ associated with isotropic hardening, the damage force Y conjugate to the damage density variable ϕ, the healing force H conjugate to the healing variable h, and M_{int}^{ve} - of phenomenological internal state variables associated with the viscoelastic processes ζ_m ($m = 1,..., M_{\text{int}}^{ve}; M_{\text{int}}^{ve} \geq 1$), such that the expenditure of the internal power can be written as:

$$P_{\text{int}} = \int_{\Gamma} \left(\sigma_{ij}\dot{\varepsilon}_{ij}^{ve} + \sum_{m=1}^{M_{\text{int}}^{ve}} \chi_m\dot{\zeta}_m + \mathbf{X}_{ij}\dot{\varepsilon}_{ij}^{vp} + \kappa\dot{p} + Y\dot{\phi} + H\dot{h} \right) dV \qquad (6.4)$$

where $\dot{p}$ is the rate of the equivalent viscoplastic strain, which is defined by:

$$\dot{p} = \sqrt{2\dot{\varepsilon}_{ij}^{vp}\dot{\varepsilon}_{ij}^{vp} / 3} \qquad (6.5)$$

Eq. (6.4) is based on the concept that the power expended by each kinematical field be expressible in terms of an associated force system consistent with its own balance. The first two terms in Eq. (6.4) represent the internal power generated because of the viscoelastic processes. The third and the fourth terms represent the internal power generated by the viscoplastic process. The third term accounts for internal power expenditure by the backstress (the residual stress) which is attributed to kinematic hardening which introduces anisotropic effects, whereas the fourth term is the internal power due to the dragstress attributing to the isotropic hardening. Moreover, the fifth and the sixth terms are the internal power expended by the damage and healing processes,

respectively. However, the kinematical fields in Eq. (6.4) are no longer independent and, therefore, special care is taken in the following in order to properly account for their couplings. Moreover, although the two state variables ε_{ij}^{vp} and p are dependent, they introduce different physics such that the viscoplastic strain ε_{ij}^{vp} results in kinematic hardening in the plastic/viscoplasticity model whereas the effective plastic strain p results in isotropic hardening in the plastic/viscoplastic model (c.f. Abu Al-Rub et al., 2007; Voyiadjis and Abu Al-Rub, 2007).

As mentioned before, the internal state variables associated with the viscoelastic process are considered as hidden state variables. Ideally speaking, these internal state variables can relate the developed constitutive model at the continuum scale to the microstructure. Although these hidden state variables finally result in the evolution of the viscoelastic strain tensor, their contribution to the stored and dissipated energies should be considered for more accurate estimation of the these energies in the viscoelastic materials (as will be shown in the next sections).

On the other hand, the external expenditure of power is defined in terms of the macroscopic body force b, a macroscopic surface traction t, and inertial forces. Therefore, the external expenditure of the power can be written as follows:

$$P_{\text{ext}} = \int_{\Gamma} b_i \dot{u}_i dV + \int_{\partial \Gamma} t_i \dot{u}_i dA - \int_{\Gamma} \rho \ddot{u}_i \dot{u}_i dV \qquad (6.6)$$

where u is a prescribed field and represents the displacement vector.

Moreover, it is desired to derive the constitutive model in the healing configuration since the common argument in CDM is that once the material is damaged, further loading can only affect the undamaged and healed material skeleton. Obviously, before the material gets damaged the healing and nominal configurations are identical.

As it was mentioned in the previous section, the healing configuration is defined as a fictitious state where the unhealed damages in the material are removed. Hence, damage and healing does not contribute to the internal expenditure of power in the healing configuration. In the healing configuration, the Cauchy stress tensor in the healing configuration $\tilde{\sigma}$, the back stress in the healing configuration $\tilde{X}$, the dragstress

in the healing space $\tilde{\kappa}$, and M_{int}^{ve} - of phenomenological internal state variables associated with the viscoelastic processes $\tilde{\zeta}_m$ ($m = 1,..., M_{\text{int}}^{ve}$; $M_{\text{int}}^{ve} \geq 1$)contribute to the internal expenditure of power, such that the expenditure of the internal power can be written as:

$$\tilde{P}_{\text{int}} = \int_{\Gamma} \left(\tilde{\sigma}_{ij} \dot{\tilde{\varepsilon}}_{ij}^{ve} + \sum_{m=1}^{M_{\text{int}}^{ve}} \tilde{\chi}_m \dot{\tilde{\zeta}}_m + \tilde{X}_{ij} \dot{\tilde{\varepsilon}}_{ij}^{vp} + \tilde{\kappa} \dot{\tilde{p}} \right) dV \tag{6.7}$$

where $\tilde{P}_{\text{int}}$ is the internal expenditure of power in the healing configuration and $\dot{\tilde{p}} = \sqrt{2\dot{\tilde{\varepsilon}}_{ij}^{vp} \dot{\tilde{\varepsilon}}_{ij}^{vp} / 3} = \left[1 - \phi(1-h) \right] \dot{p}$ by substituting Eq. (6.3)$_3$ into Eq. (6.5). However, as it will be shown in the next section, the thermodynamic forces conjugate to the damage and healing variables in the nominal configuration are always null [i.e. $Y = 0$ and $H = 0$, based on the principle of virtual power, Eqs. (6.17) and (6.18)]. Hence, by adopting the power equivalence hypothesis, it can easily be shown that Eqs. (6.4) and (6.7) are the same, such that:

$$\tilde{P}_{\text{int}} = P_{\text{int}} \tag{6.8}$$

This can be verified by substituting Eqs. (6.1), (6.3), (6.17), and (6.18) into Eq. (6.7) to obtain Eq. (6.4). It is noteworthy that the power equivalence hypothesis is used for all components of the viscoelastic power in the nominal and healing configurations (i.e. $\sum_{m=1}^{M_{\text{int}}^{ve}} \tilde{\chi}_m \dot{\tilde{\zeta}}_m = \sum_{m=1}^{M_{\text{int}}^{ve}} \chi_m \dot{\zeta}_m$ and $\tilde{\sigma}_{ij} \dot{\tilde{\varepsilon}}_{ij}^{ve} = \sigma_{ij} \dot{\varepsilon}_{ij}^{ve}$).

6.3.2. Principle of Virtual Power

The principle of the virtual power is the assertion that, given any sub-body Γ, the virtual power expended on Γ by materials or bodies exterior to Γ (i.e. external power) is equal to the virtual power expended within Γ (i.e. internal power). Eqs. (6.4) and (6.6) represent the actual expenditures of the power during a kinematical process. The virtual expenditure of the power can be defined when the prescribed fields are replaced by virtual ones. Hence, we can write internal and external expenditures of virtual power as:

$$\overset{*}{P}_{\text{int}} = \int\limits_{\Gamma} \left(\sigma_{ij} \delta\dot{\varepsilon}_{ij}^{ve} + \sum_{m=1}^{M_{\text{int}}^{ve}} \chi_m \delta\dot{\zeta}_m + X_{ij}\delta\dot{\varepsilon}_{ij}^{vp} + \kappa\delta\dot{p} + Y\delta\dot{\phi} + H\delta\dot{h} \right) dV \qquad (6.9)$$

$$\overset{*}{P}_{\text{ext}} = \int\limits_{\Gamma} b_i \delta\dot{u}_i dV + \int\limits_{\partial\Gamma} t_i \delta\dot{u}_i dA - \int\limits_{\Gamma} \rho\ddot{u}_i \delta\dot{u}_i dV \qquad (6.10)$$

where $\overset{*}{P}_{\text{int}}$ and $\overset{*}{P}_{\text{ext}}$ represent internal and external expenditures of virtual power, respectively. Note that the kinematical fields $\delta\dot{u}$, $\delta\dot{\varepsilon}^{ve}$, $\delta\dot{\zeta}$, $\delta\dot{\varepsilon}^{vp}$, $\delta\dot{p}$, $\delta\dot{\phi}$, and $\delta\dot{h}$ in Eqs. (6.9) and (6.10) are virtual, where δ is the virtual operator.

According to the principle of the virtual power, the external virtual power should be balanced by the internal expenditure of virtual power, such that:

$$\overset{*}{P}_{\text{int}} = \overset{*}{P}_{\text{ext}} \qquad (6.11)$$

Let N be a second-order tensor representing the unit direction of the viscoplastic strain tensor, $\dot{\varepsilon}^{vp}$, such that:

$$N_{ij} = \frac{\dot{\varepsilon}_{ij}^{vp}}{\left\| \dot{\varepsilon}_{ij}^{vp} \right\|} = \sqrt{\frac{2}{3}} \frac{\dot{\varepsilon}_{ij}^{vp}}{\dot{p}} \qquad (6.12)$$

Substituting Eqs. (6.9) and (6.10) into Eq. (6.11), decomposing the strain tensor into its viscoelstic and viscoplastic components, and using the divergence theorem imply:

$$\int\limits_{\Gamma} \Bigg[\left(\sigma_{ij,j} + b_i - \rho\ddot{u}_i \right)\delta\dot{u}_i$$

$$+ \left(\sqrt{\frac{3}{2}}\left(\sigma_{ij} - X_{ij} \right)N_{ij} - \kappa \right)\delta\dot{p} - Y\delta\dot{\phi} - H\delta\dot{h} - \sum_{m=1}^{M_{\text{int}}^{ve}} \chi_m \delta\dot{\zeta}_m \Bigg] dV \qquad (6.13)$$

$$+ \int\limits_{\partial\Gamma} \left(t_i - \sigma_{ij}n_j \right)\delta\dot{u}_i dA = 0$$

The fields Γ, $\delta\dot{u}$, $\delta\dot{\zeta}$, $\delta\dot{p}$, $\delta\dot{\phi}$, and $\delta\dot{h}$ may be arbitrary specified if and only if:

$$\sigma_{ij,j} + b_i = \rho\ddot{u}_i, \quad \text{in } \Gamma \qquad (6.14)$$

$$t_i = \sigma_{ij}n_j, \quad \text{on } \partial\Gamma \qquad (6.15)$$

$$\sqrt{\frac{3}{2}}\left(\sigma_{ij} - X_{ij} \right)N_{ij} - \kappa = 0, \quad \text{in } \Gamma \qquad (6.16)$$

$$Y = 0, \quad \text{in } \Gamma \qquad (6.17)$$

$$H = 0, \quad \text{in } \Gamma \tag{6.18}$$

$$\chi_m = 0, \quad \text{in } \Gamma, \quad m \in \left[1...M_{\text{int}}^{ve}\right] \tag{6.19}$$

Eq. (6.14) expresses the local static or dynamic equilibrium or macroforce balance. Eq. (6.15) defines the boundary traction as the density of the surface forces introduced. Eq. (6.16) is the viscoplastic microforce balance according to notion of Gurtin (2003) that will be used for deriving the dynamic viscoplasticity yield surface in the subsequent sections. Also, we will show that this equation is valid for both associative and non-associative plasticity/viscoplasticity. Similarly, Eq. (6.17) defines the damage microforce balance (Fremond and Nedjar, 1996) that will be used in deriving the dynamic viscodamage nucleation and growth condition. Moreover, Eq. (6.18) is the healing microforce balance which can be used to derive the healing condition and the healing evolution law. Eq. (6.19) is defined as the viscoelastic microforce balance. Eqs. (6.17), (6.18), and (6.19) are new and non-classical for viscoelastic materials. Eq. (6.19) defines the balance law for the internal work of viscoelastic process. This simple balance law results in the general partial differential equation that explains the viscoelastic processes in materials.

Using the power equivalence hypothesis allows one to express the internal expenditure of virtual power in the healed configuration. The virtual expenditure of the virtual power in the healing configuration can be defined when the prescribed fields in Eq. (6.7) are replaced by virtual ones, such that:

$$\overset{*}{\tilde{P}}_{\text{int}} = \int_{\Gamma} \left(\tilde{\sigma}_{ij} \delta \dot{\tilde{\varepsilon}}_{ij}^{ve} + \sum_{m=1}^{M_{\text{int}}^{ve}} \tilde{\chi}_m \delta \dot{\tilde{\zeta}}_m + \tilde{X}_{ij} \delta \dot{\tilde{\varepsilon}}_{ij}^{vp} + \tilde{\kappa} \delta \dot{\tilde{p}} \right) dV \tag{6.20}$$

where $\overset{*}{\tilde{P}}_{\text{int}}$ is the internal expenditure of virtual power in the healing configuration. It can easily be shown that adopting the power equivalence hypothesis implies the equivalency of the internal expenditure of virtual power in the nominal and healed configurations, such that:

$$\overset{*}{\tilde{P}}_{\text{int}} = \overset{*}{P}_{\text{int}} \tag{6.21}$$

This can be verified by substituting Eqs. (6.1) and (6.3) into Eq. (6.20) and noting that the damage and healing microforce balances in the nominal configuration are zero. Substituting Eqs. (6.1), (6.20), and (6.21) into the principle of virtual power [Eq. (6.11)] result the following equations:

$$\left[1-\phi\left(1-h\right)\right]\tilde{\sigma}_{ij,j}+b_i=\rho\ddot{u}_i, \quad \text{in } \Gamma \tag{6.22}$$

$$t_i=\left[1-\phi\left(1-h\right)\right]\tilde{\sigma}_{ij}n_j, \quad \text{on } \partial\Gamma \tag{6.23}$$

$$\sqrt{\frac{3}{2}}\left(\tilde{\sigma}_{ij}-\tilde{X}_{ij}\right)\tilde{N}_{ij}-\tilde{\kappa}=0, \quad \text{in } \Gamma \tag{6.24}$$

$$\tilde{\chi}_m=0, \quad \text{in } \Gamma, \quad m\in\left[1...M_{\text{int}}^{ve}\right] \tag{6.25}$$

Substituting Eq. (6.1) into Eqs. (6.22) and (6.23) shows that these equations are the same as Eqs. (6.14) and (6.15), respectively. Eq. (6.25) defines the balance law for internal work of viscoelastic process in the healed configuration. Moreover, Eq. (6.24) shows the microforce balance in the effective configuration, where:

$$\tilde{N}_{ij}=\frac{\dot{\tilde{\varepsilon}}_{ij}^{vp}}{\left\|\dot{\tilde{\varepsilon}}_{ij}^{vp}\right\|}=\sqrt{\frac{2}{3}}\frac{\dot{\tilde{\varepsilon}}_{ij}^{vp}}{\dot{\tilde{p}}} \tag{6.26}$$

Substituting Eq. (6.3) into Eq. (6.26) yields:

$$\tilde{N}_{ij}=N_{ij} \tag{6.27}$$

6.3.3. Non-Associative Plasticity/Viscoplasticity Based on Principle of Virtual Power

One of the challenges in the plasticity/viscoplasticity theories is that the associative plasticity/viscoplasticity theories cannot accurately predict the plastic/viscoplastic strain in pressure-dependent materials such as polymers, soils, rocks, bituminous materials, and geomaterials (e.g. Zienkiewicz et al., 1975; Oda and Nakayama, 1989; Cristescu, 1994; Florea, 1994; Pestana and Whittle, 1999; Collins and Kelly, 2002; Dormieux et al., 2006). To overcome this issue, a plastic/viscoplastic potential function different from the yield surface function is usually assumed to obtain the accurate amount of plastic/viscoplastic strain using a non-associated plastic flow rule. The plastic potential

function is usually selected based on the experiments and without any attention to the fundamental laws of thermodynamics.

Several researchers have derived the associative plasticity/viscoplasticity flow rule based on principle of virtual power (e.g. Gurtin, 2000; Fleck and Hutchinson, 2001; Gurtin, 2002; Gudmundson, 2004; Gurtin and Anand, 2005; Abu Al-Rub et al., 2007; Voyiadjis and Abu Al-Rub, 2007; Gurtin and Anand, 2009; Voyiadjis and Deliktas, 2009). Moreover, it is usually thought that the principle of virtual power leads only to associative plasticity/viscoplasticity flow rules as mentioned and shown by several researchers. Several researchers, on the other hand, have used the maximum dissipation principle to derive plasticity theories. However, it is commonly known that the maximum dissipation principle leads to associative plasticity theories (c.f. Simo and Hughes, 1998) unless the dissipation function depends on the stress in addition to the plastic strain and its rate (e.g. Collins and Houlsby, 1997; Srinivasa, 2010). However, these approaches (e.g. Collins and Houlsby, 1997; Srinivasa, 2010) suffer from two main deficiencies: (1) the forms of both the yield function and the plastic potential function are both required to inversely obtain the form for the rate of the energy dissipation as a function of the stress, plastic strain, and its rate; and (2) they do not lead to an explicit form for the plastic strain rate, instead, the stress is usually obtained as a function of the strain and strain rate which most of the time requires tedious mathematical manipulations to express the rate of the plastic strain as a function of stress.

However, it is shown here that the generalized nonassociative plasticity/viscoplasticity theories can be a direct consequence of the principle of virtual power. This will also be along the direction of Ziegler's thermodynamic approach (Ziegler, 1983) which states that the constitutive models for materials should be fully determined by the knowledge of a thermodynamic potential such as the Helmholtz free energy function and another function which is the dissipation function.

The associative plasticity/viscoplasticity theories assume that the direction of the plastic strain N is normal to the yield surface.

However, in this work, it is shown that the generalized non-associative viscoplasticity theories are direct consequences of the principle of virtual power. Let one assume for simplicity and without loss of generality that the material is simply elasto-viscoplastic with kinematic hardening. Hence, for this material the principle of virtual power can be written as follows:

$$\int_\Gamma \left(\sigma_{ij} \delta \dot\varepsilon_{ij}^e + X_{ij} \delta \dot\varepsilon_{ij}^{vp} + \kappa \delta \dot p \right) dV = \int_\Gamma b_i \delta \dot u_i dV + \int_{\partial\Gamma} t_i \delta \dot u_i dA - \int_\Gamma \rho \ddot u_i \delta \dot u_i dV \qquad (6.28)$$

Substituting the macroforce balance [Eq. (6.14)] and boundary traction equation [Eq. (6.15)] into Eq. (6.28) yields:

$$\int_\Gamma \left[\left(\sigma_{ij} - X_{ij} \right) \delta \dot\varepsilon_{ij}^{vp} - \kappa \delta \dot p \right] dV = 0 \qquad (6.29)$$

Substituting Eq. (6.12) into Eq. (6.29) yields:

$$\int_\Gamma \left[\sqrt{\frac{3}{2}} \left(\sigma_{ij} - X_{ij} \right) - \kappa \right] \delta \dot\varepsilon_{ij}^{vp} dV = 0 \qquad (6.30)$$

For an arbitrary Γ one can then write:

$$\sigma_{ij}^* \delta \dot\varepsilon_{ij}^{vp} = 0 \qquad (6.31)$$

where $\boldsymbol{\sigma}^*$ is given by:

$$\sigma_{ij}^* = \sqrt{\frac{3}{2}} \left(\sigma_{ij} - X_{ij} \right) - \kappa N_{ij} \qquad (6.32)$$

Eq. (6.31) should be satisfied for all possible cases. The possible cases which may always make this equation zero are investigated in the following:

a) *Case I:*

$$\delta \dot\varepsilon_{ij}^{vp} = 0 \qquad (6.33)$$

However, the field $\delta\boldsymbol{\varepsilon}^{vp}$ can be selected arbitrary. Therefore, this case cannot always be satisfied.

b) *Case II:*

$$\sigma_{ij}^* = 0_{ij} \qquad (6.34)$$

This case gives a plastic flow rule (or microforce balance), different than the flow rule in Eq. (6.16), and enforces co-directionality constraint by requiring that the direction of the viscoplastic strain N coincides with the direction of $(\sigma - X)$. Therefore, from Eqs. (6.32) and (6.34) one can write for this case:

$$N_{ij} = \sqrt{\frac{3}{2}} \frac{\sigma_{ij} - X_{ij}}{\kappa} \tag{6.35}$$

Moreover, for this case, one can define the yield surface f by taking the Euclidean norm of Eq. (6.34) along with Eq. (6.32) and noting that $\|N\| = 1$, such that:

$$f = \|\sigma_{ij}^*\| = \sqrt{\frac{3}{2}} \|\sigma_{ij} - X_{ij}\| - \kappa = 0 \tag{6.36}$$

However, this expression shows that Case 2, Eq. (6.34), yields an associative plastic flow rule, where one can obtain from Eq. (6.36) that the direction of the plastic flow as the normal to the yield surface, such that:

$$N'_{ij} = \frac{\partial f}{\partial (\sigma_{ij} - X_{ij})} = \sqrt{\frac{3}{2}} \frac{\sigma_{ij} - X_{ij}}{\kappa} = N_{ij} \tag{6.37}$$

Eq. (6.35) is also used in obtaining the above restriction.

c) Case III:

Another possible case, which is also the most general one, is that the stress tensor σ^* in Eq. (6.32) be perpendicular to the direction of the viscoplastic strain rate (i.e. $\sigma^* \perp N$). This does not necessarily imply that the plastic flow direction N coincides with the direction of the stress tensor $(\sigma - X)$. Eq. (6.31) can be rewritten as the inner product of σ^* and N by utilizing Eq. (6.12) and for any arbitrary value of $\delta \dot{p}$, such that:

$$\sigma_{ij}^* N_{ij} = 0 \tag{6.38}$$

However, the microforce balance in Eq. (6.16), which is equivalent to the yield function f, can easily be obtained from Eq. (6.38) and noting that $N : N = 1$, such that:

$$f = \sigma_{ij}^* N_{ij} = \sqrt{\frac{3}{2}}(\sigma - X)' - \kappa = 0 \qquad (6.39)$$

where $(\sigma - X)'$ is termed the resolved or equivalent stress since it represents the stress $\sigma - X$ resolved on the direction of plastic flow N, and is given by:

$$(\sigma - X)' = (\sigma_{ij} - X_{ij})N_{ij} \qquad (6.40)$$

It is obvious from Eq. (6.39) that the normal to the yield surface (i.e. $N' = \partial f / \partial(\sigma - X)$) does not coincide with the direction of the plastic strain rate, N. In case, N is co-directional with $(\sigma - X)$ then from Eq. (6.40) one obtains $(\sigma - X)' = \|\sigma_{ij} - X_{ij}\|$ which is the case in Eq. (6.36). One can also relate N' and N from Eq. (6.39) as follows:

$$N_{ij}' = N_{ij} + (\sigma_{kl} - X_{kl})\frac{\partial N_{kl}}{\partial(\sigma_{ij} - X_{ij})} \qquad (6.41)$$

Therefore, f in Eq. (6.36) or (6.39) are equivalent only for the case of associative plasticity (i.e. $N = N'$). In other words, taking the Euclidean norm of Eq. (6.39) and using $\|N\| = 1$ yields:

$$\sqrt{\frac{3}{2}}\|(\sigma_{ij} - X_{ij})\| \geq \kappa \qquad (6.42)$$

Which implies that $\|\sigma - X\|$ is not the equivalent stress as it is the case in Eq. (6.36). Also, this inequality reduces to an equality (i.e. $\sqrt{\frac{3}{2}}\|\sigma - X\| = \kappa$ as in Eq. (6.36)) when $\sigma - X$ is co-directional with N. However, for the general case Eq. (6.42) remains an inequality.

Now, let F be a plastic flow potential function, such that:

$$N_{ij} = M^{-1}\frac{\partial F}{\partial(\sigma_{ij} - X_{ij})}; \quad M = \left\|\frac{\partial F}{\partial(\sigma_{ij} - X_{ij})}\right\| \qquad (6.43)$$

Then the plastic strain rate is given from Eq. (6.12) as follows:

$$\dot{\varepsilon}_{ij}^{vp} = \sqrt{\frac{3}{2}} M^{-1} \dot{p} \frac{\partial F}{\partial \left(\sigma_{ij} - X_{ij} \right)} \tag{6.44}$$

The constraint between the plastic potential F and the yield surface function f can be obtained by substituting Eq. (6.43) into Eq. (6.38) along with Eq. (6.32), such that:

$$f = \left(\sigma_{ij} - X_{ij} \right) \frac{\partial F}{\partial \left(\sigma_{ij} - X_{ij} \right)} - \sqrt{\frac{2}{3}} M \kappa = 0 \tag{6.45}$$

Differentiating both sides of Eq. (6.45) with respect to the $\left(\sigma_{ij} - X_{ij} \right)$ yields:

$$\frac{\partial f}{\partial \sigma_{ij}} = \frac{\partial F}{\partial \left(\sigma_{ij} - X_{ij} \right)} + \left(\sigma_{kl} - X_{kl} \right) \frac{\partial^2 F}{\partial \left(\sigma_{kl} - X_{kl} \right) \partial \left(\sigma_{ij} - X_{ij} \right)} = 0 \tag{6.46}$$

Eq. (6.46) provides the relationship between the yield function f and the viscoplastic potential function F for nonassociative/associative plasticity/viscoplasticity theories. This relationship is general and can be used for both associative and non-associative plasticity/viscoplasticity theories.

As it was discussed earlier, in the associative viscoplasticity theories, the yield function f and the plastic potential function F are assumed to be the same or, equivalently, the direction of the plastic flow is normal to the yield surface (i.e. $N = \partial F / \partial (\sigma - X) = \partial f / \partial (\sigma - X)$. According to Eq. (6.46) the assumption of the associative viscoplasticity requires the second term in the right side of Eq. to be zero, such that:

$$\left(\sigma_{kl} - X_{kl} \right) \frac{\partial^2 F}{\partial \left(\sigma_{kl} - X_{kl} \right) \partial \left(\sigma_{ij} - X_{ij} \right)} = 0; \quad \text{when } f = F \tag{6.47}$$

Or equivalently from Eq. (6.41):

$$\left(\sigma_{kl} - X_{kl} \right) \frac{\partial N_{ij}}{\partial \left(\sigma_{kl} - X_{kl} \right)} = 0 \quad \text{when } N' = \frac{\partial f}{\partial \sigma} = \frac{\partial F}{\partial \sigma} = N \tag{6.48}$$

which means that $(\sigma - X) \perp \dfrac{\partial N}{\partial (\sigma - X)}$ as the basic assumption for associative plasticity/viscoplasticity theories. Therefore, one can conclude that Eq. (6.46) governs

the relation between the yield function and the viscoplastic potential function for both associative and non-associative viscoplasticity theories. It should be mentioned that this equation naturally implies that the yield surface and the plastic potential functions are the same for associative viscoplasticity theories.

Eqs. (6.43), (6.45), and (6.46) are derived when both isotropic and kinematic hardening are assumed. These equations are simplified to the following forms when kinematic hardening is not considered.

$$N_{ij} = M^{-1} \frac{\partial F}{\partial \sigma_{ij}}; \quad M = \left\| \frac{\partial F}{\partial \sigma_{ij}} \right\| \tag{6.49}$$

$$f = \sigma_{ij} \frac{\partial F}{\partial \sigma_{ij}} - \sqrt{\frac{2}{3}} M \kappa = 0 \tag{6.50}$$

$$\frac{\partial f}{\partial \sigma_{ij}} = \frac{\partial F}{\partial \sigma_{ij}} + \sigma_{kl} \frac{\partial^2 F}{\partial \sigma_{kl} \partial \sigma_{ij}} = 0 \tag{6.51}$$

It should be noted that the same arguments can be used for deriving associative and non-associative damage rules.

The above arguments clearly show the existence of a constraint between the yield function f and the plastic potential F in a thermodynamically consistent framework. The yield surface f can be derived directly using the microforce balance without the need for any further assumption more than the Helmholtz free energy function and the rate of the energy dissipation that will be shown in the subsequent development. On the other hand, one may solve the differential equation presented in Eq. (6.46) for thermodynamically admissible potential functions once the yield function is known. Reversely, one can use the given plastic potential function to derive its associated thermodynamically admissible yield function f. The second approach is used in this work to derive the thermodynamically consistent yield functions associated with the given plastic potential function.

6.3.4. Internal State Variables and Clausius-Duhem Inequality

The Helmholtz free energy is assumed to be a function of the following variables in the healing configuration:

$$\Psi = \Psi(\tilde{\varepsilon}_{ij}^{ve}, \tilde{\zeta}_m, \overline{p}, \phi, h, T) \tag{6.52}$$

The internal state variables associated with the viscoelastic process are considered as the hidden variables. Ideally speaking, these hidden variables can be used to relate the developed constitutive equation at continuum scale to the microstructure.

By combining the first and second laws of thermodynamics (i.e. balance of energy and entropy imbalance, respectively) and also assuming that the material density does not change during the deformation (i.e. $\dot{\rho} = 0$), the Clausius-Duhem inequality for non-isothermal conditions can be written as follows (c.f. Lemaître and Chaboche, 1990):

$$\int_{\Gamma} \left[\rho\left(\dot{\Psi} + \eta\dot{T}\right) + \frac{1}{T}q_i T_{,i} \right] dV \leq P_{\text{ext}} = P_{\text{int}} \tag{6.53}$$

Substituting Eq. (6.7) into Eq. (6.53) and noting that the sub-region Γ is arbitrary yield the following local form of the Clausius-Duhem inequality:

$$\tilde{\sigma}_{ij}\dot{\tilde{\varepsilon}}_{ij}^{ve} + \sum_{m=1}^{M_{\text{int}}^{ve}} \tilde{\chi}_m\dot{\tilde{\zeta}}_m + \tilde{X}_{ij}\dot{\tilde{\varepsilon}}_{ij}^{vp} + \tilde{\kappa}\dot{p} - \rho\left(\dot{\Psi} + \eta\dot{T}\right) - \frac{1}{T}q_i T_{,i} \geq 0 \tag{6.54}$$

which defines the rate of the energy dissipation per unit volume, Π. However, the thermodynamic forces conjugate to the damage density and healing variable (i.e. Y and H) are null according to Eqs. (6.17) and (6.18). Hence, these terms can be added Eq. (6.54) without changing the values of the rate of energy dissipation per unit volume. As it will be shown, adding these null terms will substantially simplify the derivation of the damage and healing conditions. Hence, one can rewrite Eq. (6.54) as:

$$\tilde{\sigma}_{ij}\dot{\tilde{\varepsilon}}_{ij}^{ve} + \sum_{m=1}^{M_{\text{int}}^{ve}} \tilde{\chi}_m\dot{\tilde{\zeta}}_m + \tilde{X}_{ij}\dot{\tilde{\varepsilon}}_{ij}^{vp} + \tilde{\kappa}\dot{p} + Y\dot{\phi} + H\dot{h} - \rho\left(\dot{\Psi} + \eta\dot{T}\right) - \frac{1}{T}q_i T_{,i} \geq 0 \tag{6.55}$$

Substituting the time derivative of the Helmholtz free energy into Eq. (6.55) yields:

$$\Pi = \left(\tilde{\sigma}_{ij} - \rho \frac{\partial \Psi}{\partial \tilde{\varepsilon}_{ij}^{ve}} \right) \dot{\tilde{\varepsilon}}_{ij}^{ve} + \sum_{m=1}^{M_{int}^{ve}} \left(\tilde{\chi}_m - \rho \frac{\partial \Psi}{\partial \tilde{\zeta}_m} \right) \dot{\tilde{\zeta}}_m + \left(\tilde{X}_{ij} - \rho \frac{\partial \Psi}{\partial \tilde{\varepsilon}_{ij}^{vp}} \right) \dot{\tilde{\varepsilon}}_{ij}^{vp} +$$

$$\left(\tilde{\kappa} - \rho \frac{\partial \Psi}{\partial \tilde{p}} \right) \dot{\tilde{p}} + \left(Y - \rho \frac{\partial \Psi}{\partial \phi} \right) \dot{\phi} + \left(H - \rho \frac{\partial \Psi}{\partial h} \right) \dot{h} - \rho \left(\frac{\partial \Psi}{\partial T} + \eta \right) \dot{T} - \frac{1}{T} q_i T_{,i} \geq 0 \tag{6.56}$$

From Eq. (6.56) the following classical thermodynamic state law for entropy is defined:

$$\eta = -\frac{\partial \Psi}{\partial T} \tag{6.57}$$

such that the rate of the energy dissipation from Eqs. (6.56) and (6.57) can be written as:

$$\Pi = \left(\tilde{\sigma}_{ij} - \rho \frac{\partial \Psi}{\partial \tilde{\varepsilon}_{ij}^{ve}} \right) \dot{\tilde{\varepsilon}}_{ij}^{ve} + \sum_{m=1}^{M_{int}^{ve}} \left(\tilde{\chi}_m - \rho \frac{\partial \Psi}{\partial \tilde{\zeta}_m} \right) \dot{\tilde{\zeta}}_m + \left(\tilde{X}_{ij} - \rho \frac{\partial \Psi}{\partial \tilde{\varepsilon}_{ij}^{vp}} \right) \dot{\tilde{\varepsilon}}_{ij}^{vp} +$$

$$\left(\tilde{\kappa} - \rho \frac{\partial \Psi}{\partial \tilde{p}} \right) \dot{\tilde{p}} + \left(Y - \rho \frac{\partial \Psi}{\partial \phi} \right) \dot{\phi} + \left(H - \rho \frac{\partial \Psi}{\partial h} \right) \dot{h} - \frac{1}{T} q_i T_{,i} \geq 0 \tag{6.58}$$

However, in order to obtain non-zero dissipation resulting from the viscoelasticity, viscoplasticity, and viscodamage dissipative processes, the following energetic thermodynamics conjugate forces that depend on the Helmholtz free energy are defined from Eq. (6.58), such that:

$$\tilde{\sigma}_{ij}^{ene} \equiv \rho \frac{\partial \Psi}{\partial \tilde{\varepsilon}_{ij}^{ve}} \tag{6.59}$$

$$\tilde{\chi}_m^{ene} \equiv \rho \frac{\partial \Psi}{\partial \tilde{\zeta}_m}; \quad m \in \left[1, ..., M_{int}^{ve} \right] \tag{6.60}$$

$$\tilde{X}_{ij}^{ene} \equiv \rho \frac{\partial \Psi}{\partial \tilde{\varepsilon}_{ij}^{vp}} \tag{6.61}$$

$$\tilde{\kappa}^{ene} \equiv \rho \frac{\partial \Psi}{\partial \tilde{p}} \tag{6.62}$$

$$Y^{ene} \equiv \rho \frac{\partial \Psi}{\partial \phi} \tag{6.63}$$

$$H^{ene} \equiv \rho \frac{\partial \Psi}{\partial h} \tag{6.64}$$

where "ene" designates the energetic component of the thermodynamic conjugate forces. Substituting Eqs. (6.59)-(6.64) into Eq. (6.58) implies:

$$\Pi = \left(\tilde{\sigma}_{ij} - \tilde{\sigma}_{ij}^{\text{ene}} \right) \dot{\tilde{\varepsilon}}_{ij}^{ve} + \sum_{m=1}^{M_{\text{int}}^{ve}} \left(\tilde{\chi}_m - \tilde{\chi}_m^{\text{ene}} \right) \dot{\tilde{\zeta}}_m + \left(\tilde{X}_{ij} - \tilde{X}_{ij}^{\text{ene}} \right) \dot{\tilde{\varepsilon}}_{ij}^{vp} + \left(\tilde{\kappa} - \tilde{\kappa}^{\text{ene}} \right) \dot{p}$$
$$+ \left(Y - Y^{\text{ene}} \right) \dot{\phi} + \left(H - H^{\text{ene}} \right) \dot{h} - \frac{1}{T} q_i T_{,i} \geq 0 \tag{6.65}$$

Eq. (6.65) shows that the rate of energy dissipation resulting from different mechanisms (i.e. viscoelasticity, viscoplasticity, viscodamage, and healing) is positive only if the thermodynamic conjugate forces have dissipative components as well. Hence, rewriting Eq. (6.65) implies:

$$\Pi = \tilde{\sigma}_{ij}^{\text{dis}} \dot{\tilde{\varepsilon}}_{ij}^{ve} + \sum_{m=1}^{M_{\text{int}}^{ve}} \tilde{\chi}_m^{\text{dis}} \dot{\tilde{\zeta}}_m + \tilde{X}_{ij}^{\text{dis}} \dot{\tilde{\varepsilon}}_{ij}^{vp} + \tilde{\kappa}^{\text{dis}} \dot{p} + Y^{\text{dis}} \dot{\phi} + H^{\text{dis}} \dot{h} - \frac{1}{T} q_i T_{,i} \geq 0 \tag{6.66}$$

where "dis" designates the dissipative component of the thermodynamic conjugate forces and defined as follows:

$$\tilde{\sigma}_{ij}^{\text{dis}} = \tilde{\sigma}_{ij} - \tilde{\sigma}_{ij}^{\text{ene}} \tag{6.67}$$

$$\tilde{\chi}_m^{\text{dis}} = \tilde{\chi}_m - \tilde{\chi}_m^{\text{ene}} ; \quad m \in \left[1, ..., M_{\text{int}}^{ve} \right] \tag{6.68}$$

$$\tilde{X}_{ij}^{\text{dis}} = \tilde{X}_{ij} - \tilde{X}_{ij}^{\text{ene}} \tag{6.69}$$

$$\tilde{\kappa}^{\text{dis}} = \tilde{\kappa} - \tilde{\kappa}^{\text{ene}} \tag{6.70}$$

$$Y^{\text{dis}} = Y - Y^{\text{ene}} \tag{6.71}$$

$$H^{\text{dis}} = H - H^{\text{ene}} \tag{6.72}$$

Therefore, in the current work, the energetic means that the thermodynamic conjugate forces are derived from the Helmholtz free energy function and the dissipative means that they are derived from the dissipation potential. Therefore, in order to formulate constitutive equations for the energetic and dissipative conjugate forces, one needs to know: (1) how the material stores energy which helps in assuming a mathematical form for the Helmholtz free energy, and (2) how the material dissipates energy which helps in assuming a mathematical form for the rate of energy dissipation. Furthermore, the rate of energy dissipation [Eq. (6.58)] naturally enforces the decomposition of the stress tensor into energetic and dissipative components. This decomposition results in a more comprehensive relation between the stress and the viscoelastic strain compared to the

classical relations for the viscoelastic materials. It is noteworthy to mention that, the Clausius-Duhem inequality also enforces the decomposition of the specific entropy η into energetic specific entropy (i.e. $\eta^{\text{ene}} = -\dfrac{\partial \Psi}{\partial T}$) and the dissipative specific entropy (i.e. $\eta^{\text{dis}} = \eta - \eta^{\text{ene}}$) which is related directly to the rate of energy dissipation. However, this decomposition is not used for the specific entropy in this work and the classical thermodynamic law is assumed for entropy as in Eq. (6.57) with $\eta^{\text{dis}} = 0$.

Let one assume for a moment that neither damage nor viscoplasticity occur in the material (i.e. $\dot{p} = 0$ and $\dot{\phi} = 0$) in order to explain the common argument that has been made in the literature for substituting the total stress instead of its energetic component in Eq. (6.59) [c.f. Levesque et al. (2008)]. Therefore, assuming *isothermal* conditions as well, the Clausius-Duhem inequality in Eq. (6.58) reduces to the following form:

$$\left(\tilde{\sigma}_{ij} - \rho \frac{\partial \Psi}{\partial \tilde{\varepsilon}_{ij}^{ve}} \right) \dot{\tilde{\varepsilon}}_{ij}^{ve} + \sum_{m=1}^{M_{\text{int}}^{ve}} \left(\tilde{\chi}_m - \rho \frac{\partial \Psi}{\partial \tilde{\zeta}_m} \right) \dot{\tilde{\zeta}}_m \geq 0 \qquad (6.73)$$

The commonly used argument states that the Clausius-Duhem inequality [Eq. (6.73)] is valid for all load histories. So, let the load history to be a hypothetical reversible load history such that the viscoelastic internal state variables remain constant (i.e. $\dot{\tilde{\zeta}}_m = 0$). Under this load history the second term of the inequality in Eq. (6.73) vanishes and the following constitutive law is obtained:

$$\tilde{\sigma}_{ij} = \rho \frac{\partial \Psi}{\partial \tilde{\varepsilon}_{ij}^{ve}} \qquad (6.74)$$

However, the authors believe that this argument is not consistent. The reason is that the material is assumed to be viscoelastic, and hence, the state variables $\dot{\tilde{\zeta}}_m$ are not independent of the viscoelastic strains $\tilde{\varepsilon}^{ve}$ and they evolve even under the unloading process. In other words, both $\tilde{\varepsilon}^{ve}$ and $\tilde{\zeta}_m$ evolve during the viscoelastic process whether it is loading or unloading. Hence, a more consistent framework is to admit the decomposition of the stress tensor into energetic and dissipative components as in Eq.

(6.67) such that Eq. (6.74) defines the thermodynamic law for the energetic component. The thermodynamic laws for the dissipative components are derived next.

6.3.5. Maximum Rate of the Energy Dissipation Principle

As it was shown in the previous section, the correct estimation of the rate of the energy dissipation requires the decomposition of the thermodynamic conjugate forces into energetic and dissipative components (Ziegler, 1977, 1983; Ziegler and Wehrli, 1987; Fremond and Nedjar, 1996; Shizawa and Zbib, 1999; Gurtin, 2003; Anand et al., 2005; Gurtin and Anand, 2005; Abu Al-Rub et al., 2007; Gurtin and Anand, 2009; Lele and Anand, 2009; Voyiadjis and Deliktas, 2009). However, in all of these works, except for the works of Ziegler (1977, 1983) and Shizawa and Zbib (1999), the constitutive equations for the dissipative components are merely constitutive assumptions and are not derived based on the laws of thermodynamics. However, in this work, the dissipative components of thermodynamic conjugate forces are determined directly from the rate of energy dissipation by using the maximum energy dissipation principle. Eq. (6.66)shows that the rate of the energy dissipation can be decomposed into its thermo-viscoelastic, thermo-viscoplastic, thermo-viscodamage, thermo-healing, and thermal components, such that:

$$\Pi = \Pi^{tve} + \Pi^{tvp} + \Pi^{tvd} + \Pi^{tH} + \Pi^{th} \geq 0 \qquad (6.75)$$

where Π^{tve}, Π^{tvp}, Π^{tvd}, Π^{tH}, and Π^{th} are thermo-viscoelastic, thermo-viscoplastic, thermo-viscodamage, thermo-healing, and thermal components of the rate of the energy dissipation, respectively, which are given as follows:

$$\Pi^{tve} = \tilde{\sigma}_{ij}^{\text{dis}} \dot{\tilde{\varepsilon}}_{ij}^{ve} + \sum_{m=1}^{M_{\text{int}}^{ve}} \tilde{\chi}_m^{\text{dis}} \dot{\tilde{\zeta}}_m \geq 0 \qquad (6.76)$$

$$\Pi^{tvp} = \tilde{X}_{ij}^{\text{dis}} \dot{\tilde{\varepsilon}}_{ij}^{vp} + \tilde{\kappa}^{\text{dis}} \dot{p} \geq 0 \qquad (6.77)$$

$$\Pi^{tvd} = Y^{\text{dis}} \dot{\phi} \geq 0 \qquad (6.78)$$

$$\Pi^{tH} = H^{\text{dis}} \dot{h} \geq 0 \qquad (6.79)$$

$$\Pi^{th} = -\frac{1}{T} q_i T_{,i} \geq 0 \qquad (6.80)$$

Obviously, Eqs. (6.76)-(6.80) are more restrict constraints for obtaining a positive-definite dissipation than that in Eq.(6.75). Now, constraint conditions are needed in order to maximize the rate of energy dissipation. This can be achieved by defining the following constraint conditions:

$$D^{tve} = \Pi^{tve} - \left(\tilde{\sigma}_{ij}^{\mathrm{dis}} \dot{\tilde{\varepsilon}}_{ij}^{ve} + \sum_{m=1}^{M_{\mathrm{int}}^{ve}} \tilde{\chi}_{m}^{\mathrm{dis}} \dot{\tilde{\zeta}}_{m} \right) = 0 \tag{6.81}$$

$$D^{tvp} = \Pi^{tvp} - \left(\tilde{X}_{ij}^{\mathrm{dis}} \dot{\tilde{\varepsilon}}_{ij}^{vp} + \tilde{\kappa}^{\mathrm{dis}} \dot{\tilde{p}} \right) = 0 \tag{6.82}$$

$$D^{tvd} = \Pi^{tvd} - Y^{\mathrm{dis}} \dot{\phi} = 0 \tag{6.83}$$

$$D^{tH} = \Pi^{tH} - H^{\mathrm{dis}} \dot{h} = 0 \tag{6.84}$$

$$D^{th} = \Pi^{th} + \frac{1}{T} q_i T_{,i} = 0 \tag{6.85}$$

Hence, the following objective functions Ω^{tve}, Ω^{tvp}, Ω^{tvd}, Ω^{tH}, and Ω^{th} with their corresponding Lagrange multipliers Λ^{tve}, Λ^{tvp}, Λ^{tvd}, Λ^{tH}, and Λ^{th} subjected to the constraint $D^{tve} = 0$, $D^{tvp} = 0$, $D^{tvd} = 0$, $D^{tH} = 0$, and $D^{th} = 0$, respectively, are defined, such that:

$$\Omega^{tve} = \Pi^{tve} - \Lambda^{tve} D^{tve} \tag{6.86}$$

$$\Omega^{tvp} = \Pi^{tvp} - \Lambda^{tvp} D^{tvp} \tag{6.87}$$

$$\Omega^{tvd} = \Pi^{tvd} - \Lambda^{tvd} D^{tvd} \tag{6.88}$$

$$\Omega^{tH} = \Pi^{tH} - \Lambda^{tH} D^{tH} \tag{6.89}$$

$$\Omega^{th} = \Pi^{th} - \Lambda^{th} D^{th} \tag{6.90}$$

Maximizing the above objective functions by using the necessary conditions implies:

$$\frac{\partial \Omega^{tve}}{\partial \dot{\tilde{\varepsilon}}_{ij}^{ve}} = 0 \, ; \frac{\partial \Omega^{tve}}{\partial \dot{\tilde{\zeta}}_{m}} = 0 \, ; \frac{\partial \Omega^{tvp}}{\partial \dot{\tilde{\varepsilon}}_{ij}^{vp}} = 0 \, ; \frac{\partial \Omega^{tvp}}{\partial \dot{\tilde{p}}} = 0 \, ; \frac{\partial \Omega^{tvd}}{\partial \dot{\phi}} = 0 \, ; \frac{\partial \Omega^{tH}}{\partial \dot{h}} = 0 \, ; \frac{\partial \Omega^{th}}{\partial (q_i / T)} = 0 \tag{6.91}$$

Substituting Eqs. (6.86)-(6.90) into Eq. (6.91) yield the following conjugate laws for the dissipative forces, such that:

$$\tilde{\sigma}_{ij}^{\mathrm{dis}} = \widehat{\Lambda}^{tve} \frac{\partial \Pi^{tve}}{\partial \dot{\tilde{\varepsilon}}_{ij}^{ve}} \tag{6.92}$$

$$\tilde{\chi}_m^{\mathrm{dis}} = \widehat{\Lambda}^{tve}\, \frac{\partial \Pi^{tve}}{\partial \dot{\tilde{\zeta}}_m} \tag{6.93}$$

$$\tilde{\mathrm{X}}_{ij}^{\mathrm{dis}} = \widehat{\Lambda}^{tvp}\, \frac{\partial \Pi^{tvp}}{\partial \dot{\tilde{\varepsilon}}_{ij}^{vp}} \tag{6.94}$$

$$\tilde{\kappa}^{\mathrm{dis}} = \widehat{\Lambda}^{tvp}\, \frac{\partial \Pi^{tvp}}{\partial \dot{\tilde{p}}} \tag{6.95}$$

$$Y^{\mathrm{dis}} = \widehat{\Lambda}^{tvd}\, \frac{\partial \Pi^{tvd}}{\partial \dot{\phi}} \tag{6.96}$$

$$H^{\mathrm{dis}} = \widehat{\Lambda}^{tH}\, \frac{\partial \Pi^{tH}}{\partial \dot{h}} \tag{6.97}$$

$$T_{,i} = -\widehat{\Lambda}^{th}\, \frac{\partial \Pi^{th}}{\partial \left(q_i / T \right)} \tag{6.98}$$

where

$$\widehat{\Lambda}^{tve} = 1 - \frac{1}{\Lambda^{tve}};\ \ \widehat{\Lambda}^{tvp} = 1 - \frac{1}{\Lambda^{tvp}};\ \ \widehat{\Lambda}^{tvd} = 1 - \frac{1}{\Lambda^{tvd}};\ \ \widehat{\Lambda}^{tH} = 1 - \frac{1}{\Lambda^{tH}};\ \ \widehat{\Lambda}^{th} = 1 - \frac{1}{\Lambda^{th}} \tag{6.99}$$

By substituting Eqs. (6.92)-(6.98) respectively into Eqs. (6.81)-(6.85), the Lagrange multipliers in Eq. (6.99) can be determined as:

$$\widehat{\Lambda}^{tve} = \frac{\Pi^{tve}}{\dfrac{\partial \Pi^{tve}}{\partial \dot{\tilde{\varepsilon}}_{ij}^{ve}}\, \dot{\tilde{\varepsilon}}_{ij}^{ve} + \displaystyle\sum_{m=1}^{M_{\mathrm{int}}^{ve}} \dfrac{\partial \Pi^{tve}}{\partial \dot{\tilde{\zeta}}_m}\, \dot{\tilde{\zeta}}_m} \tag{6.100}$$

$$\widehat{\Lambda}^{tvp} = \frac{\Pi^{tvp}}{\dfrac{\partial \Pi^{tvp}}{\partial \dot{\tilde{\varepsilon}}_{ij}^{vp}}\, \dot{\tilde{\varepsilon}}_{ij}^{vp} + \dfrac{\partial \Pi^{tvp}}{\partial \dot{\tilde{p}}}\, \dot{\tilde{p}}} \tag{6.101}$$

$$\widehat{\Lambda}^{tvd} = \frac{\Pi^{tvd}}{\dfrac{\partial \Pi^{tvd}}{\partial \dot{\phi}}\, \dot{\phi}} \tag{6.102}$$

$$\widehat{\Lambda}^{tH} = \frac{\Pi^{tH}}{\dfrac{\partial \Pi^{tH}}{\partial \dot{h}}\, \dot{h}} \tag{6.103}$$

$$\widehat{\Lambda}^{th} = \frac{\Pi^{th}}{\dfrac{\partial \Pi^{th}}{\partial (q_i / T)} \dfrac{q_i}{T}} \tag{6.104}$$

It is noteworthy that other constraints such as the viscoplastic microforce balance [Eq.(6.24)], the viscodamage microforce balance [Eq. (6.17)], the healing microforce balance [Eq. (6.18)], and the viscoelastic microforce balance [Eq. (6.25)] can also be applied to the objective functions which requires determination of several Lagrange multipliers. Although applying more constraints to the objective function results in a more comprehensive solution for dissipative components of the thermodynamic conjugate forces, it makes the problem more complex. This section concludes the general thermodynamic framework for determining the energetic and dissipative components of thermodynamic conjugate forces. The next following sections present the capabilities of the presented thermodynamic framework through an example that derives a temperature-dependent viscoelastic, viscoplastic, viscodamage, and healing constitutive model for time- and rate-dependent materials.

6.4. Application to Bituminus Materials

In this section, the thermodynamic framework explained in the previous sections will be used to derive a thermo-viscoelastic, thermo-viscoplastic, thermo-viscodamage, and thermo-healing constitutive equations for time- and rate-dependent materials. The objective is to derive thermodynamic consistent Schapery-type viscoelastic law, Perzyna-type viscoplastic law, damage law proposed by Darabi et al. (2011c), and a healing law suitable for time- and rate-dependent materials.

The Helmholtz free energy is decomposed into thermo-viscoelastic, thermo-viscoplastic, thermo-viscodamage, and healing components, such that:

$$\Psi(\tilde{\varepsilon}_{ij}^{ve}, \tilde{\zeta}_m, \tilde{\varepsilon}_{ij}^{vp}, \tilde{p}, \phi, h, T) = \Psi^{tve}(\tilde{\varepsilon}_{ij}^{ve}, \tilde{\zeta}_m, T) + \Psi^{tvp}(\tilde{\varepsilon}_{ij}^{vp}, \tilde{p}, T) + \\ \Psi^{tvd}(\phi, T) + \Psi^{tH}(h, T) \tag{6.105}$$

6.4.1. Thermo-Viscoelastic Constitutive Equation

Schapery (1969b) used the thermodynamics of irreversible processes and developed a single integral constitutive model for non-linear viscoelastic materials. Schapery made his viscoelastic model nonlinear by introducing the stress and/or strain-dependent scalars at various steps during the development of the constitutive theory. Recently, Levesque et al. (2008) extended the Schapery's nonlinear viscoelastic model for 3D applications based on laws of thermodynamics. Here, the procedure of Levesque et al. (2008) will be followed to derive the viscoelasticity model and couple it to viscoplasticity, viscodamage, and healing models. However, the formulation is expressed in the healing configuration and the thermodynamic conjugate forces are decomposed into energetic and dissipative components which result in a more general relationship between the stress and the viscoelastic strain, as argued in previous sections. Moreover, the viscoelastic microforce balance is used to derive viscoelastic equations.

Both the viscoelastic strain tensor and the viscoelastic internal state variables are assumed to contribute to the viscoelastic component of the Helmholtz free energy, such that the thermo-viscoelastic component of the Helmholtz free energy can be written as follows:

$$\rho \Psi^{tve} = \left[\frac{1}{2} a_0 \left(\tilde{\boldsymbol{\varepsilon}}^{ve} \right) L_{ijkl}^{(1)} \tilde{\varepsilon}_{ij}^{ve} \tilde{\varepsilon}_{kl}^{ve} + \frac{1}{2} L_{mn}^{(2)} \tilde{\zeta}_m \tilde{\zeta}_n + a_1 \left(\tilde{\boldsymbol{\varepsilon}}^{ve} \right) L_{ijm}^{(3)} \tilde{\varepsilon}_{ij}^{ve} \tilde{\zeta}_m \right] \vartheta^{ve} \qquad (6.106)$$

where $a_0 \left(\tilde{\boldsymbol{\varepsilon}}^{ve} \right)$ and $a_1 \left(\tilde{\boldsymbol{\varepsilon}}^{ve} \right)$ are nonlinear dependency scalars to make the viscoelastic model nonlinear (Schapery, 1969b); $\boldsymbol{L}^{(1)}$, $\boldsymbol{L}^{(2)}$, and $\boldsymbol{L}^{(3)}$ are positive definite coefficient matrices; and ϑ^{ve} is an Arrhenius-type temperature term for coupling temperature to the viscoelastic model.

The energetic component of the stress can be easily derived using Eqs. (6.59) and (6.106), such that:

$$\tilde{\sigma}_{ij}^{\text{ene}} = \left(A_{ijtu}^{(0)} L_{tukl}^{(1)} \tilde{\varepsilon}_{kl}^{ve} + A_{ijtu}^{(1)} L_{tum}^{(3)} \tilde{\zeta}_m \right) \vartheta^{ve} \qquad (6.107)$$

where $A_{ijtu}^{(0)}$ and $A_{ijtu}^{(1)}$ are nonlinear parameters related to the instantaneous and transient viscoelastic responses, respectively which are no longer an scalar for 3D models, such that:

$$A_{ijtu}^{(0)} = a_0 \delta_{it} \delta_{ju} + \frac{1}{2} \frac{\partial a_0}{\partial \tilde{\varepsilon}_{ij}^{ve}} \tilde{\varepsilon}_{tu}^{ve}; \quad A_{ijtu}^{(1)} = a_1 \delta_{it} \delta_{ju} + \frac{\partial a_1}{\partial \tilde{\varepsilon}_{ij}^{ve}} \tilde{\varepsilon}_{tu}^{ve} \tag{6.108}$$

Eq. (6.108) shows that the energetic component of the stress has two terms, one of which is related to instantaneous response and the other one is related to the recoverable processes associated with the viscoelastic internal state variables. These two terms are recovered upon the unloading and no energy dissipates due to these terms. However, the dissipation mechanism results from the viscoelastic strain rate and the rate of the viscoelastic internal state variables which are related to the chain mobility and friction between the polymer chains. In this work, a simple quadratic form is postulated for the viscoelastic component of the rate of energy dissipation, such that:

$$\Pi^{tve} = \left[\mu_{ijkl} \dot{\tilde{\varepsilon}}_{ij}^{ve} \dot{\tilde{\varepsilon}}_{kl}^{ve} + P_{mn} \dot{\tilde{\zeta}}_m \dot{\tilde{\zeta}}_n \right] \vartheta^{ve} \tag{6.109}$$

Parameters in Eq. (6.109) are defined as follows:

$$\mu_{ijkl} = \frac{\partial^2 \Pi^{tve}}{\vartheta^{ve} \partial \dot{\tilde{\varepsilon}}_{ij}^{ve} \partial \dot{\tilde{\varepsilon}}_{kl}^{ve}}; \quad P_{mn} = \frac{\partial^2 \Pi^{tve}}{\vartheta^{ve} \partial \dot{\tilde{\zeta}}_m \partial \dot{\tilde{\zeta}}_n} \tag{6.110}$$

The same Arrhenius-type temperature coupling terms are assumed for both temperature-dependent Helmholtz free energy and rate of energy dissipation. However, different temperature coupling terms can be assumed for the Helmholtz free energy and the rate of energy dissipation. The assumed form for the thermo-viscoelastic component of rate of energy dissipation guarantees the rate of the energy dissipation to be always positive. Another common assumption in the theory of nonlinear viscoelasticity is that the thermodynamic conjugate forces can be expressed as a nonlinear function of the evolution of the state variables (see e.g. Schapery, 1969a; Levesque et al., 2008). However, as it will be shown here, there is no need to make these assumptions and the viscoelastic laws can be derived directly using the viscoelastic microforce balance [Eq. (6.25)]. The viscoelastic microforce balance indicates that the summation of the

energetic and dissipative components of the thermodynamic forces conjugate to the viscoelastic internal state variables is zero, such that:

$$\tilde{\chi}_m = 0 \Rightarrow \tilde{\chi}_m^{\text{ene}} + \tilde{\chi}_m^{\text{dis}} = 0 \tag{6.111}$$

The energetic and dissipative components of the viscoelastic conjugate forces can be determined using Eqs., (6.60), (6.93), (6.100), (6.106), and (6.109), such that:

$$\tilde{\chi}_m^{\text{ene}} = \left[L_{mn}^{(2)} \tilde{\zeta}_n + a_1 \left(\tilde{\boldsymbol{\varepsilon}}^{ve} \right) L_{ijm}^{(3)} \tilde{\varepsilon}_{ij}^{ve} \right] \vartheta^{ve} \; ; \quad \tilde{\chi}_m^{\text{dis}} = \left[P_{mn} \dot{\tilde{\zeta}}_n \right] \vartheta^{ve} \tag{6.112}$$

Substituting Eq. (6.112) into Eq. (6.111) implies:

$$P_{mn} \dot{\tilde{\zeta}}_n + L_{mn}^{(2)} \tilde{\zeta}_n + a_1 \left(\tilde{\boldsymbol{\varepsilon}}^{ve} \right) L_{ijm}^{(3)} \tilde{\varepsilon}_{ij}^{ve} = 0 \tag{6.113}$$

Eq. (6.113) is the partial differential equation governing the viscoelastic processes. This equation relates the viscoelastic internal state variables to the viscoelastic strain tensor. Eq. (6.113) represents a coupled system of differential equations which expresses the evolution of internal variables $\tilde{\zeta}_n$ as a function of $\tilde{\varepsilon}_{ij}^{ve}$. Expressing Eq. (6.113) in a basis where the coefficient matrices are diagonal and using the Laplace transform implies:

$$\tilde{\zeta}_m(t) = -\frac{L_{ijm}^{(3)}}{L_{mm}^{(2)}} \int_0^t \left(1 - \exp[-\omega_m(t - \tau)] \right) \frac{d}{d\tau} \left(a_1 \tilde{\varepsilon}_{ij}^{ve} \right) d\tau \; ; \text{No sum on } m \tag{6.114}$$

where $\omega_m = \dfrac{L_{mm}^{(2)}}{P_{mm}}$. Eq. (6.114) shows the relation between the viscoelastic state variables and the viscoelastic strain. It is clear from Eq. (6.114) that the viscoelastic state variables $\tilde{\zeta}_m$ depend on the viscoelastic deformation history $\tilde{\varepsilon}_{ij}^{ve}$. Hence, the viscoelastic internal state variables evolve with the evolution of the viscoelastic strain. This supports the previously made argument for decomposing the total stress into its energetic and dissipative components. Also, Eq. (6.114) shows that the assumptions of assuming state variables $\tilde{\zeta}_m$ to be constant (i.e. $\dot{\tilde{\zeta}}_m = 0$) is valid only when the viscoelastic strain is constant (i.e. $\dot{\tilde{\varepsilon}}_{ij}^{ve} = 0$) which happens only in the absence of the viscoelastic processes. Hence, it is not consistent to make this argument to derive a viscoelasticity law as presented by several researchers (Levesque et al., 2008).

The dissipative component of the stress can now be obtained using Eqs. (6.92) and (6.109), such that:

$$\tilde{\sigma}_{ij}^{\text{dis}} = \widehat{\Lambda}^{tve} \frac{\partial \Pi^{tve}}{\partial \dot{\tilde{\varepsilon}}_{ij}^{ve}} = \mu_{ijkl} \dot{\tilde{\varepsilon}}_{kl}^{ve} \tag{6.115}$$

The stress as a function of the viscoelastic strain can now be obtained by substituting Eqs. (6.107), (6.114), and (6.115) into Eq. (6.67), such that:

$$\tilde{\sigma}_{ij} = \mu_{ijkl} \dot{\tilde{\varepsilon}}_{kl}^{ve} + \mathcal{G}^{ve} G_{ijtu}^{(0)} E_{tukl}^{(0)} \tilde{\varepsilon}_{kl}^{ve} +$$

$$\mathcal{G}^{ve} G_{ijtu}^{(1)} \int_0^t \left[\sum_{m=1}^M E_{tukl}^{(m)} \left(1 - \exp[-\omega_m(t-\tau)] \right) \right] \frac{d\left(g^{(2)} \tilde{\varepsilon}_{kl}^{ve} \right)}{d\tau} d\tau \tag{6.116}$$

where

$$G_{ijtu}^{(0)} E_{tukl}^{(0)} = A_{ijtu}^{(0)} L_{tukl}^{(1)} - a_1 A_{ijtu}^{(1)} L_{tum}^{(3)} \frac{L_{klm}^{(3)}}{L_{mm}^{(2)}};$$

$$G_{ijtu}^{(1)} = A_{ijtu}^{(1)}; \quad E_{tukl}^{(m)} = \frac{L_{tum}^{(3)} L_{klm}^{(3)}}{L_{mm}^{(2)}}; \quad g^{(2)} = a_1 \tag{6.117}$$

Eq. (6.116) represents a more comprehensive formulation that relates the total stress to the viscoelastic strain comparing to Levesque et al. (2008). According to notations of Duvaut and Lions (1976), the first two terms in the right hand side of Eq. (6.116) refer to the viscoelastic materials with the short memories since these two terms relate the state of stress at time t only to the strains at current time t and the immediately preceding time. However, the third term in the right hand side of Eq. (6.116) corresponds to the viscoelastic materials with long term memory since it relates the state of stresses at time t to strains at the times preceding t. For the case of linear viscoelasticity the nonlinear parameters should be always unity (i.e. $\boldsymbol{G}^{(0)} = \boldsymbol{G}^{(1)} = \boldsymbol{I}$ and $g^{(2)} = 1$).

Eq. (6.116) clearly shows that the temperature-dependency can easily be incorporated into the viscoelastic models using a temperature coupling term for all terms in the right hand side of Eq. (6.116). This approach is more general comparing to the classical Schapery-type viscoelasticity where the temperature shift factor is introduced in the definition of reduced time. The reason is that incorporation of the temperature shift factor as part of the reduced time variable only makes the third term in the RHS of Eq.

(6.116) temperature-dependent. However, using the Arrhenius-type temperature coupling term makes all terms of Eq. (6.116) to depend on temperature. Moreover, as it was mentioned earlier, two temperature coupling terms can be introduced in Eq. (6.116), one is related to Helmholtz free energy affecting the instantaneous response and the other is related to the rate of energy dissipation affecting the rate-type and the transient responses. Furthermore, using ϑ^{ve} implies that the nonlinear parameters $\boldsymbol{G}^{(0)}$, $\boldsymbol{G}^{(1)}$, and $g^{(2)}$ are not temperature-dependent which makes their calibration easier. It is noteworthy that a proper viscoelastic model can be derived for a specific material by postulating different mathematical forms for viscoelastic components of Helmholtz free energy and rate of energy dissipation.

6.4.2. Thermo-Viscoplastic Constitutive Equation

In the classical theory of continuum plasticity/viscoplasticity several experimentally motivated assumptions should be made to formulate a plasticity/viscoplasticity theory. These assumptions are the mathematical forms for yield surface and plastic potential function from which the plastic strain is determined. Most of the times these assumptions are made based on experimental observations. Hence, there is no guarantee for these experimental assumptions to satisfy fundamental laws of thermodynamic. As it was mentioned in the introduction, several researchers have tried to derive the plasticity yield surface based on the fundamental laws of thermodynamics (Gurtin, 2003; Anand et al., 2005; Gurtin and Anand, 2005; Abu Al-Rub et al., 2007; Gurtin et al., 2007; Voyiadjis and Abu Al-Rub, 2007; Abu Al-Rub, 2008a, b; Gurtin, 2008; Gurtin and Anand, 2009). However, to the authors' best knowledge they could only derive the von-Misses-type associative plasticity/viscoplasticity theory (i.e. the J_2-flow theory). In this section, the generalized non-associative viscoplasticity yield conditions and potential functions will be derived based on the viscoplastic microforce balance. Both isotropic and kinematic hardening terms are considered. Also, an evolution equation similar to Armstrong and Frederick model (1966) is derived using the presented thermodynamic framework.

T non-associative viscoplasticity can be derived based on principle of virtual power. Eq. (6.45) represents the relationship between the yield surface and the plastic potential function. In this section, the thermodynamically consistent dynamic yield surface associated with a given viscoplastic potential function will be derived. As it is shown in this section, Eq. (6.45) naturally yields to non-associative viscoplasticity for the given viscoplastic potential. The normality rule for non-associative plasticity in the healing configuration which states that the direction of the viscoplastic strains in the effective configuration is normal to the viscoplastic potential function is used. Hence, there exists a viscoplastic potential function $\tilde{F}$ for which the direction of the viscoplastic flow in the healing configuration, $\tilde{N}$, in Eq. (6.43) can be defined as:

$$\tilde{N}_{ij} = M^{-1} \frac{\partial \tilde{F}}{\partial \left(\tilde{\sigma}_{ij} - \tilde{\mathrm{X}}_{ij} \right)}; \quad M = \left\| \frac{\partial \tilde{F}}{\partial \left(\tilde{\sigma}_{ij} - \tilde{\mathrm{X}}_{ij} \right)} \right\| \tag{6.118}$$

Comparing Eqs. (6.26)and (6.118) implies:

$$\dot{\tilde{\varepsilon}}_{ij}^{vp} = \sqrt{\frac{3}{2}} \dot{p} \tilde{N}_{ij} = \sqrt{\frac{3}{2}} \left(\dot{p} M^{-1} \right) \frac{\partial \tilde{F}}{\partial \left(\tilde{\sigma}_{ij} - \tilde{\mathrm{X}}_{ij} \right)} \tag{6.119}$$

Eq. (6.119) properly relates $\tilde{N}$ and $\dfrac{\partial \tilde{F}}{\partial \left(\tilde{\sigma}_{ij} - \tilde{\mathrm{X}}_{ij} \right)}$. The modified Drucker-Prager-type

[see Eqs. (2.23) and (2.25)] is expressed in the healing configuration and assumed as the viscoplastic function, such that:

$$\tilde{F} = \tilde{\tau}^{vp} - \beta \tilde{I}_1 \tag{6.120}$$

Substituting Eq. (6.120) into Eq. (6.118) implies:

$$
\begin{aligned}
\tilde{N}_{ij} = {} & A^{-1} \frac{\sqrt{3}}{4} \left(1 + \frac{1}{d^{vp}} \right) \frac{\tilde{S}_{ij} - \tilde{\mathrm{X}}_{ij}}{\sqrt{\tilde{J}_2}} - A^{-1} \left[\frac{3}{2} \left(1 - \frac{1}{d^{vp}} \right) + \frac{\alpha}{3} \right] \delta_{ij} - \\
& A^{-1} \frac{1 - d^{vp}}{d^{vp} \tilde{J}_2^2} \left[\frac{9}{4} \tilde{J}_2 \left(\tilde{S}_{ik} - \tilde{\mathrm{X}}_{ik} \right) \left(\tilde{S}_{kj} - \tilde{\mathrm{X}}_{kj} \right) - \frac{3}{2} \tilde{J}_3 \left(\tilde{S}_{ij} - \tilde{\mathrm{X}}_{ij} \right) \right]
\end{aligned}
\tag{6.121}
$$

where

$$A^2 = \frac{3}{8}\left(1 + \frac{1}{d^{vp}}\right)^2 + \frac{\alpha^2}{3} - \frac{27}{4}\left(1 - \frac{1}{d^{vp}}\right)\left(1 + \frac{3}{d^{vp}}\right) +$$

$$\frac{3\sqrt{3}}{4}\left(1 - \frac{1}{d^{vp}}\right)\left(1 + \frac{3}{d^{vp}}\right)\frac{\tilde{J}_3}{\tilde{J}_2^{3/2}} + \qquad (6.122)$$

$$\left(1 - \frac{1}{d^{vp}}\right)^2\left[\frac{81}{16}\frac{\left(\tilde{S}_{ik} - \tilde{X}_{ik}\right)\left(\tilde{S}_{kj} - \tilde{X}_{kj}\right)\left(\tilde{S}_{im} - \tilde{X}_{im}\right)\left(\tilde{S}_{mj} - \tilde{X}_{mj}\right)}{\tilde{J}_2^2} - 9\frac{\tilde{J}_3^2}{\tilde{J}_2^3}\right]$$

Substituting Eq. (6.122) into the equation of microforce balance yields:

$$\tilde{\tau}^{vp} - \beta\tilde{I}_1 - \tilde{\kappa}A = 0 \qquad (6.123)$$

Eq. (6.123) shows the expression of the yield surface associated with the assumed viscoplastic potential function in Eq. (6.120). It is noteworthy that the term $\tilde{\kappa}A$ can be considered as the hardening function. Interestingly, Eq. (6.122) shows that the hardening function associated with this plastic potential function is stress dependent.

It should be mentioned that one of the common ways to obtain viscoplasticity theories is to treat Eq. (6.123) as the rate-independent plasticity yield surface and extend it to rate-dependent plasticity (viscoplasticity) using the overstress concept (Zener and Hollomon, 1944; Malvern, 1951; Perzyna, 1986; Perzyna and Korbel, 1998). According to this approach, the extension of the plasticity yield surface to the rate-dependent plasticity (viscoplasticity) theory is usually accompanied by the assumption that the stress state is no longer on the yield surface. Hence, an overstress function is defined in a dynamic yield surface to constrain the stress state to remain on the dynamic yield surface. Then by defining an admissible form of the plasticity Lagrange multiplier as a function of the overstress, the dynamic yield surface can be obtained (see Voyiadjis et al., 2004 for more details). However, it will be shown here that there is no need for extending Eq. (6.123) to viscoplasticity. In other words, the viscoplasticity dynamic yield surface obtains directly from Eq. (6.123) if the hardening parameter $\tilde{\kappa}$ is properly decoupled into its energetic and dissipative components (i.e. $\tilde{\kappa} = \tilde{\kappa}^{ene} + \tilde{\kappa}^{dis}$). The next step is to postulate mathematical forms for the thermo-viscoplastic component of the Helmholtz free energy Ψ^{tvp} and the rate of thermo-viscoplastic energy dissipation Π^{tvp}

in order to define the dynamic yield surface for the assumed viscoplastic potential. The following forms are postulated for these two functions:

$$\rho \Psi^{tvp} = \left[\frac{1}{2} C_1 \tilde{\varepsilon}_{ij}^{vp} \tilde{\varepsilon}_{ij}^{vp} + \kappa_0 \tilde{p} + \kappa_1 \left(\tilde{p} + \frac{1}{\kappa_2} \exp(-\kappa_2 \tilde{p}) \right) \right] \vartheta^{vp}(T) \qquad (6.124)$$

$$\Pi^{tvp} = \frac{1}{2} \left[C_2 \exp(-\gamma \tilde{p}) \dot{\tilde{\varepsilon}}_{ij}^{vp} \dot{\tilde{\varepsilon}}_{ij}^{vp} + C_3 \Gamma^{vp} \left(\frac{\dot{\tilde{p}}}{\Gamma^{vp} \vartheta^{vp}} \right)^{1+\frac{1}{N}} \right] \vartheta^{vp}(T) \qquad (6.125)$$

The energetic and dissipative components of the isotropic and kinematic hardening can be obtained using Eqs. (6.61), (6.62), (6.94), (6.95), (6.124), and (6.125), such that:

$$\tilde{\kappa}^{ene} = \left[\kappa_0 + \kappa_1 \left(1 - \exp(-\kappa_2 \tilde{p}) \right) \right] \vartheta^{vp}; \quad \tilde{\kappa}^{dis} = C_3 \left(\frac{\dot{\tilde{p}}}{\Gamma^{vp} \vartheta^{vp}} \right)^{\frac{1}{N}} \qquad (6.126)$$

$$\tilde{X}_{ij}^{ene} = C_1 \tilde{\varepsilon}_{ij}^{vp} \vartheta^{vp}; \quad \tilde{X}_{ij}^{dis} = C_2 \exp(-\gamma \tilde{p}) \dot{\tilde{\varepsilon}}_{ij}^{vp} \vartheta^{vp} \qquad (6.127)$$

Therefore, the total isotropic and kinematic hardening functions will be expressed as:

$$\tilde{\kappa} = \left[\kappa_0 + \kappa_1 \left(1 - \exp(-\kappa_2 \tilde{p}) \right) \right] \vartheta^{vp} + C_3 \left(\frac{\dot{\tilde{p}}}{\Gamma^{vp} \vartheta^{vp}} \right)^{\frac{1}{N}} \qquad (6.128)$$

$$\tilde{X}_{ij} = \left[C_1 \tilde{\varepsilon}_{ij}^{vp} + C_2 \exp(-\gamma \tilde{p}) \dot{\tilde{\varepsilon}}_{ij}^{vp} \right] \vartheta^{vp} \qquad (6.129)$$

The dynamic viscoplastic yield function associated with the assumed viscoplastic potential can now be obtained using Eqs. (6.123), (6.128), and (6.129), such that:

$$\tilde{\tau}^{vp} - \beta \tilde{I}_1 - \left[\kappa_0 + \kappa_1 \left(1 - \exp(-\kappa_2 \tilde{p}) \right) \right] A \vartheta^{vp} - C_3 A \left(\frac{\dot{\tilde{p}}}{\Gamma^{vp} \vartheta^{vp}} \right)^{\frac{1}{N}} = 0 \qquad (6.130)$$

Eq. (6.130) represents the temperature-dependent dynamic yield surface associated with the assumed viscoplastic potential [Eq. (6.120)].

Taking the time derivative of Eq. (6.127) at the reference temperature and neglecting the temperature evolution yield:

$$\dot{\tilde{X}}_{ij}^{ene} = C_1 \dot{\tilde{\varepsilon}}_{ij}^{vp}; \quad \dot{\tilde{X}}_{ij}^{dis} = -\gamma C_2 \dot{\tilde{p}} \exp(-\gamma \tilde{p}) \dot{\tilde{\varepsilon}}_{ij}^{vp} + C_2 \exp(-\gamma \tilde{p}) \ddot{\tilde{\varepsilon}}_{ij}^{vp} \qquad (6.131)$$

Adding both sides of Eqs. (6.131)$_1$ and (6.131)$_2$ implies:

$$\dot{\tilde{X}}_{ij} = C_1 \dot{\tilde{\varepsilon}}_{ij}^{vp} - \gamma \dot{\tilde{p}} \dot{\tilde{X}}_{ij}^{dis} + C_2 \exp(-\gamma \tilde{p}) \ddot{\tilde{\varepsilon}}_{ij}^{vp} \qquad (6.132)$$

Eq. (6.132) shows the equation for the evolution of the backstress. This equation can be considered as the modified Armstrong and Frederick model (Armstrong and Frederick, 1966). When the loading rate is not too high, the effect of $\ddot{\tilde{\varepsilon}}_{ij}^{vp}$ can be neglected. In this case. Eq. (6.132) reduces to:

$$\dot{\tilde{X}}_{ij} = C_1 \dot{\tilde{\varepsilon}}_{ij}^{vp} - \gamma \dot{\tilde{p}} \dot{\tilde{X}}_{ij}^{dis} \qquad (6.133)$$

The Armstrong and Frederick model for evolution of backstress can be written as:

$$\dot{\tilde{X}}_{ij} = C_1 \dot{\tilde{\varepsilon}}_{ij}^{vp} - \gamma \dot{\tilde{p}} \dot{\tilde{X}}_{ij} \qquad (6.134)$$

Eqs. (6.133) and (6.134) are similar except that the total backstress tensor in the right side of Eq. (6.134) is replaced by its dissipative component in Eq. (6.133). Also, Eq. (6.133) yields the linear kinematic hardening rule when $\gamma = 0$ (Prager, 1956). Eq. (6.133) can also be rewritten as the following form:

$$\dot{\tilde{X}}_{ij} = C_1 \dot{\tilde{\varepsilon}}_{ij}^{vp} - \gamma \dot{\tilde{p}} \dot{\tilde{X}}_{ij} + \gamma \dot{\tilde{p}} \dot{\tilde{X}}_{ij}^{ene} \qquad (6.135)$$

The first two terms represent the Armstrong and Frederick model. However, Eq. (6.135) shows that the energetic component of the kinematic hardening function should also be added to Armstrong and Frederick model.

These examples show the capabilities of the proposed framework in deriving different constitutive models for time- and rate-dependent materials. In the next sections, the presented framework will be applied in deriving viscodamage and healing loading conditions and evolution functions.

6.4.3. Thermo-Viscodamage Constitutive Equation

In classical continuum damage mechanics a damage condition is usually postulated to determine the onset of damage growth and evolution (Hayakawa and Murakami, 1997; Murakami et al., 1998). This damage function is treated very similar to plasticity theory. As a result, the extension of the damage condition to the rate-dependent one is also carried out similarly to the extension of rate-independent plasticity yield surface to the

dynamic viscoplasticity yield surface (Voyiadjis et al., 2004). However, here it will be shown that the rate-dependent damage (viscodamage) condition can be derived directly from the principle of virtual power and laws of thermodynamics. Eq. (6.17) defines the damage microforce balance. It will be shown here that the damage microforce balance is in fact the damage condition. Combining the damage microforce balance with Eq. (6.71) yields:

$$Y = 0 \;\Rightarrow\; Y^{\text{ene}} + Y^{\text{dis}} = 0 \;\Rightarrow\; Y^{\text{ene}} = -Y^{\text{dis}} \tag{6.136}$$

where Y^{ene} and Y^{dis} are given in Eqs. (6.63) and (6.96), respectively. To the best of the authors knowledge, this interesting result has been reported here for the first time. In fact, Eq. (6.136) is the damage condition criterion. Based on the mathematical form of thermo-viscodamage Helmholtz free energy Ψ^{tvd} and rate of thermo-viscodamage energy dissipation Π^{tvd} the damage condition can be rate-independent or rate-dependent. Wu et al. (2006) proposed an energy-based plastic-damage model for concrete in which the Helmholtz free energy in the presence of damage is expressed as a function of stress invariants and damage variable. Similar assumptions have been made by Voyiadjis et al. (2004), Voyiadjis and Abu Al-Rub (2006), and Abu Al-Rub and Kim (2009). Therefore, the following form is postulated for the thermo-viscodamage component of the Helmholtz free energy to consider the confinement effects, the different effects of damage in tensile and compressive loading conditions, and the effect of temperature on damage evolution and growth, such that:

$$\rho\Psi^{tvd} = \frac{1}{b_1}\left[(1-\phi)^{b_1}\left\langle \frac{\overline{\tau}^{vd} - \alpha\overline{I}_1}{b_2} \right\rangle \exp\left(b_3\overline{\varepsilon}_{eff}\right)\right]\vartheta^{vd} \tag{6.137}$$

This form is postulated in order to derive the viscodamage model proposed by Darabi et al. (2011c) [see Chapters II and III for more information]. The energetic component of the viscodamage force can now be determined using Eqs. (6.63) and (6.137), such that:

$$Y^{\text{ene}} = -(1-\phi)^{b_1-1}\left\langle \frac{\overline{\tau}^{vd} - \alpha\overline{I}_1}{b_2} \right\rangle \exp\left(b_3\overline{\varepsilon}_{eff}\right)\vartheta^{vd} \tag{6.138}$$

An expression similar to that assumed for the thermo-viscoplastic rate of energy dissipation is postulated for the rate of the thermo-viscodamage energy dissipation Π^{tvd}, such that:

$$\Pi^{tvd} = b_0 \Gamma^{vd} \left(\frac{\dot{\phi}}{\Gamma^{vd} \vartheta^{vd}} \right)^{1+\frac{1}{q}} \tag{6.139}$$

Then, the dissipative component of the damage thermodynamic force Y^{dis} can be obtained using Eqs. (6.96) and (6.139) as follows:

$$Y^{dis} = \frac{b_0}{\vartheta^{vd}} \left(\frac{\dot{\phi}}{\Gamma^{vd} \vartheta^{vd}} \right)^{\frac{1}{q}} \tag{6.140}$$

with $\hat{\Lambda}^{tvd} = (1 + 1/q)^{-1}$. The rate-dependent damage surface can be determined by substituting Eqs. (6.138) and (6.140) into Eq. (6.136), such that:

$$(1-\phi)^{b_1-1} \left\langle \frac{\overline{\tau}^{vd} - \alpha \overline{I}_1}{b_2} \right\rangle \exp\left(b_3 \overline{\varepsilon}_{eff} \right) \vartheta^{vd} - \frac{b_0}{\vartheta^{vd}} \left(\frac{\dot{\phi}}{\Gamma^{vd} \vartheta^{vd}} \right)^{\frac{1}{q}} = 0 \tag{6.141}$$

Eq. (6.141) represents the dynamic viscodamage loading condition for temperature- and rate-dependent damage (thermo-viscodamage). This equation can also be represented as a damage evolution law, such that:

$$\dot{\phi} = \Gamma^{vd} \left\langle \frac{(1-\phi)^{b_1-1} \left(\overline{\tau}^{vd} - \alpha \overline{I}_1 \right)}{b_2 b_0} \right\rangle^q \exp\left(b_3 q \overline{\varepsilon}_{eff} \right) \hat{\vartheta}^{vd} \tag{6.142}$$

where $\hat{\vartheta}^{vd} = \left(\vartheta^{vd} \right)^{2q+1}$. A simplified version of Eq. (6.142) has applied to predict the time- and rate-dependent damage response of asphalt mixes [Refer to Chapter II and Darabi et al. (2011c) for more details].

6.4.4. Thermo-Healing Constitutive Equation

As it was mentioned in the introduction part, some engineering materials have the potential to heal and retrieve part of their strength and stiffness with time. Hence, a robust continuum based model should be able to predict the healing process in addition

to the damage evolution and growth. Here, it is shown that the healing evolution law can easily be obtained from the principle of virtual power. In fact, the defined healing microforce balance [Eq. (6.18)] is the balance law governing the healing process in the materials. The healing microforce balance states that the summation of the energetic and dissipative components of the healing force should be zero, such that:

$$H = 0 \implies H^{\text{ene}} + H^{\text{dis}} = 0 \implies H^{\text{ene}} = -H^{\text{dis}} \tag{6.143}$$

where H^{ene} and H^{dis} are given in Eqs. (6.64) and (6.97), respectively. To the best of the authors knowledge, this interesting result has been reported here for the first time. In fact, the healing evolution can be easily obtained using Eq. (6.143). Different forms for the healing evolution law can be obtained based on the mathematical form of thermo-healing Helmholtz free energy Ψ^{tH} and the rate of thermo-healing energy dissipation Π^{tH}. In this work, mathematical forms are assumed for the healing components of the Helmholtz free energy and rate of energy dissipation in order to derive the healing model proposed by Abu Al-Rub et al. (2010a) to model fatigue damage in bituminous materials. To achieve this, the following forms are postulated for the healing components of the Helmholtz free energy and rate of energy dissipation, such that:

$$\rho \Psi^{tH} = \left[\frac{1}{k_1 + 1} \gamma_1 \left(1 - h \right)^{k_1 + 1} \right] \vartheta^{H,\text{ene}} \tag{6.144}$$

$$\Pi^{tH} = \left[\gamma_2 \left(1 - \phi \right)^{k_2} \dot{h}^2 \right] \vartheta^{H,\text{dis}} \tag{6.145}$$

where $\vartheta^{H,\text{ene}}$ and $\vartheta^{H,\text{dis}}$ are Arrhenius-type temperature coupling terms to couple temperature to the energetic and dissipative components of the healing model. Note that the material parameters γ_1 and γ_2 could depend on surface energy since they capture the changes in the total surface energy because of the healing of micro-cracks. Moreover, the healing component of the rate of energy dissipation is expressed as a function of healing rate and damage history. Although the healing component of the rate of energy dissipation depends on the damage density, it does not contribute to the dissipative component of the damage force. Energetic and dissipative components of the healing

force can be obtained by substituting Eqs. (6.64), (6.97), and (6.103) into Eqs. (6.144) and (6.145), such that:

$$H^{\text{ene}} = \left[-\gamma_1 \left(1 - h \right)^{k_1} \right] \vartheta^{H,\text{ene}} \tag{6.146}$$

$$H^{\text{dis}} = \left[\gamma_2 \left(1 - \phi \right)^{k_2} \dot{h} \right] \vartheta^{H,\text{dis}} \tag{6.147}$$

Substituting Eqs. (6.146) and (6.147) into the healing microforce balance [Eq. (6.143)] gives:

$$\left[\gamma_2 \left(1 - \phi \right)^{k_2} \vartheta^{H,\text{dis}} \right] \dot{h} - \left[\gamma_1 \vartheta^{H,\text{ene}} \right] \left(1 - h \right)^{k_1} = 0 \tag{6.148}$$

Eq. defines the first order differential equation governing the healing process. The healing evolution law can be obtained by rearranging Eq. such that:

$$\dot{h} = \Gamma^h \left(1 - \phi \right)^{-k_2} \left(1 - h \right)^{k_1} \vartheta^H \tag{6.149}$$

where $\Gamma^h = \gamma_1 / \gamma_2$ is the healing viscosity parameter and ϑ^H is the healing temperature coupling term. The healing viscosity parameter has the dimension $1/\sec$ and controls the rate of healing in materials.

This section concludes the derivation of the thermo-viscoelastic-viscoplastic-viscodamage-healing constitutive model. It should be noted that this constitutive model is derived only as an example. However, the presented thermodynamic framework is general and can be used to derive different constitutive models.

6.5. Heat Equation

As it was mentioned in previous sections, rate- and time-dependent materials show a wide range of mechanical responses depending on the temperature. Changes in temperature could be caused by the changes in the ambient temperature or as a result of different forms of energy dissipation accompanied by the deformation process. Moreover, a local increase in temperature influences the behavior of materials during deformation. Hence, including the temperature evolution in the constitutive models for time- and rate-dependent materials seems inevitable for accurate modeling of their

mechanical responses. In this section, the heat equation necessary for calculating the increase in temperature due to different deformation processes is derived.

The first law of thermodynamic for a sub-body Γ having the outward unit vector $\boldsymbol{n}$ normal to the boundary $\partial\Gamma$ can be written as:

$$\frac{d}{dt}\int_{\Gamma}\rho e\,dV = P_{\text{ext}} - \int_{\partial\Gamma}q_i n_i\,dA + \int_{\Gamma}\rho r_{\text{ext}}\,dV \tag{6.150}$$

where e and r_{ext} are internal energy density and the density of external heat gained by the body (e.g. through radiation), and P_{ext} is the external power which is equal to the internal power P_{int}. Meanwhile, the internal energy density e the specific entropy η and the Helmholtz free energy density Ψ are related through the following relationship:

$$\Psi = e - T\eta \tag{6.151}$$

By neglecting the changes in the mass density during the deformation, using the divergence theorem, noting that the sub-body Γ is arbitrary, using the equivalency of internal and external expenditures of power, and using the definition of internal expenditure of power [Eq. (6.7)], the first law of thermodynamic can be rewritten as follows:

$$\rho\left(\dot{\Psi} + \dot{\eta}T + \eta\dot{T}\right) - \tilde{\sigma}_{ij}\dot{\tilde{\varepsilon}}_{ij}^{ve} - \sum_{m=1}^{M_{\text{int}}^{ve}}\tilde{\chi}_m\dot{\tilde{\zeta}}_m - \tilde{X}_{ij}\dot{\tilde{\varepsilon}}_{ij}^{vp} - \tilde{\kappa}\dot{\tilde{p}} - Y\dot{\phi} - H\dot{h} + q_{i,i} - \rho r_{\text{ext}} = 0 \tag{6.152}$$

Substituting Eqs. (6.57) and (6.76)-(6.80) into Eq. (6.152) yields:

$$\rho T\dot{\eta} = \Pi^{tve} + \Pi^{tvp} + \Pi^{tvd} + \Pi^{tH} + \rho r_{\text{ext}} - q_{i,i} \tag{6.153}$$

On the other hand Eqs. (6.57) and (6.105) implies:

$$\eta = \eta^{tve} + \eta^{tvp} + \eta^{tvd} + \eta^{tH} \tag{6.154}$$

where η^{tve}, η^{tvp}, η^{tvd}, and η^{tH} are the specific entropies due to viscoelastic, viscoplastic, viscodamage, and healing processes, respectively.

$$\eta^{tve} = -\frac{\partial\Psi^{tve}}{\partial T}\;;\quad \eta^{tvp} = -\frac{\partial\Psi^{tvp}}{\partial T}\;;\; \eta^{tvd} = -\frac{\partial\Psi^{tvd}}{\partial T}\;;\; \eta^{tH} = -\frac{\partial\Psi^{tH}}{\partial T} \tag{6.155}$$

The following equations for the specific entropy can be obtained by substituting Eqs. (6.106), (6.124), (6.137), and (6.144) into Eq. (6.155), such that:

$$\eta^{tve} = \frac{1}{\rho}\left[\frac{1}{2}a_0\left(\tilde{\boldsymbol{\varepsilon}}^{ve}\right)L_{ijkl}^{(1)}\tilde{\varepsilon}_{ij}^{ve}\tilde{\varepsilon}_{kl}^{ve} + \frac{1}{2}L_{mn}^{(2)}\tilde{\zeta}_m\tilde{\zeta}_n + a_1\left(\tilde{\boldsymbol{\varepsilon}}^{ve}\right)L_{ijm}^{(3)}\tilde{\varepsilon}_{ij}^{ve}\tilde{\zeta}_m\right]Z^{ve} \qquad (6.156)$$

$$\eta^{tvp} = \frac{1}{\rho}\left[\frac{1}{2}C_1\tilde{\varepsilon}_{ij}^{vp}\tilde{\varepsilon}_{ij}^{vp} + \kappa_0\tilde{p} + \kappa_1\left(\tilde{p} + \frac{1}{\kappa_2}\exp(-\kappa_2\tilde{p})\right)\right]Z^{vp} \qquad (6.157)$$

$$\eta^{tvd} = \frac{1}{\rho b_1}\left[(1-\phi)^{b_1}\left\langle\frac{\bar{\tau}^{vd} - \alpha\bar{I}_1}{b_2}\right\rangle\exp\left(b_3\bar{\varepsilon}_{eff}\right)\right]Z^{vd} \qquad (6.158)$$

$$\eta^{tH} = \frac{1}{\rho}\left[\frac{1}{k_1+1}\gamma_1\left(1-h\right)^{k_1+1}\right]Z^{H,ene} \qquad (6.159)$$

where $Z = -\dfrac{\partial\vartheta}{\partial T}$. Taking the time derivative of Eq. (6.154) and substitute it in Eq. (6.153) and using Eqs. (6.59)-(6.64) yield:

$$\rho c_p\dot{T} = \Pi^{tve} + \Pi^{tvp} + \Pi^{tvd} + \Pi^{tH} + \rho r_{ext} - q_{i,i} -$$
$$\underbrace{\left[\frac{\partial\tilde{\sigma}_{ij}^{ene}}{\partial T}\dot{\tilde{\varepsilon}}_{ij}^{ve} + \frac{\partial\tilde{\chi}_m^{ene}}{\partial T}\dot{\tilde{\zeta}}_m + \frac{\partial\tilde{X}_{ij}^{ene}}{\partial T}\dot{\tilde{\varepsilon}}_{ij}^{vp} + \frac{\partial\tilde{\kappa}^{ene}}{\partial T}\dot{\tilde{p}} + \frac{\partial Y^{ene}}{\partial T}\dot{\phi} + \frac{\partial H^{ene}}{\partial T}\dot{h}\right]}_{\text{Thermo-mechanical coupling terms}}T \qquad (6.160)$$

where $c_p = T\dfrac{\partial\eta}{\partial T}$ is the specific heat at constant pressure. Eq. (6.160) yields a physically sound relationship for the heat equation. This equation reveals two mechanisms that contribute to the temperature evolution: (a) the thermo-mechanical coupling terms which are functions of energetic components of the thermodynamic conjugate forces; and (2) dissipation terms which are functions of the dissipative components of the thermodynamic conjugate forces appearing in different components of Π.

The relationship for the heat flux vector $\boldsymbol{q}$ can be easily determined using the principle of maximum dissipation. Therefore, an expression is needed for the thermal component of the rate of energy dissipation in Eq. (6.98). The following form is assumed for Π^{th}:

$$\Pi^{th} = \frac{1}{T}k_{ij}^{-1}q_iq_j \qquad (6.161)$$

Substituting Eq. (6.161) into Eq. (6.98) implies:

$$q_i = -k_{ij}T_{,j} \qquad (6.162)$$

with $\widehat{\Lambda}^{th} = 1/2$. Eq. (6.162) is the well-known Fourier heat conduction law. The negative sign indicates that the heat flow is opposite to the direction of temperature increase.

6.6. Conclusions

In this work, a general and comprehensive thermodynamic based framework with especial attention to the decomposition of the thermodynamic conjugate forces into energetic and dissipative components is presented to derive a temperature-dependent viscoelastic, viscoplastic, viscodamage, and healing constitutive model for time- and rate-dependent materials.

The healing natural configuration as the extension of the well-known Kachanov's effective (undamaged) configuration is used to enhance the continuum damage mechanics in modeling the healing phenomenon. Hence, the constitutive models are presented in the healing configuration which substantially simplifies the numerical implementation by avoiding the complexities associated with the direct couplings of viscoelastic and viscoplastic models to the viscodamage and healing models. The power-correlating hypothesis is used for relating stress and strain tensors in the healing and damaged configurations. This hypothesis allows one to present the constitutive model in the healing configuration (for simplicity) and yet to estimate the dissipated energy in the healed stress space (healed natural configuration) accurately.

Moreover, it is shown that the thermodynamic formulation naturally enforces the decomposition of the thermodynamic conjugate forces into energetic and dissipative components. Energetic components are derived using the Helmholtz free energy. A systematic procedure based on the principle of maximum dissipation (or maximum entropy production) is presented for deriving dissipative components directly from rate of energy dissipation. The thermodynamic framework is then used for deriving a more comprehensive version of Schapery-type viscoelastic model, Perzyna-type viscoplastic model, and a viscodamage model analogous to the Perzyna-type viscoplastic model, and

a healing model for bituminous materials. Moreover, all the derived constitutive models are coupled to temperature.

Furthermore, it is shown that the principle of virtual power can be used for deriving generalized non-associative viscoplasticity theories without further needs to assume a viscoplastic potential function independent from the yield loading condition. It is also shown that the rate-dependent terms in viscoplasticity dynamic yield surface are identical to the dissipative components of the hardening function and can be derived directly from the rate of energy dissipation. Moreover, an equation for the evolution of the backstress is proposed which can be considered as a modified version of Armstrong and Frederick model (1966) for the backstress evolution.

The viscoelastic model is derived using the viscoelastic microforce balance, obtained directly from the principle of virtual power. Similarly, the viscodamage and healing loading conditions and evolution laws are derived using the viscodamage microforce balance and healing microforce balance, respectively.

Moreover, the well-known Fourier heat conduction law is derived as a consequence of decomposing thermodynamic conjugate forces into energetic and dissipative components and using the principle of maximum dissipation. Finally, the heat equation for the presented constitutive model is derived.

CHAPTER VII

VALIDATION OF THE THERMO-VISCOELASTIC-VISCOPLASTIC-VISCODAMAGE-HEALING MODEL AGAINST THE ALF DATA

7.1. Introduction

In this chapter, the presented thermo-viscoelastic-viscoplastic-viscodamage-healing constitutive models (see Chapters II and V for detailed information on these constitutive models) is further validated against the FHWA Accelerated Load Facility (ALF) data. The experimental measurements on ALF materials are performed at North Carolina State University (NCSU) (see Kim et al., (2008) for a detailed explanation regarding the material and test procedure). Based on the available experimental data, the calibration procedure presented in Chapters II and V is modified and adopted for the available experimental data. The compressive data at high temperatures (i.e. 55°C) shows that the viscoplastic response of the asphalt mixes cannot be explained by classical hardening plasticity/viscoplasticity models. Therefore, a novel approach is introduced to capture the viscoplastic softening response (i.e. decreasing in hardening during cyclic loading) in asphalt mixtures. This approach is based on the viscoplastic memory surface in the viscoplastic strain space. Subsequently, the model is validated against the experimental data which has not been used in the calibration process. The model prediction and experimental data reveal that the thermo-viscoelastic-viscoplastic-viscodamage-healing model with the viscoplastic memory surface has the capability to predict the complex response of asphalt mixes over a wide range of temperatures, stress levels, strain rates, and loading conditions (Darabi et al., 2011a; Huang et al., 2011b).

7.2. Materials

The materials used in this study are compacted using the Superpave gyratory compactor to the dimension of 178 mm in height and 150 mm in diameter. To obtain the uniform air void distribution, the specimens are cored and cut to a height of 150 mm with a diameter 100 mm. The asphalt mixes have 5.3% binder content with approximately 4% air voids and the asphalt binder is specified as unmodified PG 70-22.

7.3. Model Calibration in Compression

The NCSU tests in compression include complex modulus test at different temperatures and repeated creep-recovery tests with different stress levels and loading/unloading times at 55°C. These tests are used to calibrate and validate the thermo-viscoelastic-viscoplastic model. Table 7.1 lists the tests which are used to calibrate the thermo-viscoelastic-viscoplastic model parameters.

Table 7.1. Summary of the test used for identification of the thermo-viscoelastic-viscoplastic model parameters.

Test	Temperature (^{o}C)	Stress level (kPa)	Confinement (kPa)	Loading time (Sec)	Rest period (Sec)
Complex Modulus test	-10, 10, 35, 55	-	140	-	-
Repeated creep-recovery test with variable loading (VL)	55	Varies	140	0.4	200

It should be noted that that most of the tests in compression are conducted at 55°C. At high temperatures, the failure mechanism of asphalt mixes is primarily related to the flow of the materials. Therefore, the damage model has not been used here to predict the degradations of the asphaltic mixes subjected to compressive loadings at high temperatures. Instead, a viscoplastic softening model is proposed to capture the flow-type response of asphalt mixes at high temperatures and in compression.

7.3.1. Identification of the Thermo-Viscoelastic Model Parameters

The dynamic modulus test is used to identify the linear viscoelastic model parameters along with the temperature coupling terms. This test is conducted at four temperatures (i.e. -10, 10, 35, and 55°C) and eight frequencies (i.e. 0.01, 0.05, 0.1, 0.5, 1, 5, 10, and 25 Hz). The strain amplitude is controlled to be low enough (i.e. 50-70 $\mu\varepsilon$) such that the material does not get damaged. The standard procedure is used to identify the viscoelastic model parameters and time-temperature shift factors using the complex compliance D^* and the phase angle θ. In other words, the master curve is first constructed for the complex compliance D^* from which the time-temperature shift factors are also identified. The next step is to calculate the storage compliance $D' = \|D^*\|\sin(\theta)$ and the loss compliance $D'' = \|D^*\|\cos(\theta)$ versus the reduced angular frequency ω_R. The Prony series coefficients and the loss and storage compliances are related through the following relationships:

$$D' = D_0 + \sum_{n=1}^{N} \frac{D_n}{1+(\omega/\lambda_n)^2} \; ; \quad D'' = \sum_{n=1}^{N}\left[\frac{1}{\lambda_n}\frac{D_n\omega}{1+(\omega/\lambda_n)^2}\right] \tag{7.1}$$

where D_n and λ_n are n^{th} Prony series coefficients and retardation times, respectively. The Prony series coefficients can then be identified by minimizing the error between the experimental and calculated loss and storage compliances, such that:

$$err = \left(\frac{D'}{D'_{Exp}}-1\right)^2 + \left(\frac{D''}{D''_{Exp}}-1\right)^2 \tag{7.2}$$

The identified model parameters at the reference temperature are listed in Table 7.2.

Figure 7.1 (a) and (b) show the complex compliance before and after the time-temperature shift.

Table 7.2. Identified viscoelastic model parameters at $T_0 = 10^o C$ and the time-temperature model parameters.

Viscoelastic Model Parameters							
n	1	2	3	4	5	6	7
λ_n (sec^{-1})	100	1	10^{-2}	10^{-3}	10^{-4}	10^{-5}	10^{-6}
D_n (kPa^{-1})	1.8×10^{-8}	5.6×10^{-8}	2.3×10^{-7}	4.4×10^{-7}	5.6×10^{-7}	3.3×10^{-7}	3.5×10^{-7}
D_0 (kPa^{-1})	3×10^{-8}						
Time-temperature shift factors ($T_0 = 10^o C$)							
$T(^o C)$		-10	10		35	55	
		1.26×10^3	1		6.3×10^{-4}	10^{-5}	

7.3.2. Identification of the Viscoplastic Model Parameters

The Variable Loading (VL) test at 55°C is used to identify the viscoplastic model parameters. This test is a repeated creep-recovery test where the loading time is 0.4 sec and the rest period is 200 sec. This test consists of several blocks where each block also consists of eight creep-recovery cycles. The deviatoric stress level starts from 137.9 kPa in the first block and increases with the factor of 1.2 for the next stress level until it reaches the last creep-recovery test within that block. For the next loading block, however, the first stress level equals to the third stress level in the previous block. Figure 7.2 shows the applied stress history for the VL test.
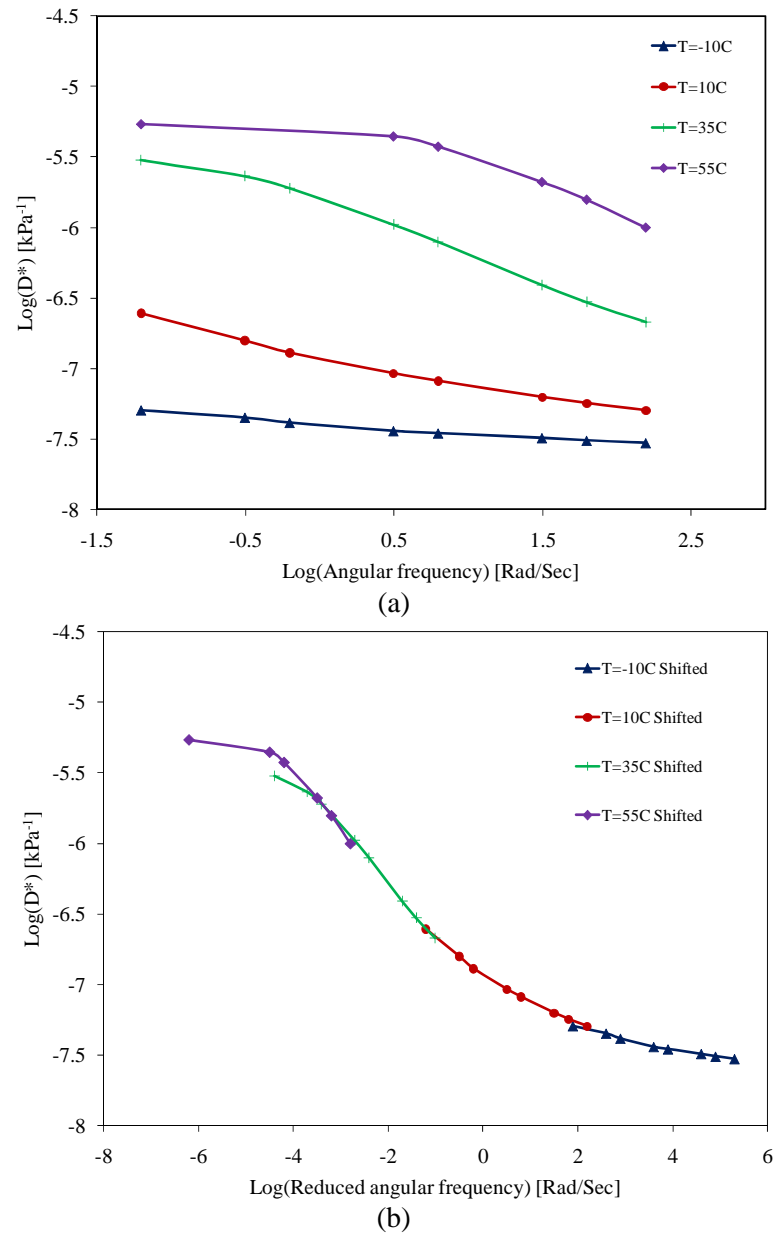
Figure 7.1. Complex modulus data in compression at different temperatures; (a) before time-temperature shift; (b) after time-temperature shift.
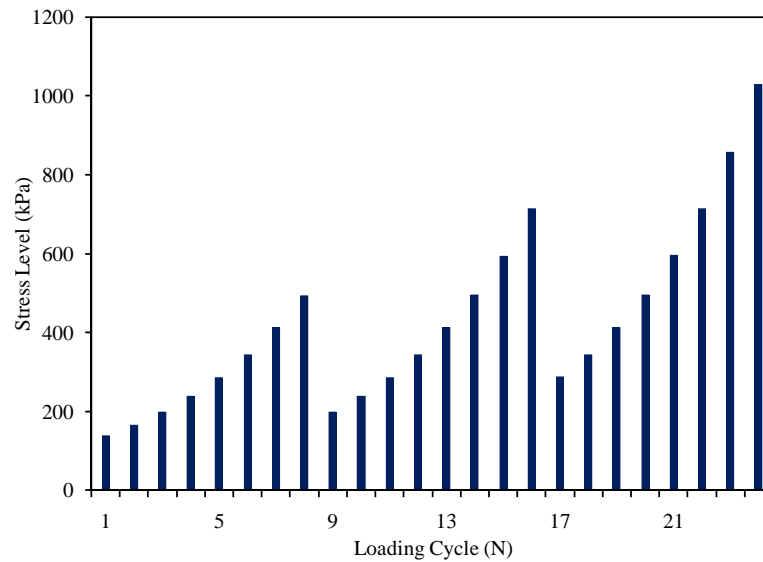
Figure 7.2. Stress history for the Variable Loading (VL) test.

Once the viscoelastic model parameters are identified, the viscoelastic and viscoplastic strain responses can be separated. The separated viscoplastic strain responses for the initial loading cycles are used to identify the viscoplastic model parameters (please refer to Chapter II and Huang et al. (2011) for more details on identification of the viscoplastic model parameters). It should be noted that the viscoplastic model parameters are identified at 55°C, whereas, the viscoelastic model parameters are identified at 10°C. Therefore, it is assumed primarily that the time-temperature shift factors are the same for the viscoelastic and viscoplastic responses. Having this assumption in hand, the identified viscoplastic model parameters are shifted to the reference temperature (i.e. $T = 10^{o}C$) using the same time-temperature shift factor identified from the dynamic modulus test. This can be achieved by simply scaling the viscoplasticity viscosity parameter Γ^{vp} [i.e. $\Gamma^{vp}\left(10^{o}C\right) = \Gamma^{vp}\left(55^{o}C\right) \times a_T\left(55, T_0 = 10^{o}C\right)$]. This simple analysis allows one to use the same time-temperature shift factor for viscoelasticity and viscoplasticity and avoids the confusion. The rest of the viscoplastic model parameters remain the same for both temperatures. Table 7.3 lists the viscoplastic model parameters at reference temperature (i.e. $T = 10^{o}C$).

Table 7.3. Viscoplastic model parameters at the reference temperature $T_0 = 10^o C$. (Note that these parameters are obtained using the viscoplastic parameters identified at 55°C and the time-temperature shift factor identified from dynamic modulus test).

α	β	σ_y^0 (kPa)	Γ^{vp} (sec^{-1})	N	κ_0 (kPa)	κ_1 (kPa)	κ_2
0.25	0.2	100	2.4×10^{-8}	1.0	50	1800	135

Figure 7.3 shows the comparison between the experimental data and model predictions for the VL test at 55°C. Figure 7.3 shows that model predictions agree well with the experimental data within the first block.
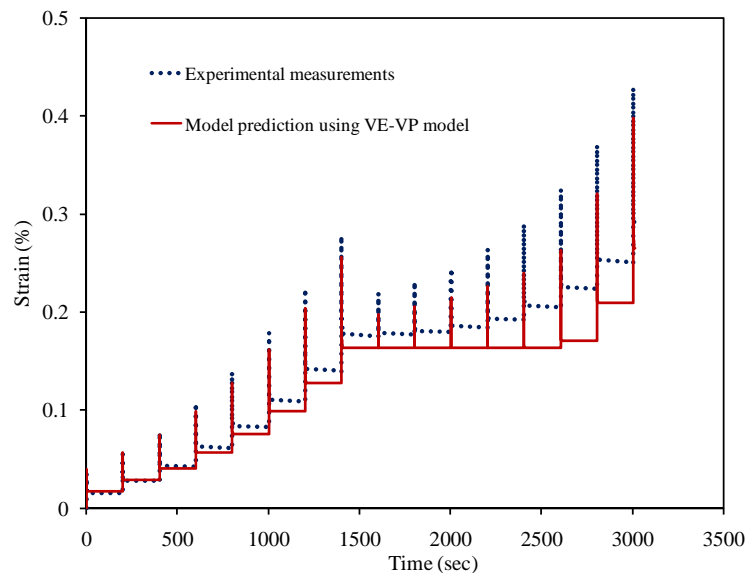
Figure 7.3. Model predictions and experimental measurements for the VL test at 55°C.

However, the model does not show more viscoplastic strain in the second block until the applied stress level exceeds its maximum value in the previous block. However, experimental measurements show that asphalt mixes progressively accumulate the permanent deformation even when the applied stress is less than its maximum value in the previous block (more viscoplastic strain is accumulated for the first four loading cycles in the second block even though the applied stress is still less than the applied stress at the end of the first block).

This distinct behavior of asphalt mixes subjected to the repeated loading at high temperatures cannot be explained by hardening plasticity and viscoplasticity theories only. In other words, the hardening plasticity/viscoplasticity theories state that the material point remains inside the yield surface (i.e. elastic/viscoelastic) when the applied stress in the subsequent loading cycle is less than the stress level in the preceding loading cycle such that no further permanent deformation is predicted. However, as it is obvious from Figure 7.3, asphalt mixes once yielded show accumulation of the plastic/viscoplastic strain in each loading cycle even if the applied stress is decreasing. Although this behavior can be explained by the viscodamage model, it is not physical to relate this degradation behavior to the damage model since at this high temperature and in compression loading conditions the material rarely experiences micro-cracking. This behavior is related in this work to the *viscoplastic softening* which will be explained in more details in the next subsection.

7.3.3. *Viscoplastic Softening Model and the Viscoplastic Softening Memory Surface*

Asphalt mixes are subjected to repeated loading during their service life. The microstructure of the asphalt mixes rearranges during the unloading and rest period especially at high temperatures. This rearrangement of the microstructure (i.e. rearragement of the aggregates) changes the mechanical properties of the asphalt mixes such that they can undergo more viscoplastic deformation during the next loading cycle. This behavior is referred to as the *viscoplastic softening,* (Saadeh et al., 2007). There are several approaches to model the viscoplastic softening in materials. The first approach is to allow the yield surface to shrink during the unloading to take into account the softening behavior. This approach has been used by Yum and Kim (2011) to predict the viscoplastic softening response of asphalt mixes at high temperatures. However, their model is augmented with more than seven model parameters which increase the number of required tests to identify the parameters. The second approach is to additively decompose the hardening/softening function κ in the viscoplastic dynamic yield surface into hardening and softening components, such that:

$$\kappa = \kappa^h + \kappa^s \tag{7.3}$$

where κ^h and κ^s are hardening and softening components of the function κ, respectively. The hardening and softening components can then be obtained by proposing certain evolution functions. The third approach is to consider the viscoplastic softening effect through the maximum saturation limit of the viscoplastic hardening function. In other words, the classical plasticity/viscoplasticity theories state that the isotropic hardening saturates for large values of the viscoplastic strains. However, if unloading occurs after the saturation point of the isotropic hardening, additional softening is observed again which causes the evolution of more plastic/viscoplastic strain under the same stress level. Therefore, the saturation limit of the isotropic hardening is not constant and changes during the unloading which is accompanied with the changes in the microstructure. For example, the saturation limit of the viscoplastic model used in this work is $\kappa_0 + \kappa_1$. In this approach, one can express the parameter κ_1 to be a decreasing function of the effective viscoplastic strain from previous loading cycles.

However, numerous other conditions should also be used in these approaches. For example, the experimental measurements show that the softening occurs when the viscoplastic strain exceeds a certain value. Therefore, one should put another condition to capture this effect in order to avoid overestimation of the viscoplastic softening. Moreover, experimental measurements usually show the presence of a lower limit for the viscoplastic softening such that the material cannot get softer than that limit. Again, another condition is required to capture this effect. More importantly, these models are usually developed for specific loading conditions and should be used with special cares for the general cases.

The last approach and the most robust approach, in the author's opinion, is to define a surface in the viscoplastic strain space instead of the stress space as the *viscoplastic softening memory surface*. The memory surface can be considered as the counterpart of the yield surface in the viscoplastic strain space. This surface can be expressed in terms of an internal state variable which memorizes the maximum experienced viscoplastic strain in the last unloading stage. The evolution of the viscoplastic softening will then be controlled by this surface. This concept has been used

for a different purpose in modeling the stabilization of the hysteresis loops in cyclic plasticity of metals (Murakami and Ohno, 1982; Ohno, 1982; Chaboche, 1989). Analogously, in this study the static viscoplastic memory surface can be defined as follows:

$$f^{vp,\text{soft}} = p - q^{vp} \leq 0 \tag{7.4}$$

where $f^{vp,\text{soft}}$ is the static viscoplastic memory surface, p is the effective viscoplastic strain, and q^{vp} is the viscoplastic internal state variable memorizing the maximum experienced viscoplastic strain for which the softening has occurred. Eq. (7.4) shows that the material does not undergo viscoplastic softening if $f^{vp,\text{soft}} \leq 0$. However, similar to the rate-dependent plasticity (i.e. viscoplasticity), the value of the static viscoplastic softening memory surface can have a positive value if the viscoplastic strain exceeds the viscoplastic softening internal state variable. The distance of the viscoplastic strain from the static viscoplastic softening memory surface controls the rate of the evolution of the viscoplastic softening internal state variable, such that one can define a dynamic viscoplastic softening memory surface as follows:

$$\chi^{vp,\text{soft}} = p - q^{vp} - \left(\frac{\dot{q}^{vp}}{\Gamma^{vp,\text{soft}}} \right)^{\frac{1}{S_1}} \leq 0 \tag{7.5}$$

where $\chi^{vp,\text{soft}}$ is the dynamic viscoplastic softening memory surface, $\Gamma^{vp,\text{soft}}$ is the viscoplastic softening viscosity parameter, and S_1 is a model parameter. The rate of the evolution of the viscoplastic softening internal state variable $\dot{q}^{vp}$ can be determined based on Eq. (7.5), such that:

$$\dot{q}^{vp} = \Gamma^{vp,\text{soft}} \left(p - q^{vp} \right)^{S_1} \tag{7.6}$$

This equation clearly shows that the rate of the viscoplastic softening internal state variable depends on the difference of the effective viscoplastic strain and the maximum value of the viscoplastic strain for which the softening has occurred. In other words, $p - q^{vp}$ is the amount of the viscoplastic strain for which the material has not yet rearranged its microstructure during the unloading (i.e. viscoplastic softening has not

occurred for this deformation). In fact, this difference is the driving force for the viscoplastic softening. Now, as the first try, one can assume that the evolution function for the saturation limit of the hardening parameter κ_1 to be a linear function of the viscoplastic softening internal state variable, such that:

$$\dot{\kappa}_1 = -S_2 \dot{q}^{vp} \tag{7.7}$$

However, Eq. (7.7) is modified as follows to consider the history effect in the viscoplastic softening model since the experimental measurements show that the rate of the viscoplastic softening decreases as the saturation limit of the hardening parameter decreases, such that:

$$\dot{\kappa}_1 = -S_2 \dot{q}^{vp} \left(\frac{\kappa_1}{\kappa_1^{\text{initial}}} \right)^{S_3} \tag{7.8}$$

Figure 7.4 shows the schematic representation of the concept of the viscoplastic softening memory surface.
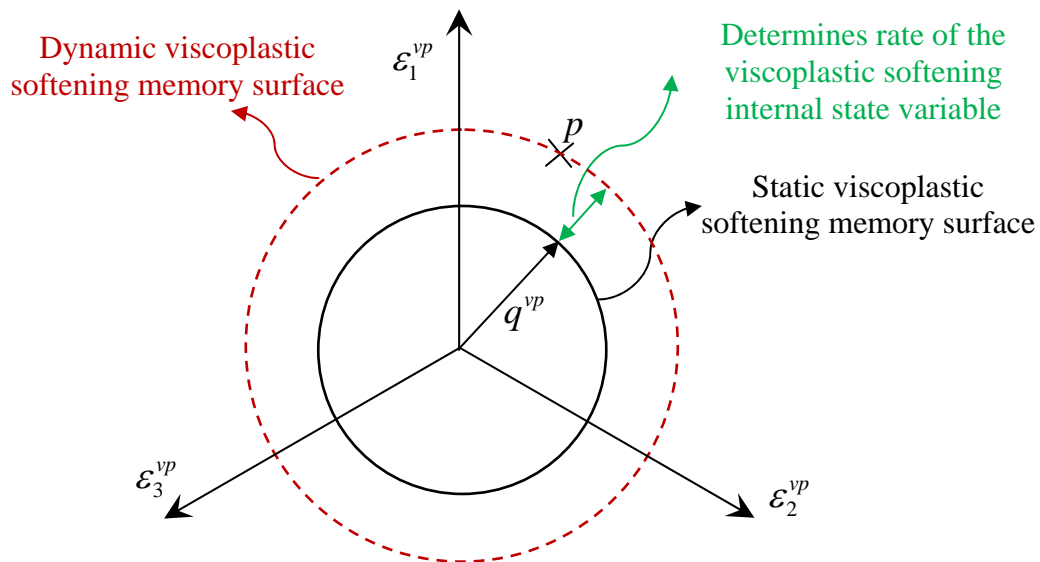

Figure 7.4. Schematic representation of the concept of the viscoplastic softening memory surface.

This approach provides a promising framework for modeling the viscoplastic softening mechanism in the materials. This dynamic viscoplastic softening memory surface distinguishs between the viscoplastic softening under extension and compressive loading conditions. The identification of the model parameters is pretty straightforward and is similar to identification of the parameters associated with the yield surface in the stress space. Therefore, one can easily conduct repeated creep-recovery tests at high temperatures and for different loading/unloading times to identify the model parameters. Alternatively, one can use the flow test to identify the viscoplastic softening model parameters. The identified model parameters associated with the ALF materials at 55°C are listed in Table 7.4.

Table 7.4. Identified viscoplastic softening model parameters.

$\Gamma^{vp,\text{soft}}$ (sec^{-1})	S_1	S_2 (kPa)	S_3
0.001	0.3	200000	2.5

The variable loading test is resimulated using the viscoplastic softening memory surface as shown in Figure 7.5. As shown in Figure 7.5 (a), inclusion of the viscoplastic softening model through the viscoplastic softening memory surface significantly enhances the model prediction of the strain response in the VL test. Moreover, the evolution of the saturation limit of the viscoplastic model (i.e. κ_1) with time is plotted in Figure 7.5 (b). This Figure shows that the material undergoes softening during the rest period. However, the viscoplastic model parameters are identified such that the softening continues until the rate of the viscoplastic strain reaches a negligible value. After that point, no softening occurs since the softening is physically related to the rearrangement of the microstructure during the unloading. Therefore, no more softening is expected once the rate of the recoverable strain in the unloading reaches zero.
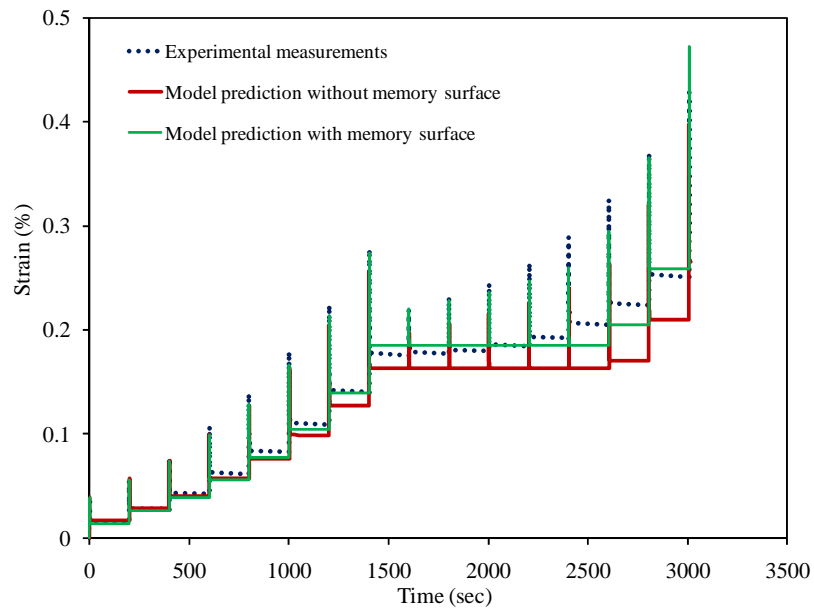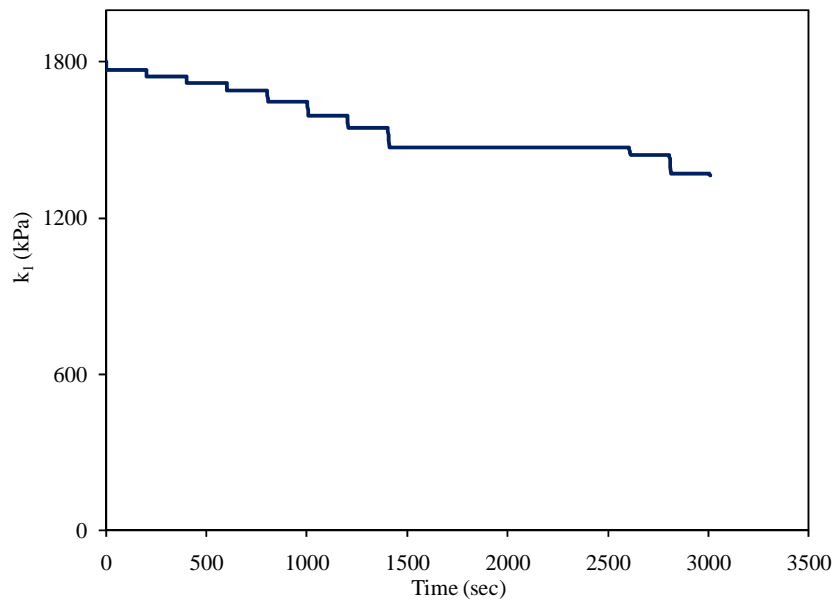
Figure 7.5. Experimental measurements and model prediction with and without viscoplastic memory surface for the variable loading test (VL) at 55$^{\mathrm{o}}$C in compression. (a) strain response; (b) evolution of the κ_1 parameter with time.

7.4. Model Validation in Compression

The calibrated VE-VP model along with the viscoplastic softening model are used to further validate the model against the experimental data listed in Table 7.5 which has not been used in the calibration process.

Table 7.5. Summary of the test used for validation of the viscoelastic-viscoplastic model with viscoplastic softening model[*]

Test	Stress level (kPa)	Loading time (Sec)	Rest period (Sec)
Repeated creep-recovery test with constant loading level and time (CLT)	827	0.1, 0.4, 1.6, 6.4	0.9
Repeated creep-recovery test with variable loading time (VT)	827	Sequence of (0.05, 0.1, 0.4, 1.6, 6.4)	0.05, 1, 200
Repeated creep-recovery test with reversed variable loading time (RVT)	827	Sequence of (6.4, 1.6, 0.4, 0.1, 0.05)	200

[*] All tests have done at 55°C and 140kPa confinement in compression

7.4.1. Model Validation against Constant Loading Time Test (CLT)

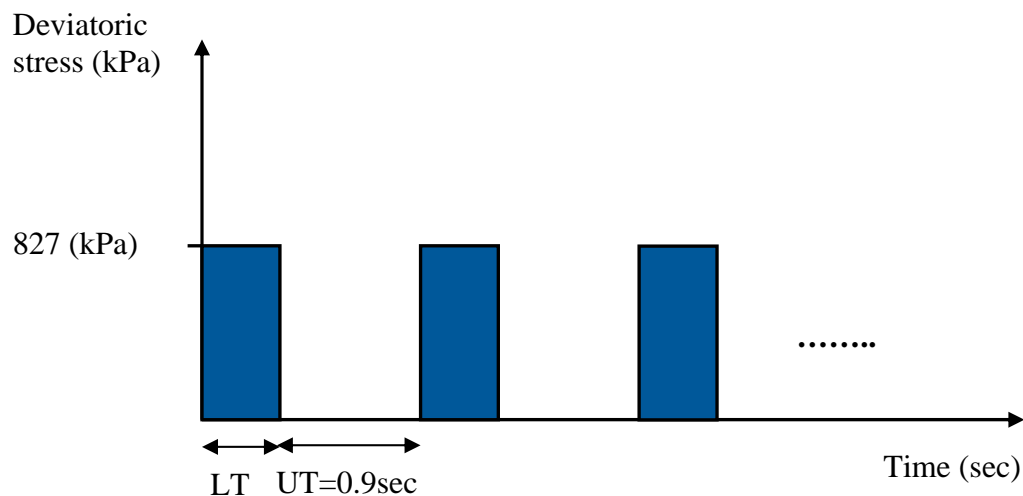Figure 7.6 schematically shows the stress history input for CLT.

Figure 7.6. Schematic representation of the stress input for the constant loading time test (CLT). NCSU database includes CLT tests for four different loading times (LT) of 0.1, 0.4, 1.6, and 6.4 sec.

The constant loading time test (CLT) is basically a simple repeated creep-recovery test with the rest periods between the loading cycles. The applied stress level, loading time, and rest period are kept constant for each test. However, this test is repeated for four loading times of 0.1, 0.4, 1.6, and 6.4 sec. The rest period in all these four tests equals to 0.9 sec. The applied deviatoric stress is also constant for these four tests and equals to 827 kPa. Figures 7.7 and 7.8 show the comparison of the model prediction with and without the memory surface with the experimental measurements when the loading times are 0.1 and 0.4sec, respectively. As shown in Figures 7.7(a) and 7.8(a), the VE-VP model shows that the viscoplastic strain saturates after the first one or two loading cycle. Therefore, it predicts no more viscoplastic strain for the next loading cycles. However, experimental measurements and model predictions with memory surface clearly show that the material can undergo more viscoplastic strain after the unloading occurs. This phenomenon can be clearly seen in Figures 7.7(b) and 7.8(b). These figures show that the material softens during the unloading by decreasing the saturation limit of the hardening function κ_1. However, the rate of softening decreases as the viscoplastic strain increases and as the hardening parameter κ_1 decreases. This behavior is related to the inclusion of the history term $\left(\dfrac{\kappa_1}{\kappa_1^{\text{initial}}} \right)^{S_3}$ in Eq. (7.8). This history term slows the rate of the viscoplastic softening as the hardening parameter κ_1 decreases. Figures 7.7 and 7.8 show that the model with the viscoplastic memory surface agrees well with the experimental measurements. Model predictions and experimental measurements for longer loading times of 1.6sec and 6.4sec are presented in Figure 7.9. Figure 7.9 shows that as the loading time increases, the viscoplastic softening model slightly overestimates the experimental measurements. It should be noted that loading times 1.6 and 6.4sec resemble very high vehicle speed which are less likely to happen in the roads and pavements. However, more experimental data is required to investigate the reason for this overestimation as the loading time increases.
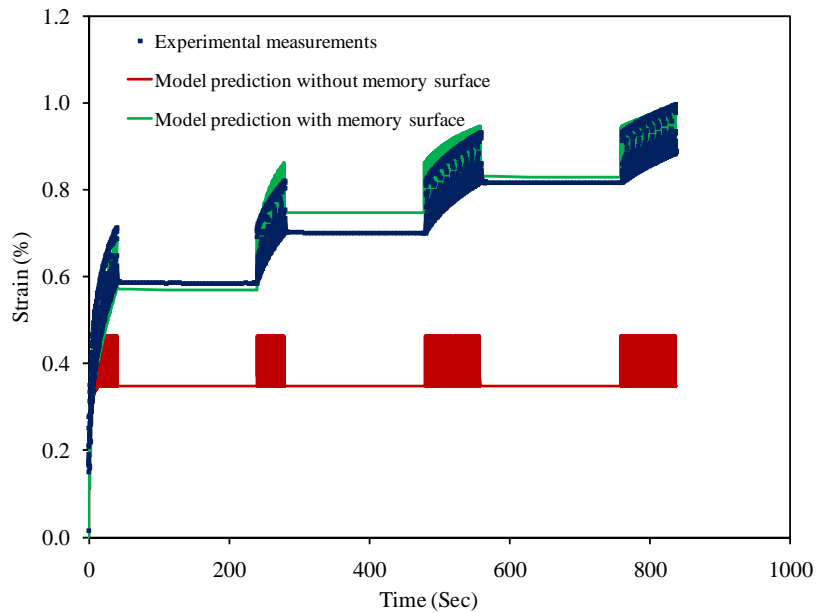
(a)
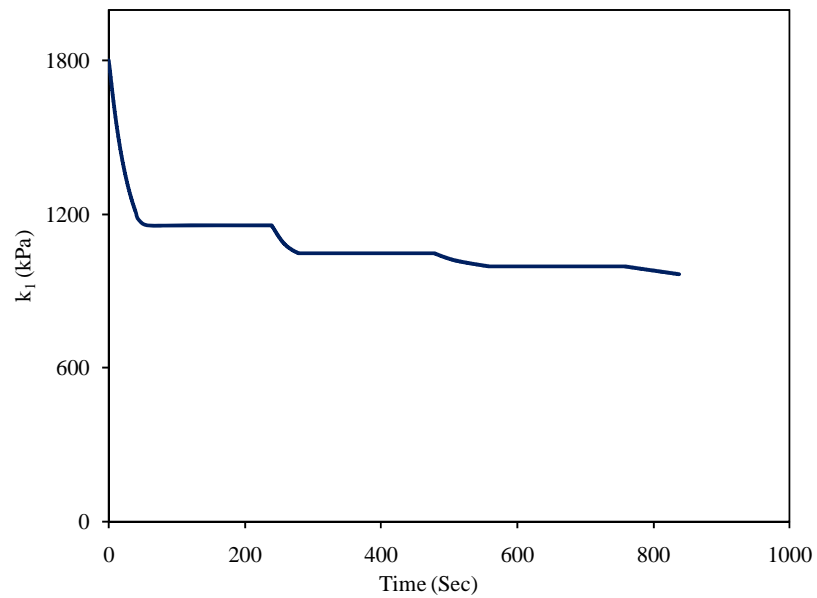
(b)

Figure 7.7. Experimental measurements and model prediction with and without viscoplastic memory surface for the constant loading and time test (CLT) at 55°C in compression when the loading time is 0.1sec. (a) strain response; (b) evolution of the κ_1 parameter with time.

(a)

(b)

Figure 7.8. Experimental measurements and model prediction with and without viscoplastic memory surface for the constant loading and time test (CLT) at 55°C in compression when the loading time is 0.4 sec. (a) strain response; (b) evolution of the κ_1 parameter with time.
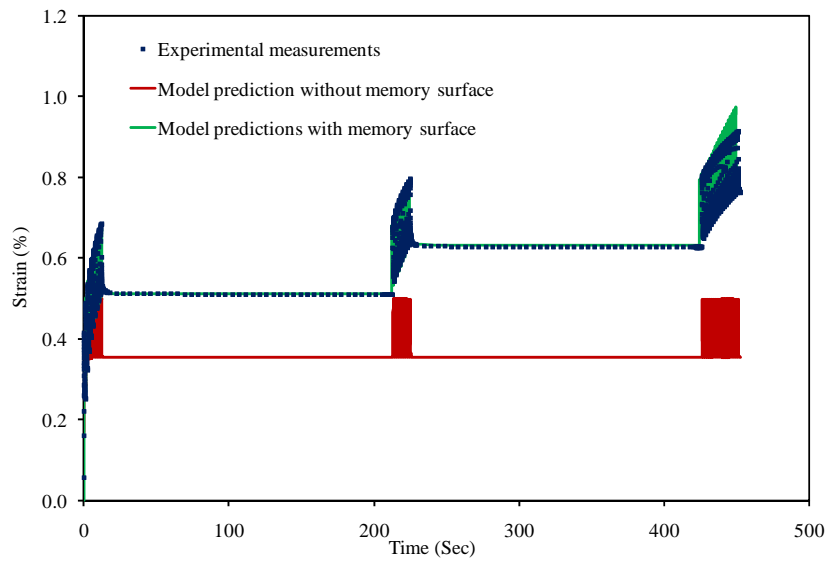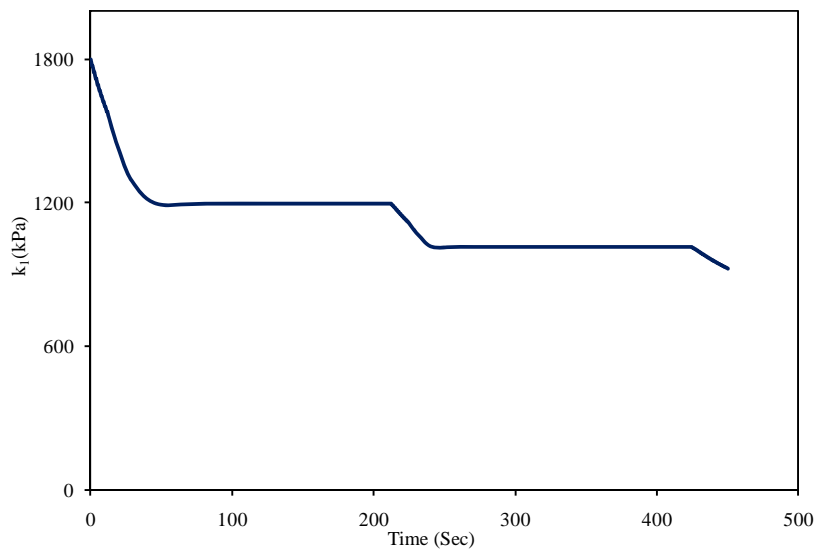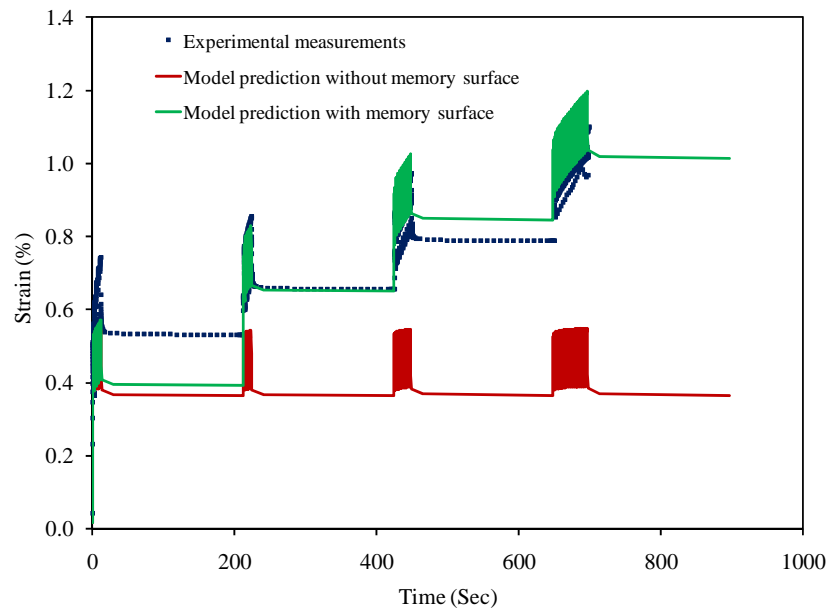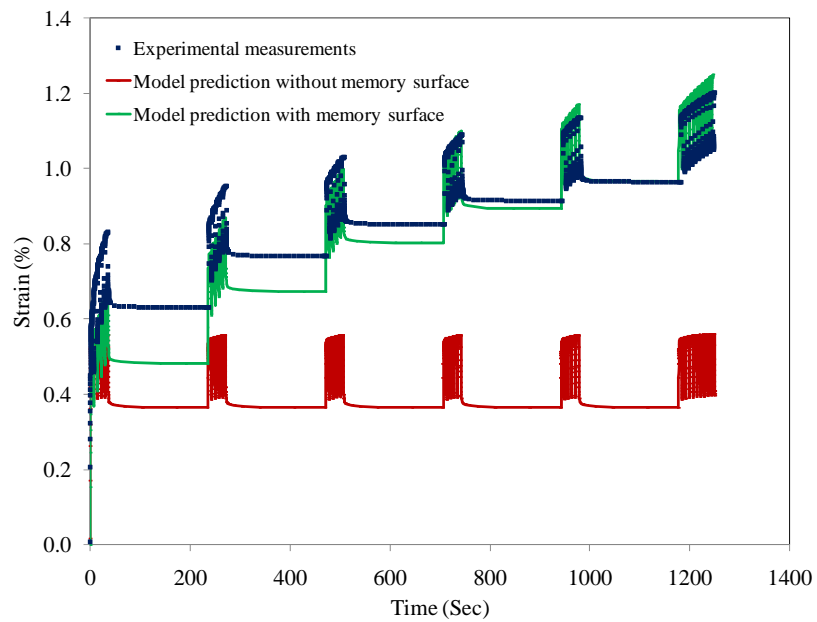
(a)

(b)

Figure 7.9. Experimental measurements and model prediction with and without viscoplastic memory surface for the constant loading and time test (CLT) at 55°C in compression. (a) loading time is 1.6sec; (b) loading time is 6.4sec.

7.4.2. Model Validation against Variable Loading Time Test (VT)

Variable loading time test (VT) is a repeated creep-recovery test where the applied deviatoric stress and the rest period between the loading cycles are kept constant and equal to 827kPa and 200sec, respectively. This test is designed to investigate the effect of loading time on mechanical response of asphalt mixes. VT consists of several blocks with each block consisting of six creep-recovery tests. The loading time in each block varies from short to long loading times with the sequence of 0.05, 0.1, 0.2, 0.4, 1.6, and 6.4 sec. The schematic representation of the stress input in VT test is shown in Figure 7.10. The unloading time (UT) remains constant during each test. However, the VT test is conducted at three different unloading times (i.e. rest periods) of 0.05, 1, and 200 sec to investigate the effect of the rest period as well.

Figure 7.10. Schematic representation of stress input in variable loading time test (VT). The unloading time (UT) is constant and equals to 200 sec.

Figures 7.11 (a), (b), and (c) show the model predictions and experimental measurements for the variable loading time test when the rest periods are 0.05, 1, and 200 sec, respectively.

(a)

(b)

Figure 7.11. Experimental measurements and model prediction with and without viscoplastic memory surface for the variable loading time test (VT) at 55°C in compression. (a) rest period is 0.05sec; (b) rest period is 1sec; (c) rest period is 200sec.
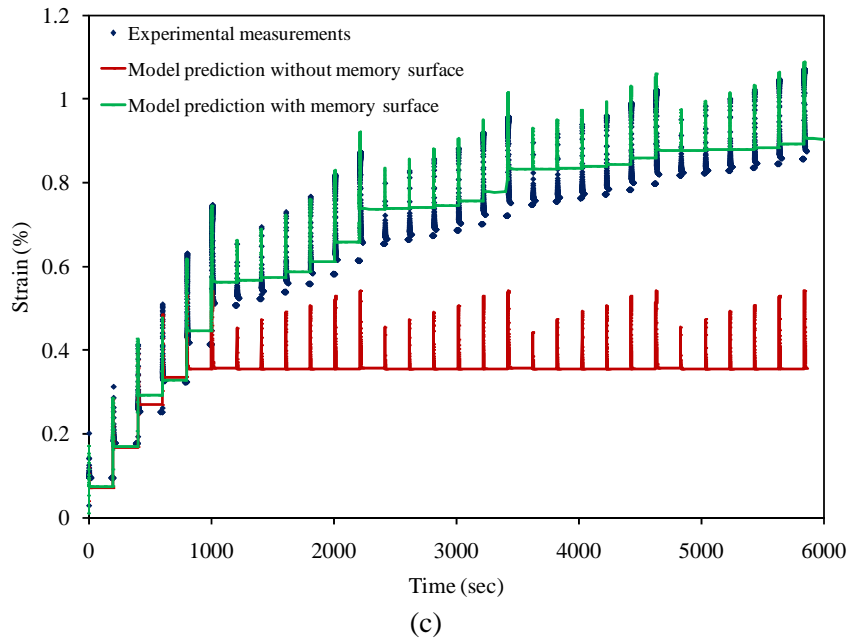
Figure 7.11. Continued.

7.4.3. Model Validation against Reversed Variable Loading Time Test (RVT)

Figure 7.12 shows the schematic representation of the stress history for the reversed variable loading time test.
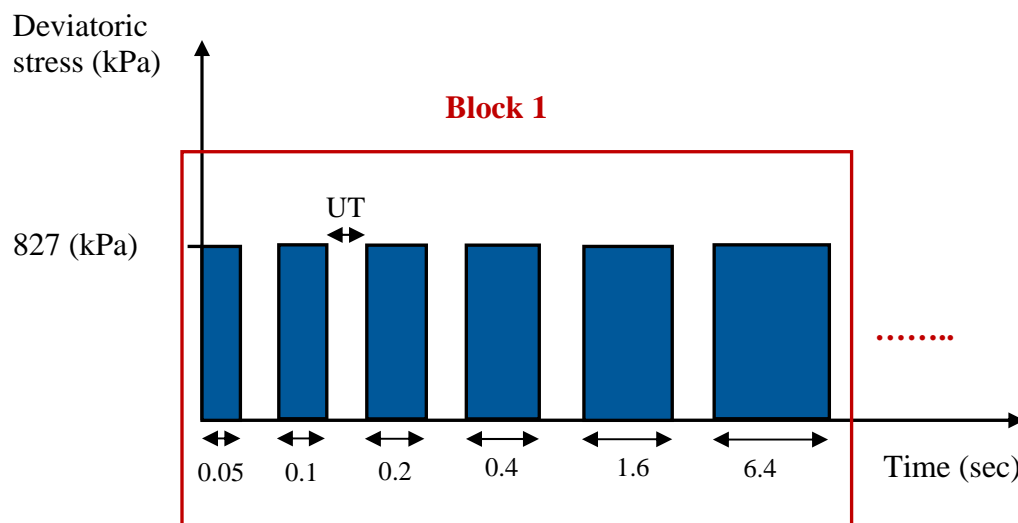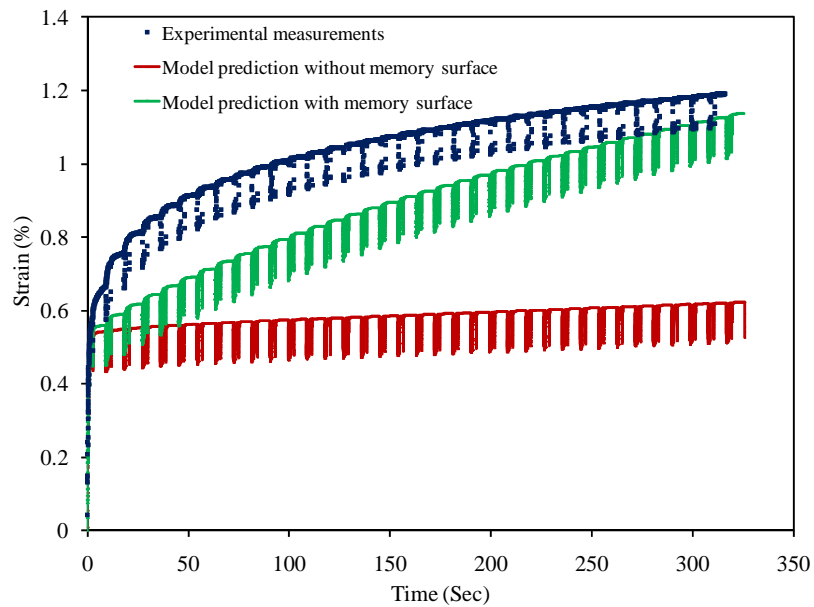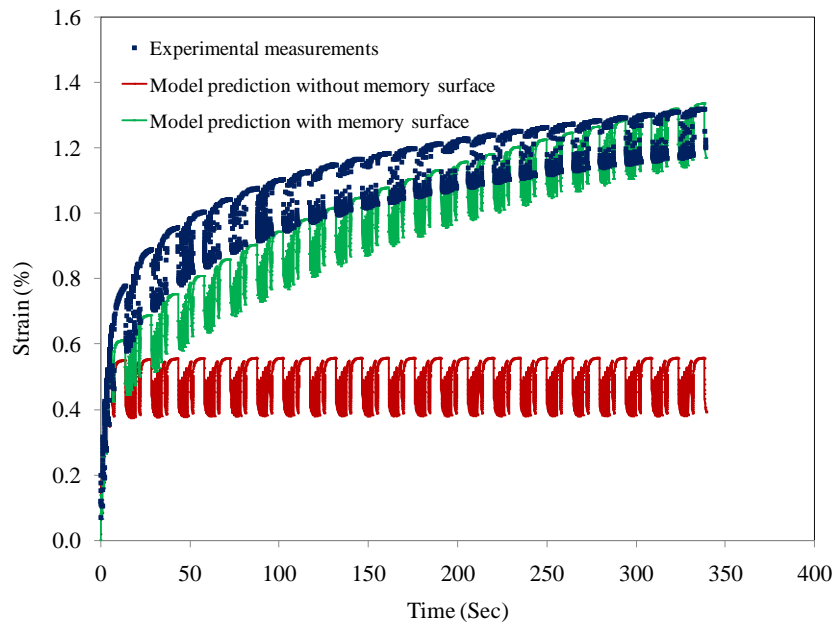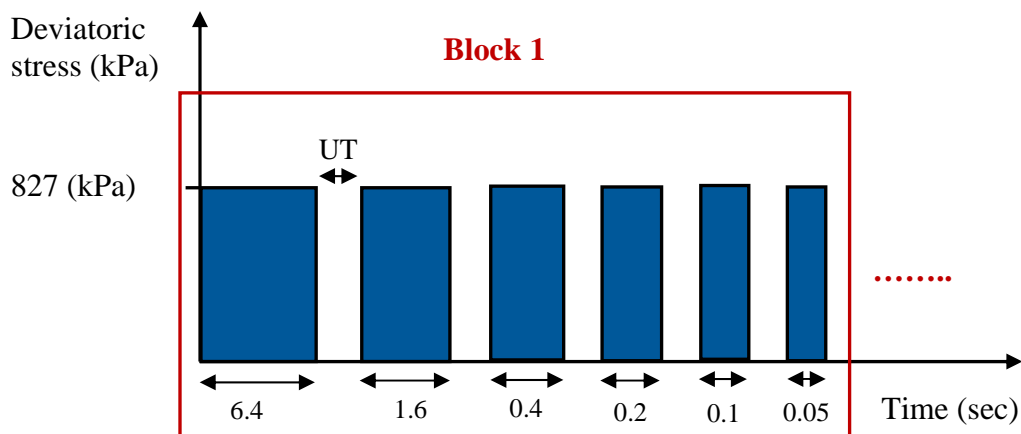

Figure 7.12. Schematic representation of stress input in the reversed various loading time test (RVT). The unloading time (UT) is constant and equals to 200 sec.

Reversed variable loading time test (RVT) is very similar to the variable loading time test (VT) with the difference that the loading time in each block starts from its maximum value and decreases to its minimum value. The applied deviatoric stress is kept constant and equal to 827kPa. However, the loading time is a sequence of 6.4, 1.6, 0.4, 0.2, 0.1, and 0.05sec. The unloading time or the rest period in this test is constant and is equal to 200sec. Figure 7.13 shows the model predictions and experimental measurements for the reversed variable loading time test. Figure 7.13 shows that the model prediction without the viscoplastic memory surface significantly underestimates the experimental measurements while the model prediction with the viscoplastic memory surface overestimates the experimental measurements.
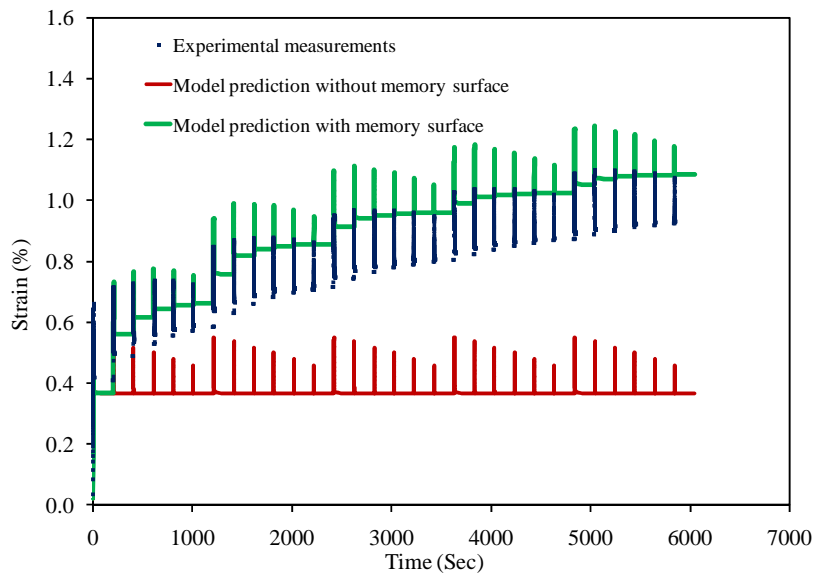
Figure 7.13. Experimental measurements and model prediction with and without viscoplastic memory surface for the reversed variable loading time test (RVT) at 55°C in compression.

7.5. Effect of Viscoplastic Softening Model on the Mechanical Response

The effect of different model parameters associated with the viscoplastic softening memory surface and the evolution function for the saturation hardening parameter κ_1 is investigated in this section. The first block of the CLT test with 0.1sec loading time and

0.9sec unloading time is selected to investigate this issue. Figure 7.14 shows the effect of the viscoplasticity softening viscosity parameter $\Gamma^{vp,\text{soft}}$ on the evolution of the viscoplasticity softening internal variable q^{vp}. As shown in Figure 7.14, the viscoplastic softening viscosity parameter controls the rate of the change in the viscoplastic internal state variable q^{vp}. For example, Figure 7.14 shows that when $\Gamma^{vp,\text{soft}} = 0.1\,\text{sec}^{-1}$, the material can fulfill its full softening potential during the rest period of 0.9sec. However, the material can only partially fulfill its softening potential when $\Gamma^{vp,\text{soft}} = 0.001\,\text{sec}^{-1}$. However, the material will fulfill its full softening potential once a long enough rest period is introduced. Figure 7.14 shows an interesting feature of the model in capturing time-dependent viscoplastic softening response. It is noteworthy that the difference between the effective viscoplastic strain p and the viscoplastic softening internal state variable q^{vp} is the driving force for the viscoplastic softening.
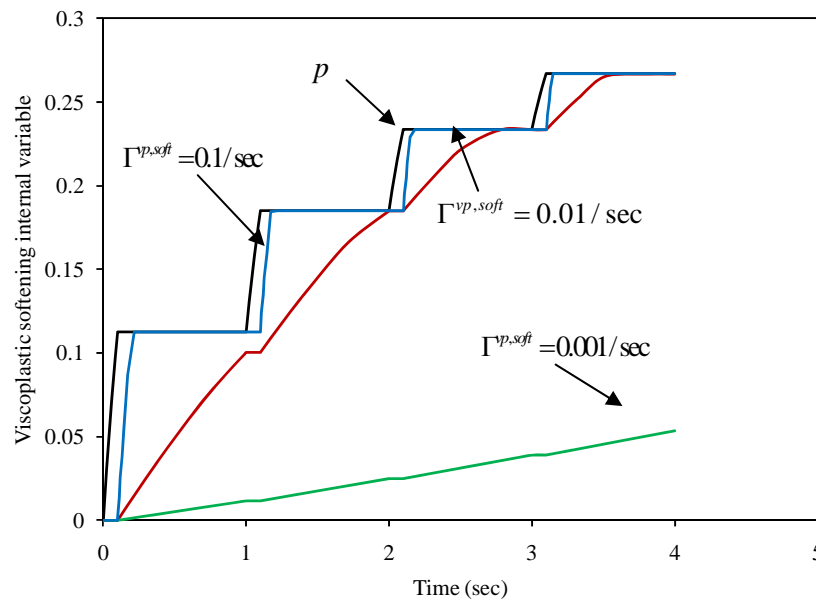
Figure 7.14. Effect of the viscoplastic softening viscosity parameter $\Gamma^{vp,\text{soft}}$ on the evolution of the viscoplastic softening internal state variable q^{vp}. The other parameters are selected as : $S_1 = 0.3$ and $S_2 = 0$.

The value of $\Gamma^{vp,\text{soft}} = 0.001\,\text{sec}^{-1}$ is selected to investigate the effect of the rate-sensitivity parameter S_1 on the evolution of the viscoplastic softening internal state variable. Figure 7.15 shows that the S_1 parameter also controls the rate of change in the viscoplastic softening internal state variable. Comparing Figures 7.14 and 7.15 shows that the parameter $\Gamma^{vp,\text{soft}}$ changes both the value and the shape of the curve for the viscoplastic softening state variable, whereas, parameter S_1 only affects the rate of the change in the viscoplastic internal state variable.

Furthermore, Figures 7.16(a) and 7.16(b) show the effect of S_2 and S_3 parameters on the softening response of materials.
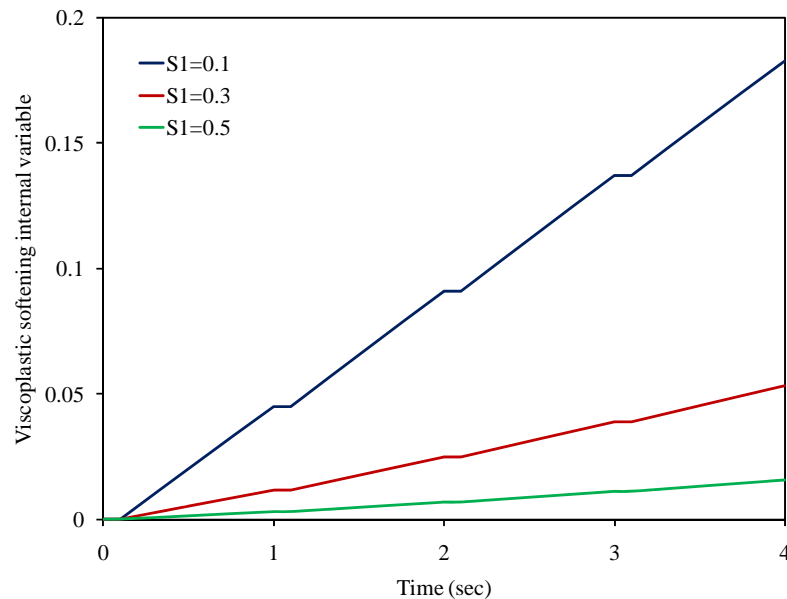
Figure 7.15. Effect of the viscoplastic softening parameter S_1 on the evolution of the viscoplastic softening internal state variable q^{vp}. The other parameters are selected as : $\Gamma^{vp,\text{soft}} = 0.001 / \sec$ and $S_2 = 0$.

(a)

(b)
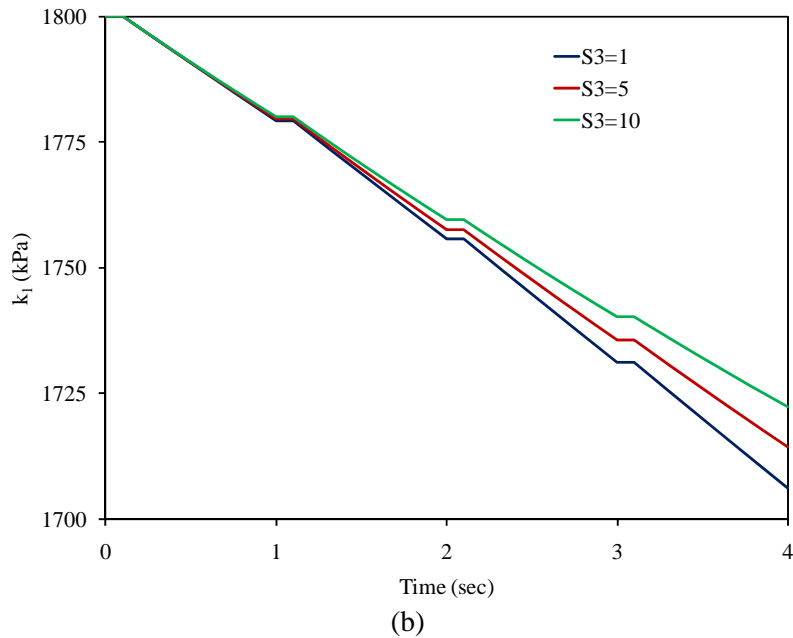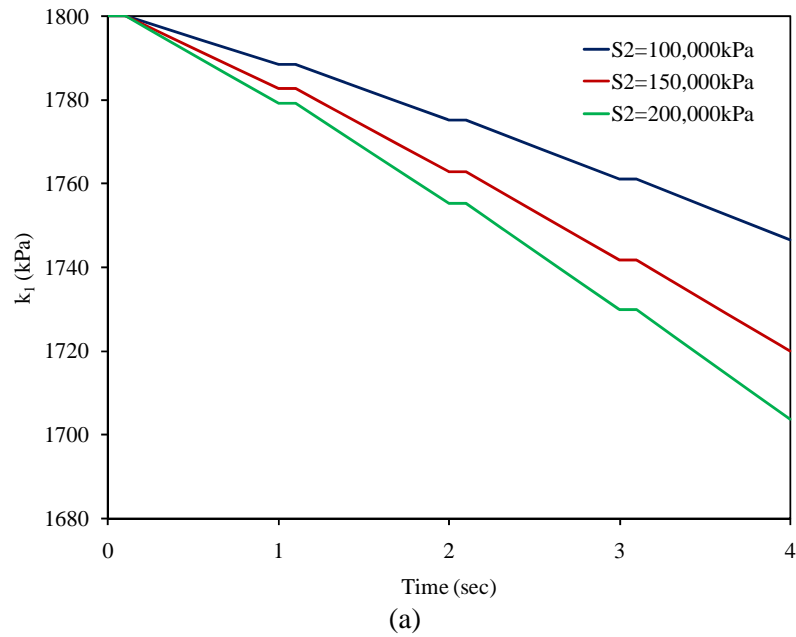
Figure 7.16. Effect of viscoplastic softening model parameters on the softening response of materials. (a) Effect of S_2 parameter when $\Gamma^{vp,\text{soft}} = 0.001/\sec$, $S_1 = 0.3$, and $S_3 = 0$; (b) Effect of S_3 parameter when $\Gamma^{vp,\text{soft}} = 0.001/\sec$, $S_1 = 0.3$, and $S_2 = 2 \times 10^5 \, \text{kPa}$.

Figure 7.16(a) shows that the softening viscoplastic response signifies as the parameter S_2 increases. However, the history model parameter S_3 controls the rate of the viscoplastic softening as the material softens.

7.6. Identification of the Model Parameters in Tension

The NCSU test data in tension include complex modulus, uniaxial constant strain rate, cyclic stress control, and cyclic strain control tests at different temperatures, strain rates, strain levels, and stress levels. The monotonic uniaxial constant strain rates at 5°C are used to calibrate the damage model, whereas, the other test data are used to further validate the model presented in Chapter II. Tables 7.6 and 7.7 list the tests which have been used to calibrate and validate the model respectively.

Table 7.6. Summary of the tests in tension used for identification of the thermo-viscodamage model parameters.

Test	Temperature (^{o}C)	Strain rate (sec^{-1})
Uniaxial constant strain rate test	5	7×10^{-6}; 2.1×10^{-5}; 3×10^{-5}; 5.5×10^{-5}

Table 7.7. Summary of the tests in tension used for validation of the thermo-viscoelastic-viscoplastic-viscodamage-model.

Test	Temperature (^{o}C)	Stress level (kPa)	Strain level ($\mu\varepsilon$)	Strain rate (sec^{-1})
Complex Modulus test	-10, 10, 35, 55			
Uniaxial constant strain arte test	12			2.7×10^{-4}; 4.6×10^{-4}
	25			5×10^{-4}; 1.5×10^{-3}; 4.5×10^{-3}; 1.35×10^{-2}
	40			3×10^{-4}; 10^{-3}; 3×10^{-3}
Cyclic stress control	5	1525		
	19	250, 750		
Cyclic strain control	5		1750	
	19		1200, 1500	

7.6.1. Viscoelastic-Viscoplastic Parameters in Tension and Time-Temperature Shift Factors

The NCSU database includes the dynamic modulus tests in both tension and compression for the same temperatures and frequencies (i.e. -10, 10, 35, and 55°C; and 0.01, 0.05, 0.1, 0.5, 1, 5, 10, and 25 Hz). It is usually argued that the viscoelastic response of asphalt mixes is controlled by the viscoelastic response of the asphalt binder. However, the viscoelastic response of asphalt binder is practically the same in tension and compression. Therefore, the viscoelastic response of asphalt mixes should also be similar in tension and compression. To investigate this issue, the complex modulus data at different temperatures are plotted versus the angular frequency ω for both tension and compression in Figure 7.17 (a). Figure 7.17 (a) shows that the viscoelastic response of asphalt mixes is the same in both tension and compression for a range of temperatures (i.e. -10°C-35°C).

However, the viscoelastic response in tension and compression deviate from each other as the temperature increases. Moreover, this deviation signifies at low angular frequencies. The reason is that asphalt mixes at high temperatures are very prone to viscoplastic deformation and cracking in compression and tension, respectively. Therefore, the measured complex compliance at high temperatures includes viscoplastic response in compression and damage response in tension. Furthermore, at low angular frequencies, the applied load remains on the specimen for a longer time which signifies the effect of the viscoplastic evolution and damage evolution in compression and tension, respectively. However, surprisingly the time-temperature shift factors in both tension and compression are the same. Figure 7.17 (b) shows the shifted complex compliance data to the reference temperature $T_0 = 10^o C$ using the same time-temperature shift factor listed in Table 7.2. Therefore, for the range of the temperatures for which the tension data are available (i.e. 5-25°C) the same viscoelastic parameters and time-temperature shift factors identified in compression can be used. Moreover, $d^{vp} = 0.78$ is used to differentiate between the viscoplastic response in tension and compression.
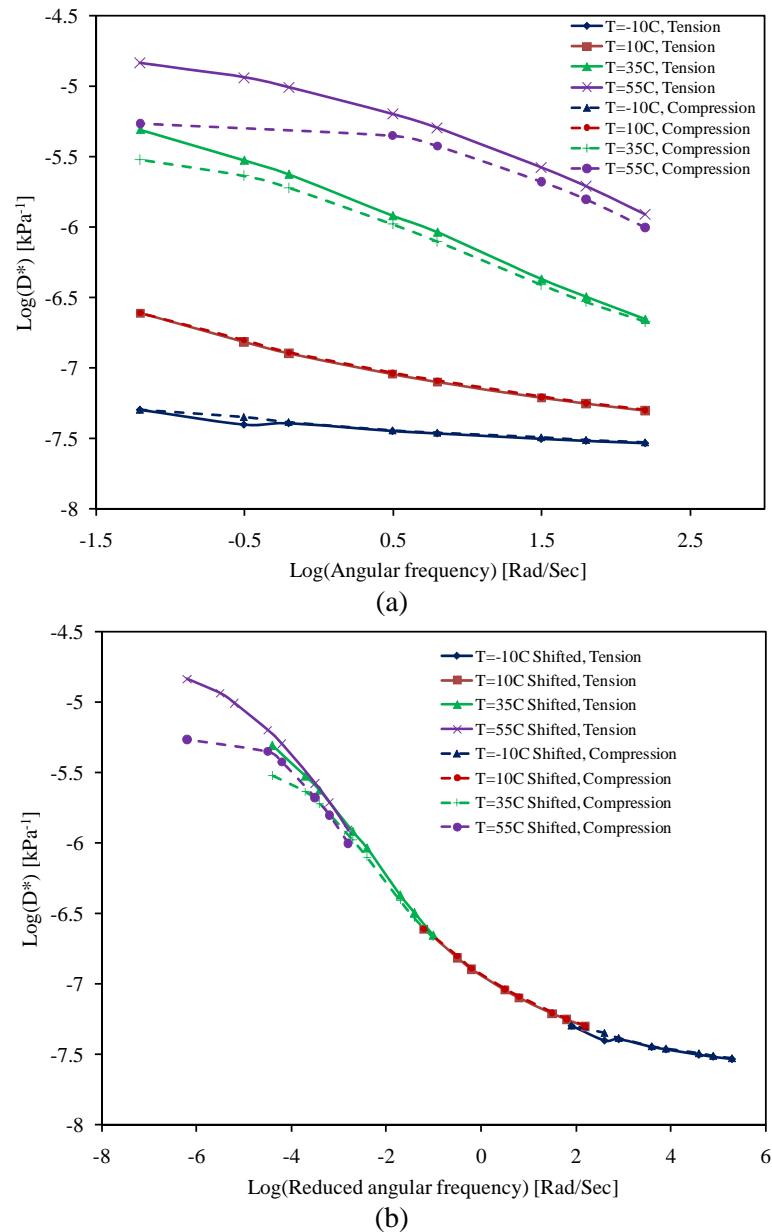
Figure 7.17. The complex compliance data at different temperatures. (a) before time-temperature shift factor; (b) after time-temperature shift.

7.6.2. Viscodamage Model Parameters in Tension

The constant uniaxial strain rate tests in tension at $5^{o}C$ are analyzed to identify the viscodamage model parameters. At this temperature, one can assume reasonably that the material is only viscoelastic since the viscoplastic response can be reasonably neglected

at low temperatures. To examine the accuracy of this assumption, the VE-VP model parameters along with the time-temperature shift factors are used to simulate the response of asphalt mixes at 5°C when the strain rate is 1×10^{-4}/sec. Figure 7.18 shows the predicted viscoplastic strain versus the total applied strain. Figure 7.18 shows that the predicted viscoplastic strain is less than 1% of the total applied strain which reasonably verifies the assumption of neglecting the viscoplastic strain at 5°C. Moreover, the constant strain rate test is selected since one can analytically obtain the response in the healing configuration and subsequently identify the damage variable.
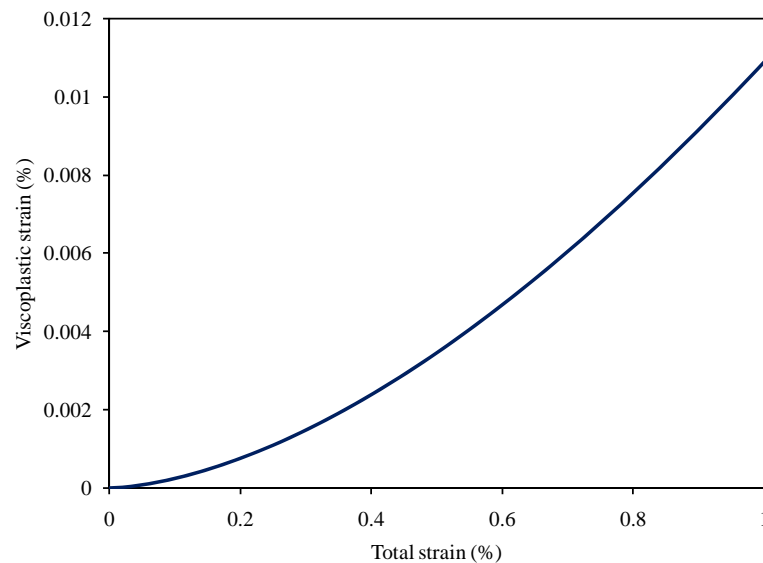
Figure 7.18. Predicted viscoplastic strain versus the total applied strain at 5°C when the strain rate is 1×10^{-4}/sec. It shows that the viscoplastic strain can be reasonably neglected at 5°C.

To show the procedure, one can assume the strain input for the constant strain rate test as follows:

$$\tilde{\varepsilon}(t) = Ct \tag{7.9}$$

where C is a constant representing the strain rate in the uniaxial constant strain rate response. The uniaxial stress output in the healing configuration can be simply obtained

using the superposition position principle for linear viscoelastic materials which could be written as one of the following equations:

$$\tilde{\sigma}(t) = \tilde{E}(0)\tilde{\varepsilon}(t) + \int_0^t \tilde{E}(t-\tau)\dot{\tilde{\varepsilon}}(\tau)d\tau \tag{7.10}$$

$$\tilde{\sigma}(t) = \tilde{E}(t)\tilde{\varepsilon}(0) + \int_0^t \tilde{E}(\tau)\dot{\tilde{\varepsilon}}(t-\tau)d\tau \tag{7.11}$$

However, Eq. (7.11) serves the purpose of the analysis better. Therefore, substituting Eq. (7.9) into Eq. (7.11) yields the following stress output for the uniaxial constant strain rate test:

$$\tilde{\sigma}(t) = C\int_0^t \tilde{E}(\tau)d\tau \tag{7.12}$$

Therefore, the stress output in the healing configuration at any given time t will be the multiplication of the strain rate by the area under the relaxation modulus-time curve. The damage density can now be identified simply by comparing the experimental measurements for the stress which can be considered as the stress in the nominal configuration and the results obtained from Eq. (7.12), such that:

$$\phi(t) = 1 - \frac{\sigma(t)}{\tilde{\sigma}(t)} \tag{7.13}$$

where $\sigma(t)$ is the experimentally measured stress at time t. This procedure is followed for several constant uniaxial strain rate tests in tension at 5°C. Note that the loading condition is monotonic. Therefore, healing will not occur such that the healing and effective configurations are the same. Figure 7.19 shows the experimental stress-strain curves which have been used in identifying the viscodamage model parameters. The identified damage densities at 5°C are plotted versus time and strain in Figures 7.20(a) and (b), respectively.
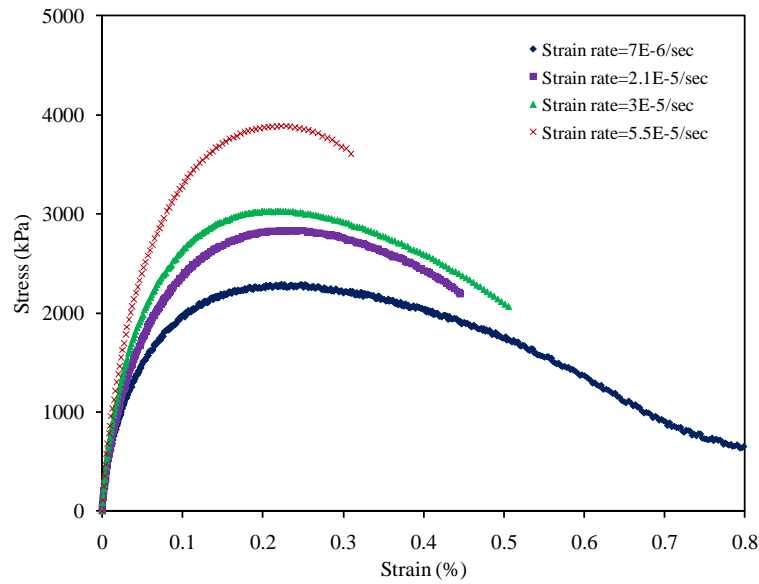
Figure 7.19. Stress-strain curves at 5°C which have been used in identifying the viscodamage model parameters.

Now, let one assume the following form for the rate of the damage density as a function of the normalized effective damage force and strain:

$$\dot{\phi} = \Gamma^{vd} f_1\left(\frac{\tilde{Y}}{Y_0}\right) f_2\left(\tilde{\varepsilon}\right) \tag{7.14}$$

where Y_0 is the damage force at the reference stress level which could be selected arbitrary.

Taking the natural logarithm of both sides implies:

$$Ln\left(\dot{\phi}\right) = Ln\left(\Gamma^{vd}\right) + Ln\left[f_1\left(\frac{\tilde{Y}}{Y_0}\right)\right] + Ln\left[f_2\left(\tilde{\varepsilon}\right)\right] \tag{7.15}$$
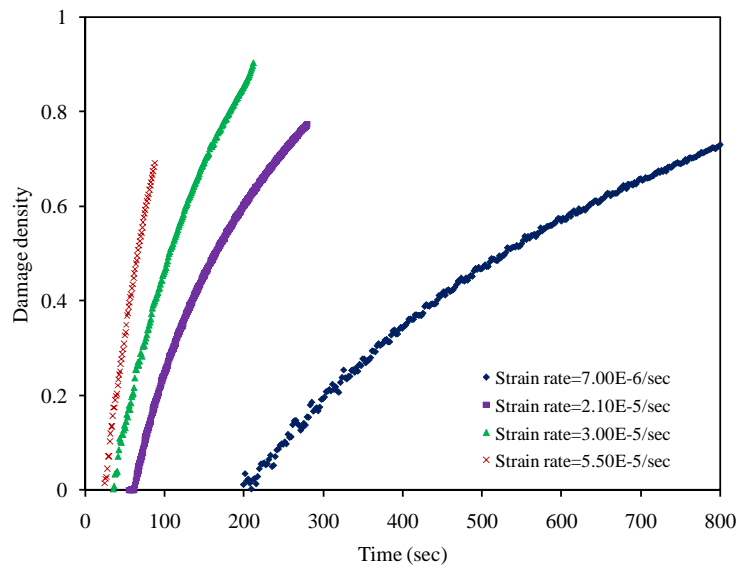
(a)
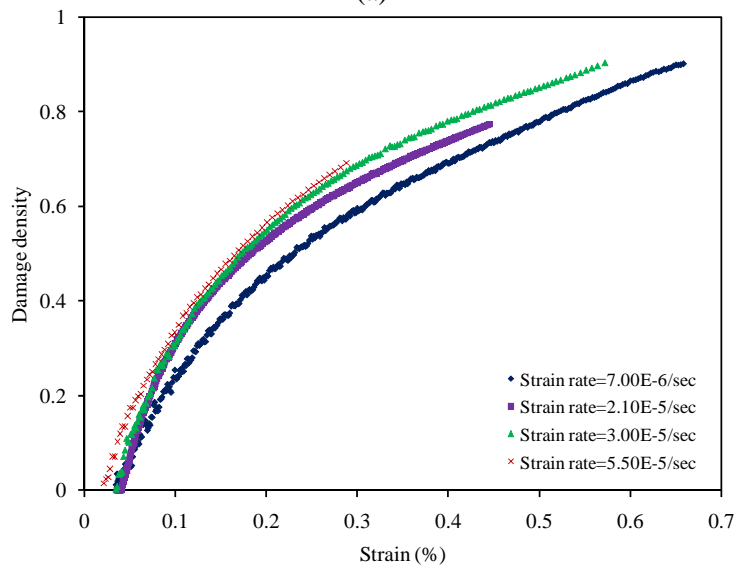
(b)

Figure 7.20. The identified damage density versus time and strain for different constant strain rate tests at 5°C.

Now, as shown in Figure 7.21, one can simply plot the rate of the damage density versus strain using experimental measurements.
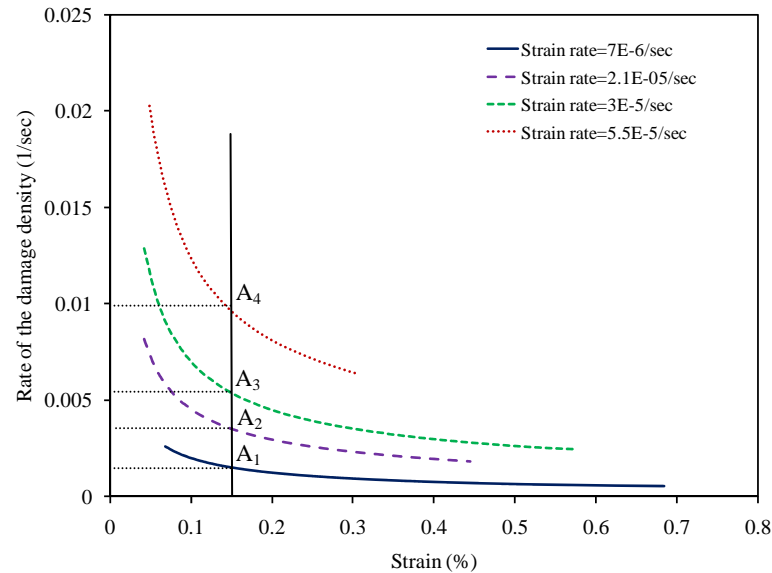
Figure 7.21. Rate of the damage density versus strain for the constant strain rate tests at 5°C.

The first and the third terms in the right hand side of Eq. (7.15) will be constant if the strain level is kept constant. To examine the f_1 function, the values of the normalized effective damage force (i.e. $\tilde{Y}/Y_0$) at four strain levels (i.e. 0.1, 0.15, 0.2, 0.25, 0.3%) are plotted versus the damage rate for several strain rates (Figure 7.22). For example, the line of 0.15% strain level in Figure 7.22 corresponds to points A_1-A_4 at Figure 7.21. Figure 7.22 clearly shows that the natural logarithm of the damage rate changes linearly with the natural logarithm of the normalized effective damage force for different strain levels. Surprisingly, the slope at all strain level lines is the same and the lines are parallel. Note that each point of the line at a fixed strain level corresponds to a constant strain rate test. Therefore, each curve at a specific strain level consists of the data at all four strain rate. Although Figure 7.22 is plotted at five different strain levels using four different constant strain rate tests, the slope of the lines are constant and the lines are parallel. This Figure clearly suggests the following form for the function f_1, such that:

$$f_1\left(\frac{\tilde{Y}}{Y_0}\right) = \left(\frac{\tilde{Y}}{Y_0}\right)^q \tag{7.16}$$

where q is the slope of the lines. Furthermore, the interception of each strain level line with the Y-axis is the summation of the first and the third terms of the right hand side of Eq. (7.15) at that strain level. Therefore, the term $Ln\left(\Gamma^{vd}\right)$ and subsequently the parameter Γ^{vd} can be identified since the strain level at each strain level line is given.
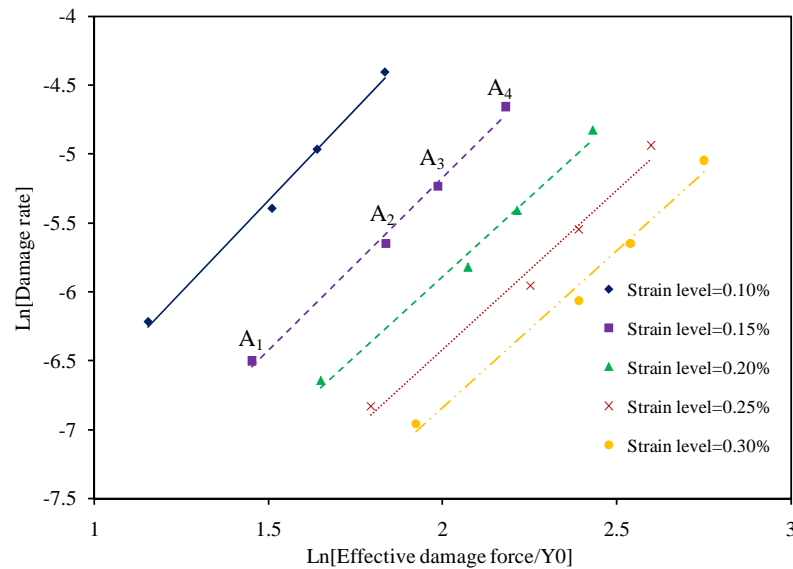
Figure 7.22. Plot of the damage rate versus the normalized effective damage density for identification of the parameters q and Γ^{vd}.

This procedure allows the identification of the parameter q independent of the other viscodamage parameters.

Similarly, as shown in Figure 7.23, one can plot the rate of the damage density versus the effective damage force using the experimental measurements and Eq. (7.12).
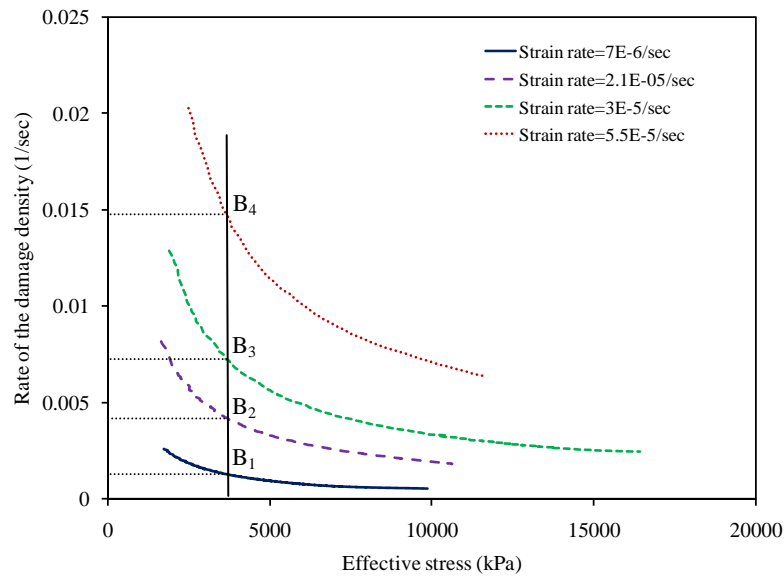
Figure 7.23. Rate of the damage density versus the effective damage force $\tilde{Y}$ for constant strain rate tests at 5°C.

The first and the second terms of the right side of Eq. (7.15) are constant if the effective damage force is kept constant. Therefore, one can fix the effective stress, and therefore the effective damage force, and plot the damage rate versus strain for the fixed values of the damage force in order to specify the function f_2. This plot is presented in Figure 7.24. The line of 3000kPa effective stress in Figure 7.24 corresponds to points B_1-B_4 at Figure 7.23. Figure 7.24 also shows that the changes in the rate of the damage density versus strain for constant effective stress are linear. Therefore, the function f_2 will have the following form with k being the slope of the lines in Figure 7.24.

$$f_2\left(\tilde{\varepsilon}\right) = \tilde{\varepsilon}^k \tag{7.17}$$
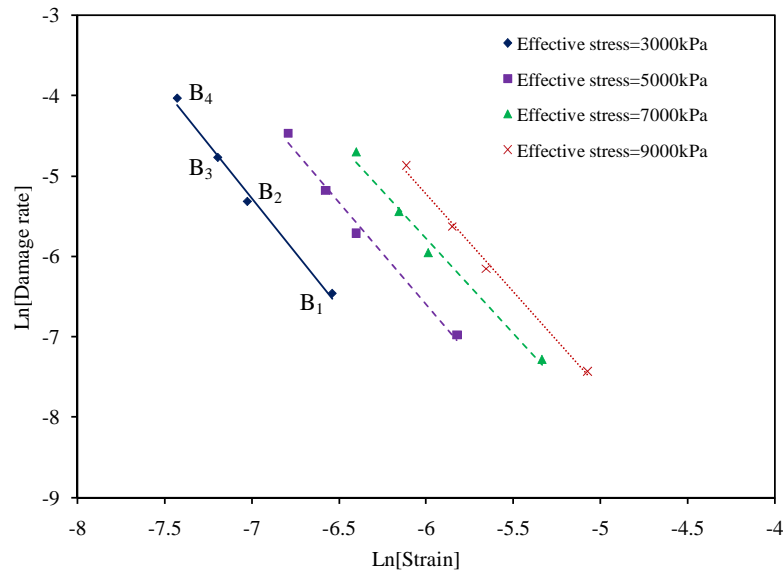
Figure 7.24. Plot of the damage rate versus the strain for identification of the parameters k and Γ^{vd}.

The interception with the Y-axis at a specific effective stress corresponds to the summation of the first and the second terms in right side of Eq. (7.15). Therefore, the viscodamage viscosity parameter Γ^{vd} can be identified for each line of the effective stress in Figure 7.24. It is interesting that the viscodamage viscosity parameters identified from different lines of Figures 7.22 and 7.24 ranges between $10^{-12} - 6 \times 10^{-12}$ /sec with the average of 4×10^{-12}/sec which shows the robustness of the presented procedure for identification of the viscodamage model parameters. Therefore, the viscodamage model presented in Chapter II is slightly modified such that the exponential term of the effective strain is substituted by a power law. This change has been made since the experimental data did not show a linear correlation between $Ln(\dot{\phi})$ and strain ε [please see Figure 7.25] such that the exponential-type functions are not a reasonable form for the f_2 function.

Note that the viscodamage model parameters are identified at 5°C, whereas, the viscoelastic and viscoplastic parameters are expressed at the reference temperature (i.e. $T_0 = 10^{o}C$). Therefore, the viscodamage model parameters are shifted to the reference

temperature using the same time-temperature shift factor identified from the dynamic complex compliance test by scaling the viscodamage viscosity parameter such that $\Gamma^{vd}\left(10^{o}C\right)=\Gamma^{vd}\left(5^{o}C\right)\times a_{T}\left(5,T_{0}=10^{o}C\right)$. The assumption for this conversion is that the same time-temperature shift factor can also be used for the damage model. This issue will be investigated with more details in the following subsections. The viscodamage model parameters at the reference temperature are listed in Table 7.8.
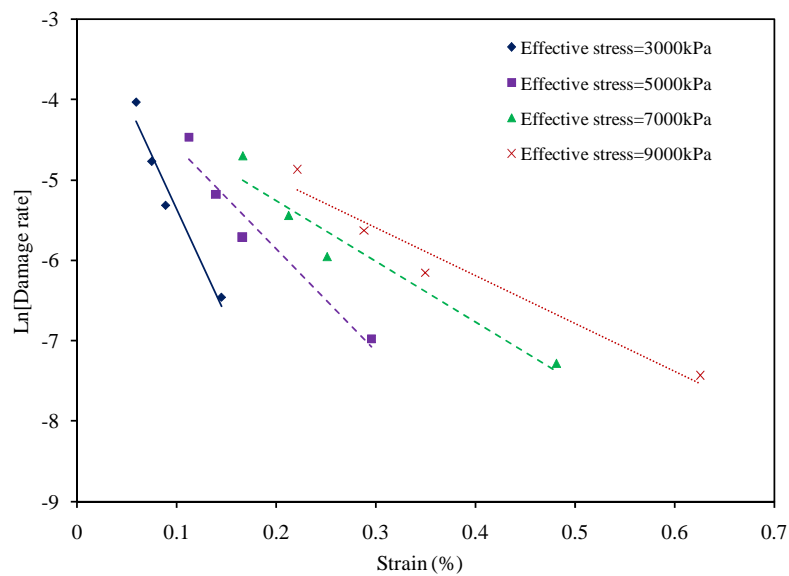
Figure 7.25. Plot of the natural logarithm of the damage rate versus strain for different strain rates at 5°C showing that the damage rate does not correlate with an exponential function of strain.

Table 7.8. Viscodamage model parameters at the reference temperature $T_{0}=10^{o}C$. (Note that these parameters are obtained using the viscodamage parameters identified at 5°C and the time-temperature shift factor identified from dynamic modulus test).

Γ^{vd} sec^{-1}	Y_{0} kPa	q	k
2.14×10^{-11}	1000	2.41	-2.53

7.7. Validation of the Model against the Uniaxial Constant Strain Rate Tests in Tension

The identified thermo-viscoelastic-viscoplastic-viscodamage model parameters are used to validate the model against the constant strain rate tests at different temperatures and strain rates. Figure 7.26 shows the model prediction and experimental measurements for the constant strain rate tests at 5°C and at different strain rates. It should be noted that the same time-temperature shift factor identified from the dynamic modulus test is used for all components of the model (i.e. viscoelastic-viscoplastic-viscodamage). Figure 7.26 clearly shows that the model is capable of predicting the rate-dependent response of asphalt mixes. It should be noted that the experimental measurements shown in Figure 7.26 have been used to identify and calibrate the viscodamage model parameters.

(a)

Figure 7.26. Model predictions and experimental measurements for the constant strain rate test in tension at 5°C when strain rates are: (a) 7×10^{-6}/sec; (b) 2.1×10^{-5}/sec; (c) 3×10^{-5}/sec; (d) 5.5×10^{-5}/sec.

Figure 7.26. Continued.

Moreover, the model is also used to predict the response of the asphalt mixes subjected to constant strain rate tests at 12°C, 25°C, and 40°C as well. Figure 7.27 shows the model predictions and experimental measurements for two strain rates at 12°C. Figures 7.27 (a) and (b) show that the model predictions agree well with the experimental data when the damage is activated. The plots of the damage density versus strain for the constant strain rate tests at 12°C are shown in Figure 7.28.

Figure 7.27. Model predictions and experimental measurements for the constant strain rate test in tension at 12°C when strain rates are: (a) 2.7×10^{-4}/sec; (b) 4.6×10^{-4}/sec.

Furthermore, Figure 7.29 shows further validation of the model at 25°C and for four different strain rates. Also, Figure 7.30 shows the predicted damage density versus strain for different strain rates at 25°C.
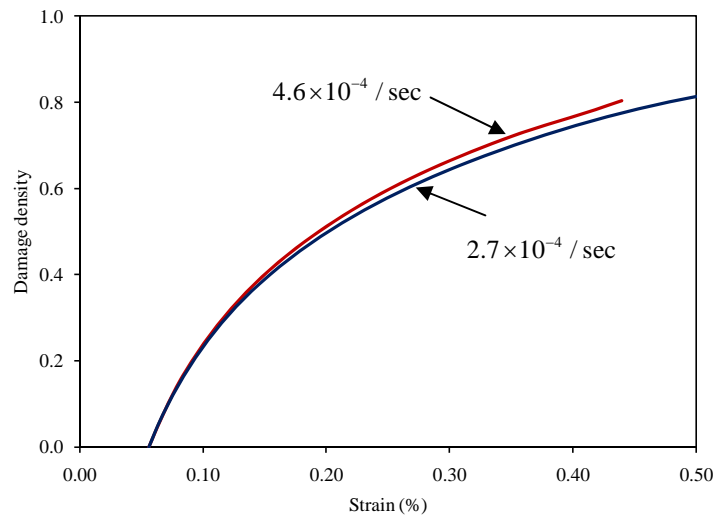
Figure 7.28. Predicted damage density versus strain for the constant strain rate test at 12°C.
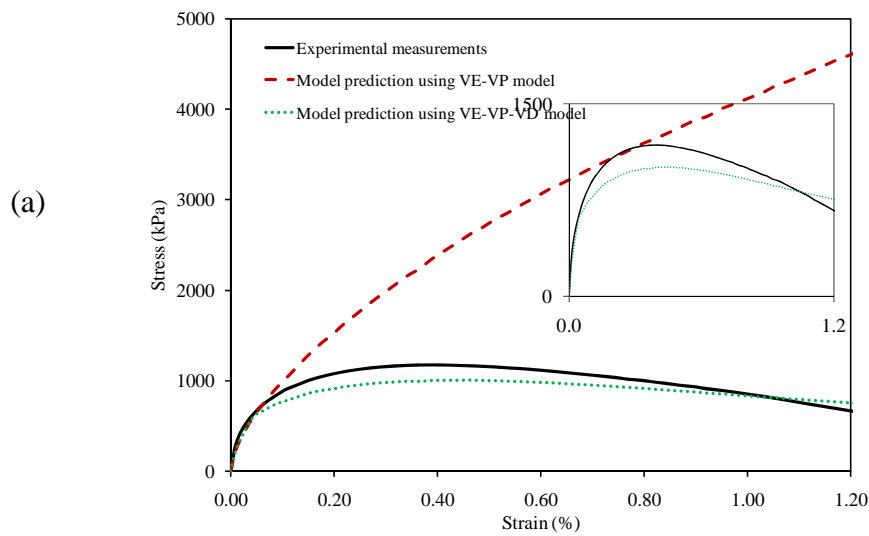
Figure 7.29. Model predictions and experimental measurements for the constant strain rate test in tension at 25°C when strain rates are: (a) 5×10^{-4}/sec; (b) 1.5×10^{-3}/sec; (c) 4.5×10^{-3}/sec; (d) 1.35×10^{-2}/sec.

Figure 7.29. Continued.
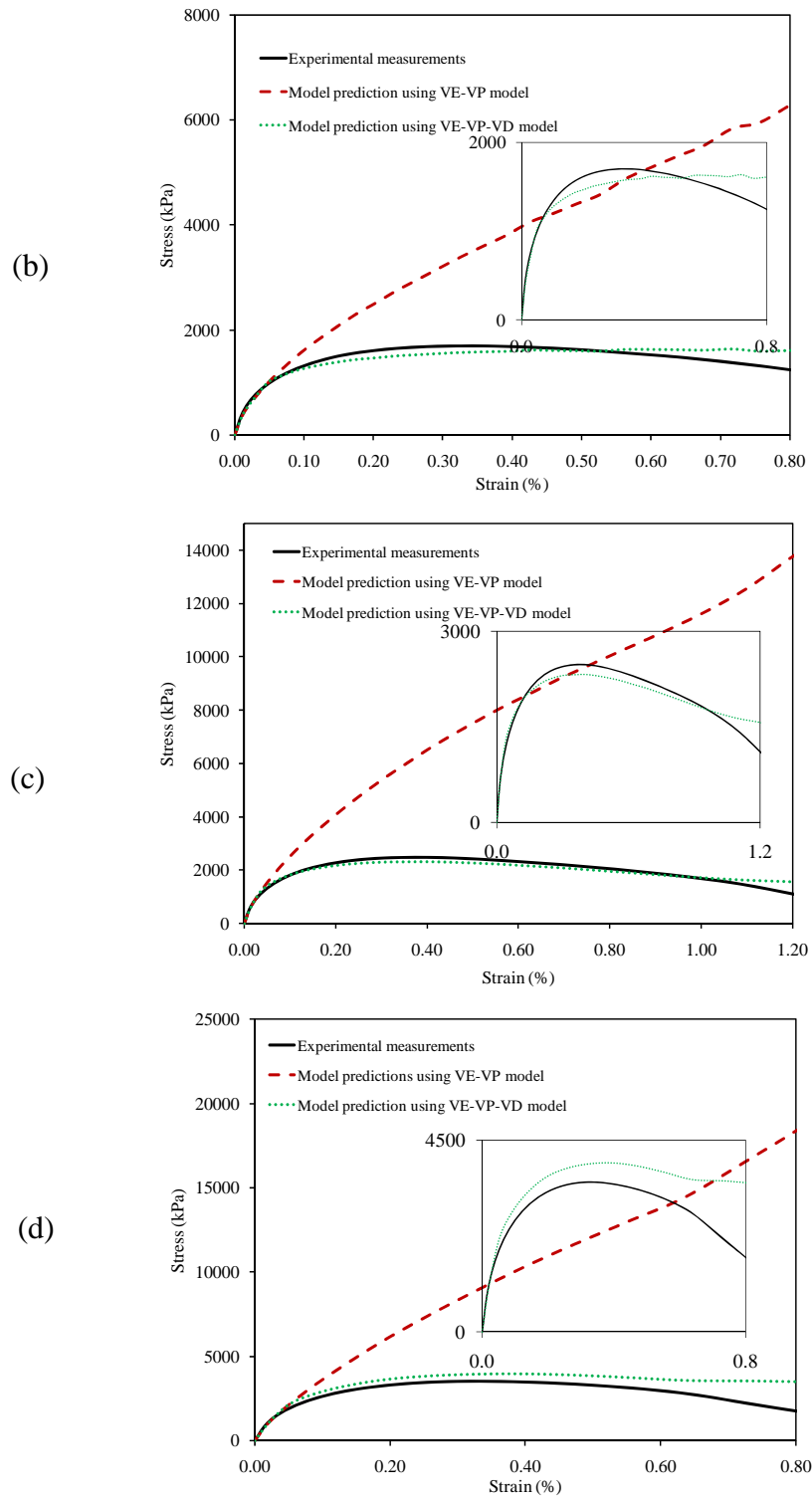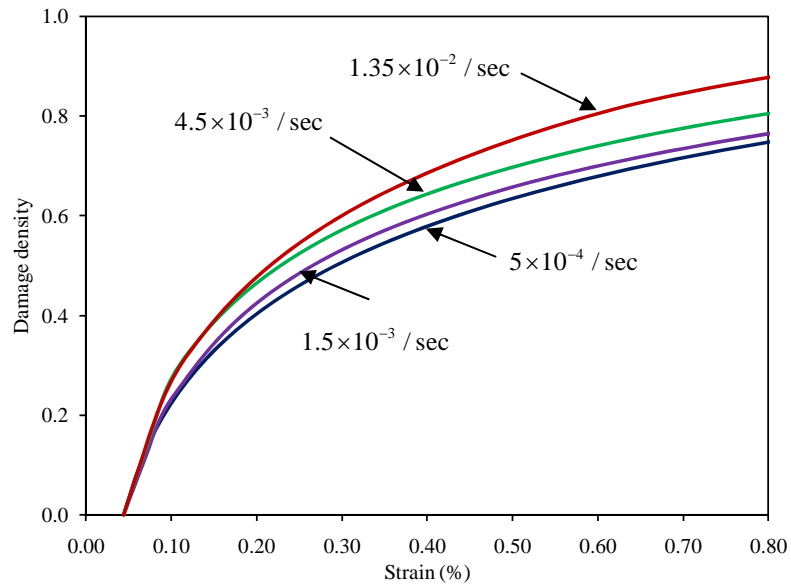
Figure 7.30. Predicted damage density versus strain for the constant strain rate test at 25$^\mathrm{o}$C.

The model is further validated at 40$^\mathrm{o}$C for the constant strain rate test at several strain rates. Figure 7.31 shows the model predictions and experimental measurements for the stress-strain response at several strain rates. As it is shown in Figure 7.31 model agrees well with the experimental data.
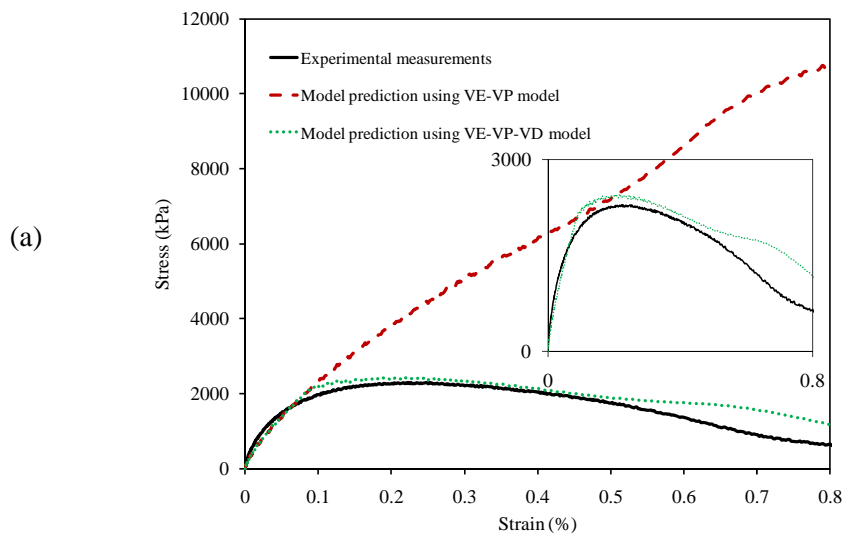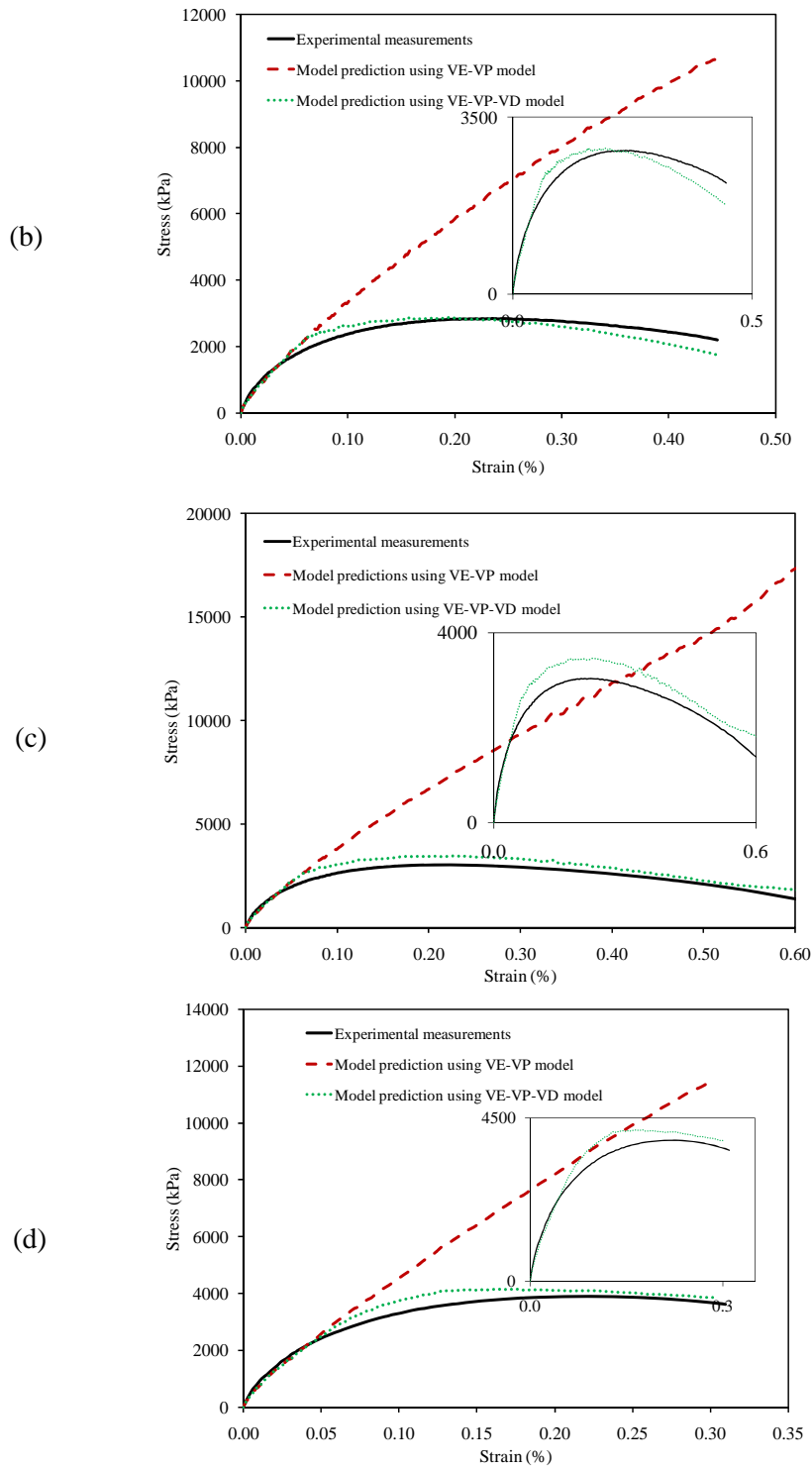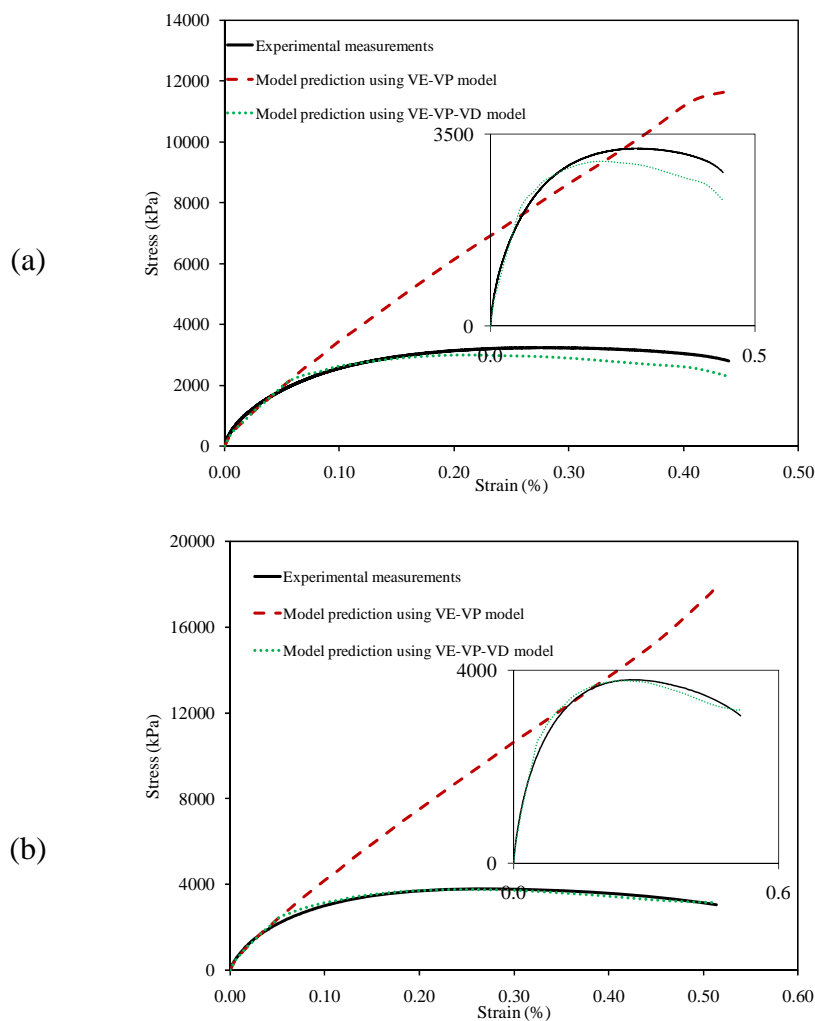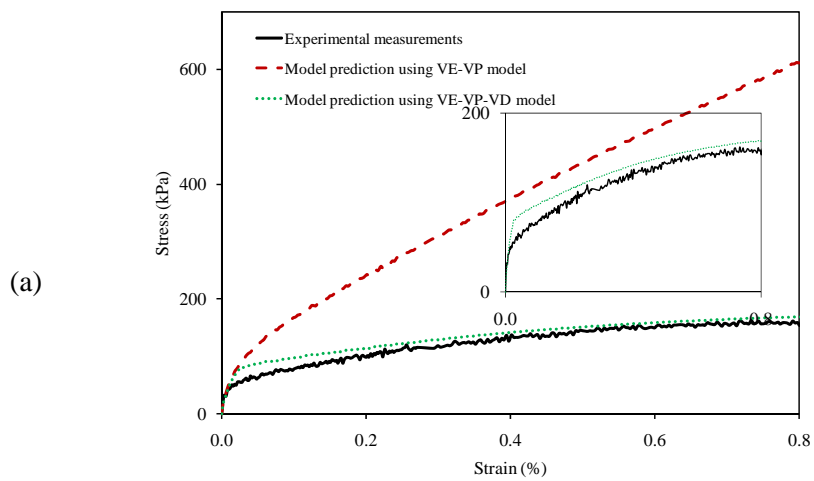

Figure 7.31. Model predictions and experimental measurements for the constant strain rate test in tension at 40$^\mathrm{o}$C when strain rates are: (a) 3×10^{-4}/sec; (b) 10^{-3}/sec; (c) 3×10^{-3}/sec.

(b)

(c)

Figure 7.31. Continued.
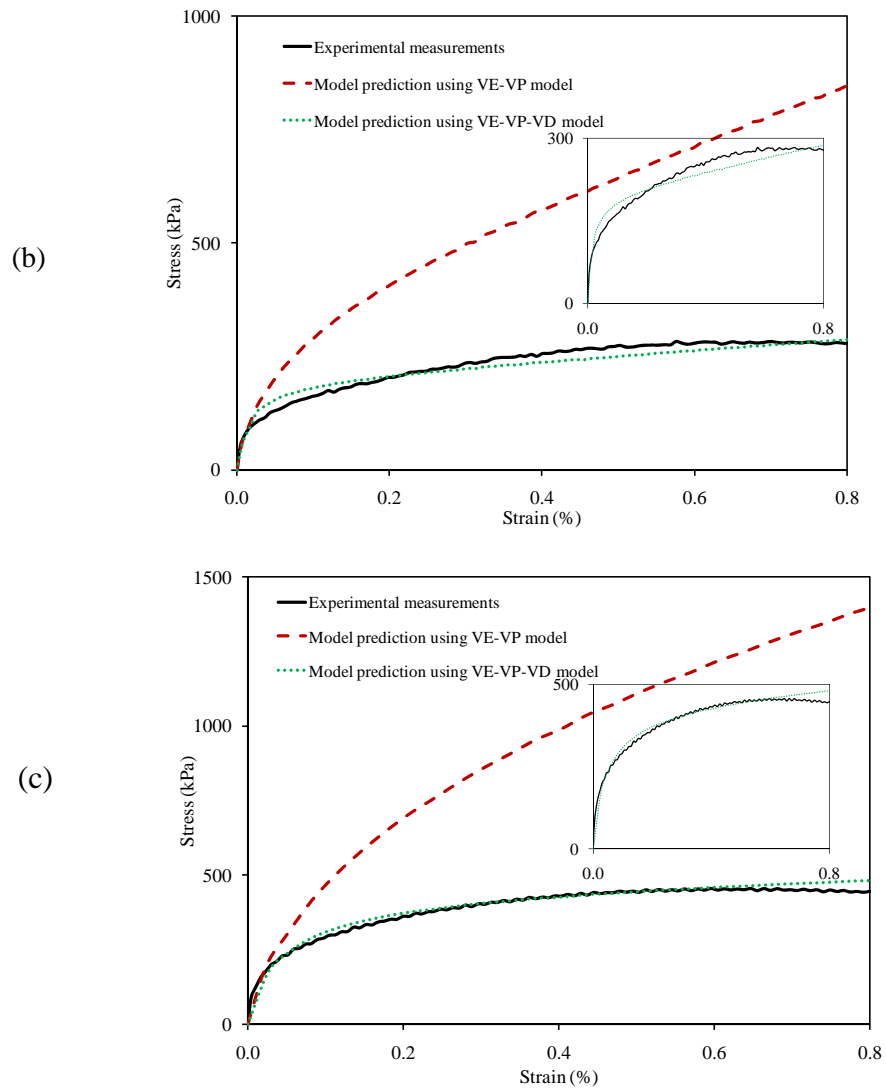
Moreover, the damage density versus strain is plotted in Figure 7.32.
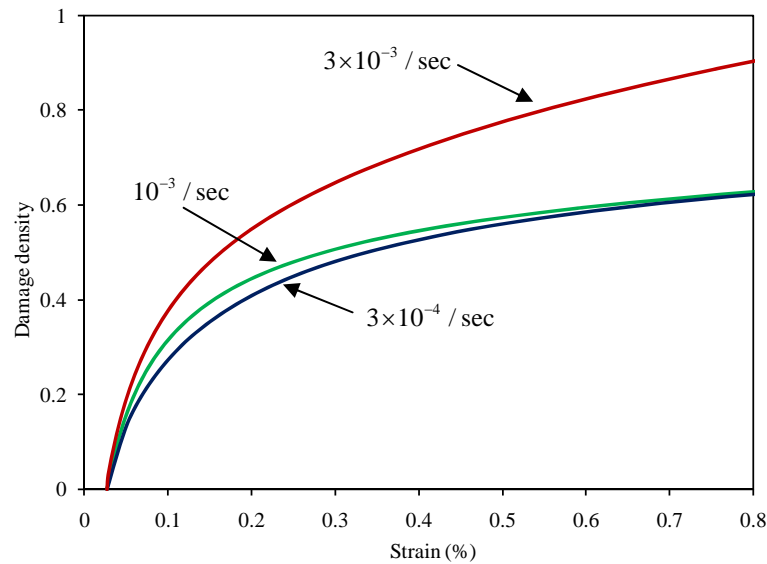
Figure 7.32. Predicted damage density versus strain for the constant strain rate test at 40°C.

Figures 7.20, 7.28, 7.30, and 7.32 clearly show that the model predicts higher damage value at fixed strain levels as the strain rate increases. This is in agreement with experimental measurements on asphalt mixes. Predictions presented in this section clearly shows that the proposed damage model is capable of predicting the rate- and temperature response of asphalt mixes subjected to monotonic loading. Moreover, it is usually recommended to identify the damage model parameters at low temperatures for which the material is expected to undergo severe micro-cracking as the strain level increases. The reason is that if the model can predict the severe damage condition, it might also perform well at higher temperatures for which the rate of the damage growth decreases.

The viscoelastic-viscoplastic-viscodamage model parameters along with the time-temperature shift factors are also used to predict the response of the asphalt mixes subjected to cyclic loading at 5 and 19°C. However, it should be mentioned that the time-temperature shift factors for the damage model at 12°C, 19°C, 25°C, and 40°C are assumed to be slightly different from the time-temperature shift factor identified from the dynamic modulus test. However, this difference is negligible such that one can consider the asphalt mix used in this study a thermo-rheological simple material for

viscoelastic, viscoplastic, and viscodamage components. Figure 7.33 shows the comparison between the time-temperature shift factors for the damage model and the viscoelastic-viscoplastic model.
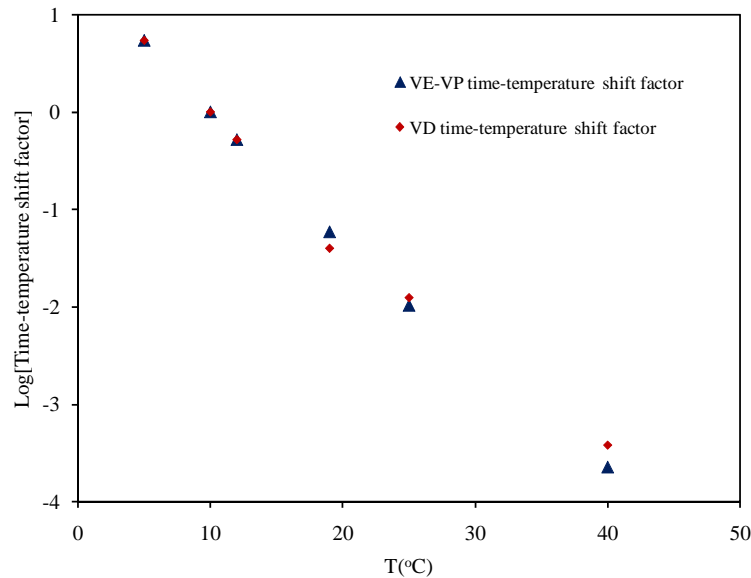
Figure 7.33. Comparison of the viscodamage time-temperature shift factor and the viscoelastic-viscoplastic time-temperature shift factor (identified from dynamic modulus test) when the reference temperature is 10°C.

7.8. Validation of the Model against the Cyclic Stress Controlled Tests in Tension

The model is further validated against the cyclic stress controlled tests in tension. This test is performed at 5°C and 19°C and for multiple stress amplitude. This test applies a cyclic stress input with the frequency of 4cycles/sec, such that the stress input can be written as follows:

$$\sigma = -\frac{\sigma_{\max}}{2} + \frac{\sigma_{\max}}{2}\cos(8\pi t) \tag{7.18}$$

where $\sigma_{\max}$ is the stress amplitude. The schematic presentation of the stress history in this test is shown in Figure 7.34. t_f in Figure 7.34 can be considered as the failure time. The number of loading cycles until which the material fails is therefore $4 \times t_f$.

Figures 7.35(a) and (b) show the model predictions using viscoelastic-viscoplastic model and the experimental measurements at initial loading cycles and intermediate loading cycles for 750kPa stress amplitude, respectively. Figure 7.35(a) shows that the model agrees reasonably well with experimental data for initial cycles. However, as shown in Figure 7.35(b), model predictions deviates significantly from the experimental data. This deviation should be compensated for with the viscodamage model. As shown in Figure 7.36, the viscodamage component significantly enhances the prediction of the cyclic response of asphalt mixes at large number of loading cycles.
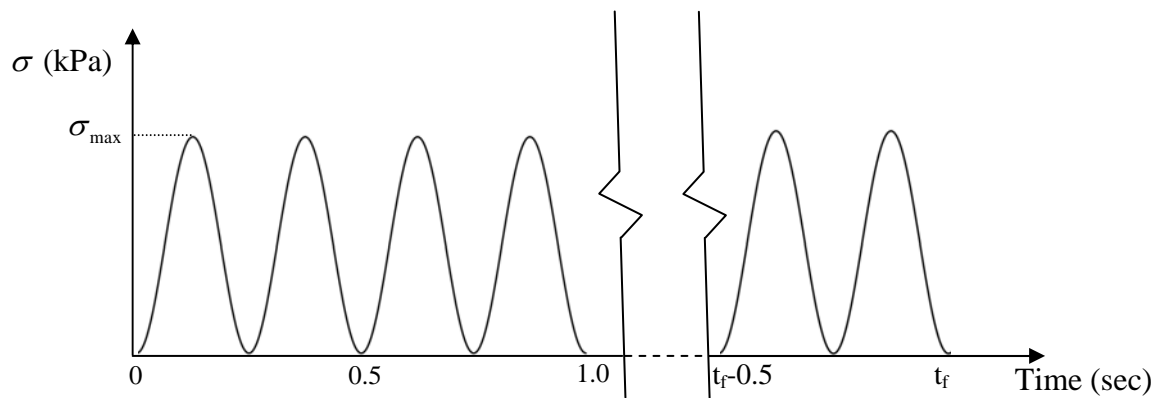
Figure 7.34. Schematic representation of loading history for Controlled Stress cyclic test in tension.

Figure 7.37 shows the model predictions and experimental data of the strain response for the cyclic stress control test at 19°C when the stress amplitude is 750kPa.
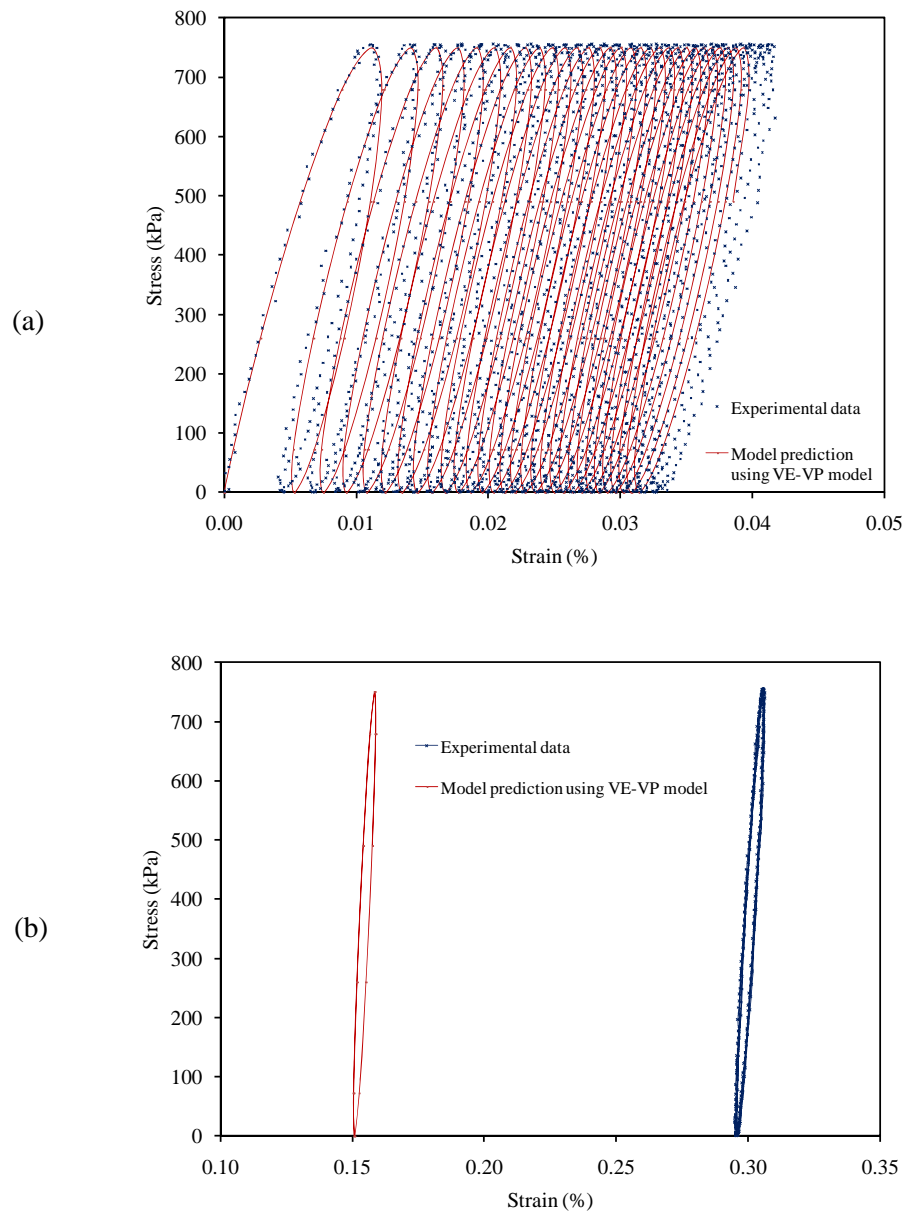
Figure 7.35. Compasrison of the model prediction using viscoelastic-viscoplastic model and experimental data for the cyclic stress control test at 19°C when the stress amplitude is 750kPa. (a) Loading cycles 1-30; (b) Loading cycles 970-980.
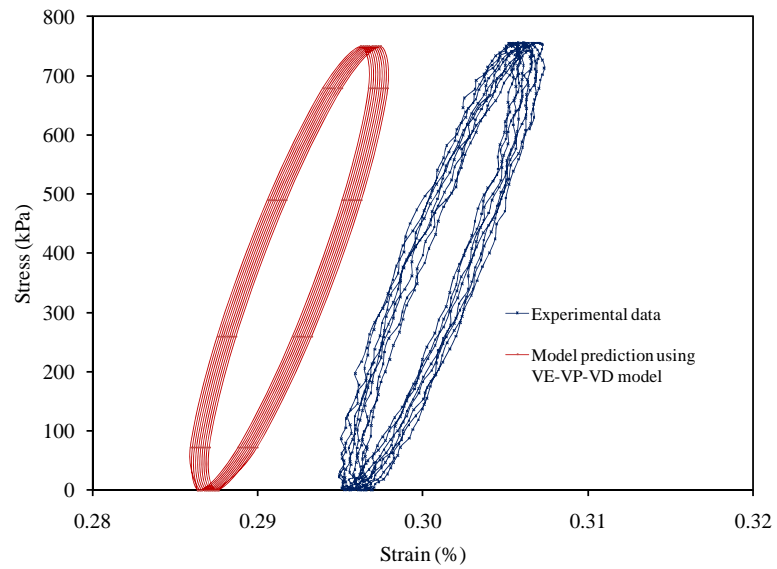
Figure 7.36. Comparison of the VE-VP-VD model prediction and experimental data for loading cycles 970-975 at 19°C when the stress amplitude is 750kPa.
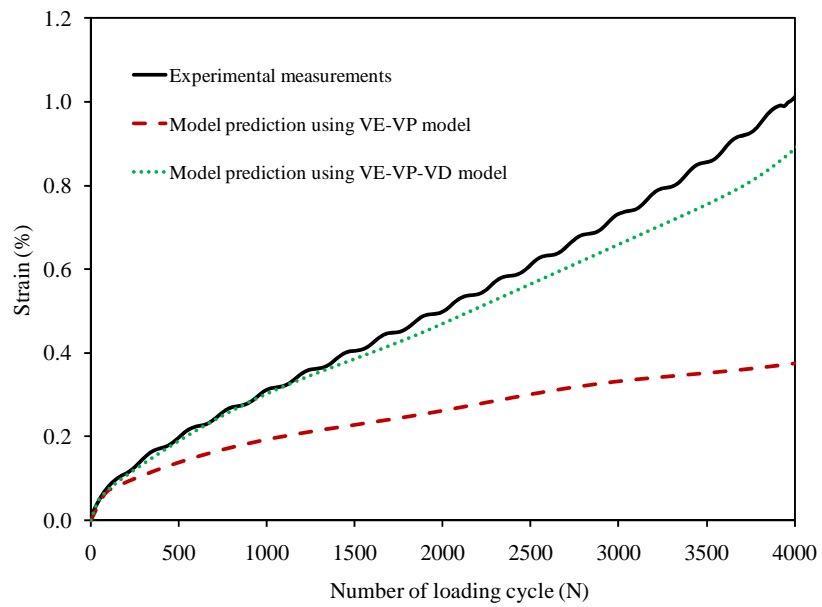
Figure 7.37. Comparison of the experimental data and model predictions with and without damage component for the strain response in the cyclic stress control test at 19°C when the stress amplitude is 750kPa.

Moreover, Figure 7.38 shows model predictions and experimental measurements for the same test and temperature when the stress amplitude is 250 kPa.
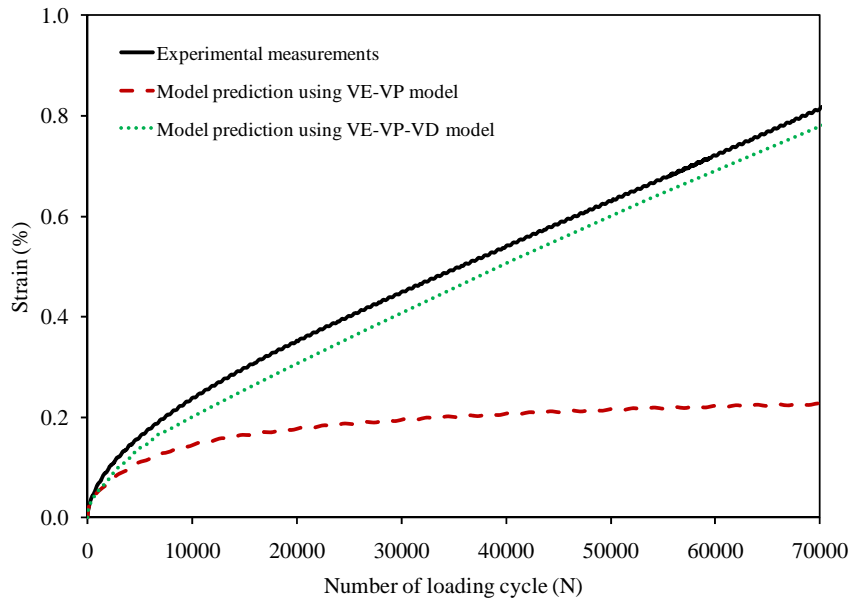
Figure 7.38. Comparison of the experimental data and model predictions with and without damage component for the strain response in the cyclic stress control test at 19°C when the stress amplitude is 250kPa.

Figure 7.38 shows that the model prediction without damage saturates very fast and significantly underestimates the experimental measurements. However, model predictions agree reasonably well when the viscodamage component of the model is activated. The NCSU database also includes the cyclic control stress test at 5°C when the stress amplitude is 1525kPa. The identified model predictions along with the time-temperature shift factors shown in Figure 7.33 are used to predict the strain response of the cyclic control stress test at 5°C. As shown in Figure 7.39, the presented thermo-viscoelastic-viscoplastic-viscodamage model is capable of predicting the cyclic response of the asphalt mixes at different temperatures. Although Figures 7.37-7.39 show that the damage model slightly underestimates the experimental measurements, it significantly enhances the model predictions without the damage model.
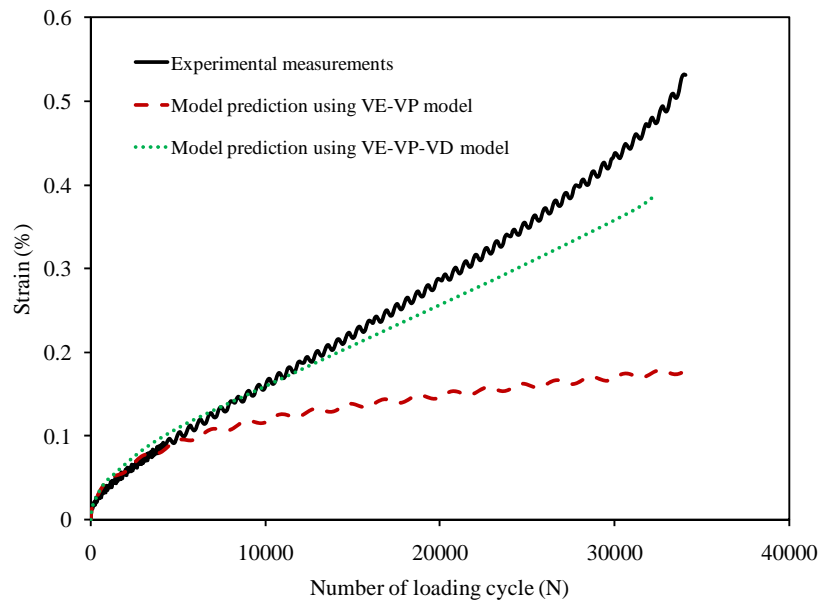
Figure 7.39. Comparison of the experimental data and model predictions with and without damage component for the strain response in the cyclic stress control test at 5°C when the stress amplitude is 1525kPa.

7.9. Validation of the Model against the Cyclic Strain Controlled Tests in Tension

It is usually very difficult to conduct the cyclic strain controlled tests. The reason is that for the stress controlled tests, one can apply the stress to the specimen by controlling the applied force from the machine ram. However, although one can control the applied strain from the machine ram, the strain at the middle of the specimen is not the same as the applied strain at the end of the specimen. This effect is referred to as the *end plate effects*. Therefore, the common practice is to apply the cyclic controlled strain at the end of the specimens and measure the strain at the middle of the specimen using LVDTs. This test is referred to as controlled crosshead cyclic loading (refer to Kim et al., 2008). Figure 7.40 shows the schematic representation of the strain input for the controlled crosshead cyclic loading.
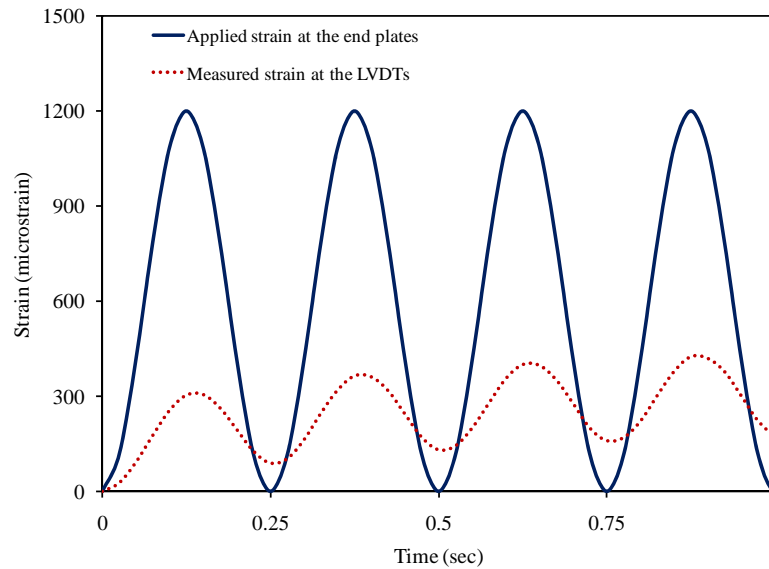
Figure 7.40. Schematic representation of the applied strain from the machine ram and the measured strain at the LVDTs for cyclic strain control tests.

The NCSU database includes cyclic strain controlled tests in tension at 5 and 19$^{\text{o}}$C and at several strain amplitudes. However, the frequency of the loading at 5$^{\text{o}}$C and 19$^{\text{o}}$C are 10 cycles/sec and 4 cycles/sec, respectively, such that the applied strain at the end of the specimen can be written as:

$$\varepsilon = -\frac{\varepsilon_{\max}}{2} + \frac{\varepsilon_{\max}}{2}\cos\left(2\pi f t\right) \tag{7.19}$$

where f is the frequency which is 4cycles/sec and 10cycles/sec at temperatures 19$^{\text{o}}$C and 5$^{\text{o}}$C, respectively.

As it is schematically shown in Figure 7.40, the measured strain at the LVDTs does not have constant amplitudes. Therefore, to simulate these tests, the measured strain values versus time are fed as the strain input into the Abaqus software. The identified viscoelastic-viscoplastic-viscodamage model parameters along with the time-temperature shift factors presented in Figure 7.33 are used to predict the cyclic strain controlled tests in tension. However, the constitutive models usually do not perform well in capturing the response for both stress and strain controlled tests. The reason is that the

controlled strain tests usually show initial responses which are related to initial stretch or initial densification of the material.

To capture this effect, the instantaneous compliance is adjusted such that the model predictions agree with the experimental data at initial cycles. Figure 7.41 shows the strain amplitude measured at the LVDTs for the cyclic strain controlled test when the strain amplitude applied at the end plates is 1200 $\mu\varepsilon$.
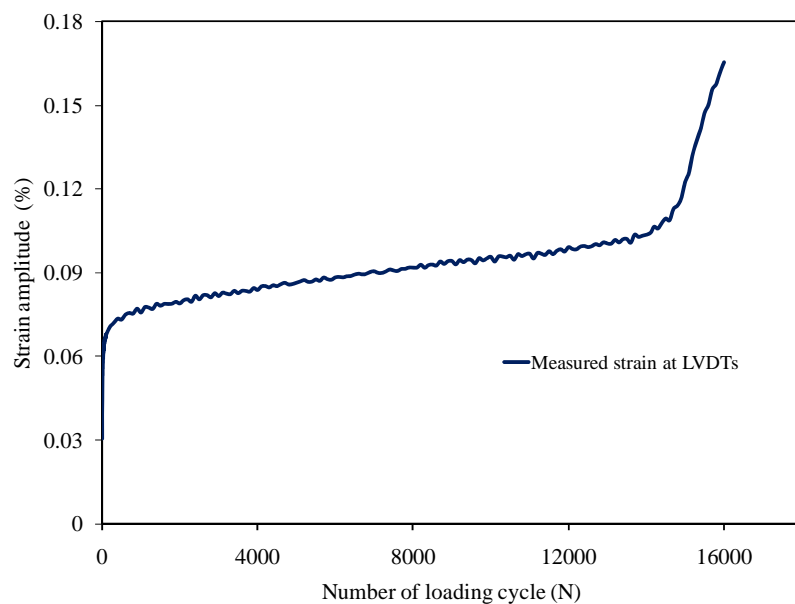
Figure 7.41. Measured strain amplitude at LVDTs for the cyclic strain controlled test when the applies strain amplitude at the end plates is 1200 $\mu\varepsilon$.

The identified VE-VP-VD model parameters along with the time temperature shift factors are used to predict the response for the cyclic strain controlled tests. Figure 7.42 (a) and (b) show the measured stress-strain response and the model predictions for initial and intermediate cycles, respectively.
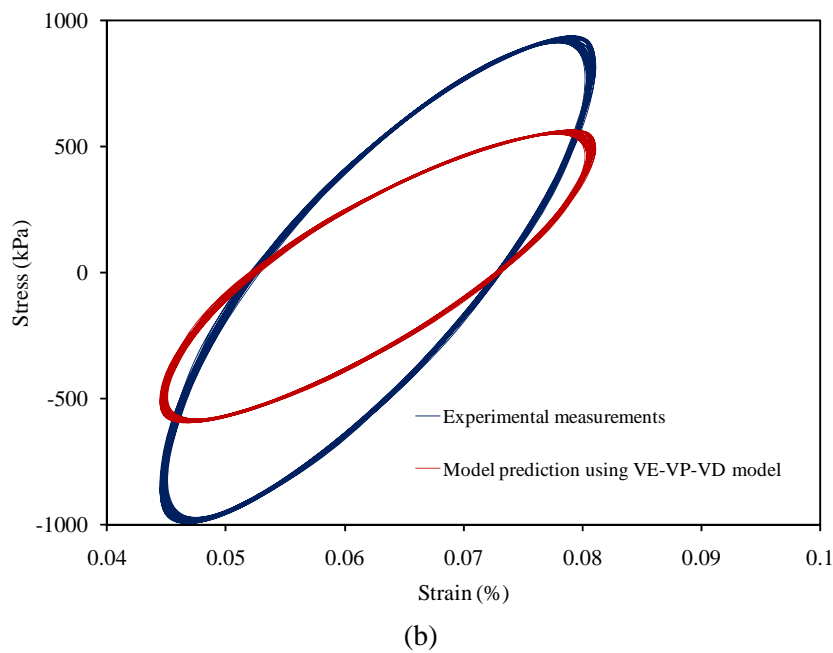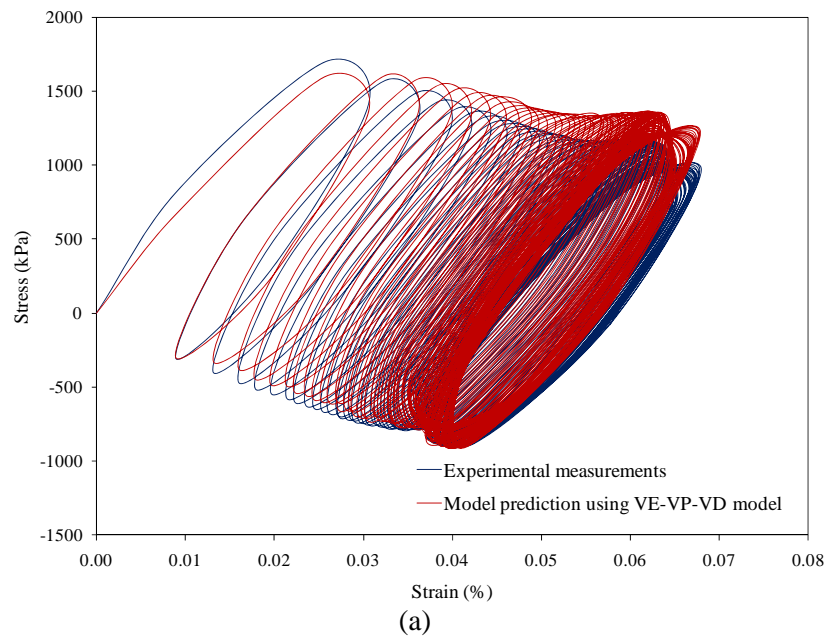
Figure 7.42. Measured and predicted stress-strain response for the cyclic strain controlled test when the strain amplitude applied at the end plates is 1200 $\mu\varepsilon$. (a) cycles 1-50; (b) cycles 22200-2250.

As shown in Figure 7.42 (a), the model predicts the experimental measurements well for the initial cycles. However, the VE-VP-VD model significantly underestimates the stress output as the number of loading cycles increase. Figure 7.43 shows the model prediction and experimental measurements for the stress amplitude versus number of loading cycles. Figure 7.43 shows that the model prediction using VE-VP model significantly overestimates the stress input, whereas, the model prediction using VE-VP-VD model significantly underestimates the stress output such that in predicts premature failure. In other words, the VE-VP-VD model significantly overestimates the damage parameter as compared to experimental measurements.
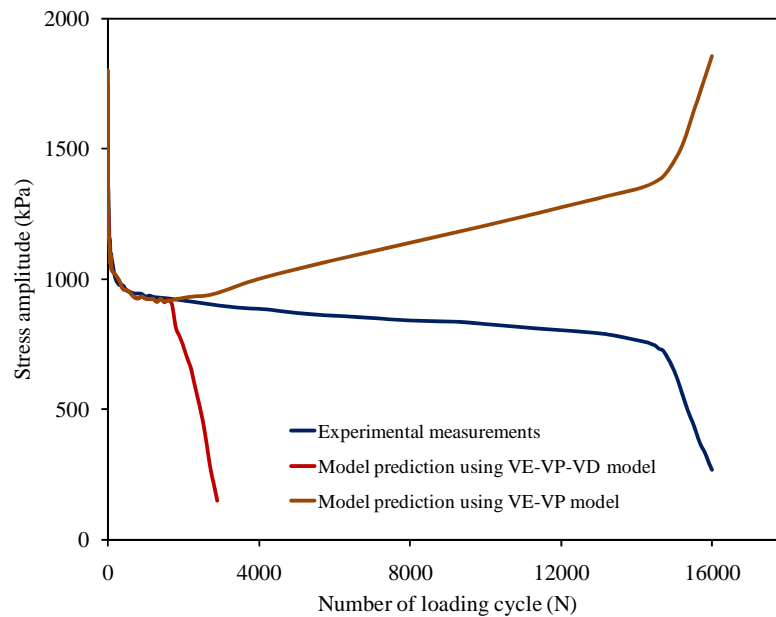
Figure 7.43. Measured and predicted stress amplitude for the cyclic controlled strain test when the applied strain amplitude at the end plates is 1200 $\mu\varepsilon$.

It is usually argued that the model parameters identified from the strain controlled tests do not yield satisfactory results for the stress controlled tests. However, as shown in previous subsections, the viscodamage model parameters are identified using the constant strain rate tests which are strain control tests. These model parameters resulted in satisfactory model predictions for both strain control tests (i.e. cyclic stress

controlled) and strain controlled tests with monotonic loading (i.e. constant strain rate tests). However, the model fails for the cyclic strain controlled tests. This issue is explained based on the viscoelasticity theory. Figure 7.44 shows schematic representation of the strain input and stress output for the cyclic strain controlled tests.
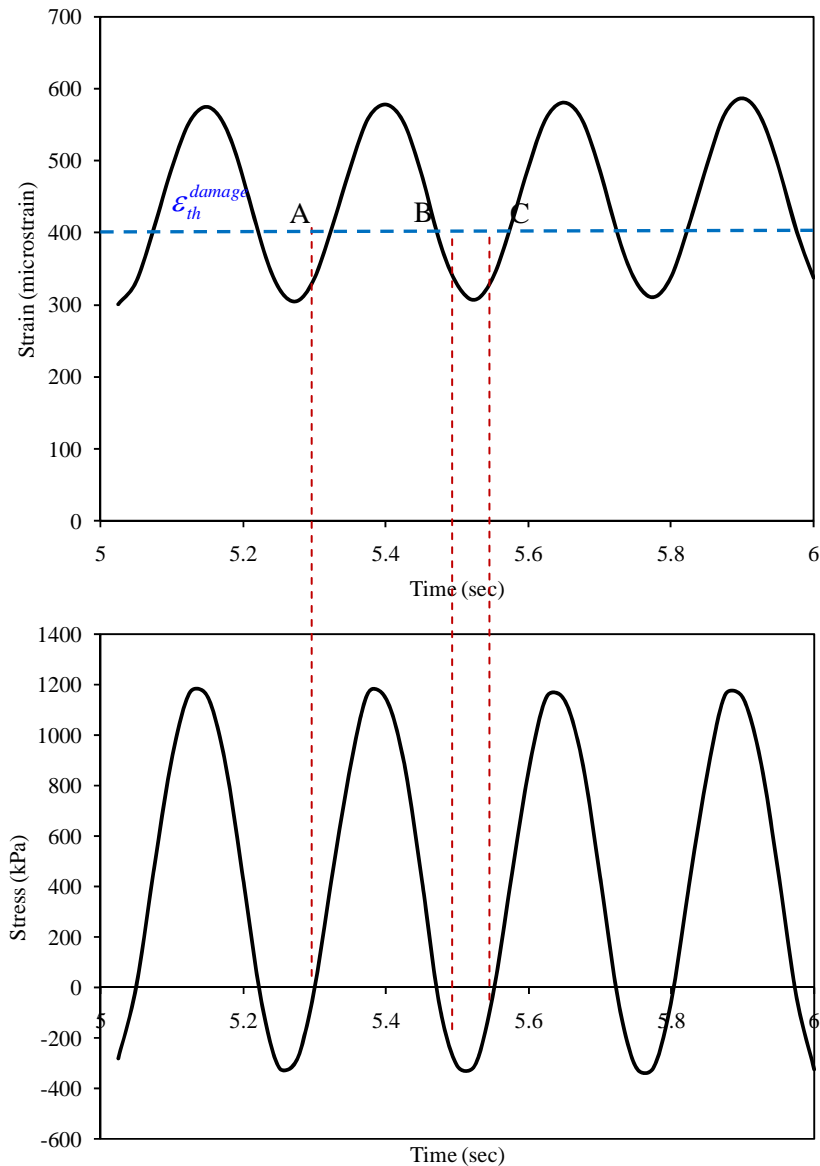
Figure 7.44. Schematic representation of the strain input and stress output for the cyclic strain controlled tests.

Let one assume that the damage occurs if the tensile strain is larger than the threshold value (i.e. $\varepsilon_{th}^{damage}$). Therefore, for strain values larger than $\varepsilon_{th}^{damage}$ damage may nucleate and propagate. For example, let one assume a very simple case where the material already contains a single crack with the length a_0 at point "A" as shown in Figure 7.45(a).

| a_0 | a | $a - \Delta a$ |

Point "A" Point "B" Point "C"
(a) (b) (c)
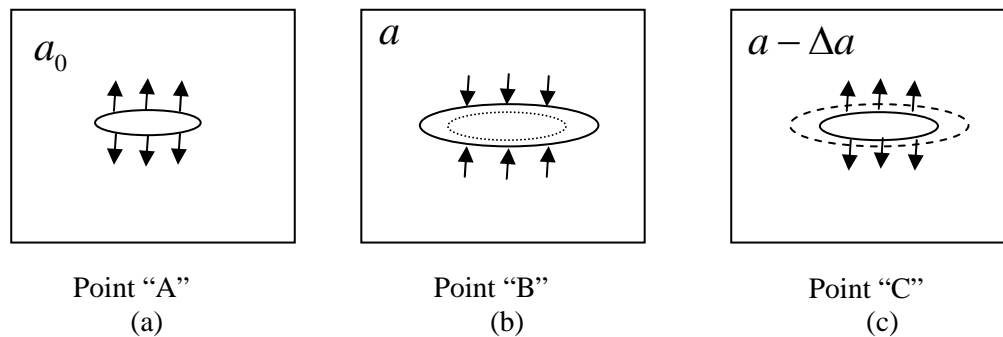
Figure 7.45. Schematic representation of crack growth and crack closure/healing in the cyclic strain controlled tests (Points shown in this figure correspond to the points shown in Figure 7.44).

The strain remains larger than $\varepsilon_{th}^{damage}$ when moving from point "A" to point "B" as shown in Figure 7.44 (a) such that the crack length increases to a_1 which is larger than a_0 as shown in Figure 7.45 (b). It should be noted that the stress is also tensile from point "A" and close to point "B" which also causes the crack to propagate and increase its length from a_0 to a. However, it is well-known that the viscoelastic materials have fading memory. In other words, during the loading stage (when strain rate is positive) the stress increases. However, the stress starts relaxing and fading away with time. On the other hand, during the unloading stage (when the strain rate is negative) the stress decreases such that at some point it becomes negative. The reason is that the resulted negative increment in the stress due to the decrease in the strain level in the unloading region is more than the resulted positive increment in the stress due to the increase in the strain level in the preceding loading region. In other words, a large portion of the

resulted positive stress increment in the preceding loading region has already faded away since it has been applied before the current unloading stage such that the decrease in the stress exceeds the increase in the stress and causes the material to feel compression although the total strain is still in tension. On the other hand, from point "B" to point "C" the strain value is less than the threshold damage strain $\varepsilon_{th}^{damage}$. Moreover, as discussed, the material feels compressive stress in this region. Therefore, as shown in Figure 7.45 (b) the crack faces tend to attract each other and create a bond. As a result, the crack length decreases from a at point "B" to $a - \Delta a$ at point "C". It should be noted that this phenomenon can be referred to as crack closure. However, as mentioned in the previous chapters, the asphalt binder and as a result the asphalt mixes has the tendency to heal at low strain levels. Moreover, moving from tensile stresses to compressive stresses may enhance the healing capabilities. Therefore, without inclusion of the healing component the induced damage is overestimated such that the model without healing model predicts unrealistic failure as shown in Figure 7.43. Since the time interval for which the strain values is less than the damage threshold strain $\varepsilon_{th}^{damage}$ and the tensile stress changes to compressive stress is short, a very simplified version of the healing model presented in Chapter V is postulated here to explain this distinct behavior, such that one can write:

$$\dot{h} = \Gamma^h \qquad (7.20)$$

where Γ^h is the healing viscosity parameter. As mentioned in Chapter V, the healing viscosity parameter should be identified from the repeated creep-recovery tests with rest periods. However, the NCSU database does not possess this test in tension. Therefore, the healing viscosity parameter is identified based on the deviation between the VE-VP-VD model predictions and experimental measurements. The identified healing parameters along with the VE-VP-VD model parameters and time-temperature shift factors are used to predict the cyclic strain controlled tests at different temperatures and for different strain amplitudes. The healing viscosity parameter is identified to be 6.5×10^{-3}/sec.

Figure 7.46 shows the measured stress-strain response and the model predictions with and without healing component for the intermediate cycles of the cyclic strain controlled test at 19°C when the applied strain amplitude is 1200 $\mu\varepsilon$. As shown in Figure 7.46, the healing model significantly enhances the prediction of the stress-strain response at intermediate cycles.
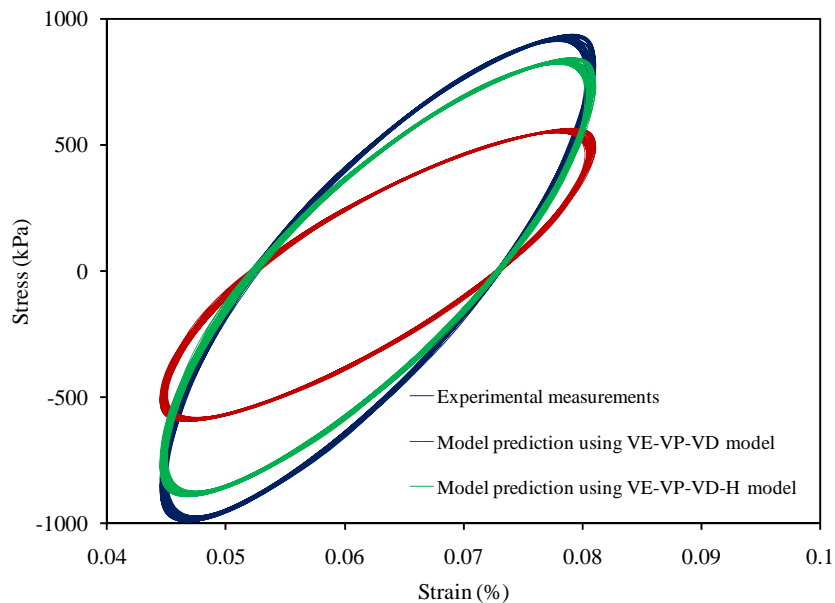
Figure 7.46. Measured and predicted stress-strain response at intermediate cycles (i.e. cycles 2200-2250) for the cyclic strain controlled test when the strain amplitude applied at the end plates is 1200 $\mu\varepsilon$.

Figure 7.47 shows the measured and predicted stress amplitude versus number of loading cycles at 19°C when the applied strain amplitude is 1200 $\mu\varepsilon$. This figure shows that the VE-VP-VD model predict the failure after 3500 loading cycles. However, the experimental measurements and model predictions with the healing component show that the material can tolerate the loading up to 16000 loading cycles.

Figure 7.48(b) shows the model predictions and experimental measurements for the stress amplitude for the cyclic strain controlled test at 19°C when the applied strain

amplitude at the end plates is 1500 $\mu\varepsilon$. The measured strain at LVDTs is shown in Figure 7.48 (a).
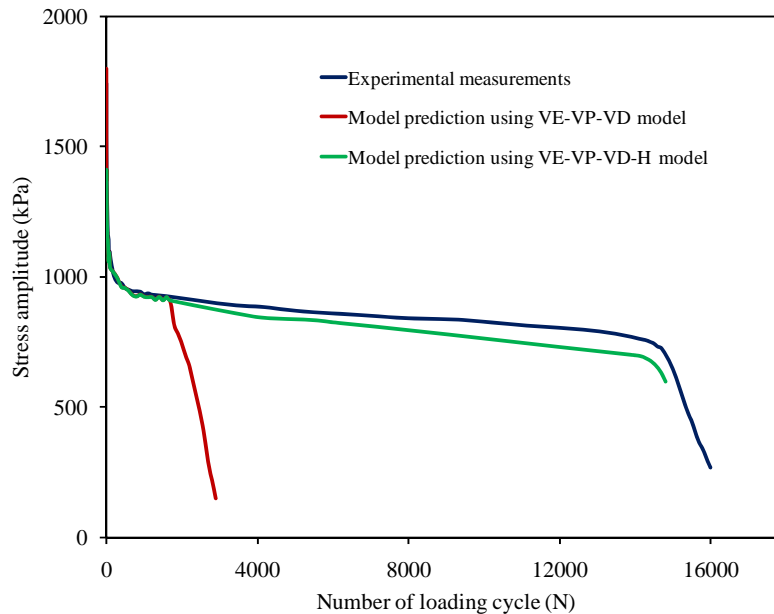
Figure 7.47. Measured and predicted stress amplitude for the cyclic controlled strain test when the applied strain amplitude at the end plates is 1200 $\mu\varepsilon$.

Figure 7.48(b) clearly shows that the inclusion of the healing in the constitutive model significantly enhances the model predictions for the cyclic strain controlled test.

The VE-VP-VD-H model parameters along with the time-temperature shift factors are used to predict the cyclic strain controlled test at 5°C. It should be noted that more experimental data is required to identify the healing and its associated temperature coupling term model parameters. However, the healing and damage time-temperature shift factors are assumed to be the same. Figure 7.49 (a) shows the measured LVDTs' strain amplitude at 5°C for the cyclic strain controlled test when the applied strain amplitude at the end plates is 1750 $\mu\varepsilon$. The experimental and model prediction for the strain history shown in Figure 7.49(a) is shown in Figure 7.49(b). The predictions shown in this chapter clearly show that the model can reasonably predict the time-, temperature-

and rate-dependent response of asphalt mixes under both monotonic and cyclic loading conditions.

(a)

(b)
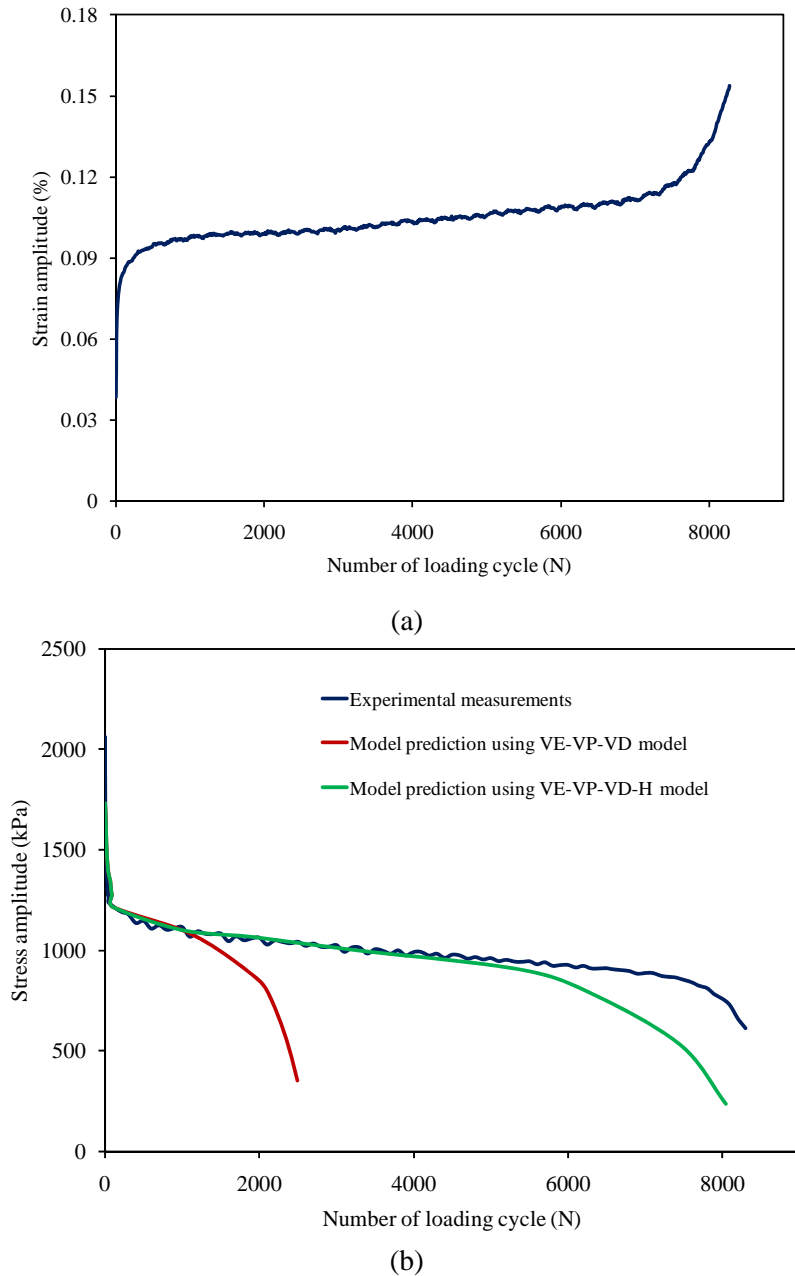
Figure 7.48. Experimental measurements and model predictions for the cyclic strain controlled test at 19°C when the applied strain amplitude at the end plates is 1500 $\mu\varepsilon$. (a) The amplitude of the measured strains at LVDTs versus the number of loading cycles; (b) The tensile stress amplitude versus number of loading cycles.
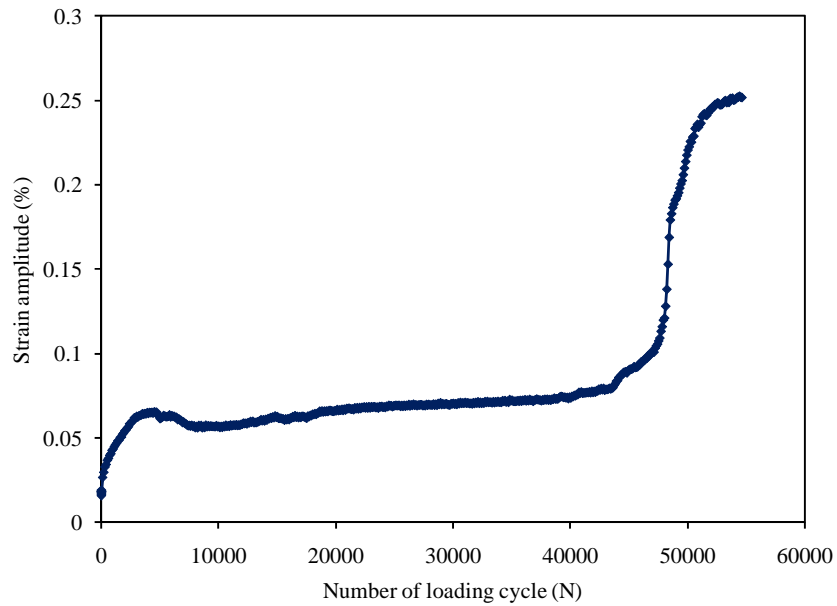
(a)
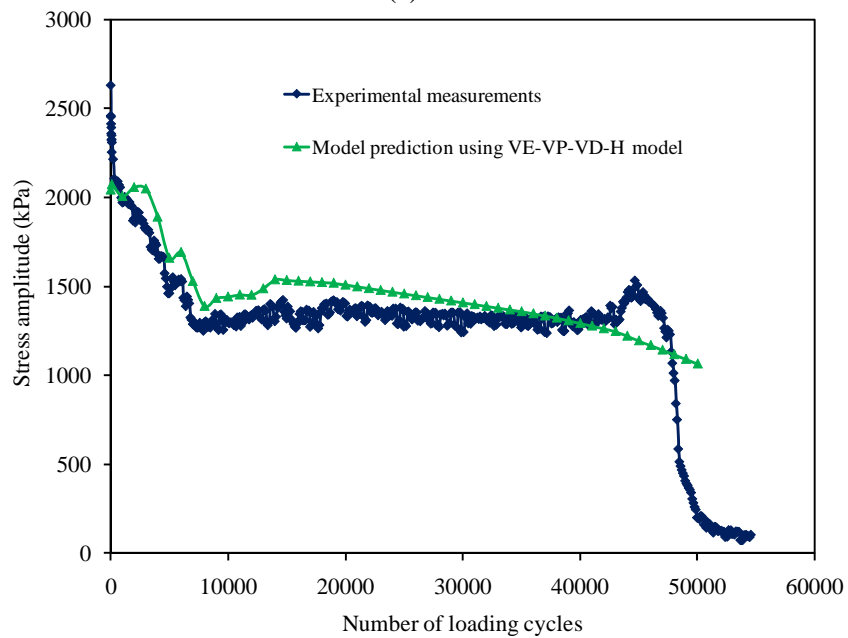
(b)

Figure 7.49. Experimental measurements and model predictions for the cyclic strain controlled test at 5°C when the applied strain amplitude at the end plates is 1750 $\mu\varepsilon$. (a) The amplitude of the measured strains at LVDTs versus the number of loading cycles; (b) The tensile stress amplitude versus number of loading cycles.

7.10. Conclusions

The thermo-viscoelastic-viscoplastic-viscodamage-healing model presented in Chapter II is modified and further validated against an extensive experimental data from the NCSU database. It is shown that the classical plasticity/viscoplasticity theories are not capable of predicting the viscoplastic response of asphalt mixes at high temperatures.

A novel computational technique to model the viscoplastic softening in asphalt mixes is proposed. This model is based on the definition of a viscoplastic softening memory surface in the viscoplastic strain space. The viscoplastic softening memory surface is defined as a function of the effective viscoplastic strain and an internal variable memorizing the maximum viscoplastic strain for which the softening has already occurred. This memory surface can be considered as the counterpart of the viscoplastic dynamic yield surface in the viscoplastic strain space. The viscoelastic-viscoplastic model with the viscoplastic memory surface is then validated against creep-recovery tests in compression at 55°C for different stress levels, loading times, and rest periods.

The calibrated viscoelastic-viscoplastic model is then used to identify the damage response of asphalt mixes in tension. A straightforward procedure for identification of the viscodamage model parameters is proposed. This procedure is based on the analysis of the constant strain rate tests at several strain rates. The identified viscodamage model parameters are then used to predict the mechanical response of asphalt mixes at multiple temperatures (i.e. 5, 12, 19, 25, and 40). The tension data include constant strain rate, dynamic modulus, cyclic stress controlled, and cyclic strain controlled tests at multiple temperatures, strain rates, stress amplitudes, and strain amplitudes. Comparison of the model predictions and experimental measurements show that the viscodamage model predicts the constant strain rate tests as well as the cyclic controlled stress tests very well. However, it fails to capture the response for the cyclic strain controlled tests.

It is shown that this discrepancy is related to the healing mechanism that occurs during the cyclic strain controlled tests. The model predictions with the viscodamage and

healing models show that the inclusion of the micro-damage healing remedies this problem and yields reasonable responses comparing to the experimental measurements.

CHAPTER VIII
NUMERICAL TECHNIQUE FOR FINITE ELEMENT IMPLEMENTATION OF GRADIENT-DEPENDENT CONTINUUM DAMAGE MECHANICS THEORIES

8.1. Introduction

The ultimate goal of developing a multi-physics constitutive model for asphalt mixes is to predict the performance of these materials during their service lives. However, the asphalt pavements are subjected to millions of loading cycles during their service life. Therefore, it is imperative to develop robust, yet simple, computational techniques for numerical implementation of the multi-physics constitutive equations and performance simulation of the pavements. However, the difference between the stiffness of the constituents of the asphalt mixes causes the strain and the induced damages to localize in binder phases causing instabilities and mesh-dependent results in the FE simulations. In other words, as the loading increases, asphalt binder undergoes a substantial strain levels comparing to the applied strain to the HMA. For example, strain in the binder could range between average of eight times and a maximum of 510 times the bulk strain of the mixture (Kose et al., 2000) and some regions within the mastic can experienced strain levels as high as 30 times the applied strain (Masad and Somadevan, 2002). These localizations lead to the mesh-dependent results in the FE simulations specially at softening regions such that the traditional local continuum theories fail to predict physical response. One alternative to remedy this problem is to use and implement non-classical gradient-dependent continuum theories (see Dessouky, 2005 for an example). Therefore, a general framework for implementation of the nonlocal damage theories is proposed. The proposed implementation procedure will be used in the next chapter to simulate the performance of asphalt pavements.

In general, failure of most of the materials is accompanied with the observation of localization phenomenon and softening. In the softening region, most of the specimen's deformation occurs within one or more narrow bands (i.e. inside the binder

for the case of asphalt mixes) while the rest of specimen usually exhibits unloading (Pamin, 1994). Depending on the material parameters; loading type and distribution; loading rate, geometry, and boundary conditions the orientation and width of these localization bands change. The physical origin of localization and various types of size-scale effects lies at the micro-scale of observation. Material deformation patterns are heterogeneous at the micro-scale; upon loading this heterogeneity causes a severe nonlinear behavior and local weakness of the material, which is an instability initiating strain localization (Pamin, 1994).

Continuum damage mechanics proposed initially by Kachanov (1958) seems to be well-adopted to describe the material response due to the existence, nucleation, and growth of micro-cracks and micro-voids. This approach has been used by several researchers for modeling damage in different materials. However, the assumption of variation of deformation in a sufficiently smooth manner is implicitly embedded in these classical theories since they are expressed in terms of averaged stress and strain. But this is not the case when strain or damage localization occurs. As the strain and damage defects localize over narrow regions, the material increasingly displays localization and the finite element simulations become highly affected by the mesh size and alignment causing non-physical predictions of the damage regions, damage distribution across the localized region, and the failure of the structure. In addition, the size of the fracture process zone becomes controlled by the size of one element in the finite element simulations. Therefore, the characteristic length scale governing the variations of those defects and their average interactions over multiple length scales falls far below the scale of the local state variables of classical theories of continuum mechanics. In these cases, damage theories and the boundary value problem in the presence of damage-induced softening will become ill-posed. In other words, continuum theories suffer from mesh-dependency problems when strain or damage localizes over a narrow region and the material response shows the softening behavior. This mesh-dependent response is because of the lack of an intrinsic length scale in the governing equations of the classical continuum theories. Therefore, the condition for the loss of ellipticity (or hyperbolicity

in dynamic problems) of the governing differential equations leads to ill-posed solution when strain or damage localization occurs such that the width of softening zone will always be of the thickness of one element, regardless of the element size (e.g. de Borst et al., 1993; Mühlhaus, 1995; Alehossein and Korinets, 2000).

For quasi-static loading conditions, well-posed solutions and restoring the ellipticity of the governing equations can be obtained by enhancing the local damage models by nonlocal measure(s). This can be achieved either by using the nonlocal integral approach (e.g.Pijaudiercabot and Bazant, 1987; Bazant and Pijaudiercabot, 1988; Comi, 2001; Ferrara and di Prisco, 2001) or the gradient-enhanced approach (e.g. Aifantis, 1984; Lasry and Belytschko, 1988; deBorst and Muhlhaus, 1992; Zbib and Aifantis, 1992; de Borst et al., 1993; deBorst and Pamin, 1996; Peerlings et al., 1996; Nedjar, 2001; Voyiadjis and Abu Al-Rub, 2003; Abu Al-Rub and Voyiadjis, 2005b, 2006; Challamel et al., 2009). Although these nonlocal theories have provided many useful results, there are still some difficulties in their numerical implementation which are mostly due to the higher-order of the governing equations in the localized region. As an example, the consistency condition of damage surface becomes a differential equation and is not an algebraic one anymore. Moreover, there are also some complexities due to higher-order boundary conditions which are necessary for mathematical consistency and need to be prescribed on the moving elastic-damage boundary (Abu Al-Rub and Voyiadjis, 2005a).

The computational technique usually followed for integrating the gradient-dependent constitutive relations was first proposed by de Borst and co-workers (e.g. Mühlhaus and Aifantis, 1991; deBorst and Muhlhaus, 1992; Pamin, 1994; deBorst and Pamin, 1996). In their work, the plasticity/damage flow/growth conditions depend on the Laplacian of an equivalent kinematic measure (hardening/softening internal state variables), and the consistency conditions result in differential equations with respect to the plastic/damage Lagrange multipliers. These multipliers are considered as fundamental unknowns (additional degrees of freedom) having a role similar to that of displacements and are discretized in addition to the usual discretization of the

displacements in the finite element method. The consistency condition is written in a weak form and solved simultaneously with the equilibrium equation. Because of the presence of high-order derivatives in the weak form of the (initial) boundary value problem, there is a need for numerically expensive C^1-continuous conditions on the shape functions or penalty-enhanced C^0 class functions for the interpolation of the plastic/damage multipliers in the finite element context. C^2 and higher continuity are also needed if fourth-order or higher-order gradient terms are incorporated; otherwise the gradient terms lose their presence. Therefore, Hermitian or mixed formulations are unavoidable for a consistent finite element formulation. Moreover, for the inelastic process a standard return mapping algorithm is performed, in which the values of the kinematic fields at an integration point are interpolated from their nodal values. This approach has been discussed thoroughly in Voyiadjis et al. (2001; 2004), and used intensively by many other authors (e.g. Ramaswamy and Aravas, 1998a, b; Aifantis et al., 1999; Nedjar, 2001). The disadvantage of this approach is that it gives rise to many numerical difficulties that require considerable modifications to the existing finite element codes, which makes their implementation not an easy or a direct task.

In this work, numerical implementation of a simple nonlocal gradient-enhanced elastic-damage model is presented as an example. Although the proposed numerical approach is applied to this elastic-damage model as a simple example, it can be easily adapted to a more complex constitutive nonlocal damage models. Therefore, the elastic-damage model is assumed here for simplicity and in order to emphasize and demonstrate the steps necessary for a direct numerical implementation of nonlocal gradient-dependent damage theories in existing finite element codes such as Abaqus. In the nonlocal models the explicit incorporation of a material length scale parameter scales the width of the damaged zone, thus preventing strain localization into a line with consequent zero energy dissipation, and eliminates the mesh-dependent behavior in the softening regions. Moreover, in order to avoid using the numerically expensive C^1-continous condition on the shape function and penalty-enhanced C^0 class functions for the interpolation of the damage multipliers, and also eliminate large modification of

existing finite element codes, the direct numerical algorithm of Abu Al-Rub and Voyiadjis (2005a) is extended here to nonlocal gradient-damage-type models and for three dimensional problems. In this approach, the nonlocal consistency condition is transformed into a linear set of algebraic equations that depend on the material parameters and the current co-ordinates of the Gauss integration points. These sets of linear equations are solved for the damage densities at all the integration points simultaneously. The gradients of the damage variable at each integration point in the local element are evaluated from the derivatives of a polynomial that interpolates the value of the damage densities from the surrounding elements. So, there is no need to consider a damage variable as a degree of freedom, and obviously there is no need for introducing high-order continuous shape functions (Abu Al-Rub et al., 2010b).

8.2. Continuum Damage Model

Evolution (i.e. nucleation and growth) of micro-damages (micro-cracks and micro-voids) due to different mechanical and environmental loading conditions can be effectively modeled using a continuum damage mechanics (CDM) based model. However, since most of the materials are very heterogeneous at the scale of micro-damages, local damage modeling in materials requires some generalization of CDM such that it is unreasonable to assume micro-cracks and micro-voids to be randomly distributed. In fact, material behavior is also controlled by the distribution of micro-damages within the material such that it is undesirable to simulate damage density evolution as a function of stress or strain state of the desired point only (i.e. locally). Therefore, one should also include the effect of damage density from the neighboring points around the point in study (nonlocality).

8.2.1. Local Continuum Damage Model

The classical relationship between the nominal and effective stress tensors in the CDM is recalled here, such that:

$$\boldsymbol{\sigma} = \left(1 - \phi\right)^{\gamma} \bar{\boldsymbol{\sigma}} \tag{8.1}$$

where $\gamma = 2$ is considered in this work. In order to calculate the damage density in Eq. (8.1), a procedure analogous to the classical plasticity theory is commonly used through defining a damage flow rule and a damage growth surface (Abu Al-Rub and Voyiadjis, 2003). Hence, a damage surface G is defined that determines whether a stress state results in damage or not, such that:

$$G = \overline{Y} - Y_{th} - \kappa^d\left(\phi\right) \leq 0 \tag{8.2}$$

where $\overline{Y}$ is the damage force, which can be interpreted as the energy release rate as in classical fracture mechanics, Y_{th} is the damage threshold, and $\kappa^d\left(\phi\right)$ is the damage hardening function. In this work, the damage force $\overline{Y}$ is considered to have a modified Drucker-Prager form, such that:

$$\overline{Y} = \overline{\tau} - \alpha \overline{I}_1 \tag{8.3}$$

where $\overline{\tau}$ is defined earlier in Chapter II. Although one can simply assume a nonlinear damage hardening function, a linear isotropic damage hardening is considered for simplicity, such that:

$$\kappa^d\left(\phi\right) = \kappa\phi \tag{8.4}$$

where κ is a material parameter that controls the rate of damage evolution. To determine the damage density, one can use a damage flow rule analogous to classical plasticity flow rule, such that:

$$\dot{\phi} = \dot{\lambda}^d \frac{\partial G}{\partial \overline{Y}} \tag{8.5}$$

where $\dot{\lambda}^d$ is the damage multiplier. In this case, one can easily show that the damage multiplier is identical to the damage variable. The Kuhn-Tucker loading/unloading conditions should also be satisfied for the damage surface and the damage multiplier, such that:

$$G \leq 0, \qquad \dot{\lambda}^d \geq 0, \qquad \dot{\lambda}^d G = 0 \tag{8.6}$$

Moreover, the damage multiplier can be determined using the damage consistency condition (i.e. $\dot{G} = 0$). In this work, by making use of the damage consistency condition, one can derive damage density equation very simply as:

$$\phi = \beta \left\langle \frac{\overline{Y}}{Y_{th}} - 1 \right\rangle \qquad (8.7)$$

where $\beta = \frac{Y_{th}}{\kappa}$ is a material parameter that controls the rate of damage evolution and $\langle \ \rangle$ is the Macaulay bracket.

8.2.2. Nonlocal Damage Model

The definition in Eq. (8.1) may be considered as the average stress acting on the effective area of the material. In order to give it a general physical meaning, it is necessary to use the corresponding damage-free material (intact material) in the meso-scale to represent the 'effective' concept of Eq. (8.1) for a macroscopically damaged material. Thus, a proper correlating hypothesis between the two material scale levels, the meso- and macro-scales, can be obtained by enhancing nonlocality through using a nonlocal measure for the damage variable (Voyiadjis et al., 2004; Voyadjis and Abu Al-Rub, 2006; Abu Al-Rub and Voyiadjis, 2009), such that one can rewrite Eq. (8.7) as follows:

$$\hat{\phi} = \beta \left\langle \frac{\overline{Y}}{Y_{th}} - 1 \right\rangle \qquad (8.8)$$

where the superimposed ^ designates the nonlocal measure. In a nonlocal integral-type damage theory, the damage variable ϕ can be replaced by an averaged (nonlocal) quantity $\hat{\phi}$, such that:

$$\hat{\phi}(x) = \frac{1}{V} \int_V h(\xi) \phi(x + \xi) dV \qquad (8.9)$$

where V is the body volume, x is the point of interest, ξ designates the local location of a material point within the localized damaged zone, and $h(\xi)$ is a nonlocal weight function that decays smoothly with distance $\|\xi\|$ and fades away for the points outside the limits of an internal characteristic material length scale ℓ. However, by expanding $\phi(x + \xi)$ into a Taylor series around the point $x = 0$ and assuming an isotropic

weighting function $h(\xi)$, which results in disappearing of higher-order gradients with odd orders, and neglecting higher than second-order terms, the following expression for $\hat{\phi}$ can be derived (de Borst et al., 1993):

$$\hat{\phi} = \phi + \ell^2 \nabla^2 \phi \tag{8.10}$$

where $\nabla^2 \phi$ is the second-order gradient (or Laplacian) of ϕ and ℓ is the intrinsic material length scale parameter which is related to the material microstructure. Voyiadjis and Abu Al-Rub (2005) showed that ℓ is not constant but evolves with deformation. In this study, however, ℓ is assumed constant for simplicity in demonstrating the robustness of the proposed computational technique in calculating $\nabla^2 \phi$ within a finite element context. Extending this technique to variable ℓ is a straightforward.

Replacing the local damage density by its nonlocal counterpart Eq. (8.8) along with Eq. (8.2), one can obtain an expression for the nonlocal damage surface, which is still governed by the loading-unloading conditions in Eq. (8.6), such that:

$$G = \overline{Y} - Y_{th} - \kappa^d \left(\phi + \ell^2 \nabla^2 \phi \right) = 0 \tag{8.11}$$

This condition should be satisfied in order to calculate the final value of the damage density.

In order to calculate the nonlocal damage density in Eq. (8.10), the second-order damage gradient $\nabla^2 \phi$ is needed, which is the main reason that makes the numerical implementation of gradient-dependent damage theories in finite element codes difficult. However, Abu Al-Rub and Voyiadjis (2005a) have proposed a numerical technique that can be effectively used in evaluating first-, second-, and higher-order gradient terms without the need to formulate a new higher-order element with additional degrees of freedom in the finite element method. Therefore, to evaluate $\nabla^2 \phi$ at an arbitrary integration point m, the approach proposed by Abu Al-Rub and Voyiadjis (2005a) for strain gradient plasticity theories is extended here for nonlocal gradient-dependent damage theories. Also, this approach is extended here for three-dimensional (3D) problems. These extensions will be detailed in the following section.

8.3. Computation of the Nonlocal Damage Density

In the numerical approach of Abu Al-Rub and Voyiadjis (2005a), the gradient at each integration point m is evaluated from the derivatives of a polynomial function that interpolates the values of local variables at neighboring points. In this study, the values of ϕ at integration point m and its neighbors are needed to calculate $\nabla^2\phi$. Hence, one can write:

$$\nabla^2\phi_m = \sum_{n=1}^{N_{GP}} g_{mn}\phi_n \qquad (8.12)$$

where N_{GP} is the number of Gauss integration points that are used for calculating $\nabla^2\phi_m$. The computation of coefficients g_{mn} for 3D problems is described below. In the following, matrix notation is used for convenience.

It is noteworthy that Abu Al-Rub and Voyiadjis (2005a) employed integration points of eight elements, the first neighbors, around the element in which the arbitrary integration point m is located to calculate the gradient terms. However, this approach is restricted to the regular finite element meshes. Moreover, for different mesh densities the interaction length which is the largest distance that affects the nonlocal average at an arbitrary point m is different such that the interaction length for coarse meshes is greater than the interaction length for fine meshes. Therefore, in this study all integration points of the finite element mesh are used to calculate the gradient terms, which makes the numerical approach even simpler than that in Abu Al-Rub and Voyiadjis (2005a). Therefore, in this approach the interaction length is the same for all mesh densities, and it can easily be used for both regular and irregular finite element meshes. Another method for extending Abu Al-Rub and Voyiadjis (2005a) approach to irregular meshes is through using the connectivity matrix for determining the neighboring points. In this method, one can easily consider the second and third nearest neighbors for calculating the gradient terms depending on different meshes such that the interaction length remains constant for all mesh densities. However, this method is not used here.

In order to determine g_{mn} in Eq. (8.12), a complete second-order polynomial function is used to interpolate the damage density around point m. Hence, one can write:

$$\phi = \boldsymbol{a}^T \boldsymbol{v} \tag{8.13}$$

where $\boldsymbol{a}$ is the coefficients vector, $\boldsymbol{v}$ is the variables vector, and the superimposed "T" designates the transpose of a matrix. For three dimensional problems, one can write the following expressions for $\boldsymbol{a}$ $\boldsymbol{v}$:

$$\boldsymbol{a}^T = \begin{bmatrix} a_0 & a_1 & a_2 & a_3 & a_4 & a_5 & a_6 & a_7 & a_8 & a_9 \end{bmatrix}, \text{ and}$$
$$\boldsymbol{v}^T = \begin{bmatrix} 1 & x & y & z & xy & yz & xz & x^2 & y^2 & z^2 \end{bmatrix} \tag{8.14}$$

It is noteworthy that one can assume other higher-order polynomials for Eq. (8.14) to achieve higher accuracy in calculating the higher-order gradients. This is one of the major strengths of the proposed approach without worrying about formulating C^1 or higher-order finite elements or penalty enhanced C^0 elements. However, Eq. (8.14) is the minimum order for a polynomial that can be assumed so that non-zero values for $\nabla^2 \phi$ can be calculated.

To obtain the coefficients vector $\boldsymbol{a}$, the minimization method by least squares can be used. Moreover, the interpolation is made in the global coordinate system (x, y, z) of the generated finite element mesh with N_{GP} integration points. The coefficients vector $\boldsymbol{a}$ can then be expressed using the following equation:

$$\boldsymbol{\Phi} = \boldsymbol{M}^T \boldsymbol{a} \tag{8.15}$$

where the matrix $\boldsymbol{M}$ and $\boldsymbol{\Phi}$ are defined as follows:

$$M = \begin{bmatrix} 1 & 1 & ... & 1 \\ x_1 & x_2 & ... & x_{N_{GP}} \\ y_1 & y_2 & ... & y_{N_{GP}} \\ z_1 & z_2 & ... & z_{N_{GP}} \\ x_1 y_1 & x_2 y_2 & ... & x_{N_{GP}} y_{N_{GP}} \\ y_1 z_1 & y_2 z_2 & ... & y_{N_{GP}} z_{N_{GP}} \\ x_1 z_1 & x_2 z_2 & ... & x_{N_{GP}} z_{N_{GP}} \\ x_1^2 & x_2^2 & ... & x_{N_{GP}}^2 \\ y_1^2 & y_2^2 & ... & y_{N_{GP}}^2 \\ z_1^2 & z_2^2 & ... & z_{N_{GP}}^2 \end{bmatrix} \tag{8.16}$$

$$\Phi = \begin{bmatrix} \phi_1 & \phi_2 & ... & \phi_{N_{GP}} \end{bmatrix}^T \tag{8.17}$$

Multiplying both sides of Eq. (8.15) by M implies:

$$M\Phi = Ha \tag{8.18}$$

where $H = MM^T$ is a symmetric square matrix which can be expanded as follows:

$$H = \sum_{n=1}^{N_{GP}} \begin{bmatrix} 1 & x_n & y_n & z_n & x_n y_n & y_n z_n & x_n z_n & x_n^2 & y_n^2 & z_n^2 \\ & x_n^2 & x_n y_n & x_n z_n & x_n^2 y_n & x_n y_n z_n & x_n^2 z_n & x_n^3 & x_n y_n^2 & x_n z_n^2 \\ & & y_n^2 & y_n z_n & x_n y_n^2 & y_n^2 z_n & x_n y_n z_n & x_n^2 y_n & y_n^3 & y_n z_n^2 \\ & & & z_n^2 & x_n y_n z_n & y_n z_n^2 & x_n z_n^2 & x_n^2 z_n & y_n^2 z_n & z_n^3 \\ & & & & x_n^2 y_n^2 & x_n y_n^2 z_n & x_n^2 y_n z_n & x_n^3 y_n & x_n y_n^3 & x_n y_n z_n^2 \\ & & & & & y_n^2 z_n^2 & x_n y_n z_n^2 & x_n^2 y_n z_n & y_n^3 z_n & y_n z_n^3 \\ & \text{Symm} & & & & & x_n^2 z_n^2 & x_n^3 z_n & x_n y_n^2 z_n & x_n z_n^3 \\ & & & & & & & x_n^4 & x_n^2 y_n^2 & x_n^2 z_n^2 \\ & & & & & & & & y_n^4 & y_n^2 z_n^2 \\ & & & & & & & & & z_n^4 \end{bmatrix} \tag{8.19}$$

It is obvious that H is computed only once for small deformation problems and needs to be updated at each loading increment for finite deformation problems. The damage density and its Laplacian can be determined using Eqs. (8.13) and (8.18), such that:

$$\phi = a^T v = \left(H^{-1} M\Phi \right)^T v = \left(H^{-1} \sum_{n=1}^{N_{GP}} \phi_n v_n \right)^T v \tag{8.20}$$

$$\nabla^2 \phi = \left(H^{-1} M\Phi \right)^T \nabla^2 v = \left(H^{-1} \sum_{n=1}^{N_{GP}} \phi_n v_n \right)^T \nabla^2 v \tag{8.21}$$

Hence, for integration point m one can write:

$$\nabla^2 \phi_m = \nabla_{xx}\phi_m + \nabla_{yy}\phi_m + \nabla_{zz}\phi_m \tag{8.22}$$

Substituting Eq. (8.20) into Eq. (8.22) gives:

$$\nabla^2 \phi_m = \sum_{n=1}^{N_{GP}} \left(\boldsymbol{v}_n^T \boldsymbol{H}^{-1}\nabla_{xx}\boldsymbol{v}_m + \boldsymbol{v}_n^T \boldsymbol{H}^{-1}\nabla_{yy}\boldsymbol{v}_m + \boldsymbol{v}_n^T \boldsymbol{H}^{-1}\nabla_{zz}\boldsymbol{v}_m \right)\phi_n \tag{8.23}$$

Coefficients g_{mn} can be calculated by comparing Eqs. (8.12) and (8.23), such that:

$$g_{mn} = \boldsymbol{v}_n^T \boldsymbol{H}^{-1}\nabla_{xx}\boldsymbol{v}_m + \boldsymbol{v}_n^T \boldsymbol{H}^{-1}\nabla_{yy}\boldsymbol{v}_m + \boldsymbol{v}_n^T \boldsymbol{H}^{-1}\nabla_{zz}\boldsymbol{v}_m \tag{8.24}$$

The coefficients g_{mn} depend only on the (x, y, z) coordinates of the Gauss integration points. Thus, as stated previously, these coefficients are computed only once for small deformations and at each loading increment for finite deformations.

Since the damage densities around a point is estimated by a second-order polynomial function as described in Eq.(8.13), it is worthy to note that:

$$\frac{\partial^2 \boldsymbol{v}}{\partial x^2} = \begin{bmatrix} 0 & 0 & 0 & 0 & 0 & 0 & 0 & 2 & 0 & 0 \end{bmatrix};$$

$$\frac{\partial^2 \boldsymbol{v}}{\partial y^2} = \begin{bmatrix} 0 & 0 & 0 & 0 & 0 & 0 & 0 & 0 & 2 & 0 \end{bmatrix}; \tag{8.25}$$

$$\frac{\partial^2 \boldsymbol{v}}{\partial z^2} = \begin{bmatrix} 0 & 0 & 0 & 0 & 0 & 0 & 0 & 0 & 0 & 2 \end{bmatrix}$$

Such that if one uses Eq. (8.25) in Eq. (8.24), a simple equation for calculation the coefficients g_{mn} can be written as follows:

$$g_{mn} = 2\left[\text{8th row of } \boldsymbol{H}^{-1} + \text{9th row of } \boldsymbol{H}^{-1} + \text{10th row of } \boldsymbol{H}^{-1} \right]\boldsymbol{v}_n \tag{8.26}$$

Having the information of neighboring points in hand, one can calculate the second-order damage gradient terms easily by employing Eqs. (8.26) and (8.12).

Once the effective stress is calculated, the damage driving force can then be calculated and compared with the damage threshold Y_{th} in order to check for damage initiation. Therefore, upon damage occurrence, one should satisfy Eq. (8.11) to calculate the final nonlocal damage density at each integration point m.

Substituting Eq. (8.12) into Eq. (8.11) gives:

$$G_m = \bar{Y}_m - Y_{th} - \kappa^d \phi_m - \kappa^d \ell^2 \sum_{n=1}^{N_{GP}} g_{mn} \phi_n = 0; \quad m \in \{1,...N_{GP}\} \tag{8.27}$$

which should be satisfied for all integration points simultaneously. Furthermore, Eq. (8.27) expresses a set of linear algebraic equations for determining the damage densities at all integration points. Therefore, one can define the following expressions:

$$\boldsymbol{C} = \begin{bmatrix} 1 + \ell^2 g_{11} & \ell^2 g_{12} & \cdots & \ell^2 g_{1N_{GP}} \\ \ell^2 g_{21} & 1 + \ell^2 g_{22} & \cdots & \ell^2 g_{2N_{GP}} \\ \vdots & \vdots & \ddots & \vdots \\ \ell^2 g_{N_{GP}1} & \ell^2 g_{N_{GP}2} & \cdots & 1 + \ell^2 g_{N_{GP}N_{GP}} \end{bmatrix} \tag{8.28}$$

$$\boldsymbol{F} = \begin{bmatrix} \dfrac{\bar{Y}_1 - Y_{th}}{\kappa^d} & \dfrac{\bar{Y}_2 - Y_{th}}{\kappa^d} & \cdots & \dfrac{\bar{Y}_{N_{GP}} - Y_{th}}{\kappa^d} \end{bmatrix} \tag{8.29}$$

such that Eq. (8.27) can be expressed in a matrix format as follows:

$$\boldsymbol{C}\boldsymbol{\Phi} = \boldsymbol{F} \tag{8.30}$$

The above linear-system of equations can be solved for the damage density vector $\boldsymbol{\Phi}$ by calculating the inverse of the square matrix $\boldsymbol{C}$. Eqs. (8.28) and (8.30) show that the square matrix $\boldsymbol{C}$ is of the order $N_{GP} \times N_{GP}$ which seems to be very expensive to solve. However, it should be noted that the matrix $\boldsymbol{C}$ remains constant for the small deformation problems. Therefore, one can calculate matrix $\boldsymbol{C}$ and its inverse $\boldsymbol{C}^{-1}$ at the beginning of the simulation and store it to solve Eq. (8.30) for the rest of the simulation. Therefore, the proposed approach will have an initial computational cost to calculate $\boldsymbol{C}$ and $\boldsymbol{C}^{-1}$. However, this initial cost will be compensated eventually since there is no need to calculate these matrices at each increment. On the other hand, by considering the damage density as an additional degree of freedom, the required high-order continuous shape functions (e.g. C^1 class or penalty-enhanced C^0 class functions) should be used at each increment to calculate the gradient terms, which makes these approaches difficult to implement and computationally expensive.

8.4. Nonlocal Gradient-Dependent Tangent Moduli

To complete the proposed nonlocal algorithmic procedure discussed above, the nonlocal continuum elastic-damage tangent stiffness $E_t^{ed} = \Delta\sigma / \Delta\varepsilon$ and the nonlocal consistent (algorithmic) elastic-damage stiffness $E_t^{alg} = d\Delta\sigma / d\Delta\varepsilon$ that can be used for accelerating convergence are derived in this section. E_t^{ed} can be used if small time steps are employed, whereas E_t^{alg} can be used for large time steps are employed.

The relationship between the stress increment and the strain increment between the time t and $t + \Delta t$ at integration point m can be written as:

$$\Delta\sigma_m = E_{t,m}^{ed} : \Delta\varepsilon_m \tag{8.31}$$

The stress increment for the elastic-damage materials can be written as:

$$\Delta\sigma_m = \left(1 - \phi_m\right)^2 \bar{E} : \Delta\varepsilon_m - 2\Delta\phi_m \left(1 - \phi_m\right) \bar{E} : \varepsilon_m \tag{8.32}$$

The damage consistency condition (i.e. $\Delta G = 0$) for the integration point m can be written using Eq. (8.27), such that:

$$\Delta G_m = N_m : \Delta\sigma_m + \frac{\partial G}{\partial \phi_m}\Delta\phi_m + \frac{\partial G}{\partial \nabla^2 \phi_m}\nabla^2\Delta\phi_m = 0 \tag{8.33}$$

where $N = \dfrac{\partial G}{\partial \sigma}$ can be expressed as follows:

$$N = \sqrt{\frac{3}{4}}\left(1 + \frac{1}{d}\right)\frac{\bar{S}}{\sqrt{\bar{J}_2}} - \frac{1-d}{2d\bar{J}_2^2}\left[\frac{9}{2}\bar{J}_2\bar{S}.\bar{S} - 3\bar{J}_3\bar{S}\right] - \left[\frac{3}{2}\left(1 - \frac{1}{d}\right) + \frac{\alpha}{3}\right]\mathbf{1} \tag{8.34}$$

where $\mathbf{1}$ is the second-order identity tensor. Substituting Eqs. (8.12) and (8.32) into Eq. (8.33) and performing some mathematical manipulations, the nonlocal elastic-damage tangent stiffness can be expressed as follows:

$$E_{t,m}^{ed} = \left(1 - \phi_m\right)^2 \bar{E} - \frac{2\left(1 - \phi_m\right)}{L_m}\left(\bar{E} : \varepsilon_m \otimes N_m : \bar{E}\right) \tag{8.35}$$

where $\otimes$ indicates the dyadic tensor product and L_m is the nonlocal damage softening modulus at integration point m which is given by:

$$L_m = \kappa^d \left(1 + \ell^2 g_{mn}\right) + \frac{\kappa^d \ell^2}{\Delta\phi_m} \sum_{n=1, n \neq m}^{N_{GP}} g_{mn} \Delta\phi_n \tag{8.36}$$

One can retrieve the local elastic-damage stiffness when the intrinsic length scale is set to zero (i.e. $\ell = 0$). Furthermore, Eq. (8.35) defines the nonlocal continuous operator $\boldsymbol{E}_t^{ed}$. However, as mentioned earlier, small time increments should be used with the nonlocal elastic-damage tangent stiffness tensor in order to ensure the convergence. To increase the rate of convergence for large time increments, the nonlocal consistent (algorithmic) tangent stiffness modulus is more appropriate. Differentiating Eq. (8.32) at integration point m and noting that ($d\boldsymbol{\varepsilon}_m = d\Delta\boldsymbol{\varepsilon}_m$ and $d\phi_m = d\Delta\phi_m$), one can write the following expression:

$$\begin{aligned} d\Delta\boldsymbol{\sigma}_m = &\left[\left(1 - \phi_m\right)^2 - 2\Delta\phi_m\left(1 - \phi_m\right)\right]\bar{\boldsymbol{E}} : d\Delta\boldsymbol{\varepsilon}_m \\ &- 2\left(1 - \phi_m\right)\left[\bar{\boldsymbol{E}} : \Delta\boldsymbol{\varepsilon}_m + \left(1 - \frac{\Delta\phi_m}{1 - \phi_m}\right)\bar{\boldsymbol{E}} : \boldsymbol{\varepsilon}_m\right]d\Delta\phi_m \end{aligned} \tag{8.37}$$

Substituting Eqs. (8.12) and (8.27) into Eq. (8.33) and then differentiating the resulting expression, the following equation for $d\Delta\phi_m$ at integration point m can be obtained:

$$d\Delta\phi_m = \frac{1}{L_m}\left[d\boldsymbol{N}_m : \bar{\boldsymbol{E}} : \Delta\boldsymbol{\varepsilon}_m + \boldsymbol{N}_m : \bar{\boldsymbol{E}} : d\Delta\boldsymbol{\varepsilon}_m\right] \tag{8.38}$$

where

$$d\boldsymbol{N}_m = \frac{\partial \boldsymbol{N}}{\partial \Delta\bar{\boldsymbol{\sigma}}_m} : \frac{\partial \Delta\bar{\boldsymbol{\sigma}}_m}{\partial \Delta\boldsymbol{\varepsilon}_m} : d\Delta\boldsymbol{\varepsilon}_m = \boldsymbol{T}_m : \bar{\boldsymbol{E}} : d\Delta\boldsymbol{\varepsilon}_m \tag{8.39}$$

where $\boldsymbol{T}$ is expressed in components format as follows:

$$\begin{aligned} T_{ijkl} = &\sqrt{\frac{3}{4}}\left(1 + \frac{1}{d}\right)\bar{J}_2^{-1/2}\left[P_{ijkl}^I - \frac{1}{2}\bar{J}_2^{-1}P_{ijkl}^{II}\right] - \frac{9}{4}\left(1 - \frac{1}{d}\right) \times \\ &\left[6\bar{J}_2^{-2}\bar{J}_3 P_{ijkl}^I - \frac{2}{3}\left(2\bar{J}_2^{-3}\bar{J}_3 + \bar{J}_2^{-1}\right)P_{ijkl}^{II} - \bar{J}_2^{-1}\left(P_{ljik}^{III} - \frac{2}{3}P_{ijkl}^{III} + P_{iljk}^{III} - \bar{J}_2^{-1}P_{klij}^{IV}\right) + \bar{J}_2^{-2}P_{ijkl}^{IV}\right] \end{aligned} \tag{8.40}$$

with the forth-order tensors $\boldsymbol{P^I}$, $\boldsymbol{P^{II}}$, $\boldsymbol{P^{III}}$, and $\boldsymbol{P^{IV}}$ defined as follows:

$$P_{ijkl}^I = \delta_{ik}\delta_{jl} - \frac{1}{3}\delta_{ij}\delta_{mn} \tag{8.41}$$

$$P_{ijkl}^{II} = \overline{S}_{ij}\overline{S}_{kl} \tag{8.42}$$

$$P_{ijkl}^{III} = \overline{S}_{ij}\delta_{kl} \tag{8.43}$$

$$P_{ijkl}^{IV} = \overline{S}_{ij}\overline{S}_{km}\overline{S}_{ml} \tag{8.44}$$

Substituting Eqs. (8.38) and (8.39) into Eq. (8.37) gives:

$$d\Delta\boldsymbol{\sigma}_m = \boldsymbol{E}_{t,m}^{\mathrm{alg}} : d\Delta\boldsymbol{\varepsilon}_m \tag{8.45}$$

where $\boldsymbol{E}_{t,m}^{\mathrm{alg}}$ is the nonlocal consistent (algorithmic) tangent modulus and is given by:

$$
\begin{aligned}
\boldsymbol{E}_{t,m}^{\mathrm{alg}} = &\left(1 - \frac{\Delta\phi_m}{1-\phi_m}\right)\boldsymbol{E}_{t,m}^{ed} - \left(1-\phi_m\right)\Delta\phi_m\overline{\boldsymbol{E}} \\
&- \frac{2\left(1-\phi_m\right)}{L_m}\left(\overline{\boldsymbol{E}} : \boldsymbol{\varepsilon}_m \otimes \Delta\boldsymbol{\varepsilon}_m : \overline{\boldsymbol{E}} : \boldsymbol{T}_m : \overline{\boldsymbol{E}} + \overline{\boldsymbol{E}} : \Delta\boldsymbol{\varepsilon}_m \otimes \boldsymbol{N}_m : \overline{\boldsymbol{E}}\right)
\end{aligned}
\tag{8.46}
$$

This concludes the necessary steps for the numerical implementation of the nonlocal gradient-dependent damage model in a finite element code. This proposed numerical approach is implemented in the well-known finite element code Abaqus (2008) through the user material subroutine UMAT. It is noteworthy that the majority of the existing numerical implementation approaches of gradient-dependent damage and plasticity theories require the use of two subroutines in Abaqus; namely, UMAT, which is used for material constitutive modeling, and UEL, which is used for formulating a new element with additional degrees of freedom. In the current approach the use of UEL subroutine is avoided which saves a lot of time and effort for those who are interested in implementing gradient-dependent theories.

One of the most challenging issues of the proposed algorithm is the nonlocal integration of the damage model using only the UMAT subroutine in Abaqus. UMAT provides an access only to the local integration point and not all the integration points that are needed to calculate the damage gradient. To implement the proposed algorithm using UMAT, the coordinates of all integration points are saved globally when Abaqus calls UMAT at increment zero. As a result, at the beginning of the first increment the coordinates of all integration points are available. Hence, by using Eqs.(8.19) and (8.26), the nonlocal coefficients g_{mn} are calculated and saved globally at the beginning of the

first increment. It is noteworthy to mention that at each increment Abaqus calls UMAT for all integration points at least twice. This makes the nonlocal implementation easier. In other words, all the required local variables, including the damage force, are updated at the end of the first UMAT call. Therefore, at the end of the first UMAT call, C and F matrices [Eqs. (8.28) and (8.29)] are calculated; then, the nonlocal damage variables for all integration points are calculated at once by solving Eq. (8.30). Then, at the second UMAT call the nominal stresses and continuum or consistent tangent moduli are updated using the updated nonlocal damage variables and the effective local variables. For convenience, a step-by-step description of the discussed algorithm is illustrated in Figure 8.1.

However, it should be emphasized that the above description of the numerical implementation of the proposed nonlocal algorithm within the commonly used commercial finite element software Abaqus can be adapted to implement nonlocal damage theories in any other finite element codes. In the following, the robustness of the proposed numerical approach in solving the mesh-dependency problem when simulating damage localization is demonstrated.

8.5. Numerical Examples

In the absence of a physically motivated length scale which would govern the width of the shear band, the numerical solutions are susceptible to mesh densification. In other words, damage density and as a result strain localization within the shear band changes dramatically with refining the mesh. Incorporating an internal length scale in the continuum description can remedy the mesh sensitivity of the numerical results. The potential of the current gradient-dependent damage computational approach as presented in the previous section in solving the mesh sensitivity problem associated with the formation of damaged localized shear bands is demonstrated through the following numerical examples.
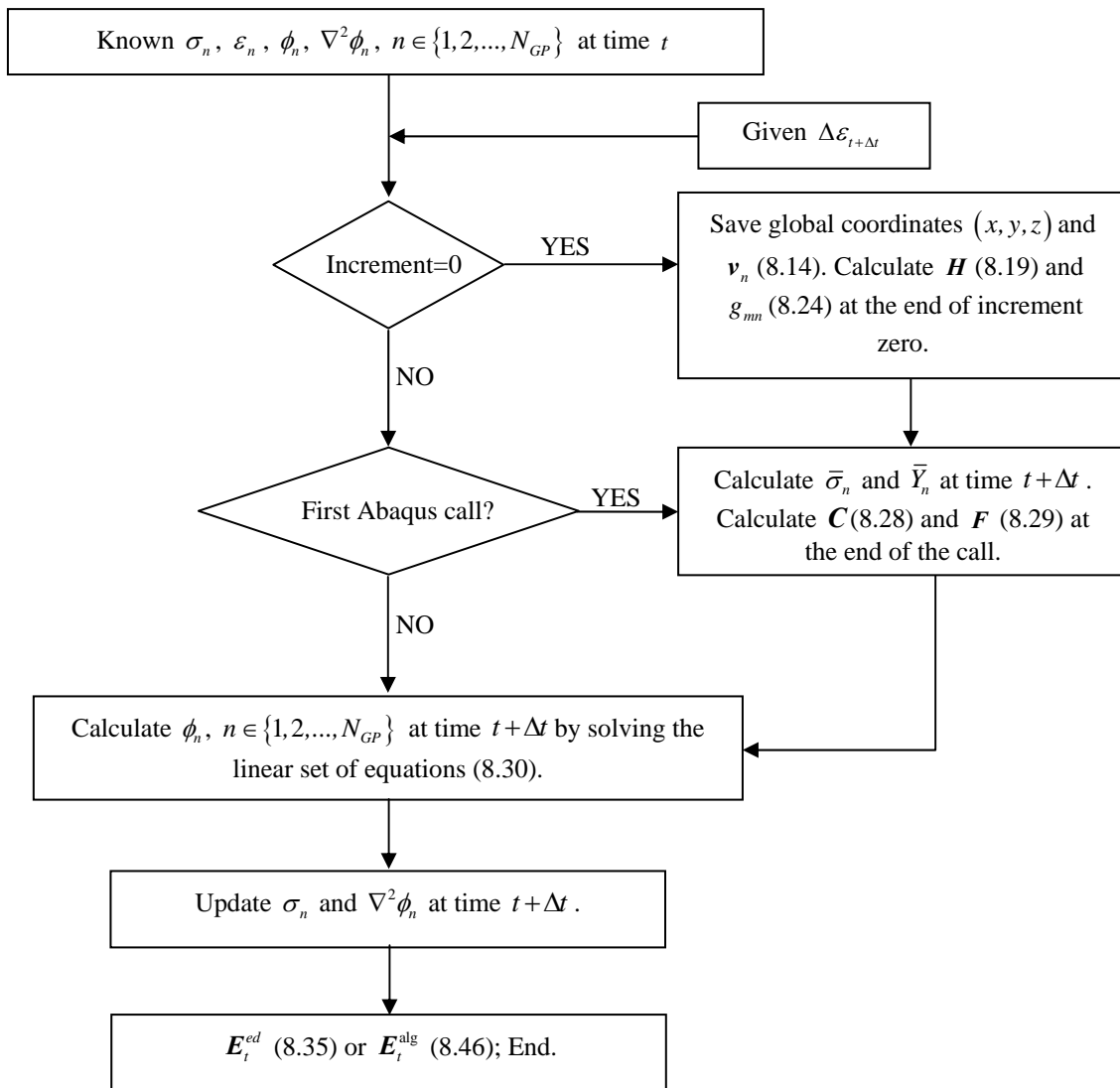
Figure 8.1. Flow chart of the numerical integration algorithm for the proposed nonlocal gradient-dependent damage model.

8.5.1. Fixed Plate in Tension

Mesh-dependent results of finite element predictions can be easily shown by the example of plane strain plate subjected to tensile loading at the top edge and fixed boundary condition at the bottom edge as shown in Figure 8.2. The bottom edge of the plate is fixed and the upper edge is constrained to remain horizontal while a vertical deformation equivalent to a tensile force is applied. The forces per unit area at both sides

of the specimen are set to zero. Dimensions of the specimen are $10\mu m\times20\mu m$, and a strain equal to 3.5% is applied at its upper edge in the positive -direction. The Young's modulus and Poisson's ratio are assumed to be $\overline{E}=200\text{GPa}$ and $\nu=0.49$, respectively. Moreover, the values for $\alpha=0$ and $\beta=0.1$ are assumed. First the local elastic-damage model is used to conduct the simulations with a zero length scale parameter (i.e. $\ell=0$). Simulations are performed for four different mesh densities. Four-node plane strain quadrilateral element with four integration points is used in this example. The fixed boundary condition causes the damage and strain to localize within a band and forms two crossed shear bands as shown in Figure 8.3.
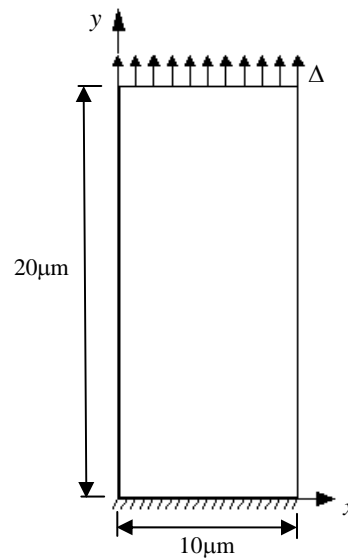
Figure 8.2. Uniaxial tension test configuration with dimensions $10\mu m\times20\mu m$ and fixed boundary condition at the bottom edge.

Figure 8.3 shows that the localized zone and shear band tend to occupy the minimum possible area. As mesh density increases the width of shear band decreases and tends to become a line which is not realistic and physical. Damage Localization of deformation in a narrow band is caused by the accumulation of micro-cracks and micro-voids; hence, very similar to strain localization, damage also localizes within a shear

band which is shown in Figure 8.4. Furthermore, Figure 8.4 shows clearly the mesh-dependency through the width of the localized damage band and the damage distribution being more severe for the fine meshes.
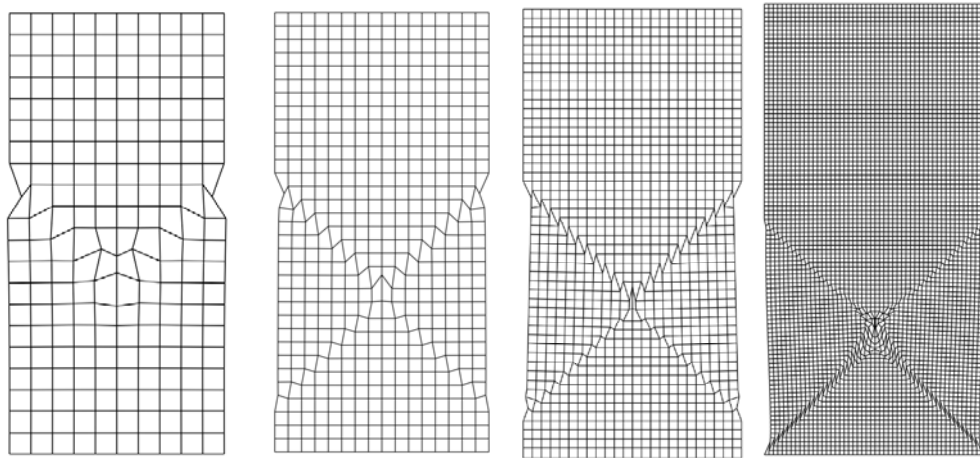
Figure 8.3. Mesh-dependent deformation patterns for four mesh densities when using the local damage model with $\ell = 0$. Non-physical response; the finer the mesh the smaller the shear band's width.

Figures 8.5 and 8.6 illustrate the damage density distributions across the shear band and the load-displacement diagrams, respectively, for the different meshes when $\ell = 0$.

It is obvious from Figure 8.5 that increasing the mesh density causes the shear band width to become narrower and the damage density to become larger, which is a nonphysical phenomenon upon mesh densification. In other words, more damage accumulates within smaller area. Figure 8.6 shows that the local damage model predicts very sudden failure after the peak load, where different post-peak responses are predicted for different mesh densities.
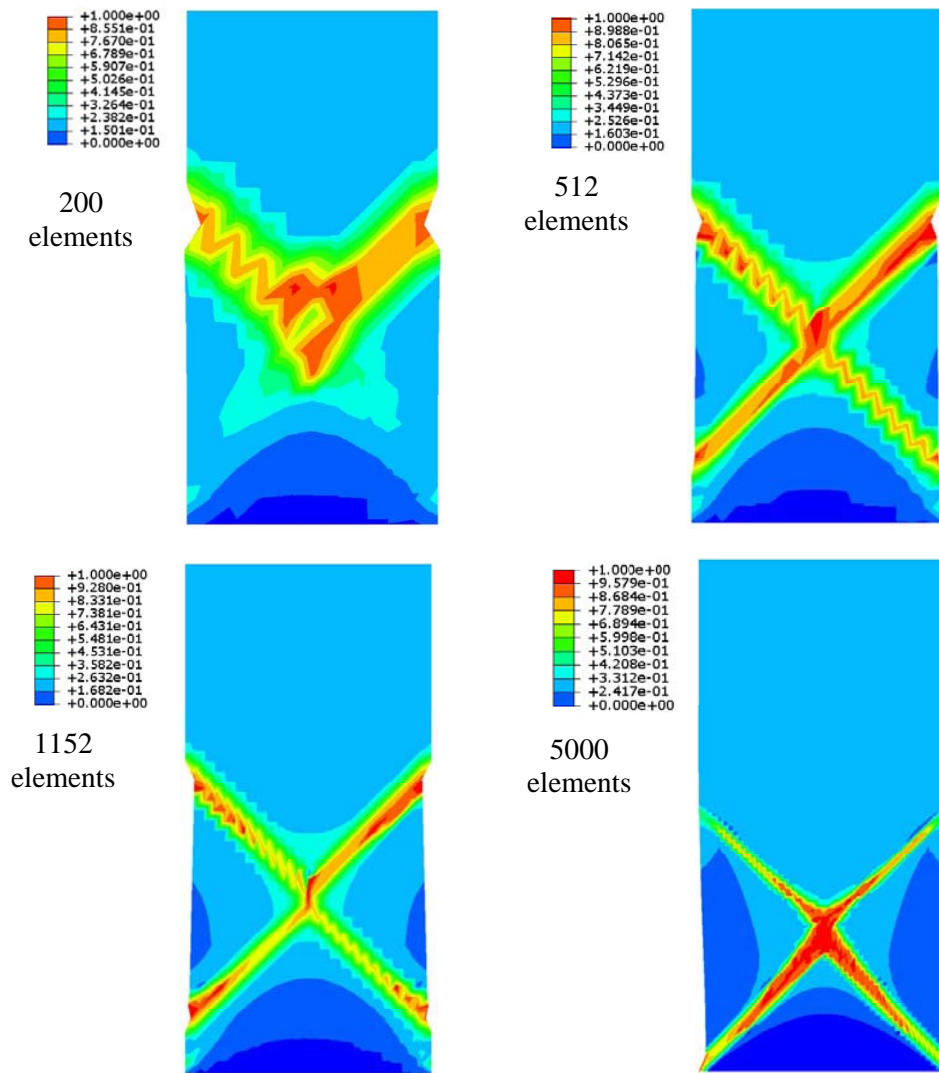
Figure 8.4. Mesh-dependent damage density contours for four mesh densities when using the local damage model with $\ell = 0$. Non-physical response; damage tends to localize over the smallest possible area.
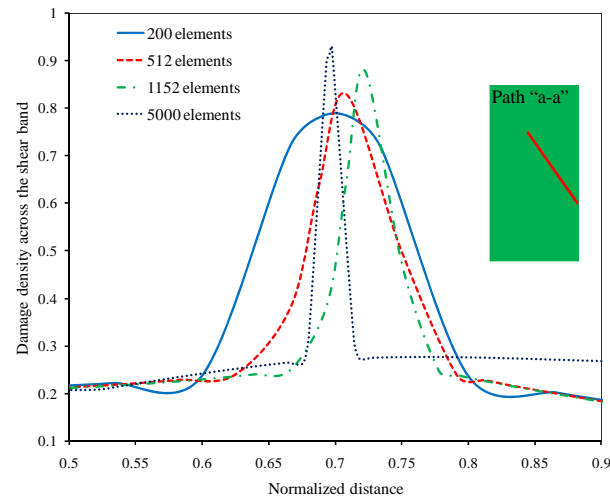
Figure 8.5. Mesh-dependent results of damage density across the shear band (along path 'a-a") when using the local damage model with $\ell = 0$. Non-physical response; damage tends to localize over the smallest possible area.
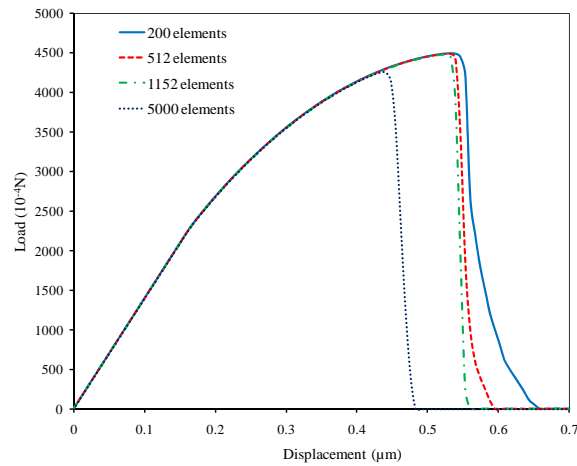
Figure 8.6. Mesh-dependent results of the load-displacement diagram when using the local damage model with $\ell = 0$. Responses are not the same in the softening region.

Now, in order to show the potential of the gradient-enhanced algorithm in eliminating the mesh-sensitivity problem, the same boundary value problem is simulated using the nonlocal damage algorithm with a material length scale equal to $\ell = 1\mu m$. The

results are shown in Figures 8.7-8.10. Figures8. 7 and 8.8 illustrate the deformation patterns and the damage density contours, respectively, for the different mesh densities.
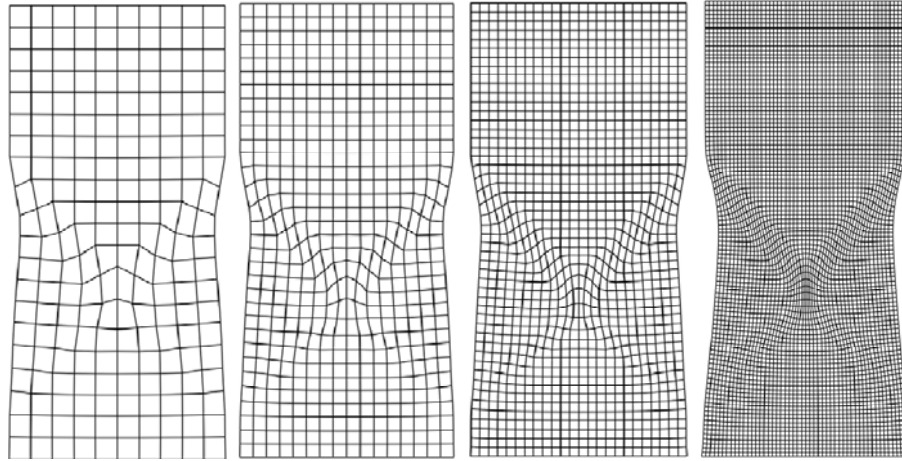
Figure 8.7. Mesh-independence deformation patterns for the nonlocal damage when $\ell = 1\mu m$.

It is obvious that the incorporation of an intrinsic material length scale through the gradient damage theory has alleviated to a great extent the mesh-dependent problem such that the width of the shear band remains approximately the same and does not change much with changing the mesh density. The same observation can be seen for the damage density contours shown in Figure 8.8. The damage density across the shear band is also plotted in Figure 8.9, where it can be seen that the width of the damage localization zone is to a great extent independent of the mesh density as compared to the local simulations in Figure 8.5. Furthermore, Figure 8.10 shows the most interesting results, where the post-peak response is completely independent of the mesh density. In fact, by introducing the gradient of damage density in the current simple damage model, the nonlocality does not allow few elements to undergo excessive deformation that results in a sudden decrease of the specimen loading capacity, but the deformation and damage density within the integration points change smoothly which results in regularizing the numerical results.
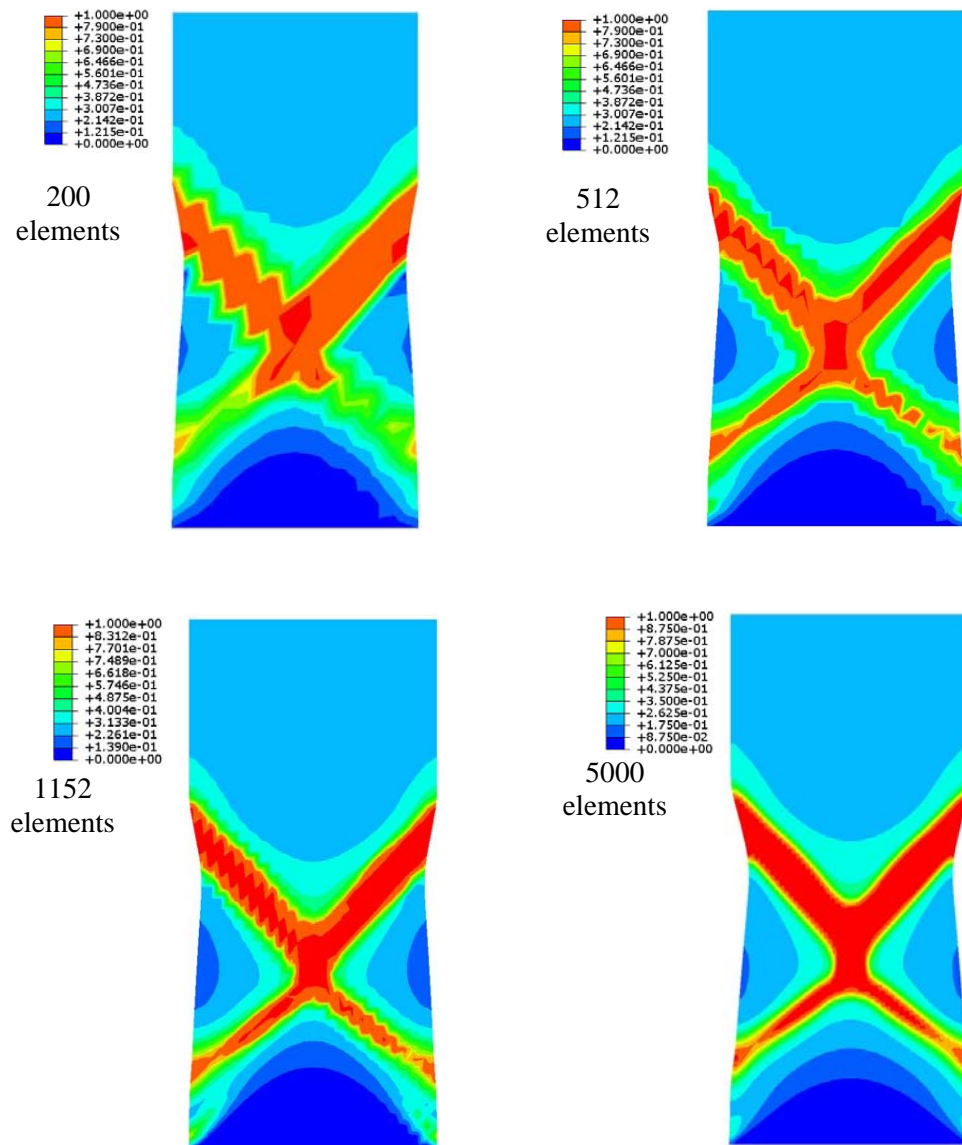
Figure 8.8. Mesh-independent results of the damage density contour on deformed configuration using the nonlocal damage model when $\ell = 1\mu m$. Damage accumulation and width of shear band are mesh insensitive.
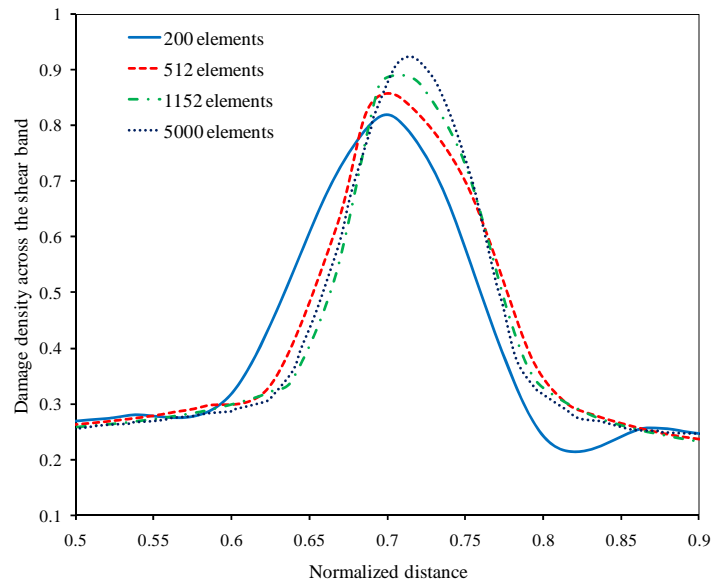
Figure 8.9. Mesh-independent results of damage density distribution across the shear band, along the path 'a-a', when $\ell = 1\mu m$.
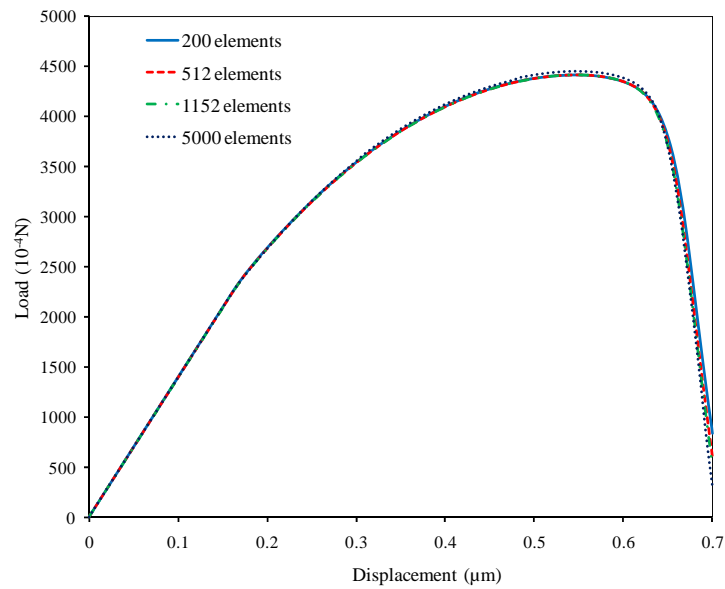
Figure 8.10. Mesh-independent results of the predicted load-displacement diagrams when $\ell = 1\mu m$.

8.5.2. Strip in Tension

In the previous section, damage localization and evolution of a shear band in a plane strain plate under tension was studied, and the ability of the nonlocal damage algorithm in successfully providing mesh-objective results is demonstrated. In this section, the same material properties are considered; however, the geometry is changed and enhanced with an imperfection in order to enforce the formation of a shear band in a specific direction. This is a common benchmark problem that is used to assess the ability of damage/plasticity theory in achieving mesh-objective results. The problem geometry, loading, and boundary conditions are shown in Figure 8.11. The strip is constrained at the bottom and a displacement of $1\mu m$ is applied at the upper edge of the strip. Similar to the previous section, four different meshes of 200, 512, 1152, and 5000 elements are considered. A four-node plane strain quadrilateral element with four integration points is used in the following simulations. Due to the specimen's geometric imperfection, the shear band initiates at the bottom left corner and evolves with an inclination of 45°. In this case, the nonlinearity in geometry is investigated in the formation of a shear band and in the distribution of the damage density across the shear band.
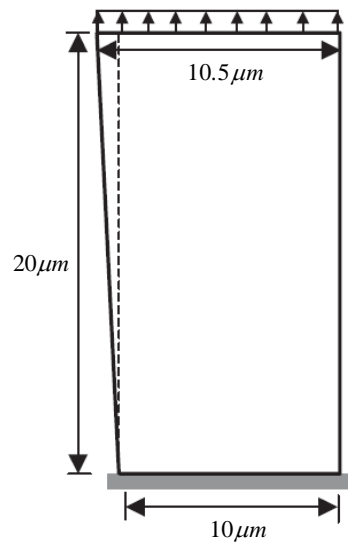
Figure 8.11. The geometry of the strip in tension.

In Figure 8.12 the obtained deformation patterns for all meshes when setting $\ell = 0$ are plotted. It can be observed easily that the width of the shear band is determined by the element size when utilizing the classical continuum damage mechanics. Deformation is localized almost within one element width.
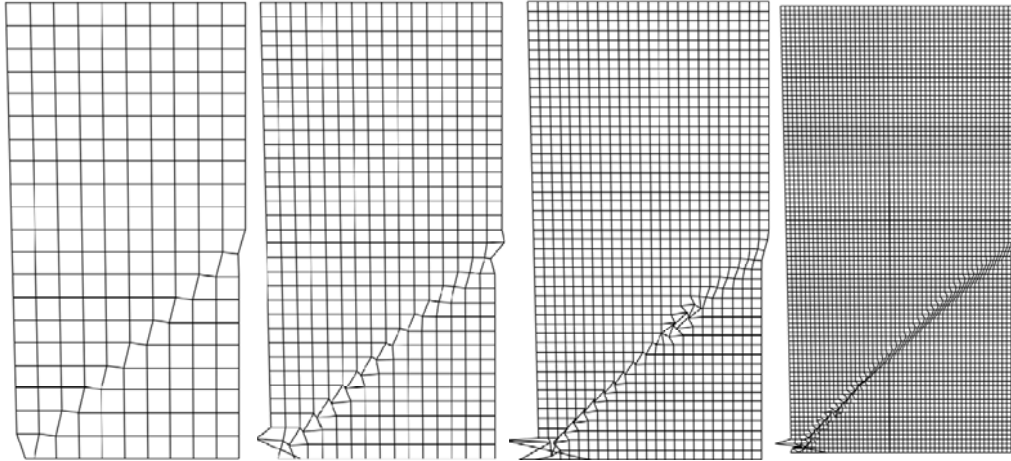
Figure 8.12. Mesh-dependence of deformation patterns for the strip with an imperfection under tension when $\ell = 0$. Non-physical response; deformation localizes within one element.

Mesh-dependence is also obvious from the damage density contours plotted in Figure 8.13 and the damage density across the shear band presented in Figure 8.14, where the width of the shear band is strongly dependent on the mesh density.
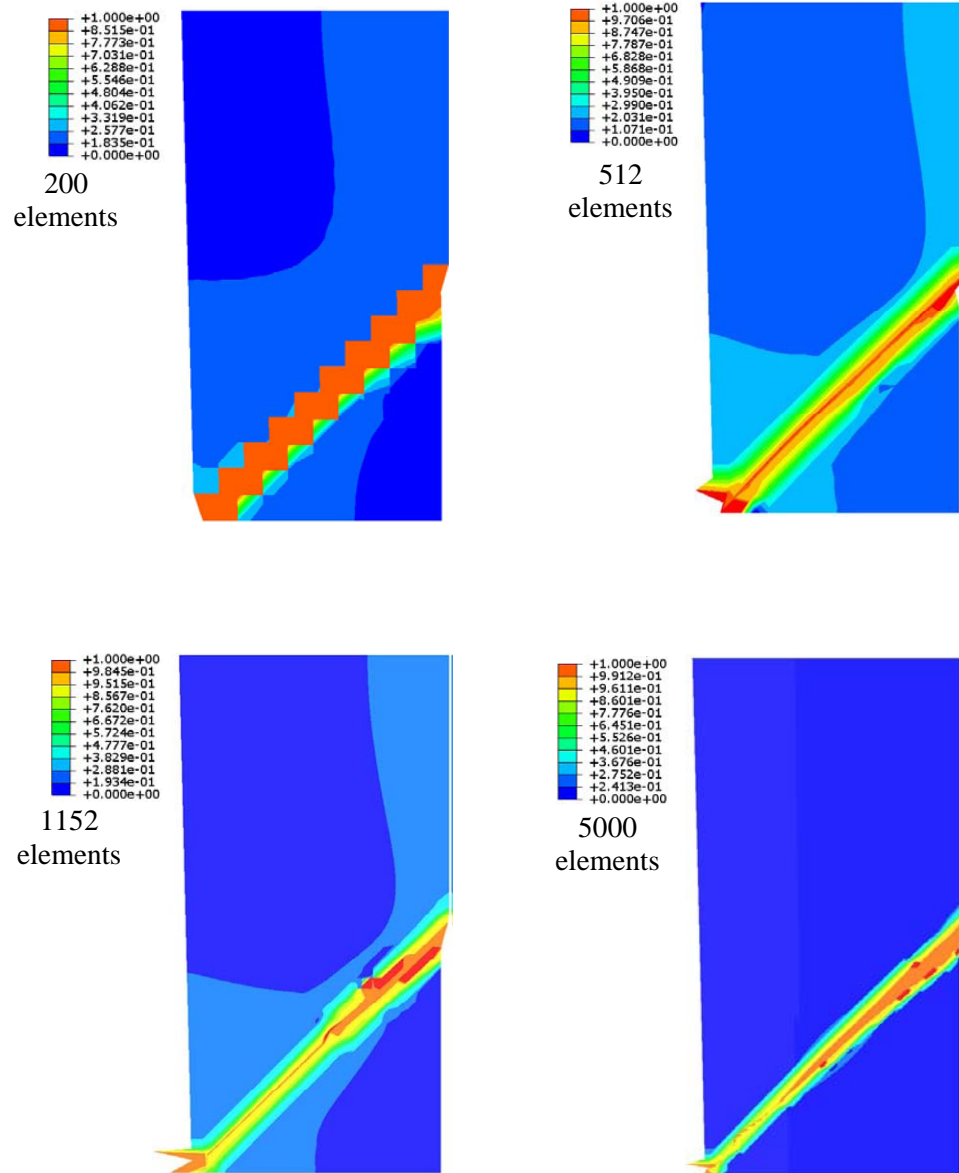
Figure 8.13. Mesh-dependent results of damage density contour on deformed configuration using the classical continuum damage model with $\ell = 0$.

It should be noted that damage density value could not be more than one; hence, the localization phenomenon appears in the form of width of the shear band not the maximum value for damage density.
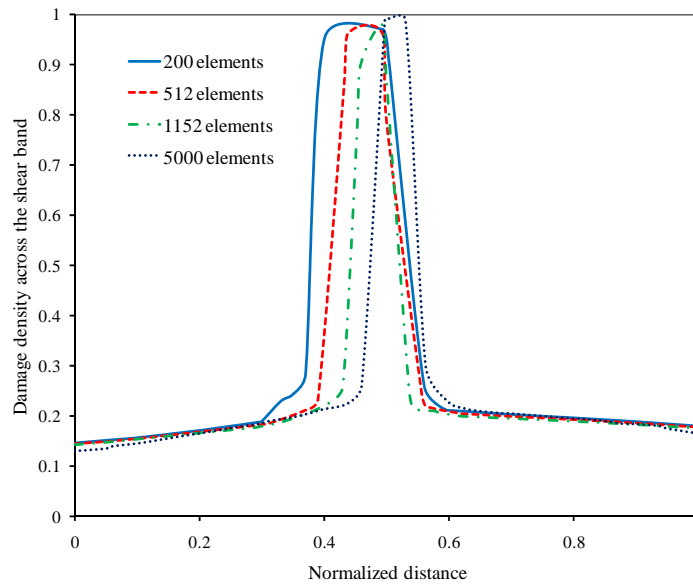
Figure 8.14. Damage density across the shear band when $\ell = 0$. Width of the localized zone depends on the mesh density.

Nonlocal damage gradient algorithm is employed to remedy the mesh sensitivity problem. Material properties of the specimen are assumed to be the same in both examples. Hence, the same length scale of $\ell = 1\mu m$ is also considered here to keep the field equations well-posed. Figures 8.15 and 8.16 illustrate respectively the deformation patterns and damage density contours for different mesh densities. As it is obvious from the figures, the nonlocal damage algorithm solves the mesh-dependency problem to a great extent. Moreover, a damage density across the shear band is depicted in figure 8.17, which also confirms mesh-independent shear band width. In order to show the effect of nonlocal damage on the post-peak response, the load-displacement diagrams for all mesh densities for both local, $\ell = 0$, and nonlocal, $\ell = 1\mu m$, cases are plotted in Figure 8.18. It is very clear from this figure that the current nonlocal damage model with the proposed computational algorithm predicts mesh-independent post-peak response whereas the local damage model is mesh-dependent. Also, it is obvious from this figure that a non-zero length scale delays damage and smooth it out during the deformation process.
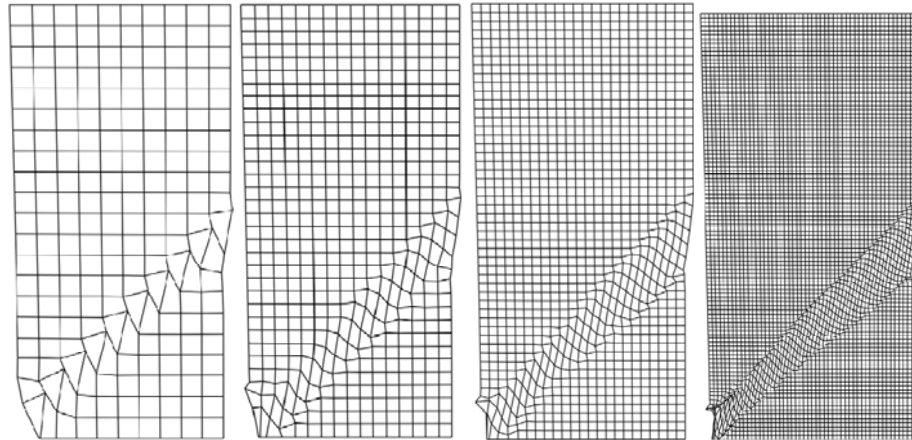
Figure 8.15. Mesh-independent deformation patterns when $\ell = 1\mu m$.
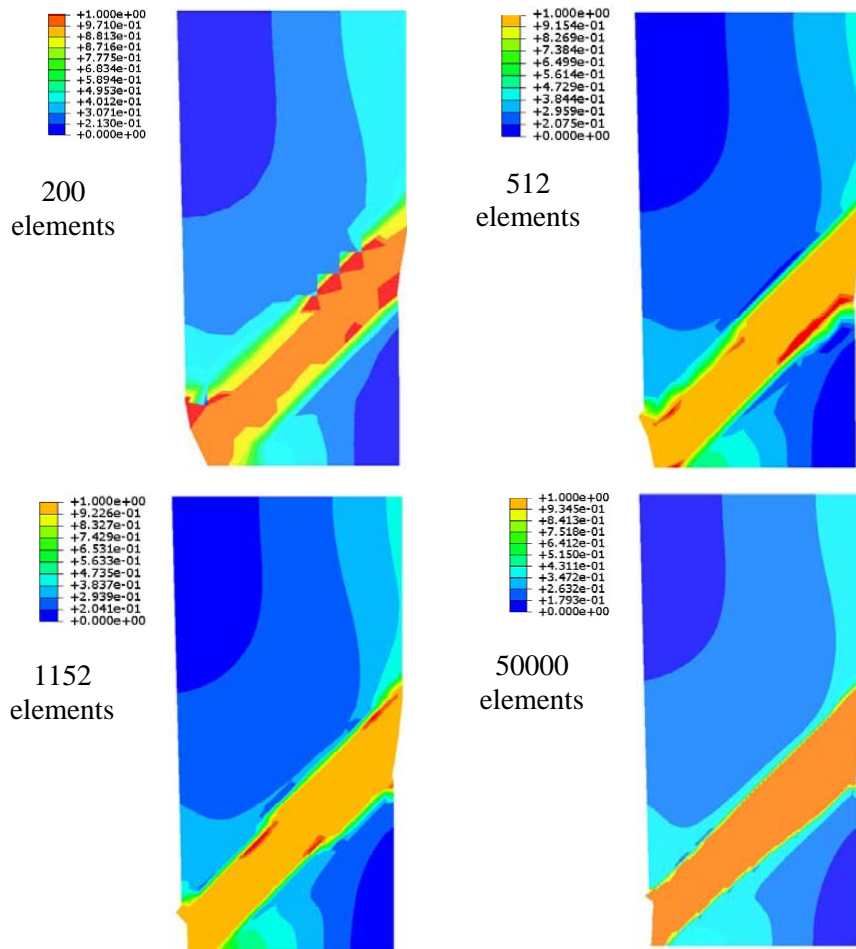
Figure 8.16. Mesh-independent results of damage density contour on deformed configurations when $\ell = 1\mu m$. Width of the shear band is almost the same for all mesh densities.
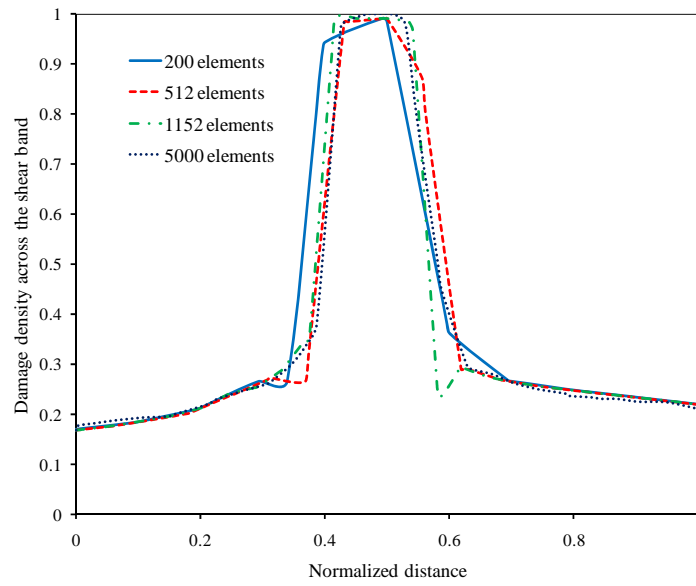
Figure 8.17. Mesh-independent results of damage density across the shear band when $\ell = 1 \mu m$.
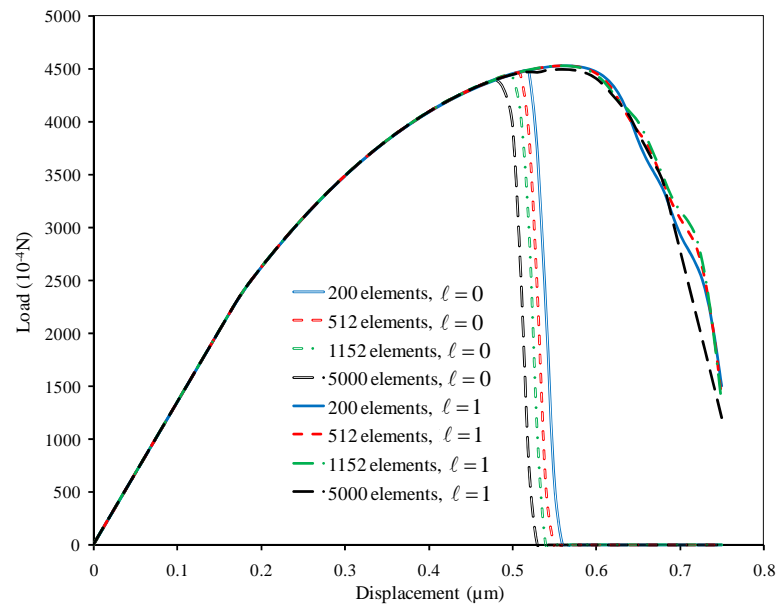
Figure 8.18. Load-Displacement diagrams showing the results for $\ell = 0$ and $\ell = 1 \mu m$.

8.6. Effect of Different Parameters on Damage Localization

8.6.1. Effect of Parameters α and β

In this section, the effect of material constants α in the damage force equation Eq. (8.3) and β in Eq. (8.8), on the location and width of shear band is investigated. The parameter α defines the material sensitivity to confinement whereas the parameter β represents the rate of damage growth. These parameters are selected as $\alpha = 0$ and $\beta = 0.1$ in the previous examples. To study the effect of these parameters on the development of damage localization, the nonlocal damage case for $\ell = 1\mu m$ is simulated for the intermediate mesh density for the fixed plate in tension examples.

The parameter α in Eq. (8.3) controls the material sensitivity due to confinement and mean stress. In other words, α describes the fact that specimen with higher compressive mean stress can tolerate more load without going to a damaged state. However, in this problem the applied stress is tensile, so it is expected that the regions with higher tensile stresses become damaged faster. The simulation results presented in Figure 8.19(a) confirms the pressure sensitive results.

One can explain that due to Poisson's effect, regions that are closer to the bottom edge boundary undergo higher tensile stresses which can be characterized by the negative mean stress. Hence, these regions should go to the damage region earlier. As it is obvious from Figure 8.19(a), increasing the value of α causes the shear band to move slightly toward the bottom edge and for large values of α the damaged region is very close to the bottom. Furthermore, the load displacement diagram for different values of α is also shown in Figure 8.19(b). This figure shows that increasing the parameter α induces a softening effect and causes the specimen to go to the softening region faster.

$\alpha = 0$ $\alpha = 0.1$ $\alpha = 0.2$ $\alpha = 0.25$

(a)

(b)
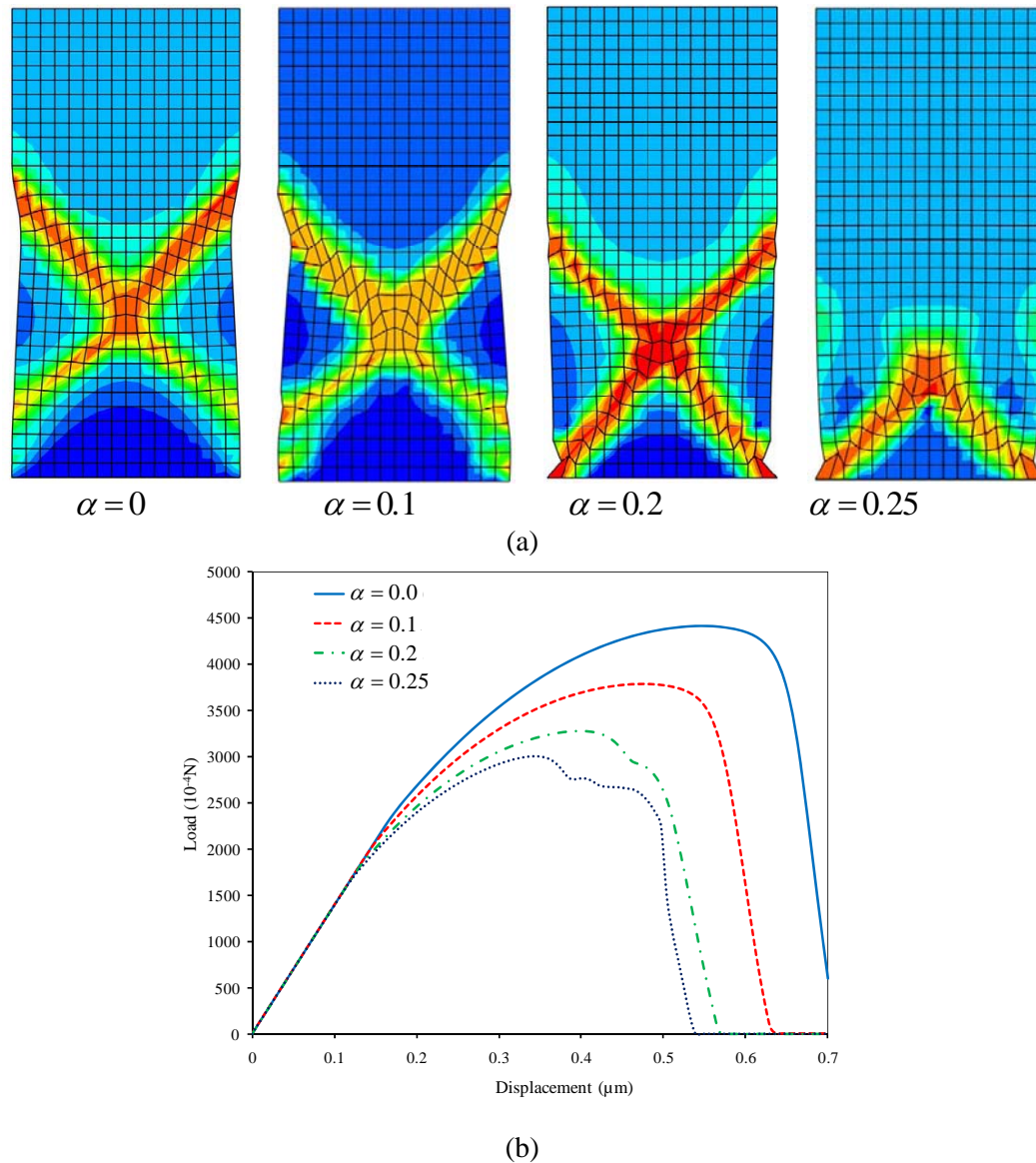
Figure 8.19. Model predictions using the nonlocal damage model when $\ell = 1\mu m$. (a) Damage density contour on the deformed shape for different values of α; (b) load-displacement diagrams for different values of α.

The effect of the damage growth rate parameter β is shown in Figure 8.20. The damage density contours are plotted in Figure 8.20(a). It can be seen that the width of shear band increases as the damage growth rate increases. To clarify the change in the shear band width, damage variable across the shear band is plotted in Figure 8.20(b), which confirms the increase in shear band width upon the increase in damage growth

rate. As it is expected, damage grows and distributes within the specimen faster for larger damage growth rates. This effect can be seen clearly in the load-displacement diagrams shown in Figure 8.20(c). Thus, higher damage growth rates make the specimen to undergo the softening region faster and exhibits higher degree of softening.

(a)

(b)
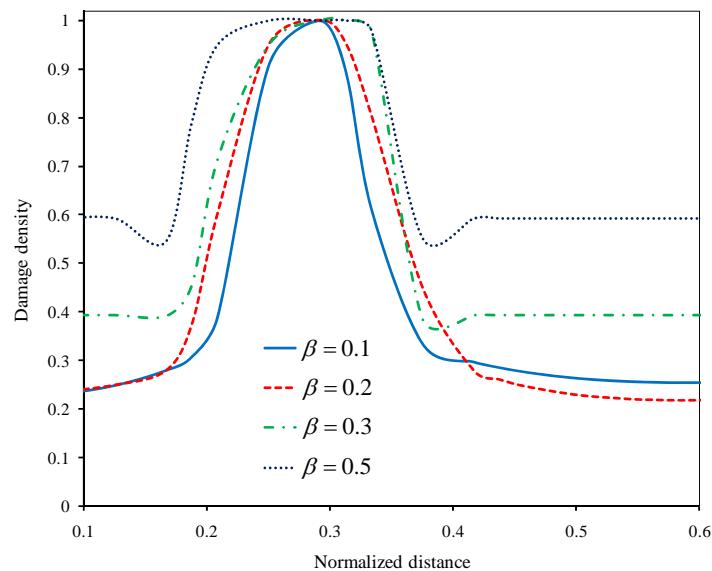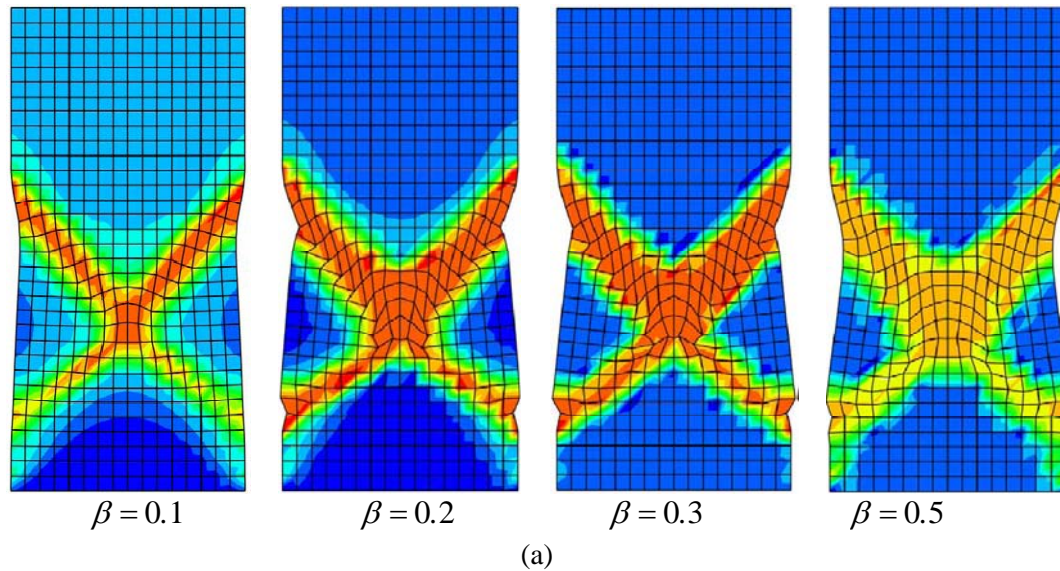
Figure 8.20. The effect of β on (a) damage density contour on deformed shape, (b) damage density across the shear band, (c) load-displacement diagram. Results are for $\ell = 1\mu m$.
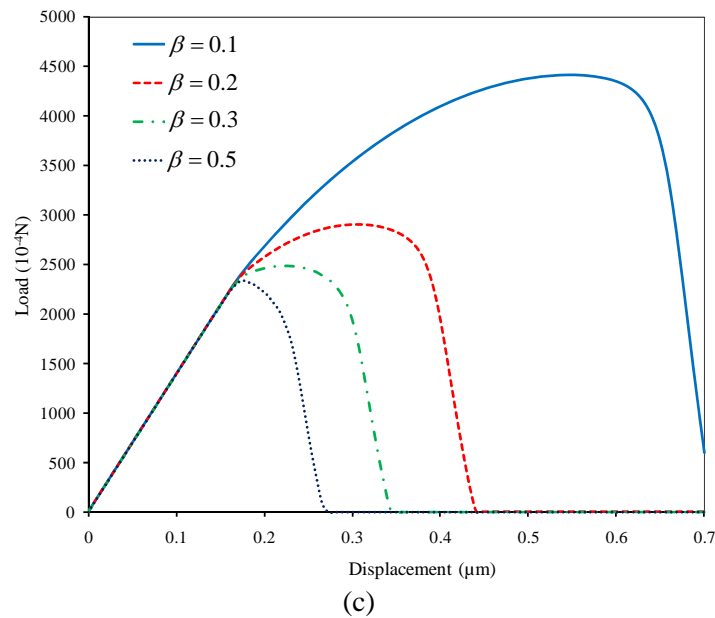
(c)

Figure 8.20. Continued.

From Figures 8.19 and 8.20, one can conclude that α controls the location of shear band and causes the shear band to form in regions with smaller confinement, whereas β controls the width of the shear band and rate of softening behavior.

8.6.2. Length Scale Effect

In this section, the effect of the length scale value on the width of shear band, deformation pattern, and damage distribution across the shear band is presented. To this aim, the fixed plate in tension with 1152 elements is selected. The specimens are loaded until complete failure. Deformation patterns, damage density across the shear band, and load-displacement diagrams are shown in Figures 8.21(a), 8.21(b), and 8.21(c), respectively, for different values of ℓ. Figure 8.21(a) clearly shows that the width of the shear band depends on the length scale value such that the larger the length scale value the broader the shear band width as also clearly shown in Figure 8.21(b), which is a known result (Pamin, 1994). This shows that the proposed computational algorithm yield reasonable and physically known behavior. The damage distribution across the shear band and the load-displacement diagrams for various length scales are shown in Figures

8.21(b) and 8.21(c), respectively. Figure 8.21(b) shows that increasing the length scale value causes the damage density to regularize more in the specimen. Figure 8.21(c) shows that the length scale value is the parameter that delays damage initiation and growth. Hence, materials with larger length scale values tolerate higher stresses compared to the materials with smaller length scale values.

$$\ell = 1\mu m \qquad \ell = 3\mu m \qquad \ell = 6\mu m \qquad \ell = 10\mu m$$

(a)
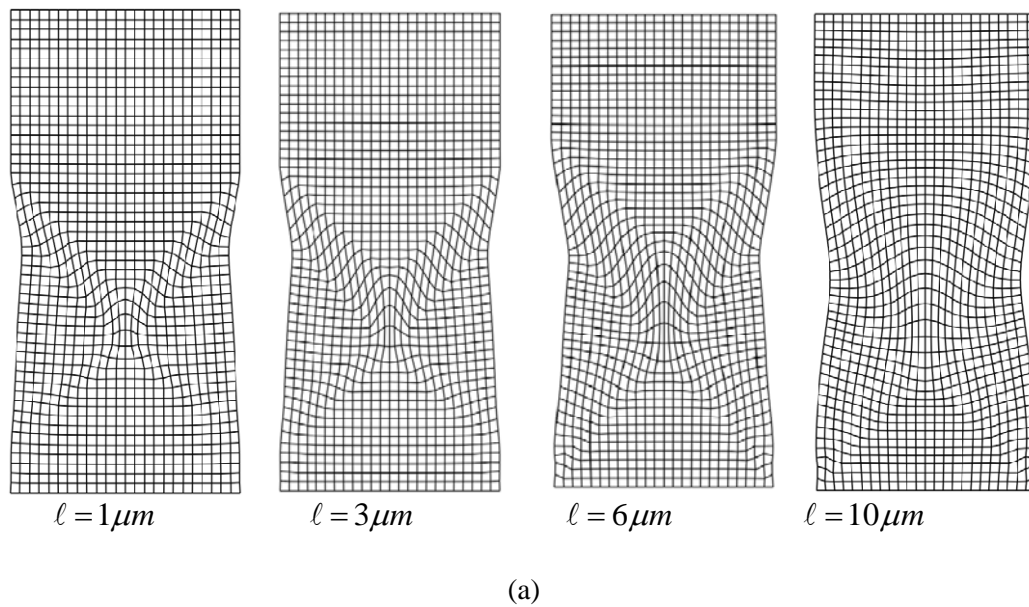
Figure 8.21. Effect of ℓ on (a) deformed pattern, (b) damage density across the shear band, (c) load-displacement diagram. Nonlocal damage for $\ell = 1,3,6,$ and $10\mu m$.
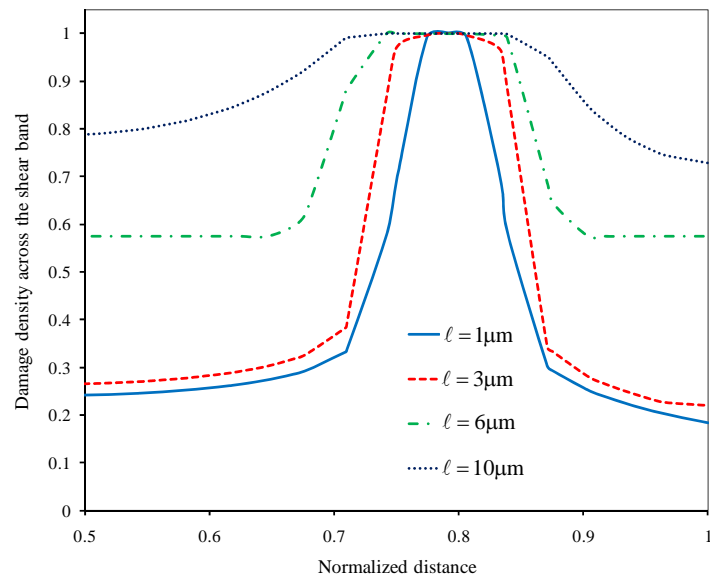
(b)
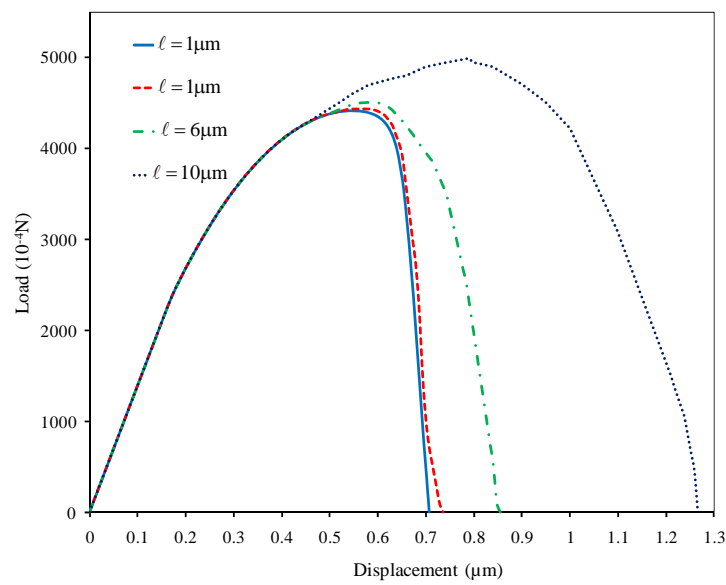
(c)

Figure 8.21. Continued.

8.7. Conclusions

Localization of deformation and damage is associated with the softening behavior in the stress-strain response. Unfortunately, when using classical continuum damage theories, this softening behavior in the stress-strain diagram causes instabilities that result in the

loss of well-posedness of the governing partial differential equations and in turn lead to mesh-dependent results and non-physical description of damage evolution and failure. As shown by many authors, a very effective way to remedy this problem is through the nonlocal gradient-enhanced damage theory. However, one of the most challenging issues when dealing with this type of theories is their implementation in the finite element codes. In this work, a simple and straightforward computational approach is presented for numerically integrating the nonlocal constitutive equations with little effort required to modify an existing finite element code. Hence, by using this approach, one can avoid the common practice in introducing high-order continuous shape functions (e.g. C^1 class or penalty-enhanced C^0 class functions) with additional degrees of freedom in a finite element code to calculate the gradient terms, which is computationally difficult and expensive. A simple algorithm for satisfying damage consistency condition is proposed which can be implemented easily in a finite element code. Numerical algorithm presented in this paper is implemented in the well-known finite element code Abaqus via the user material subroutine UMAT. The effectiveness and robustness of the proposed approach in alleviating the mesh-dependency problem when simulating damage localization and the post-peak response are illustrated through two numerical examples. The examples show that results of the shear band converge to a unique solution upon mesh densification and clearly show that the proposed computational algorithm works well in integrating the nonlocal damage theories. Moreover, a parametric study on the effect of the material constants associated with the presented elastic-damage model is conducted with special emphasis placed on their effect on the size of the localized damage zone and the post-peak response. Finally, the proposed numerical algorithm can be easily adapted by more complex constitutive models that incorporate the effect of higher-order gradients.

The proposed general numerical technique along with the developed constitutive model will be employed in the next chapter to investigate the best way for predicting the performance simulation of asphalt pavements.

CHAPTER IX

FINITE ELEMENT AND CONSTITUTIVE MODELING TECHNIQUES FOR PREDICTING RUTTING IN ASPHALT PAVEMENTS

9.1. Introduction

This chapter focuses on a comprehensive evaluation of the effects of different finite element (FE) modeling techniques and material constitutive models on predicting rutting in asphalt pavements under repeated loading conditions. Different simplified two-dimensional (2D) and more realistic three-dimensional (3D) loading techniques are simulated and compared for predicting asphalt rutting. This study also evaluates and compares the rutting performance predictions using different material constitutive behaviors such as viscoelastic-viscoplastic, elasto-viscoplastic, and coupled viscoelastic, viscoplastic, and viscodamage behaviors.
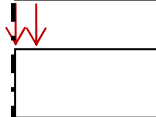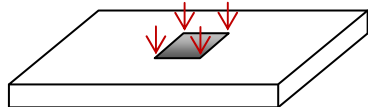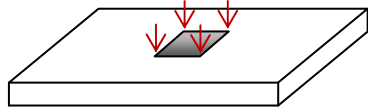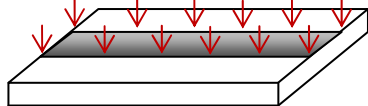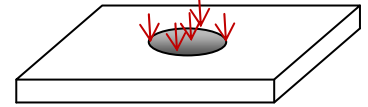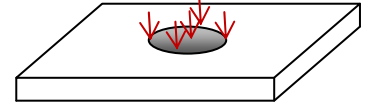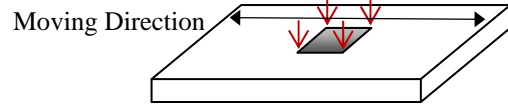
Rutting is one of the most serious distresses in asphalt pavements affecting the pavement performance and service life. Therefore, the accurate simulation of rutting in asphalt pavements is essential for improving their performance and management. The main mechanism of rutting is the accumulation of permanent deformation that increases progressively with increasing number of loading cycles. However, the complex nature of the applied loading conditions, very large number of loading cycles (millions of loading cycles), and complex constitutive behavior of asphaltic materials make the accurate prediction of rutting a very difficult and challenging task. Even with the current state-of-the-art in computational power, conducting 3D finite element (FE) rutting performance simulations for pavements subjected to millions of wheel loading cycles and considering realistic wheel tracking and environmental loading conditions is almost impossible. Therefore, an evaluation of a simplified numerical model with efficient and realistic loading conditions and material constitutive models that can simulate the pavement rutting performance for a very large number of loading cycles is desirable. In order to accurately simulate the pavement response, the computer simulations should have the

capability to capture the response by considering structural loading, boundary conditions, and material constitutive behavior. Therefore, realistic loading and boundary conditions should be imposed, and an accurate material constitutive model should be utilized. The material model should be able to describe the inelastic-damage behavior of asphalt under different stress levels, loading rates, and temperatures.

At the material level, experimental measurements show that the deformation response of asphaltic materials is time-, rate-, and temperature-dependent such that the accurate constitutive model should at least consider the couplings between the temperature, viscoelasticity, viscoplasticity, and viscodamage models. Therefore, the constitutive model presented in Chapter II is used here to investigate the effect of each component of the constitutive model on rutting performance simulation of asphalt pavements.

In terms of the FE modeling of asphaltic pavements under simplified loading conditions, several FE studies have been conducted in order to predict the rutting performance. Lu and Wright (1998) constructed a two-dimensional (2D) plane strain FE model to represent a three layers pavement structure and employed the Perzyna's viscoplastic model to predict the permanent deformation under large number of loading cycles assuming a pulse loading. Pulse loading is commonly used to represent a wheel moving load. However, the implicit assumption in conducting 2D plane strain FE simulations is that the loading condition is represented as an infinite load strip in the traffic direction (see Table 9.1). Similarly, Hunter et al. (2007) have also conducted 2D plan strain FE simulations of the Wheel Tracking Test in order to predict rutting performance assuming a pulse loading. However, Hunter et al. (2007) have used a power law viscoplasticity constitutive model and neglected viscoelasticity and damage evolution. Their simulations show that the shape of rutting is significantly different than that obtained experimentally. Kettil et al. (2007) have conducted 2D axisymmetric FE simulations and compared two different loading assumptions; pulse loading and equivalent loading (see Table 9.1).

Table 9.1. Summary of simulated loading assumptions.

Mode	Loading approach	Loading Area	Schematic representation of loading modes
1 (2D)	Pulse loading (plane strain)	One wheel	
2 (2D)	Equivalent loading (plane strain)	One wheel	
3 (2D)	Pulse loading (axisymmetric)	One wheel	
4 (2D)	Equivalent loading (axisymmetric)	One wheel	
5 (3D)	Pulse loading	One wheel	
6 (3D)	Equivalent loading	One wheel	
7 (3D)	Pulse loading	Whole wheel path	
8 (3D)	Equivalent loading	Whole wheel path	
9 (3D)	Pulse loading	Circular loading area	
10 (3D)	Equivalent loading	Circular loading area	
11 (3D)	Moving loading	One wheel	Moving Direction

The equivalent loading assumption, which is another commonly adapted loading assumption to represent a wheel moving load, applies the wheel loading over the

respective accumulative loading time neglecting the unloading time periods. Results from this study showed that the equivalent loading assumption gives comparable rutting performance predictions from the pulse loading assumption such that by assuming an equivalent loading one can save significant amount of computational time. However, this conclusion is based on assuming an elasto-viscoplastic material behavior neglecting the viscoelastic and damage behavior of asphaltic materials. Cho et al. (1996) compared the rutting predictions from 2D plane strain, 2D axisymmetric, and 3D FE simulations assuming a linear elastic behavior of the asphalt material. Huang et al. (2001) conducted 2D and 3D axisymmetric simulations of asphalt pavement sections using an elasto-viscoplastic model. Results of this research showed that the 3D FE analysis gives more accurate predictions as compared to field measurements. Huang (1995) proposed a step loading function to simulate a large number of loading cycles of a moving load in 3D FE simulations. This loading function accumulates each wheel pass time to produce a total cumulative loading time and then applies a single load step to a set of elements in the middle of the whole wheel path. Hua (2000) improved the cumulative loading time approach by Huang (1995). The improved approach also accumulates each single loading time, and then applies a single step loading on the whole wheel path to represent the moving wheel loading in 3D simulations. However, in both of these works [i.e. Huang (1995) and Hua (2000)] an elasto-viscoplastic model is used for validating the proposed loading models. Huang (2001), Hua and White (2002), and Park et al. (2005) used an elasto-viscoplastic model along with the cumulative loading time approach to represent a large number of loading cycles. Saleeb et al. (2005) used a visco-elasto-plastic model to conduct a 3D FE simulation with a moving loading model by applying the loading on one set of elements and then moving forward to the next set of elements. However, most of the aforementioned FE simulations have focused on the effect of loading modes. To the authors' best knowledge, no study yet has used a comprehensive constitutive model incorporating nonlinear viscoelasticity, viscoplasticity, and viscodamage for simulating rutting performance of asphalt pavements.

The main objective of this work is to study the effect of different simplified wheel loading assumptions on 2D and 3D FE rutting simulations of asphalt layers using different constitutive behaviors; namely, elasto-viscoplastic, viscoelastic-viscoplastic, and coupled viscoelastic-viscoplastic-viscodamage constitutive behaviors. Different simplified two-dimensional (2D) and more realistic three-dimensional (3D) finite element (FE) loading techniques that represent the commonly conducted Wheel Tracking Test are simulated and compared to predict asphalt rutting performance.

The simulations show that the assumption of the equivalency between a pulse loading and an equivalent loading, which are commonly used as simplified loading assumptions for predicting rutting, is reasonable for viscoelastic-viscoplastic and elasto-viscoplastic constitutive behaviors. However, these loading assumptions and material constitutive models overestimate rutting as damage grows. Results show that the 2D plane strain FE simulations significantly overestimate rutting as compared to the rutting performance predictions from more realistic 3D FE simulations (Abu Al-Rub et al., 2011).

9.2. Material Constitutive Model

The coupled thermo-viscoelastic-viscoplastic-viscodamage constitutive model presented in Chapter II is used to conduct this study. This constitutive model is not presented in this chapter in order to avoid the repetition. Please refer to Chapter II for a comprehensive and detailed description of the constitutive model.

9.3. Description of the Finite Element Simulations

This section presents the description of 2D and 3D FE rutting simulations of a test asphalt slab in a Wheel Tracking Test, and the description of the employed wheel loading assumptions for simplifying the FE simulations.

9.3.1. Geometry of the Finite Element Model

This study simulates the Wheel Tracking Test as an example to investigate the effect of various commonly adapted loading assumptions on rutting predictions. Based on this analysis, one can draw conclusions about the suitability and computational cost of each loading assumption in predicting the rutting in asphaltic layers. The geometry of the Wheel Tracking Test is illustrated in Figure 9.1.
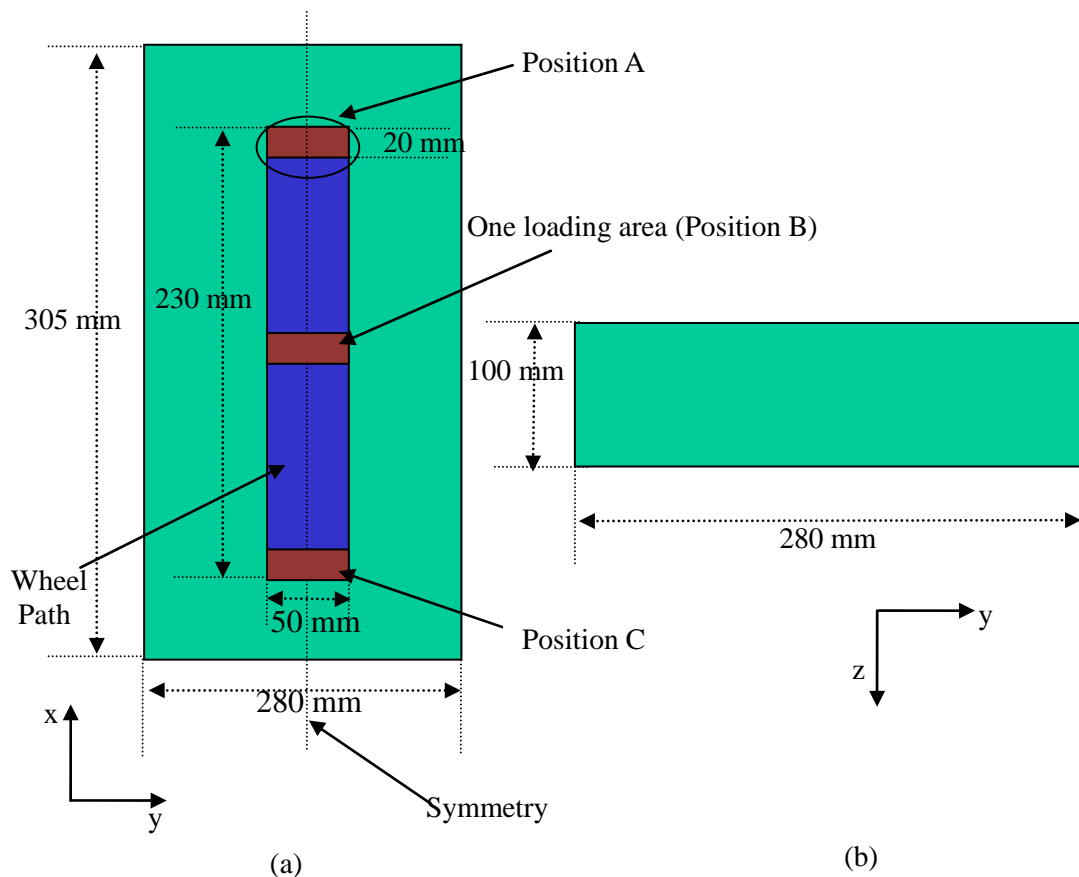
Figure 9.1. The geometry of the simulated Wheel Tracking Test. (a) X-Y plane; (b) Y-Z plane.

The wheel tracking test consists of an asphalt slab of dimensions of $305 \times 280 \times 100$ mm^3 in length, width, and depth, respectively. A wheel load is applied at the middle of the slab along the width and moved bake and forth along the length of the slab. The

wheel moves with a speed of 40 passes per minute over a wheel path of 230mm length, which is equivalent to a 0.55 km/hr speed. The wheel loading area is assumed as a rectangular shape with dimensions of 20×50 mm^2 in width and length, respectively. The employed asphalt layer, dimensions of the loading area, and the wheel speed are from the Wheel Tracking Test conducted by Hunter et al. (2007). The loading is applied as a step load within each loading cycle. Because of the symmetric nature of the wheel loading condition and the slab's geometry, the finite element model can be reduced to a half of the slab by constraining the horizontal direction on the vertical edge of the model to represent the middle of the slab.

The 3D and 2D finite element meshes showing the applied wheel loading are shown in Figures 9.2(a) and 9.2(b), respectively.

(a)   (b)
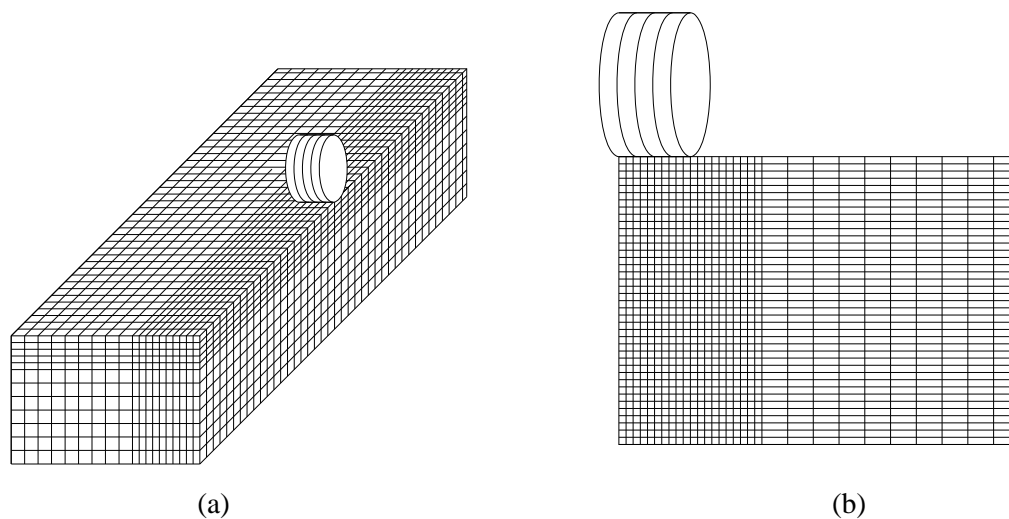
Figure 9.2. The FE mesh in (a) the 3D simulations and (b) the 2D simulations.

The boundary conditions in both 2D and 3D FE models are imposed such that the horizontal direction on the opposite side of the symmetric boundary is fixed; while the bottom of the slab is fixed in the vertical direction. The used element types in the 2D FE simulations in Abaqus are plane strain four-node element with reduced integration (CPE4R) for plane strain analysis, and axisymmetric four-node element with reduced

integration (CAX4R) for axisymmetric analysis; whereas, 3D eight-node element with reduced integration (C3D8R) is used for conducting 3D FE simulations. Moreover, a maximum element aspect ratio of 2 is used for the 2D and 3D elements, respectively. According to the performed convergence studies for the 2D simulations, 2.5×2.5 mm^2 elements are used under and close to the loads, whereas, the maximum element size of 5×5 mm^2 is used for the area far from the loading path. For the 3D simulations, $2.5 \times 2.5 \times 2.5$ mm^3 elements are used under the load and close to loading path, whereas, the maximum element size of $5 \times 5 \times 5$ mm^3 is used for the regions that are far from the loading path. From a convergence study that is not reported here, the constructed 2D and 3D meshes were sufficient to get converged results that are independent of the mesh density. The loading level is 770 kPa and is applied on the top of the asphalt layer with different loading scenarios as described in the next section. For simplicity, the shape of the applied load is assumed rectangular. Moreover, frictional and tangential loadings from the contact of the wheel with the asphalt top surface are neglected in this study.

9.3.2. Applied Wheel Loading Assumptions

The loading modes (or loading assumptions) can be categorized into two main types (see Table 9.1): (1) *loading duration* such as pulse loading, equivalent loading, and moving loading; and (2) *loading area* such as applying the loading on one wheel area, on the whole wheel path, and on a circular loading area that represents the axisymmetric analysis. Considering the combination of those loading categories, four loading modes can be considered in the 2D simulations; whereas seven loading modes can be considered in the 3D simulations (see Table 9.1). Those loading modes are applied to the 2D and 3D FE models and then the results are compared in terms of the rutting performance in order to find an efficient loading mode, but simple enough, for the prediction of rutting under very large number of repeated loading cycles. Therefore, the objective from simulating these loading scenarios is to identify a loading assumption that allows one to predict effectively and with minimum computational cost the rutting performance of asphaltic layers over a large number of repeated loading cycles without the need of complicated and computationally expensive rutting performance simulations.

9.3.2.1. Wheel loading assumptions in 2D simulations

In the 2D FE simulations, two cases are considered for the area on which the loading is applied: (1) the loading is applied on an infinite stripe bar along the length of the pavement; (2) the loading is applied on a circular area at the middle of the pavement. The first case is simulated using 2D plane strain FE models, whereas the second case is simulated using 2D axisymmetric FE models. Moreover, two loading durations are assumed for each of the cases. The first loading duration is a pulse loading in which the wheel load is applied with a loading time period of 0.109 sec and then the load is removed for 0.109 sec as shown in Table 9.1 and Figure 9.3.
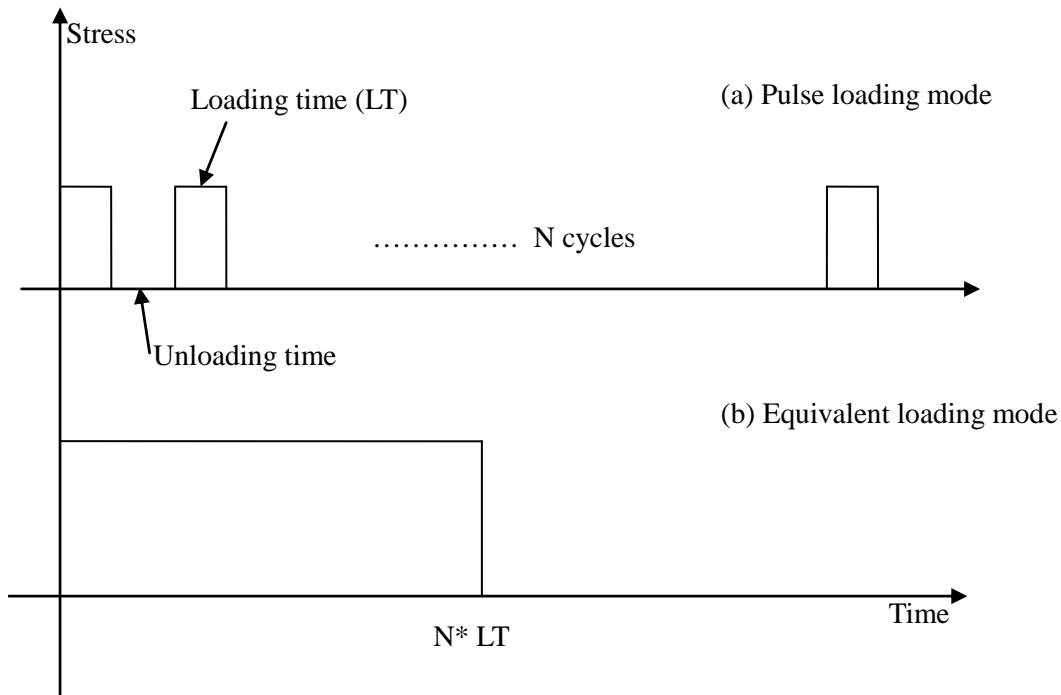
Figure 9.3. The sketch of equivalent and pulse loading modes. Equivalent loading is obtained by substituting pulse loading by a one step equivalent loading whose duration is equal to the summation of loading times in pulse loading.

The simulated total loading-unloading cycles in this case are 1000 cycles. The loading scheme is shown in Figure 9.3(a). The second loading duration is the equivalent

loading mode (Mode 2) as shown in Table 9.1 and Figure 9.3(b). This loading assumption represents the equivalent loading time by accumulating the loading time from all loading cycles and then applying the wheel loading at once in one loading cycle for the period of accumulated time such that the unloading or resting time is neglected. The advantage of this loading model is that only one step loading is applied instead of applying large number of loading steps, and thus reducing greatly the computational cost. Hence, four loading assumptions are considered in the 2D simulations (see Table 9.1).

9.3.2.2. Wheel loading assumptions in 3D simulations

In the 3D FE simulations as compared to the 2D simulations, one can specify the loading location and apply more realistic loading conditions. In the 3D simulations, seven wheel loading scenarios can be simulated. The fifth loading assumption (Mode 5) as shown in Table 9.1 assumes a pulse loading (as described in Modes 1 and 3) where the load is applied at the center of the asphalt layer (position B in Figure 9.1) with one wheel loading area. As shown in Figure 9.3 the loading duration is 0.109 sec and also 0.109 sec for the unloading within each cycle. A 1000 loading-unloading cycles are applied in this case. The sixth loading scenario (Mode 6) assumes an equivalent loading time (as described in Modes 2 and 4) where one wheel loading area is applied at position B in Figure 9.1 Loading modes 7 and 8 assume a pulse loading (loading time of 0.109 sec and unloading time of 0.109 sec) and an equivalent time loading, respectively. Both modes 7 and 8 assume the loading over the whole wheel path (shown in Figure 9.1). Moreover, a circular loading area is assumed for modes 9 and 10. A pulse loading and an equivalent time loading are assumed for loading modes 9 and 10, respectively. Finally, the last loading mode is the moving loading (Mode 11) where the wheel movement is simulated by applying the wheel loading on one set of elements (one loading area) at the beginning of the wheel path (position A in Figure 9.1). This load remains on the shaded area shown in Figure 9.4(a) for 0.109 sec $(t_2 - t_1)$ and then moving it forward to the next set of elements shown in Figure 9.4(b). The load remains on the same set of elements shown in Figure 9.4(b) for the same loading duration of 0.109 sec $(t_3 - t_2)$ and then moves to

another set of elements shown in Figure 9.4(c) until it reaches to the end of the wheel path (position C in Figure 9.1). This loading mode, which is illustrated in Figure 9.4, is the most realistic one as compared to the aforementioned loading modes. This approach of simulating the moving load is followed in the current study due to its simplicity and the significant reduction in the computational cost as compared to explicitly simulating a real tire with considering dynamic effects.

$t = t_1$

(a)

$t = t_2$

(b)

$t = t_3$

(c)
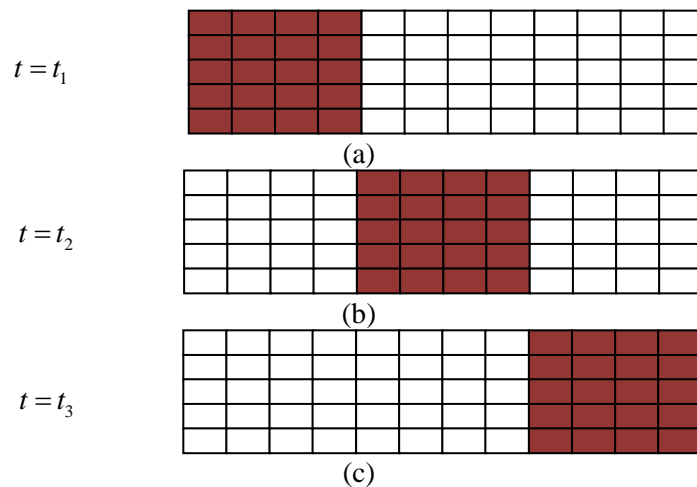
Figure 9.4. A schematic representation of the simplified wheel moving loading scenario. The shaded area is the region at which the wheel load is applied over a set of elements and then moved in the traffic direction to a new set of elements.

It should be noted that one would expect different rutting results using plane strain simulations (loading modes 1 and 2) or using their 3D counterparts (loading modes 7 and 8) comparing to the realistic loading conditions. However, the qualitative comparison of the changes in the results using these simplifications is of great importance in deciding on when to use these simplifications depending on the problem under study.

9.4. Material Parameters

The asphalt mix used in the Wheel Tracking test is the same as the asphalt mix used in Chapter II. Therefore, the viscoelastic, viscoplastic, and viscodamage model parameters

along with the time-temperature shift factors reported in Chapter II are used to simulate the rutting performance in this section. However, during some preliminary simulations, it is found that the identified viscodamage material parameters in Darabi et al. (2011c) did not cause noticeable amount of damage at the largest number of loading cycles simulated in this study. Therefore, in order to investigate the effect of damage evolution on rutting performance predictions, the material parameters for the viscodamage model are modified in such a way that signifies the effect of damage. These assumed material parameters are listed in Table 9.2.

Table 9.2. Assumed viscodamage model parameters for inducing early damage growth.

$\Gamma^{vd}\left(\sec^{-1}\right)$	$Y_0\left(\mathrm{kPa}\right)$	q	k
5×10^{-5}	500	10^{-5}	300

9.5. Rutting Predictions

Three different constitutive behaviors; elastic-viscoplastic, viscoelastic-viscoplastic, and viscoelastic-viscoplastic-viscodamage, are considered here in order to conduct a comprehensive study on the effects of: (1) different simplified loading assumptions as listed in Table 9.1, and (2) different material constitutive behaviors on the 2D and 3D rutting performance predictions of asphaltic layers. The elasto-viscoplastic behavior is simulated by turning off the viscoelastic and viscodamage constitutive models, whereas the viscoelastic-viscoplastic behavior is simulated by turning off the viscodamage constitutive model.

Since permanent (viscoplastic) displacement is not considered as a degree of freedom at the element's nodes in the classical finite element method, it is not possible to calculate the permanent surface deformation (i.e. rutting) directly. However, the magnitude of rutting can be calculated numerically by integrating the magnitude of the viscoplastic deformation through the pavement's thickness. This can be achieved by

dividing the thickness of the asphalt layer into a number of sub-layers, such that the rutting depth can be calculated as follows:

$$u_{rutting} = \sum_{i=1}^{k} \varepsilon^{vp(i)} h^{(i)}$$

(9.1)

where $u_{rutting}$ is the permanent displacement (rutting), $\varepsilon^{vp(i)}$ is the vertical viscoplastic strain at i^{th} layer through the depth of the asphalt layer, and $h^{(i)}$ is the ith layer thickness. In the following, the rutting is only calculated at the center of the slab (position B in Figure 9.1) for the purpose of conducting the numerical comparisons.

9.5.1. 2D Simulation Results

As it was mentioned, four loading scenarios can be assumed for performing the 2D FE simulations for predicting rutting as shown in Table 9.1 (i.e. Mode 1: plane strain-pulse loading; Mode 2: plane strain-equivalent loading; Mode 3: axisymmetric-pulse loading; and Mode 4: axisymmetric-equivalent loading). In the 2D plane strain simulations, it is assumed that the loading is applied as an infinite strip along the length of the asphalt layer. The corresponding 3D loading modes for the 2D loading modes 1 and 2 are loading modes 7 and 8, respectively. Furthermore, for the 2D axisymmetric simulations, the loading is assumed to be applied on a circular area. Hence, the corresponding 3D loading modes for the 2D loading modes 3 and 4 are loading modes 9 and 10. Figures 9.5 and 9.6 show the rutting versus loading cycles assuming a viscoelastic-viscoplastic constitutive behavior at temperatures 20 °C and 40 °C, respectively. Figures 9.5 and 9.6 show that the rutting values obtained from the pulse and equivalent loading cases are comparable. However, the difference depends on the employed constitutive model and decreases as the temperature increases. The 2D simulation results assuming an elasto-viscoplastic material behavior are shown in Figure 9.7. This figure shows that an elasto-viscoplastic constitutive behavior leads to prediction of the same rutting values for pulse and equivalent loading cases when the only difference is the loading duration (i.e. pulse loading versus equivalent loading).
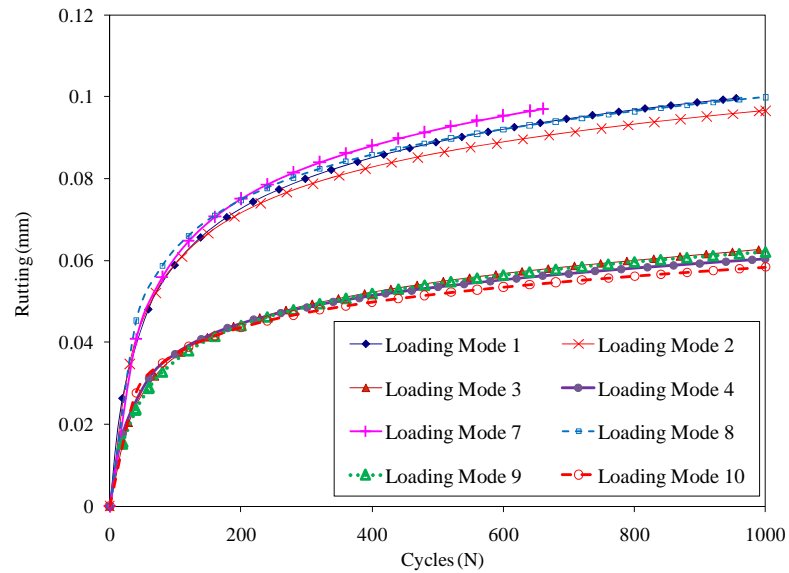
Figure 9.5. The rutting results for 2D plane strain and axisymmetric and their corresponding 3D FE simulations at temperature 20 ^{o}C assuming a nonlinear viscoelastic and viscoplastic material constitutive behavior.
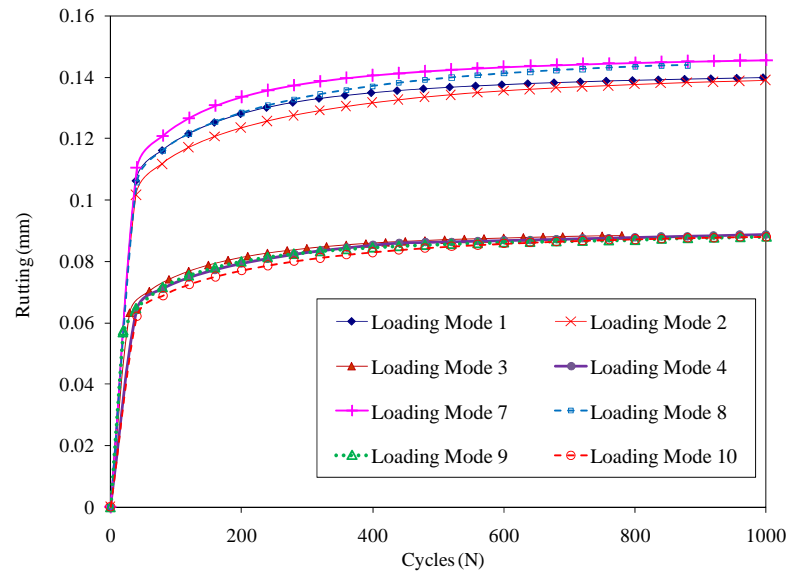
Figure 9.6. The rutting results for 2D plane strain and axisymmetric and their corresponding 3D FE simulations at temperature 40 ^{o}C assuming a nonlinear viscoelastic and viscoplastic material constitutive behavior.
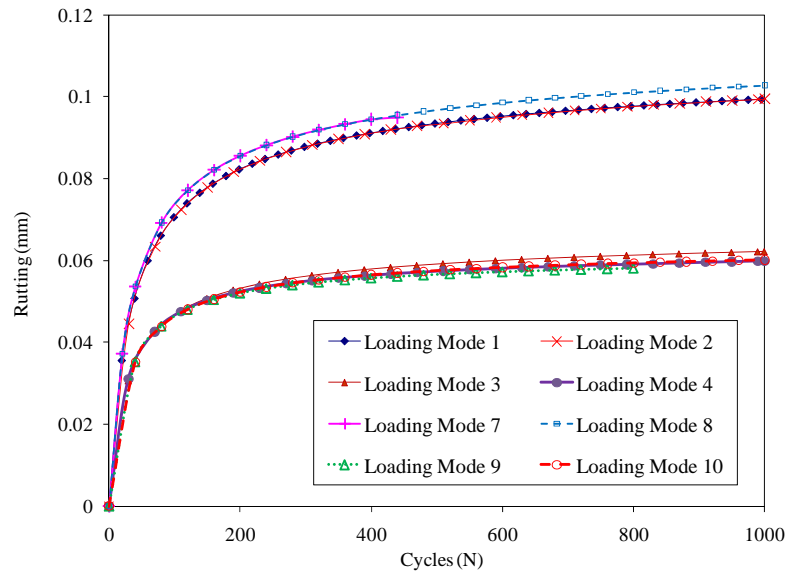
Figure 9.7. The rutting results for 2D plane strain and axisymmetric and their corresponding 3D FE simulations at temperature $20\,^{\circ}\text{C}$ assuming an elasto-viscoplastic material constitutive behavior.

The 2D simulation results for loading modes 1-4 when damage is activated are shown in Figure 9.8. Figure 9.8 shows that when damage is activated the simulation results for loading modes 1 and 2 could be very different. This is attributed to the viscous behavior of the damage law. In other words, changing the loading duration has a significant effect on the value of damage density since the damage law is time-dependent. These observations clearly show that the differences in rutting values using different simplified loading assumptions are also model-dependent. For example, these differences are magnified when the damage component of the model is added to the viscoelastic-viscoplastic constitutive model. Also, one may expect greater differences if other material mechanisms such as the viscoplastic softening (i.e. decrease levels of viscoplastic hardening during each loading cycle due to rearrangements in the material's microstructure) which is related to the loading history is considered. In other words, any material mechanism which is related to the loading history could magnify the differences in calculated rutting values using the simplified loading assumptions and realistic loading scenarios since the simplified loading assumptions do not capture the real loading history. Therefore, it should be emphasized that the rutting predictions from a

specific simplified loading assumption completely depends on the employed constitutive model and one cannot generalize the conclusions from a specific loading assumption independent of the employed constitutive model.
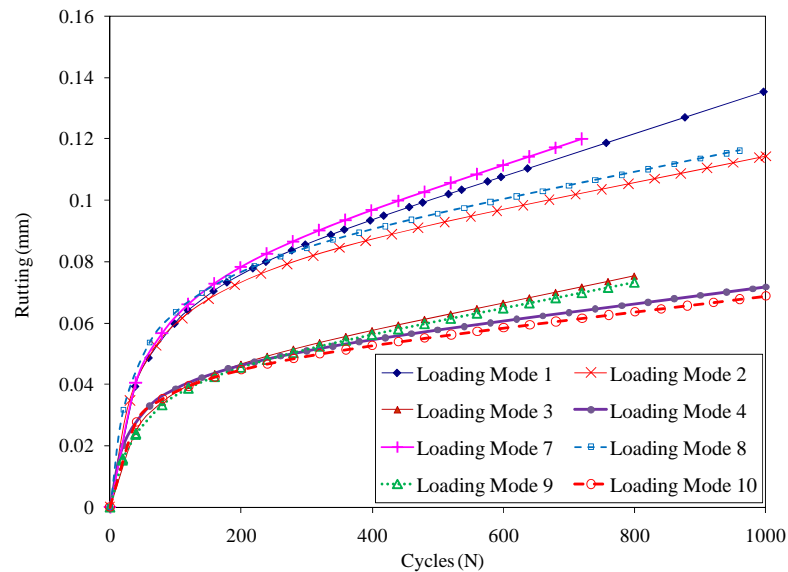
Figure 9.8. The rutting results for 2D plane strain and axisymmetric and their corresponding 3D FE simulations at temperature 20 $^{\circ}$C using the coupled viscoelastic-viscoplastic-viscodamage material constitutive model.

The same trend is also obtained from the simulation results of loading modes 3 and 4. The results of loading modes 7 and 8, which are the 3D counterparts of loading modes 1 and 2, respectively, are also presented in Figures 9.5-9.8. These figures show that the results of loading modes 1 and 7, and the results of loading modes 2 and 8 are very similar. Details of the 3D simulations are presented in the following section.

As an example, the viscoplastic strain and damage contours at different loading cycles for loading mode 1 is plotted in Figures 9.9 and 9.10, respectively, for the viscoelastic-viscoplastic-viscodamage model. Figure 9.9 shows that the maximum viscoplastic strain occurs at the half top portion of the pavement. Figure 9.10 shows that the maximum damage occurs at the top of the middle part of the asphalt layer which is exactly the region where the maximum viscoplastic strain occurs. However, as it is clear

from Figure 9.10, damage does not distribute toward bottom part of the asphalt layer instead it localizes at the top of the middle part of the asphalt layer that eventually causes macro-cracks at that region. These macro-cracks then propagate toward the surface of the asphalt layer.

It is noteworthy that due to the large computational cost the rutting simulations of this study are conducted up to 1000 loading cycles which is much lower than the actual number of loading cycles in the wheel tracking tests. Hence, it is not a surprise that FE predicted values for the surface rutting is lower than the actual rutting values in the wheel tracking tests which are conducted for huge number of cycles.
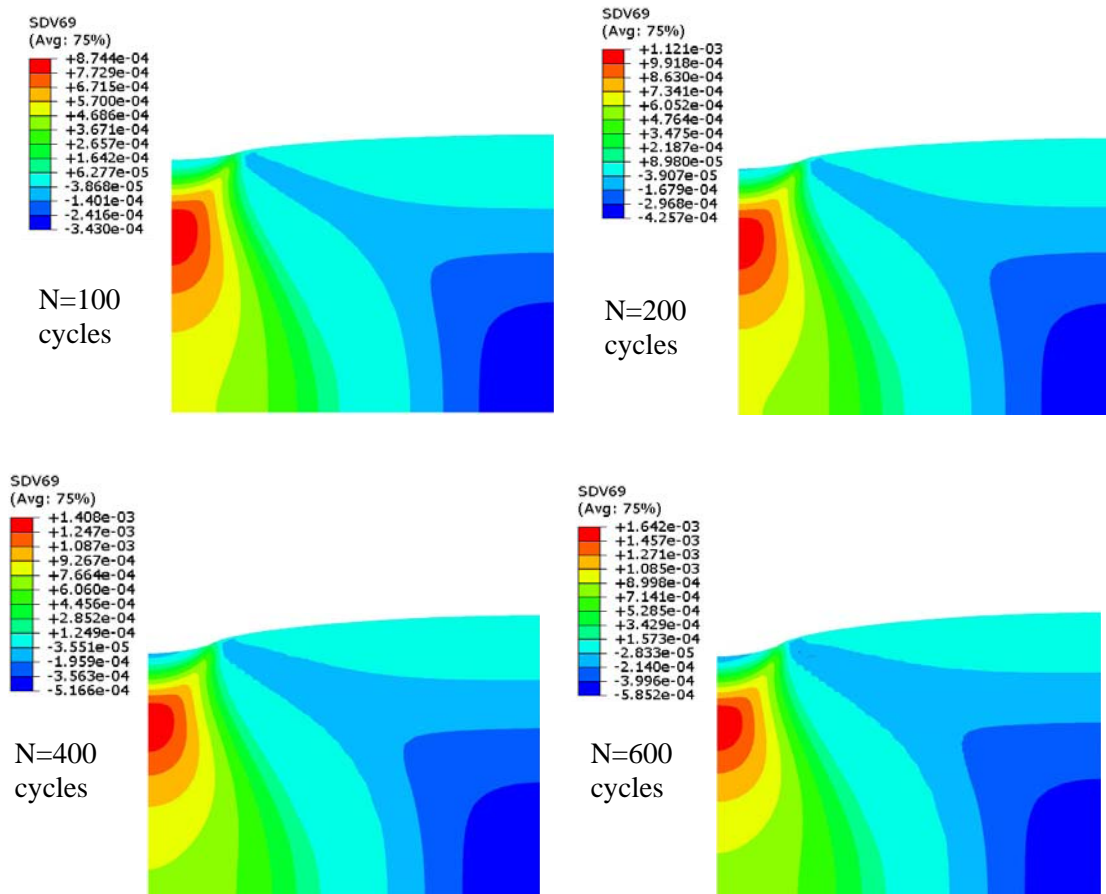
Figure 9.9. Viscoplastic strain distribution contours at different loading cycles for the 2D FE analysis when using the coupled viscoelastic-viscoplastic-viscodamage constitutive model at $T = 20^{o}C$ when simulating the pulse loading (loading mode 1).
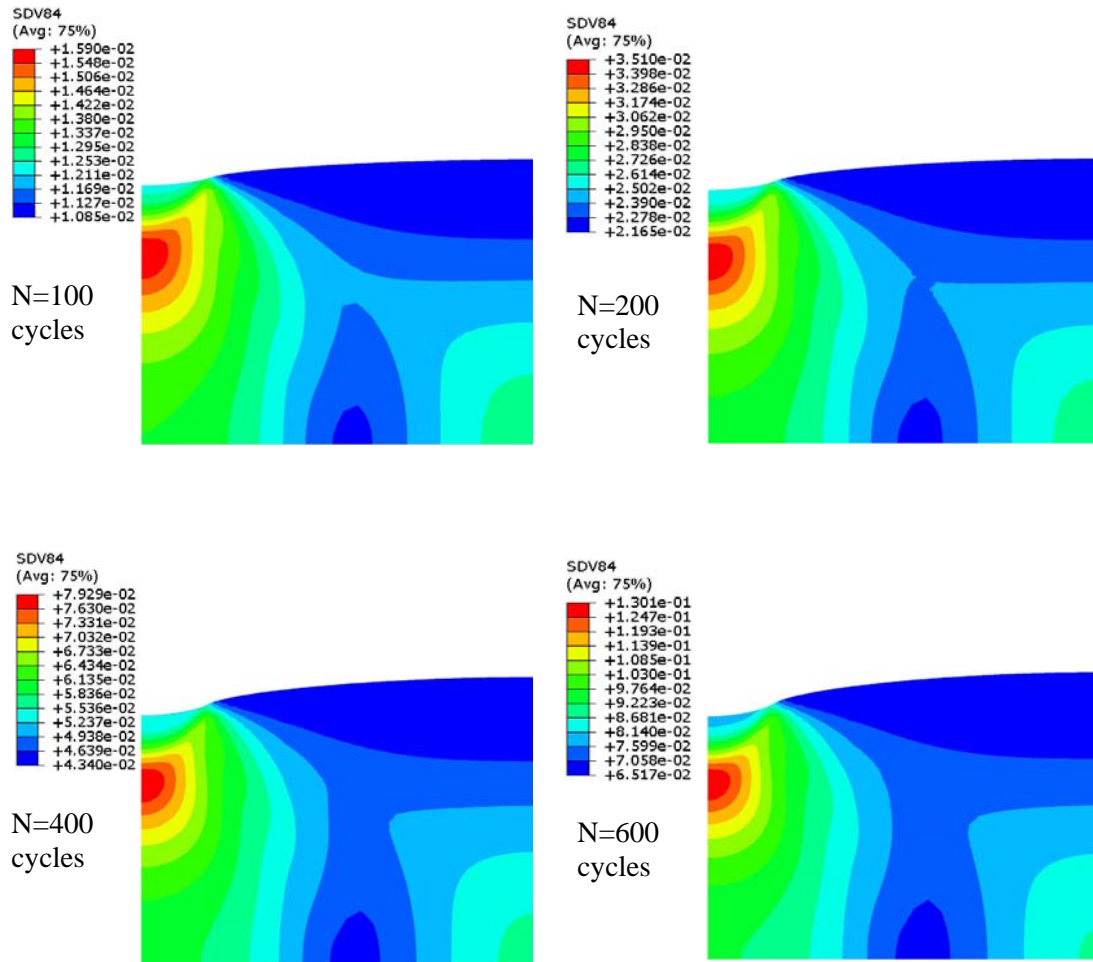
Figure 9.10. Damage distribution contours at different loading cycles for the 2D FE analysis when using the coupled viscoelastic-viscoplastic-viscodamage constitutive model at $T = 20^o C$ when simulating the pulse loading (loading mode 1).

However, the main purpose of this study is qualitative comparisons of rutting values obtained from different simplified assumptions on the constitutive model and on the imposed loading scenario with the most realistic constitutive model and loading scenario, which are viscoelastic, viscoplastic, viscodamage model and the moving load scenario, respectively, are used as a reference for qualifying the rutting predictions. Although this study provides a qualitative comparison between different assumptions for low number of loading cycles, the trend for larger number of loading cycles is expected

to be similar. The authors are currently working on developing an extrapolation technique that could be used to extrapolate the 3D simulation results obtained from low number of loading cycles to the simulation results for a large number of loading cycles.

9.5.2. 3D Simulation Results

Seven simplified loading scenarios are simulated for the 3D case. Figures 9.11 and 9.12 show the rutting predictions versus the number of loading cycles at temperatures $20\,^{\circ}$C and $40\,^{\circ}$C, respectively.
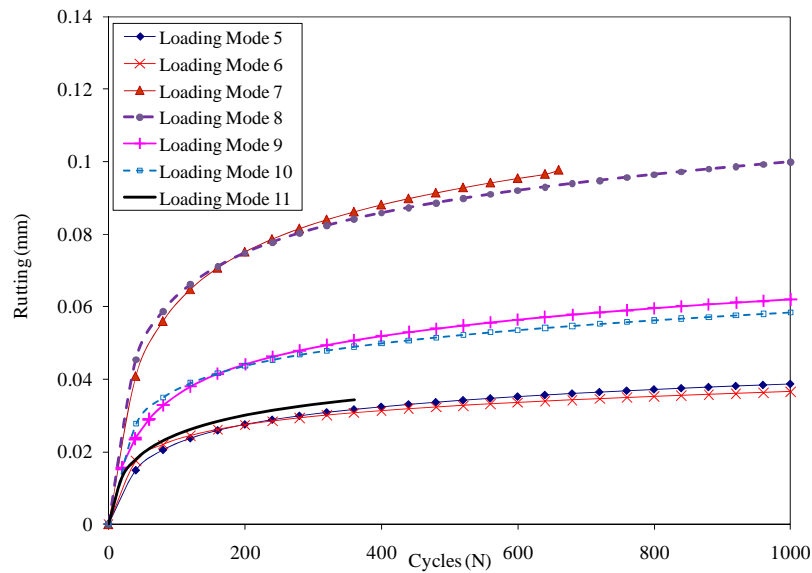
Figure 9.11. The rutting simulation results from 3D FE analysis at temperature $20\,^{\circ}$C assuming a nonlinear viscoelastic and viscoplastic material constitutive behavior.

These results are obtained assuming that asphalt material behavior is viscoelastic-viscoplastic with no damage. Since the rutting predictions from the moving load (Mode 11) are the closest to the real loading in a Wheel Tracking Test, these figures show that applying the loading over the whole wheel path (Modes 7 and 8) results in a significant error in predicting rutting as compared to the moving load (mode 11). Figures 9.11 and 9.12 show that the axisymmetric assumption also overestimates the rutting value as compared to the most realistic loading mode (mode 11). However, these figures

show that cases when the wheel loading is only applied on one wheel loading area (Modes 5 and 6) reasonably predict the simulation results of loading mode 11. Due to the very large computational cost in conducting the moving load simulations, the results are obtained up to about 400 and 500 cycles at temperatures 20 ^{o}C and 40 ^{o}C, respectively. In terms of the effect of the pulse and equivalent loading conditions (Mode 5 versus 6; Mode 7 versus 8; Mode 9 versus 10), one can notice from Figures 9.11 and 9.12 that the rutting predictions are close when applying Mode 5 versus Mode 6, Mode 7 versus Mode 8, and Mode 9 versus Mode 10.
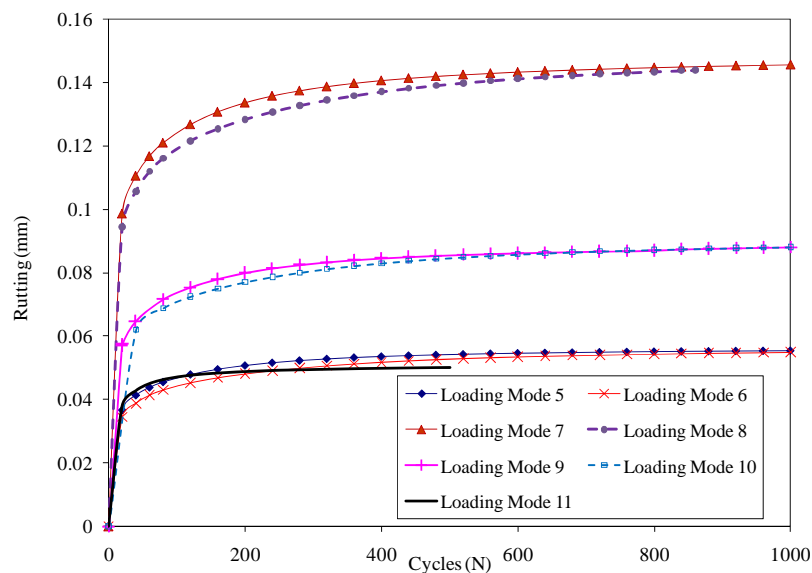
Figure 9.12. The rutting simulation results from 3D FE analysis at temperature 40 ^{o}C assuming a nonlinear viscoelastic and viscoplastic material constitutive behavior.

Figure 9.13 shows the relationship between the rutting predictions and the number of loading cycles when assuming an elasto-viscoplastic material constitutive behavior with no viscoelasticity and no damage. Figure 9.13 shows that using pulse and equivalent loading modes give comparable predictions when assuming that the loading area is the same. This observation is compatible with the 2D simulation results shown in Figure 9.7. As inferred from the results in Figures 9.11 and 9.12, the rutting predictions from the loading Modes 5 and 6 are close to that from the moving loading mode (Mode

11). However, when assuming loading Modes 7, 8, 9, and 10 the rutting is over predicted significantly.
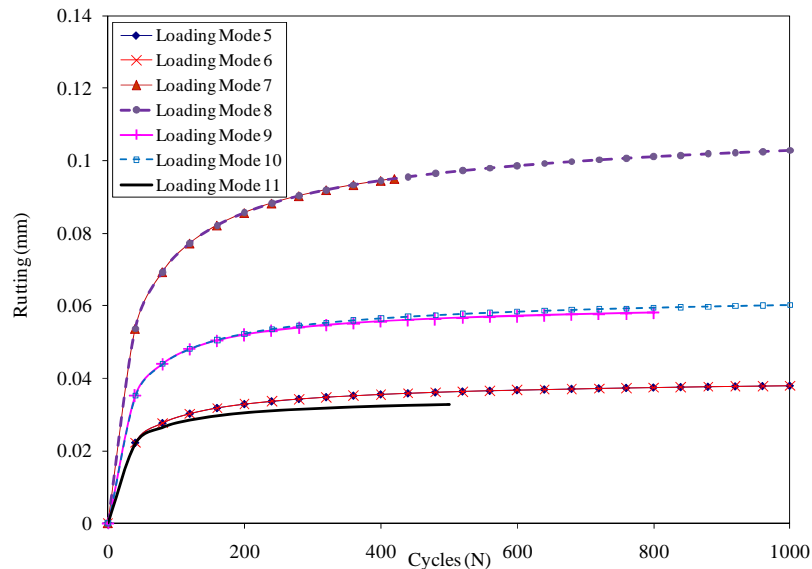
Figure 9.13. The rutting simulation results from 3D FE analysis at temperature $20\,^{\circ}\text{C}$ assuming an elasto-viscoplastic material constitutive behavior.

In order to study the effect of damage on rutting using different loading modes in the 3D simulations, the viscoelastic-viscoplastic-viscodamage constitutive model is now used. Figure 9.14 shows the corresponding results at temperature $20\,^{\circ}\text{C}$.

It is clear from Figure 9.14 that the rutting predictions are different for each loading mode and the difference increases as damage grows. Figure 9.14 also shows that when damage is activated, results from loading mode 11 (i.e. moving load) significantly deviates from the results of loading modes 5 and 6 as compared to that in Figures 9.11-9.13. This is attributed to the viscous behavior of the damage law. In other words, changing the loading duration has a significant effect on the value of damage density since the damage law is time-dependent. Moreover, it is found that the identified viscodamage material parameters in Darabi et al. (2011c) did not cause noticeable amount of damage at the largest number of loading cycles simulated in this study.
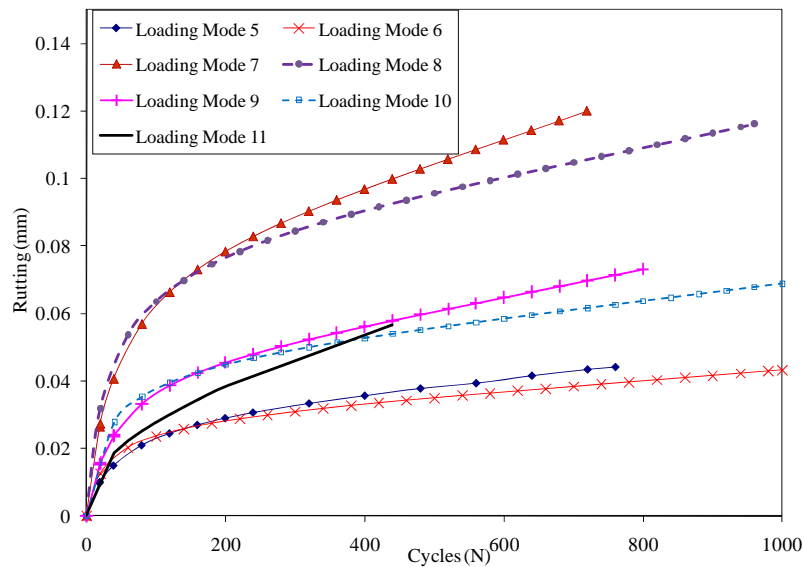
Figure 9.14. The rutting simulation from 3D FE analysis at temperature 20 °C using the coupled viscoelastic-viscoplastic-viscodamage material constitutive model.

Therefore, in order to investigate the effect of damage evolution on rutting performance predictions, the material parameters for the viscodamage model are modified in such a way that signifies the effect of damage. These assumed material parameters also contribute in magnifying the differences in the predicted rutting values using loading modes 5 and 6. The total loading duration for loading mode 11 is larger than the loading duration for other loading modes and, therefore, the rate of rutting accumulation and damage density from loading mode 11 are greater than those from other loading modes (i.e. modes 5-10). Figure 9.15 shows the evolution of the maximum damage density (occurring at the center of the loading and 30 mm from the top surface) for different loading modes, where the damage density evolves differently depending on the loading model and loading duration, but is much more important for loading mode 11 which causes the noticeable deviation from loading modes 5-10. Hence, one can conclude that it is not accurate to substitute the pulse loading with equivalent loading in the presence of significant damage. Also, substitution of loading mode 11 (moving load) with loading modes 5 and 6 may cause significant error when damage is activated. Figure 9.16 compares the rutting predictions for loading mode 11 when different

constitutive models are used. These results show that the effect of using different loading assumptions totally depends on the material constitutive model adapted for conducting the rutting simulations.
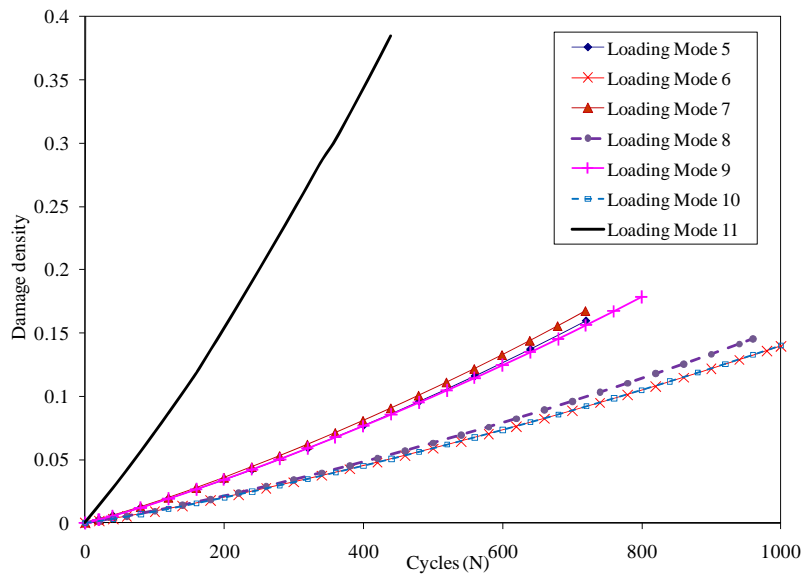
Figure 9.15. The evolution of the damage density from 3D FE analysis at temperature $20\,^{o}C$ using the coupled viscoelastic-viscoplastic-viscodamage material constitutive model.
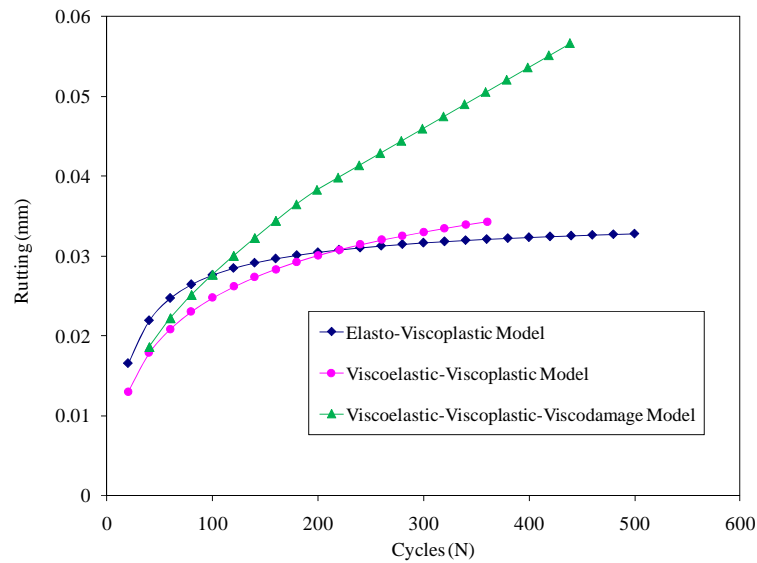
Figure 9.16. Comparing the rutting predictions from the 3D FE simulations using different constitutive models at temperature $20\,^{o}C$ for loading mode 11.

As an example, the evolution of viscoplastic strain distribution at different loading cycles for the loading mode 7 is plotted in Figure 9.17. Figure 9.17 shows that the maximum viscoplastic strain occurs at the top of the middle part of the asphalt layer which is consistent with the 2D predictions in Figure 9.9 and previous studies. Moreover, it also shows that as the number of loading cycles increases, the compressive viscoplastic strain extends toward both top and bottom of the pavement which contributes to more permanent deformation.
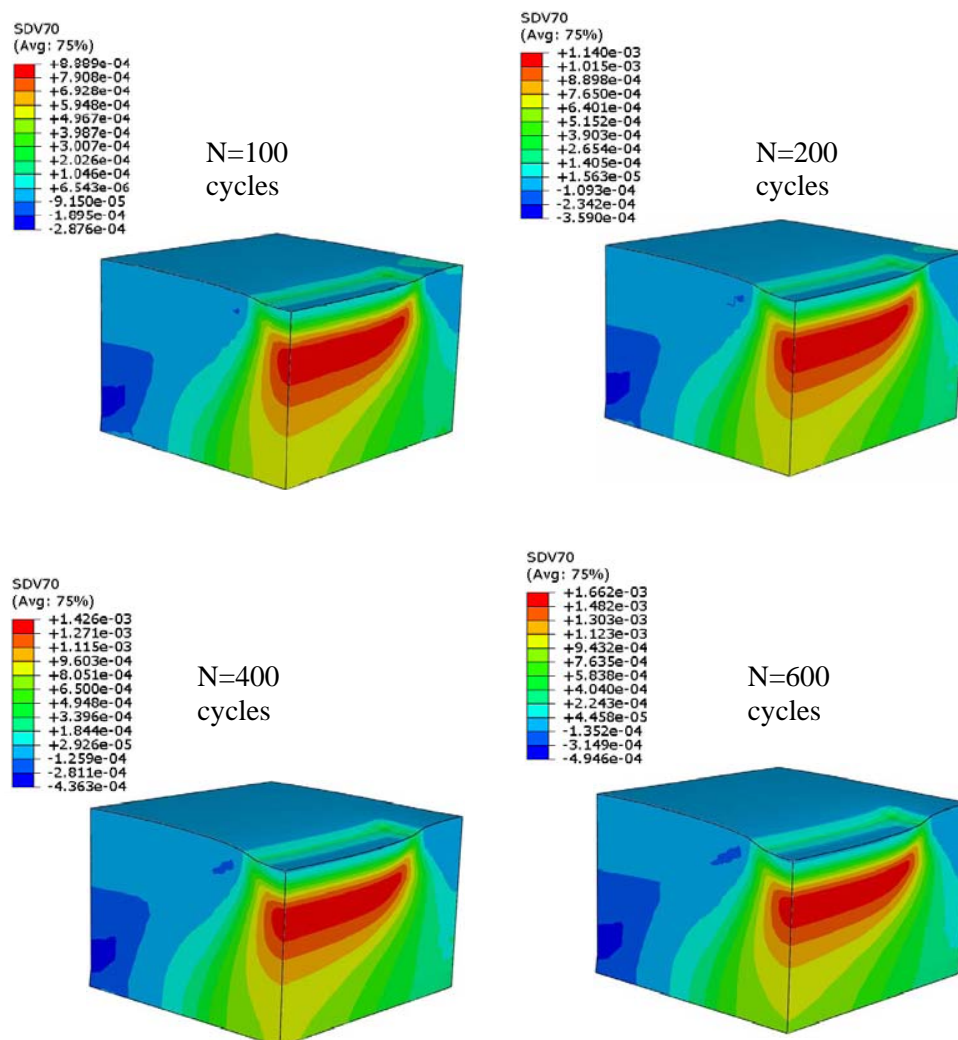
Figure 9.17. Viscoplastic strain distribution contours at different loading cycles for the 3D FE analysis when using the coupled viscoelastic-viscoplastic-viscodamage constitutive model at $T = 20^o C$ when simulating the pulse loading (loading mode 5).

Also, damage distribution contours are plotted for the same problem in Figure 9.18 which shows that the maximum damage occurs at the top of the middle part of asphalt layer which is exactly the region where the maximum viscoplastic strain occurs. The results in Figure 9.17 and 9.18 are consistent with the 2D viscoplasticity and damage contours (Figures 9.9 and 9.10).
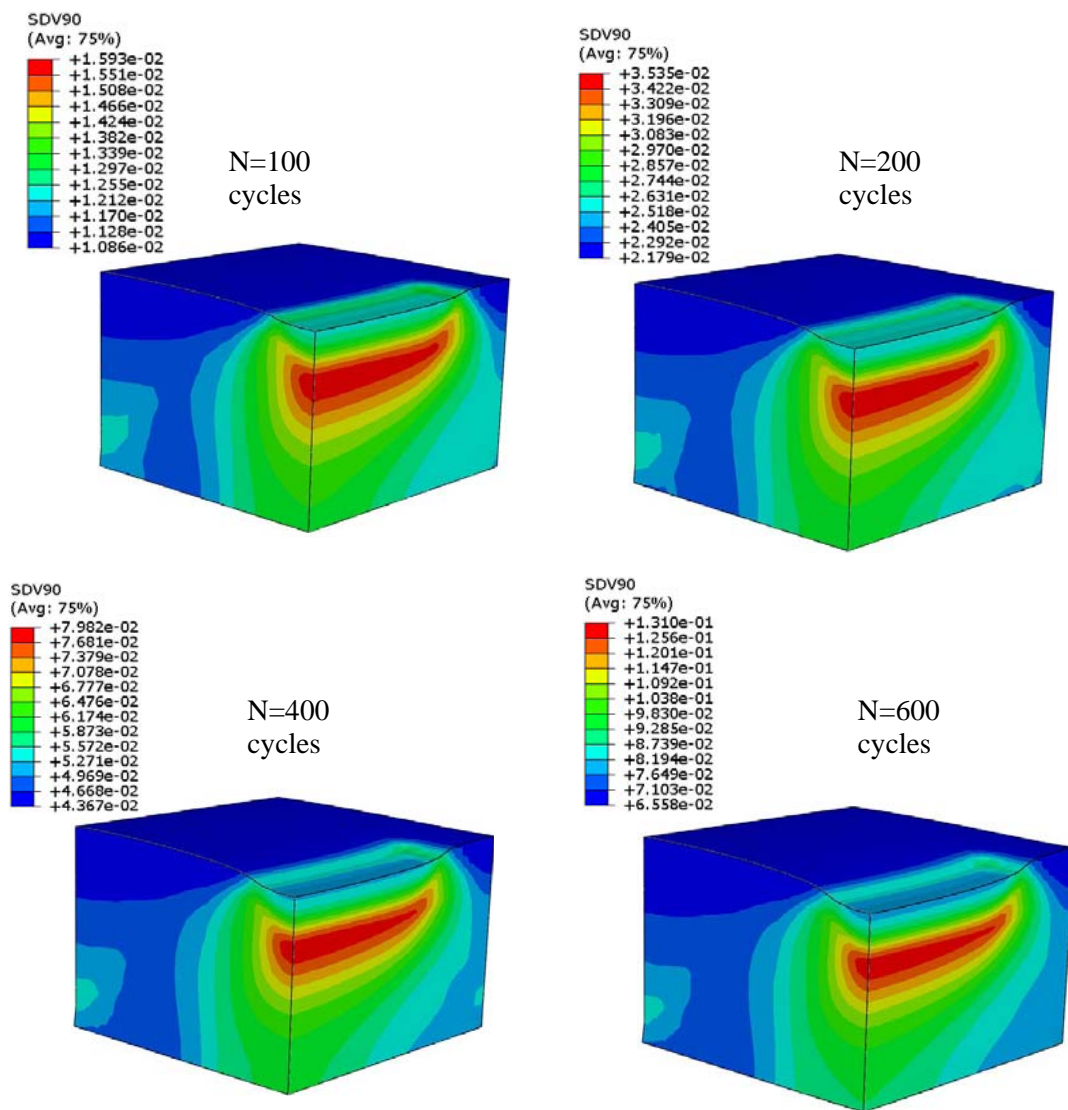
Figure 9.18. Damage distribution contours at different loading cycles for the 3D FE analysis when using the coupled viscoelastic-viscoplastic-viscodamage constitutive model at 20°C when simulating the pulse loading (loading mode 5).

From the 3D FE predictions of rutting (Figures 9.11-9.14), one can conclude that the simplified loading and constitutive assumptions can significantly affect the rutting predictions. The difference between the rutting values using the moving load (Mode 11), which is the most realistic one, and using the equivalent loading mode (Mode 8), which is the most common loading assumption in the literature, exceeds 100% in some cases. Moreover, assuming the equivalency between the pulse loading modes (Modes 7 and 9) and the equivalent loading modes (Modes 8 and 10) totally depend on the assumed constitutive model. This assumption yields almost similar results for an elasto-viscoplastic constitutive model. It could also be reasonable for a viscoelastic-viscoplastic constitutive mode; however, special care should be taken in the presence of damage since the results of these two loading cases could be totally different; depending on the damage level.

The conducted simulations show that rutting predictions in asphaltic pavements using the simplified assumptions such as the 2D analysis instead of the 3D analysis and using the equivalent loading assumption instead of the pulse loading assumption will significantly overestimate rutting, but, on the other hand, significantly reduce the computational cost. However, due to the very large computational cost needed to predict the rutting using 3D FE simulations with a complex coupled viscoelastic, viscoplastic, and viscodamage constitutive mode, it is imperative that an extrapolation technique to very large number of cycles is developed based on 3D FE simulations.

9.6. Extrapolation of the Rutting in 3D

The conducted simulations show that rutting predictions in pavements using the simplified assumptions such as the 2D analysis instead of the 3D analysis and using the equivalent loading mode instead of the pulse loading mode will significantly overestimate rutting, but will significantly reduce the computational cost. However, the 2D simulations as well as the equivalent load assumption give qualitative agreements with the 3D simulations and the pulse load assumption. Therefore, in this section a simple yet accurate method for extrapolating the results of 3D FE analysis based on the

results of 2D FE analysis is proposed. The extrapolation equation is expressed as follows:

$$Rutting^{3D,N} = \frac{Rutting^{3D,N_{ref}}}{Rutting^{2D,N_{ref}}} \times Rutting^{2D,N} \qquad (9.2)$$

where $Rutting^{3D,N}$ is the extrapolated rutting at N cycles for 3D, $Rutting^{3D,N_{ref}}$ and $Rutting^{2D,N_{ref}}$ are the calculated rutting at a reference cycle in 3D and 2D simulations, respectively. The reference cycles are chosen as 20, 100, 300, 400, and 500 for comparison. $Rutting^{2D,N}$ is the calculated rutting after N cycles in the 2D simulation.

For the purpose of extrapolation, the loading mode in the 2D simulations is chosen as the equivalent loading (Mode 2) since it is computationally inexpensive. The loading mode in the 3D simulations is assumed to be the moving loading (Mode 11) since it is the most realistic one as compared to the actual loading condition of the Wheel Tracking Test. Figures 9.19 (a) and 9.19(b) show the extrapolated results at temperatures 20 ^{o}C and 40 ^{o}C, respectively, when assuming a nonlinear viscoelastic and viscoplastic constitutive behavior. Figure 9.19(c) shows the extrapolation results at temperature 20 ^{o}C when assuming an elasto-viscoplastic constitutive behavior. These figures show that using the reference rutting at low number of cycles (20th cycle) does not yield accurate extrapolation comparing to the calculated rutting from 3D. Moreover, for the viscoelastic-viscoplastic constitutive model at temperature 20 ^{o}C, using the reference rutting at 100th cycle yields an accurate extrapolation such that increasing the reference cycle does not affect the extrapolated rutting. Generally, the extrapolated rutting using the reference rutting at 400th cycle yield accurate extrapolations to the calculated rutting from the 3D simulations at cycle 500th for the viscoelastic-viscoplastic model at temperature 40 ^{o}C and the elasto-viscoplastic model at 20 ^{o}C. The errors are around 1.2%. Hence, the proposed extrapolation technique based on the 2D rutting predictions gives an efficient method to predict and to extrapolate the rutting from the 3D simulations to large number of loading cycles.
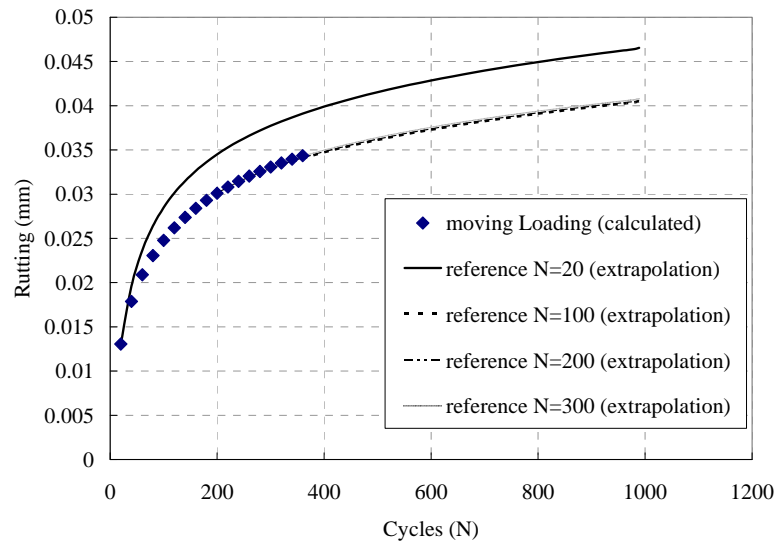
(a)
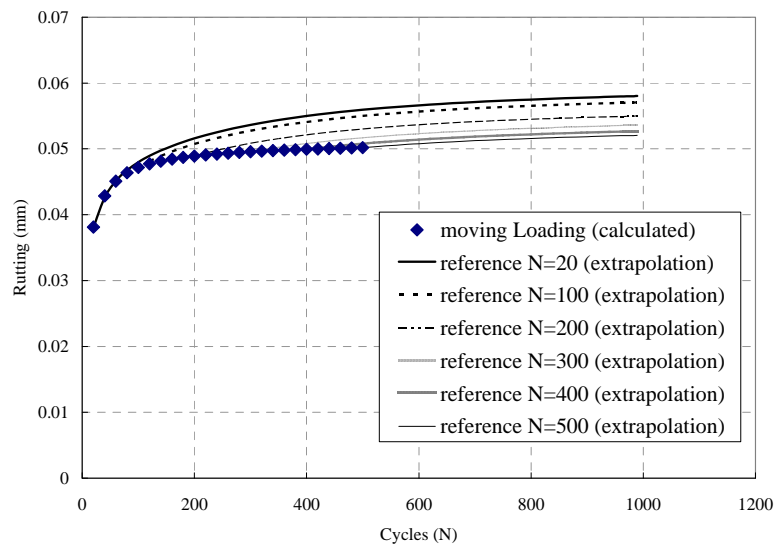
(b)

Figure 9.19. The extrapolation of the 3D rutting predictions based on the 2D predictions for: (a) the viscoelastic and viscoplastic model at temperature 20 ^{o}C, (b) the viscoelastic and viscoplastic model at temperature 40 ^{o}C, and (c) the elasto-viscoplastic model at temperature 20 ^{o}C.
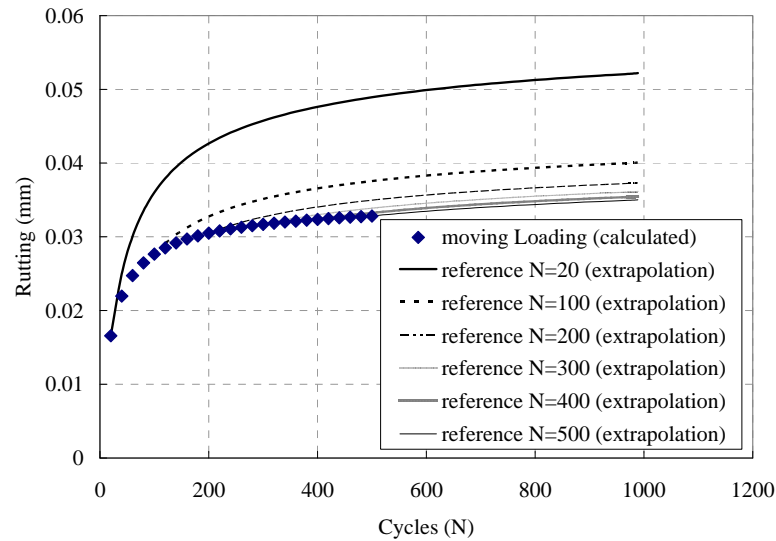
(c)

Figure 9.19. Continued.

9.7. Comparison with Experimental Results

In this section, the Wheel Tracking Test is modeled using the viscoelastic-viscoplastic-viscodamage constitutive model and the results are compared with experimental measurements. Since the experimental data are available at temperature 35 ^{o}C, the simulation is performed at temperature 35 ^{o}C. The asphalt mixture is described as 10 mm Dense Bitumen Macadam (DBM) which is a continuously graded mixture with asphalt binder content of 5.5%. Granite aggregates and an asphalt binder with a penetration grade of 70/100 are used in preparing the asphalt mixtures. The material parameters associated with the nonlinear viscoelastic, viscoplastic, and viscodamage constitutive equations are presented in Chapter II. The slabs of DMB materials with the dimensions of $305 \times 280 \times 100$ mm^3 are manufactured using a roller compactor. Materials are compacted in rigid molds using a roller compactor designed to simulate the action of the site compaction plant. The mold was moved back and forth under the rolling compactor to simulate a rolling action. The steel wheel applies 770 kPa moving load to the center of the slab with the frequency of 40 passes per minute. The total number of 96000 loading cycles is applied to the slab and the rutting depth is measured every five minutes. Figure

9.20 shows the comparison between the experimental measurements and the 2D simulation results and the 3D extrapolation results. The 2D finite element simulates the rutting up to 96000 cycles; while the 3D finite element only simulates the rutting up to 1000 cycles (i.e. $N_{ref} = 1000$). Then, the extrapolation technique [Eq.(9.2)] is employed to predict the rutting in 3D up to 96000 cycles. The results show that the rutting from the 2D simulation significantly overestimates the experimental measurements. However, the extrapolated results are with reasonable agreement with the experimental measurements where the error at loading cycle 96000 is about 10%. Moreover, the rate of rutting from the 3D extrapolation is comparable to the experiment measurements.
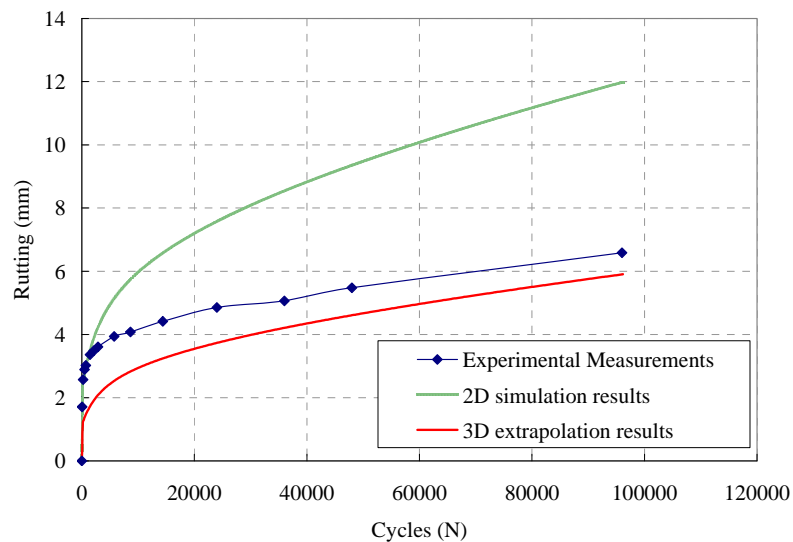
Figure 9.20 Comparing 2D FE rutting predictions and extrapolated results with experimental data from a Wheel Tracking Test (from Nottingham database) at temperature of $35\,^{\circ}$C.

Moreover, ALF database also includes the rutting performance simulation at $64\,^{\circ}$C. The model parameters for the ALF mixtures with the unmodified binder identified and presented in Chapter VII. These model parameters are also used to predict the ALF rutting performance. However, as mentioned in Chapter VII, at high temperatures such as $64\,^{\circ}$C, one does not expect nucleation of cracks and voids under compressive loading

modes. Instead, the material undergoes viscoplastic softening. Figure 9.21 schematically represents the asphalt layer section for the ALF rutting performance tests.
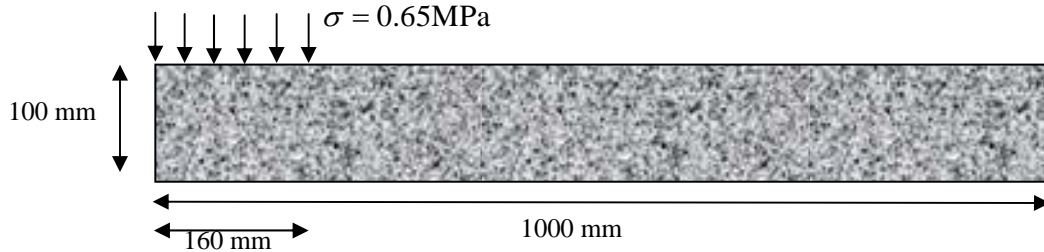
Figure 9.21. Schematic representation of the half of the asphalt layer model for the ALF rutting performance data.

The simulation results with and without the viscoplastic softening model is compared with the experimental measurements on ALF data in Figure 9.22.
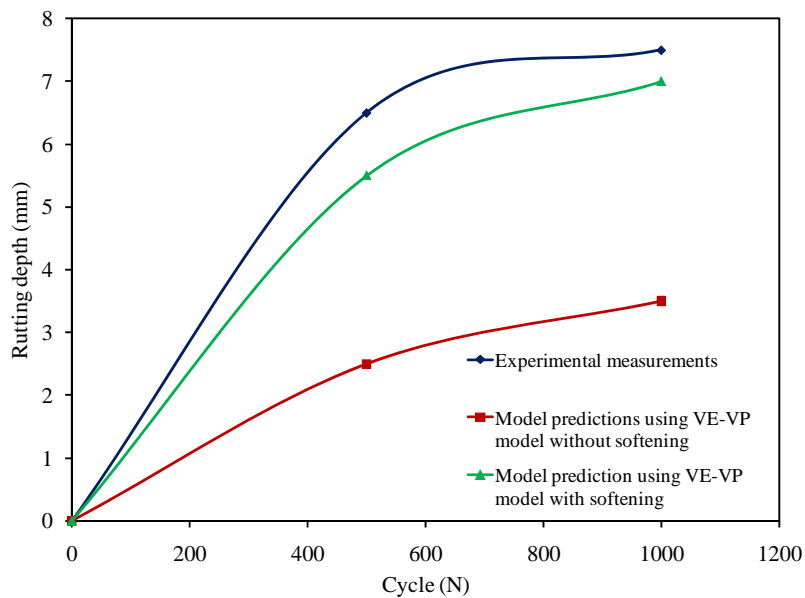
Figure 9.22. Experimental measurements and model predictions of the rutting performance for the ALF data.

Figure 9.22 clearly shows that the model without the viscoplastic softening significantly underestimates the experimental data. However, when the viscoplastic softening is included, the model predicts reasonable results for the rutting depth which agrees well with the experimental results. It should be noted that the same model parameters listed in Chapter VII are used to conduct the model predictions.

9.8. Conclusions

This chapter thoroughly investigates the FE prediction of the rutting in asphalt pavements which is one of the most challenging and important distresses in asphalt pavements.

The effect of different loading and constitutive behavior assumptions that greatly simplify the rutting performance predictions in asphalt pavements are systematically investigated. Three material constitutive behaviors are considered for studying the effects of viscoelasticity, viscoplasticity, and viscodamage models on the rutting depth in the Wheel Tracking Test. 2D and 3D FE simulations with different loading assumptions are simulated to study the difference between 2D and 3D simulations and to study the effect of different performance loading assumptions (e.g. pulse loading and equivalent loading) on the predicted rutting depth.

Simulation results show that certain simplified loading scenarios significantly overestimate the rutting performance. It is shown that the 2D simulations significantly overestimate the rutting depth as compared to the 3D moving loading case which is the most realistic case considered in this study. It is also shown that the accuracy of the assumption of equivalency between the pulse loading and the equivalent time loading, which have been extensively assumed by many researchers in predicting rutting, totally depends on the assumed material constitutive behavior (i.e. elasto-viscoplastic, viscoelastic-viscoplastic, or viscoelastic-viscoplastic- viscodamage). Therefore, one cannot generalize the conclusions from a specific loading assumption independent of the employed constitutive model. The pulse loading and equivalent time loading simplifications give comparable rutting predictions when the wheel loading is applied on

the same area of the wheel's path and the damage evolution is neglected. Therefore, depending on the level of damage, the results can deviate progressively as damage grows.

Moreover, an extrapolation technique is proposed to extrapolate the rutting performance simulation results to large number of loading cycles. The model predictions are finally compared to the experimental measurements for Nottingham and ALF mixes.

CHAPTER X
CONCLUSIONS AND RECOMMENDATIONS

As mentioned and shown in different chapters of this work, bituminous materials and asphalt mixes clearly show time-, rate-, and temperature-dependent responses. This makes the constitutive modeling of these materials very challenging and difficult. However, the main objectives of such constitutive modeling are: (1) to obtain a robust model that considers the main mechanisms contributing to the response of asphalt mixes subjected to mechanical, thermal, and mechanical loading conditions; and (2) to effectively use the derived constitutive model to predict the performance of asphalt pavements during their service lives.

10.1. Summary of the Findings

It is shown that thermo-viscoelastic, thermo-viscoplastic, thermo-viscodamage, micro-damage healing, and viscoplastic softening are the necessary mechanisms for predicting the thermo-mechanical response of asphalt mixes.

10.1.1. Thermo-Viscoelasticity

It is shown that the Schapery's nonlinear model can effectively be used to capture the thermo-viscoelastic response of asphalt mixes over a range of temperatures. It is shown that the viscoelastic model parameters can be effectively identified using either dynamic modulus tests or creep-recovery tests at different temperatures. It is also argued, however, that the dynamic modulus test yields more promising model parameters for the asphalt mixes since it these tests are usually conducted at several loading frequencies, and therefore, can capture the response at different loading rates.

10.1.2. Thermo-Viscoplasticity

This work used the Perzyna's viscoplasticity model to capture the irrecoverable strain response of asphalt mixes. It is shown that the Perzyna's viscoplastic model can be used to predict the viscoplastic response of asphalt mixes over a range of temperatures,

excluding high temperatures, using the same time-temperature shift factors identified from the dynamic modulus tests. However, the time-temperature shift factor should be introduced in both flow rule and viscoplastic dynamic yield surface. Moreover, this work uses a modified Drucker-Prager type yield surface and plastic potential that distinguishes between the loading conditions in compression and extension. This modified yield function introduces one more model parameter and enables the model to capture the viscoplastic response in both extension and compressive loading modes using the same model parameters. Furthermore, a straightforward procedure for identifying the viscoplastic model parameters based on the creep part of the creep-recovery test is introduced.

10.1.3. Thermo-Viscodamage

It is shown that the inclusion of the damage component in the constitutive models is crutial in accurate prediction of the mechanical response of bituminous materials. Distinct responses such as secondary and tertiary creep; post peak response in the stress-strain diagram; and fatigue life of bituminous materials and asphalt mixes cannot be predicted without the damage component of the constitutive model.

Moreover, it is shown that the damage response of asphalt mixes is time-, temperature-, and rate-dependent such that a delay-damage (viscodamage) model is required to accurately model the damage response of asphalt mixes.

Therefore, the continuum damage mechanics framework is used to propose a viscodamage model for asphalt mixes in Chapter II. The proposed viscodamage model is implemented using the concept of the effective stress space along with a transformation hypothesis to relate stress and strain tensors in the nominal and effective configurations. The use of the effective stress concept in continuum damage mechanics greatly simplifies the numerical implementation of the highly nonlinear constitutive models presented in this study. However, a physically-based transformation hypothesis is also required to relate the stress and strain tensors in the effective configuration to the associated quantities in the nominal (damaged configuration). It is argued that the best transformation hypothesis for the asphalt mixes is the power equivalence hypothesis.

Postulating the power equivalence hypothesis along with using the continuum damage mechanics based on the effective stress space are both numerically and physically interesting. In other words, the effective stress space significantly simplifies the numerical implementation and at the same time the power equivalence hypothesis makes these simplifications physically sound since it allows the accurate estimation of the dissipated energy in the effective configuration.

Analysis of extensive experimental data shows that the viscodamage response of asphalt mixes should be sensitive to the stress level, strain level, temperature, loading path, confinement level, and loading modes. The stress dependency of the damage model is captured using a damage force with a modified Drucker-Prager-type function. The advantage of using this form of damage force is that it makes the damage model sensitive to the confinement level and also distinguishes between the damage response in compression and extension loading modes. Moreover, it is shown that the damage evolution function is not independent of the loading history. In other words, different loading paths damage the material differently. This history effect is captured by incorporating a simple history term in the viscodamage evolution function.

Extensive experimental data are analyzed to decide on the form of the damage evolution function. The analysis show linear relationship between the rate of the damage density variable versus the damage force when plotted in log-log scale. It is shown that the slope of the rate of the damage density versus damage force in log-log scale is almost constant regardless of the strain level. Therefore, a power law form is selected for the dependency of the damage evolution function on the damage force. The same procedure is used to develop proper function for the dependency of the damage evolution function on the effective total strain level. It is shown that for different damage forces in the effective configuration the damage evolution function changes linearly with the effective total strain in the log-log scale. The slope of this depency was also constant which suggests a power law relation between the damage evolution function and the effective total strain level. It should be noted that including the total effective strain enhances the couplings between the damage model and the rest of the constitutive model. Moreover,

the viscodamage model is coupled to temperature using an exponential multiplicative term in the viscodamage evolution law. Also, it is shown that the incorporation of the damage history in the viscodamage evolution function adds interesting features to the viscodamage model.

Systematci and simple procedures are developed to identify the viscodamage model parameters based on either two creep tests at different stress levels which show secondary and tertiary creep responses or several constant strain rate tests, whichever are available in the experimental data.

The proposed viscodamage model along with the identified model parameters are used to predict the response of asphalt mixes against other sets of experimental data which have not been used in calibration processes. Experimental data from the Nottingham and NCSU database are used to validate the viscodamage model. Results show that the viscodamage model is capable of capturing damage response of asphalt mixes subjected to different loading conditions in tension and compression loading modes, different temperatures, stress levels, strain rate levels, and loading/unloading times. It is shown that both secondary and tertiary creep can be captured at different stress levels and temperatures. Also, the model predicts the uniaxial constant strain rate tests at different temperatures and strain rates reasonably well. Reasonable predictions are also resulted for the repeated creep-recovery data. The experimental data on cyclic stress-controlled and strain-controlled loading conditions verify the capability of the proposed viscodamage model in capturing the fatigue life of asphalt mixes under realistic loading conditions.

10.1.4. Micro-Damage Healing

A novel continuum damage mechanics-based framework is proposed in this work to enhance the continuum damage mechanics theories in modeling the micro-damage healing phenomenon in materials that tend to self-heal. This framework is proposed by extending the concept of the effective configuration and effective stress to the healing configuration. Three well-known transformation hypotheses of the continuum damage mechanics theories (i.e. strain, elastic strain energy, and power equivalence hypotheses)

are also extended for the materials with healing ability. Analytical relations are derived for each transformation hypothesis to relate the strain tensors, secant stiffness moduli, and tangent stiffness moduli in the damaged (nominal) and healing configurations.

The developed general micro-damage healing framework is then applied to asphalt mixes to model the healing phenomenon in asphalt mixes which occurs under different loading conditions. The proposed micro-damage healing model is coupled with temperature-dependent nonlinear viscoelastic, viscoplastic, and viscodamage constitutive models that can predict the highly nonlinear mechanical responses of asphalt mixtures subjected to repeated loading conditions.

Moreover, motivated by previously developed micromechanical- and fracture-based healing models, a phenomenological healing equation is proposed for the evolution of the micro-damage healing internal state variable. The healing evolution equation is time, temperature, and loading/unloading history dependent model that explicitly affect the stress state and the viscoelastic, viscoplastic, and viscodamage response of the material while undergoing micro-damage healing. Moreover, an attempt is made to relate the material parameter that controls the rate of healing to the surface energy and bond strength of the material. Finally, a straightforward procedure to identify the healing model parameters using the repeated creep-recovery tests with different rest periods is proposed.

10.1.5. Viscoplastic Softening

It is shown that the classical plasticity/viscoplasticity models are not sufficient to explain the viscoplastic response of asphalt mixes subjected to repeated loadings at high temperatures.

It is argued that the microstructure of the asphalt mixes rearranges during the unloading and rest period especially at high temperatures. This rearrangement of the microstructure (i.e. relocation of the aggregates) changes the mechanical properties of the asphalt mixes such that they can undergo more viscoplastic deformation during the next loading cycle. However, the classical viscoplastic models show that the material only undergoes more viscoplastic deformation when the applied stress exceeds its

applied maximum level. This distinct behavior of the asphalt mixes is referred to as the *viscoplastic softening.*

Alternative methods to model the viscoplastic softening response of asphalt mixes at high temperatures are discussed. A novel method to simulate the viscoplastic softening model is then proposed. This method is based on the introduction of a viscoplasticity memory surface in the viscoplastic strain space. This surface is formulated very similar to the viscoplastic dynamic yield surface in the stress space which allows the application of the well-known procedures for identifying the yield surface in the stress space for the identification of the viscoplasticity memory surface in the strain space. An internal state variable, viscoplastic softening internal state variable, that memorizes the maximum experienced viscoplastic strain during the last unloading is introduced. This internal state variable is then used to construct a robust viscoplastic softening model for asphalt mixes.

10.1.6. Thermodynamic Consistency of the Proposed Model

This work presents a general and comprehensive thermodynamic based framework with especial attention to the decomposition of the thermodynamic conjugate forces into energetic and dissipative components to derive a temperature-dependent viscoelastic, viscoplastic, viscodamage, and healing constitutive model for time- and rate-dependent materials.

The healing configuration as the extension of the well-known Kachanov's effective (undamaged) configuration is defined to enhance the continuum damage mechanics in modeling the healing phenomenon. Hence, the constitutive models are presented in the healing configuration which substantially simplifies the numerical implementation by avoiding the complexities associated with the direct couplings of viscoelastic and viscoplastic models to the viscodamage and healing models. The power-correlating hypothesis is used to relate stress and strain tensors in the healing and damaged configurations. This hypothesis allowed one to present the constitutive model in the healing configuration (for simplicity) and yet to estimate the dissipated energy in the healing stress space accurately.

Moreover, it is shown that the thermodynamic formulation naturally enforces the decomposition of the thermodynamic conjugate forces into energetic and dissipative components. Energetic components are derived using the Helmholtz free energy. A systematic procedure based on the principle of maximum dissipation (or maximum entropy production) is presented for deriving dissipative components directly from rate of the energy dissipation. The thermodynamic framework is then used for deriving a more comprehensive version of Schapery-type viscoelastic model, Perzyna-type viscoplastic model, and a viscodamage model analogous to the Perzyna-type viscoplastic model, and a healing model for bituminous materials and asphalt mixes. Moreover, all the derived constitutive models are coupled to temperature. It is shown that the presented thermodynamic framework yields a simpler and more comprehensive form for temperature-dependent viscoelastic models where there is no need for using the temperature shift factor in the definition of the reduced time. Instead, a temperature coupling term can be used for making the viscoelasticity model temperature-dependent.

Furthermore, it is shown that the principle of virtual power can be used for deriving generalized non-associative viscoplasticity theories without further needs to assume a viscoplastic potential function independent from the yield loading condition. It is also shown that the rate-dependent terms in viscoplasticity dynamic yield surface are identical to the dissipative components of the hardening function and can be derived directly from the rate of energy dissipation.

For the first time, the viscoelastic model is derived using the viscoelastic microforce balance, obtained directly from the principle of virtual power. Similarly, the viscodamage and healing loading conditions and evolution laws are derived using the viscodamage microforce balance and healing microforce balance, respectively.

Finally, equations for the thermo-mechanical coupling terms are derived which can be used to investigate the temperature evolution during the deformation.

10.1.7. Model Validation

The presented thermo-viscoelastic-viscoplastic-viscodamage-healing constitutive model is validated against extensive experimental measurements. This model is first

validated against the Nottingham data base over creep, creep-recovery, repeated creep-recovery, and constant strain rate tests at different stress levels, strain rates, loading times, unloading times in both tension and compression at 10, 20, and 35°C. It is shown that the model is capable of predicting time-, rate-, and temperature-dependent response of asphalt mixes.

The model is also validated against the ALF data. These data include compression tests at 55°C. It is shown that the classical plasticity/viscoplasticity models cannot predict the viscoplastic response of asphalt mixes at high temperatures. Therefore, a viscoplastic softening model is proposed to capture the viscoplastic response of asphalt mixes at high temperatures. The model is then validated against different kinds of repeated creep-recovery tests with different stress levels, loading times, and rest periods. Experimental measurements and model predictions clearly show that the model is capable of predicting the viscoplastic response of asphalt mixes at high temperatures.

The model is also validated against constant strain rate tests, dynamic modulus tests, cyclic stress controlled tests, and cyclic strain controlled tests at different temperatures in tension. It is shown that the viscoelastic-viscoplastic-viscodamage-healing model yield reasonable predictions of the experimental data.

10.1.8. Performance Simulations

This work presents a thorough investigation of the FE prediction of rutting, one of the most challenging and important distresses in asphalt pavements. The effect of different loading and constitutive behavior assumptions that greatly simplify the rutting performance predictions in asphalt pavements are systematically investigated. Three material constitutive behaviors are considered for studying the effects of viscoelasticity, viscoplasticity, and viscodamage models on the rutting depth in the Wheel Tracking Test. 2D and 3D FE simulations with different loading assumptions are simulated to study the difference between 2D and 3D simulations and to study the effect of different performance loading assumptions (e.g. pulse loading and equivalent loading) on the predicted rutting depth.

Simulation results show that certain simplified loading scenarios significantly overestimate the rutting performance. It is shown that the 2D simulations significantly overestimate the rutting depth as compared to the 3D moving loading case which is the most realistic case considered in this study. It is also shown that the accuracy of the assumption of equivalency between the pulse loading and the equivalent time loading, which have been extensively assumed by many researchers in predicting rutting, totally depends on the assumed material constitutive behavior (i.e. elasto-viscoplastic, viscoelastic-viscoplastic, or viscoelastic-viscoplastic- viscodamage). Therefore, one cannot generalize the conclusions from a specific loading assumption independent of the employed constitutive model. The pulse loading and equivalent time loading simplifications give comparable rutting predictions when the wheel loading is applied on the same area of the wheel's path and the damage evolution is neglected. Therefore, depending on the level of damage, the results can deviate progressively as damage grows.

Finally, the presented techniques and extrapolation techniques are used to predict the rutting performance of Wheel Tracking tests for the Nottingham and ALF mixes. Model predictions and experimental measurements show that the model is capable of predicting the rutting performance in asphalt pavements within a reasonable accuracy.

10.2. Recommended Areas of Future Research

- *Development of multiphysics constitutive models that include aging and moisture induced damage as well:* The ultimate goal of such constitutive models is to predict the response of asphalt pavements subjected to realistic loading and environmental conditions. Therefore, it is extremely important to include the effect of environmental conditions such as moisture induced damage and aging in the constitutive models.

- *Including statistical analysis and probabilistic and stochastic approaches into the constitutive models:* Experimental measurements show high variability even for the same test and same mix in some cases. The constitutive models as discussed in this

work predict one determined response under the loading conditions. However, the experimental measurements show a range for the response of the materials. Therefore, the constitutive model will be more robust and realistic if it can also predict a range instead a determinant response under a specific loading condition. This important issue can be incorporated into the constitutive models by considering statistical analysis and probabilistic approaches.

- *Extending the constitutive model for the anisotropic cases:* This study presents the isotropic damage and healing response of asphalt mixes. However, the asphalt mixes are highly heterogeneous and anisotropic. Therefore, extension of the proposed healing configuration to the anisotropic cases and subsequently proposing anisotropic damage and healing models will be helpful in ensuring the robustness of the constitutive model for different loading paths and conditions.

- *Extending the constitutive model to the large deformation theories:* This study postulates the small deformation theories for asphalt mixes. This assumption is reasonable for asphalt mixes under a range of temperatures. However, at high temperatures, the asphalt mixes may undergo finite deformations such that the small deformation theories may fail in predicting reasonable predictions of the mechanical response of asphalt mixes. Moreover, even at low and intermediate temperatures, the asphalt mixes may experience finite strains as high damage densities. Furthermore, even though the experienced strain level at mixture level is small, the strain at the binder phase could be large due to the strain localization. Therefore, extending the current formulation to large deformation theories will be helpful in analyzing the asphalt mixes at high temperatures and high damage densities as well as conducting the micro-mechanical simulations considering binder, aggregate, and FAM phases.

- *More investigation of the viscoplastic softening response of asphalt mixes:* This study presents a robust and theoretically sound framework for the modeling of the viscoplastic softening in asphalt mixes using the viscoplastic memory surface. The viscoplastic memory surface provides a sound framework for modeling such phenomena. However, more experimental data should be analyzed to obtain the

proper evolution equation for the viscoplastic softening model based on the viscoplastic memory surface.

- *Investigation of the healing mechanism of asphalt mixes and binders during the cyclic strain controlled tests:* Investigations on the cyclic response of asphalt mixes (see Chapter VII) reveals that the asphalt mixes have the capability to heal partially during the cyclic strain controlled tests. The careful investigation of the healing mechanism of asphalt mixes subjected to such loading conditions will be, therefore, of significant importance.

- *Investigation of the couplings between the Environmental conditions and mechanical loadings:* As mentioned in the introduction chapter, the environmental conditions might have significant effect on the mechanical response of asphalt pavements during its service life. For example, aging makes the pavements more prone to cracking and damage. Subsequently, more micro-cracks increases the porosity of the pavement which allows more oxygen and moisture diffusion. Obviously, this coupling accelerates the aging and moisture damage in pavements progressively. Therefore, considering the couplings between these mechanisms through robust constitutive models will significantly enhance the more accurate prediction of the asphalt pavement performance.

- *Considering more realistic loading conditions such as shear loading for the rutting and fatigue damage performance of asphalt mixes:* This study only considers the normal stress for the prediction of the rutting in asphalt mixes. However, the measurements of the force interaction between the wheel and the pavement surface shows that the shear stresses could be dominant in some cases which can significantly affect the prediction of the rutting and fatigue damage performance simulations in asphalt mixes.

- *Development of the robust and simple extrapolation techniques:* Another important issue in the performance simulation of the rutting and fatigue damage in pavements is the number of loading cycles. Pavements are subjected to millions of loading cycles during their service lives. Even with the state of the art computational

capacities, it is not possible to simulate the 3D performance simulations using realistic constitutive models. Therefore, development of robust and simple extrapolation techniques will be of crucial importance in enabling the realistic simulation of the pavements performances.

REFERENCES

Abaqus, 2008. Version 6.8. Habbit, Karlsson and Sorensen, Inc, Providence, RI.

Abdulshafi, A., Majidzadeh, K., 1985. Combo viscoelastic-plastic modeling and rutting of aphaltic mixtures. Transportation Research Board, Washington, D.C. 968, 19-31.

Abu Al-Rub, R.K., 2008a. Interfacial gradient plasticity governs scale-dependent yield strength and strain hardening rates in micro/nano structured metals. International Journal of Plasticity 24, 1277-1306.

Abu Al-Rub, R.K., 2008b. Modeling the interfacial effect on the yield strength and flow stress of thin metal films on substrates. Mechanics Research Communications 35, 65-72.

Abu Al-Rub, R.K., Darabi, M.K., Huang, C.w., Masad, E., Little, D., 2011. Comparing finite element and constitutive modelling techniques for predicting rutting of asphalt pavements. International Journal of Pavement Engineering, In press.

Abu Al-Rub, R.K., Darabi, M.K., Little, D.N., Masad, E.A., 2010a. A micro-damage healing model that improves prediction of fatigue life in asphalt mixes. International Journal of Engineering Science 48, 966-990.

Abu Al-Rub, R.K., Darabi, M.K., Masad, E.A., 2010b. A straightforward numerical technique for finite element implementation of nonlocal gradient-dependent continuum damage mechanics theories. International Journal of Theoretical and Applied Multiscale Mechanics 1, 352-385.

Abu Al-Rub, R.K., Kim, S.M., 2009. Predicting mesh-independent ballistic limits for heterogeneous targets by a nonlocal damage computational framework. Composites Part B-Engineering 40, 495-510.

Abu Al-Rub, R.K., Masad, E.A., Huang, C.W., 2009. Improving the sustainability of asphalt pavements through developing a predictive model with fundamental material properties. Southwest University Transportation Center, Texas Transportation Institute, College Station, TX, 1-45.

Abu Al-Rub, R.K., Voyiadjis, G.Z., 2003. On the coupling of anisotropic damage and plasticity models for ductile materials. International Journal of Solids and Structures 40, 2611-2643.

Abu Al-Rub, R.K., Voyiadjis, G.Z., 2005a. A direct finite element implementation of the gradient-dependent theory. International Journal for Numerical Methods in Engineering 63, 603-629.

Abu Al-Rub, R.K., Voyiadjis, G.Z., 2005b. A finite strain plastic-damage model for high velocity impacts using combined viscosity and gradient localization limiters: Part i - theoretical formulation. International Journal of Damage Mechanics 15, 293-334.

Abu Al-Rub, R.K., Voyiadjis, G.Z., 2006. A physically based gradient plasticity theory. International Journal of Plasticity 22, 654-684.

Abu Al-Rub, R.K., Voyiadjis, G.Z., 2009. Gradient-enhanced coupled plasticity-anisotropic damage model for concrete fracture: Computational aspects and applications. International Journal of Damage Mechanics 18, 115-154.

Abu Al-Rub, R.K., Voyiadjis, G.Z., Bammann, D.J., 2007. A thermodynamic based higher-order gradient theory for size dependent plasticity. International Journal of Solids and Structures 44, 2888-2923.

Aifantis, E.C., 1984. On the microstructural origin of certain inelastic models. Journal of Engineering Materials and Technology, ASME 106, 326-330.

Aifantis, E.C., Oka, F., Yashima, A., Adachi, T., 1999. Instability of gradient dependent elasto-viscoplasticity for clay. International Journal for Numerical and Analytical Methods in Geomechanics 23, 973-994.

Alehossein, H., Korinets, A., 2000. Mesh-independent finite difference analysis using gradient-dependent plasticity. Communications in Numerical Methods in Engineering 16, 363-375.

Anand, L., Gurtin, M.E., Lele, S.P., Gething, C., 2005. A one-dimensional theory of strain-gradient plasticity: Formulation, analysis, numerical results. Journal of the Mechanics and Physics of Solids 53, 1789-1826.

Ando, K., Chu, M.C., Tsuji, K., Hirasawa, T., Kobayashi, Y., Sato, S., 2002. Crack healing behaviour and high-temperature strength of mullite/sic composite ceramics. Journal of the European Ceramic Society 22, 1313-1319.

Armstrong, P.J., Frederick, C.O., 1966. A mathematical representation of the multiaxial bauschinger effect. CEGB Report RD/B/N/73. Berkeley Nuclear Laboratories, Berkeley, CA.

Arrington, E.D., Smith, W.J., Chambers, H.G., Bucknell, A.L., Davino, N.A., 1996. Complications of iliac crest bone graft harvesting. Clinical Orthopaedics and Related Research 329, 300-309.

Barbero, E.J., Greco, F., Lonetti, P., 2005. Continuum damage-healing mechanics with application to self-healing composites. International Journal of Damage Mechanics 14, 51-81.

Bari, S., Hassan, T., 2000. Anatomy of coupled constitutive models for ratcheting simulation. International Journal of Plasticity 16, 381-409.

Bazant, Z.P., Pijaudiercabot, G., 1988. Nonlocal continuum damage, localization instability and convergence. Journal of Applied Mechanics, ASME 55, 287-293.

Beijer, J.G.J., Spoormaker, J.L., 2002. Solution strategies for fem analysis with nonlinear viscoelastic polymers. Computers & Structures 80, 1213-1229.

Belloni, G., Bernasconi, G., Piatti, G., 1979. Creep damage models. In: Creep of Engineering Materials and Structures. Applied Science Publishers, London.

Bhasin, A., Bommavaram, R., Greenfield, M.L., Little, D.N., 2011. Use of molecular dynamics to investigate self-healing mechanisms in asphalt binders. Journal of Materials in Civil Engineering (ASCE) 23, 485-492.

Bhasin, A., Little, D.N., Bommavaram, R., Vasconcelos, K., 2008. A framework to quantify the effect of healing in bituminous materials using material properties. Road Materials and Pavement Design 9, 219-242.

Biot, M.A., 1954. Theory of stress-strain relations in anisotropic viscoelasticity and relaxation phenomena. Journal of Applied Physics 25, 1385-1391.

Bond, I., Trask, R., Williams, G., Williams, H., 2007. Autonomic self-healing and damage visualisation in fibre reinforced polymer composites. Structural Health Monitoring: Quantification, Validation, and Implementation 1, 1364-1372.

Boubakar, M.L., Vang, L., Trivaudey, F., Perreux, D., 2003. A meso-macro finite element modelling of laminate structures part ii: Time-dependent behaviour. Composite Structures 60, 275-305.

Bousshine, L., Chaaba, A., De Saxce, G., 2001. Softening in stress-strain curve for drucker-prager non-associated plasticity. International Journal of Plasticity 17, 21-46.

Brown, E.N., Sottos, N.R., White, S.R., 2002. Fracture testing of a self-healing polymer composite. Experimental Mechanics 42, 372-379.

Brown, E.N., White, S.R., Sottos, N.R., 2005. Retardation and repair of fatigue cracks in a microcapsule toughened epoxy composite - part ii: In situ self-healing. Composites Science and Technology 65, 2474-2480.

Burgers, J.M., 1939. Mechanical considerations, model systems phenomenological theories of relaxation and of viscosity. . In: First Report on Viscosity and Plasticity, second ed. Nordemann Publishing Company, Inc., New York, Prepared by the committee for the study of viscosity of the academy of sciences at Amsterdam.

Carpenter, S.H., Shen, S., 2006. A dissipated energy approach to study HMA healing in fatigue. 85th Annual Meeting of the Transportation Research Board Washington D.C.

Cela, J.J.L., 2002. Material identification procedure for elastoplastic drucker-prager model. Journal of Engineering Mechanics (ASCE) 128, 586-591.

Chaboche, J.L., 1989. Constitutive equations for cyclic plasticity and cyclic viscoplasticity. International Journal of Plasticity 5, 247-302.

Chaboche, J.L., 2003. Damage mechanics. Comprehensive Structural Integrity 2, 213-284.

Challamel, N., Casandjian, C., Lanos, C., 2009. Some closed-form solutions to simple beam problems using nonlocal (gradient) damage theory. International Journal of Damage Mechanics 18, 569-598.

Chehab, G., Kim, Y.R., Schapery, R.A., Witczack, M., Bonaquist, R., 2002. Time-temperature superposition principle for asphalt concrete mixtures with growing damage in tension state. Asphalt Paving Technology 71, 559–593.

Chehab, G.R., Kim, Y.R., Schapery, R.A., Witczak, M.W., Bonaquist, R., 2003. Characterization of asphalt concrete in uniaxial tension using a viscoelastoplastic continuum damage model. Journal of the Association of Asphalt Paving Technologists (AAPT) 72, 315-355.

Chen, W.F., Mizuno, E., 1990. Nonlinear analysis in soil mechanics: Theory and implementation. Elsevier Science Publishing Company Inc., New York.

Cho, Y., McCullough, B.F., Weissmann, J., 1996. Considerations on finite-element method application in pavement structural analysis. Transportation Research Board, Washington, D.C. 1539, 96–101.

Christen, R.M., 1968. On obtaining solutions in nonlinear viscoelasticity. Journal of Applied Mechanics 35, 129-134.

Cicekli, U., Voyiadjis, G.Z., Abu Al-Rub, R.K., 2007. A plasticity and anisotropic damage model for plain concrete. International Journal of Plasticity 23, 1874-1900.

Coleman, B.D., Gurtin, M.E., 1967. Thermodynamics with internal state variables. Journal of Chemical Physics 47, 597-613.

Coleman, B.D., Noll, W., 1963. The thermodynamics of elastic materials with heat conduction and viscosity. Archive for Rational Mechanics and Analysis 13, 167-178.

Collins, I.F., Houlsby, G.T., 1997. Application of thermomechanical principles to the modelling of geotechnical materials. Proceedings of the Royal Society of London A 453, 1975-2001.

Collins, I.F., Kelly, P.A., 2002. A thermomechanical analysis of a family of soil models. Geotechnique 52, 507-518.

Collop, A.C., Scarpas, A.T., Kasbergen, C., de Bondt, A., 2003. Development and finite element implementation of stress-dependent elastoviscoplastic constitutive model with damage for asphalt. Transportation Research Board, Washington, D.C. 1832, 96-104.

Comi, C., 2001. A non-local model with tension and compression damage mechanisms. European Journal of Mechanics a-Solids 20, 1-22.

Cordebois, J., Sidoroff, F., 1982. Anisotropic damage in elasticity and plasticity. Journal De Mecanique Theorique Et Appliquee, 45-60.

Cozzarelli, F.A., Bernasconi, G., 1981. Non-linear creep damage under one-dimensional variable tensile-stress. International Journal of Non-Linear Mechanics 16, 27-38.

Cristescu, N., 1994. A procedure to determine nonassociated constitutive-equations for geomaterials. International Journal of Plasticity 10, 103-131.

Darabi, M.K., Abu Al-Rub, R.K., 2011. A thermodynamic framework for constitutive modeling of time- and rate- dependent materials, part 1: Theory. Unpublished paper, Texas A&M University, College Station, TX.

Darabi, M.K., Abu Al-Rub, R.K., Huang, C.w., Masad, E., Little, D., 2011a. On viscoplastic softening and damage response of asphalt mixes. Unpublished paper, Texas A&M University, College Station, TX.

Darabi, M.K., Abu Al-Rub, R.K., Little, D.N., 2011b. A continuum damage mechanics-based framework for modeling micro-damage healing. International Journal of Solids and Structures, In press.

Darabi, M.K., Abu Al-Rub, R.K., Masad, E.A., Huang, C.-W., Little, D.N., 2011c. A thermo-viscoelastic-viscoplastic-viscodamage constitutive model for asphaltic materials. International Journal of Solids and Structures 48, 191-207.

Darabi, M.K., Abu Al-Rub, R.K., Masad, E.A., Little, D.N., 2011d. Thermodynamic based model for coupling temperature-dependent viscoelastic, viscoplastic, and viscodamage constitutive behavior of bituminous materials. International Journal for Numerical and Analytical Methods in Geomechanics DOI: 10.1002/nag.1030.

Davison, L., Stevens, A.L., 1973. Thermomechanical constitution of spalling elastic bodies. Journal of Applied Physics 44, 668-674.

Davison, L., Stevens, A.L., Kipp, M.E., 1977. Theory of spall damage accumulation in ductile metals. Journal of the Mechanics and Physics of Solids 25, 11-28.

de Borst, R., Sluys, L.J., Mühlhaus, H.-B., Pamin, J., 1993. Fundamental issues in finite element analysis of localization of deformation. Engineering Computations 10, 99-121.

deBorst, R., Muhlhaus, H.B., 1992. Gradient-dependent plasticity - formulation and algorithmic aspects. International Journal for Numerical Methods in Engineering 35, 521-539.

deBorst, R., Pamin, J., 1996. Some novel developments in finite element procedures for gradient-dependent plasticity. International Journal for Numerical Methods in Engineering 39, 2477-2505.

Dessouky, S.H., 2005. Multiscale approach for modeling hot mix asphalt. Ph.D. Dissertation, Texas A&M University.

Di Benedetto, H., Mondher, N., Sauzeat, C., Olard, F., 2007. Three-dimensional thermo-viscoplastic behavior of bituminous materials. Road Material Pavement 8, 285-316.

Dormieux, L., Barthelemy, J.F., Maghous, S., 2006. Strength of a composite reinforced by rigid inclusions: The case of a drucker-prager matrix with non associated plastic flow rule. Comptes Rendus Mecanique 334, 111-116.

Dornowski, W., Perzyna, P., 2002. Localized fracture phenomena in thermo-viscoplastic flow processes under cyclic dynamic loadings. Acta Mechanica 155, 233-255.

Drucker, D.C., Gibson, R.E., Henkel, D.J., 1957. Soil mechanics and work-hardening theories of plasticity. Transactions American Society of Civil Engineers 122, 338-346.

Duvaut, G., Lions, J.L., 1976. Inequalities in mechanics and physics. Springer-Verlag, New York.

Eggeler, G., Hornbogen, E., Yawny, A., Heckmann, A., Wagner, M., 2004. Structural and functional fatigue of niti shape memory alloys. Materials Science and Engineering a-Structural Materials Properties Microstructure and Processing 378, 24-33.

Erkens, S.M.J.G., 2002. Asphalt concrete response : Determination, modeling and prediction. Delft University Press, The Netherlands.

Fanella, D., Krajcinovic, D., 1985. Continuum damage mechanics of fiber reinforced-concrete. Journal of Engineering Mechanics (ASCE) 111, 995-1009.

Ferrara, L., di Prisco, M., 2001. Mode i fracture behavior in concrete: Nonlocal damage modeling. Journal of Engineering Mechanics (ASCE) 127, 678-692.

Fleck, N.A., Hutchinson, J.W., 2001. A reformulation of strain gradient plasticity. Journal of the Mechanics and Physics of Solids 49, 2245-2271.

Florea, D., 1994. Nonassociated elastic viscoplastic model for bituminous concrete. International Journal of Engineering Science 32, 87-93.

Fremond, M., Nedjar, B., 1996. Damage, gradient of damage and principle of virtual power. International Journal of Solids and Structures 33, 1083-1103.

Gazonas, G.A., 1993. A uniaxial nonlinear viscoelastic constitutive model with damage for m30 gun propellant. Mechanics of Materials 15, 323-335.

Ghorbel, E., 2008. A viscoplastic constitutive model for polymeric materials. International Journal of Plasticity 24, 2032-2058.

Gibson, N.H., Kutay, M.E., Keramat, D., Youtchef, J., 2009. Multiaxial strain response of asphalt concrete measured during flow number performance test. Journal of the Association of Asphalt Paving Technologists (AAPT) 78, 25-66.

Gibson, N.H., Schwartz, C.W., Schapery, R.A., Witczak, M.W., 2003. Viscoelastic, viscoplastic, and damage modeling of asphalt concrete in unconfined compression. Transportation Research Record 1860, Transportation Research Board, Washington, D. C., 3-15.

Graham, M.A., 2009. Damaged viscoelastic-viscoplastic model for asphalt mixes, Civil Engineering. Texas A&M University, College Station, Texas.

Gudmundson, P., 2004. A unified treatment of strain gradient plasticity. Journal of the Mechanics and Physics of Solids 52, 1379-1406.

Guo, Y.F., Guo, W.L., 2006. Self-healing properties of flaws in nanoscale materials: Effects of soft and hard molecular dynamics simulations and boundaries studied using a continuum mechanical model. Physical Review B 73, 1-7.

Gurtin, M.E., 2000. On the plasticity of single crystals: Free energy, microforces, plastic-strain gradients. Journal of the Mechanics and Physics of Solids 48, 989-1036.

Gurtin, M.E., 2002. A gradient theory of single-crystal viscoplasticity that accounts for geometrically necessary dislocations. Journal of the Mechanics and Physics of Solids 50, 5-32.

Gurtin, M.E., 2003. On a framework for small-deformation viscoplasticity: Free energy, microforces, strain gradients. International Journal of Plasticity 19, 47-90.

Gurtin, M.E., 2008. A finite-deformation, gradient theory of single-crystal plasticity with free energy dependent on densities of geometrically necessary dislocations. International Journal of Plasticity 24, 702-725.

Gurtin, M.E., Anand, L., 2005. A theory of strain-gradient plasticity for isotropic, plastically irrotational materials. Part i: Small deformations. Journal of the Mechanics and Physics of Solids 53, 1624-1649.

Gurtin, M.E., Anand, L., 2009. Thermodynamics applied to gradient theories involving the accumulated plastic strain: The theories of aifantis and fleck and hutchinson and their generalization. Journal of the Mechanics and Physics of Solids 57, 405-421.

Gurtin, M.E., Anand, L., Lele, S.P., 2007. Gradient single-crystal plasticity with free energy dependent on dislocation densities. Journal of the Mechanics and Physics of Solids 55, 1853-1878.

Haj-Ali, R.M., Muliana, A.H., 2004. Numerical finite element formulation of the schapery non-linear viscoelastic material model. International Journal for Numerical Methods in Engineering 59, 25-45.

Hallberg, H., Ryttberg, K., Ristinmaa, M., 2009. Model describing material-dependent deformation behavior in high-velocity metal forming processes. Journal of Engineering Mechanics (ASCE) 135, 345-357.

Han, L.H., Elliott, J.A., Bentham, A.C., Mills, A., Amidon, G.E., Hancock, B.C., 2008. A modified drucker-prager cap model for die compaction simulation of pharmaceutical powders. International Journal of Solids and Structures 45, 3088-3106.

Hassan, T., Corona, E., Kyriakides, S., 1992. Ratcheting in cyclic plasticity, part ii: Multiaxial behavior. International Journal of Plasticity 8, 117-146.

Hayakawa, K., Murakami, S., 1997. Thermodynamical modeling of elastic-plastic damage and experimental validation of damage potential. International Journal of Damage Mechanics 6, 333-363.

Henriksen, M., 1984. Nonlinear viscoelastic stress analysis. A finite element approach. Computers & Structures 18, 133-139.

Houlsby, G.T., 1981. A study of plasticity theories and their application to soils. Ph.D. Thesis, University of Cambridge.

Houlsby, G.T., 1982. A derivation of the small-strain incremental theory of plasticity from thermodynamics. Proceedings of International Union of Theoretical and Applied Mechanics Conference on Deformation and Failure of Granular Materials, Delft, 109-118.

Hua, J., 2000. Finite element modeling and analysis of accelerated pavement testing devices and rutting phenomenon. Dissertation. Purdue University, West Lafayette, IN.

Hua, J., White, T., 2002. Study of nonlinear tire contact pressure effects on HMA rutting. International Journal of Geomechanics, ASCE 2, 353–376.

Huang, B., Mohammad, L., Wathugala, W., 2002. Development of a thermoviscoplastic model for HMA mixtures. Journal of the Association of Asphalt Paving Technologists 71, 594-618.

Huang, B., Mohammad, L.N., Rasoulian, M., 2001. Threedimensional numerical simulation of asphalt pavement at Louisiana accelerated loading facility Transportation Research Board, Washington, D.C. 1764, 44-58.

Huang, C.W., 2008. Development and numerical implementation of nonlinear viscoelastic-viscoplastic model for asphalt materials. Ph.D. Dissertation, Texas A&M University.

Huang, C.W., Abu Al-Rub, R.K., Masad, E., Little, D., 2011a. Three dimensional simulations of asphalt pavement performance using a nonlinear viscoelastic-viscoplastic model. ASCE Journal of Materials in Civil Engineering 23, 56-68.

Huang, C.W., Darabi, M.K., Masad, E., Abu Al-Rub, R.K., Little, D., 2011b. Development, characterization and validation of the nonlinear viscoelastic and viscoplastic model of asphalt mixtures. Unpublished paper, Texas A&M University, College Station, TX.

Huang, C.W., Masad, E., Muliana, A.H., Bahia, H., 2007. Nonlinearly viscoelastic analysis of asphalt mixes subjected to shear loading. Mechanics of Time-Dependent Materials 11, 91-110.

Huang, H., 1995. Analysis of accelerated pavement tests and finite element modeling of rutting phenomenon. Ph.D. Dissertation, Purdue University, West Lafayette, IN.

Hunter, A.E., Airey, G.D., Harireche, O., 2007. Numerical modeling of asphalt mixture wheel tracking experiments. International Journal of Pavement Engineering and Asphalt Technology 8, 52-71.

Ingram, J.D., Cemal Eringen, A., 1967. A continuum theory of chemically reacting media--ii constitutive equations of reacting fluid mixtures. International Journal of Engineering Science 5, 289-322.

Jacobsen, S., Marchand, J., Boisvert, L., 1996. Effect of cracking and healing on chloride transport in opc concrete. Cement and Concrete Research 26, 869-881.

Kachanov, L.M., 1958. On time to rupture in creep conditions (in russian). Izviestia Akademii Nauk SSSR, Otdelenie Tekhnicheskikh Nauk 8, 26-31.

Kachanov, L.M., 1986. Introduction to continuum damage mechanics. M. Nijhoff, Dordrecht , Boston, MA.

Karsan, I.D., Jirsa, J.O., 1969. Behavior of concrete under compressive loadings. ASCE Journal of the Structural Division 95, 2543-2563.

Kattan, P.I., Voyiadjis, G.Z., 1993. A plasticity-damage theory for large deformation of solids -ii. Applications to finite simple shear. International Journal of Engineering Science 31, 183-199.

Kessler, M.R., 2007. Self-healing: A new paradigm in materials design. Proceedings of the Institution of Mechanical Engineers Part G-Journal of Aerospace Engineering 221, 479-495.

Kessler, M.R., White, S.R., 2001. Self-activated healing of delamination damage in woven composites. Composites Part a-Applied Science and Manufacturing 32, 683-699.

Kettil, P., Lenhof, B., Runesson, K., Wiberg, N.E., 2007. Simulation of inelastic deformation in road structures due to cyclic mechanical and thermal loads. Computers & Structures 85, 59-70.

Kim, B., Roque, R., 2006. Evaluation of healing property of asphalt mixture. Transportation Research Board, Washington, D.C. 1970, 84-91.

Kim, Y.R., Allen, D.H., Little, D.N., 2007. Computational constitutive model for predicting nonlinear viscoelastic damage and fracture failure of asphalt concrete mixtures. International Journal of Geomechanics 7, 102-110.

Kim, Y.R., Guddati, M.N., Underwood, B.S., Yun, T.Y., Subramanian, V., Heidari, A.H., 2005. Characterization of ALF mixtures using the viscoelastoplastic continuum damage model. Final report, Feheral Highway Administration. Washington, DC.

Kim, Y.R., Guddati, M.N., Underwood, B.S., Yun, T.Y., Subramanian, V., Savadatti, S., Thirunavukkarasu, S., 2008. Development of a multiaxia viscoelastoplastic continuum damage model. Final report, DTFH61-05-RA-00108 Project.

Kim, Y.R., Little, D.N., 1989. Evaluation of healing in asphalt concrete by means of the theory of nonlinear viscoelasticity. Transportation Research Board, Washington, D.C. 1228, 198-210.

Kim, Y.R., Little, D.N., 1990. One-dimensional constitutive modeling of asphalt concrete. Journal of Engineering Mechanics (ASCE) 116, 751-772.

Kim, Y.R., Whitmoyer, S.L., Little, D.N., 1994. Healing in asphalt concrete pavements: Is it real? Transportation Research Board, Washington, D.C. 1454, 89-96.

Koneru, S., Masad, E., Rajagopal, K.R., 2008. A thermomechanical framework for modeling the compaction of asphalt mixes. Mechanics of Materials 40, 846-864.

Kose, S., Guler, M., Bahia, H.U., Masad, E., 2000. Distribution of strains within hot-mix asphalt binders : Applying imaging and finite-element techniques. Asphalt Binders 1728, 21-27.

Krajcinovic, D., 1996. Damage mechanics. Elsevier, Amsterdam.

Kringos, N., Drescher, A., Scarpas, T., 2010. On the behavior of a parallel elasto-visco-plastic model for asphaltic materials. Mechanics of Materials 42, 109-117.

Kringos, N., Scarpas, A., Kasbergen, C., 2007. Three- dimensional elastovisco-plastic finite element model for combined physical–mechanical moisture induced damage in asphaltic mixtures. Journal Association Asphalt Paving Technologists 76, 495-524.

Krishnan, J.M., Rajagopal, K.R., 2003. Review of the uses and modeling of bitumen from ancient to modern times. Applied Mechanics Reviews 56, 149-214.

Krishnan, J.M., Rajagopal, K.R., 2004. Thermodynamic framework for the constitutive modeling of asphalt concrete: Theory and applications. Journal of Materials in Civil Engineering (ASCE) 16, 155-166.

Krishnan, J.M., Rajagopal, K.R., 2005. On the mechanical behavior of asphalt. Mechanics of Materials 37, 1085-1100.

Krishnan, J.M., Rao, C.L., 2000. Mechanics of air voids reduction of asphalt concrete using mixture theory. International Journal of Engineering Science 38, 1331-1354.

Lai, J.J., Bakker, A., 1996. 3-d schapery representation for non-linear viscoelasticity and finite element implementation. Computational Mechanics 18, 182-191.

Lasry, D., Belytschko, T., 1988. Localization limiters in transient problems. International Journal of Solids and Structures 24, 581-597.

Lee, C., Cozzarelli, F.A., Burke, K., 1986. One-dimensional strain-dependent creep damage in inhomogeneous materials. International Journal of Non-Linear Mechanics 21, 303-314.

Lee, H., Peng, K., Wang, J., 1985. An anisotropic damage criterion for deformation instability and its application to forming limit analysis of metal plates. Engineering Fracture Mechanics 21, 1031-1054.

Lee, H.J., Daniel, J.S., Kim, Y.R., 2000. Continuum damage mechanics-based fatigue model of asphalt concrete. Journal of Materials in Civil Engineering (ASCE) 12, 105-112.

Lee, H.J., Kim, Y.R., 1998. Viscoelastic continuum damage model of asphalt concrete with healing. Journal of Engineering Mechanics (ASCE) 124, 1224-1232.

Lee, J.H., Fenves, G.L., 1998. Plastic-damage model for cyclic loading of concrete structures. Journal of Engineering Mechanics (ASCE) 124, 892-900.

Lele, S.P., Anand, L., 2009. A large-deformation strain-gradient theory for isotropic viscoplastic materials. International Journal of Plasticity 25, 420-453.

Lemaître, J., 1992. A course on damage mechanics. Springer-Verlag, New York.

Lemaître, J., 1996. A course on damage mechanics, 2nd ed. Springer, New York.

Lemaître, J., 2002. Continuum damage mechanics of materials and structures - introduction to continuum damage mechanics. Continuum Damage Mechanics of Materials and Structures, 235-258.

Lemaître, J., Chaboche, J.-L., 1990. Mechanics of solid materials. Cambridge University Press, , Cambridge, UK.

Lemaître, J., Desmorat, R., 2005. Engineering damage mechanics: Ductile, creep, fatigue and brittle failures. Springer, New York.

Lemaître, J., Desmorat, R., Sauzay, M., 2000. Anisotropic damage law of evolution. European Journal of Mechanics a-Solids 19, 187-208.

Levesque, M., Derrien, K., Baptiste, D., Gilchrist, M.D., 2008. On the development and parameter identification of schapery-type constitutive theories. Mechanics of Time-Dependent Materials 12, 95-127.

Levesque, M., Derrien, K., Mishnaevsky, L., Baptiste, D., Gilchrist, M.D., 2004. A micromechanical model for nonlinear viscoelastic particle reinforced polymeric composite materials - undamaged state. Composites Part a-Applied Science and Manufacturing 35, 905-913.

Little, D.N., Bhasin, A., 2007. Exploring mechanisms of healing in asphalt mixtures and quantifying its impact. In: van der Zwaag, S. (Ed.). Self healing materials. Springer, Dordrecht, The Netherlands, 205-218.

Lu, Y., Wright, P.J., 1998. Numerical approach of visco-elastoplastic analysis for asphalt mixtures. Computers & Structures 69, 139-147.

Lubarda, V.A., Krajcinovic, D., 1995. Some fundamental issues in rate theory of damage-elastoplasticity. International Journal of Plasticity 11, 763-797.

Lubliner, J., 1990. Plasticity theory. Collier Macmillan, New York.

Lubliner, J., 2008. Plasticity theory. Dover Publications, Mineola, New York.

Lytton, R.L., Uzan, J., Fernando, E.G., Roque, R., Hiltunen, D.R., Stoffels, S.M., 1993. Development and validation of performance prediction models and specifications for asphalt binders and paving mixes. SHRP-A-357, Strategic Highway Research Program, National Research Council, Washington D.C.

Malvern, L.E., 1951. The propagation of longitudinal waves of plastic deformation in a bar of material exhibiting a strain-rate effect. Journal of Applied Mechanics, ASME 18, 203-208.

Masad, E., Dessouky, S., Little, D., 2007. Development of an elastoviscoplastic microstructural-based continuum model to predict permanent deformation in hot mix asphalt. International Journal of Geomechanics 7, 119-130.

Masad, E., Huang, C.W., Airey, G., Muliana, A., 2008. Nonlinear viscoelastic analysis of unaged and aged asphalt binders. Construction and Building Materials 22, 2170-2179.

Masad, E., Huang, C.W., DAngelo, J., Little, D., 2009. Characterization of asphalt binder resistance to permanent deformation based on nonlinear viscoelastic analysis of multiple stress creep recovery (mscr) test. Journal of the Association of Asphalt Paving Technologists (AAPT) 78, 471–501.

Masad, E., Somadevan, N., 2002. Microstructural finite-element analysis of influence of localized strain distribution on asphalt mix properties. Journal of Engineering Mechanics (ASCE) 128, 1105-1114.

Masad, E., Tashman, L., Little, D., Zbib, H., 2005. Viscoplastic modeling of asphalt mixes with the effects of anisotropy, damage and aggregate characteristics. Mechanics of Materials 37, 1242-1256.

Miao, S., Wang, M.L., Schreyer, H.L., 1995. Constitutive models for healing of materials with application to compaction of crushed rock-salt. Journal of Engineering Mechanics (ASCE) 121, 1122-1129.

Mirmiran, A., Zagers, K., Yuan, W., 2000. Nonlinear finite element modeling of concrete confined by fiber composites. Finite Elements in Analysis and Design 35, 79-96.

Modaressi, H., Laloui, L., Aubry, D., 1994. Thermodynamical approach for camclay-family models with roscoe-type dilatancy rules. International Journal of Numerical and Analytical Methods in Geomechanics 18, 133-138.

Mühlhaus, H.B., 1995. Continuum models for materials with microstructure. Wiley, New York.

Mühlhaus, H.B., Aifantis, E.C., 1991. A variational principle for gradient plasticity. International Journal of Solids and Structures 28, 845-857.

Muliana, A.H., Haj-Ali, R., 2008. A multi-scale framework for layered composites with thermo-rheologically complex behaviors. International Journal of Solids and Structures 45, 2937-2963.

Murakami, S., Hayakawa, K., Liu, Y., 1998. Damage evolution and damage surface of elastic-plastic-damage materials under multiaxial loading. International Journal of Damage Mechanics 7, 103-128.

Murakami, S., Ohno, N., 1982. A constitutive equation of creep based on the concept of a creep-hardening surface. International Journal of Solids and Structures 18, 597-609.

Nedjar, B., 2001. Elastoplastic-damage modeling including the gradient of damage: Formulation and computational aspects. International Journal of Solids and Structures 38, 5421–5451.

Oda, M., Nakayama, H., 1989. Yield function for soil with anisotropic fabric. Journal of Engineering Mechanics (ASCE) 115, 89-104.

Odqvist, F.K.G., Hult, J., 1961. Some aspects of creep rupture. Arkiv For Det Fysiske 19, 379-382.

Ohno, N., 1982. A constitutive model of cyclic plasticity with a nonhardening strain region. Journal of Applied Mechanics, ASME 49, 721-726.

Ortiz, M., 1985. A constitutive theory for the inelastic behavior of concrete. Mechanics of Materials 4, 67-93.

Palermo, D., Vecchio, F.J., 2004. Compression field modeling of reinforced concrete subjected to reversed loading: Verification. ACI Structural Journal 101, 155-164.

Pamin, J., 1994. Gradient-dependent plasticity in numerical simulation of localization phenomena. Dissertation, Delft University of Technology, The Netherlands.

Park, D.W., Epps Martin, A., Masad, E.A., 2005. Effects of nonuniform tire contact stresses on pavement response. Journal of Transportation Engineering, ASCE, 873–879.

Park, S.W., Kim, Y.R., Schapery, R.A., 1996. A viscoelastic continuum damage model and its application to uniaxial behavior of asphalt concrete. Mechanics of Materials 24, 241-255.

Peerlings, R.H.J., deBorst, R., Brekelmans, W.A.M., deVree, J.H.P., 1996. Gradient enhanced damage for quasi-brittle materials. International Journal for Numerical Methods in Engineering 39, 3391-3403.

Perl, M., Uzan, J., Sides, A., 1983. Visco-elasto-plastic constitutive law for a bituminous mixture under repeated loading. Transportation Research Board, Washington, D.C., 20-27.

Perzyna, P., 1963. The constitutive equations for rate-sensitive materials. Quarterly of Applied Mathematics 20, 321-332.

Perzyna, P., 1971. Thermodynamic theory of viscoplastcity. Advances in Applied Mechanics 11, 313-354.

Perzyna, P., 1986. Internal state variable description of dynamic fracture of ductile solids. International Journal of Solids and Structures 22, 797-818.

Perzyna, P., Korbel, K., 1998. Analysis of the influence of various effects on criteria for adiabatic shear band localization in single crystals. Acta Mechanica 129, 31-62.

Pestana, J.M., Whittle, A.J., 1999. Formulation of a unified constitutive model for clays and sands. International Journal for Numerical and Analytical Methods in Geomechanics 23, 1215-1243.

Pijaudiercabot, G., Bazant, Z.P., 1987. Nonlocal damage theory. Journal of Engineering Mechanics (ASCE) 113, 1512-1533.

Prager, S., Tirrell, M., 1981. The healing-process at polymer-polymer interfaces. Journal of Chemical Physics 75, 5194-5198.

Prager, W., 1956. A new method of analyzing stresses and strains in work-hardening plastic solids. Journal of Applied Mechanics, ASME 23, 493-496.

Rabotnov, I.U.N., 1969. Creep problems in structural members. North-Holland Pub. Co., Amsterdam, London,.

Rajagopal, K.R., 1995. Multiple configurations in continuum mechanics. Report, Institute for Computational and Applied Mechanics, University of Pittsburgh.

Rajagopal, K.R., Tao, L., 1996. Mechanisc of mixtures. World Scientific, Singapore.

Rajagopal, K.R., Wineman, A.S., 1992. A constitutive equation for nonlinear solids which undergo deformation induced microstructural changes. International Journal of Plasticity 8, 385-395.

Ramaswamy, S., Aravas, N., 1998a. Finite element implementation of gradient plasticity models - part i: Gradient-dependent yield functions. Computer Methods in Applied Mechanics and Engineering 163, 11-32.

Ramaswamy, S., Aravas, N., 1998b. Finite element implementation of gradient plasticity models - part ii: Gradient-dependent evolution equations. Computer Methods in Applied Mechanics and Engineering 163, 33-53.

Ramm, W., Biscoping, M., 1998. Autogenous healing and reinforcement corrosion of water-penetrated separation cracks in reinforced concrete. Nuclear Engineering and Design 179, 191-200.

Ravindran, P., Krishnan, J.M., Masad, E., Rajagopal, K.R., 2009. Modelling sand–asphalt mixtures within a thermodynamic framework: Theory and application to torsion experiments. International Journal of Pavement Engineering 10, 115-131.

Reinhardt, H.W., Jooss, M., 2003. Permeability and self-healing of cracked concrete as a function of temperature and crack width. Cement and Concrete Research 33, 981-985.

Rice, J.R., 1971. Inelastic constitutive relations for solids: An internal-variable theory and its application to metal plasticity. Journal of the Mechanics and Physics of Solids 19, 433-455.

Rodeo, S.A., Arnoczky, S.P., Torzilli, P.A., Hidaka, C., Warren, R.F., 1993. Tendon-healing in a bone tunnel: A biomechanical and histological study in the dog. Journal of Bone and Joint Surgery-American 75A, 1795-1803.

Rong, M.Z., Zhang, M.Q., Zhang, W., 2007. A novel self-healing epoxy system with microencapsulated epoxy and imidazole curing agent. Advanced Composites Letters 16, 167-172.

Saadeh, S., Masad, E., 2010. On the relationship of microstructure properties of asphalt mixtures to their constitutive behavior. International Journal of Materials and Structural Integrity 4, 186-214.

Saadeh, S., Masad, E., Little, D., 2007. Characterization of hot mix asphalt using anisotropic damage viscoelastic-viscoplastic model and repeated loading. ASCE Journal of Materials in Civil Engineering 19, 912-924.

Saal, R.N.J., Labout, J.W.A., 1940. Rheological properties of asphaltic bitumens. The Journal of Physical Chemistry 44, 149-165.

Sadd, M.H., Dai, Q.L., Parameswaran, V., Shukla, A., 2003. Simulation of asphalt materials using finite element micromechanical model with damage mechanics. Bituminous Paving Mixtures 1832, 86-95.

Sadkin, Y., Aboudi, J., 1989. Viscoelastic behavior of thermo-rheologically complex resin matrix composites. Composites Science and Technology 36, 351-365.

Saleeb, A., Liang, R.Y., A., Q.H., Powers, D., 2005. Numerical simulation techniques for HMA rutting under loaded wheel tester. International Journal of Pavement Engineering 6, 57-66.

Scarpas, 2004. A mechanics based computational platform for pavement engineering. Master of Science, University of Canterbury, New Zealand.

Schapery, R.A., 1964. Application of thermodynamics to thermomechanical fracture birefringent phenomena in viscoelastic media. Journal of Applied Physics 35, 1451-1465.

Schapery, R.A., 1966. A theory of non-linear thermo-viscoelasticity based on irreversible thermodynamics. Proceedings of the Fifth U.S. National Congress of Applied Mechanics 5, 511-530.

Schapery, R.A., 1969a. Further development of a thermodynamic constitutive theory: Stress formulation. Purdue University, Purdue Resarch Foundation, Lafayette, IN.

Schapery, R.A., 1969b. On the characterization of nonlinear viscoelastic materials. Polymer Engineering & Science 9, 295-310.

Schapery, R.A., 1975a. Theory of crack initiation and growth in viscoelastic media .1. Theoretical development. International Journal of Fracture 11, 141-159.

Schapery, R.A., 1975b. Theory of crack initiation and growth in viscoelastic media .2. Approximate methods of analysis. International Journal of Fracture 11, 369-388.

Schapery, R.A., 1975c. Theory of crack initiation and growth in viscoelastic media .3. Analysis of continuous growth. International Journal of Fracture 11, 549-562.

Schapery, R.A., 1984. Correspondence principles and a generalized j integral for large deformation and fracture-analysis of viscoelastic media. International Journal of Fracture 25, 195-223.

Schapery, R.A., 1987. Deformation and fracture characterization of inelastic composite-materials using potentials. Polymer Engineering and Science 27, 63-76.

Schapery, R.A., 1989. On the mechanics of crack closing and bonding in linear viscoelastic media. International Journal of Fracture 39, 163-189.

Schapery, R.A., 1990. A theory of mechanical-behavior of elastic media with growing damage and other changes in structure. Journal of the Mechanics and Physics of Solids 38, 215-253.

Schapery, R.A., 1999. Nonlinear viscoelastic and viscoplastic constitutive equations with growing damage. International Journal of Fracture 97, 33-66.

Schwartz, C.W., Gibson, N., Schapery, R.A., 2002. Time-temperature superposition for asphalt concrete at large compressive strains. Transportation Research Board, Washington, D.C. 1789, 101-112.

Seibi, A.C., Sharma, M.G., Ali, G.A., Kenis, W.J., 2001. Constitutive relations for asphalt concrete under high rates of loading. Asphalt Mixtures, 111-119.

Shen, S., Airey, G.D., Carpenter, S.H., Huang, H., 2006. A dissipated energy approach to fatigue evaluation. International Journal of Materials and Pavement Design 7, 47-69.

Shen, S., Carpenter, S.H., 2005. Application of dissipated energy concept in fatigue endurance limit testing. Transportation Research Board, Washington, D.C. 1929, 165-173.

Shizawa, K., Zbib, H.M., 1999. A thermodynamical theory of gradient elastoplasticity with dislocation density tensor. I: Fundamentals. International Journal of Plasticity 15, 899-938.

Si, Z., Little, D.N., Lytton, R.L., 2002. Characterization of microdamage and healing of asphalt concrete mixtures. Journal of Materials in Civil Engineering (ASCE) 14, 461-470.

Sides, A., Uzan, J., Perl, M., 1985. A comprehensive viscoelasto-plastic characterization of sand-asphalt compressive and tensile cyclic loading. Journal of Testing and Evaluation 13, 49-59.

Sima, J.F., Roca, P., Molins, C., 2008. Cyclic constitutive model for concrete. Engineering Structures 30, 695-706.

Simo, J.C., 1987. On a fully three-dimensional finite-strain viscoelastic damage model: Formulation and computational aspects. Computer Methods in Applied Mechanics and Engineering 60, 153-173.

Simo, J.C., 1998. Numerical analysis and simulation of plasticity. In: Ciarlet, P.G., Lions, J.L. (Eds.), Handbook of numerical analysis, Vol. 6. Elsevier, Amsterdam, pp. 183-499.

Simo, J.C., Hughes, T.J.R., 1998. Computational inelasticity. Springer, New York.

Sinha, B.P., Gerstle, K.H., Tulin, L.G., 1964. Stress–strain relations for concrete under cyclic loading. ACI Journal Proceedings 61, 195–212.

Sousa, J.B., Weissman, S., 1994. Modeling permanent deformation of asphalt concrete mixtures. Journal of the Association of Asphalt Paving Technologists (AAPT) 63, 224-257.

Sousa, J.B., Weissman, S., Sackman, J., Monismith, C.L., 1993. Nonlinear elastic viscous with damage model to predict permanent deformation of asphalt concrete mixtures. Transportation Research Board, Washington, D.C. 1384, 80-93.

Srinivasa, A.R., 2010. Application of the maximum rate of dissipation criterion to dilatant, pressure dependent plasticity models. International Journal of Engineering Science 48, 1590-1603.

Strauer, B.E., Brehm, M., Zeus, T., Kostering, M., Hernandez, A., Sorg, R.V., Kogler, G., Wernet, P., 2002. Repair of infarcted myocardium by autologous intracoronary mononuclear bone marrow cell transplantation in humans. Circulation 106, 1913-1918.

Sullivan, R.W., 2008. Development of a viscoelastic continuum damage model for cyclic loading. Mechanics of Time-Dependent Materials 12, 329-342.

Tan, S.A., Low, B.H., Fwa, T.F., 1994. Behavior of asphalt concrete mixtures in triaxial compression. Journal of Testing and Evaluation 22, 195-203.

Tao, L., Humphrey, J.D., Rajagopal, K.R., 2001. A mixture theory for heat-induced alterations in hydration and mechanical properties in soft tissues. International Journal of Engineering Science 39, 1535-1556.

Tashman, L., 2003. Microstructure viscoplastic continuum model for permanent deformation in asphalt pavements. Ph.D. Dissertation, Texas A&M University.

Tashman, L., Masad, E., Little, D., Zbib, H., 2005. A microstructure-based viscoplastic model for asphalt concrete. International Journal of Plasticity 21, 1659-1685.

Touati, D., Cederbaum, G., 1998. Postbuckling of non-linear viscoelastic imperfect laminated plates part i: Material considerations. Composite Structures 42, 33-41.

Truesdell, C., 1969. Rational thermodynamics. McGraw-Hill, New York.

Underwood, B.S., Kim, Y.R., Guddati, M., 2006. Characterization and performance prediction of ALF mixtures using a viscoelastoplastic continuum damage model. Journal of the Association of Asphalt Paving Technologists (AAPT) 75, 577-636.

Uzan, J., 2005. Viscoelastic-viscoplastic model with damage for asphalt concrete. Journal of Materials in Civil Engineering (ASCE) 17, 528-534.

Voyadjis, G.Z., Abu Al-Rub, R.K., 2006. A finite strain plastic-damage model for high velocity impacts using combined viscosity and gradient localization limiters: Part ii - numerical aspects and simulations. International Journal of Damage Mechanics 15, 335-373.

Voyiadjis, G.Z., Abed, F.H., 2006. A coupled temperature and strain rate dependent yield function for dynamic deformations of bcc metals. International Journal of Plasticity 22, 1398-1431.

Voyiadjis, G.Z., Abu Al-Rub, R.K., 2003. Thermodynamic based model for the evolution equation of the backstress in cyclic plasticity. International Journal of Plasticity 19, 2121-2147.

Voyiadjis, G.Z., Abu Al-Rub, R.K., 2005. Gradient plasticity theory with a variable length scale parameter. International Journal of Solids and Structures 42, 3998-4029.

Voyiadjis, G.Z., Abu Al-Rub, R.K., 2007. Nonlocal gradient-dependent thermodynamics for modeling scale-dependent plasticity. International Journal for Multiscale Computational Engineering 5, 295-323.

Voyiadjis, G.Z., Abu Al-Rub, R.K., Palazotto, A.N., 2004. Thermodynamic framework for coupling of non-local viscoplasticity and non-local anisotropic viscodamage for

dynamic localization problems using gradient theory. International Journal of Plasticity 20, 981-1038.

Voyiadjis, G.Z., Deliktas, B., 2000. A coupled anisotropic damage model for the inelastic response of composite materials. Computer Methods in Applied Mechanics and Engineering 183, 159-199.

Voyiadjis, G.Z., Deliktas, B., 2009. Mechanics of strain gradient plasticity with particular reference to decomposition of the state variables into energetic and dissipative components. International Journal of Engineering Science 47, 1405-1423.

Voyiadjis, G.Z., Deliktas, B., Aifantis, E.C., 2001. Multiscale analysis of multiple damage mechanics coupled with inelastic behavior of composite materials. ASCE Journal of Engineering Mechanics 127, 636-645.

Voyiadjis, G.Z., Kattan, P.I., 1990. A coupled theory of damage mechanics and finite strain elasto-plasticity--ii. Damage and finite strain plasticity. International Journal of Engineering Science 28, 505-524.

Voyiadjis, G.Z., Kattan, P.I., 1992. A plasticity-damage theory for large deformation of solids .1. Theoretical formulation. International Journal of Engineering Science 30, 1089-1108.

Voyiadjis, G.Z., Kattan, P.I., 1993. Damage of fiber-reinforced composite-materials with micromechanical characterization. International Journal of Solids and Structures 30, 2757-2778.

Voyiadjis, G.Z., Kattan, P.I., 1999. Advances in damage mechanics: Metals and metals matrix composites. Elsevier, Oxford.

Voyiadjis, G.Z., Park, T., 1999. The kinematics of damage for finite-strain elasto-plastic solids. International Journal of Engineering Science 37, 803-830.

Voyiadjis, G.Z., Shojaei, A., Li, G., 2011. A thermodynamic consistent damage and healing model for self healing materials. International Journal of Plasticity 27, 1025-1044.

Voyiadjis, G.Z., Thiagarajan, G., 1997. Micro and macro anisotropic cyclic damage-plasticity models for mmcs. International Journal of Engineering Science 35, 467-484.

Wang, L., Wang, X., Mohammad, L., Wang, Y., 2004. Application of mixture theory in the evaluation of mechanical properties of asphalt concrete. Journal of Engineering Mechanics (ASCE) 16, 167-174.

Wang, W.M., Sluys, L.J., deBorst, R., 1997. Viscoplasticity for instabilities due to strain softening and strain-rate softening. International Journal for Numerical Methods in Engineering 40, 3839-3864.

Weitsman, Y., 1988. A continuum damage model for viscoelastic materials. Journal of Applied Mechanics, ASME 55, 773-780.

Werner, S., Grose, R., 2003. Regulation of wound healing by growth factors and cytokines. Physiological Reviews 83, 835-870.

White, S.R., Caruso, M.M., Moore, J.S., 2008. Autonomic healing of polymers. Mrs Bulletin 33, 766-769.

White, S.R., Sottos, N.R., Geubelle, P.H., Moore, J.S., Kessler, M.R., Sriram, S.R., Brown, E.N., Viswanathan, S., 2001. Autonomic healing of polymer composites. Nature 409, 794-797.

Wool, R.P., Oconnor, K.M., 1981. A theory of crack healing in polymers. Journal of Applied Physics 52, 5953-5963.

Wu, J.Y., Li, J., Faria, R., 2006. An energy release rate-based plastic-damage model for concrete. International Journal of Solids and Structures 43, 583-612.

Yasko, A.W., Lane, J.M., Fellinger, E.J., Rosen, V., Wozney, J.M., Wang, E.A., 1992. The healing of segmental bone defects, induced by recombinant human bone morphogenetic protein (rhbmp-2): A radiographic, histological, and biomechanical study in rats. Journal of Bone and Joint Surgery-American 74A, 659-670.

Yin, T., Rong, M.Z., Zhang, M.Q., 2008. Self-healing of cracks in epoxy composites. Multi-Functional Materials and Structures 47-50, 282-285.

Yuan, Y.C., Yin, T., Rong, M.Z., Zhang, M.Q., 2008. Self healing in polymers and polymer composites. Concepts, realization and outlook: A review. Express Polymer Letters 2, 238-250.

Yum, T., Kim, Y.R., 2011. Modeling of viscoplastic rate-dependent hardening-softening behavior of hot mix asphalt in compression. Mechanics of Time-Dependent Materials 15, 89-103.

Zbib, H.M., Aifantis, E.C., 1992. On the gradient-dependent theory of plasticity and shear banding. Acta Mechanica 92, 209-225.

Zener, C., Hollomon, J.H., 1944. Effect of strain rate upon plastic flow of steel. Journal of Applied Physics 15, 22-32.

Zhang, Z., Roque, R., Birgisson, B., 2001a. Evaluation of laboratory-measured crack growth rate for asphalt mixtures. Transportation Research Board, Washington, D.C. 1767, 67-75.

Zhang, Z., Roque, R., Birgisson, B., Sangpetgnam, B., 2001b. Identification and verification of a suitable crack growth law for asphalt mixtures. Journal of the Association of Asphalt Paving Technologists (AAPT) 70, 206-241.

Ziegler, H., 1969. Zum plastischen potential in der bodenmechanik. Zeitschrift Fur Angewandte Mathematik Und Physik 20, 659-675.

Ziegler, H., 1977. An introduction to thermodynamics. North-Holland Pub. Co., Amesterdam.

Ziegler, H., 1983. An introduction to thermomechanics, 2nd edn. North-Holland Pub. Co., Amesterdam.

Ziegler, H., Wehrli, C., 1987. The derivation of constitutive relations from the free energy and the dissipation function. In: Theodore, Y.W., John, W.H. (Eds.), Advances in Applied Mechanics, Elsevier, Amsterdam, pp. 183-238.

Zienkiewicz, O.C., Humpheson, C., Lewis, R.W., 1975. Associated and non-associated visco-plasticity and plasticity in soil mechanics. Geotechnique 25, 671-689.

Zolochevsky, A., Voyiadjis, G.Z., 2005. Theory of creep deformation with kinematic hardening for materials with different properties in tension and compression. International Journal of Plasticity 21, 435-462.

VITA

Masoud Darabi Konartakhteh was born in Shiraz, Iran. He received his Bachelor of Science in Civil Engineering from Sharif University of Technology in August 2002. He entered the graduate school at Sharif University of Technology and received his Master of Science in the area of Mechanics of Structures and Materials Engineering under the guidance of Professor Hossein M. Shodja in May 2005. Afterwards, he worked with the Alisaz Company, a construction company, from 2005-2008 as a field engineer, and later as an engineering manager, where he was involved in construction of heavy concrete structures such as cement plants and water intakes. He left the Alisaz Company in 2008 to begin his doctoral studies at Texas A&M University under the supervision of Dr. Rashid K. Abu Al-Rub and Dr. Eyad Masad. Two years and nine months later he completed the research presented in this dissertation in the area of Materials and he received his Ph.D. in August 2011 from the Department of Civil and Environmental Engineering at Texas A&M University. Masoud has been involved in research projects in several areas, such as computational mechanics, advanced constitutive modeling, mechanics of materials, damage-healing mechanics, and effect of environmental conditions on mechanical response of materials. He has nearly 15 publications published in several prestigious journals and conference proceedings in the field of computational mechanics and materials. He has also participated in over 6 world and national conferences. His future plans involve continued research on computational mechanics and mechanics of materials, which he finds fascinating.

Department of Civil Engineering

Texas A&M University

3136 TAMU

College Station, TX, 77843-3136